School of Earth and Planetary Sciences

Proterozoic crustal evolution of NE Australia during the supercontinent Nuna Assembly: new insights from a coupled thermochronological and geophysical study

Jiangyu Li

This thesis is presented for the Degree of
Doctor of Philosophy
of
Curtin University

May 2021

DECLARATION

To the best of my knowledge and belief, this thesis contains no material previously published by any other person except where due acknowledgement has been made. This thesis contains no material which has been accepted for the award of any other degree or diploma in any university.

The author acknowledges that the copyright of published works contained within this thesis resides with the copyright holder(s) of those works. I warrant that I have obtained, where necessary, permission from the copyright owners to use any third-party copyright material reproduced in the thesis (e.g., questionnaires, unpublished letters), or to use any of my own published work (e.g., journal articles) in which the copyright is held by another party (e.g., publisher, co-author).

Signature: Jiangyu Li May 19^{th}, 2021

Jiangyu Li Date

ABSTRACT

While it is generally accepted that NE Australia collided with NW Laurentia during the final assembly of the supercontinent Nuna at ca. 1.6 Ga through the Isan Orogeny, uncertainties remain on clear recognition of allochthonous terranes in the orogen, the delineation of crustal boundaries, detailed syn- to post-orogenic tectonic processes, and the overall crustal architecture of the orogen. To quantitatively investigate the spatial and temporal crustal evolution of NE Australia during the assembly of the supercontinent Nuna, high-precision $^{40}Ar/^{39}Ar$ thermochronological data were acquired along an E-W transect across the Proterozoic Mount Isa and Georgetown inliers in NE Australia. This is to examine the cooling history, which, when combined with known metamorphic P-T paths and other pressure estimates, to infer timing and magnitude of syn- to post-orogenic exhumation. Aeromagnetic and gravity analyses, along with a reinterpretation of seismic profiles, were also conducted to explore the crustal architecture and orogenic evolution through integration with the surface geology, published isotopic data, and the new thermo-geochronological results.

In the filtered aeromagnetic and gravity grid, a N-S trending, steep anomaly gradient was revealed on the eastern margin of the Mount Isa Inlier, coincident with the Gidyea Fault (others refer to as the Gidyea Suture Zone) previously recognized from the seismic reflection data. The N-S to NNE trending, deep-seated Pilgrim Fault is joined with the Gidyea Fault east of the Canobie Domain, and is inferred in this study to be a terrane boundary between the western-central belt and eastern belt of the Mount Isa Inlier. Between the Mount Isa and Georgetown inliers, a seismically identified, west-dipping, crustal dissecting fault (the Empress Suture Zone) is interpreted as a suture zone with additional smaller-scale thrusts antithetic to the main structure. The presence of duplexed crustal architecture between the Mount Isa and Georgetown inliers indicates crustal thickening occurred along the Empress Suture Zone, and is interpreted to be associated with the westward docking of the Georgetown Inlier. Compiled Nd isotopic data shows that the Georgetown Inlier shared the same isotopic characteristics post ca. 1.56 Ga, indicating the unification of the Georgetown Inlier with the North Australian Craton after the assembly of the supercontinent Nuna.

Newly acquired $^{40}Ar/^{39}Ar$ thermochronological results provide constraints on the syn- to post-orogenic thermal history of NE Australia following the assembly of Nuna. In the Mount Isa Inlier, where intense crustal imbrication occurred during the Proterozoic continental collision, the central, and eastern belts cooled heterogeneously through ~525–330 °C, primarily between 1.53 and 1.48 Ga, whereas the western belt did not cool to muscovite closure temperature (~425 °C) until ca. 1.40 Ga. Contrasting cooling history across post-metamorphic fault zones record the reactivation of inherited normal (i.e., early basinal) and reverse (i.e., orogenic) faults. Estimated exhumation rates are generally low (<~0.5 mm yr-1), consistent with modest local relief of <~1000 m, which is comparable to modern analogs, and suggests a 'soft' collision during the continental assembly with limited crustal thickening. Exhumation and cooling in the eastern belt were contemporaneous with felsic magmatism (1.55–1.48 Ga). Limited exhumation compare to distinguishable cooling rate variation suggests that the region may have maintained an elevated thermal gradient during that time due to widespread magmatism intrusions. Magmatism transitioning from trondhjemitic to A-type granitoids over this period suggests progressive heating of the source region, and is ascribed to lower crust delamination in this study. The heterogeneous exhumation of the Mount Isa Inlier was interpreted to reflect extensional faulting during orogenic collapse stage following the assembly of Nuna.

The Georgetown Inlier, 200 km to the east, was also applied with high-precision $^{40}Ar/^{39}Ar$ thermochronology to evaluate the regional orogenic evolution. Due to multiple Palaeozoic thermal impacts, only eight (out of 23) high-precision $^{40}Ar/^{39}Ar$ ages were resolved. These analyses show that cooling following the ca. 1.6 Ga crustal thickening/metamorphic event was diachronous across the region. The western and central belts cooled heterogeneously through ~525–330 °C, primarily between 1.54 and 1.50 Ga, whereas the eastern belt did not cool to hornblende closure temperature (~525 °C) until ca. 1.49 Ga. Contrasting cooling histories across post-metamorphic fault zones record the reactivation of orogenic reverse faults. Restricted to the Croydon domain, rapid cooling occurred during ca. 1.548–1.536 Ga with an estimated minimal cooling rate of $8.1^{+6.6}_{-3.9}$ °C/Ma, which is interpreted to represent magmatism-related cooling. This event is accompanied by an episode of crustal melting and a slow cooling ($0.7^{+1.2}_{-0.7}$ °C/Ma) in the little-metamorphosed western domain. Cooling behaviours across the Mount Isa and Georgetown inliers reveal that, the widespread ca. 1.5 Ga post-orogenic regional extension and cooling, accompanied by magmatism, occurred synchronously with a westward younging trend. This widespread crustal melting and differential exhumation event is interpreted to be due to the delamination of the orogenic root, occurred ca. 50 Myr after the final assembly of Nuna .

.

ACKNOWLEDGEMENTS

This research would not have been possible without the support of the following people:

- My supervisor Zheng-Xiang Li – thank you for your continuous support and words of encouragement throughout this long journey. Thank you for taking me as your student despite the little knowledge I had, and my lack of sufficient research training, at the time. Your consistent guidance and instructions have transformed me to who I am today. I am thankful for all the time and effort you made through the Ph.D. journey. Thank you for setting a good role model of a critically thinking scientist for me.
- My co-supervisor Amaury Pourteau – thank you for your continuous support and placing all your trust in me. You inspired me to find my personal values and life goals. When I was lost in this endeavour journey, you always guided me back gently. Thanks for every day you spent on me and offering everything you could give. It was really my luck to have you as my supervisor.
- My co-supervisor Fred Jourdan – thank you for all the effort you have put into guiding me along the path of $^{40}Ar/^{39}Ar$ geochronology. You showed me how a top argon specialist should be. You are a very close friend who always kept his door open to me. I am very proud to be your student.
- My colleagues Adam, Silvia – Thanks for tolerating my immature and naive behaviour when I gradually started my research. Thanks for being patient with me and taught me sedimentology and metamorphic petrology during the Queensland field seasons. Thanks for being a big brother and sister and looking after me.
- Collaborative researchers and academia friends Bill Collins, Hugo Olierook, Chris Elder, Chris Spencer, Brendan Murphy – I have learned a lot from you guys through daily discussions. Your profound knowledge, clear logic, and good memory are the things that I admire most during my Ph.D. study.
- My colleagues Yebo, Chuan, Hammed, Dan, Luc, Josh, Lei – you have all invested way more time in me than you will ever get credit for. I am grateful for the accompany and support you have given me throughout the years.

- Thesis examiners: Prof. David Giles and Dr. Richard A. Spikings – Both examiners are thanked for their fair and thorough examination of the thesis, and for giving the many great feedbacks. I deeply appreciate your kindness and patience.
- Sponsors – I would like to thank the China Scholarship Council (CSC) and a joint Curtin International Postgraduate Research Scholarship (CIPRS) for providing me my Ph.D. stipend, and the Australian Research Council grant to Professor ZX Li (FL150100133) for covering my research costs. I thank the Institute for Geoscience Research (TIGeR) at Curtin University and ARC Centre of Excellence for Core to Crust Fluid Systems (CCFS) for providing conference travel support. I thank Schlumberger for their provision of Petrel E&P, and Sigma Zone for providing a student license of the Quantum XL program for making Monte Carlo simulations.
- Technical staff at Curtin University: Celia Mayers, Zdenka Martelli, Adam Frew, Andy Wieczorek, Brad McDonald – The time I spent picking grains, working in the lab, and sharing laughter with you will always remain some of my fondest memories of the past years.
- My friends Huan Li, Shiyong Zhao, Jiaxin He, Yurong Liu, Peter Chen, Nicole Zhang, Susu Zhang, Zixian Deng, Zefang Shen, and friends in the WA Fujian Association—Yours accompany through my Ph.D. journey has brought me a lot of joys and hope when times were tough.
- My ex-girlfriend Jenna – Thank you for your continuous understanding and support throughout half of my Ph.D. journey. The only thing I regretted is that I could have been nicer to you when we were together. You taught me how to grow up and let me become a better person. I sincerely wish you happiness and joyfulness whatever you do and wherever you are.
- My family – Thank you for giving me life and letting me experience this wonderful world. I will use the rest of my life to protect you.

List of Publications Included as Part of this Thesis

This thesis includes three research papers that are either published, in press or nearly ready for submission at the time of writing this document. The final chapter summarizes the three data papers and put them into a coherent synthesis. The research papers, conference presentations, and other relevant co-authored publications are given below.

Peer-reviewed journal articles:

Li, J., Pourteau, A., Li, Z. X., Jourdan, F., Nordsvan, A. R., Collins, W. J. & Volante, S. (2020) Heterogeneous Exhumation of the Mount Isa Orogen in NE Australia After 1.6 Ga Nuna Assembly: New High-Precision $^{40}Ar/^{39}Ar$ Thermochronological Constraints. *Tectonics*, 39(12), e2020TC006129.

Li, J., Li, Z.-X., Pourteau, A., Jourdan, F., Volante, S., Olierook, H. K. H., Nordsvan, A. R., & Collins, W. J. Crustal extrusion and orogenic collapse in the Georgetown Inlier of NE Australia after 1.6 Ga Nuna assembly: new insights from Ar thermochronology. *Tectonics.* (in prep.)

Li, J., Olierook, H. K. H., Li, Z.-X., Nordsvan, A. R., Collins, W. J., Elder, C., Volante, S., Pourteau, A., & Doucet, L.S. Proterozoic tectonic evolution of North Queensland, Australia: insights from seismic reflection profile reinterpretation, *Earth-Science Reviews.* (in prep.)

Conference presentations:

Li, J., Pourteau, A., Jourdan, F., Volante, S. Nordsvan, A. R., & Li, Z.-X., 2017, November, Thermal history of Proterozoic NE Australia: Insights into Nuna assembly and breakup. In *CCFS Whole-of-Centre Meeting*, *Conference Abstracts*, Cairns, Australia

Li, J., Pourteau, A., Jourdan, F., Volante, S. Nordsvan, A. R., & Li, Z.-X., 2018, October, Proterozoic tectonic evolution of North Queensland, Australia: new insights from thermal cooling history. In *Australian Geoscience Council Convention Conference Abstracts,* Adelaide, Australia

Li, J., Olierook, H. K. H., Li, Z.-X., Nordsvan, A. R., Collins, W. J., Pourteau, A., Volante, S., Elder, C., & Doucet, L. S., 2021, February, Proterozoic crustal evolution of NE Australia during Nuna assembly: insights from geophysical and radiogenic isotope data. In *Australia Earth Sciences Convention Conference Abstracts*, Tasmania, Australia

Other relevant co-authored publications:

Pourteau, A., Smit, M. A., Li, Z.-X., Collins, W. J., Nordsvan, A. R., Volante, S. & **Li, J.** (2018) 1.6 Ga crustal thickening along the final Nuna suture. *Geology*, 46(11), 959-962.

Gan, B., Diwu, C., Yan, J., Wang, T. & **Li, J.** (2020a) Formation and stabilization of the Dunhuang Block, NW China: Constraints from the Late Paleoproterozoic A-type granites of the Dunhuang Complex. *Precambrian Research*, 346.

Gan, B., Li, Z., Song, Z. & **Li, J**. (2020b) Middle Cambrian granites in the Dunhuang Block (NW China) mark the early subduction of the southernmost Paleo-Asian Ocean. *Lithos*, 372-373.

Volante, S., Collins, W. J., Blereau, E., Pourteau, A., Spencer, C., Evans, N. J., Barrote, V., Nordsvan, A. R., Li, Z. X. & **Li, J**. (2020a) Reassessing zircon-monazite thermometry with thermodynamic modelling: insights from the Georgetown igneous complex, NE Australia. *Contributions to Mineralogy and Petrology*, 175(12).

Volante, S., Collins, W. J., Pourteau, A., Li, Z. X., **Li, J.** & Nordsvan, A. R. (2020b) Structural Evolution of a 1.6 Ga Orogeny Related to the Final Assembly of the Supercontinent Nuna: Coupling of Episodic and Progressive Deformation. *Tectonics*, 39(10).

Volante, S., Pourteau, A., Collins, W. J., Blereau, E., Li, Z.-X., Smit, M., Evans, N. J., Nordsvan, A. R., Spencer, C. J., McDonald, B. J., **Li, J.** & Guenter, C. (2020c) MultipleP-T-d-tpaths reveal the evolution of the final Nuna assembly in northeast Australia. *Journal of Metamorphic Geology*, 38(6), 593-627

El Dien, H.G., Li, Z.X., Anbar, M.A., Doucet, L.S., Murphy, J.B., Evans, N.J., Xia, X.P. and **Li, J.,** 2021a. Two-stage crustal growth in the Arabian-Nubian shield: Initial arc accretion followed by plume-induced crustal reworking. *Precambrian Research*, *359*, p.106211.

El Dien, H.G., Li, Z.X., Abu Anbar, M., Doucet, L.S., Murphy, J.B., Evans, J.N., Xia, X.P., **Li, J**., 2021b. The largest plagiogranite on Earth formed by re-melting of juvenile proto-continental crust. *Communications Earth & Environment, 2*(1), pp.1-16.

Brennan, D.T., Link, P.K., Li, Z.X., Martin, L., Johnson, T., Evans, N.J. and Li, J., 2022. Closing the “North American Magmatic” gap: Crustal evolution of the Clearwater Block from multi-isotope and trace element zircon data. *Precambrian Research*, *369*, p.106533.

Curtin University

Authorship Agreement Form

The Curtin University Authorship, Peer Review and Publication of Research Findings Policy and Procedures[1] which references the Australian Code for the Responsible Conduct of Research[2], provides clear guidelines regarding attribution of authorship. This form is to assist researchers in capturing discussions around intended publications arising from joint work. It does not replace copyright or certification forms required by publishers.

1. Research

Project Title:	Proterozoic crustal evolution of NE Australia during the supercontinent Nuna Assembly: new insights from a coupled thermochronological and geophysical study		
Project identifier (if applicable)			
Principal Investigator	Zheng-Xiang Li		
Other named investigator/s#	Jiangyu Li	**Role**	Ph.D. Student
Other researcher/s#	Dr. Amaury Pourteau	**Role**	Investigator
Other researcher/s#	Prof. Fred Jourdan	**Role**	Investigator

Insert additional rows if required

2. Publications/Outputs – the intended outputs from the above research are identified below

Pub#	Description (e.g. method paper)	Publication Type (Conference, journal article etc)
1	**Li, J.,** Pourteau, A., Li, Z. X., Jourdan, F., Nordsvan, A. R., Collins, W. J. & Volante, S. (2020) Heterogeneous Exhumation of the Mount Isa Orogen in NE Australia After 1.6 Ga Nuna Assembly: New High-Precision $^{40}Ar/^{39}Ar$ Thermochronological Constraints. *Tectonics*, 39(12), e2020TC006129.	Journal article (published)
2	**Li, J. Y.**, Li, Z.-X., Pourteau, A., Jourdan, F., Volante, S., Olierook, H. K. H., Nordsvan, A. R., & Collins, W. J. A two-stage cooling history for the Georgetown Inlier in NE Australia after 1.6 Ga Nuna assembly: new insights into the late-orogenic crustal tectono-magmatic history. In preparation for *Tectonics*	Journal article (in prep)
3	**Li, J. Y.**, Olierook, H. K. H., Li, Z.-X., Nordsvan, A. R., Collins, W. J., Elder, C., Volante, S., Pourteau, A., & Doucet, L.S. Proterozoic tectonic evolution of North Queensland, Australia: insights from seismic reflection profile reinterpretation. In preparation for submission to *Earth-Science Reviews*.	Journal article (in prep)

Insert additional rows if required

3. Proposed order of authors

(add rows as required for additional authors and/or if authorship will differ between multiple outputs)

Pub*	Author**	Corresponding? Y/N
1	1. Jiangyu Li	Y
1	2. Amaury Pourteau	N
1	3. Zheng-Xiang Li	N
1	4. Fred Jourdan	N
1	5. Adam Nordsvan	N

[1] http://policies.curtin.edu.au/findapolicy/#A

[2] https://www.nhmrc.gov.au/guidelines-publications/r39

Curtin University

Authorship Agreement Form

1	6. William Joseph Collins	N
1	7. Silvia Volante	N
1	Named Acknowledgement: Caroline Perkins; I. W. Withnall; G.M. Gibson; Hugo Olierook; Celia Mayers	N
2	1. Jiangyu Li	Y
2	2. Zheng-Xiang Li	N
2	3. Amaury Pourteau	N
2	4. Fred Jourdan	N
2	5. Silvia Volante	N
2	6. Hugo Olierook	N
2	7. Adam Nordsvan	N
2	8. William Joseph Collins	N
2	Named Acknowledgement: Adelia; Simon Terry; Celia Mayers	N
3	1. Jiangyu Li	Y
3	2. Hugo Olierook	N
3	3. Zheng-Xiang Li	N
3	4. Adam Nordsvan	N
3	5. William Joseph Collins	N
3	6. Chris Elders	N
3	7. Silvia Volante	N
3	8. Amaury Pourteau	N
3	Named Acknowledgement: Matthew Greenwood	

* If multiple publications are intended under table 2, and author inclusion and order is the same, then insert "All"

** Attribution of authorship, and role of corresponding author, may have some discipline differences, however, in all cases, inclusion must be based upon substantive intellectual contribution as defined under the Policy. Acceptance should also be sought where intending to name an individual in the acknowledgements.

4. Confirmation of agreement

(add rows as required)

Author Name and Affiliation (if other than Curtin)	Author Signature	Date
1. Zheng-Xiang Li		
2. Amaury Pourteau		
3. Fred Jourdan		
4. Adam Nordsvan		
5. Silvia Volante		
6. Hugo Olierook		

All authors should maintain a copy of this completed form for their reference

Table of Contents

List of Tables

List of Figures

Chapter 1

Introduction

1.1 Supercontinent cycles and Nuna configuration

The concept of a ‘supercontinent’ was initially proposed by Wegener (1912), referring to a landmass formed via the assembly of all of Earth’s continents in a certain time range. This hypothesis was further developed by Sutton (1963), proposing a ‘chelogenic cycle’, during which the supercontinent would periodically aggregate and disperse. With recent improvements on Precambrian paleomagnetic data and intensive research on global orogenic events, the complexities of crustal evolution, tectonic histories and their association with supercontinent cycles have been better constrained and addressed over the last three decades (Evans et al., 2016; Li et al., 2019; Mitchell et al., 2012; Murphy & Nance, 2013; Rogers & Santosh, 2003). It is widely accepted that several episodes of supercontinents have existed over the past ca. 2.5 Ga, including (1) Pangea (Wagener 1912), formed at ca. 0.3 Ga (van Staal et al., 1998; Murphy et al., 2009); (2) Rodinia (McMenamin and MacMenamin, 1990), complete after the Greenville Orogeny around 1.0 Ga (Dalziel, 1992; Meert and Powell, 2001; Powell et al., 1994) or 0.9 Ga (Li et al., 2008); and (3) Nuna/Columbia (Evans & Mitchell 2011; Meert et al., 2002; Roger and Santosh 2002; Zhao et al., 2002, 2004) or Hudsonland (Pesonen et al., 2003), assembled during the Mesoproterozoic period at ca. 1.8–1.6 Ga (Furlanetto et al., 2013; Pisarevsky et al. 2014; Pourteau et al., 2018; Verbaas et al., 2018; Zhang et al. 2012). Although intensive research has contributed to the present understanding of the assembly of the supercontinent Nuna (Condie, 2002; Hartmann, 2002; Kirscher et al., 2020; Meert, 2002; Pourteau et al., 2018; Rogers and Santosh, 2002; Wilde et al., 2002; Zhao et al., 2002), debate remains on the exact manner of the continental amalgamation and related orogenic processes

(Betts et al. 2008; Eglington et al. 2013; Nordsvan et al., 2018; Pisarevsky et al. 2014; Pourteau et al., 2018; Volante et al., 2020a; Zhang et al. 2012).

1.2 NE Australia in Nuna reconstruction and its relationship with Laurentia.

In most Nuna reconstructions, Australia is connected with NW Laurentia (Fig. 1.1a; Evans & Mitchell, 2011; Evans et al., 2016; Rogers & Santosh, 2002; Zhang et al., 2012; Zhao et al., 2002) with the final accretion at ca. 1.60 Ga (Betts et al., 2016; Kirscher et al., 2019; Nordsvan et al., 2018; Pisarevsky et al., 2014; Pourteau et al., 2018; Volante et al., 2020b). In western Laurentia, this final Nuna amalgamation event was recorded by the Racklan and Forward orogenies (Furlanetto et al., 2013; Thorkelson et al., 2005). In northeast Australia, coeval orogenesis was recorded by the Isan and Jana orogenies of the Mount Isa and Georgetown inliers (Fig. 1.1c), respectively (Betts et al., 2008; Boger & Hansen, 2004; Withnall, 1996; Withnall & Hutton, 2013). Here, we collectively call the orogen across the Mount Isa and Georgetown inliers, linked to the ca. 1.6 Ga collisional event, the Isa orogen, given distinct names referred to the two adjacent inliers. Recent investigations of the sedimentary provenance (Nordsvan et al*.,* 2018) and metamorphic record (Pourteau et al., 2018) suggest that the Georgetown Inlier of NE Australia might represent part of an allochthonous terrane of Laurentian heritage that collided with the North Australia Craton at ca. 1.60 Ga during the assembly of the supercontinent Nuna. In the Mount Isa and Georgetown inliers, the ca. 1.60 Ga orogeny resulted in medium-pressure and medium-temperature (*MP–MT*) metamorphism followed by regional, high temperature and low-pressure metamorphism (Abu Sharib & Sanislav, 2013; Bell & Rubenach, 1983; Boger and Hansen, 2004; Volante et al., 2020a), atypical of modern-style continent-continent collisions (Dong et al., 2011; Yin and Harrison, 2000). It is generally thought that supercontinent amalgamation involves large scale orogenesis representing the closure of wide oceans (Brown, 2007; Johnson et al., 2012). However, the collisional processes prevalent during the ca. 1.6 Ga Isan orogenies remain cryptic due to a lack of clearly diagnostic plate-boundary features such as: (1) exposed ophiolites or accretionary complexes, (2) pre-collisional arc magmatism, and (3) high-pressure metamorphic rocks reflecting significant crustal thickening (Boger and Hansen, 2004 ; Pourteau et al., 2018; Foster & Rubenach, 2006; Volante et al., 2020a, 2020b). Although seismic transects across the Mount Isa and Georgetown inliers have led to the identification of concealed Proterozoic terrane boundaries in NE Australia (Korsch et al., 2012), details regarding the timing and nature of crustal boundaries, terrane accretionary process, and orogenic evolutionary history remain elusive.

Understanding tectonic processes during continental collision requires detailed knowledge of the timing and duration of the associated deformation, metamorphism and crustal exhumation (Johnson et al., 2012; Kearey et al., 2009). Resolving orogenic crustal architecture and recognizing terrane suture zones are also essential for determining terrane amalgamation process. In this study, high-precision $^{40}Ar/^{39}Ar$ thermochronology of igneous and metamorphic rocks from the Mount Isa and Georgetown inliers were used to decipher the cooling history associated with the ca. 1.6 Ga Isan Orogeny. Isotopically derived thermal histories can be used to infer the denudation of an uplifted region, and thus, provide insights into orogenic and crustal evolution processes (McDougall & Harrison 1999, Skipton et al., 2017, Stübner et al., 2018). Aeromagnetic and gravity analyses, along with a reinterpretation of seismic profiles, were also conducted to explore the crustal architecture and orogenic evolution through integrating with the surface geology, published isotopic data, and the new thermo-geochronological results.

1.3 Study Area

This thesis focuses on the Protozoic rocks of the Mount Isa and Georgetown inliers (Fig. 1.1c), which are the two largest Proterozoic inliers in NE Australia (Withnall & Hutton, 2013). The Proterozoic Mount Isa Inlier preserves evidence of ca. 1.90–1.50 Ga sedimentation and igneous activity (Betts et al., 1998; Foster & Austin, 2008; Jackson et al., 2000; Neumann et al., 2006; Neumann & Fraser, 2007; Withnall and Hutton, 2013), and has been subjected to poly-phase shortening, widespread, generally low-pressure metamorphism, and syn- to post-orogenic magmatism at ca. 1.60–1.50 Ga (Abu Sharib & Sanislav, 2013; Betts, 1999; Mark, 2001; Page, 1983; Reinhardt, 1992b; Sayab, 2006, 2009; Wyborn, 1998). The Georgetown Inlier exposes >ca. 1.70–1.56 Ga sedimentary and mafic volcanic rocks (Black et al., 1998, 2005; Geological Survey of Queensland, 2011; Withnall & Hutton, 2013), which were regionally deformed and locally metamorphosed up to granulite facies during the Jana Orogeny (Cihan et al., 2006; Pourteau et al., 2018; Volante et al., 2020a), and later were intruded by ca. 1.56–1.54 Ga S-type and locally I-type plutons (Black & McCulloch, 1990). Thus, the long Proterozoic sedimentary and magmatic records of the Mount Isa (400 Myr) and Georgetown Inlier (>150 Myr) make them excellent natural laboratories for studying the Proterozoic crustal evolution of the North Australian Craton, and its association with the assembly of the supercontinent Nuna.

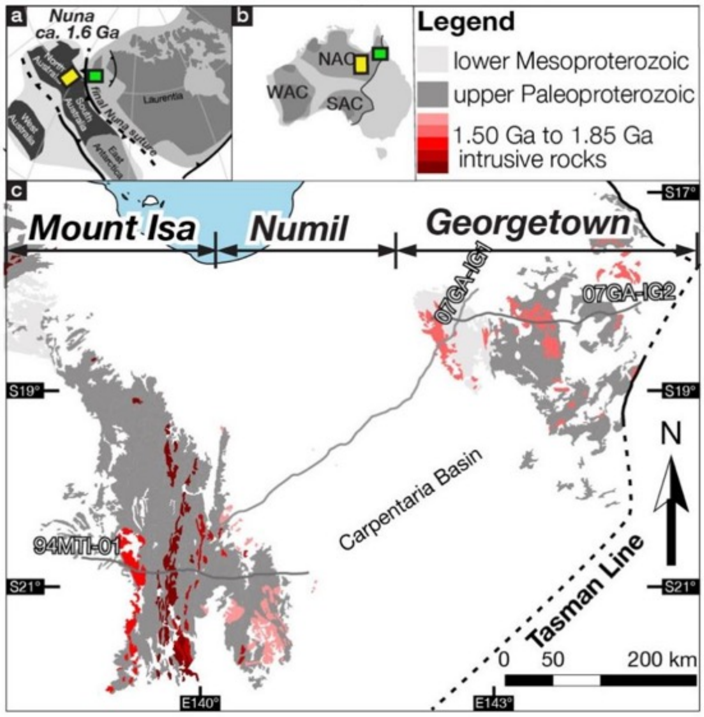

Fig. 1.1: a. Paleogeographic reconstruction of the Proterozoic supercontinent Nuna at ca. 1.60 Ga (adapted from Pourteau et al., 2018) showing the location of NE Australia (yellow and green box each represents the Mount Isa and Georgetown inliers, respectively). b. Present-day map of Australia with Australian cratons, and showing the location of study area. NAC, North Australian Craton; SAC, South Australian Craton; WAC, West Australian Craton. C. Simplified map of the NE Australian Proterozoic inliers (Modified after Pourteau et al., 2018) with E-W and NE-SW trending seismic transects, including 94MTI–01, 07GA–IG1, and 07GA–IG2. The discontinuous black line 'Tasman Line' depicts the eastern edge of the North Australia Craton (NAC).

1.3.1 The Mount Isa Inlier

The Mount Isa Inlier of NE Australia consists of high-grade metamorphic and crystalline basement rocks (the >1.85 Ga Kalkadoon–Leichhardt Complex; Blake, 1987; Etheridge et al., 1987) that are overlain by three successive superbasins including the ca. 1.8–1.74 Ga Leichhardt Superbasin, the ca. 1.73–1.69 Ga Calvert

Superbasin, and the ca. 1.67–1.58 Ga Isa Superbasin (Fig. 1.2; Betts et al., 2006; Blake, 1987; Foster & Austin, 2008; Jackson et al., 2000; Neumann et al., 2006). At ca. 1.60 Ga, sedimentation was disrupted throughout most of the Mount Isa Inlier by a predominately E–W shortening event—the Isan Orogeny (Abu Sharib and Sanislav, 2013; Betts et al., 2006; Blake, 1987; Giles et al., 2006), with the supracrustal rocks being metamorphosed to sub-greenschist to upper amphibolite facies at low-pressure condition (Giles & Nutman, 2002; Rubenach 1992; Rubenach et al., 2008; Sayab, 2006). Syn- to post-orogenic magmatic events occurred between ca. 1.60 and 1.50 Ga (Betts, 1999; Mark, 2001; Page, 1983; Wyborn, 1998). Separated by major N–S to NE-SW trending major faults, the Mount Isa Inlier was initially divided into three major belts (Day et al., 1983) (Fig. 1.2): the western belt, west of the George Creek and Mount Isa faults; the eastern belt, east of the Fountain Range and Pilgrim Faults; and the intervening central belt. It was further subdivided into 15 fault bound domains based on their discrete sedimentary records and geophysical characteristics (Withnall & Hutton, 2013).

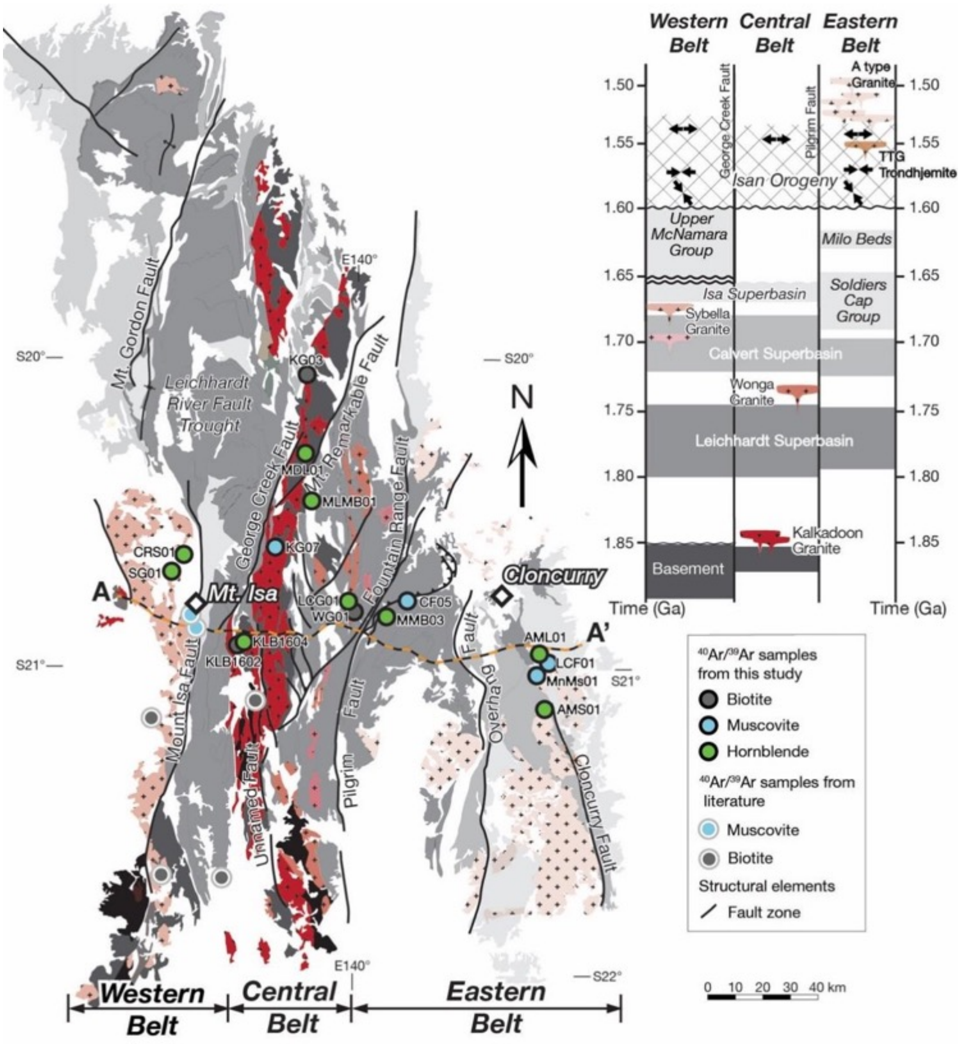

Fig. 1.2: Simplified lithological map of the Mount Isa Inlier showing the basement, successive stratigraphic packages (or "superbasins"), magmatic intrusions and main fault zones, modified from Blake, (1987). Dark gray regions are exposed Proterozoic rocks of the Mount Isa Inlier. $^{40}Ar/^{39}Ar$ sample locations from this study and selective results from literature are shown in green (hornblende), blue (muscovite) and grey dots (biotite). Transect A–A' shows the trace of Geoscience Australia geophysical imaging profile 94MTI-1. Stratigraphic columns are modified after Betts et al. (2006) and Withnall et al. (2013). Relative tectonic regimes during the Isan Orogeny are adapted from Bell et al., 1992; Bell, 1991; Giles et al., 2006; O'Dea et al., 2006; Rubenach et al, 2008 and Sharib & Sanislav., 2013.

1.3.2 The Georgetown Inlier

The Georgetown Inlier exposes >ca. 1.70–1.56 Ga sedimentary and mafic volcanic rocks (Black et al., 1998, 2005; Geological Survey of Queensland, 2011; Withnall & Hutton, 2013), which have been subjected to poly-phase deformation and metamorphism, and syn- to post-orogenic magmatism at ca. 1.60–1.55 Ga, ascribed to the Jana Orogeny (Cihan et al., 2006; Pourteau et al., 2018; Volante et al., 2020a, Black & McCulloch, 1990; Black et al., 2005). A recent petrostructural study (Volante et al., 2020a) has divided the Georgetown Inlier into three distinct geological domains based on their structural characteristics and metamorphic grades, from west to east, the western, central, and eastern domains (Fig. 1.3). The Croydon domain is added in in this study to reflect the westernmost volcanic and subvolcanic rocks of the Georgetown Inlier (Fig. 1.3).

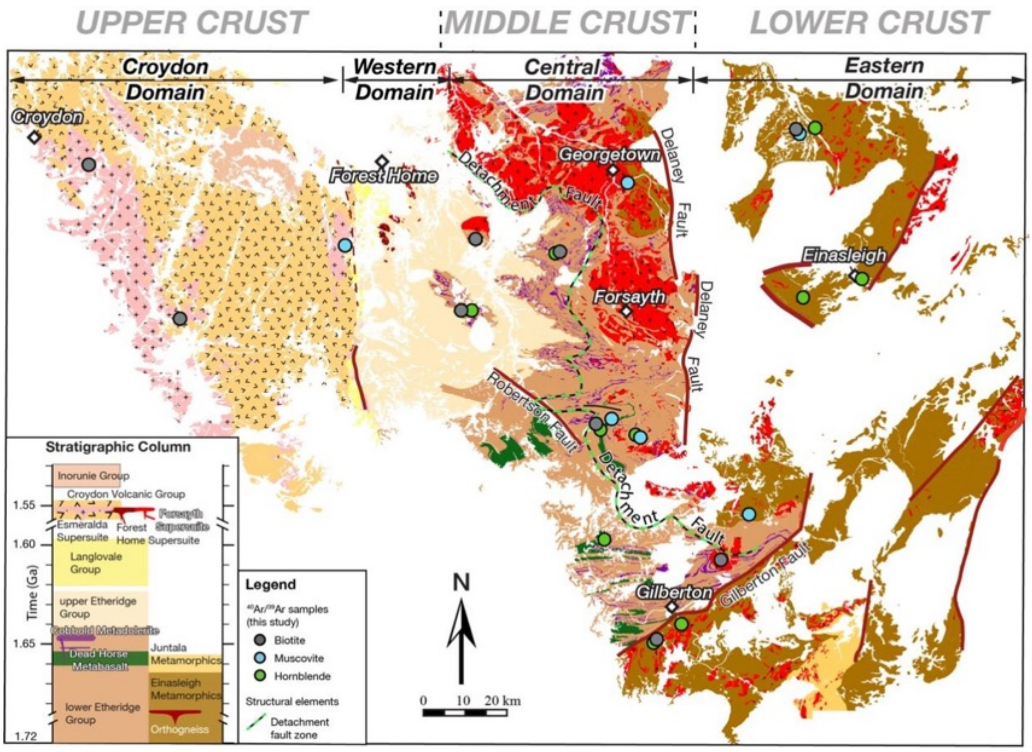

Fig. 1.3: Simplified lithological map of the Georgetown Inlier, modified from Bain et al. (1985), showing the successive stratigraphic packages (or "superbasins"), magmatic intrusions and main fault zones. ^{40}Ar/^{39}Ar sample locations from this study are shown in green (hornblende), blue (muscovite) and grey dots (biotite). The discontinuous green and black line depicts the regional detachment fault separating the upper-crustal western domain against lower-crustal central domain (Volante et al., 2020a). Stratigraphic columns are modified after Withnall et al. (2013) and Neumann and Fraser. (2007).

1.4 Research Objectives

This thesis aims to better understand the Proterozoic crustal evolution of NE Australia and resolve the terrane accretionary process during the assembly of the supercontinent Nuna from the following aspects:

(1) Recognize how many different tectonic or structural domains

E-W and NE-SW trending seismic reflection surveys across the Proterozoic inliers in NE Australia (Fig. 1.1) were reinterpreted in combination with filtered aeromagnetic and gravity images and the surface geological data to delineate the crustal architecture of the orogen. Whole-rock Nd and Hf isotopic data from igneous rocks of different crustal domains were also aggregated to recognized varying crustal characteristics and mantle input.

(2) Identify terrane suture zones and evaluate their formation timing and nature

In combination with seismic reinterpretation, aeromagnetic and gravity data allow us to trace the continuity of crustal provinces and identify the transect or offset features. The terrane suture zones can be recognized as sharp gradient variations responses on aeromagnetic and gravity grids, or on seismic reflections image as lithosphere-scale structures which offset the Moho. To further investigate the timing and nature of terrane suturing events, sedimentary records and structural evolution histories from individual domains separated by the major crustal boundaries are also incorporated to discuss the autochthonous signature of each terrane and evaluate their accretionary timing and process.

(3) Establish the orogenic evolution and processes involved

In this study, high-precision $^{40}Ar/^{39}Ar$ thermochronology was conducted along an E-W transect across the Mount Isa and Georgetown inliers to decipher the syn- to post-orogenic cooling history. Geochronological results, combined with published petrological and metamorphic records, were used to reconstruct retrograde *P–T* paths of individual domains. Cooling rate calculations were conducted to monitor the cooling history across the major fault zones, evaluate the controlling factors, and aid the determination of the driving mechanism for the post-orogenic crustal exhumation.

Combined with an updated understanding of the structural and metamorphic evolutionary processes (Volante, 2020a, b, c; Pourteau et al., 2018, 2020), this work aims to establish a complete crustal evolutionary process of NE Australia syn- to post-the assembly of the supercontinent Nuna.

1.5 Thesis Structure

This thesis starts with an introduction section that reviews the scientific questions regarding the exact manner of the assembly of the supercontinent and the related orogenic processes, specifically for NE Australia. It continues with a methodology section (Chapter 2) before presenting a series of published papers or manuscripts prepared for peer-reviewed journals, addressing the crustal evolutionary history of NE Australia during the supercontinent amalgamation event. The text and figures for the published works (Chapters 3) and works currently under peer-review (Chapters 4) or in preparation for submission (Chapter 5) are reproduced in full, but are reformatted in this thesis to meet the format consistency need. Thus, some unavoidable repetition may appear between chapters, particularly in the geological background sections. This thesis is summarized by a conclusion section (Chapter 6) emphasizing the major scientific contributions of this study. Copies of the reprint permissions for published manuscripts from the publisher can be found in Appendix A at the end of the relevant chapters. A brief introduction for the following chapters is presented below:

Chapter 2: Methodology

This chapter outlines the field work and samples collected from the study areas. It also contains details of sample preparation and mineral separation methods as well as $^{40}Ar/^{39}Ar$ thermochronological analytical processes. Sample lithology and thin section descriptions proximal to $^{40}Ar/^{39}Ar$ thermochronological analyses are presented with more detail in Chapters 3 and 4. The Monte Carlo simulation method for calculating the closure temperature of individual minerals and the cooling rate of mineral pairs is described. Methods for geophysical data acquisition and processing are also included in this section.

Chapter 3:

Heterogeneous exhumation of the Mount Isa orogen in NE Australia after 1.6 Ga Nuna assembly: new high-precision $^{40}Ar/^{39}Ar$ thermochronological constraints (this chapter is published in *Tectonics*).

This chapter investigates the Proterozoic tectonic evolution of the NE Australian orogen during the assembly of the supercontinent Nuna. High-precision $^{40}Ar/^{39}Ar$ thermochronological data from igneous and metamorphic rocks were acquired in the Mount Isa Inlier, NE Australia, where intense crustal imbrication occurred during the Proterozoic continental collision. The thermochronology results are combined with petrological examination to reconstruct the pressure-temperature evolution of individual structural domains. This chapter shows a contrasting cooling history of the Mount Isa Inlier across post-metamorphic fault zones, which is explained as associated with the reactivation of inherited normal (i.e., early basinal) and reverse (i.e., orogenic) faults. The regional exhumation period can be closely linked with the regional magmatism transition stage from ca. 1.55 Ga localized trondhjemite to voluminous A-type granitoids at ca. 1.54–1.49 Ga, and carry implications for the post-orogenic exhumation kinematic following the assembly of the supercontinent Nuna.

Chapter 4: Proterozoic cooling of the Georgetown Inlier in NE Australia after 1.6 Ga Nuna assembly: new insights into the late-orogenic crustal tectono-magmatic history (this chapter is in preparation for *Tectonics*).

This chapter reports high-precision $^{40}Ar/^{39}Ar$ thermochronology data from the Georgetown Inlier, NE Australia. Together with published data from the adjacent Mount Isa Inlier (two hundred kilometers to the west), this study establishes a temporal and spatial crustal evolution of NE Australia during the supercontinent Nuna assemblage. The cooling history suggests that the tectonic regime had transited to a post-orogenic extension and cooling environment by ca. 1.55 Ga, accompanied by a westward younging magmatic event. This widespread crustal melting and differential exhumation event is interpreted to be due to orogenic root delamination, occurred ca. 50 Myr after the final assembly of Nuna.

Chapter 5: Proterozoic crustal evolution of NE Australia during Nuna assembly: new insights from coupled geophysical and radiogenic isotope data (this chapter is close to submission, formatted for *Earth Science Review*).

This chapter used aeromagnetic and gravity data, along with a reinterpretation of seismic profiles and the surface geological data to explore the crustal architecture and evolutionary history of NE Australia during the final assembly of the Proterozoic supercontinent Nuna. Previously recognized crustal boundaries and newly identified lithosphere suture zone are discussed regarding their formation timing and nature. Published geochronological data, Neodymium and Hf isotopic data, sedimentary records and structural evolution histories are also incorporated into this work to present a unified model synthesizing the Proterozoic crustal evolution of NE Australia at ca. 1.74–1.60 Ga in the reconstruction of the supercontinent Nuna.

Chapter 6: Conclusions

This chapter outlines the scientific contributions of this work. A summary of the previous chapters brings together the major output of this research. Scientific questions raised as the research objective of this thesis are addressed using the newly acquired knowledge.

1.6 References

Abu Sharib, A. S. A. A., & I. V. Sanislav (2013), Polymetamorphism accompanied switching in horizontal shortening during Isan Orogeny: Example from the Eastern Fold Belt, Mount Isa Inlier, Australia, *Tectonophysics*, *587*, 146-167.

Abu Sharib, A. S. A. A. (2012) Foliation intersection axes (FIAs) preserved within porphyroblasts: resolving plan view orthogonal refolding, Eastern Fold Belt, Mt Isa Inlier. *Australian Journal of Earth Sciences*, 59(4), 571-598.

Bell, T. H. & Rubenach, M. J. (1983) Sequential Porphyroblast Growth and Crenulation Cleavage Development during Progressive Deformation. *Tectonophysics, 92(1-3)*, 171-194.

Bell, T. H. (1991), The role of thrusting in the structural development of the Mount Isa Mine and its relevance to exploration in the surrounding region, *Economic Geology, 86(8)*, 1602-1625.

Bell, T., J. Reinhardt, & R. Hammond (1992), Multiple foliation development during thrusting and synchronous formation of vertical shear zones, *Journal of Structural Geology, 14(7),* 791-805.

Betts, P. G., Lister, G. S. & O'Dea, M. G. (1998) Asymmetric extension of the Middle Proterozoic lithosphere, Mount Isa terrane, Queensland, Australia. *Tectonophysics, 296(3-4),* 293-316.

Betts, P. G. (1999), Palaeoproterozoic mid-basin inversion in the northern Mt Isa terrane, Queensland, *Australian Journal of Earth Sciences, 46(5),* 735-748.

Betts, P. G., D. Giles, G. Mark, G. S. Lister, B. R. Goleby, & L. Ailleres (2006), Synthesis of the proterozoic evolution of the Mt Isa Inlier, *Australian Journal of Earth Sciences, 53(1),* 187-211.

Betts, P. G., D. Giles, & B. F. Schaefer (2008), Comparing 1800-1600 Ma accretionary and basin processes in Australia and Laurentia: Possible geographic connections in Columbia, *Precambrian Research, 166(1-4),* 81-92.

Black, L. P. & McCulloch, M. T. (1990) Isotopic Evidence for The Dependence of Recurrent Felsic Magmatism on New Crust Formation - An example from the Georgetown Region of Northeastern Australia. *Geochimica Et Cosmochimica Acta, 54(1),* 183-196.

Black, L. P., Gregory, P., Withnall, I. W. & Bain, J. H. C. (1998) U-Pb zircon age for the Etheridge Group, Georgetown region, north Queensland: implications for relationship with the Broken Hill and Mt Isa sequences. *Australian Journal of Earth Sciences, 45(6),* 925-935.

Black, L. P., Withnall, I. W., Gregory, P., Oversby, B. S. & Bain, J. H. C. (2005) U-Pb zircon ages from leucogneiss in the Etheridge Group and their significance for the early history of the Georgetown region, north Queensland. *Australian Journal of Earth Sciences, 52(3),* 385-401.

Blake, D. H. (1987), Geology of the Mount Isa Inlier and environs, Queensland and Northern Territory, Bulletin - Bureau of Mineral Resources, Geology & Geophysics, Australia, 225.

Boger, S. D. & Hansen, D. (2004) Metamorphic evolution of the Georgetown Inlier, northeast Queensland, Australia; evidence for an accreted Palaeoproterozoic terrane? *Journal of Metamorphic Geology, 22(6),* 511-527.

Brown, M. (2007) Metamorphic conditions in orogenic belts: A record of secular change. *International Geology Review, 49(3),* 193-234.

Cihan, M., Evins, P., Lisowiec, N. & Blake, K. (2006) Time constraints on deformation and metamorphism from EPMA dating of monazite in the Proterozoic Robertson River Metamorphics, NE Australia. *Precambrian Research, 145(1-2),* 1-23.

Condie, K. C. (2002) The supercontinent cycle: Are there two patterns of cyclicity? *Journal of African Earth Sciences, 35(2),* 179-183.

Dalziel, I. W. D. (1991) Pacific margins of Laurentia and East Antarctica-Australia as a conjugate rift pair: evidence and implications for an Eocambrian supercontinent. *Geology, 19(6),* 598-601.

Day, RW, Whitaker, WG, Murray, CG, Wilson, IH & Grimes, KG 1983, Queensland Geology. *A companion volume to the 1:2 500 000 scale geological map (1975), publication no. 383,* Geological Survey of Queensland, Brisbane.

Dong, Y., Zhang, G., Neubauer, F., Liu, X., Genser, J. & Hauzenberger, C. (2011) Tectonic evolution of the Qinling orogen, China: Review and synthesis. *Journal of Asian Earth Sciences, 41(3),* 213-237.

Eglington, B. M., Pehrsson, S. J., Ansdell, K. M., Lescuyer, J. L., Quirt, D., Milesi, J. P. & Brown, P. (2013) A domain-based digital summary of the evolution of the Palaeoproterozoic of North America and Greenland and associated unconformity-related uranium mineralization. *Precambrian Research, 232,* 4-26.

Etheridge, M. A., R. W. R. Rutland, & L. A. I. Wyborn (1987), Orogenesis and tectonic process in the early to middle Proterozoic of northern Australia, *Precambrian Lithospheric Evolution, 17,* 131-147.

Evans, D. A. D. & Mitchell, R. N. (2011) Assembly and breakup of the core of Paleoproterozoic-Mesoproterozoic supercontinent Nuna. *Geology, 39(5),* 443-446.

Evans, D.A., Veselovsky, R.V., Petrov, P.Y., Shatsillo, A.V. and Pavlov, V.E., 2016. Paleomagnetism of Mesoproterozoic margins of the Anabar Shield: A hypothesized billion-year partnership of Siberia and northern Laurentia. *Precambrian Research*, *281*, pp.639-655.

Foster, D. & Austin, J. (2008) The 1800–1610Ma stratigraphic and magmatic history of the Eastern Succession, Mount Isa Inlier, and correlations with adjacent Paleoproterozoic terranes. *Precambrian Research, 163(1-2),* 7-30.

Foster, D. R. W. & Rubenach, M. J. (2006) Isograd pattern and regional low-pressure, high-temperature metamorphism of pelitic, mafic and calc-silicate rocks along an east – west section through the Mt Isa Inlier. *Australian Journal of Earth Sciences, 53(1),* 167-186.

Furlanetto, F., Thorkelson, D. J., Daniel Gibson, H., Marshall, D. D., Rainbird, R. H., Davis, W. J., Crowley, J. L. & Vervoort, J. D. (2013) Late Paleoproterozoic terrane accretion in northwestern Canada and the case for circum-Columbian orogenesis. *Precambrian Research, 224,* 512-528.

Geological Survey of Queensland, (2011): North-West Queensland Mineral and Energy Province Report. Queensland Department of Employment, Economic Development and Innovation, Brisbane.

Gibson, G. M., D. C. Champion, I. W. Withnall, N. L. Neumann, & L. J. Hutton (2018), Assembly and breakup of the Nuna supercontinent: Geodynamic constraints from 1800 to 1600 Ma sedimentary basins and basaltic magmatism in northern Australia, *Precambrian Research, 313,* 148-169.

Giles, D., & A. P. Nutman (2002), SHRIMP U-Pb monazite dating of 1600-1580 Ma amphibolite facies metamorphism in the southeastern Mt Isa Block, Australia, *Australian Journal of Earth Sciences, 49(3),* 455-465.

Giles, D., L. Ailléres, D. Jeffries, P. Betts, & G. Lister (2006), Crustal architecture of basin inversion during the Proterozoic Isan Orogeny, Eastern Mount Isa Inlier, Australia, *Precambrian Research, 148(1-2),* 67-84.

Hartmann, L.A., (2002). The Mesoproterozoic supercontinent Atlantica in the Brazilian shield—review of geological and U–Pb zircon and Sm–Nd isotopic evidence. *Gondwana Res. 5,* 157–164

Jackson, M. J., Scott, D. L. & Rawlings, D. J. (2000) Stratigraphic framework for the Leichhardt and Calvert Superbasins: review and correlations of the pre-1700 Ma successions between Mt Isa and McArthur River. *Australian Journal of Earth Sciences, 47(3),* 381-403.

Johnson, M. R. W. & Harley, S. L. (2012) Orogenesis The Making of Mountains Preface.

Kearey, P., K. A. Klepeis, & F. J. Vine (2009), *Global tectonics,* John Wiley & Sons.

Korsch, R. J., Huston, D. L., Henderson, R. A., Blewett, R. S., Withnall, I. W., Fergusson, C. L., Collins, W. J., Saygin, E., Kositcin, N., Meixner, A. J., Chopping, R., Henson, P. A., Champion, D. C., Hutton, L. J., Wormald, R., Holzschuh, J. & Costelloe, R. D. (2012) Crustal architecture and geodynamics of North Queensland, Australia: Insights from deep seismic reflection profiling. Tectonophysics, 572-573, 76-99.

Li, J. Y., Li, Z.-X., Pourteau, A., Jourdan, F., Volante, S., Olierook, H. K. H., Nordsvan, A. R., & Collins, W. J. Crustal extrusion and orogenic collapse in the Georgetown Inlier of NE Australia after 1.6 Ga Nuna assembly: new insights from Ar thermochronology. *Tectonics.* (In Review)

Li, Z. X., Bogdanova, S. V., Collins, A. S., Davidson, A., De Waele, B., Ernst, R. E., Fitzsimons, I. C. W., Fuck, R. A., Gladkochub, D. P., Jacobs, J., Karlstrom, K. E., Lu, S., Natapov, L. M., Pease, V., Pisarevsky, S. A., Thrane, K. & Vernikovsky, V. (2008) Assembly, configuration, and break-up history of Rodinia: A synthesis. Precambrian Research, 160(1-2), 179-210.

Li, Z.X., Mitchell, R.N., Spencer, C.J., Ernst, R., Pisarevsky, S., Kirscher, U. and Murphy, J.B., 2019. Decoding Earth's rhythms: modulation of supercontinent cycles by longer superocean episodes. *Precambrian Research*, *323*, pp.1-5.

Liu, Y., Mitchell, R. N., Li, Z.-X., Kirscher, U., Pisarevsky, S. A. & Wang, C. (2021) Archean geodynamics: Ephemeral supercontinents or long-lived supercratons. *Geology.*

Mark, G. (2001), Nd isotope and petrogenetic constraints for the origin of the Mount Angelay igneous complex: implications for the origin of intrusions in the Cloncurry district, NE Australia, *Precambrian Research, 105(1),* 17-35.

Mark, G., A. Wilde, N. H. S. Oliver, P. J. Williams, and C. G. Ryan (2005), Modeling outflow from the Ernest Henry Fe oxide Cu–Au deposit: implications for ore genesis and exploration, *Journal of Geochemical Exploration, 85(1),* 31-46.

Mark, G., Foster, D. R. W., Pollard, P. J., Williams, P. J., Tolman, J., Darvall, M. & Blake, K. L. (2004) Stable isotope evidence for magmatic fluid input during large-scale Na-Ca alteration in the Cloncurry Fe oxide Cu-Au district, NW Queensland, Australia. *Terra Nova, 16(2),* 54-61.

McDougall, I., and Harrison, T.M., (1999). Geochronology and Thermochronology by the ^{40}Ar/^{39}Ar Method. Oxford University Press on Demand.

McMenamin, M. A. S., & MacMenamin, D. L. S. (1990). *The emergence of animals: The Cambrian breakthrough.* New York: Columbia University Press.

Meert, J. G. (2002) Paleomagnetic Evidence for a Paleo-Mesoproterozoic Supercontinent Columbia. *Gondwana Research, 5(1),* 207-215.

Meert, J.G. and Powell, C.M., (2001). Assembly and break-up of Rodinia: introduction to the special volume. *Precambrian Research, 110*, pp.1-8.

Mitchell, R.N., Kilian, T.M. and Evans, D.A., 2012. Supercontinent cycles and the calculation of absolute palaeolongitude in deep time. *Nature*, *482*(7384), pp.208-211.

Moores, E. M. (1991) Southwest US-East Antarctic (SWEAT) connection: a hypothesis. *Geology, 19(5),* 425-428.

Murphy, J. B., Nance, R. D. & Cawood, P. A. (2009) Contrasting modes of supercontinent formation and the conundrum of Pangea. *Gondwana Research, 15(3-4),* 408-420.

Murphy, J.B. and Nance, R.D., 2013. Speculations on the mechanisms for the formation and breakup of supercontinents. *Geoscience Frontiers*, *4*(2), pp.185-194.

Neumann and Geoffrey L. Fraser, e. (2007) *Geochronological synthesis and Time-Space plots for Proterozoic Australia.* (Vol. 2007). Canberra, Australia: Geoscience Australia.

Neumann, N. L., Southgate, P. N., Gibson, G. M. & McIntyre, A. (2006) New SHRIMP geochronology for the Western Fold Belt of the Mt Isa Inlier: Developing a 1800 - 1650 Ma event framework. *Australian Journal of Earth Sciences, 53(6),* 1023-1039.

Nordsvan, A. R., Collins, W. J., Li, Z.-X., Spencer, C. J., Pourteau, A., Withnall, I. W., Betts, P. G. & Volante, S. (2018) Laurentian crust in northeast Australia: Implications for the assembly of the supercontinent Nuna. *Geology, 46(3),* 251-254.

O'Dea, M. G., P. G. Betts, T. MacCready, & L. Aillères (2006), Sequential development of a mid-crustal fold-thrust complex: evidence from the Mitakoodi Culminationin the eastern Mt Isa Inlier, Australia, *Australian Journal of Earth Sciences, 53(1),* 69-90.

Page, R. (1983) Timing of superposed volcanism in the Proterozoic Mount Isa inlier, Australia. *Precambrian Research, 21(3-4),* 223-245.

Pesonen, L. J., Elming, S. A., Mertanen, S., Pisarevsky, S., D'Agrella, M. S., Meert, J. G., Schmidt, P. W., Abrahamsen, N. & Bylund, G. (2003) Palaeomagnetic configuration of continents during the Proterozoic. *Tectonophysics, 375(1-4),* 289-324.

Piper, J.D.A., (1982). The Precambrian paleomagnetic record: the case for the Proterozoic Supercontinent. *Earth Planet. Sci. Lett. 59*, 61–89.

Piper, J.D.A., (2000). The Neoproterozoic Supercontinent: Rodinia or Palaeopangaea? *Earth Planet. Sci. Lett. 176,* 131–146.

Pisarevsky, S. A., Elming, S.-A., Pesonen, L. J. & Li, Z.-X. (2014) Mesoproterozoic paleogeography: Supercontinent and beyond. *Precambrian Research, 244,* 207-225.

Pourteau, A., Smit, M. A., Li, Z.-X., Collins, W. J., Nordsvan, A. R., Volante, S. & Li, J. (2018) 1.6 Ga crustal thickening along the final Nuna suture. *Geology, 46(11),* 959-962.

Pourteau, A., Doucet, L. S., Blereau, E. R., Volante, S., Johnson, T. E., Collins, W. J., Li, Z.-X. & Champion, D. C. (2020) TTG generation by fluid-fluxed crustal melting: Direct evidence from the Proterozoic Georgetown Inlier, NE Australia. *Earth and Planetary Science Letters, 550*. 116548

Powell, C. M., Preiss, W. V., Gatehouse, C. G., Krapez, B. & Li, Z. X. (1994) South Australian record of a Rodinian epicontinental basin and its Mid-Neoproterozoic Breakup (Similar-To-700 Ma) to form the Palaeo-Pacific Ocean. *Tectonophysics, 237(3-4),* 113-140.

Reinhardt, J. (1992a), The Corella Formation of the Rosebud Syncline (central Mount Isa Inlier): deposition, deformation, and metamorphism, *In Detailed studies of the Mount Isa Inlier* (Vol. 243, pp. 229-256). Australian Geological Survey Organization Bulletin.

Reinhardt, J. (1992b), Low-pressure, high-temperature metamorphism in a compressional tectonic setting: Mary Kathleen Fold Belt, northeastern Australia, G*eological Magazine, 129(1)*, 41-57.

Rogers, J. J. W. & Santosh, M. (2002) Configuration of Columbia, a Mesoproterozoic supercontinent. *Gondwana Research, 5(1),* 5-22.

Rubenach, M. J. (1992), Proterozoic low-pressure/high-temperature metamorphism and an anticlockwise P–T–t path for the Hazeldene area, Mount Isa Inlier, Queensland, Australia, *Journal of Metamorphic Geology, 10(3),* 333-346.

Rubenach, M. J., D. R. W. Foster, P. M. Evins, K. L. Blake, & C. M. Fanning (2008), Age constraints on the tectonothermal evolution of the Selwyn Zone, Eastern Fold Belt, Mount Isa Inlier, *Precambrian Research, 163(1-2),* 81-107.

Sayab, M. (2006) Decompression through clockwise P–T path: implications for early N–S shortening orogenesis in the Mesoproterozoic Mt Isa Inlier (NE Australia).*Journal of Metamorphic Geology*, *24*(2), 89-105.

Sayab, M. (2009) Tectonic significance of structural successions preserved within low-strain pods: Implications for thin- to thick-skinned tectonics vs. multiple near-orthogonal folding events in the Palaeo-Mesoproterozoic Mount Isa Inlier (NE Australia). *Precambrian Research, 175(1-4),* 169-186.

Skipton, D.R., Schneider, D.A., Kellett, D.A. and Joyce, N.L., (2017). Deciphering the Paleoproterozoic cooling history of the northeastern Trans-Hudson Orogen, Baffin Island (Canada), using 40Ar/39Ar step-heating and UV laser thermochronology. *Lithos, 284*, pp.69-90.

Sutton, J., (1963). Long-term cycles in the evolution of the continents. *Nature, 198(4882),* pp.731-735.

Stübner, K., Grujic, D., Dunkl, I., Thiede, R. and Eugster, P., (2018). Pliocene episodic exhumation and the significance of the Munsiari thrust in the northwestern Himalaya. *Earth and Planetary Science Letters, 481,* pp.273-283.

Thorkelson, D. J., Abbott, J. A., Mortensen, J. K., Creaser, R. A., Villeneuve, M. E., McNicoll, V. J. & Layer, P. W. (2005) Early and Middle Proterozoic evolution of Yukon, Canada. *Canadian Journal of Earth Sciences, 42(6),* 1045-1071.

Van Staal, C.R., Dewey, J.F., Mac Niocaill, C. and McKerrow, W.S., (1998). The Cambrian-Silurian tectonic evolution of the northern Appalachians and British Caledonides: history of a complex, west and southwest Pacific-type segment of Iapetus. *Geological Society, London, Special Publications, 143(1),* pp.197-242.

Verbaas, J., Thorkelson, D.J., Crowley, J., Davis, W.J., Foster, D.A., Gibson, H.D., Marshall, D.D. and Milidragovic, D., 2018. A sedimentary overlap assemblage links Australia to northwestern Laurentia at 1.6 Ga. *Precambrian Research*, *305*, pp.19-39.

Volante, S., Pourteau, A., Collins, W. J., Blereau, E., Li, Z.-X., Smit, M., Evans, N. J., Nordsvan, A. R., Spencer, C. J., McDonald, B. J., Li, J. & Guenter, C. (2020a) MultipleP-T-d-tpaths reveal the evolution of the final Nuna assembly in northeast Australia. *Journal of Metamorphic Geology, 38(6),* 593-627.

Volante, S., Collins, W. J., Pourteau, A., Li, Z. X., Li, J. & Nordsvan, A. R. (2020b) Structural Evolution of a 1.6 Ga Orogeny Related to the Final Assembly of the Supercontinent Nuna: Coupling of Episodic and Progressive Deformation. *Tectonics, 39(10).*

Volante, S., Collins, W. J., Blereau, E., Pourteau, A., Spencer, C., Evans, N. J., Barrote, V., Nordsvan, A. R., Li, Z. X. & Li, J. (2020c) Reassessing zircon-monazite thermometry with thermodynamic modelling: insights from the Georgetown igneous complex, NE Australia. *Contributions to Mineralogy and Petrology, 175(12).*

Wang, C., Mitchell, R. N., Murphy, J. B., Peng, P. & Spencer, C. J. (2020) The role of megacontinents in the supercontinent cycle. *Geology. 49*(4), 402-406.

Wegener, A., (1912). Die entstehung der kontinente. *Geologische Rundschau, 3(4),* pp.276-292.

Wilde, S.A., Zhao, G. and Sun, M., (2002). Development of the North China Craton during the late Archaean and its final amalgamation at 1.8 Ga: some speculations on its position within a global Palaeoproterozoic supercontinent. *Gondwana Research, 5(1),* pp.85-94.

Withnall, I. W. (1996) *Stratigraphy, structure and metamorphism of the Proterozoic Etheridge and Langlovale Groups, Georgetown region, north Queensland.* Australian Geological Survey Organisation Record (15).

Withnall, I. W. & Hutton, L. J. (2013) *Proterozoic - North Australian Craton. Geology of Queensland,* 23-112.

Withnall, I., Hutton, LJ., Armit, RJ., Betts, PG., Blewett, RS., Champion, DC. & Jell, PA., (2013) *Geology of Queensland Introduction*.

Wyborn, L. (1998) Younger ca 1500 Ma granites of the Williams and Naraku Batholiths, Cloncurry district, eastern Mt Isa Inlier: Geochemistry, origin, metallogenic significance and exploration indicators. *Australian Journal of Earth Sciences, 45(3),* 397-411.

Yin, A. & Harrison, T. M. (2000) Geologic evolution of the Himalayan-Tibetan orogen. *Annual Review of Earth and Planetary Sciences, 28(1),* 211-280.

Zhang, S., Li, Z.-X., Evans, D. A. D., Wu, H., Li, H. & Dong, J. (2012) Pre-Rodinia supercontinent Nuna shaping up: A global synthesis with new paleomagnetic results from North China. *Earth and Planetary Science Letters, 353-354,* 145-155.

Zhao, G., Cawood, P. A., Wilde, S. A. & Sun, M. (2002) Review of global 2.1–1.8 Ga orogens: implications for a pre-Rodinia supercontinent. *Earth-Science Reviews, 59(1-4),* 125-162.

Zhao, G., Sun, M., Wilde, S. A. & Li, S. (2004) A Paleo-Mesoproterozoic supercontinent: assembly, growth and breakup. *Earth-Science Reviews, 67(1-2),* 91-123.

Appendix A:
Supplementary materials to Chapter 1

Attached at the end of the thesis.

Chapter 2

Methodology

2.1 Field work and sample collection

Geological fieldwork to North Queensland was conducted in two field seasons: one in 2017, from 12 May to 19 July in both the Mount Isa and Georgetown inliers; and one in 2018 in the Georgetown Inlier, from 03 to 17 March. Field tasks include field observations, geological mapping, structural measurements, and sample collection. I targeted the least weathered mafic or high-grade metamorphic rocks for hornblende $^{40}Ar/^{39}Ar$ thermochronological dating, and felsic intrusion or metapelitic rocks for muscovite and biotite dating. In the Mount Isa Inlier (Fig. 1.2), Proterozoic rocks were sampled across major fault zones and metamorphic gradients, and were pinned to the interpreted seismic profile 94MTI-01 (Geoscience Australia; MacCready et al., 2006) to ensure structural control and investigate the activity of the major, deep-rooted fault zones. Extra samples were collected to the north and south of the E-W profile for detecting possible lateral variations within each domain. In the Georgetown Inlier (Fig. 1.3), samples were collected along an E–W and a N–S transects across the Georgetown Inlier, intersecting various crustal domains. A total of 160 rock samples were collected for petrological study and for $^{40}Ar/^{39}Ar$ thermochronological dating to investigate the regional syn- to post-orogenic cooling history, and examine the timing and magnitude of crustal motions.

2.2 Laboratory work

The robustness of the expected data relies on a thorough selection of freshest samples, cautious thin section examination, meticulous mineral picking, and careful laboratory procedures, which are fully described in detail below:

2.2.1 Thin section preparation and microscopic examination

To ensure the highest quality of samples (unaltered target minerals), a total of 90 thin sections were prepared and examined using optical microscopy and scanning electron microscopy. The rock samples for thin sections were cut and polished with progressively finer grades of diamond paste (9–1μm thick) by service provider Yu'neng Petrology and Mineral Service Company (China) and Minerex Services Pty Ltd (Western Australia). The relative abundance of minerals (both transparent and opaque) and their textural relationships were analysed at Curtin University using a Nikon Eclipse optical microscope under transmitted and reflected lights.

2.2.2 Mineral separation

Rock samples were examined by optical microscopy to pick the least weathered samples with minimal evidence of hydrothermal alteration. Selected rocks were crushed and sieved to extract 250–350 μm grains, which were then washed in acetone and rinsed with deionized water. Optically fresh and homogeneous grains of hornblende, muscovite and biotite were handpicked under a binocular microscope. Grains with inclusions or intergrowths of other K-bearing mineral phases were avoided. Hornblende aliquots were further leached in diluted HF and rinsed with distilled water in an ultrasonic cleaner to remove impurities.

2.2.3 $^{40}Ar/^{39}Ar$ analysis

Selected sample grains were sent to irradiation before conducting $^{40}Ar/^{39}Ar$ analyses. Sample aliquots and reference Fish Canyon sanidine standard (FCs) (to monitor neutron flux) were loaded into the 14 large wells of an aluminium disc measuring 1.9 cm in diameter and 0.3 cm in depth. The discs were Cd-shielded and irradiated for 40 hours in Oregon State university nuclear reactor (USA) (Color, USA). For the FCs reference material, the age of 28.294 ± 0.036 Ma (1 standard deviation, SD) (Renne et al., 2011) was used. A neutron fluence parameter *J* values were calculated from the mean J-values computed from standard grains within the small pits. Specific *J* values applied for each measurement are listed in Appendix C for samples dated from the Mount Isa Inlier, and Appendix D for Georgetown Inlier samples, respectively. An automated air pipette was used to monitor the mass discrimination and provided a mean value of 1.003786 ± 0.07 per dalton (atomic mass unit). The correction factors for interfering isotopes were $(^{39}Ar/^{37}Ar)_{Ca} = 6.95 \times 10^{-4}$ (± 1.3%), $(^{36}Ar/^{37}Ar)_{Ca} = 2.65 \times 10^{-4}$ (± 0.84%) and $(^{40}Ar/^{39}Ar)_{K} = 7.30 \times 10^{-4}$ (± 12.4%; Renne et al., 2013).

A total of 50 signal grains $^{40}Ar/^{39}Ar$ analyses were measured at the Western Australian Argon Isotope Facility at Curtin University.

MAP 215:50 mass spectrometer: All the analyses were conducted on single-grain aliquots, which maximizes data accuracy as it enables determining ^{40}Ar concentrations directly within single grains and prevents the mixing of different age populations. Single grains were step-heated using a 110 W Spectron Laser System by rastering a continuous Nd-YAG (IR, 1064 nm) laser over the sample for 1 min for homogeneous heating. The released gas was purified in a stainless-steel extraction line using two SAES AP10 getters and one GP50 getter. Ar isotopes in the released gas were measured in static mode with a MAP 215–50 mass spectrometer, with a Balzers SEV 217 electron multiplier using 9–10 cycles of peak hopping. Blanks were monitored every 3 to 4 steps and typical ^{40}Ar blanks range from 1×10^{-16} to 2×10^{-16} mol. A blank was monitored after every 4 steps, with a typical ^{40}Ar range of 3×10^{-16} – 5×10^{-16} mol. Raw mass-spectrometer data were reduced using the Argus program written by M.O. McWilliams, and run under a LabView environment.

ARGUS mass spectrometer: selected single crystals were step-heated using a continuous 100 W PhotonMachine© CO2 (IR, 10.6 μm) laser fired on the crystals during 60 seconds. Each of the standard crystals was fused in a single step. The gas was purified in an extra low-volume stainless steel extraction line of 240cc and using one SAES AP10 and one GP50 getter. Ar isotopes were measured in static mode using a low volume (600 cc) ARGUS VI mass spectrometer from Thermofisher© (Phillips and Matchan, 2013) set with a permanent resolution of ~200. Measurements were carried out in multi-collection mode using four faradays to measure mass 40 to 37 and a 0-background compact discrete dynode ion counter to measure mass 36. We measured the relative abundance of each mass simultaneously using 10 cycles of peak-hopping and 33 seconds of integration time for each mass. Detectors were calibrated to each other electronically and using Air shot beam signals.

2.2.4 $^{40}Ar/^{39}Ar$ data processing and management

Ages were calculated using the ArArCALC software (Koppers, 2002), considering the atmospheric or trapped $^{40}Ar/^{36}Ar$ ratio of 298.56 ± 0.3 (Lee et al., 2006) and a decay constant recommended by Renne et al. (2011). Plateau ages were calculated from the mean of all plateau steps, weighted by the inverse variance of the analytical error of each step, and were reported with an uncertainty of 2σ. The criteria used to determine an age plateau are as follow: plateaus should contain ~70% or more of the total measured ^{39}Ar, with at least 3 consecutive steps agreeing at 95% confidence level, and satisfy a probability of fit (p) >0.05 (Hansma et al., 2016). Mini-plateaus are defined similarly but encompass only 50–70% of the measured ^{39}Ar, and are considered less robust than plateau ages. None-plateaus ages were not exclusively discarded, but were further discussed on their geological meaning after combining the petrological observation with argon step-age spectra interpretation. A summary of the dated sample lithologies, sample locations and $^{40}Ar/^{39}Ar$ analytical ages were listed in the Table B.2.1

of Appendix B. Ar isotope data corrected for blanks, mass discrimination, and radioactive decay can be found in the Table C.3.3 of Appendix C for samples dated from the Mount Isa Inlier, and in the Table D.4.3 of Appendix D for the Georgetown Inlier samples.

2.3 ^{40}Ar/^{39}Ar thermochronology

^{40}Ar/^{39}Ar dating is based on the decay of ^{40}K to radiogenic ^{40}Ar with a half-life of ca. 1.25 Ga (Sigurgeirsson, 1962). ^{39}Ar is produced by ^{39}K neutron irradiation prior to degassing. Since ^{40}K/^{39}K ratio is fixed for natural K, the ^{40}K isotope can be calculated using the ^{39}Ar production rate during the neutron irradiation. Thus, argon-argon ages can be calculated utilizing the following formular (1) by determining the ^{40}Ar/^{39}Ar ratios via gas source mass spectrometry.

$$t=\frac{1}{\lambda}[1+\left(\frac{^{40}\mathrm{Ar}^*}{^{40}\mathrm{K}}\right)\left(\frac{\lambda}{\lambda_e}\right)] \qquad (1)$$

The retention of ^{40}Ar in a given system is controlled by thermally activated diffusion (Harrison 1981). Below a certain temperature (so-called “closure temperature”), Argon is retained, so that the Argon isotopic systems record the timing at which the system “closed”. Despite notable variations due to grain size and cooling rate, the closure temperatures for biotite, muscovite, and hornblende are typically in the order of 310 °C (Harrison et al., 1985), 405 °C (Harrison et al., 2009), and 500 °C (Harrison 1981), respectively, at a cooling rate of 10°C/Ma. Theoretically, with Ar being progressively released at each step of the heating process, the individual step calculated using the ^{40}Ar/^{39}Ar ratio should be equal within errors. Thus, whether a plateau is present or not is a good indicator for determining if the sample remained in a closed system. When available, a plateau age can be calculated by averaging the step ages calculated from at least 70% ^{40}Ar release over three heating steps.

2.3.1 Argon thermal diffusion and diffusive modelling

Argon diffusion is believed to follow the Arrhenius Law where the diffusion activity rate is controlled by the temperature effect. For a thermal activity process, the diffusion coefficient (D) is defined by:

$$D = D_0 e^{-E_a/RT} \qquad (2)$$

Where D_0 is the pre-exponential factor, E_a is the activation energy, R is the gas constant and T is the absolute temperature. The diffusion coefficient (D) can also be calculated by:

$$\frac{\partial c}{\partial t} = \mathrm{D}\nabla^2 c \qquad (3)$$

In this formular, c is the argon concentration and D is the diffusion coefficient. By measuring Argon concentration under different absolute temperatures, both active energy (E_a) and diffusion coefficient (D) can be determined. This calculation is based on the assumption that mineral is in a spherical geometry, and D/a^2 is the partition coefficient. For a single rate-limited thermally activated process, the activation energy (E_a) and the pre-exponential factor (A/D_0) can both be determined via utilizing Arrhenius plot:

$$\ln(k) = \ln(A) - \frac{E_a}{R}\left(\frac{1}{T}\right) \qquad (4)$$

As pressure can reduce the argon diffusivity during a thermal event, thus, the activity energy (Q) needs to be modified by adding a pressure correction (PV) at the zero pressure (Ea)

$$Q = Ea + PV \qquad (5)$$

Therefore, argon diffusion activity is particularly dependant on pressure (P), temperature (T) and mineral geometric factors (a). In this study, the argon diffusive parameters from published work (Grove and Harrison, 1996; Harrison 1981; Harrison et al., 1985; Harrison et al., 2009; Scibiorski et al., 2015) were applied after careful comparison and examination of the dated minerals' chemical composition and crystallization conditions.

Theoretically, with Ar being progressively released, the step ages calculated via $^{40}Ar/^{39}Ar$ ratios should be equal within errors. Thus, whether a plateau is present or not is a good indicator of whether the sample has remained as a closed system. However, argon distribution within a mineral is not ideally homogenous and can be impacted by other factors. For example, the apparent argon ages dated from a grain centre and its boundary could be different due to argon concentration differences. To test different impacts on argon apparent ages, argon diffusion modelling, which allows simulating argon diffusion profiles in minerals, are usually used to clarify impacts by factors such as mineral reside time, cooling rate, gain size and PT condition (Wheeler, 1996; Lister; Skipton 2018; Warren et al., 2012a). Argon diffusion modelling is usually performed on the Diffrag (Wheeler, 1996), which is a finite-difference algorithm that simulates argon diffusion profiles and produces the apparent age profile under a given condition. The quantitative prediction of diffusion profile can thus be compared with a in-situ core-to-rim argon profils to investigate its P-T-t history. However, previous studies showed that the numerical models for mineral diffusion can be artificial due to mineral contamination (Jong 2009；Jong, 2012). For example, research shows that the earlier degassing of minor younger biotite inclusions in hornblende could produce apparent-loss age spectra, despite careful handpicking during the mineral separating stage (Jong, 2012). Thus, for non-plateau age spectrum, extra cautions need to be taken on the age interpretation through petrological observations.

2.3.2 Closure temperature calculation

For any specific sample, the argon closure temperature can be calculated using *Dodson* (1973)'s mathematical formulation:

$$T_c = \frac{Q/R}{\text{In}\left(\frac{ART_{ic}^2(D_0/a^2)}{Q(dT/dt)}\right)} \quad (2)$$

where Q is the activation energy, R the constant of perfect gases, A the geometric factor, T_{ic} the initial closure temperature value, D_0 the diffusion coefficient, a the effective diffusion radius, assumed as grain dimension of each mineral (radius for sphere and cylinder, and half-length for a plane sheet), and dT/dt the cooling rate.

As previously discussed, argon diffusive parameters can be determined by measuring argon concentration under different heating temperature. However, the single grains dated from this study were heated using a continuous laser for homogeneous heating, thus the partition coefficient and activation energy were not directed measured from this study. For hornblende, we use activation energy (64.1 ± 1.7 kcal/mol), diffusion coefficient ($0.024^{+0.053}_{-0.011}$ cm^2/s), and volume constant (55) from Harrison (1981) assuming a spherical geometry of dated grains. For muscovite, we use activation energy (63 ± 7 kcal/mol), diffusion coefficient ($2.3^{+70}_{-2.2}$ cm^2/s), and volume constant (55) from Harrison et al. (2009) assuming a spherical geometry of dated grains. For biotite, as the ^{40}Ar diffusivity increases with Fe content, we use the parameters for Fe-mica biotite, and chose activation energy (50.5 ± 2.2 kcal/mol), diffusion coefficient ($0.4^{+0.96}_{-0.28}$ cm^2/s), and volume constant (27) from Grove and Harrison. (1996) assuming a cylindrical geometry of dated grains.

Despite notable different initial closure temperatures were used in the literature, we chose the values summarised in Schaen et al. (2020), and take 320 ±10 °C for biotite (Harrison et al., 1985), 390 ±10 °C for muscovite (Harrison et al., 2009), and 510 ±10 °C for hornblende

(Harrison 1981) at the same effective diffusion dimension of 100 mm and cooling rate of 10 °C/m.y. The effective diffusion radius (a) was based on the grain sizes of the dated mineral. Specific parameter values for calculating the closure temperature of each sample are summarized in Table B.2.2 of Appendix B. The initial cooling rates (dT/dt) are assessed from the metamorphic stage to the time of mineral's closure temperature (as defined by Dodson, 1973).

2.3.3 Cooling rate calculation

Specific closure temperatures for hornblende, muscovite and biotite and their associated cooling ages were used to calculate cooling rates for different mineral pairs dated in this study within individual tectonic domains. The duration, magnitude, and rates of the rock cooling, thus, can be estimated and utilized to build crustal thermal model, and constrain spatial-temporal variations. Uncertainties while calculating the closure temperature and cooling rate were estimated using Monte Carlo simulation, with detailed explanation described below. In areas where closure temperature constraints for biotite are unavailable (for example the Sybella Domain, Mount Isa Inlier), the closure temperatures from previous single-grain argon dating (Spikings et al.., 2002) were recalculated and used.

2.3.4 Mount Calo simulation

Although specific parameters (e.g., A, R, E, D_0) were applied to the calculation the argon closure temperature, uncertainties associated with some of the parameters (E, D_0 and a) have also been taken into account via the Monte Carlo simulation method developed by Scibiorski et al. (2015). This approach minimizes error-correlation in closure temperature estimation and cooling rate calculation by taking the cooling ages (with errors) of paired minerals and closure temperature ranges into consideration. Each Monte Carlo simulation involved 10,000 trials on the Microsoft Excel add-on program Quantum XL (SigmaZone inc.), and the maximal range of possible closure temperatures (or cooling rate) was estimated. The probability distributions and values of parameters used for the Monte Carlo Simulation are listed in Table B.2.3 of Appendix B. Representative probability histograms showing the distribution of each Monte Carlo simulation of either closure temperature or cooling rate are given in more detail in appendix Fig. C.3.8–3.9 and appendix Fig. D.4.2–4.3, respectively. Average closure temperatures estimated for hornblende, muscovite and biotite in our samples are 518 ± 53 °C, 405 ± 49 °C, and 329 ± 57 °C (2σ). The occasional right-tailed skew of the cooling rate histograms is due to the large ranges of mathematically calculated cooling rates by Monte Carlo simulation.

2.4 Geophysical data acquisition and filtering

2.4.1 Aeromagnetic and gravity data acquisition and process

The publicly available, high-resolution airborne aeromagnetic and gravity data from this study cover an area of ~785,700 km^2, and were merged by the Geological Survey of Queensland from individual State, Federal government, open range and multi-client surveys (Greenwood et al., 2018; Roger, 2014; https://geoscience.data.qld.gov.au). The data have been levelled to account for variations in line spacing, direction and flight height using data from the Australia Wide Airborne Geophysical Survey (AWAGS). Small offsets occur related to levelling at the regional scale, but do not pose a problem for our investigation.

Filtering of the acquired geophysical grids had been conducted by the Geological Survey of Queensland and this study to enhance the geophysical signals and resolve source bodies at different crustal levels. The total magnetic intensity (TMI) grid was reduced-to-magnetic-pole (RTP) (Geological Survey of Queensland; Greenwood et al., 2018), using a background field value of 50696 nT, an inclination of –50.56° and declination of 6.11°, to reduce dipole effect and bring the anomalies directly over their geological sources. The gravity data were corrected to reduces free-air correction and produce Bouguer gravity grid, showing gravity anomalies that are more representative of local geology (Geological Survey of Queensland; Roger, 2014). Upward continuation, which calculates the expected potential field measurement at an arbitrary distance (in this case 10 km) above the surface, is applied to RTP magnetic data to attenuate the subsurface wavelength (e.g., Blakely, 1995) and image the basement anomaly signature. We applied a low pass filter to the Bouguer gravity grid to remove subsurface high frequency and short wavelength responses and intensity geophysical signals from buried source bodies. Data processing and filtering were conducted via Geosoft Oasis montaj®, which allows visualizing multiple superimposed datasets for integrated spatial analysis. The upward continued aeromagnetic image is projected as an 80% transparent color scale intensity layer overlying the regional RTP aeromagnetic image to facilitate data interpretation.

2.4.2 Seismic data data acquisition and processing

The publicly available, seismic data used in this study (http://www.ga.gov.au/about/projects/resources/seismic/qld-datasets) was acquired from two reflection surveys, including the L138 Mount Isa survey in 1994 and the L184 Isa-Georgetown survey in 2007. The L138 Mount Isa survey was conducted by the Australian Geological Survey Organization under the auspices of the Australian Geodynamics Cooperative Research Centre (Goleby et al., 1996; MacCready et al., 1998), and the L184 survey was conducted in a collaborative program involving Australian Government's Onshore Energy Security Programme, the Queensland Government's smart mining and Smart Exploration initiatives and Auscope (Korsch et al., 2012; Spampinato et al., 2015). The L138 seismic data were acquired along two seismic lines (94MTI-01 and 94MTI-02) using explosives as an energy source and a 120 channels array, with the shot interval of 240 m (MacCready et al., 1998). The L184 seismic survey was acquired along two lines (07GA-IG1 and 07GA-IG2), using three Hemi-60 (60 000 lb) peak force vibrators as the energy source (Korsch et al., 2012), with an 80 m vibration point interval. Two-D seismic reflective data of line 94MTI-01 was collected with a total length of 255 km at 20 s two-way travel time (TWT). The seismic reflective data for line of 94MTI-02 was collected at a total length of 32 km. For the line 07GA-IG1 and 07GA-IG2, the seismic traverse lengths are 440 km and 240 km, respectively. CDP lines used for geological interpretation are 10-fold for line 94MTI-01 in the L138 survey (Goleby et al., 1996), 60-fold for line 07GA-IG1, and 75-fold for line 07GA-IG2 in the L184 survey (Korsch et al., 2012). Seismic sections were grid referenced to AGD84, AMG Zone 54, and displayed assuming an average crustal velocity of 6 km s^{-1} at a vertical to horizontal scale of 1:4. More details about the seismic survey and associate experiments parameters are provided in Goleby et al. (1996) and Jones et al. (2009).

In this study, we chose three most extended E–W to NE–SW seismic transects (94MTI-01, 07GA-IG1, and 07GA-IG) across the Mount Isa and Georgetown inliers to best image the crustal architectures of the Proterozoic orogens in NE Australia. Seismic data were optimized using Schlumberger Petrel E&P to amplify the reflective signals. To further aid visualization and interpretation at large-scale, seismic images were uploaded into the tile display at HIVE (Hub for Immersive Visualisation and eResearch), Curtin University, and displayed on an array of 12 full-HD LCD panels at a resolution of 24 million active pixels.

2.5 References

Blakely, R.J., 1995. Potential Theory in Gravity and Magnetic Applications. Cambridge University Press, New York.

Dodson, M. H. (1973), Closure temperature in cooling geochronological and petrological systems, Contributions to Mineralogy and Petrology, 40(3), 259-274.

Greenwood, M., 2018. Queensland Digital Exploration Reports System (QDEX).

Goleby, B.R., Drummond, B.J. and MacCready, T., (1996). The Mount Isa Geodynamic Transect—the deep seismic reflection profile south of Mount Isa and Cloncurry. *AGSO Research Newsletter*, *24*, pp.6-8.

Grove, M., & T. M. Harrison (1996), ^{40}Ar* diffusion in Fe-rich biotite, *American Mineralogist*, *81*(7-8), 940-951.

Hansma, J., E. Tohver, C. Schrank, F. Jourdan, & D. Adams (2016), The timing of the Cape Orogeny: New 40 Ar/ 39 Ar age constraints on deformation and cooling of the Cape Fold Belt, South Africa, *Gondwana Research*, *32*, 122-137.

Harrison, T. M. (1981), Diffusion of ^{40}Ar in hornblende, *Contributions to Mineralogy & Petrology*, *78*(3), 324-331.

Harrison, T. M., I. Duncan, & I. McDougall (1985), Diffusion of ^{40}Ar in biotite: Temperature, pressure and compositional effects, *Geochimica et Cosmochimica Acta*, *49*(11), 2461-2468. http://doi.org/10.1016/0016-7037(85)90246-7.

Harrison, T. M., J. Célérier, A. B. Aikman, J. Hermann, & M. T. Heizler (2009), Diffusion of ^{40}Ar in muscovite, *Geochimica et Cosmochimica Acta*, *73*(4), 1039-1051.

Jones, L., Maher, J., Costelloe, R., Holzschuh, J., Nakamura, A., Saygin, E., (2009). 2007 Isa-Georgetown-Charters towers seismic survey – acquisition and processing. *Australian Institute of Geoscientists Bulletin 49,* 149–152.

Koppers, A. A. P. (2002), ArArCALC - software for Ar-40/Ar-39 age calculations, *Computers & Geosciences*, *28*(5), 605-619.

Korsch, R. J., D. L. Huston, R. A. Henderson, R. S. Blewett, I. W. Withnall, C. L. Fergusson, W. J. Collins, E. Saygin, N. Kositcin, A. J. Meixner, R. Chopping, P. A. Henson, D. C. Champion, L. J. Hutton, R. Wormald, J. Holzschuh, and R. D. Costelloe (2012), Crustal architecture and geodynamics of North Queensland, Australia: Insights from deep seismic reflection profiling, Tectonophysics, 572-573, 76-99.

Lee, J. Y., K. Marti, J. P. Severinghaus, K. Kawamura, H. S. Yoo, J. B. Lee, & J. S. Kim (2006), A redetermination of the isotopic abundances of atmospheric Ar, *Geochimica et Cosmochimica Acta*, *70*(17), 4507-4512.

Li, J. Y., Pourteau, A., Li, Z.-X., Jourdan, F., Nordsvan, A. R., Collins, W. J., & Volante, S. 2020, Heterogeneous exhumation of the Mount Isa orogen in NE Australia after 1.6 Ga Nuna assembly: new high-precision 40Ar/39Ar thermochronological constraints, Tectonics, 10.1029/2020TC006129

MacCready, T. (2006), Structural cross-section based on the Mt Isa deep seismic transect, Australian Journal of Earth Sciences, 53(1), 5-26.

Renne, P. R., G. Balco, K. R. Ludwig, R. Mundil, & K. Min (2011), Response to the comment by W.H. Schwarz et al. on "Joint determination of K-40 decay constants and Ar-40*/K-40 for the Fish Canyon sanidine standard, and improved accuracy for Ar-40/Ar-39 geochronology" by PR Renne et al. (2010), Geochimica Et Cosmochimica Acta, 75(17), 5097-5100.

Roger, C., 2014. Queensland Digital Exploration Reports System (QDEX).

Scibiorski, E., E. Tohver, & F. Jourdan (2015), Rapid cooling and exhumation in the western part of the Mesoproterozoic Albany-Fraser Orogen, Western Australia, *Precambrian Research*, *265*, 232-248.

Sigurgeirsson, T. (1962). Age dating of young basalts with the potassium argon method. *Unpublished Report Physics Laboratory, University of Iceland (in Icelandic (English translation by L. Kristjansson, University of Iceland, 1973))*.

Spikings, R. A., D. A. Foster, B. P. Kohn, & G. S. Lister (2002), Post-orogenic (< 1500 Ma) thermal history of the Palaeo-Mesoproterozoic, Mt. Isa province, NE Australia, Tectonophysics, 349(1-4), 327-365.

Appendix B:
Supplementary materials to Chapter 2

Attached at the end of the thesis.

Chapter 3

Heterogeneous exhumation of the Mount Isa orogen in NE Australia after 1.6 Ga Nuna assembly: new high-precision $^{40}Ar/^{39}Ar$ thermochronological constraints

This chapter was published as:

Li, J., Pourteau, A., Li, Z. X., Jourdan, F., Nordsvan, A. R., Collins, W. J. & Volante, S. (2020) Heterogeneous Exhumation of the Mount Isa Orogen in NE Australia After 1.6 Ga Nuna Assembly: New High-Precision $^{40}Ar/^{39}Ar$ Thermochronological Constraints. *Tectonics*, 39(12), e2020TC006129.

but minor edits were made here to accommodate thesis examiners' comments and edits.

Abstract

The ca. 1.60 Ga Isan Orogeny in NE Australia has been ascribed to the collision of Australia and Laurentia (North America), marking the final assembly of the Proterozoic supercontinent Nuna. However, details regarding the tectonic evolution of the orogen remain poorly constrained. To investigate the late- to post-orogenic thermal evolution and exhumation history, $^{40}Ar/^{39}Ar$ dating was conducted on hornblende, muscovite, and biotite in the Mount Isa Inlier, NE Australia, where intense crustal imbrication occurred during the Proterozoic continental collision. Published thermochronological results were recalculated using the current decay constant. Petrological examination and calculation of sample-specific $^{40}Ar/^{39}Ar$ closure temperatures and cooling rates were used to reconstruct the pressure-temperature evolution of individual structural domains. Diachronous cooling histories are revealed between the western, central and eastern belts, of the Mount Isa Inlier, over a temperature range of ~525 to 330 °C, mainly between 1.53 and 1.48 Ga. Contrasting cooling across post-metamorphic fault zones records the reactivation of inherited normal (i.e., early basinal) and reverse (i.e., orogenic) faults. Estimated exhumation rates are generally low (<~0.5 mm yr^{-1}), consistent with modest local relief of <~1000 m which is comparable to modern analogs, and suggest a 'soft' collision with limited crust thickening. Exhumation shortly following orogenesis was contemporaneous with felsic magmatism (1.55–1.48 Ga) in the eastern belt. Magmatism transitioning from trondhjemitic to A-type granitoids over this period suggests progressive heating of the orogen

base, which is interpreted to have been caused by lower crust delamination. The thermochronological data reveal a regionally heterogeneous exhumation history controlled by orogenic collapse and extensional faulting following the final assembly of the supercontinent Nuna.

3.1 Introduction

Despite the period of global orogenesis between ca. 2.10 and 1.80 Ga, the supercontinent Nuna (also known as Columbia; Evans & Mitchell, 2011; Evans et al., 2016; Rogers & Santosh, 2002; Zhang et al., 2012; Zhao et al., 2002) was not completely assembled until the juxtaposition of Australia with Laurentia (North America) at ca. 1.60 Ga (Fig. 3.1a) (Betts et al., 2016; Kirscher et al., 2019, 2020; Nordsvan et al., 2018; Pehrsson et al., 2016; Pisarevsky et al., 2014). In western Laurentia, this final Nuna amalgamation event was recorded by the Racklan and Forward orogenies (Furlanetto et al., 2013; Thorkelson et al., 2005). In northeast Australia coeval orogenesis was recorded by the Isan and Jana orogenies of the Mount Isa and Georgetown inliers (Fig. 3.1b), respectively (Betts et al., 2008; Pourteau et al., 2018; Volante et al., 2020a, b; Withnall & Hutton, 2013).

In the Mount Isa Inlier (Fig. 3.1), the Isan Orogeny resulted in large-scale crustal imbrication and regional metamorphism characterised by high thermobaric gradients (Abu Sharib & Sanislav, 2013; Bell & Rubenach, 1983; MacCready, 2006; Page & Bell, 1986), atypical of modern-style continental collision. It is generally thought that supercontinent amalgamation involves large-scale orogenesis representing the closure of wide oceans event (Brown, 2007; Johnson et al., 2012). However, the collisional processes during the Isan Orogeny remain cryptic due to a general lack of clearly diagnostic plate-boundary features such as: (1) exposed ophiolites or accretionary complexes, (2) pre-collisional arc magmatism, and (3) high-pressure metamorphic rocks reflecting significant crustal thickening (Foster & Rubenach, 2006; Pourteau et al., 2018). Nevertheless, recent investigations of sedimentary provenance (Nordsvan et al*.*, 2018) and metamorphic record (Pourteau et al., 2018) suggest that the Georgetown Inlier of NE Australia might represent part of an allochthonous terrane that collided with the North Australia Craton during the Isan Orogeny. The exact nature of this collisional event remains ambiguous.

Understanding tectonic processes during continental collision requires detailed knowledge of the timing and duration of the associated deformation, metamorphism and crustal exhumation

(Johnson et al., 2012; Kearey et al., 2009). Isotopic dating techniques that are sensitive to temperature and cooling rate have the potential to date thermal events and constrain cooling history. Such thermal records can be linked to exhumation histories, and thus provide insights into orogenic and crustal evolution (McDougall & Harrison 1999, Skipton et al., 2017, Stübner et al., 2018). In this study, high-precision $^{40}Ar/^{39}Ar$ thermochronology from igneous and metamorphic rocks from the Mount Isa Inlier are used to decipher the cooling history associated with the Isan Orogeny. Sampling was conducted along an E–W corridor (transect A–A' in Fig. 3.1) across different crustal domains of the inlier. Thermochronological results, combined with the metamorphic and magmatic records, are used to reconstruct and compare the cooling history across different crustal domains. This enables us to discuss about the kinematics of post-orogenic faulting and the driving mechanism of the post-orogenic crustal exhumation.

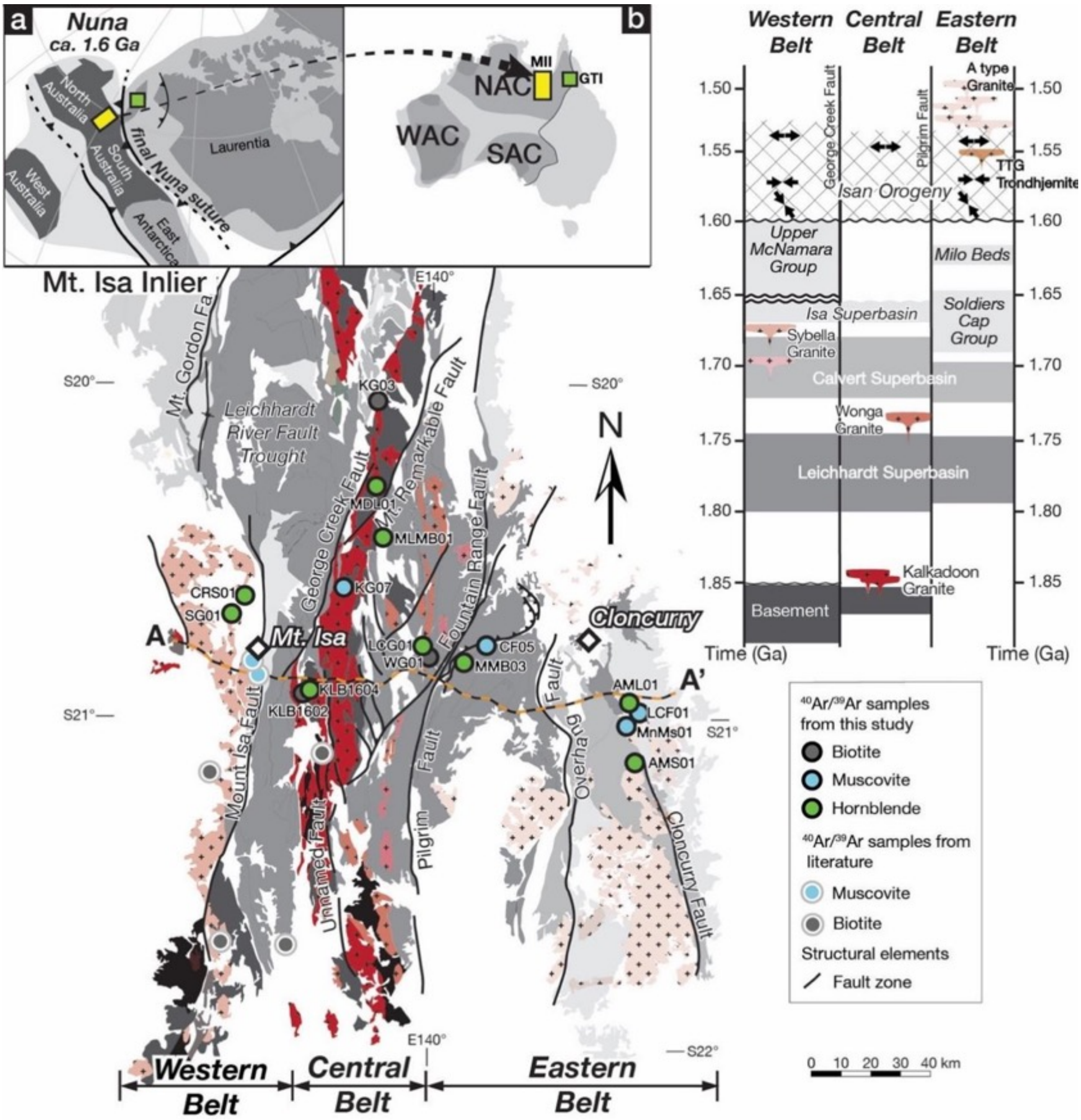

Fig. 3.1: Simplified lithological map of the Mount Isa Inlier showing the successive stratigraphic packages (or "superbasins"), the main fault zones, $^{40}Ar/^{39}Ar$ sample locations from this study and selective results from literature (relative selective criteria is described in section 2.24 and 3.3.2.). Transect A–A' shows the trace of Geoscience Australia geophysical imaging profile 94MTI-1. Inset a: Palaeogeographic reconstruction of the NE Australia at ca. 1.60 Ga (Pourteau et al., 2018) showing the inferred location of the study area (yellow box) and Georgetown Inlier (green box) along the final Nuna suture zone. Inset b: Location of the study area to the Australian cratons. NAC, North Australian Craton;

WAC, West Australian Craton; SAC, South Australian Craton, MII, Mount Isa Inlier; GTI, Georgetown Inlier.

3.2 Geological setting

3.2.1 Regional geology

The Mount Isa Inlier of NE Australia consists of high-grade metamorphic and crystalline basement rocks (the >1.85 Ga Kalkadoon–Leichhardt Complex; Blake, 1987; Etheridge et al., 1987) that are overlain by three successive superbasins including the ca. 1.8–1.74 Ga Leichhardt Superbasin, the ca. 1.73–1.69 Ga Calvert Superbasin, and the ca. 1.67–1.58 Ga Isa Superbasin (Betts et al., 2006; Blake, 1987; Foster & Austin, 2008; Jackson et al., 2000; Neumann et al., 2006). The Inlier has been subjected to poly-phase shortening, widespread, generally low-pressure metamorphism, and syn- to post-orogenic magmatism at ca. 1.60–1.50 Ga (Abu Sharib & Sanislav, 2013; Betts, 1999; Mark, 2001; Page, 1983; Reinhardt, 1992b; Sayab, 2006, 2009; Wyborn, 1998). These events have been collectively ascribed to the Isan Orogeny (Bell et al., 1992), marking the collision between NE Australia and NW Laurentia (Betts et al., 2006; Furlanetto et al., 2013; Gibson et al., 2018; Pourteau et al., 2018). The Mount Isa Inlier has been subdivided into 15 fault bound domains (Withnall & Hutton, 2013; 11 of them are shown in Fig. 3.2) based on their discrete sedimentary records and geophysical characteristics. For simplicity, the Mount Isa Inlier can also be divided into three major belts (Day et al., 1983) (Fig. 3.1) separated by major N–S to NE–SW major faults: the western belt, west of the George Creek and Mount Isa faults; the eastern belt, east of the Fountain Range and Pilgrim faults; and the intervening central belt.

In the western belt, the Leichhardt Superbasin silici-clastic, and mafic volcanic rocks formed in a N–S-striking rift (Bain et al., 1992; Jackson et al., 2000; O'Dea et al., 1997) and were subsequently folded ca. 1.73 Ga (Blaikie et al., 2017; Jackson et al., 2000). Locally, these rocks are overlain by bimodal volcanics and fluvial to shallow-marine sedimentary rocks of the Calvert Superbasin (Derrick, 1982; Gibson et al., 2008; Jackson & Southgate, 2000; O'Dea et al., 1997), which are in turn overlain by the ca. 1.67–1.59 Ga carbonaceous and clastic sandstones of the Isa Superbasin (Betts & Lister, 2001; Betts et al., 1998; Southgate et al., 2000). The ca. 1.66 Ga Sybella batholith intruded the basement and the Leichardt succession in the Sybella Domain at shallow crustal levels (Connors & Page, 1995; Gibson et al., 2008; Page & Bell, 1986), causing contact metamorphism that locally reached amphibolite facies

(Blenkinsop, 2005). The Mount Isa Fault zone, which separates the Sybella and Leichhardt River domains, marks a significant metamorphic boundary, with generally greenschist-facies rocks to the east and amphibolite-facies rocks to the west (Foster & Rubenach, 2006; Rubenach, 1992). Regional metamorphism along the western flank of the Mount Isa Fault zone was dated with garnet Nd-Sm at ca. 1575 Ma (Duncan et al., 2006; Hand & Rubatto, 2002).

The central belt exposes high-grade metamorphic and crystalline basement rocks on the western horst (the >1.85 Ga Kalkadoon-Leichhardt Complex; Blake, 1987; Etheridge et al., 1987), which are overlain by the ca. 1.79 Ga bimodal volcanic rocks in a graben along the eastern margin (Bain et al., 1992; Jackson et al., 2000). The graben is filled with Leichhardt Superbasin siliciclastic fluvial to shallow marine sediments associated with NW–SE extension (Eriksson et al., 1994; Jackson et al., 2000; Neumann et al., 2009), which are in turn overlain locally by Calvert Superbasin shallow marine sandstones and Isa Superbasin dolomitic sandstones (Jackson et al., 2000; Page et al., 1997). At ca. 1.74–1.73 Ga, the granitic Wonga suite (with subordinate gabbro) intruded the eastern central belt along a N–S mid-crustal detachment zone (Gibson et al., 2008; Holcombe et al., 1991; Oliver et al., 1991; Pearson, 1992). Amphibolite facies contact metamorphism occurred under an elevated thermal regime during granite intrusion (Oliver et al., 1991). The central belt was folded during the Isan Orogeny, with metamorphism generally being of upper greenschist facies but up to upper amphibolite facies in the Mary Kathleen Domain (Foster, 2003; Foster & Rubenach, 2006; Hand & Rubatto, 2002; Reinhardt, 1992a).

In the eastern belt, the Leichhardt Superbasin succession contains ca. 1.76–1.74 Ga bimodal felsic and mafic volcanics, sandstone, and carbonate rocks (Beardsmore et al., 1988; Foster & Austin, 2008; Jackson & Southgate, 2000; Page, 1998; Page & Sun, 1998), and was locally intruded by ca. 1.75–1.74 Ga granites (Page & Sun, 1998). The Leichhardt succession was overlain by shallow-marine sedimentary rocks of the Calvert Superbasin in the Doherty Domain (Gibson et al., 2012; Southgate et al., 2013), and, further east, by ca. 1.68–1.66 Ga quartzite, and basalt of the Soldiers Cap Group in the Cloncurry Domain, considered part of the Isan Superbasin (Foster & Austin, 2008; Page & Sun, 1998). The metamorphic grade varies across major faults and within individual domains (Foster & Rubenach, 2006; Sayab, 2006). To the west of the Cloncurry Fault, the metamorphism was in the lower greenschist facies in the Doherty and Mitakoodi domains (Foster & Rubenach, 2006) (Fig. 3.1). To the east, the Cloncurry Domain exhibits greenschist to upper amphibolite facies metamorphic assemblages

(Fig. 3.2), with prograde garnet formed at ca. 1.60 Ga (Pourteau et al., 2018) and peak monazite at ca. 1.59–1.58 Ga (Giles & Nutman, 2002; Hand & Rubatto, 2002). At ca. 1.55 Ga, the eastern belt was intruded by a minor trondhjemite pluton (Mark, 2001; Page & Sun, 1998) near the Cloncurry Fault (Fig. 3.1), and by voluminous ca. 1.54–1.49 Ga A-type granite plutons of the Williams and Naraku batholiths (Mark, 2001; Pollard et al., 1998; Wyborn, 1998).

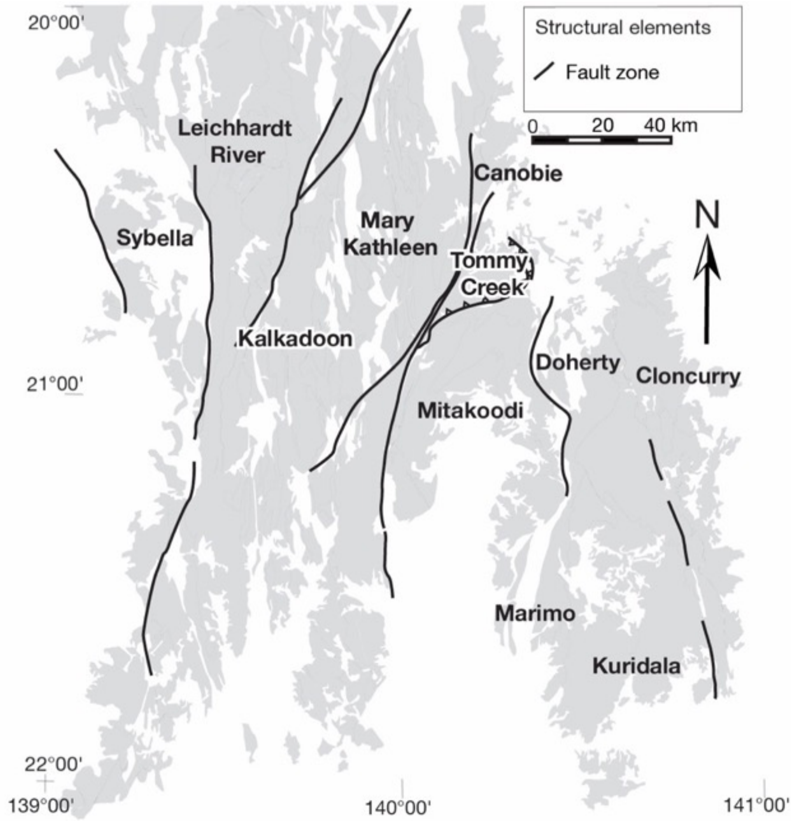

Fig. 3.2: Geological domains of the Mount Isa Inlier (Withnall & Hutton, 2013) separating by geophysical boundaries or major faults. Dark grey regions are exposed Proterozoic rock of the Mount Isa Inlier.

3.2.2 Orogenic evolution

Although the kinematic evolution of the Isan Orogeny is complex and controversial (Betts et al., 2006; Connors & Lister, 1995; Giles et al., 2006a; O'Dea & Lister, 1995; O'Dea et al., 1997b), most studies suggest that the orogeny is poly-phase and initiated at ca. 1.60 Ga with N–S crustal shortening in the western belt, reversing early E-W-trending normal basinal faults (Bell et al., 1992; Bell, 1983, 1991; Betts et al., 2006; Blake, 1987; Lister et al., 1999; O'Dea & Lister, 1995; O'Dea et al., 1997a). This early Isan orogenic phase was coeval with NW-directed folding and thrusting along mylonitic detachments in the eastern belt, with thin-skinned nappe stacking developed at low– to medium–P/T conditions (Betts et al., 2006; Giles et al., 2006; MacCready, 2006; O'Dea et al., 2006). Continuous deformation evolved into thick-skinned, E–W shortening, producing N–S-striking basement-rooted reverse faults and upright to steeply inclined folds at all scales (Betts et al., 2000; Blenkinsop et al., 2008; MacCready, 2006; MacCready et al., 1998; O'Dea et al., 2006). Although early geochronological studies suggest that the dominant E–W shortening event occurred ca. 1.55–1.53 Ga (Connors & Page, 1995; Foster & Rubenach, 2000; Page, 1983; Pollard & Perkins, 1997; Rubenach & Barker, 1998), more recent studies indicate that the metamorphism associated with the deformation occurred ca. 1.60–1.58 Ga (Abu Sharib & Sanislav, 2013; Duncan et al., 2006; Foster & Rubenach, 2006; Gauthier et al., 2001; Giles & Nutman, 2002; Hand & Rubatto, 2002; Pourteau et al., 2018). Following the Isan Orogeny, the regional deformation was interpreted to be transpressional (Lister et al., 1999; O'Dea et al., 1997b), with crustal shortening accommodated by conjugate NW-striking sinistral and NE-striking dextral faults along inherited early normal faults (Lister et al., 1999). The activity of these faults has not been precisely dated, but it certainly represents a post-orogenic deformational phase (Betts et al., 2006; Williams & Phillips, 1992).

3.3 Previous thermochronology results

3.3.1 State-of-the-art

Several geochronological studies have previously tackled the thermal history of the Mount Isa Inlier (Perkins & Wyborn, 1998; Richards et al., 1963; Spikings te al., 2001; 2002). Cooling age populations of ~1.77 Ga from the western belt and 1.45–1.40 Ga from the central belt, obtained via the K/Ar method on biotite and muscovite from ca. 1.86–1.67 Ga granitoids, were interpreted as an Isan Orogeny-related thermal event that affected only the central belt, which marked a 'metamorphic discontinuity' across the George Creek boundary fault (Richards et al., 1963). Given the analytical limitations of the K/Ar method (Kelley, 2002), subsequent studies applied the $^{40}Ar/^{39}Ar$ method on K-bearing minerals across the inlier (Perkins & Wyborn, 1998; Pollard & Perkins, 1997; Spikings et al., 2001, 2002). Hornblende and muscovite $^{40}Ar/^{39}Ar$ ages from igneous and metamorphic rocks showed an early phase of cooling at 1.45–1.39 Ga, and biotite and K-feldspar revealed a later stage cooling at 1.28–1.0 Ga (Spikings et al., 2001, 2002). The early phase of cooling was correlated with exhumation and shearing in the Arunta Inlier of central Australia and the Gawler Craton in South Australia. The later phase of cooling was interpreted to record thermal relaxation after the intrusion of ~1.11 Ga dolerite dykes in the central belt of the Mount Isa Inlier (Spikings et al., 2002). Hydrothermal hornblende and biotite associated with copper mineralization were dated using the $^{40}Ar/^{39}Ar$ method, and yielded a consistent age of ca. 1.53 Ga for both the western and eastern belts (Baker et al., 2001; Perkins et al., 1999). Syn-kinematic muscovite from the Cloncurry Fault (eastern belt) and the Mount Isa Fault zone (10 km southwest of the Mount Isa town) was dated at ca. 1.51 Ga (Baker et al., 2001) and ca. 1.40 Ga (Perkins et al., 1999), respectively. The youngest cooling event was dated by apatite fission-track thermochronology (i.e., below ~120 °C) at ca. 0.39 and 0.23 Ga, and is thought to be associated with far-field effects of orogenic events in central or eastern Australia (Spikings et al., 1997).

3.3.2 Re-assessment of available $^{40}Ar/^{39}Ar$ data

Crustal cooling within the Mount Isa inlier has been the subject of numerous studies, and is fundamental to our understanding of the Proterozoic crustal evolution of NE Australia. However, after plotting existing $^{40}Ar/^{39}Ar$ ages along an E–W transect across the Mount Isa Inlier (Fig. 3.3), these date show contrasting information: (1) a large apparent age gap of ~140 m.yr appears between peak metamorphism (at ca. 1.59 Ga) and the subsequent cooling event (mainly from ca. 1.45 Ga); (2) Hornblende with higher closure temperature of 500°C (Harrison, 1981) yielded contradictory younger dates than biotite (T ≈ 310 °C; Harrison et al., 1985) in places such as the Kalkadoon Domain (ca. 1453 Ma biotite vs. ca. 1419 Ma hornblende); (3) Individual structural domains yielded heterogeneous $^{40}Ar/^{39}Ar$ ages for the same mineral, e.g., biotite from the Sybella Domain yielding a range of dates between 1.12 Ga and 1.44 Ga (Fig. 3.3).

Several factors could explain contrasting $^{40}Ar/^{39}Ar$ ages produced by K-bearing minerals (Warren et al., 2012b; Uunk et al., 2018). As both K and Ar are mobile elements prone to redistribution by weathering or reheating, Ar loss is particularly common and would produce spuriously young ages if potassium remains fixed (Cerling et al., 1985; Clauer, 1981; Kelley, 1998), especially if the mineral experienced several thermal overprints or show multiple diffusion behaviour. Trapped Ar with $^{40}Ar/^{36}Ar$ greater than the modern atmospheric composition can be sequestered in melt or fluid inclusions from the mantle, magmas, or deep crustal fluids, and caused extraneous Ar effect (e.g., Lanphere and Dalrymple, 1976). Plutonic and volcanic rock that contain inherited argon antecrysts or xenocrysts could also incorporate pre-eruption/intrusion history of argon decay (Andersen et al., 2017; Chen et al., 1996; Singer et al., 1998; Renne et al., 2012). In addition, argon diffusive behaviour can have strongly influenced by pressure and temperature conditions. Inherited radiogenic Ar would not completely lost from the mineral if the peak pressure is ~1 GPa or higher, despite being above its closure temperature (Warren et al., 2012b, Schaen et al., 2020).

Thus, to fully acknowledge and utilize previous results, the published data, summarized in Table C.3.1, were fully evaluated and recalculated using an updated argon decay constant of 0.576 ± 0.002 E-10 1/a (Renne et al., 2011) with the recalculated age spectra presented in Fig. C.3.1–3.4 of Appendix C. We define reproduced plateau ages following the criteria of Schaen et al. (2020) and Hansma et al. (2016), that is a plateau must: (1) have a low scatter with a p-value >0.05, and encompass at least 70% of ^{39}Ar released (or 50% for an acceptable but less reliable age) with mini-plateaus over a minimum of three consecutive steps agreeing at 95% confidence level; (2) The majority of the plateau steps not showing ascending or descending slopes (Sharp and Renne, 2005). Other non-plateau scatter ages were also carefully examined, and possible causes discussed, including (i) heterogeneous, partial resetting of the argon isotopic system (see Warren et al., 2012), (ii) multiple argon diffusion domains leading to argon loss due to mineral lattice defects (through e.g., dissolution or exsolution; McDougall & Harrison, 1999), (iii) radiogenic argon released from pre-existing muscovite being trapped in the newly generated muscovite within the same rock, causing the excess argon effect (McDonald et al., 2018), and (iv) radiogenic ^{40}Ar displaced by hydrothermal fluids through chemical reactions (e.g., Miller et al., 1991).

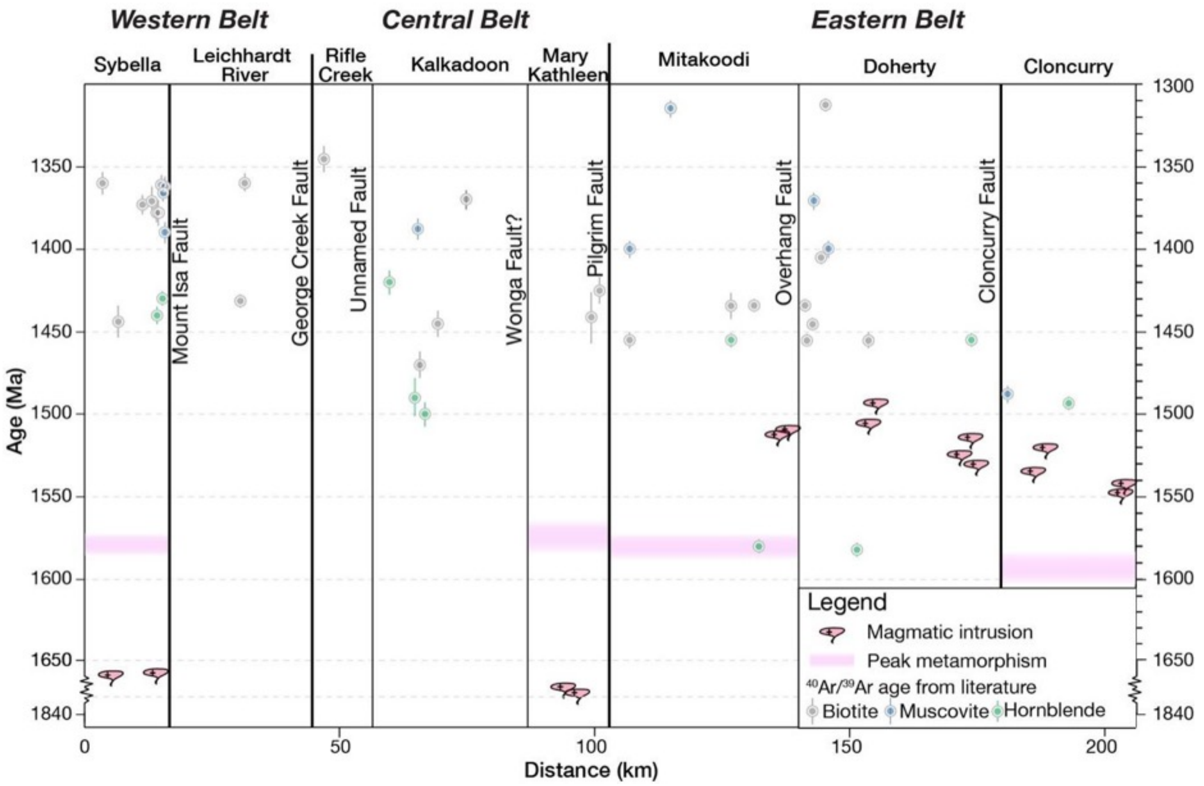

Fig. 3.3. Time vs distance plot of previously published $^{40}Ar/^{39}Ar$ ages along a W–E transect across the Mount Isa Inlier (line A–A' in Fig. 3.1) (Pollard & Perkins, 1997; Perkins & Wyborn, 1998; Spikings et al., 2001; 2002).

3.4 Methodology

3.4.1 Sample Strategy and Petrology

Sixteen samples were collected from an E–W transect aligned with the deep-seismic profile (Fig. 3.1: 94MTI-01; Geoscience Australia). Samples taken closest to the transect are for investigating E–W variations in the cooling record. Samples to the north or south of the profile are for detecting possible lateral variations within each domain. The sampling was optimized to better understand the timing, kinematics, and magnitudes of fault movement along major fault zones, and to compare the evolution of the crustal zones with various metamorphic grades. Detailed petrographic features are described in the section 3.5.1 with the outcrop and thin section photos provided in Figs. 3.5–3.7.

3.4.2 $^{40}Ar/^{39}Ar$ analysis

Selected sample grains were sent to irradiation before conducting $^{40}Ar/^{39}Ar$ analyses. After irradiation, a total of sixteen signal grains $^{40}Ar/^{39}Ar$ analyses were measured at the Western Australian Argon Isotope Facility at Curtin University. All the analyses were conducted on single-grain aliquots, which maximizes data accuracy as it enables determining ^{40}Ar concentrations directly within single grains and prevents the mixing of different age populations. Detailed $^{40}Ar/^{39}Ar$ thermochronology analysis methodology were summarized in Chapter 2 (section 2.3). A summary of dated sample lithologies, sample locations and $^{40}Ar/^{39}Ar$ analytical ages were listed in the Table B.2.1 of Appendix B. Ar isotope data corrected for blanks, mass discrimination, and radioactive decay can be found in the Table C.3.3 of Appendix.

In the closure temperature calculation, initial closure temperature value (T_{i_c}) refers to those published from argon diffusion experiments, i.e., 510 °C for hornblende (Harrison, 1981), 390 °C for muscovite (Harrison et al., 2009), and 320 °C for biotite (Harrison et al., 1985) at a cooling rate of 10 °C/Ma. The effective diffusion radius (a) was based on the grain sizes of the dated mineral. The initial cooling rates (dT/dt) are assessed from the peak metamorphic stage to the time of mineral's closure temperature (as defined by Dodson, 1973). Peak metamorphic ages were summarized from previous work (Gautier et al., 2001; Hand & Rubatto, 2002; Rubenach, 2008; Pourteau et al., 2018), and listed in Table C.3.2 of Appendix C. The peak temperature map (Fig. 3.4) was modified from Foster and Rubenach (2006) and references therein. Probability histograms of Monte Carlo simulation for the dated minerals' closure temperature calculation are given in the Fig. C.3.5 of Appendix C.

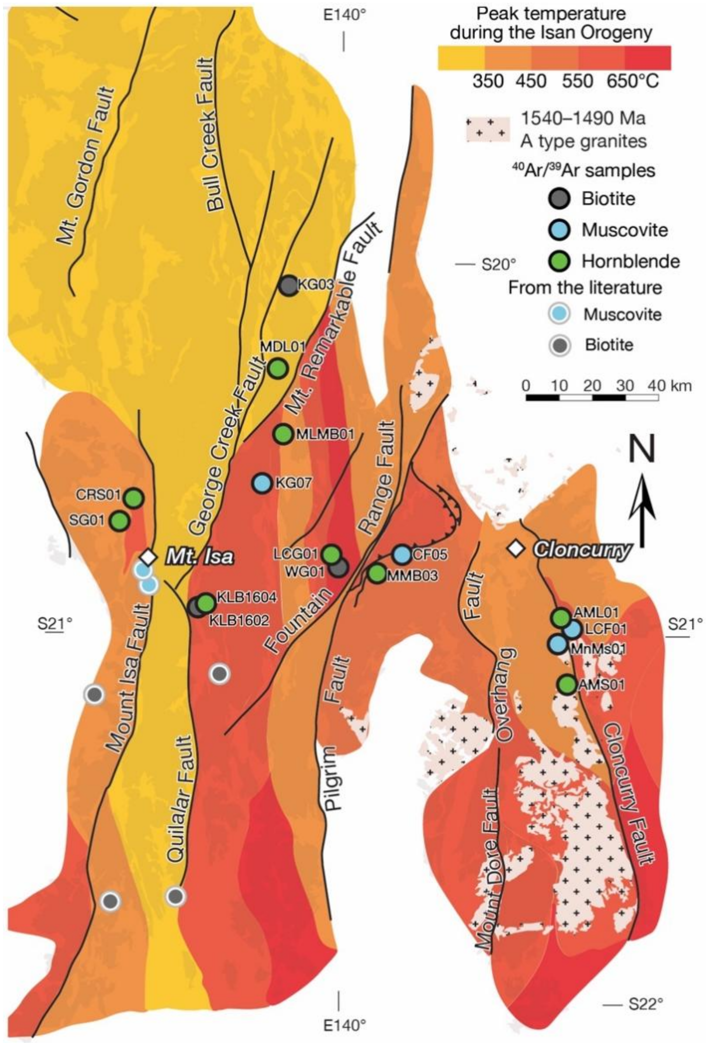

Fig. 3.4: Peak temperature map of the Mount Isa Inlier during the Isan Orogeny at ca. 1.59–1.57 Ga, modified from Foster & Rubenach (2006) after integrating estimated peak metamorphism temperature (Blenkinsop, 2005; Page & Sun, 1998; Gautier et al., 2001; Giles & Nutman, 2002; Hand & Rubatto, 2002; Rubenach et al., 2008; Pourteau et al., 2018).

3.4.3 Cooling rate

Specific closure temperatures for hornblende, muscovite and biotite were used to calculate cooling rates for different mineral pairs dated in this study within individual tectonic domains. Nine previously reported ages were selected following the age filtering criteria defined in section 2.24 and 3.3.2, and incorporated into Figs. 3.8–3.10, with the calculated cooling rates listed in Table 3.1 and plotted in a time vs distance diagram (Fig. 3.11). Uncertainties for the closure temperature and cooling rate calculations were estimated using Monte Carlo simulation, with the probability histograms showing the simulation results given in the Fig. C.3.6 of Appendix C.

3.5 Results

3.5.1 Petrography

Sample descriptions are organized broadly from west to east in their respective domains. Outcrop and thin section photos are provided in Figs. 3.5–3.7.

(1) Sybella Domain

Sample SG01 is a potassium-rich A-type granite (Fig. 3.5A & a) collected from the Sybella Batholith, west of the Mount Isa Fault zone (Fig. 3.1). This rock mainly comprises quartz, K-feldspar, plagioclase, biotite, amphibole, and accessory minerals including apatite and zircon. The granite is medium to coarse-grained and characterized by cm-sized K-feldspar phenocrysts with albite or oligoclase rims. The rock has a foliation that is defined by preferentially orientated amphibole, biotite, K-feldspar and quartz–opaque aggregates. The penetrative foliation identified in the Sybella Granite is parallel to both intrusive margins and the fabric in the country-rock. *Sample CRS01* is a foliated amphibolite (Fig. 3.5B & b) of the May Downs Gneiss from the country-rock of the Sybella Granite that was collected 5 km northeast of SG01 (Fig. 3.1). The sample comprises mainly amphibole, plagioclase, quartz, and minor biotite. A pervasive foliation fabric is defined by the preferred orientation of dark green amphibole, with aggregated plagioclase and quartz filled interstitially. Locally, euhedral light green amphibole grow at a high angle to the matrix foliation suggests that it is post-kinematic.

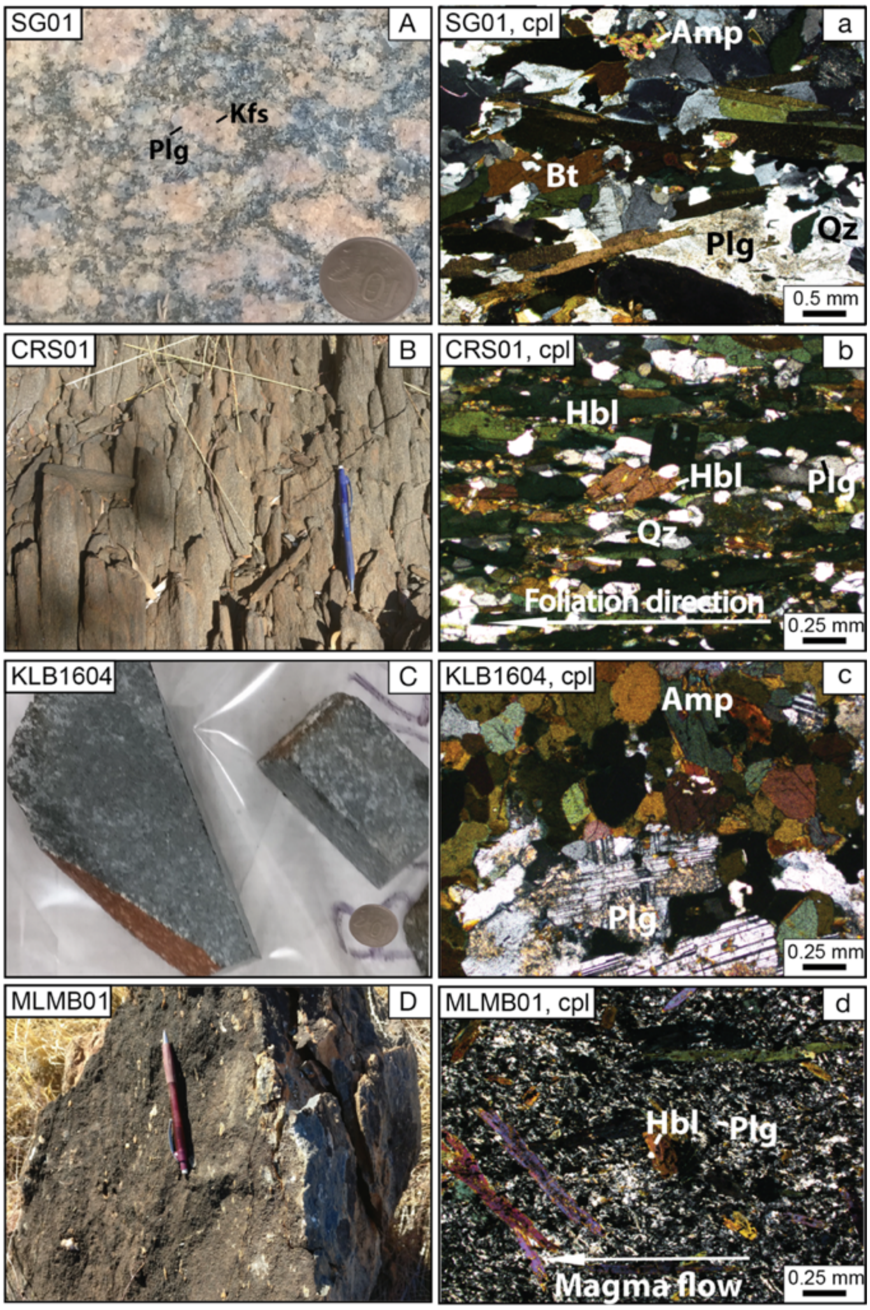

Fig. 3.5: (A & a) ca. 1.67 Ga Sybella Granite, Sybella Domain. Centimetre-sized K-feldspar phenocrysts presenting albite or oligoclase rims. (B & b) ca. 1.89 Ga amphibolite, May Downs Gneiss, Sybella Domain. Minor secondary light green amphibole grew over the dominant foliation defined by shape preferred orientation of green amphibole and plagioclase. (C & c) ca. 1.89 Ga Kurbayia Metamorphic amphibolite, Kalkadoon Domain. Minor overgrowth of light green amphibole rims around amphibole crystals. (D & d) ca. 1.79 Ga Magna Lynn metabasalt, Kalkadoon Domain. Oriented light green amphibole phenocrysts define volcanic flow texture in the groundmass of fine-grained plagioclase. Mineral abbreviations in Figs. 3.5–3.7 are followed by Whitney and Evans (2010). Qz = Quartz, Plg = Plagioclase, Kfs = K-feldspar, Bt = Biotite, Amp = Amphibole, Hbl = Hornblende, Ttn = Titanite, Ser = Sericite, Ep = Epidote. Cpl = Cross polar light.

(2) Kalkadoon Domain

Sample KLB1604 is an amphibolite (Fig. 3.5C & c) collected from the Kurbayia Metamorphic Complex in the Kalkadoon Domain (Fig. 3.1). The sample comprises millimetre-sized brown amphibole, plagioclase and minor quartz and ilmenite. Amphibole is subhedral, commonly dark brown and dark green, and shares straight contacts with plagioclase and quartz. Plagioclase are primarily euhedral with minor grains displaying subhedral crystal form. Locally, overgrowth of light green amphibole rims around amphibole crystals and fine-grained aggregates of sericite replacing plagioclase suggest overprinting. *Sample KLB1602* is a biotite-bearing gneiss collected from the Kurbayia Metamorphic Complex (Fig. 3.1), 0.5 km west of KLB1604. The sample comprises quartz, biotite, plagioclase and accessory apatite and zircon. It has a foliation that is defined by preferentially orientated biotite alternating with quartz-feldspathic layers. *Sample MLMB01* is a metabasalt (Fig. 3.5D & d) collected from the Magna Lynn Metabasalt, 10 km south of the Mount Remarkable Fault (Fig. 3.1). The sample is composed of oriented light green to dark blue prismatic amphibole phenocrysts and groundmass of fine-grained plagioclase and quartz-amphibole-opaque. The light green amphibole is slightly altered by chlorite, suggesting a low-grade greenschist-facies metamorphic overprint. *Sample KG03* is a medium to coarse-grained, biotite granite (Fig. 3.6A & a) from the Kalkadoon Supersuite (Fig. 3.1). The sample comprises coarse quartz, plagioclase, biotite and K-feldspar phenocrysts, rare hornblende, and accessory zircon, apatite, and monazite. The sample retains its primary igneous texture, with small bulging recrystallized subhedral quartz aggregates growing interstitially between primary igneous mineral phases, and to some extent, between microcracks.

(3) Mary Kathleen Domain

Sample LCG01 is a metagabbro (Fig. 3.6B & b) collected from the Lunch Creek Gabbro in the Mary Kathleen Domain (Fig. 3.1). The sample is composed of plagioclase, amphibole, quartz, biotite, and minor pyroxene. Pyroxene is locally preserved but mostly replaced by dark brown amphibole. Plagioclase is partially replaced by fine-grained aggregates of sericite, epidote and minor chlorite. Quartz grew interstitially between plagioclase and amphibole grains. *Sample WG01* is a hornblende–biotite-bearing granite (Fig. 3.6C & c) collected from the Wonga Suite, 3 km south of sample LCG01. The sample is composed of quartz, plagioclase, biotite, K-feldspar, hornblende, and accessory minerals including titanite and apatite. The sample has a well-foliated augen texture, with biotite-rich layers wrapping porphyroblasts of quartz aggregates. Subhedral quartz subgrains are found recrystallized in interstitial space, or within larger crystals in a polygonised texture.

Fig. 3.6: (A & a) ca. 1.86 Ga Kalkadoon Granite, Kalkadoon Domain. Minor recrystallised subhedral quartz aggregates growing interstitial between primary igneous mineral phases. (B & b) ca. 1.74 Ga Lunch Creek metagabbro, Mary Kathleen Domain. Pyroxene is locally preserved but largely replaced by dark brown amphibole. (C & c) ca. 1.74 Ga Wonga Granite, Mary Kathleen Domain. Subhedral quartz subgrains recrystallized in interstitial space, or within larger crystals or ribbon grains in a polygonized texture. (D & d) ca. 1.76 Ga Corella muscovite schist, Mitakoodi Domain. Euhedral biotite, muscovite and felsic-rich domains define the foliation.

(4) Mitakoodi Domain

Sample MMB03 is a foliated metabasalt collected from the Malbon Group in the Mitakoodi Domain (Fig. 3.1). It comprises millimetre-sized amphibole porphyroblasts in a matrix of prismatic euhedral amphibole, and elongated aggregates of plagioclase and quartz. Amphibole porphyroblasts are subhedral grains in dark green to brown colour. Plagioclase shows concentric zoning and is partially altered by sericite and carbonate. *Sample CF05* is a muscovite-schist (Fig. 3.6D & d) collected from the Malbon Group, 8 km northeast of MMB03. The sample comprises quartz, biotite, plagioclase, muscovite and accessory ilmenite. The dominant foliation is defined by alternating mica-rich layers, marked by preferred orientation of euhedral biotite, muscovite and felsic-rich domains (quartz+plagioclase).

(5) Doherty Domain

Sample AMS01 is a foliated metadolerite (Fig. 3.7A & a) collected from the Soldiers Cap Group in the Doherty Domain, west of the Cloncurry Fault (Fig. 3.1). The sample comprises mainly millimetre-sized amphibole, which are foliated along with mildly sericitized feldspar. Amphibole crystals are subhedral to anhedral grains of light brown to dark green colours, and have straight contacts with the surrounding plagioclase. A minor second generation of euhedral brown amphibole occurs along the foliation, indicating a later-stage thermal overprint. *Sample MnMs01* is a biotite-bearing schist (Fig. 3.7B & b) collected from the Mount Norna Quartzite, 10 km north of AMS01 (Fig. 3.1). The sample is strongly foliated with the pervasive fabric defined by shape preferred orientation of biotite and minor muscovite alternating with quartzo-feldspathic-rich domains. Quartz has undulose extinction, suggesting intra-crystalline deformation. The dominant foliation is interpreted to have formed during the Isan Orogeny, correlative with amphibolite facies metamorphism documented in the Snake Creek anticline (Rubenach & Barker, 1998; Sharib & Sanislav, 2013).

(6) Cloncurry Domain

Sample AML01 is an amphibolite (Fig. 3.7C & c) collected from the Snake Creek anticline, east of the Cloncurry Fault (Fig. 3.1). The sample comprises amphibole, plagioclase, minor relicts of clinopyroxene, rare orthopyroxene and minor interstitial quartz and magnetite. Primary dark green porphyritic amphibole occurs as centimetre-sized grains that have a decomposed core with corrosional relic texture. Plagioclase occurs as fine mm-scale grains with weak oscillatory zoning. Secondary light green amphiboles are millimetre-sized and euhedral, suggesting an overprint origin. *Sample LCF01* is a muscovite schist (Fig. 3.7D & d) collected from the Snake Creek anticline, 4 km southwest of AML01. The sample has a pervasive foliation defined by the alignment of euhedral muscovite and minor brown biotite, interlayered with flattened quartz grains.

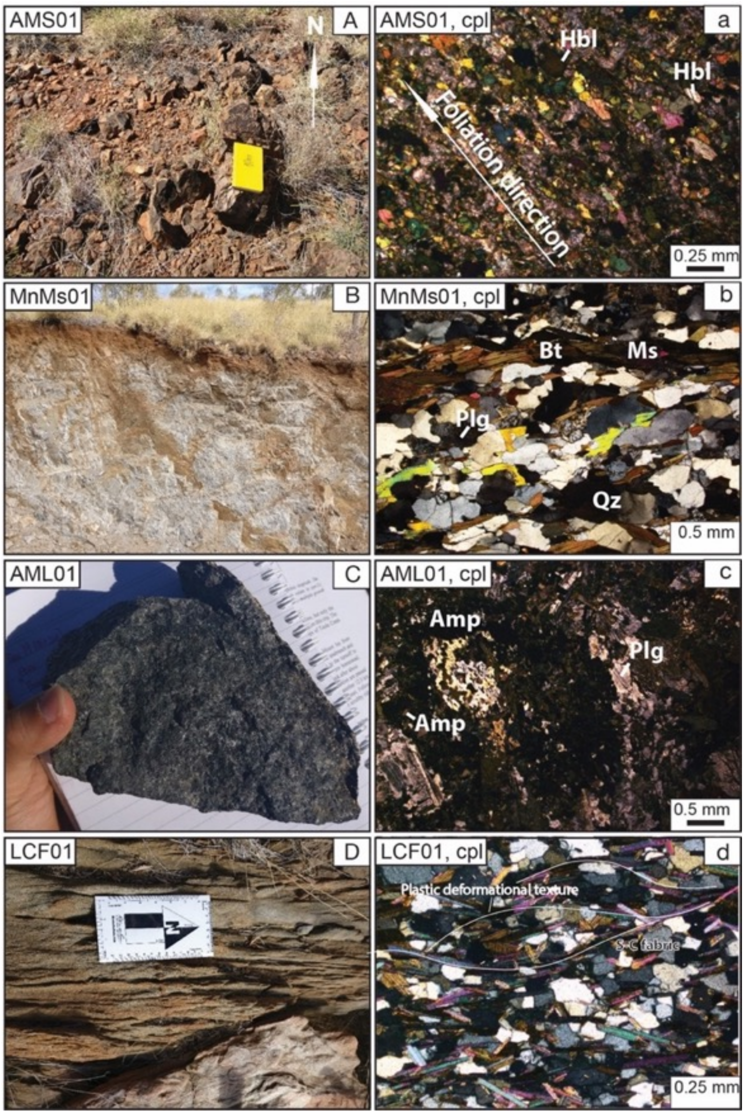

Fig. 3.7: (A & a) ca. 1.68 Ga Soldiers Cap amphibolite, Doherty Domain. Minor second generation of euhedral brown amphibole grew parallel to the dominant foliation. (B & b) ca. 1.67 Ga Mount Norna muscovite schist, Doherty Domain. Pervasive fabric is defined by orientated biotite and minor muscovite alternating with a quartzo-feldspathic-rich domain. (C & c) ca. 1.68 Ga Soldiers Cap amphibolite, Cloncurry Domain. Primary centimetre-sized porphyritic amphibole locally being replaced by secondary euhedral millimetre-sized light green amphibole. (D & d) ca. 1.66 Ga Llewellyn Creek muscovite schist, Cloncurry Domain. Planar fabric is defined by the alignment of euhedral muscovite and minor brown biotite.

3.5.2 $^{40}Ar/^{39}Ar$ ages

Sixteen analyses, including 9 hornblende, 4 muscovite, and 3 biotite single-grain aliquots, yielded flat ^{39}Ar release spectra (Figs. 3.8–3.10). These results were combined with the recalculated ages from previous studies to produce the most accurate $^{40}Ar/^{39}Ar$ thermochronological dataset available for this region.

(1) Western Belt

In the western belt, hornblende sample SG01 from the Sybella Granite yielded a plateau age of 1523 ± 7 Ma with 69% of ^{39}Ar released in the last six steps at a mean square weighted deviation (MSWD) value of 2.13 and a p-value of 0.06 (Fig. 3.8). The K/Ca shows a consistent ratio of 0.210 ± 0.006 over the plateau with low variation on each step, which indicates a homogenous signature of the dated mineral. Five kilometres northeast of SG01, from the country-rock of the Sybella granite, amphibole from sample CRS01 yielded a plateau age of 1505 ± 6 Ma (81.3% ^{39}Ar released; MSWD = 0.89, p=0.52) over 9 steps (Fig. 3.8). A previous study dated muscovite and biotite cooling ages from the Sybella granite and reported $^{40}Ar/^{39}Ar$ ages of ca. 1400 Ma and 1370 Ma, respectively (Spikings et al., 2002).

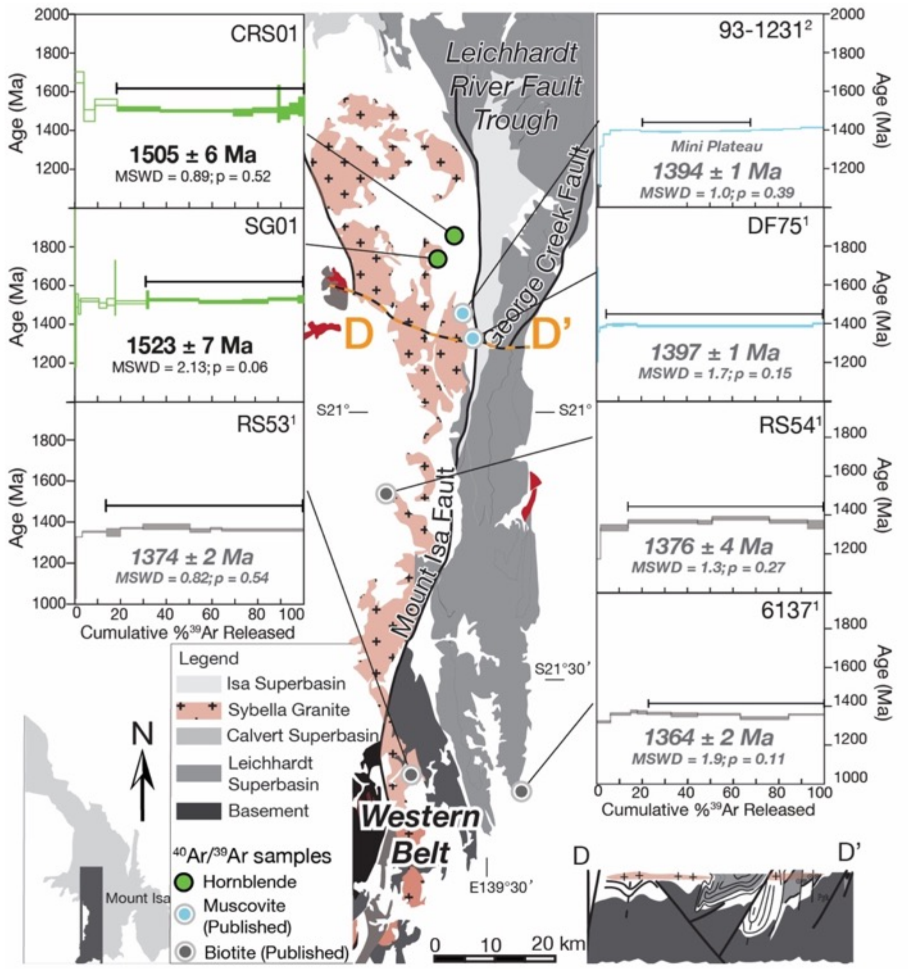

Fig. 3.8: Simplified lithological map and cross-section (modified after MacCready, 2006) of the western belt show sample locations and $^{40}Ar/^{39}Ar$ age spectra. Spectra with ages in light grey and italic are the $^{40}Ar/^{39}Ar$ results recalculated from the literature: 1 = Spikings et al. (2002); 2 = Perkins et al. (1999). Spectra with plateaus in green, blue, and dark grey are from this study.

(2) Central Belt

Of the 8 samples collected from the central belt of the Mount Isa Inlier, 4 hornblende, 3 biotite and 1 muscovite analyses gave robust $^{39}Ar/^{40}Ar$ ages (Fig. 3.9). The oldest cooling age was produced from hornblende in a migmatic amphibolite (KLB1604) of the Kalkadoon Domain (ca. 1.85 Ga high-grade metamorphic rock, Page & Williams, 1988), which yielded a plateau age of 1843 ± 6 Ma (74% of ^{39}Ar released at 10 steps; MSWD = 0.72, p=0.69). One kilometer to the west, biotite from a biotite gneiss (KLB1602) gave a plateau age of 1454 ± 5 Ma (91% of ^{39}Ar released at 10 steps; MSWD = 0.90, p=0.52). Further to the northeast, muscovite from the Kalkadoon granite (KG07) yielded a plateau age of 1490 ± 6 Ma (94% of ^{39}Ar released at 14 steps; MSWD = 0.28, p=0.99). Within the same domain, hornblende from metabasalt

MLMB01 yielded a plateau age of 1521 ± 11 Ma (100% of ^{39}Ar released at 8 steps; MSWD = 1.26, p=0.36). Across the Mount Remarkable Fault further north, hornblende from the metadolerite MDL01 yielded a similar age of 1527 ± 3 Ma (100% of ^{39}Ar released at 15 steps; MSWD = 0.32, p=0.1). Biotite from the ca. 1.86 Ga Kalkadoon granite (KG03), 15 km further north, yielded a plateau age of 1534 ± 5 Ma (90% of ^{39}Ar released at 9 steps; MSWD = 1.13, p=0.34). To the east, between the Pilgrim Fault and the Kalkadoon–Leichhardt basement (Fig. 3.6), hornblende from meta-gabbro (LCG01) in the Mary Kathleen Domain yielded a mini-plateau age of 1549 ± 10 Ma (66% of ^{39}Ar released at 6 steps; MSWD = 0.32, p=0.90), while biotite from a nearby Wonga Granite (WG01) produced a plateau age of 1489 ± 6 Ma (98% of ^{39}Ar released at 12 steps; MSWD = 0.54, p=0.89).

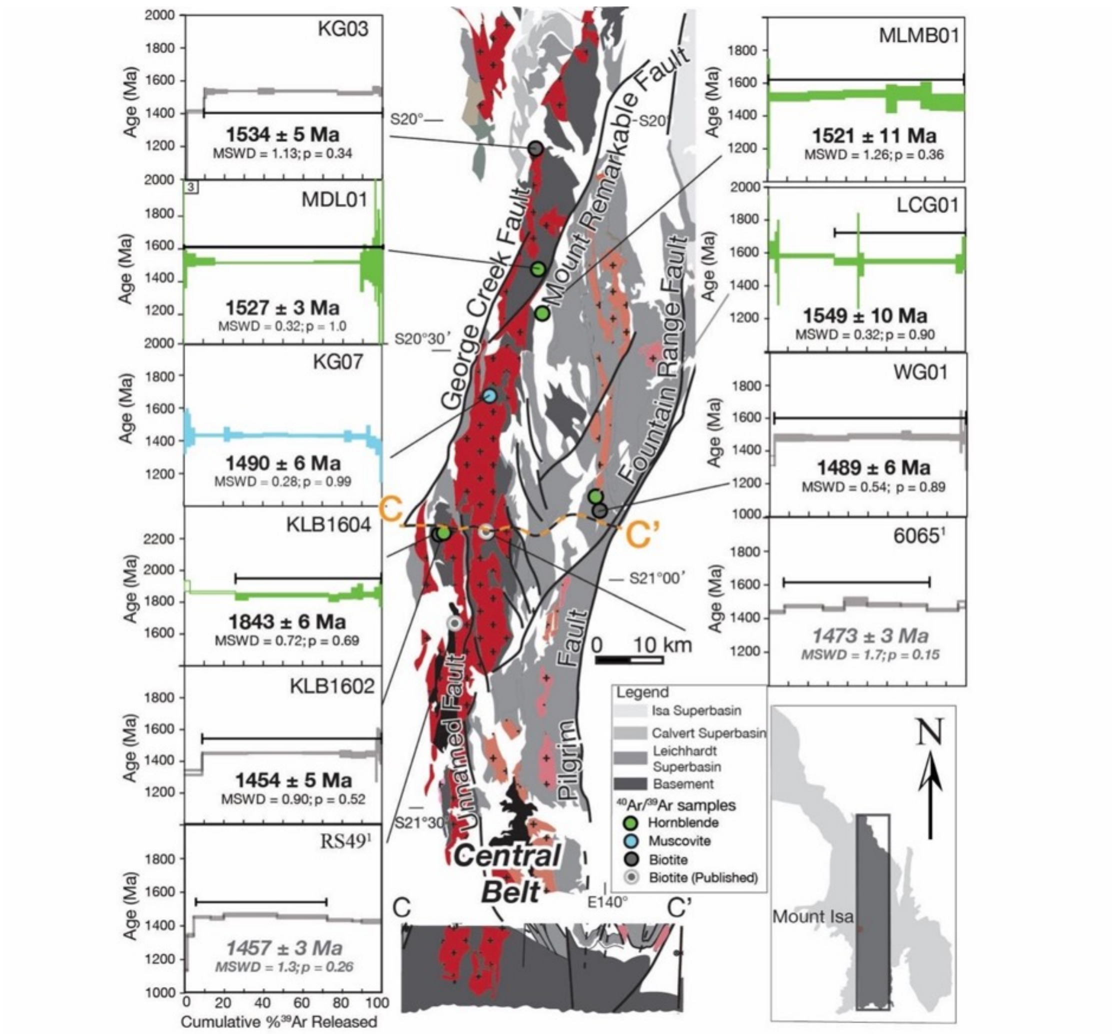

Fig. 3.9: Simplified lithological map and cross-section (modified after MacCready, 2006) of the central belt show sample locations and ^{40}Ar/^{39}Ar age spectra. Spectra with ages in light grey and italic are the ^{40}Ar/^{39}Ar results recalculated from the literature: 1 = Spikings et al. (2002). Spectra with ages in dark black and plateaus in green, blue and dark grey are from this study.

(3) Eastern Belt

In the eastern belt, 3 hornblende and 3 muscovite aliquots gave 6 robust $^{39}Ar/^{40}Ar$ ages (Fig. 3.10). In the western Mitakoodi Domain, hornblende from a metabasalt (MMB03) gave a plateau age of 1512 ± 5 Ma (84% of ^{39}Ar released at 10 steps; MSWD=0.49, p=0.88), while muscovite from nearby muscovite schist sample CF05 yielded a plateau age of 1474 ± 11 Ma (100.0% ^{39}Ar released at 4 steps; MSWD=1.82, p=0.14). Further east in the Doherty Domain, between the Cloncurry and Overhang faults (Fig. 3.10), a hornblende age of 1534 ± 8 Ma (93% ^{39}Ar released at 8 steps; MSWD=0.84, p=0.55) was obtained for amphibolite sample AMS01, and a muscovite age of 1479 ± 5 Ma (99% ^{39}Ar released at 16 steps; MSWD=1.1, p=0.35) for muscovite schist sample MnMs01. For comparison, hornblende from amphibolite (AML01) in the Cloncurry Domain, east of the Cloncurry Fault, produced a plateau age of 1504 ± 7 Ma (100% of ^{39}Ar released at 18 steps; MSWD=1.02, p=0.42), while muscovite from a nearby muscovite schist sample (LCF01) yielded an Argon plateau age of 1483 ± 6 Ma (100% of ^{39}Ar released at 14 steps; MSWD=0.5, p=0.93).

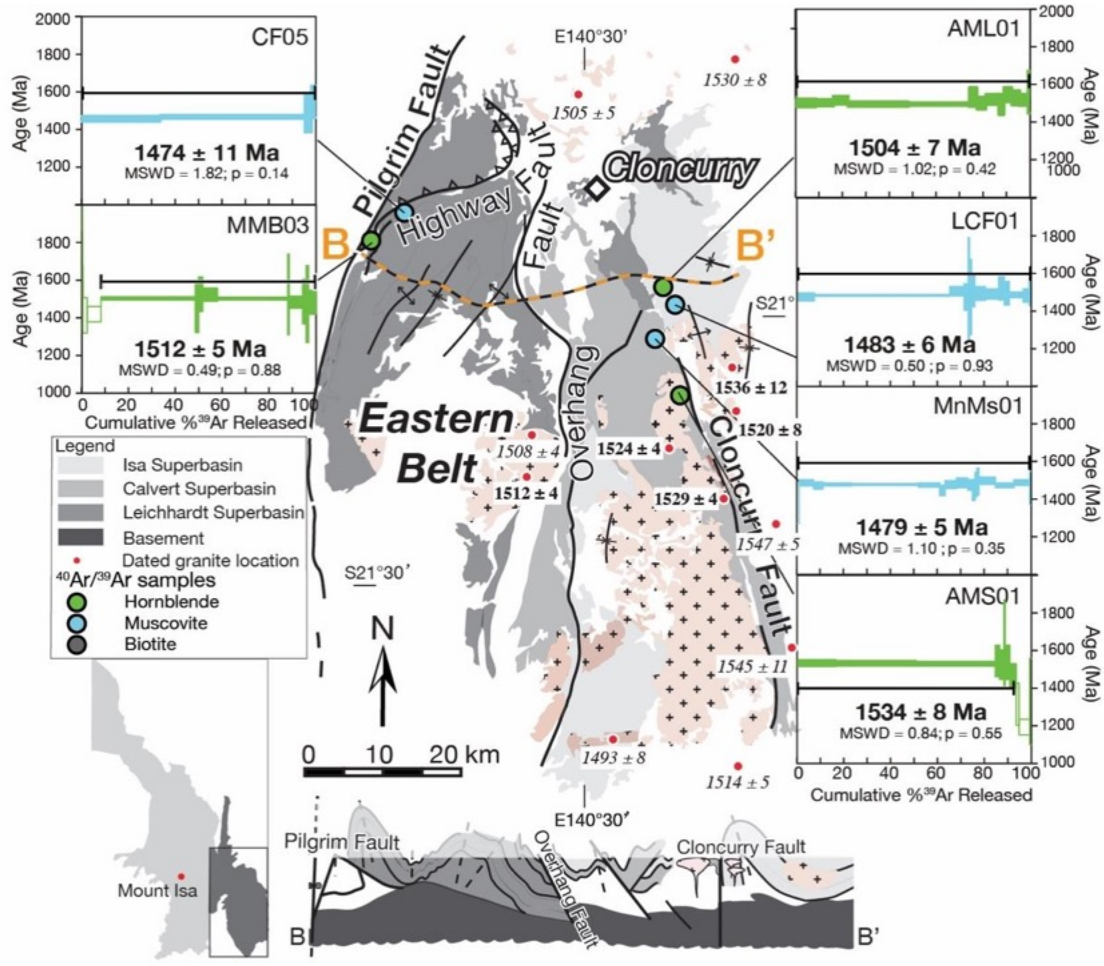

Fig. 3.10: Simplified lithological map and cross-section of the eastern belt (modified after MacCready, 2006) show $^{40}Ar/^{39}Ar$ age spectra and sample locations. Red dots represent the sample location of the ca. 1550 to 1490 Ma granites dated from the literature: ages in bold are from Pollard and McNaughton (1997), ages in italic are from Page and Sun (1998).

3.5.3 $^{40}Ar/^{39}Ar$ age interpretation

$^{40}Ar/^{39}Ar$ thermochronological dating is based on the assumptions that (1) all the radiogenic ^{40}Ar should be produced from the decay of ^{40}K, (2) the system remained in a closed system without being interrupted by hydrothermal fluids interactions, and (3) radiogenic ^{40}Ar residual will be completely degassed at conditions above the mineral's closure temperature. Thus, to justify if the $^{40}Ar/^{39}Ar$ ages reported in this study are consistent with the above assumption and represent mineral cooling ages, several factors need to be considered.

First, homogeneity of the dated samples has been examined using optical microscopy and scanning electron microscopy to avoid inclusions or intergrowth of other K-bearing mineral phases. Most selected minerals are homogenous and least weathered crystals, thus, should not have potassium addition and extraneous Ar effect (e.g., Lanphere and Dalrymple, 1976). Although minor alteration was observed from Lunch Creek Gabbro sample LCG01 and Mitakoodi metabasalt sample MMB03 (see section 3.5.1), the selected hornblende aliquots were further leached in diluted HF and rinsed with distilled water in an ultrasonic cleaner to remove impurities.

Second, data inspection. Theoretically, with Ar being progressively released, the step ages calculated via $^{40}Ar/^{39}Ar$ ratios should be equal within errors. Thus, whether a plateau is present or not is a good indicator of if the sample remained as a closed system. The $^{40}Ar/^{39}Ar$ data reported in this research consist of at least three or more consecutive steps that comprise 70% of released ^{39}Ar. The normal isochron spectra show a similar portion of $^{40}Ar/^{36}Ar$ vs. $^{39}Ar/^{36}Ar$ and a corresponding steady minimum plateau age at each step heating, suggesting consistent diffusion in a closure system with low external impact.

Third, as most of the dated minerals were collected from high-grade metamorphic areas that experienced high thermobaric gradients at low pressure and high temperature conditions during the peak-metamorphism, the residual radiogenic Ar trapped in the dated grains is unlikely to have survived the metamnorphism (Uunk et al., 2018). That is because high peak-metamorphism temperatures and partial melting likely have led to dry post-thermal-peak conditions, inhibiting late mica recrystallization. As the study area did not record multiple thermal overprints, the dated minerals are less likely to show multiple diffusion behaviour.

Based on the above observations, the step-heating ages from this study are interpreted to record post thermal-peak cooling through the closure temperatures of the minerals, rather than ages of late re- (or neo-)crystallization, reheating or hydrothermal episodes.

3.5.4 Cooling rate estimation

To monitor the cooling behaviour within and between different tectonic domains, cooling rate calculations were conducted using specific closure temperatures from different mineral pairs (detailed procedures are described in section 2.3 and 3.4). The calculated results are listed in Table 3.1 and plotted in the cooling rate vs distance diagram (Fig. 3.11). In the western belt, the Sybella Domain recorded an initial cooling from 535 ± 54 °C (Hbl) to 506 ± 54 °C (Hbl) during 1.52–1.50 Ga at $1.6^{+1.6}_{-0.6}$ °C/Ma, followed by a slower cooling from 506 ± 54 °C (Hbl) to 393 ± 48 °C (Ms) between 1.50 Ga and 1.40 Ga at $1.1^{+0.1}_{-0.1}$ °C/Ma, and lastly, cooling from 393

± 48 °C (Ms) to 330 ± 58 °C (Bt) during 1.40–1.37 Ga at $3.0^{+1.6}_{-0.8}$ °C/Ma (Fig. 3.11). In the central belt, west of the Pilgrim Fault, the Mary Kathleen Domain recorded cooling from 521 ± 46 °C (Hbl) to 328 ± 56 °C (Bt) between 1.55–1.49 Ga at $3.2^{+1.7}_{-1.4}$ °C/Ma, while the Kalkadoon Domain further west cooled from 514 ± 54 °C (Hbl) to 369 ± 52 °C (Ms) during 1.52–1.49 Ga at $4.9^{+3.2}_{-2.5}$ °C/Ma, and 369 ± 52 °C (Ms) to 324 ± 58 °C (Bt) between 1.49 and 1.47 Ga at $2.7^{+4.3}_{-2.7}$ °C/Ma (Fig. 3.11). In the eastern belt, the Mitakoodi Domain, in the west, recorded cooling from 488 ± 54 °C (Hbl) to 398 ± 50 °C (Ms) between 1.51–1.47 Ga at $2.4^{+1.8}_{-1.6}$ °C /Ma. The Doherty Domain, between the Cloncurry and Overhang faults, recorded a cooling rate of $1.3^{+1.5}_{-1.0}$ °C/Ma from 472 ± 48 °C (Hbl) to 399 ± 50 °C (Ms) during 1.53–1.48 Ga. To the east of the Cloncurry Fault, the Cloncurry Domain appears to have cooled from 516 ± 52 °C (Hbl) to 385 ± 48 °C (Ms) between 1.50 Ga and 1.48 Ga at a rate of $6.3^{+5.0}_{-3.3}$ °C/Ma (Fig. 3.11).

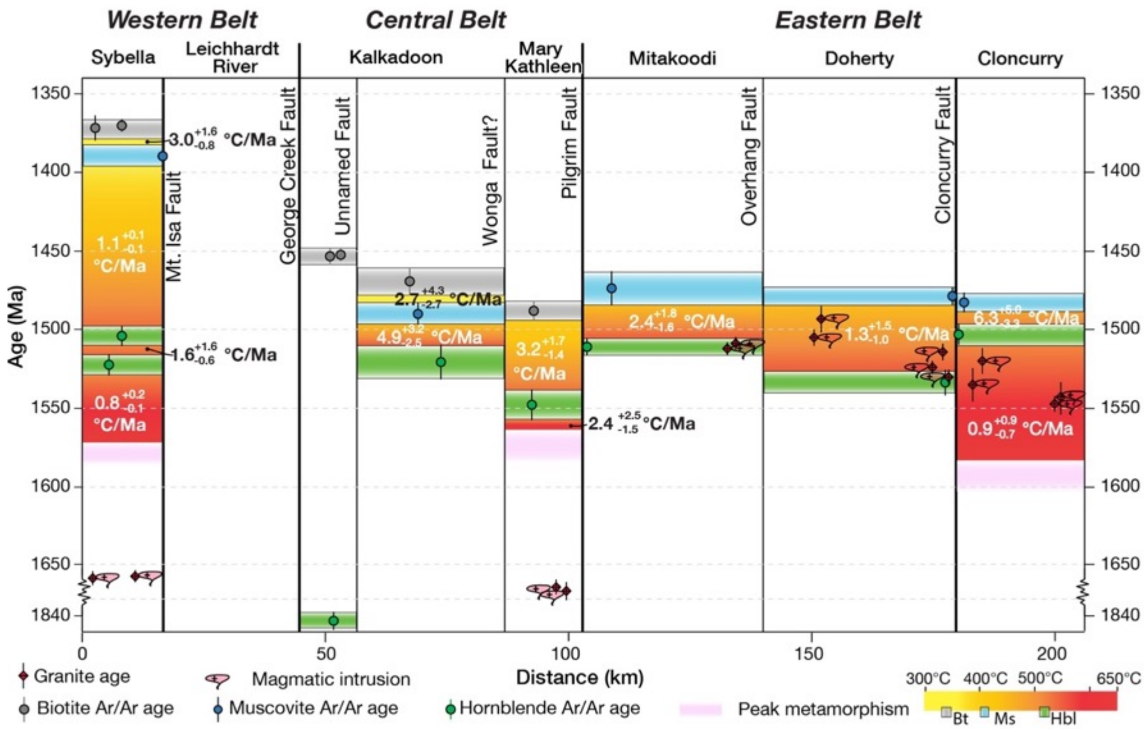

Fig. 3.11: Time vs distance plot of $^{40}Ar/^{39}Ar$ ages along a W–E transect across the Mount Isa Inlier (line A–A' in Fig. 3.1). Different domains are subdivided by the major boundary faults. Each of the green, blue and grey bars represents the cooling age dated from the hornblende, muscovite and biotite, respectively.

Table 1: Cooling rates calculated from mineral pairs of hornblende, muscovite, and biotite from each tectonic domain at specific closure temperatures.

Domain	**Cooling rate $^{I3}_{I1}$(°C/Ma)**	**Cooling period (Ma)**	**Mineral Pair**	**Cooling temperature (°C ± 2 SD)**
Eastern Belt				
Cloncurry Domain	$0.9^{+0.9}_{-0.7}$ °C/Ma	1585–1504 Ma	Metamorphism–Hbl	590 ± 10 516 ± 52
	$6.3^{+5.0}_{-3.3}$ °C/Ma	1504–1483 Ma	Hbl–Ms	516 ± 52 385 ± 48
(**Average cooling rate**)	$2.0^{+0.8}_{-0.7}$ °C/Ma	1585–1483 Ma	Metamorphism–Ms	590 ± 10 385 ± 48
Doherty Domain	$1.3^{+1.5}_{-1.0}$ °C/Ma	1534–1479 Ma	Hbl–Ms	472 ± 48 399 ± 50
Mitakoodi Domain	$2.4^{+1.8}_{-1.6}$ °C/Ma	1511–1474 Ma	Hbl–Ms	488 ± 54 398 ± 50
Central Belt				
Mary Kathleen Domain	$2.4^{+2.5}_{-1.5}$ °C/Ma	1585–1549 Ma	Metamorphism–Hbl	610 ± 30 521 ± 46
Mary Kathleen Domain	$3.2^{+1.7}_{-1.4}$ °C/Ma	1549–1489 Ma	Hbl–Bt	521 ± 46 328 ± 56
(**Average cooling rate**)	$2.9^{+0.8}_{-0.7}$ °C/M	1585–1489 Ma	Metamorphism–Bt	610 ± 30 328 ± 56
Central Kalkadoon Domain	$4.9^{+3.2}_{-2.5}$ °C/Ma	1521–1490 Ma	Hbl–Ms	514 ± 54 369 ± 52
Central Kalkadoon Domain	$2.7^{+4.3}_{-2.7}$ °C/M	1490–1473 Ma	Ms–Bt	369 ± 52 324 ± 58
(**Average cooling rate**)	$4.0^{+2.4}_{-2.0}$ °C/Ma	1521–1473 Ma	Hbl–Bt	514 ± 54 324 ± 58
Western Belt				
Sybella Domain	$0.8^{+0.2}_{-0.1}$ °C/Ma	1575–1523 Ma	Metamorphism–Hbl	575 ± 50 535 ± 54
Sybella Domain	$1.6^{+1.6}_{-0.6}$ °C/Ma	1523–1505 Ma	Hbl–Hbl	535 ± 54 506 ± 52
Sybella Domain	$1.1^{+0.1}_{-0.1}$ °C/Ma	1505–1397 Ma	Hbl–Ms	506 ± 52 393 ± 48
Sybella Domain	$3.0^{+1.6}_{-0.8}$ °C/Ma	1397–1376 Ma	Ms–Bt	393 ± 48 330 ± 58
(**Average cooling rate**)	$1.2^{+0.1}_{-0.1}$ °C/Ma	1575–1376 Ma	Metamorphism–Bt	575 ± 50 330 ± 58

3.6 Discussion

3.6.1 Diachronous cooling and exhumation of the crustal domains

To further evaluate the main controlling factors on the cooling ages from the different tectonic domains, the $^{40}Ar/^{39}Ar$ thermochronological results are combined with published geochronological and petrological constraints (Blenkinsop, 2005; Foster & Rubenach, 2006; Pourteau et al., 2018; Rubenach, 1992, 2008; Sayab et al., 2006) to reconstruct retrograde P–T paths (Fig. 3.12), and decipher the timing of the various fault zones and the exhumation histories of the crustal domains (Figs. 3.13).

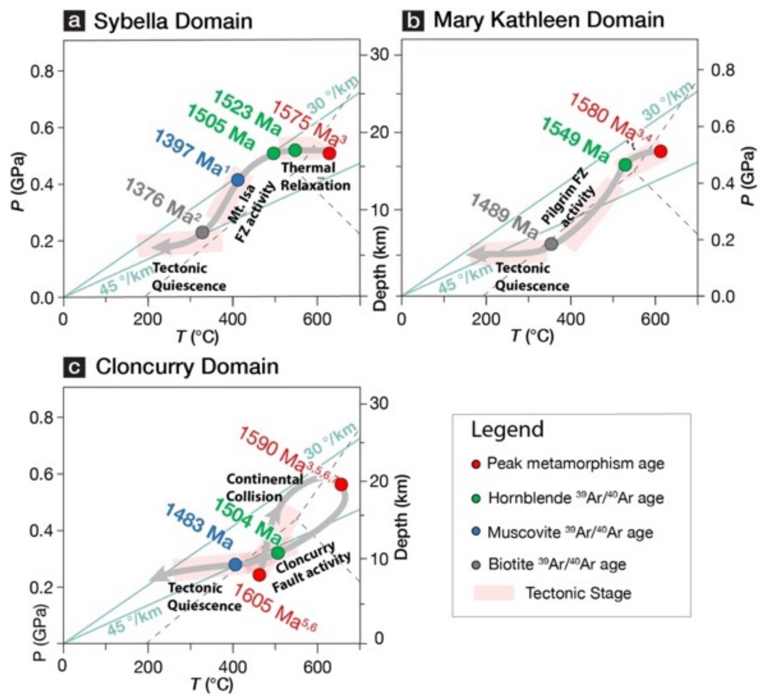

Fig. 3.12: Reconstructed P–T evolution and tectonic interpretation of the Sybella (Fig. 3.12a, following Rubenach, 1992; Blenkinsop, 2005), Mary Kathleen (Fig. 3.12b, following Reinhardt, 1992a, b; Hand & Rubatto, 2002), and Cloncurry domains (Fig. 3.12c, following Sayab et al., 2006; Foster & Rubenach, 2006; Rubenach et al., 2008; Pourteau et al., 2018). Dashed lines represent the limits of stability of the aluminosilicate polygraphs silicates. The green lines represent the 30°C/km geothermal gradient extends 25 km through the crust, and are used as a guide to constrain thermal relaxation during periods of tectonic quiescence, i.e., stages of long-term continental erosion. Peak metamorphism ages and $^{39}Ar/^{40}Ar$ age are referred from previous works: 1= Perkins et al., 1999; 2 = Spikings et al., 2002; 3 = Hand & Rubatto, 2002; 4 = Rubenach et al., 2006; 5 = Rubenach et al., 2008; 6 = Pourteau et al., 2018; 7 = Giles & Nutman, 2002.

(1) Western Belt

The Sybella Domain recorded prograde metamorphism at ca. 1575 Ma, marked by the successive growth of cordierite and andalusite to sillimanite, suggesting heating from 520–550 °C at 0.3–0.4 GPa to ~560–650 °C at 0.4–0.6 GPa (Blenkinsop, 2005). Retrograde kyanite (Rubenach, 1992) indicates near isobaric cooling through hornblende closure temperatures of 535 ± 50 °C at 1523 ± 7 Ma and of 506 ± 54 °C at 1505 ± 6 Ma (Fig. 3.12a). This initial cooling was coeval with most of the other domains in the inlier. However, biotite cooled below ~320 °C >130 m.yr. later at ca. 1375 Ma (Spikings et al., 2002). Given that muscovite near the Mount Isa Fault was dated at ca. 1400 Ma, only ~20 m.yr. before biotite cooled, we suggest that the Sybella Domain cooling below ~320 °C was associated with the activation of the Mount Isa Fault. With muscovite closure temperature of 393 ± 48 °C recalculated from the published result (Spikings et al., 2002), the Mount Isa Fault zone likely had accommodated significant exhumation of the Sybella Domain, possibly from ~14 km to ~9 km (Fig. 3.13c–d) at a rate of ~0.25 mm yr^{-1} and with a maximum cooling rate of $3.0^{+1.6}_{-0.8}$ °C/Ma.

(2) Central Belt

In the western Kalkadoon Domain of the central belt (Fig. 3.9), the ca. 1.87–1.84 Ga amphibolite-facies basement (Bierlein et al., 2008; Page & Williams, 1988) preserves a post-Barramundi Orogeny cooling age of ca. 1.84 Ga through 506 ± 52 °C. The cooling of the high-grade basement shortly after the Barramundi Orogeny is consistent with normal faulting activity of the George Creek Fault (which bounds the basement horst to the east; Fig. 3.1) during deposition of the Leichhardt Superbasin (Bain et al., 1992; Jackson & Southgate, 2000). We, therefore, infer that the cooling of the western Kalkadoon Domain through ~510 °C was associated with the exhumation of the basement in a Leichhardt-aged horst. On the other hand, the eastern Kalkadoon Domain cooled through 514 ± 54 °C at ca. 1.52 Ga (Fig. 3.11). The contrasting thermal records from the two segments of the Kalkadoon Domain suggest that either the eastern segment was buried during the Isan Orogeny (with the domain tilting to the east possibly caused by west-verging thrusts and/or the loading of foreland basin deposits) and was subsequently exhumed at ca. 1.52 Ga (Fig. 3.13a–b), or there was a crustal-scale boundary fault between the western and eastern Kalkadoon Domain.

Further to the northeast, biotite from north of the Mount Remarkable Fault cooled below ~330 °C at ca. 1535 Ma, 15 Ma earlier than the hornblende cooling below ~550 °C to the south of the fault. The thermal discontinuity separated by the Mount Remarkable Fault is consistent with the metamorphic isograd jump across this fault (Fig. 3.4; Foster and Rubenach, 2006), suggesting that the Mount Remarkable Fault is a crustal boundary between the northern and southern sections of the central belt.

The Mary Kathleen Domain records the shortest duration (10–30 m.yr.) from metamorphic peak temperature (~600 °C) at ca. 1575 Ma (Reinhardt, 1992a, b; Hand & Rubatto, 2002) to cooling through 521 ± 46 °C at 1549 ± 10 Ma (Fig. 3.9b). The kyanite growth after sillimanite reported from schist in the Mary Kathleen Domain (Reinhardt, 1992a) suggests that cooling below ~550 °C (i.e. the temperature of the aluminium silicate triple point) took place near peak pressure (~0.5 GPa; Reinhardt et al., 1992a). This well-constrained anticlockwise P-T-t path represents an episode of relatively rapid decompression and exhumation immediately following peak metamorphism (Figs. 3.11 & 3.12b). We interpret this significant early (ca. 1.57 Ga to ca. 1.55 Ga) decompression and cooling below the Ar closure temperature of biotite (~330 °C) to reflect the activation of the sub-vertical but slightly east-dipping Pilgrim Fault as a normal fault which exhumed the amphibolite facies Mary Kathleen Domain (Fig. 3.13a–b). The relative sense of vertical motion along this fault may have reversed afterwards, leading to the cooling of the Mitakoodi Domain to its east through the hornblende closure temperature (~488 °C) at ca. 1.51 Ga (Figs. 3.11 & 3.13b–c).

In the central belt, biotite $^{40}Ar/^{39}Ar$ ages become progressively younger westward (Fig. 3.11). Because no systematic difference in closure temperature can be resolved, we infer that cooling of the central belt was diachronous: from 1550 to 1520 Ma for hornblende (~520 °C) and 1490 to 1460 Ma for biotite (~330 °C). The lack of post-1600 Ma magmatic record in the central and western belts precludes magmatic cooling as a mechanism for cooling in the central belt. Therefore, we attribute the diachronous cooling to differential tectonic exhumation within the central belt, either by E–W block tilting, or by east to west diachronous uplifting of horsts with the Mary Kathleen Domain the earliest, and the western Kalkadoon Domain the latest (Figs. 3.11 & 3.13b–c).

(3) Eastern Belt

The metamorphic history in the Cloncurry Domain near the sample locality recorded heating from 450–520 °C at 0.3–0.45 GPa (1605 Ma) to 520–630 °C at 0.45–0.6 GPa (1590 Ma, Fig. 3.12c) (Foster & Rubenach, 2006; Giles & Nutman, 2002; Pourteau et al., 2018; Rubenach et al., 2008; Sayab, 2006). The successive overgrowths of cordierite and andalusite by kyanite and, later, by sillimanite before their being replaced by andalusite indicate a clockwise P–T path culminating at moderate pressures (Fig. 3.12c, Abu Sharib & Sanislav, 2013; Foster & Rubenach, 2006; Rubenach & Lewthwaite, 2002; Rubenach et al., 2008). Our $^{40}Ar/^{39}Ar$ results indicate that the Cloncurry Domain cooled to 516 ± 52 °C at 1504 ± 7 Ma, i.e. ≥70 m.yr. after the peak metamorphism at a cooling rate of ca. $0.9^{+0.9}_{-0.7}$ °C/Ma, and through 385 ± 48 °C at 1483 ± 6 Ma, with an accelerated cooling rate of $6.3^{+5.0}_{-3.3}$ °C/Ma.

All domains of the eastern belt cooled synchronously through ~400 °C at ca. 1480 Ma, although their cooling through ~520 °C occurred diachronously between 1535 Ma and 1505 Ma (Fig. 3.11). For example, the cooling in the Cloncurry Domain occurred at ca. 1505 Ma, 20–30 m.yr. later than the adjacent Doherty Domain. Further west, the Mitakoodi Domain shows an intermediate cooling age at 1512 ± 5 Ma. The heterogeneous cooling age between different geological domains cannot be explained by systematic differences in mineral closure temperature (Table B.2.2). We thus evaluate two alternative driving mechanisms for the cooling of the eastern belt: post-magmatic thermal relaxation, and tectonic exhumation.

Mechanism 1: cooling ages in the eastern belt represent resetting of the argon systematics associated with local granitic intrusions. Granitic intrusions in the eastern belt near the sample localities were dated at ca. 1.53 Ga to 1.51 Ga (Page & Sun, 1998; Pollard & McNaughton, 1997), comparable to the range of the hornblende $^{40}Ar/^{39}Ar$ cooling ages of between ca. 1.53 and 1.50 Ga. The best example for argon systematics resetting is preserved in the Doherty Domain, where the hornblende dated from an amphibolite adjacent to Mount Angelay granite gave an $^{40}Ar/^{39}Ar$ cooling age within error of the granite (1534 ± 8 Ma vs 1529 ± 4 Ma; Pollard & McNaughton, 1997). Nevertheless, it is unlikely that cooling ages in the eastern belt were all related to granite emplacement. For example, hornblende from an amphibolite near the ca. 1.53 Ga Saxby granite yielded a ca. 1.50 Ga $^{40}Ar/^{39}Ar$ cooling age, which is too young to be related to the magmatic cooling. In the Mitakoodi Domain, the dated hornblende from the Mitakoodi metabasalt is too distant (45 km) from the nearest ca. 1.51 Ga Wimberu granite to acquire an argon resetting age. Thus, magmatism alone cannot account for the cooling history of this domain.

Mechanism 2: initial cooling (through ~520 °C) within the eastern belt was controlled by normal faulting. In this case, the Doherty Domain, which records the oldest cooling age in the eastern belt, exhumed earliest at ca. 1.53 Ga due to normal faulting of the east-dipping

Cloncurry Fault (Blenkinsop, 2008). This was followed by the exhumation of the Mitakoodi and Cloncurry domains at ca. 1.51–1.50 Ga (Fig. 3.13b, c). This interpretation involves repeated activation of the domain-bounding faults with varying fault kinematics. After ca. 1.50 Ga, the eastern belt appears to have behaved as a coherent crustal block, all recording statistically indistinguishable ca. 1480 Ma muscovite $^{40}Ar/^{39}Ar$ ages (Figs. 3.11 & 3.13).

In summary, the post-orogenic evolution of the Mount Isa Inlier was characterized by heterogeneous but consistently slow cooling and exhumation, driven mostly by diachronous fault movements. The earliest cooling was recorded in the western Kalkadoon Domain with a post-Barramundi Orogeny cooling age. This is consistent with high-grade basement exhumation shortly after the Barramundi Orogeny due to normal fault activation. Differential cooling behaviour between western and eastern Kalkadoon Domain suggest different crustal burial during the Isan Orogeny with the western section buried to a shallower level than the eastern section. Reconstructed fault movements indicate that both pre-Isan basin-controlling normal faults (e.g., the Pilgrim and Cloncurry faults; Blenkinsop et al., 2008) and Isan aged reverse faults (e.g., the Overhang Fault; Baker et al., 2001) were re-activated as post-orogenic normal faults during a post-Isan extensional phase.

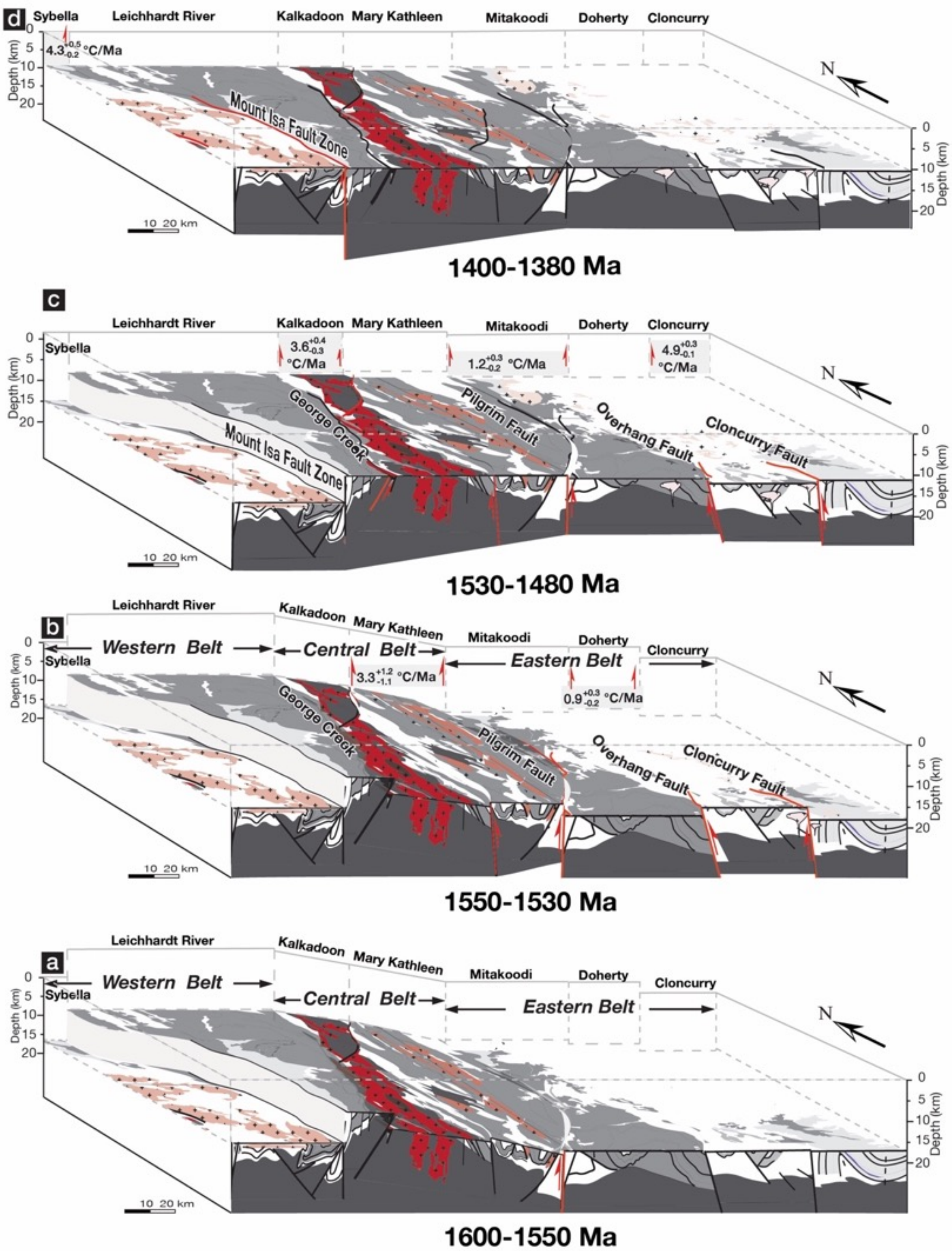

Fig. 3.13: Interpretation of the exhumation history in the Mount Isa Inlier from 1600 Ma to 1380 Ma. a. 1600–1550 Ma: Presently exposed domains were at different crustal levels, as indicated by different pressure conditions during the Isan Orogeny. b. 1550–1530 Ma: Post-orogenic extension was accommodated along pre-existing, generally steep faults. The Pilgrim Fault acted as an east-dipping normal fault, accommodating differential vertical motion between the central and eastern belts. **c.** 1530–1480 Ma: Extensional faulting continued. In the central belt, the eastern Kalkadoon Domain was exhumed either through block tilting to the west, or differential uplift relative to the western Kalkadoon and Mary Kathleen domains. **d.** 1400–1380 Ma: Following a period of tectonic quiescence, the Mount Isa fault was finally re-activated when the remainder of the inlier remained a coherent crustal block.

3.6.2 Final assembly of Nuna by 'soft' collision

The uncommon association of crustal shortening with low–P/T metamorphism and counter-clockwise P–T evolutions observed during the Isan Orogeny, as well as in other Mesoproterozoic orogenic belts (i.e., the Halls Creek orogen) in Australia, have been noticed and debated for over four decades (Bell, 1983; Bell et al., 1992; Betts et al., 2006, 2007; Etheridge et al., 1987; Foster & Rubenach, 2006; Loosveld, 1989; Rubenach, 1992; O'Dea et al., 1997a). Here, we complement and add to the previous studies, and discuss the tectonic regimes of the unusual Isan Orogeny by incorporating our reconstruction of the regional post-orogenic cooling and exhumation history.

According to a worldwide database of mountain ranges actively undergoing denudation/exhumation, surface erosion shares a linear relationship with topographic relief (Pinet & Souriau, 1988). In the Mount Isa Inlier, the exhumation following the Isan Orogeny was likely facilitated by a combination of post-orogenic normal faulting and surface erosion. The average post-peak metamorphic exhumation rates estimated for the individual crustal domains of the Mount Isa Inlier (between 1 and 6 °C/Ma) suggest an overall erosion rate of less than <0.5 mm yr^{-1}. By taking a uniformitarian approach and applying the updated relationship between erosion rate and regional-scale relief of Montgomery and Brandon (2002), the slow exhumation rates suggest that, following the Isan Orogeny, the Mount Isa Inlier had a local relief of less than 1000 m above sea-level. This is consistent with previous studies which suggest that the Isan Orogeny was associated with low-elevation mountain ranges (McLaren et al., 2005), and had limited tectonic burial (reflected by low peak pressure conditions; Fig. 3.12) and scarce post-orogenic molasse-type flexural sedimentary basins (McConachie et al., 1993; Southgate et al., 2000). The shallowness of crustal imbrication (Abu-Sharib & Sanislav, 2013; Bell, 1991; MacCready, 2006) and width of the resulting orogenic belt formed during the juxtaposition of Australia against Laurentia at ca. 1.60 Ga were previously proposed to have resulted in a 'soft collision' (Nordsvan et al., 2018b) of possibly thin and hot continental regions (McLaren et al., 2005; Pourteau et al., 2018).

3.6.3 Post-orogenic exhumation: insight into the orogen's thermal regime

Mechanisms that drive orogenic exhumation vary from orogen to orogen due to their distinct tectonic and thermal regimes. To determine the exhumation mechanism of Proterozoic orogens, it may benefit from a comparison with well-studied modern analogs. Modern orogens can be subdivided into three categories: 'small cold orogens' (SCOs), 'transitional orogens' (TOs) and 'large hot orogens' (LHOs) based on their thermal regimes and magnitude (Beaumont et al., 2006; Jamieson et al., 2002). Although no quantitive criteria (e.g. specific sizes or temperature values) have been provided to classify the orogeny types, orogens such as the Cascadia, Pyrenees, and Abitibi are regarded as SCOs, whereas, Tibet, Grenvillian, Variscan, Andes, and Trans Hudson are considered as LHOs (Beaumont et al., 2006).While SCOs are characterized by rigid crust deformation with little ductile deformation, LHOs (such as the Himalayan) typically undergo prolonged crustal heating and develop a central elevated plateau above a weak lower crust (Jamieson & Beaumont, 2013). Syn-to post-orogenic collapse is thought to be common for LHOs, which is driven by the isostatic instability of hot, thickened, melt-weakened lower crust underneath the plateau (Jamieson & Beaumont, 2013). For example, LHOs like the Variscan, Svecofennian and Grenvillian orogens all contain metamorphic core complexes or "core complex-like systems" involving domal uplift or vertical extrusion of mid-to-lower crustal rocks (Korja et al., 2009; Pascual et al., 2013; Rivers, 2012; Schulmann et al., 2008). By contrast, SCOs are comparatively cold and rheologically stronger, and tend not to result in orogenic collapse but with erosion being the dominant mechanism for exhumation (Jamieson & Beaumont, 2013). The Mount Isa Orogen, which had a high thermal regime (McLaren et al., 2005) and large lateral extent (over 120000 km^2), is more comparable with LHO type orogens.

3.6.4 Exhumation history and driving mechanism for the Mount Isa Inlier

In the Mount Isa Inlier, the ca. 1530–1480 Ma interval was marked by cooling and exhumation throughout the entire inlier. This was broadly coeval with voluminous ca. 1550–1490 Ma magmatism in the eastern belt. The chemical composition and temporal evolution of this magmatic phase may, therefore, provide constraints on the tectonic mechanisms that controlled exhumation. Late- to post-orogenic intrusions in the eastern belt consist of localized ca. 1550 Ma trondhjemite (Mark, 2001) west of the Cloncurry Fault and widespread voluminous ca. 1540–1490 Ma A-type granitoids. The trondhjemite, which is typically foliated, is characterized by high Al_2O_3 contents, low heavy rare earth element, and no Sr anomaly, suggesting that it was derived by partial melting of a hydrated mafic source possibly at >0.8–1.0 GPa (Mark, 2001). By contrast, the A-type intrusive rocks range from monzodiorite and monzogranite to syenogranite, and exhibit Sr and Eu negative anomalies with elevated high field strength element contents (Mark, 2001; Blenkinsop, 2005), were likely produced at >900

°C and <0.8–1.0 GPa from a tonalitic to granodioritic source (Mark, 2001). Thus, magmatic transition from local trondhjemite to widespread A-type granitoids at ca. 1.54 Ga may indicate an elevated heating and decompressional melting from the lower crust.

By integrating the magmatic evolution with regional terrane exhumation history, we propose the alternative scenario where crustal delamination triggered regional magmatism and crustal exhumation. The geochemical evolution of magmatism from ca. 1550 to 1490 Ma indicates heating in the lower crust of the eastern Mount Isa Inlier, and is broadly contemporaneous with the early exhumation and cooling of the middle crust, as constrained by the $^{39}Ar/^{40}Ar$ ages. We note that the ca. 1550–1490 Ma intrusions are restricted to the eastern belt that recorded crustal thickening during the ca. 1600 Ma orogeny (Pourteau et al., 2018) Therefore, we propose that, as suggested for other orogens (e.g., England & Houseman, 1989; Jiménez-Munt et al., 2008; Li et al., 2010; Meng et al., 2012; Yao et al., 2012), lower crustal heating in the Mount Isa Inlier was caused by the delamination of a predominantly mafic lower crust (Fig. 3.14a & b), possibly due to eclogitisation. Delamination of the dense orogenic root would be accompanied by crustal isostatic rebound and extension (orogenic collapse; Li et al., 2010). Water released from the eclogitized mafic lower crust might have triggered the generation of the 1550 Ma trondhjemite at moderate temperatures (~800 °C; Mark, 2001) and driven a pressure decrease due to orogenic collapse (Li et al., 2010). The subsequent local influx of hot asthenospheric mantle would have resulted in high-temperature magmatism (>900 °C) generation of A-type granites during 1540–1490 Ma (Fig. 3.14b).

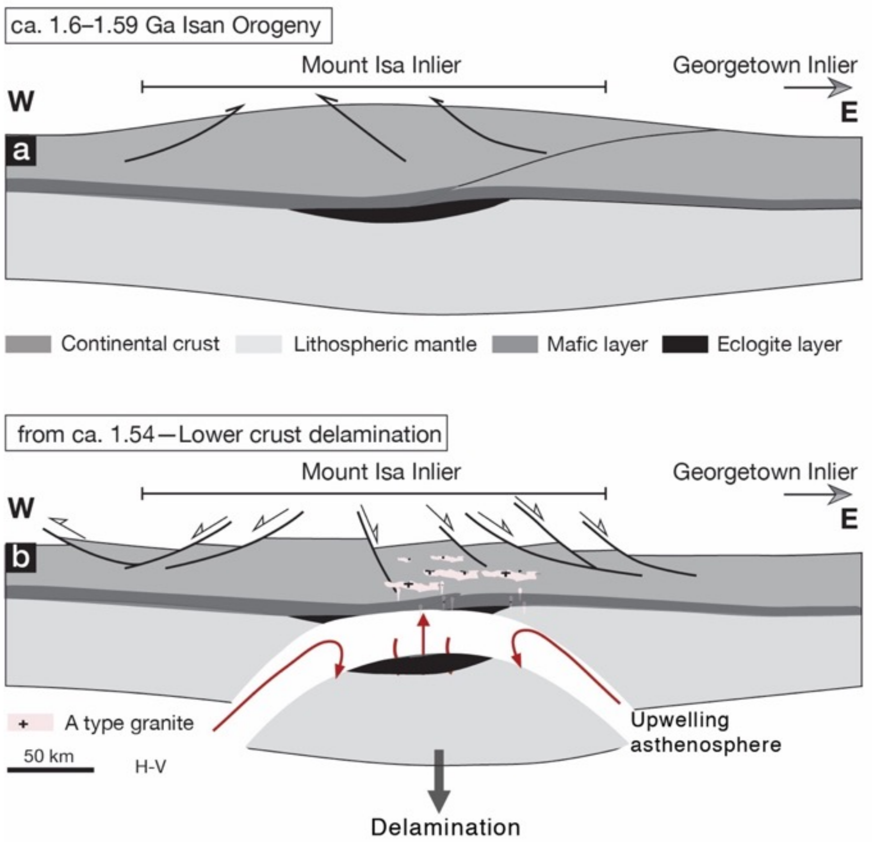

Fig. 3.14: Conceptional model for the tectonic evolution of the Mount Isa Inlier from 1600 Ma to 1540 Ma. a. The ca. 1600 Ma continental collision event in the Mount Isa Inlier recorded westward accretion of the Georgetown Inlier with local crustal thickening within the eastern belt. b. The locally thickened crust was delaminated and replaced by the upwelling asthenosphere. Elevated geotherm by hot mantle upwelling, together with water released from the sinking lower crust and reduced pressure caused by orogenic collapse, induced widespread post-kinematic felsic to mafic magmatism.

3.6.5 Slow cooling Proterozoic orogens

To compare the cooling behaviour of the Mount Isan orogen with global orogens, the cooling rates reported in this study were plotted with that from global orogens younger than 2.5 Ga (Fig. 3.15). A decreasing cooling rate trend is observed as the age of the orogens increase (Dunlap, 2000). Phanerozoic orogens commonly experienced medium to fast cooling (>50 °C/Ma), whereas Precambrian orogens rarely cooled faster than 10°C/Ma, except for the Albany-Fraser orogen where fast exhumation was controlled by transpressional faulting (Scibiorski et al., 2015). Similar to other Precambrian orogens, the Mount Isa Inlier also shows a slow cooling signature. Although further investigations may be needed before determining the dominate mechanism for the cooling of Precambrian orogens, the slow cooling is usually interpreted associated with: (1) radiogenic heating by radioactive elements from buried intrusions (McLaren et la., 1999); (2) slow erosion during the tectonic quiescence stages (Scibiorski et al., 2015); and, (3) partial resetting of the argon closure system after long-term isothermal residence below the nominal closure temperature (Dunlap, 2000; Warren et al., 2012). In the Mount Isa Inlier, radiogenic heating by radioactive elements from the granite has been reported to have generated steep upper crustal thermal gradients prior to the Isan Orogeny (McLaren et al., 2005). Thus, we propose that the slow cooling during the Isan Orogeny may have been caused by the combination of low-elevation (thus slow erosion) due to a soft-collision, and possibly radiogenic heating by existing granites in the crust (McLaren et al., 2005).

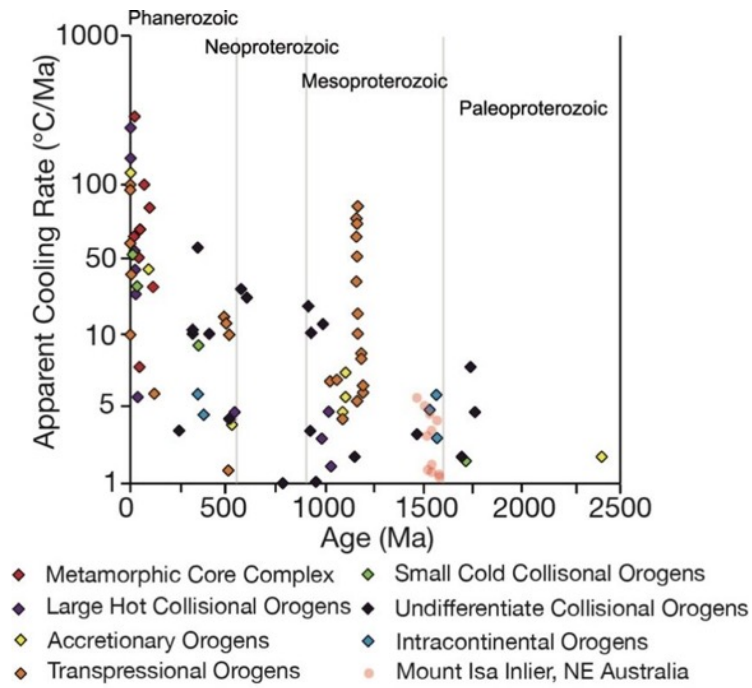

Fig. 3.15: Plot of global orogenic cooling rates (modified after Scibiorski et al., 2015). Orogens are categorized by tectonic settings with the cooling rates of previous studies source from Scibiorski et al. (2015) and references therein. New data from the Mount Isa Inlier are shown in pink diamonds.

3.7 Conclusions

New high-precision $^{39}Ar/^{40}Ar$ thermochronological data reveal a diachronous, but consistently slow (generally <5 °C/Ma) cooling of the Mount Isa Inlier following the ca. 1.60 Ga Isan Orogeny. Following the Isan orogeny, the central and eastern belts recorded a more rapid cooling at ca. 1.50–1.48 Ga at a cooling rate of 3–5 °C/Ma, compared a synchronous cooling event at a somewhat lower rate (1 °C/Ma) in the western belt. While the central and eastern belts cooled heterogeneously through ~525–330 °C between 1.53 and 1.48 Ga, the western belt did not cool to muscovite closure temperature (~425 °C) until ca. 1.40 Ga. Contrasting cooling histories across post-metamorphic fault zones are best explained by reactivation of inherited basinal faults and orogenic reverse faults during the orogenic collapse stage.

The documented prolonged and slow exhumation history suggests that the Isan Orogen was associated with a moderately thickened crust with relatively low relief (likely <1000 m according to modern analogs). The post-orogenic exhumation of the Mount Isa Inlier, together with limited tectonic burial, the relative paucity of regional-scale syn-orogenic sedimentary basins, and the breadth of orogenic deformation, point to a 'soft collision' of a previously thinned (and hot) east Australian continental margin with west Laurentia during the final assembly of the supercontinent Nuna. Such an orogen is atypical of modern collisional orogens, but is consistent with Precambrian orogens with higher geothermal gradients. The occurrence of trondhjemite (ca. 1550 Ma) to A-type magmatism (1540–1490 Ma) in the eastern belt during this exhumation process, together with our geochronological constraints on the diachronous normal faulting in the inlier, led us to propose that following the ca. 1600 Ma peak Isan Orogeny, part of the mafic lower crust was delaminated due to eclogitisation and was replaced by hot mantle materials, resulting in the collapse and exhumation of the orogen.

Acknowledgments

This study was supported by a China Scholarship Council and a Curtin Research Scholarship to JYL, and an Australian Research Council Laureate Fellow grant (FL150100133) to ZXL. We thank Caroline Perkins for providing argon released data for recalibrating of $^{40}Ar/^{39}Ar$ ages, I. W. Withnall and G.M. Gibson for introducing the Mount Isa Inlier field geology and fruitful discussions, Sigma Zone company for providing student licence for Quantum XL program to make Monte Carlo simulation possible, Hugo Olierook and Celia Mayers for their assistance during the $^{40}Ar/^{39}Ar$ data producing, and Josh Beardmore for helping proof reading the manuscript. Datasets for this research are available at http://doi.org/10.4121/uuid:bfd7c070-ca86-4f3f-82dd-5bfedf7f0d1b, and included in these references: Page and Sun. 1998, Perkins and Wyborn. 1998, Perkins. 1999 and Spikings et al. 2001, 2002.

3.8 References

Abu Sharib, A. S. A. A., & I. V. Sanislav (2013), Polymetamorphism accompanied switching in horizontal shortening during Isan Orogeny: Example from the Eastern Fold Belt, Mount Isa Inlier, Australia, *Tectonophysics*, *587*, 146-167.

Bain, J., C. Heinrich, & G. Henderson (1992), Stratigraphy, structure, and metasomatism of the Haslingden Group, east Moondarra area, Mount Isa: a deformed and mineralised Proterozoic multistage rift-sag sequence, in *Detailed Studies of the Mount Isa Inlier*, edited, pp. 125-136, AGSO Bulletin.

Baker, T., C. Perkins, K. L. Blake, & P. J. Williams (2001), Radiogenic and stable isotope constraints on the Genesis of the Eloise Cu-Au deposits, Cloncurry district, Northwest Queensland, *Economic Geology*, *96*(4), 723-742.

Beardsmore, T., S. Newbery, & W. Laing (1988), The Maronan Supergroup: an inferred early volcanosedimentary rift sequence in the Mount Isa Inlier, and its implications for ensialic rifting in the Middle Proterozoic of northwest Queensland, *Precambrian Research*, *40*, 487-507.

Bell, T. H. (1983), Thrusting and duplex formation at Mount Isa, Queensland, Australia, *Nature*, *304*(5926), 493-497.

Bell, T. H., & M. J. Rubenach (1983), Sequential Porphyroblast Growth and Crenulation Cleavage Development during Progressive Deformation, *Tectonophysics*, *92*(1-3), 171-194.

Bell, T. H. (1991), The role of thrusting in the structural development of the Mount Isa Mine and its relevance to exploration in the surrounding region, *Economic Geology*, *86*(8), 1602-1625.

Bell, T., J. Reinhardt, & R. Hammond (1992), Multiple foliation development during thrusting and synchronous formation of vertical shear zones, *Journal of Structural Geology*, *14*(7), 791-805.

Betts, P. G., G. S. Lister, & M. G. O'Dea (1998), Asymmetric extension of the Middle Proterozoic lithosphere, Mount Isa terrane, Queensland, Australia, *Tectonophysics*, *296*(3-4), 293-316.

Betts, P. G. (1999), Palaeoproterozoic mid-basin inversion in the northern Mt Isa terrane, Queensland, *Australian Journal of Earth Sciences*, *46*(5), 735-748.

Betts, P. G., L. Ailleres, D. Giles, & M. Hough (2000), Deformation history of the Hampden Synform in the Eastern fold Belt of the Mt Isa terrane, *Australian Journal of Earth Sciences*, *47*(6), 1113-1125.

Betts, P. G., & G. S. Lister (2001), Comparison of the 'strike-slipe' versus 'episodic rift-sag' models for the origin of the Isa superbasin, *Australian Journal of Earth Sciences*, *48*(2), 265-280.

Betts, P. G., D. Giles, G. Mark, G. S. Lister, B. R. Goleby, & L. Ailleres (2006), Synthesis of the proterozoic evolution of the Mt Isa Inlier, *Australian Journal of Earth Sciences*, *53*(1), 187-211.

Betts, P. G., D. Giles, B. F. Schaefer, & G. Mark (2007), 1600–1500 Ma hotspot track in eastern Australia: implications for Mesoproterozoic continental reconstructions, *Terra Nova*, *19*(6), 496-501.

Betts, P. G., D. Giles, & B. F. Schaefer (2008), Comparing 1800-1600 Ma accretionary and basin processes in Australia and Laurentia: Possible geographic connections in Columbia, *Precambrian Research*, *166*(1-4), 81-92.

Betts, P. G., D. Giles, J. Foden, B. F. Schaefer, G. Mark, M. J. Pankhurst, C. J. Forbes, H. A. Williams, N. C. Chalmers, and Q. Hills (2009), Mesoproterozoic plume-modified orogenesis in eastern Precambrian Australia, *Tectonics*, *28*(3).

Betts, P. G., R. J. Armit, J. Stewart, A. R. A. Aitken, L. Ailleres, P. Donchak, L. Hutton, I. Withnall, & D. Giles (2016), Australia and Nuna, *Geological Society, London, Special Publications*, *424*(1), 47-81.

Bierlein, F., L. Black, J. Hergt, & G. Mark (2008), Evolution of Pre-1.8Ga basement rocks in the western Mt Isa Inlier, northeastern Australia—Insights from SHRIMP U–Pb dating and in-situ Lu–Hf analysis of zircons, *Precambrian Research*, *163*(1-2), 159-173.

Bird, P. (1979), Continental delamination and the Colorado Plateau, *Journal of Geophysical Research: Solid Earth*, *84*(B13), 7561-7571.

Blaikie, T. N., P. G. Betts, R. J. Armit, & L. Ailleres (2017), The ca. 1740–1710 Ma Leichhardt Event: Inversion of a continental rift and revision of the tectonic evolution of the North Australian Craton, *Precambrian Research*, *292*, 75-92. http://doi.org/10.1016/j.precamres.2017.02.003.

Blake, D. H. (1987), Geology of the Mount Isa Inlier and environs, Queensland and Northern Territory, *Bulletin - Bureau of Mineral Resources, Geology & Geophysics, Australia*, *225*.

Blenkinsop, T. G., C. R. Huddlestone-Holmes, D. R. W. Foster, M. A. Edmiston, P. Lepong, G. Mark, J. R. Austin, F. C. Murphy, A. Ford, & M. J. Rubenach (2008), The crustal scale architecture of the Eastern Succession, Mount Isa: The influence of inversion, *Precambrian Research*, *163*(1-2), 31-49.

Blenkinsop, Tom G (2005) Total systems analysis of the Mount Isa eastern succession. Report. Predictive Mineral Discovery CRC.

Boger, S. D., & D. Hansen (2004), Metamorphic evolution of the Georgetown Inlier, northeast Queensland, Australia; evidence for an accreted Palaeoproterozoic terrane?, *Journal of Metamorphic Geology*, *22*(6), 511-527.

Brown, M. (2007), Metamorphic conditions in orogenic belts: A record of secular change, *International Geology Review*, *49*(3), 193-234.

Collins, W. J. (2002). Hot orogens, tectonic switching, and creation of continental crust. *Geology*, *30*(6), 535-538.

Connors, K. A., & G. S. Lister (1995), Polyphase deformation in the western Mount Isa Inlier, Australia: episodic or continuous deformation?, *Journal of structural geology*, *17*(3), 305-328.

Connors, K. A., & R. W. Page (1995), Relationships between magmatism, metamorphism and deformation in the western Mount Isa Inlier, Australia, *Precambrian Research*, *71*(1-4), 131-153.

Derrick, G. (1982), A Proterozoic Rift-Zone At Mount-Isa, Queensland, And Implications For Mineralization, *BMR Journal of Australian Geology & Geophysics*, *7*(2), 81-92.

Dodson, M. H. (1973), Closure temperature in cooling geochronological and petrological systems, *Contributions to Mineralogy and Petrology*, *40*(3), 259-274.

Dunlap, W. J. (2000), Nature's diffusion experiment: The cooling-rate cooling-age correlation. *Geology*, *28*(2), 139-142.

Duncan, R. J., A. R. Wilde, K. Bassano, & R. Maas (2006), Geochronological constraints on tourmaline formation in the Western Fold Belt of the Mount Isa Inlier, Australia: Evidence for large-scale metamorphism at 1.57Ga?, *Precambrian Research*, *146*(3-4), 120-137.

England, P., & G. Houseman (1989), Extension during Continental Convergence, with Application to the Tibetan Plateau, *Journal of Geophysical Research-Solid Earth and Planets*, *94*(B12), 17561-17579.

Eriksson, K., E. Simpson, & M. Jackson (1994), Stratigraphical Evolution of a Proterozoic Syn-Rift to Post-Rift Basin: Constraints on the Nature of Lithospheric Extension in the Mount Isa Inlier, Australia, *Tectonic controls and signatures in sedimentary successions*, 203-221.

Etheridge, M. A., R. W. R. Rutland, & L. A. I. Wyborn (1987), Orogenesis and tectonic process in the early to middle Proterozoic of northern Australia, *Precambrian Lithospheric Evolution*, *17*, 131-147.

Evans, D. A. D., & R. N. Mitchell (2011), Assembly and breakup of the core of Paleoproterozoic-Mesoproterozoic supercontinent Nuna, *Geology*, *39*(5), 443-446.

Evans, D. A. D., R. V. Veselovsky, P. Y. Petrov, A. V. Shatsillo, & V. E. Pavlov (2016), Paleomagnetism of Mesoproterozoic margins of the Anabar Shield: A hypothesized billion-year partnership of Siberia and northern Laurentia, *Precambrian Research*, *281*, 639-655.

Foster, D. (2003), Proterozoic low-pressure metamorphism in the Mount Isa Inlier, northwest Queensland, Australia, with particular emphasis on the use of calcic amphibole chemistry as temperature-pressure indicators, *PhD thesis James Cook University*.

Foster, D. R. W., & M. J. Rubenach (2006), Isograd pattern and regional low-pressure, high-temperature metamorphism of pelitic, mafic and calc-silicate rocks along an east – west section through the Mt Isa Inlier, *Australian Journal of Earth Sciences*, *53*(1), 167-186.

Foster, D., & J. Austin (2008), The 1800–1610Ma stratigraphic and magmatic history of the Eastern Succession, Mount Isa Inlier, and correlations with adjacent Paleoproterozoic terranes, *Precambrian Research*, *163*(1-2), 7-30.

Foster, D., & M. Rubenach (2000), High radiogenic heat-producing granites and metamorphism-An example from the western Mount Isainlier, Australia: Comment, *Geology*, *28*(7), 671.

Furlanetto, F., D. J. Thorkelson, H. Daniel Gibson, D. D. Marshall, R. H. Rainbird, W. J. Davis, J. L. Crowley, & J. D. Vervoort (2013), Late Paleoproterozoic terrane accretion in northwestern Canada and the case for circum-Columbian orogenesis, *Precambrian Research*, *224*, 512-528.

Gauthier, L., G. Hall, H. Stein, & U. Schaltegger (2001), The Osborne deposit, Cloncurry district: A 1595 Ma Cu-Au skarn deposit, *A Hydrothermal Odyssey, New Developments in Metalliferous Hydrothermal Systems Research*, *59*, 58-59.

Gibson & Hitchman (2005) 3D Basin Architecture and Mineral Systems in the Mt Isa Western Succession. Report. Predictive Mineral Discovery CRC.

Gibson, G. M., D. C. Champion, I. W. Withnall, N. L. Neumann, & L. J. Hutton (2018), Assembly and breakup of the Nuna supercontinent: Geodynamic constraints from 1800 to 1600 Ma sedimentary basins and basaltic magmatism in northern Australia, *Precambrian Research*, *313*, 148-169.

Gibson, G. M., M. J. Rubenach, N. L. Neumann, P. N. Southgate, & L. J. Hutton (2008), Syn- and post-extensional tectonic activity in the Palaeoproterozoic sequences of Broken Hill and Mount Isa and its bearing on reconstructions of Rodinia, *Precambrian Research*, *166*(1-4), 350-369.

Gibson, G. M., P. A. Henson, N. L. Neumann, P. N. Southgate, & L. J. Hutton (2012), Paleoproterozoic-earliest Mesoproterozoic basin evolution in the Mount Isa region, northern Australia and implications for reconstructions of the Nuna and Rodinia supercontinents, *Episodes*, *35*(1), 131-141.

Giles, D., & A. P. Nutman (2002), SHRIMP U-Pb monazite dating of 1600-1580 Ma amphibolite facies metamorphism in the southeastern Mt Isa Block, Australia, *Australian Journal of Earth Sciences*, *49*(3), 455-465.

Giles, D., L. Ailléres, D. Jeffries, P. Betts, & G. Lister (2006), Crustal architecture of basin inversion during the Proterozoic Isan Orogeny, Eastern Mount Isa Inlier, Australia, *Precambrian Research*, *148*(1-2), 67-84.

Grebennikov, A. V. (2014). A-type granites and related rocks: Petrogenesis and classification. *Russian Geology and Geophysics*, *55*(9), 1074-1086.

Grove, M., & T. M. Harrison (1996), ^{40}Ar* diffusion in Fe-rich biotite, *American Mineralogist*, *81*(7-8), 940-951.

Hand, M., & D. Rubatto (2002), The scale of the thermal problem in the Mount Isa Inlier, *Geological Society of Australia Abstracts*, *67*.

Hannan K. W., Golding S. D., Herbert H. K. & Krouse H. R. (1993). Contrasting alteration assemblages in metabasites from Mount Isa, Queensland: implications for copper ore genesis. Economic Geology 88, 1135 – 1175.

Hansma, J., E. Tohver, C. Schrank, F. Jourdan, & D. Adams (2016), The timing of the Cape Orogeny: New 40 Ar/ 39 Ar age constraints on deformation and cooling of the Cape Fold Belt, South Africa, *Gondwana Research*, *32*, 122-137.

Harrison, T. M. (1981), Diffusion of ^{40}Ar in hornblende, *Contributions to Mineralogy & Petrology*, *78*(3), 324-331.

Harrison, T. M., I. Duncan, & I. McDougall (1985), Diffusion of 40Ar in biotite: Temperature, pressure and compositional effects, *Geochimica et Cosmochimica Acta*, *49*(11), 2461-2468.

Harrison, T. M., J. Célérier, A. B. Aikman, J. Hermann, & M. T. Heizler (2009), Diffusion of 40Ar in muscovite, *Geochimica et Cosmochimica Acta*, *73*(4), 1039-1051.

Holcombe, R. J., P. J. Pearson, & N. H. S. Oliver (1991), Geometry of a Middle Proterozoic extensional décollement in northeastern Australia, *Tectonophysics*, *191*(3-4), 255-274.

Jackson, M. J., & P. N. Southgate (2000), Evolution of three unconformity-bounded sandy carbonate successions in the McArthur River region of northern Australia: the Lawn, Wide and Doom Supersequences in a proximal part of the Isa Superbasin, *Australian Journal of Earth Sciences*, *47*(3), 625-635.

Jackson, M. J., D. L. Scott, & D. J. Rawlings (2000), Stratigraphic framework for the Leichhardt and Calvert Superbasins: review and correlations of the pre-1700 Ma successions between Mt Isa and McArthur River, *Australian Journal of Earth Sciences*, *47*(3), 381-403.

Jiménez-Munt, I., M. Fernàndez, J. Vergés, & J. P. Platt (2008), Lithosphere structure underneath the Tibetan Plateau inferred from elevation, gravity and geoid anomalies, *Earth and Planetary Science Letters*, *267*(1-2), 276-289.

Johnson, M. R., Harley, S. L., & Harley, S. (2012). *Orogenesis: the making of mountains*. Cambridge University Press.

Jourdan, F., G. Féraud, H. Bertrand, & M. Watkeys (2007), From flood basalts to the inception of oceanization: Example from the $^{40}Ar/^{39}Ar$ high-resolution picture of the Karoo large igneous province, *Geochemistry, Geophysics, Geosystems*, *8*(2).

Kearey, P., K. A. Klepeis, & F. J. Vine (2009), *Global tectonics*, John Wiley & Sons.

Kelley, S. (2002), Excess argon in K-Ar and Ar-Ar geochronology, *Chemical Geology*, *188*(1-2), 1-22.

Kirscher, U., Liu, Y., Li, Z. X., Mitchell, R. N., Pisarevsky, S. A., Denyszyn, S. W., & Nordsvan, A. (2019). Paleomagnetism of the Hart Dolerite (Kimberley, Western Australia)–A two-stage assembly of the supercontinent Nuna?. *Precambrian Research, 329, 170-181*.

Kirscher, U., R. N. Mitchell, Y. Liu, A. R. Nordsvan, G. M. Cox, S. A. Pisarevsky, C. Wang, L. Wu, J. B. Murphy, and Z.-X. Li (2020), Paleomagnetic constraints on the duration of the Australia-Laurentia connection in the core of the Nuna supercontinent, *Geology*.

Koppers, A. A. P. (2002), ArArCALC - software for Ar-40/Ar-39 age calculations, *Computers & Geosciences*, *28*(5), 605-619.

Lally, J. H. (1997), The structural history of the central eastern fold belt, Mount Isa Inlier, Northwest Queensland, Australia, *The Structural History of the Central Eastern Fold Belt, Mount Isa Inlier, Northwest Queensland*.

Lee, J. Y., K. Marti, J. P. Severinghaus, K. Kawamura, H. S. Yoo, J. B. Lee, & J. S. Kim (2006), A redetermination of the isotopic abundances of atmospheric Ar, *Geochimica et Cosmochimica Acta*, *70*(17), 4507-4512.

Li, Z.X., Li, X.H., Wartho, J.A., Clark, C., Li, W.X., Zhang, C.L., & Bao, C.M., 2010. Magmatic and metamorphic events during the early Paleozoic Wuyi–Yunkai orogeny, south- eastern South China: new age constraints and pressure–temperature conditions, *Geological Society of America Bulletin* 122, 772–793.

Lister, G. S., M. G. O'Dea, & I. Somaia (1999), A tale of two synclines: Rifting, inversion and transpressional popouts at Lake Julius, northwestern Mt Isa terrane, Queensland, *Australian Journal of Earth Sciences*, *46*(2), 233-250.

Loosveld, R. J. H. (1989), The synchronism of crustal thickening and high T/low P metamorphism in the Mount Isa Inlier, Australia 1. An example, the central Soldiers Cap belt, *Tectonophysics*, *158*(1-4), 173-190.

MacCready, T. (2006), Structural cross-section based on the Mt Isa deep seismic transect, *Australian Journal of Earth Sciences*, *53*(1), 5-26.

Maccready, T., B. R. Goleby, A. Goncharov, B. J. Drummond, & G. S. Lister (1998), A framework of overprinting orogens based on interpretation of the Mount Isa deep seismic transect, *Economic Geology*, *93*(8), 1422-1434.

Mark, G. (2001), Nd isotope and petrogenetic constraints for the origin of the Mount Angelay igneous complex: implications for the origin of intrusions in the Cloncurry district, NE Australia, *Precambrian Research*, *105*(1), 17-35.

McConachie, B., M. Barlow, J. Dunster, R. Meaney, & A. Schaap (1993), The Mount Isa Basin—definition, structure and petroleum geology, *The APPEA Journal*, *33*(1), 237-257.

McDougall, I., and Harrison, T.M., 1999. *Geochronology and Thermochronology by the 40Ar/39Ar Method*. Oxford University Press on Demand.

Meng, L., Z.-X. Li, H. Chen, X.-H. Li, and X.-C. Wang (2012), Geochronological and geochemical results from Mesozoic basalts in southern South China Block support the flat-slab subduction model, *Lithos*, *132*, 127-140.

Montgomery, D. R., & M. T. Brandon (2002), Topographic controls on erosion rates in tectonically active mountain ranges, *Earth and Planetary Science Letters*, *201*(3-4), 481-489.

Neumann, N. L., G. M. Gibson, & P. N. Southgate (2009), New SHRIMP age constraints on the timing and duration of magmatism and sedimentation in the Mary Kathleen Fold Belt, Mt Isa Inlier, Australia, *Australian Journal of Earth Sciences*, *56*(7), 965-983.

Neumann, N. L., P. N. Southgate, G. M. Gibson, & A. McIntyre (2006), New SHRIMP geochronology for the Western Fold Belt of the Mt Isa Inlier: Developing a 1800 - 1650 Ma event framework, *Australian Journal of Earth Sciences*, *53*(6), 1023-1039.

Nordsvan, A. R., W. J. Collins, Z.-X. Li, C. J. Spencer, A. Pourteau, I. W. Withnall, P. G. Betts, & S. Volante (2018a), Laurentian crust in northeast Australia: Implications for the assembly of the supercontinent Nuna, *Geology*, *46*(3), 251-254.

Nordsvan, A. R., W. J. Collins, & Z.-X. Li (2018b), A Piece of North America Is Now in Queensland, Australian Science,

O'Dea, M. G., & G. S. Lister (1995), The role of ductility contrast and basement architecture in the structural evolution of the Crystal Creek block, Mount Isa Inlier, NW Queensland, Australia, *Journal of Structural Geology*, *17*(7), 949-960.

O'Dea, M. G., G. S. Lister, P. G. Betts, & K. S. Pound (1997a), A shortened intraplate rift system in the Proterozoic Mount Isa terrane, NW Queensland, Australia, *Tectonics*, *16*(3), 425-441.

O’Dea, M. G., G. S. Lister, T. Maccready, P. G. Betts, N. H. S. Oliver, K. S. Pound, W. Huang, R. K. Valenta, N. H. S. Oliver, & R. K. Valenta (1997b), Geodynamic evolution of the Proterozoic Mount Isa terrain, *Geological Society, London, Special Publications*, *121*(1), 99-122.

O'Dea, M. G., P. G. Betts, T. MacCready, & L. Aillères (2006), Sequential development of a mid-crustal fold-thrust complex: evidence from the Mitakoodi Culminationin the eastern Mt Isa Inlier, Australia, *Australian Journal of Earth Sciences*, *53*(1), 69-90.

Oliver, N. H., R. J. Holcombe, E. J. Hill, & P. J. Pearson (1991), Tectono-metamorphic evolution of the Mary Kathleen Fold Belt, northwest Queensland: A reflection of mantle plume processes?, *Australian Journal of Earth Sciences*, *38*(4), 425-455.

Page, R. W. (1983), Chronology of Magmatism, Skarn Formation, and Uranium Mineralization, Mary-Kathleen, Queensland, Australia, *Economic Geology*, *78*(5), 838-853.

Page, R. W. (1998), Links between Eastern and Western fold belts in the Mount Isa Inlier, based on SHRIMP U-Pb studies, *Geological Society of Australia Abstracts*, *49*.

Page, R. W., & I. Williams (1988), Age of the Barramundi Orogeny in northern Australia by means of ion microprobe and conventional U-Pb zircon studies, *Precambrian Research*, *40*, 21-36.

Page, R. W., & S. S. Sun (1998), Aspects of geochronology and crustal evolution in the Eastern Fold Belt, Mt Isa Inlier, *Australian Journal of Earth Sciences*, *45*(3), 343-361.

Page, R. W., & T. H. Bell (1986), Isotopic and Structural Responses of Granite to Successive Deformation and Metamorphism, *The Journal of Geology*, *94*(3), 365-379.

Page, R., S. Sun, & T. MacCready (1997), New geochronological results in the central and eastern Mount Isa Inlier and implications for mineral exploration, paper presented at Geodynamics and Ore Deposits Conference Abstracts, Australian Geodynamics Cooperative Research Centre.

Pearson, P. (1992), Synkinematic emplacement of the Middle Proterozoic Wonga batholith into a midcrustal extensional shear zone, Mount Isa Inlier, Queensland, Australia, *Detailed Studies of the Mount Isa Inlier*, 289-328.

Pehrsson, S. J., B. M. Eglington, D. A. D. Evans, D. Huston, & S. M. Reddy (2016), Metallogeny and its link to orogenic style during the Nuna supercontinent cycle, *Geological Society, London, Special Publications*, *424*(1), 83-94.

Perkins, C., C. A. Heinrich, & L. A. Wyborn (1999), 40 Ar/39 Ar geochronology of copper mineralization and regional alteration, Mount Isa, Australia, *Economic Geology*, *94*(1), 23-36.

Perkins, C., & L. A. I. Wyborn (1998), Age of Cu-Au mineralisation, Cloncurry district, eastern Mt Isa Inlier, Queensland, as determined by (40)Ar/(39)Ar dating, *Australian Journal of Earth Sciences*, *45*(2), 233-246.

Pinet, P., & M. Souriau (1988), Continental erosion and large-scale relief, *Tectonics*, *7*(3), 563-582.

Pisarevsky, S. A., S.-A. Elming, L. J. Pesonen, & Z.-X. Li (2014), Mesoproterozoic paleogeography: Supercontinent and beyond, *Precambrian Research*, *244*, 207-225.

Pollard, P. J., G. Mark, & L. C. Mitchell (1998), Geochemistry of post-1540 Ma granites in the Cloncurry district, northwest Queensland, *Economic Geology and the Bulletin of the Society of Economic Geologists*, *93*(8), 1330-1344.

Pollard, P., & C. Perkins (1997), $^{40}Ar/^{39}Ar$ geochronology of alteration and Cu-Au-Co mineralization in the Cloncurry district, Mount Isa Inlier, Australia, *AMIRA P438 Cloncurry Base Metals and Gold Final Report*.

Pollard, P., & N. McNaughton (1997), U/Pb geochronology and Sm/Nd isotope characterization of Proterozoic intrusive rocks in the Cloncurry district, Mount Isa inlier, Australia, *AMIRA P438 Cloncurry Base Metals and Gold Final Report, Section*, *4*, 19.

Pourteau, A., M. A. Smit, Z.-X. Li, W. J. Collins, A. R. Nordsvan, S. Volante, & J. Li (2018), 1.6 Ga crustal thickening along the final Nuna suture, *Geology*, *46*(11), 959-962.

Ra¨mo¨o. t. & Haapala I. 1995. One hundred years of rapakivi granite. Mineralogy and Petrology 52, 129–185.

Reinhardt, J. (1992a), The Corella Formation of the Rosebud Syncline (central Mount Isa Inlier): deposition, deformation, and metamorphism, *Detailed studies of the Mount Isa Inlier*, 229-255.

Reinhardt, J. (1992b), Low-pressure, high-temperature metamorphism in a compressional tectonic setting: Mary Kathleen Fold Belt, northeastern Australia, *Geological Magazine*, *129*(1), 41-57.

Renne, P. R., G. Balco, K. R. Ludwig, R. Mundil, & K. Min (2011), Response to the comment by W.H. Schwarz et al. on "Joint determination of K-40 decay constants and Ar-40*/K-40 for the Fish Canyon sanidine standard, and improved accuracy for Ar-40/Ar-39 geochronology" by PR Renne et al. (2010), *Geochimica Et Cosmochimica Acta*, *75*(17), 5097-5100.

Richards, J. R., J. A. Cooper, & A. W. Webb (1963), Potassium-argon ages on micas from the Precambrian region of North-Western Queensland, *Journal of the Geological Society of Australia*, *10*(2), 299-312.

Rogers, J. J. W., & M. Santosh (2002), Configuration of Columbia, a mesoproterozoic supercontinent, *Gondwana Research*, *5*(1), 5-22.

Rubenach, M. J. (1992), Proterozoic low-pressure/high-temperature metamorphism and an anticlockwise P–T–t path for the Hazeldene area, Mount Isa Inlier, Queensland, Australia, *Journal of Metamorphic Geology*, *10*(3), 333-346.

Rubenach, M. J., & A. J. Barker (1998), Metamorphic and metasomatic evolution of the Snake Creek Anticline, Eastern Succession, Mt Isa Inlier, *Australian Journal of Earth Sciences*, *45*(3), 363-372.

Rubenach, M. J., & K. A. Lewthwaite (2002), Metasomatic albitites and related biotite-rich schists from a low-pressure polymetamorphic terrane, Snake Creek Anticline, Mount Isa Inlier, north-eastern Australia: microstructures and P-T-d paths, *Journal of Metamorphic Geology*, *20*(1), 191-202.

Rubenach, M. J., D. R. W. Foster, P. M. Evins, K. L. Blake, & C. M. Fanning (2008), Age constraints on the tectonothermal evolution of the Selwyn Zone, Eastern Fold Belt, Mount Isa Inlier, *Precambrian Research*, *163*(1-2), 81-107.

Sayab, M. (2006), Decompression through clockwise P–T path: implications for early N–S shortening orogenesis in the Mesoproterozoic Mt Isa Inlier (NE Australia).

Sayab, M. (2009), Tectonic significance of structural successions preserved within low-strain pods: Implications for thin- to thick-skinned tectonics vs. multiple near-orthogonal folding events in the Palaeo-Mesoproterozoic Mount Isa Inlier (NE Australia), *Precambrian Research*, *175*(1-4), 169-186.

Scibiorski, E., E. Tohver, & F. Jourdan (2015), Rapid cooling and exhumation in the western part of the Mesoproterozoic Albany-Fraser Orogen, Western Australia, *Precambrian Research*, *265*, 232-248.

Skipton, D.R., Schneider, D.A., Kellett, D.A. and Joyce, N.L., 2017. Deciphering the Paleoproterozoic cooling history of the northeastern Trans-Hudson Orogen, Baffin Island (Canada), using 40Ar/39Ar step-heating and UV laser thermochronology. *Lithos*, *284*, pp.69-90.

Southgate, P. N., D. L. Scott, T. T. Sami, J. Domagala, M. J. Jackson, N. P. James, & T. K. Kyser (2000), Basin shape and sediment architecture in the Gun Supersequence: A strike-slip model for Pb–Zn–Ag ore genesis at Mt Isa, *Australian Journal of Earth Sciences*, *47*(3), 509-531.

Southgate, P. N., N. L. Neumann, & G. M. Gibson (2013), Depositional systems in the Mt Isa Inlier from 1800 Ma to 1640 Ma: Implications for Zn–Pb–Ag mineralisation, *Australian Journal of Earth Sciences*, *60*(2), 157-173.

Spikings, R. A., D. A. Foster, & B. P. Kohn (1997), Phanerozoic Denudation History of the Mount Isa Inlier, Northern Australia: Response of a Proterozoic Mobile Belt to Intraplate Tectonics, *International Geology Review*, *39*(2), 107-124.

Spikings, R. A., D. A. Foster, B. P. Kohn, & G. S. Lister (2001), Post-orogenic (<1500 Ma) thermal history of the Proterozoic Eastern Fold Belt, Mount Isa Inlier, Australia, *Precambrian Research*, *109*(1-2), 103-144.

Spikings, R. A., D. A. Foster, B. P. Kohn, & G. S. Lister (2002), Post-orogenic (< 1500 Ma) thermal history of the Palaeo-Mesoproterozoic, Mt. Isa province, NE Australia, *Tectonophysics*, *349*(1-4), 327-365.

Stübner, K., Grujic, D., Dunkl, I., Thiede, R. and Eugster, P., 2018. Pliocene episodic exhumation and the significance of the Munsiari thrust in the northwestern Himalaya. *Earth and Planetary Science Letters*, *481*, pp.273-283.

Thorkelson, D. J., J. A. Abbott, J. K. Mortensen, R. A. Creaser, M. E. Villeneuve, V. J. McNicoll, & P. W. Layer (2005), Early and Middle Proterozoic evolution of Yukon, Canada, *Canadian Journal of Earth Sciences*, *42*(6), 1045-1071.

Verbaas, J. (2018), A sedimentary overlap assemblage links Australia to northwestern Laurentia at 1.6 Ga, *Precambrian Research*.

Volante, S., Pourteau, A., Collins, W. J., Blereau, E., Li, Z.-X., Smit, M., Evans, N. J., Nordsvan, A. R., Spencer, C. J., McDonald, B. J., Li, J., Günter, C. (2020a). Multiple P-T-d-t paths reveal the evolution of the final Nuna assembly in northeast Australia. Journal of Metamorphic Geology, 38(6), 593-627.

Volante, S., Collins, W. J., Pourteau, A., Li, Z. X., Li, J., & Nordsvan, A. R. (2020b) Structural evolution of a 1.6 Ga orogeny related to the final assembly of the supercontinent Nuna: coupling of episodic and progressive deformation. Tectonics, e2020TC006162.

Whalen, J. B., K. L. Currie, & B. W. Chappell (1987), A-Type Granites - Geochemical Characteristics, Discrimination and Petrogenesis, *Contributions to Mineralogy and Petrology*, *95*(4), 407-419.

White, W. M. (2013). *Geochemistry*. John Wiley & Sons.

Williams, P. J., & G. N. Phillips (1992), Cloncurry mapping project 1990: geology of the Selwyn Range (McKinlay River and Maramungee Creek areas), *Contributions - James Cook University, Economic Geology Research Unit*, *40*.

Wilson, I. H., G. M. Derrick, & D. J. Perkin (1984), Eastern Creek Volcanics - Their geochemistry and possible Role in copper mineralization at Mount Isa, Queensland, *Bmr Journal of Australian Geology & Geophysics*, *9*(4), 317-328.

Withnall, I. W., & L. J. Hutton (2013), Proterozoic - North Australian Craton, *Geology of Queensland*, 23-112.

Wyborn, L. (1998), Younger ca 1500 Ma granites of the Williams and Naraku Batholiths, Cloncurry district, eastern Mt Isa Inlier: Geochemistry, origin, metallogenic significance and exploration indicators, *Australian Journal of Earth Sciences*, *45*(3), 397-411.

Wyborn, L., R. Page, & M. McCulloch (1988), Petrology, geochronology and isotope geochemistry of the post-1820 Ma granites of the Mount Isa Inlier: mechanisms for the generation of Proterozoic anorogenic granites, *Precambrian Research*, *40-41*(C), 509-541.

Yao, W.-H., Z.-X. Li, W.-X. Li, X.-C. Wang, X.-H. Li, & J.-H. Yang (2012), Post-kinematic lithospheric delamination of the Wuyi–Yunkai orogen in South China: Evidence from ca. 435Ma high-Mg basalts, *Lithos*, *154*, 115-129.

Zhang, S., Z.-X. Li, D. A. D. Evans, H. Wu, H. Li, & J. Dong (2012), Pre-Rodinia supercontinent Nuna shaping up: A global synthesis with new paleomagnetic results from North China, *Earth and Planetary Science Letters*, *353-354*, 145-155. http://doi.org/10.1016/j.epsl.2012.07.034.

Zhao, G., P. A. Cawood, S. A. Wilde, & M. Sun (2002), Review of global 2.1–1.8 Ga orogens: implications for a pre-Rodinia supercontinent, *Earth-Science Reviews*, *59*(1-4), 125-162.

Appendix C: Supplementary materials to Chapter 3

Attached at the end of the thesis.

Chapter 4

Orogenic collapse in the Georgetown Inlier of NE Australia after 1.6 Ga Nuna assembly: new insights from Ar thermochronology

This chapter will be submitted to *Tectonics* as:

Li, J., Li, Z.-X., Pourteau, A., Jourdan, F., Volante, S., Olierook, H. K. H., Nordsvan, A. R., & Collins, W. J. Orogenic collapse in the Georgetown Inlier of NE Australia after 1.6 Ga Nuna assembly: new insights from Ar thermochronology. *Tectonics*. (in preparation)

Abstract

Characterising the timing and magnitude of vertical and lateral motions of rocks within continental terranes is critical for understanding crustal evolution and orogenic development. In the Georgetown Inlier of NE Australia, the ca. 1.6 Ga crustal thickening/metamorphic event has been ascribed to the collision between NW Laurentia and NE Australia during the final assembly of Nuna. Although recent structural and metamorphic analyses have revealed the timing and nature of the collisional event, little is known about the timing and kinematics of post-collisional crustal exhumation. Here we evaluate the late- to post-collisional orogenic evolution through establishing the cooling history of each crustal domain using high-precision $^{40}Ar/^{39}Ar$ thermochronology. Due to multiple Palaeozoic thermal overprints, only eight (out of twenty) high-precision $^{40}Ar/^{39}Ar$ ages are resolved and show that cooling following the ca. 1.6 Ga crustal thickening/metamorphic event was diachronous across the region. Restricted to the Croydon domain, the fastest cooling was recorded by the ca. 1.55 Ga Esmeralda granite, which cooled between ca. 1.548 and 1.536 Ga at a cooling rate of $8.1^{+6.6}_{-3.9}$°C/Ma. The central domain recorded a cooling from the peak metamorphic stage at ca. 1.55 Ga to hornblende cooling age of ca. 1.53 Ga at $3.3^{+4.1}_{-3.0}$°C/Ma, and then to biotite cooling age of ca. 1.50 Ga at $4.0^{+1.7}_{-2.2}$°C/Ma. The little-metamorphosed western domain recorded the slowest cooling of $0.7^{+1.2}_{-0.7}$°C/Ma at ca. 1.6(?)–1.53 Ga. A rapid cooling occurred in the eastern domain from ca. 1.55 Ga with an estimated cooling rate of $3.4^{+4.3}_{-1.5}$°C/Ma. The post-1.55 Ga regional cooling is interpreted to represent the post-collisional extension that is correlatable with orogenic collapse reported in the neighbouring Mount Isa Inlier. This new work builds on previous structural, petrological

and geochronological studies, and leads to the recognition of a possible crustal melting and differential exhumation event during orogenic collapse across the NE Australian orogenic belts, ca. 50 Myr after the final assembly of Nuna.

4.1 Introduction

Despite the widespread record of global orogenesis between ca. 2.10 and 1.80 Ga, the supercontinent Nuna (also known as Columbia; Evans & Mitchell, 2011; Evans et al., 2016; Rogers & Santosh, 2002; Zhang et al., 2012; Zhao et al., 2002) was not completely assembled until the juxtaposition between Australia and Laurentia (North America) at ca. 1.60 Ga (Fig. 4.1a) (Betts et al., 2016; Kirscher et al., 2019; Nordsvan et al., 2018; Pisarevsky et al., 2014; Pourteau et al., 2018; Volante et al., 2020b). Recent investigations of the sedimentary provenance (Nordsvan et al*.,* 2018) and metamorphic record (Pourteau et al., 2018) suggest that the Georgetown Inlier, now preserved in the North Australian Craton, might represent part of an allochthonous terrane of Laurentian heritage that collided with the North Australia Craton during the ca. 1.60 Ga crustal thickening/metamorphic event. Although metamorphic and structural studies have begun to address the timing and nature of continental collision (Volante et al., 2020a; 2020b), details involving the orogenic evolution and its implication for supercontinent reconstruction remain a matter of debate (Gibson et al., 2018; 2019; 2020; Pourteau et al., 2018; Volante et al., 2020a). In the Georgetown Inlier, the ca. 1.60 Ga crustal thickening/metamorphic event resulted in medium-pressure and medium-temperature (*MP–MT*) metamorphism followed by regional, high temperature and low-pressure metamorphism (Boger and Hansen, 2004; Hills, 2003; Volante et al., 2020a), atypical of modern-style continent-continent collisions (Dong et al., 2011; Yin and Harrison, 2000). Although collision has been postulated as a driving mechanism for orogenesis, there is a lack of evidence for Phanerozoic-style orogenesis such as high pressure metamorphism event or exposed accretionary complexes (Boger and Hansen, 2004; Volante et al., 2020a, 2020b).

Understanding tectonic processes require detailed knowledge of the timing and duration of crustal motions and deformational history (Johnson et al., 2012; Kearey et al., 2009). Thermal histories can partly record the denudation of uplifted regions, and thus provide insights into orogenic processes (McDougall & Harrison 1999; Skipton et al., 2017; Stübner et al., 2018). In this study, high-precision $^{40}Ar/^{39}Ar$ thermochronological data from igneous and metamorphic rocks of the Georgetown Inlier were used to decipher the cooling history associated with the 1.6 Ga crustal thickening/metamorphic event. Thermochronological results, combined with published metamorphic and magmatic records, were used to reconstruct and compare the cooling history across different crustal domains, infer the kinematics of late-to post-orogenic faulting, and discuss the driving mechanism for post-peak metamorphic crustal exhumation.

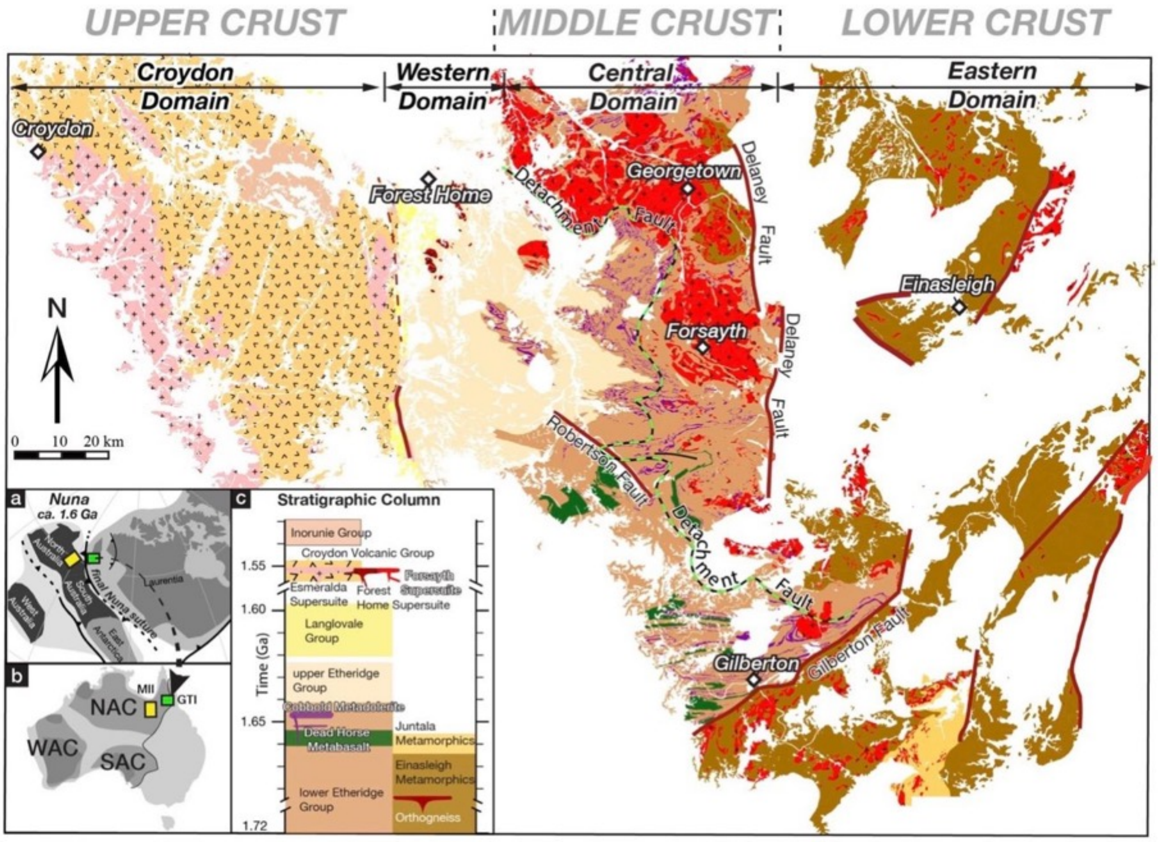

Fig. 4.1: Simplified lithological map of the Georgetown Inlier showing the successive stratigraphic packages and the main fault zones. The geometry of the detachment fault is modified after Volante et al. (2020b). The crustal domains consist of the western, central, and eastern domains from west to east based on their distinct structural and metamorphic evolution (Volante et al., 2020a). The Croydon domain represents the westernmost region of the Georgetown Inlier. Inset a: Paleogeographic reconstruction of NE Australia at ca. 1.60 Ga (Pourteau et al., 2018) showing the inferred location of the study area (the Georgetown Inlier; green box) and Mount Isa Inlier (yellow box) along the final Nuna suture zone (Olierook et al., 2021). Inset b: Location of the study area to the Australian cratons. NAC, North Australian Craton; WAC, West Australian Craton; SAC, South Australian Craton, MII, Mount Isa Inlier; GTI, Georgetown Inlier. Inset c: Stratigraphic column of the Georgetown Inlier.

4.2 Geological background of the Georgetown Inlier

The Georgetown Inlier exposes ca. 1.72–1.56 Ga sedimentary and mafic volcanic rocks (Black et al., 1998, 2005; Geological Survey of Queensland, 2011; Withnall & Hutton, 2013), which have been subjected to poly-phase deformation and metamorphism, and syn- to post-orogenic magmatism at ca. 1.60–1.55 Ga, ascribed to the Jana Orogeny (Cihan et al., 2006; Pourteau et al., 2018; Volante et al., 2020a, Black & McCulloch, 1990; Black et al., 2005). A recent petrostructural study (Volante et al., 2020a) has divided the Georgetown Inlier into three distinct geological domains based on their structural characteristics and metamorphic grades, from west to east, the western, central, and eastern domains (Fig. 4.1). The Croydon domain is added in this study to reflect the westernmost volcanic and subvolcanic rocks of the Georgetown Inlier (Fig. 4.1).

According to geochronological data and depositional settings, three dominantly marine sedimentary stratigraphic sequences are recognized in the Georgetown Inlier, including: (1) the 1.72–1.60 Ga Etheridge Group (subdivided into upper and lower sequences, Withnall et al., 1997); (2) the ca. 1.57–1.56 Ga Langlovale Group (Withnall & Mackenzie, 1983); and (3) the ca. 1.55 Ga Croydon Volcanic Group (Black et al., 1998; Withnall, 1996; Withnall et al., 2013). The lower Etheridge Group (ca. 1.72–1.65 Ga; Withnall et al., 2013; Neumann & Kositcin, 2011), exposed in the central domain, comprises paralic (Withnall, 1996) to deep marine (Lambeck, 2011) siliciclastic, calcareous and carbonaceous sedimentary rocks, interlayered with ca. 1.66–1.65 Ga mafic intrusions (Baker et al., 2010; Black et al., 1998), and is thought to represent the protolith of the high-grade migmatitic Einasleigh Metamorphics (paragneiss, calc-silicate gneiss, amphibolite, and sometimes orthogneiss) to the east (Withnall et al., 1988; Black et al., 2005; Neumann & Kositcin, 2011). The upper Etheridge Group (ca. 1.65–1.60 Ga, GSQ, 2011; Withnall et al., 2013), exposed in the western domain, comprises tidal-flat deltaic carbonaceous mudstone, representing a stratigraphically section younging toward the west (Withnall et al., 1988; Withnall & Henderson, 2012). The overlying Langlovale Group (ca. 1.57–1.56 Ga, Geological Survey of Queensland, 2011; Withnall & Mackenzie, 1983) that unconformably(?) overlies the Etheridge Group on the west (Withnall et al., 1997; Withnall & Hutton, 2013), is in turn overlain unconformably by and faulted against the Croydon Volcanic Group in the Croydon domains (Fig. 4.1). Based on filed relationship observations, a recent study suggests that the Langlovale Group overlies the upper Etheridge Group conformably (Nordsvan et al., 2018). Regional structural analysis suggests that the early D_1 fabric is preserved in both the Langlovale Group and the underlying Etheridge Group (Volante et al., 2020b).

The Georgetown Inlier was subjected to multiple deformational and metamorphic events syn- to post-ca. 1.60 Ga (Nordsvan et al., 2018, Pouteau et al., 2018; Volante et al., 2020a, 2020b). Recent structural and petrological analyses further indicate that the ca. 1.6 Ga orogeny started with an E–W compressional event under a *MP–MT* condition (D_1/M_1, in Volante et al., 2020a; Pourteau et al., 2018), and formed moderately SE-plunging, upright folds and NNE-striking S_1 fabric in the western and central domains (Volante et al., 2020b). The orogenesis evolved to a subsequent *LP*–high-*T* (*HT*) metamorphism event, occurred synchronous with ca. 1.55 Ga widespread regional magma intrusion (Volante et al., 2020a), and was interpreted by Volante et al. (2020a) to represent a regional E–W extensional stage (D_2/M_2).

According to the age and petrological characteristics of the ca. 1.56–1.55 Ga granitoid intrusions, these intrusions in the Georgetown Inlier could be further divided into: (1) the ca. 1.56–1.55 Ga Forsayth Supersuite (Champion & Heinemann, 1994; Anderson et al., 2017); (2) the ca. 1.56 Ga Forest Home Trondhjemite (Neumann & Kositcin, 2011); and (3) the ca. 1.55 Ga Esmeralda Supersuite and synchronous Croydon Volcanics (Champion, 1991; Black and McCulloch, 1990; Withnall and Hutton, 2013). The Forsayth Supersuite is a weakly to strongly deformed porphyritic, biotite-muscovite S-type granite that are found mostly in the central domain with minor occurrences in the western and eastern domains (Champion & Heinemann, 1994; Volante et al., 2020c). The Forest Home Trondhjemite is an I-type, fine- to medium-grained biotite trondhjemite intruding the upper Etheridge Group in the western domain (Champion, 1991; Mackenzie, 1980). The Esmeralda Supersuite is an S-type granite restricted to the Croydon domain, assimilated country rocks and intruded the Etheridge and Langlovale groups (Withnall & Hutton, 2013). The coeval Croydon Volcanic Group comprises felsic ignimbrite and rhyolite, erupted subaerially in the Croydon region at ca. 1.55 Ga (Black & McCulloch, 1990; Withnall, 1996; Withnall and Hutton, 2013; Volante et al., 2020c), and is overlain by the non-deformed Inorunie Group (Withnall et al., 1997), marking a tectonic quiescence post-1.55 Ga in this region.

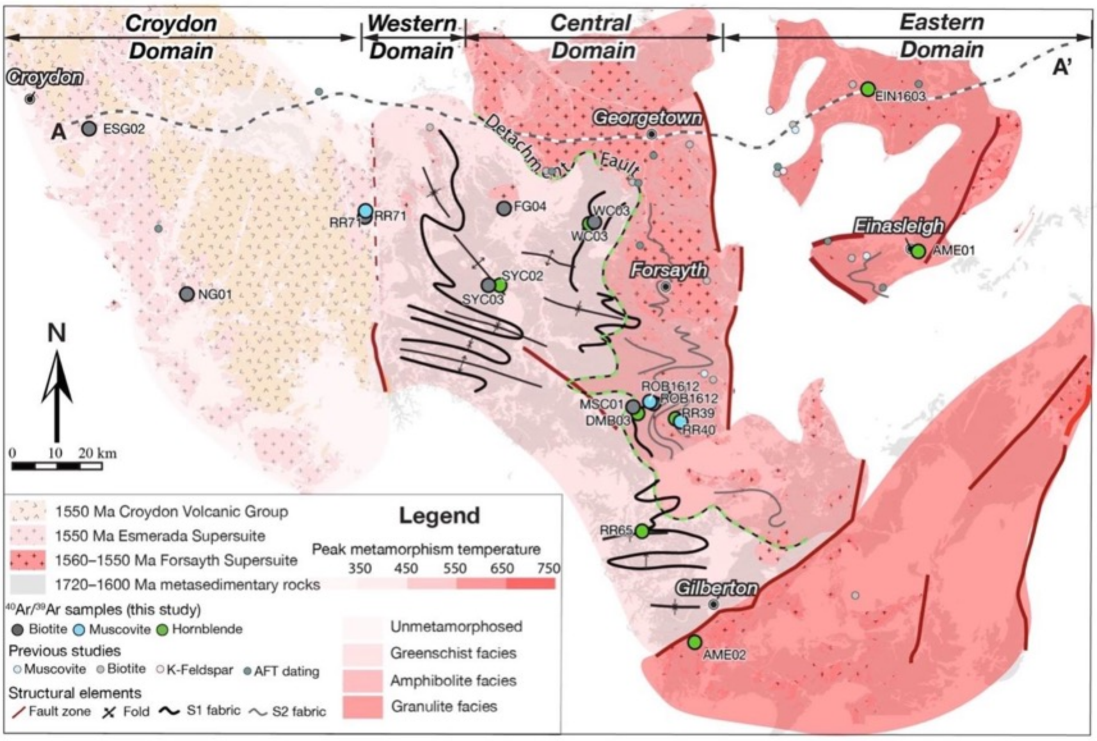

Fig. 4.2: Metamorphic temperature map of the different metamorphic domains of the Georgetown modified after Volante et al. (2020a). Structural features are also added as foliation trajectories (modified after Volante et al., 2020b). ^{40}Ar/^{39}Ar sample locations from this study and pervious thermochronology dating locations from literature (Black et al., 1979; Spikings et al., 2001) are shown in big and small circles. Transect A–A' shows the trace of Geoscience Australia geophysical imaging profile 07GA–IG2.

4.2.1 Evaluation of previously published thermochronological data

Crustal cooling within the Georgetown Inlier has been the subject of previous studies (Black et al., 1979; Richards et al., 1966; Spiking et al., 2001). The earliest thermochronological study used K-Ar analysis to date multiply-deformed and poly-metamorphosed rocks of the Georgetown Inlier (Richards et al., 1966), and yielded consistent ca. 430–415 Ma muscovite K-Ar ages, regarded as being related to the Palaeozoic magmatic thermal disturbance (Richards et al., 1966). Subsequent studies applied Rb-Sr whole-rock and K-Ar dating on Proterozoic and Paleozoic metamorphic and granitic rocks across the inlier (Black et al., 1979). Five structural metamorphic events were interpreted to have occurred between ca. 1.57 and 0.30 Ga (Black et al., 1979). The first two thermal events occurred at ca. 1.57 and 1.47 Ga, and were interpreted to be associated with regional tight folding and prograde metamorphic events, respectively

(Black et al., 1979). Subsequent thermal episodes were ascribed to retrogressive metamorphism and Palaeozoic igneous intrusions (Black et al., 1979).

Given the analytical limitations of the K/Ar and whole-rock Rb/Sr methods (Begemann et al., 2001; Kelley, 2002), Spikings et al. (2001) applied the $^{40}Ar/^{39}Ar$ method on biotite and alkali feldspar, together with apatite fission-track (AFT) dating, on Proterozoic metamorphic and granitic rocks to quantify the regional cooling and exhumation history. Four periods of non-linear cooling were identified in the Georgetown Inlier with the crust cooling from ~320°C to 60°C between the Neoproterozoic and mid-Cretaceous–Holocene. The Neoproterozoic cooling was correlated with the rifting event that separated Laurentia and Gondwana during the supercontinent Rodinia breakup. The latter phase of Palaeozoic cooling was ascribed to the northeastern Australian Precambrian basement cooling due to the far-field effects of the Delamerian Orogeny in South Australia. The latest Cretaceous and Holocene cooling events were associated with crustal exhumation related to activity along the Delaney Fault (Spikings et al., 2001).

Although those previous work set the foundation for better understanding the Proterozoic crustal evolution of the Georgetown Inlier, after plotting existing $^{40}Ar/^{39}Ar$ ages (Table D.4.1 in Appendix D) along an E–W transect across the Georgetown Inlier (Fig. 4.3), an apparent age gap of ~100 Ma appears between collisional metamorphism (at ca. 1.59 Ga) and the subsequent cooling event (mainly from ca. 1.49 Ga). Individual structural domains also yielded heterogeneous $^{40}Ar/^{39}Ar$ ages for the same type of mineral. For example, biotite from the central domain yields a range of ages between ca. 1.49 and 0.45 Ga (Fig. 4.3), indicate multiple thermal overprinting. Most of the $^{40}Ar/^{39}Ar$ ages cluster around ca. 450–370 Ma, closely following the regional Silurian-aged granite intrusions (Black et al., 1979; Richards et al., 1966; Spiking et al., 2001), as no medium- or high-temperature thermochronology has been applied to the Georgetown Inlier (e.g., garnet geospeedometry or hornblende $^{40}Ar/^{39}Ar$ thermochronology).

Several factors could lead to contrasting $^{40}Ar/^{39}Ar$ ages being produced by the same mineral system, such as weathering, mineral alteration, fluid interaction or multiple argon diffusions as discussed in section 3.3.2. To evaluate the significance and quality of the previous results, all published data (Table D.4.1) were recalculated using an updated argon decay constant of 0.576 ± 0.002 E-10 1/a (Renne et al., 2011) with the recalculated age spectra presented in Fig. D.4.1 of Appendix D.

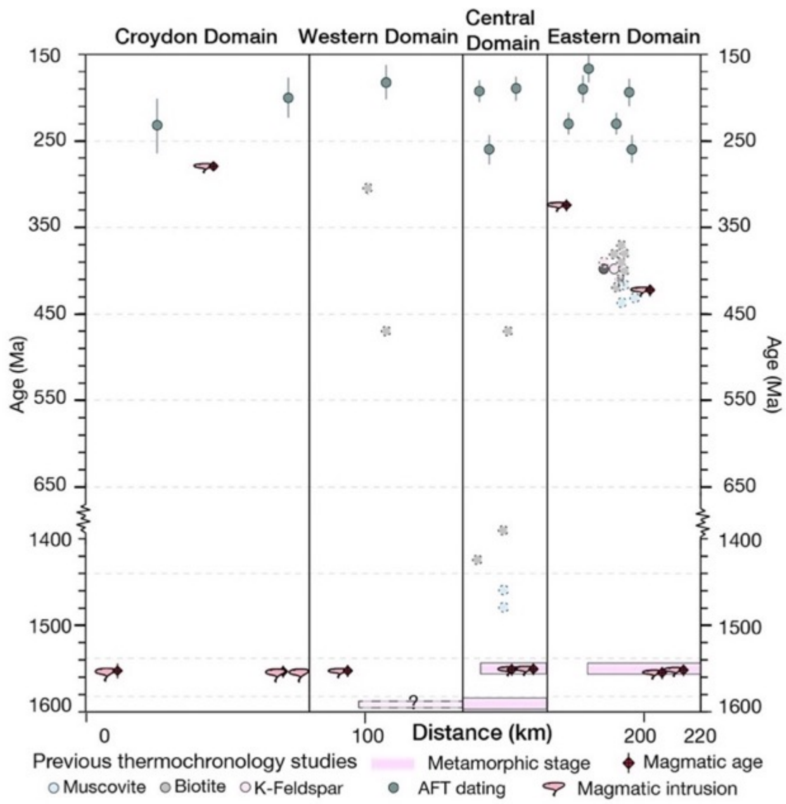

Fig. 4.3: Time vs distance plot of previously published thermochronology ages (Black et al., 1979; Richards et al., 1966; Spikings et al., 2001) along an E-W transect across the Georgetown Inlier (line A–A' in Fig. 4.1). Solid circles represent argon plateau ages, and semi circles are total fusion or unclassified ages recalculated from previous data. Dots in dark green represent apatite fission-track (AFT) ages from Spikings et al. (2001). Magmatic ages are from Black and McCulloch (1990), Black and Withnall (1993), Neumann and Kositcin (2011), and Kositcin et al. (2015).

4.3 Methodology

4.3.1 Sample collection

Twenty samples were collected along an E–W and a N–S transects across the Georgetown Inlier, intersecting various crustal domains (Fig. 4.2). To better understand the timing, kinematics, and magnitudes of fault movements, our sampling strategy targeted areas along major fault zones or crustal-scale tectonic contacts and locations within different crustal levels recording distinct metamorphic evolutions (Volante et al., 2020a).

4.3.2 $^{40}Ar/^{39}Ar$ analysis

Selected sample grains were sent to irradiation before conducting $^{40}Ar/^{39}Ar$ analyses. After irradiation, a total of 20 signal grains $^{40}Ar/^{39}Ar$ analyses were performed at the Western Australian Argon Isotope Facility at Curtin University. A summary of the Ar isotope data corrected for blanks, mass discrimination, and radioactive decay can be found in Table D.4.3 of Appendix D. The detailed analytical methodology is outlined in section 2.2.3 of the Methodology Chapter. Closure temperature and cooling rate calculation of dated minerals

Method for argon closure temperature calculation can be find in section 3.4.4. We use the activation energy, diffusion coefficient, and volume constant of Harrison (1981) for hornblende, Harrison et al. (2009) for muscovite, and Grove & Harrison (1996) for biotite. Initial closure temperature value (T_{i_c}) refers to those published from $^{40}Ar/^{39}Ar$ diffusion experiments; here we used the values summarised by Schaen et al. (2020) and chose 510 ± 10°C for hornblende (Harrison, 1981), 390 ± 10 °C for muscovite (Harrison et al., 2009), and 320 ± 10 °C for biotite (Harrison et al., 1985) at a cooling rate of 10°C/Ma, and effective diffusion dimension of 100 mm. The initial cooling rates (dT/dt) are assessed from the ca. 1.6 Ga *MP–MT* event (D_1/M_1, in Volante et al., 2020a) to the time of a minerals closure temperature (as defined by Dodson, 1973), representing a minimal (conservative) estimation as the crustal exhumation may have started substantially later than the metamorphism stage. The *MP–MT* event and ages were summarized from previous work (Black et al., 1998; Boger and Hansen, 2004; Cihan et al., 2006; Neumann and Kositcin, 2011; Pourteau et al., 2018; Volante et al., 2020a, 2020c) and compiled in Table D.4.2 of Appendix D. The effective diffusion radius (a) was based on the grain sizes of the dated mineral. Detailed parameter values of the closure temperatures calculating for each sample are listed in Table B.2.2 in Appendix B.

Cooling rate values were calculated utilizing subtraction values of specific closure temperatures for hornblende, muscovite and biotite dated in this study to divide their cooling age difference. To incorporate data error estimations into the cooling rate calculations, Monte Carlo simulations were applied to take the cooling ages of the paired minerals and closure temperature ranges into consideration (detailed descriptions summarized in section 2.3 of the Methodology Chapter). Representative probability histograms showing the distribution of Monte Carlo simulation results for closure temperature and cooling rate values are given in Fig. D.4.2 and Fig. D.4.3 of Appendix D, respectively.

4.4 Results

4.4.1 Petrography

For this study, seventeen samples were collected in the Georgetown Inlier with their sample lithology, locations, and $^{40}Ar/^{39}Ar$ analytical ages summarized in Table 4.1. Samples petrographic description is organized from west to east across the inlier (see below), with outcrop photos and thin section microphotographs provided in Figs. 4.4–4.7.

(1) Croydon Domain

Sample ESG02 is a medium- to coarse-grained, biotite-bearing S-type granite from the Esmeralda Supersuite, 5 km west of Croydon Township (Fig. 4.2). The sample comprises quartz, plagioclase, K-felspar, biotite, muscovite, amphibole and accessory ilmenite, apatite and zircon. Megacrysts of plagioclase and coarse-grained quartz show granular texture. Plagioclase is partially replaced by fine-grained sericite aggregates (Fig. 4.4 A & a). *Sample NG01* is a fine-to medium-grained biotite-bearing S-type granite from the Nonda Granite, 46 km southeast of ESG02 (Fig. 4.2). The sample comprises quartz, plagioclase, K-felspar, biotite, white mica and accessory apatite and zircon. Quartz occurs either as fine subhedral grains, which have straight contacts with plagioclase, or as an interstitial phase between plagioclase grains. Plagioclase crystals are euhedral and elongated grains partially altered by carbonate or sericite (Fig. 4.4 B & b). *Sample RR71* is a coarse-grained, biotite-bearing, S-type granite collected from the Esmeralda Supersuite, 13 km southwest of the Langlovale Station (Fig. 4.2). The sample comprises quartz, orthoclase, plagioclase, biotite and accessory ilmenite, apatite, monazite, zircon (Fig. D.4.4 C & c). This sample gave a U-Pb zircon age of 1550 ± 6 Ma (Volante et al., 2020c). Detail petrological descriptions can be find in Volante et al. (2020c).

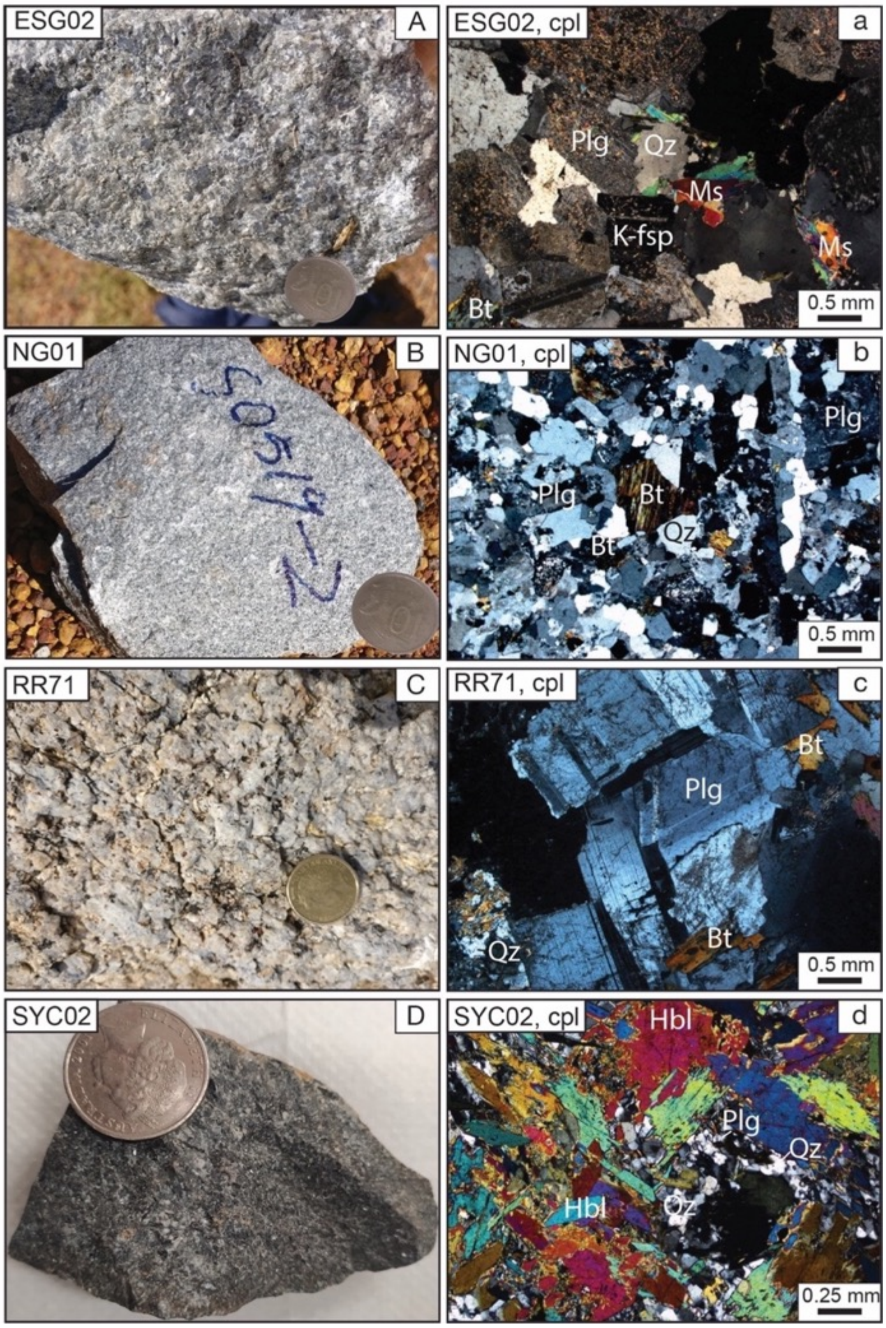

Fig. 4.4: (A & a) Esmeralda Supersuite, Croydon Domain. Megacrysts of plagioclase and coarse-grained quartz showing granular texture. (B & b) Nonda Granite, Croydon Domain. Quartz and plagioclase are subhedral in fine grains with straight contacts, showing subvolcanic texture. (C & c) Esmeralda Granite, Croydon Domain. K-feldspar megacrysts and quartz are subhedral with straight contacts, preserving granular texture. (D & d) Cobbold Metadolerite, Western Domain. Primary green to brown amphibole occurs as porphyroblast in a matrix of poikilitic plagioclase and quartz, and is partially replaced by secondary light green euhedral amphibole. Mineral abbreviations in Figs. 4.4–4.7 are followed by Whitney and Evans (2010): Qz = Quartz, Plg = Plagioclase, K-fsp = K-feldspar, Bt = Biotite, Ms = Muscovite, Amp = Amphibole, Hbl = Hornblende, Ep = Epidote, Chl = Chlorite, Grt= Garnet, St= Staurolite, Mg= Magnetite, Zo = Zoisite. Cpl = Cross polar light. Spl = single polar light.

(2) Western Domain

Sample SYC02 is an amphibolite collected 35 km southeast of RR71 (Fig. 4.2). The sample comprises amphibole, quartz, plagioclase and minor sericite. Primary porphyblastic amphibole is green to brown, preserved in poikilitic plagioclase- and quartz-bearing matrix. Secondary, euhedral, medium to fine-grained amphibole grew over the primary amphibole crystals with no preferred orientation (Fig. 4.4 D & d). *Sample SYC03* is a low-grade foliated phyllite collect adjacent to SYC02. The pervasive cleavage is defined by the shape preferred orientation of quartz grains (Fig. 4.5 A & a). White mica are 0.4 mm-sized phenocrysts in a fine-grained quartz-bearing matrix, partial replaced by chlorite. *Sample FG04* is a coarse-grained, biotite-bearing S-type granite collected from the Forsayth Supersuite, 20 km northeast of SYC03 (Fig. 4.2). The sample comprises quartz, plagioclase, orthoclase, biotite and accessory hornblende, ilmenite, apatite. Plagioclase is partially replaced by epidote (zoisite). Muscovite and recrystallized quartz grew as fine-grained aggregates around biotite megacrysts (Fig. 4.5 B & b). *Sample WC03* is an amphibolite collected 20 km east of FG04 (Fig. 4.2). The sample comprises amphibole, plagioclase, microcline, quartz, biotite and secondary chlorite. Quartz grains locally occur as vermicular inclusions in orthoclase or as an interstitial phase (Fig. 4.5 C & c). Amphibole is euhedral, shares straight contacts with plagioclase and quartz. *Sample RR65* is a foliated metabasalt collected from the Dead Horse Metabasalt, 70 km south of WC03 (Fig. 4.2). This sample consists of amphibole, plagioclase, quartz and minor white mica. The foliation is defined by alternating amphibole-rich and plagioclase- and quartz-rich layers (Fig. 4.5 D & d). Primary porphyroblastic amphibole is partially replaced by chlorite at the rims, and by minor secondary prismatic amphibole in the core.

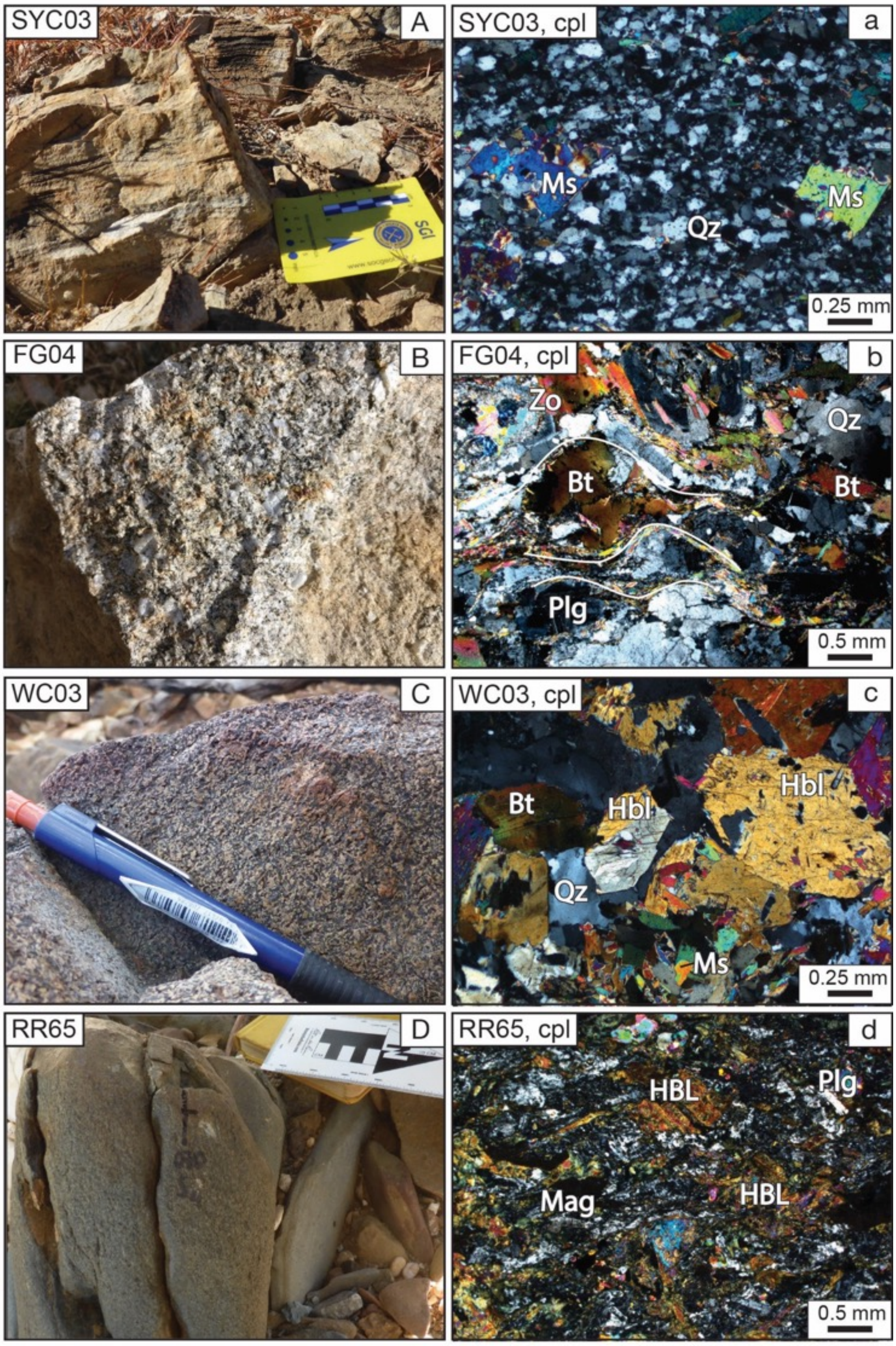

Fig. 4.5: (A & a) Mica schist from Lane Creek Formation, Western Domain. White mica crystals within a quartz-bearing matrix. (B & b) Forsayth Supersuite, Western Domain. Recrystallised fine-grained white mica wraps biotite porphyroblast and defines a tectonic fabric. (C & c) Cobbold Metadolerite, Western Domain. The light green euhedral amphibole was partially replaced by biotite and epidote. (D & d) Dead Horse Metabasalt, Western Domain. Primary porphyroblastic amphibole is partially replaced by chlorite at the rims.

(3) Central Domain

Sample ROB1612 is a garnet-staurolite schist collected from the lower Etheridge Group, 30 km north of RR65. The sample comprises quartz, muscovite, biotite, staurolite, garnet, plagioclase, and accessories ilmenite, monazite, and zircon (Fig. 4.6 A & a). Garnet Lu–Hf geochronology and metamorphic *P*-*T* estimation has been applied to this sample by Pourteau et al. (2018) with metamorphic garnet porphyroblasts dated at 1598 ± 6 Ma. Detailed petrological descriptions are in Pourteau et al. (2018). *Sample DMB03* is a metabasalt collected from the Dead Horse Metabasalt, 7 km southwest of ROB1612 (Fig. 4.2). The sample comprises amphibole, plagioclase, quartz and white mica. The dominant foliation is defined by dark green amphibole, with elongated plagioclase and quartz aggregates (Fig. 4.6 B & b). *Sample MSC01* is a low-grade phyllitic schist from the Corbett Formation, 3.6 km north of DMB03 (Fig. 4.2). The sample comprises quartz, plagioclase, white mica and biotite. Subhedral biotite and quartz porphyroblasts are wrapped by the matrix foliation defined by micaceous layers (Fig. 4.6 C & c). *Sample RR39* is an amphibolite collected 10 km southeast of MSC01 (Fig. 4.2). The sample comprises coarse-grained amphibole, plagioclase, quartz, minor sericite and chlorite. Granoblastic green amphibole is subhedral and commonly altered by chlorite or by opaque iron-rich minerals (Fig. 4.6 D & d). Oscillatory zoned plagioclase phenocrysts locally occur as elongated prismatic grains, commonly replaced by fine-grained aggregates of sericite. *Sample RR40* is a mica schist collected 1 km northwest of RR39 (Fig. 4.2). The sample comprises quartz, biotite, muscovite and minor garnet. The pervasive foliation is defined by schistous muscovite and brown biotite interlayered with flattened and elongated quartz grains (Fig. 4.7 A & a). Quartz grains are subhedral, elongated, and exhibit undulose extinction.

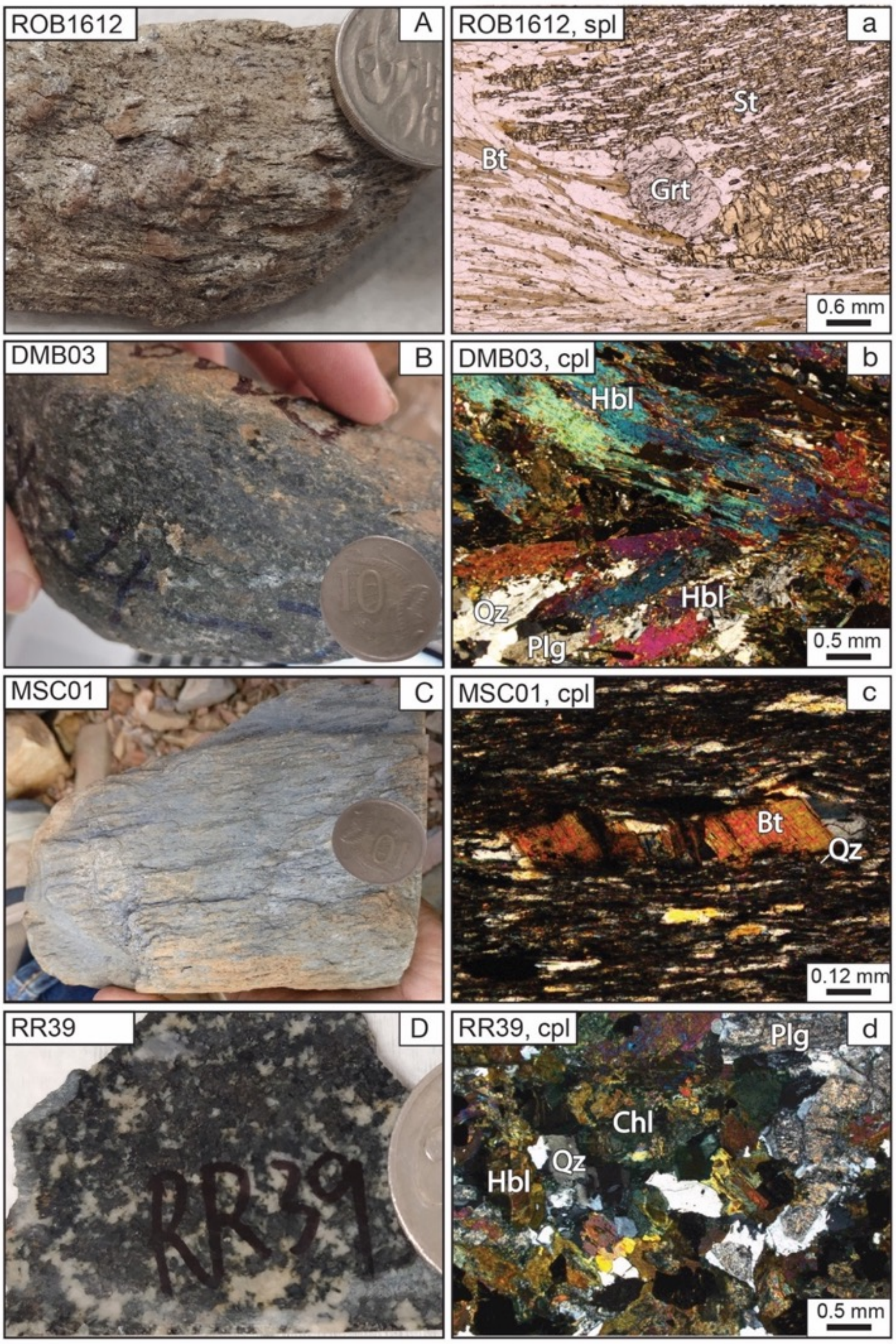

Fig. 4.6: (A & a) Garnet-staurolite schist from Corbett Formation, Central Domain. Porphyritic garnet grain contains inclusion trails of quartz, and is wrapped by the matrix foliation of biotite, muscovite and staurolite and micaceous layers. (B & b) Dead Horse Metabasalt, Central Domain. Porphyritic amphibole is replaced by euhedral elongated amphibole crystals. Secondary fine-grained quartz and plagioclase are interstitial between the porphyritic amphibole grains. (C & c) muscovite schist from Corbett Formation, Central Domain. Biotite porphyroblasts wrapped by the foliated micaceous fine grain aggregates. (D & d) Amphibolite from Daniel Creek Formation, central domain. Dark green amphibole is subhedral and has straight contact with plagioclase. Amphibole is commonly altered by chlorite or replaced by opaque iron-rich minerals.

(4). Eastern Domain

Sample EIN1603 is a foliated amphibolite collected 40 km northwest of the Einasleigh township (Fig. 4.2). The foliation is defined by amphibole with flattened quartz and plagioclase grains. Plagioclase show lamellae textures and share straight contacts with amphibole. Brown amphibole grains are subdural, partially replaced by quartz and chlorite at the rims (Fig. 4.7 B & b). *Sample AME01* is a migmatitic amphibolite from the Einasleigh migmatitic complex, 800 m northeast to the Einasleigh Town (Fig. 4.2). This sample comprises amphibole, plagioclase, quartz, minor biotite and ilmenite. The pervasive foliation is defined by brown amphibole alternated with quartz and plagioclase-bearing layers. The amphibole is subhedral to anhedral, shows straight contact with the plagioclase, and is locally altered by chlorite at the rims (Fig. 4.7 C & c). *Sample AME02* is an amphibolite collected south of the Gilberton Fault, 20 km southeast of RR65 (Fig. 4.2). The sample comprises amphibole, plagioclase, quartz, epidote and minor sericite. Coarser-grained amphibole is partially replaced by fine-grained, green amphibole (Fig. 4.7 D & d). Locally, amphibole porphyroblasts are pseudomorphed by epidote aggregate.

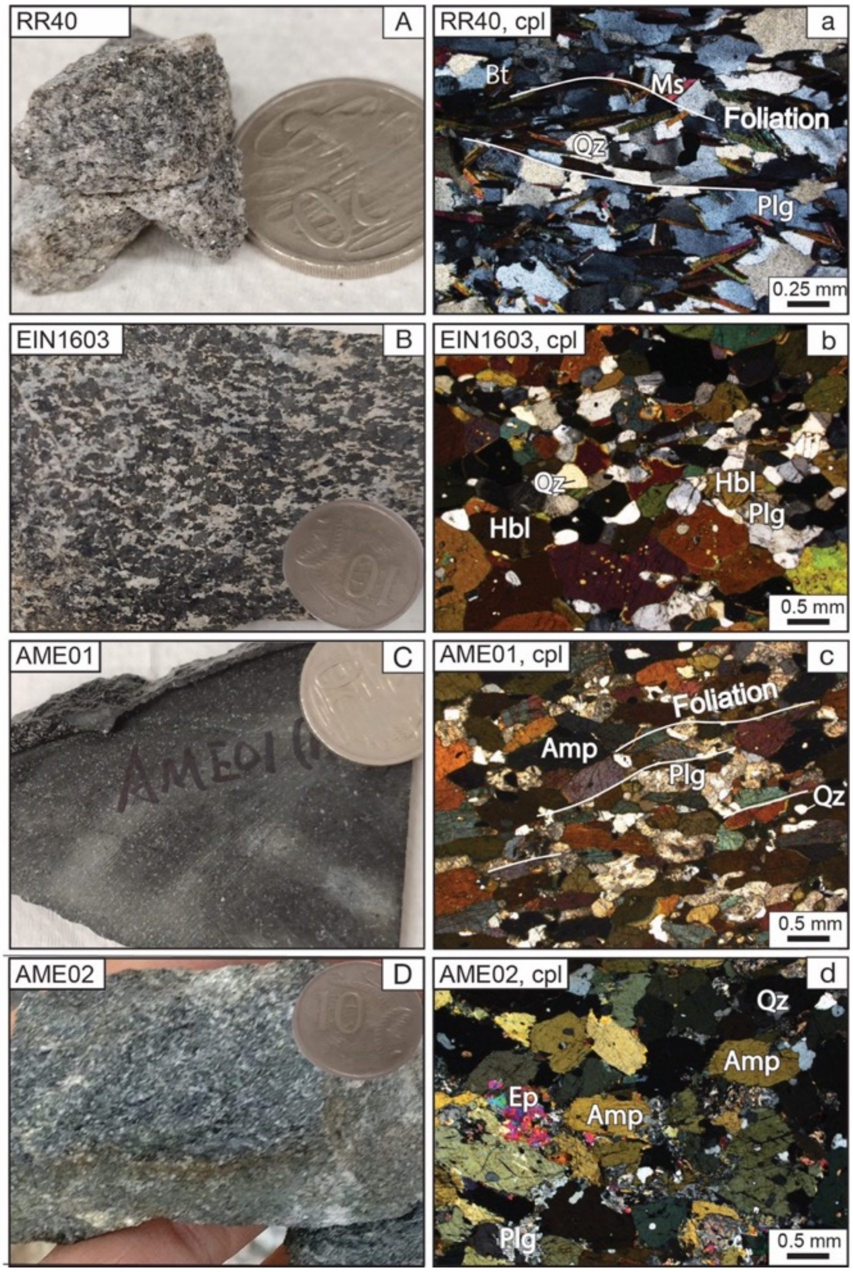

Fig. 4.7: (A & a) Muscovite schist of Daniel Creek Formation, Central Domain. The pervasive foliation is defined by the alignment of euhedral muscovite and minor brown biotite, interlayering with flattened quartz grains. (B & b) Amphibolite from Einasleigh Metamorphics, Eastern Domain. Dominant foliation defined by elongated amphibole and flattened quartz and plagioclase grains. (C & c) Amphibolitic migmatite of Einasleigh Metamorphics, Eastern Domain. Brown amphibole shows straight contact with the plagioclase, and elongates with minor quartz and plagioclase along the foliation direction. (D & d) Amphibolite from the Einasleigh Metamorphics, Eastern Domain. Primary light green porphyritic amphibole preserves corrosion relic texture with corrosion zones being replaced by quartz and plagioclase.

4.4.2 Cooling ages

Twenty single-grain analyses were conducted, including nine hornblende, three muscovite, and eight biotite. However, due to the regional thermal interference caused by Palaeozoic intrusions, multiple samples have recorded retrograde alterations or hydrothermal overprint (e.g., *SYC03, RR39, AME01*), and yield either Palaeozoic ages or perturbed age spectra suggesting Paleozoic ages (Fig. D.4.4). Among them, only eight samples yielded Proterozoic plateau ages ($n = 6$), and mini-plateau ages ($n = 2$) from several mineral types (Fig. 4.8). Sample locations and analytical results are summarized in Table 4.1.

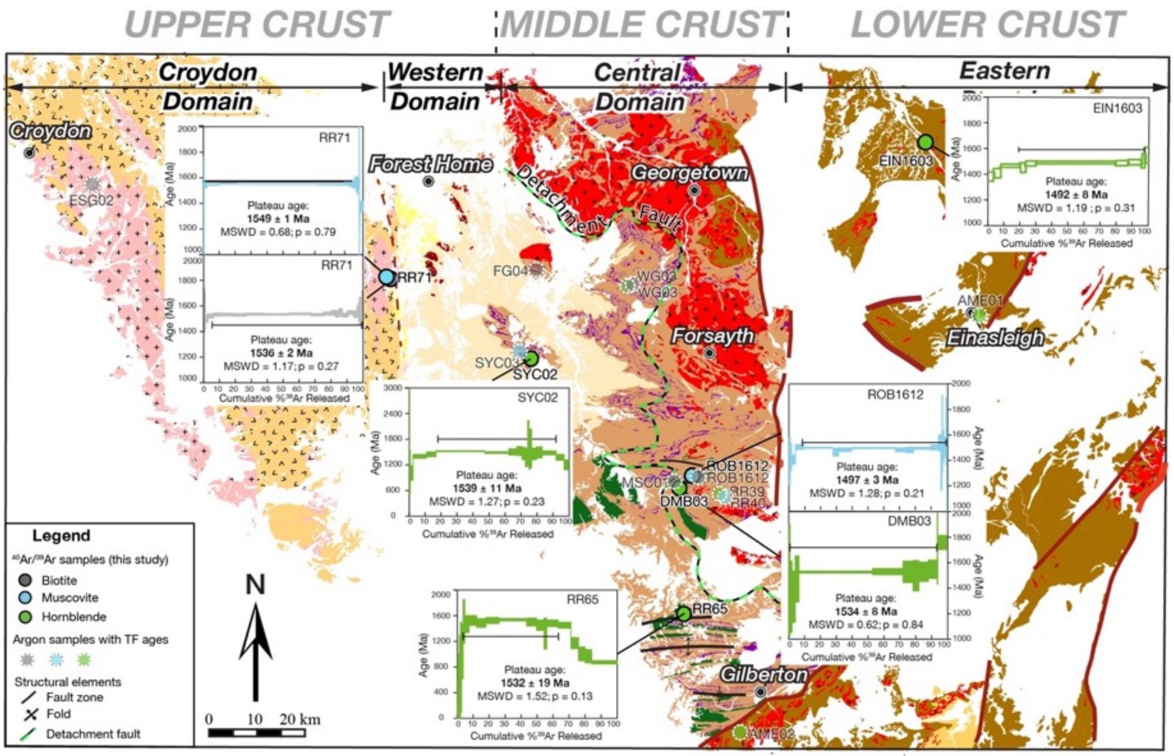

Fig. 4.8: Geological map of the Georgetown Inlier with sample locations and plateau $^{40}Ar/^{39}Ar$ age spectra of this study. Green, blue and gray dots each represent $^{40}Ar/^{39}Ar$ sample locations for hornblende, muscovite and biotite dating, respectively. Samples that produced robust plateaus are shown with solid dots along with their respective age spectra, while samples that failed to produce an age are shown in semi circles with age spectra compiled in Fig. D.4.4 of Appendix D.

Table 2: Argon thermochronology results of the dated sample from the Georgetown Inlier.

Sample ID	$^{40}Ar/^{39}Ar$ dates phase	Lithology	Argon age (Ma)	Age type	Latitude	Longitude
Croydon Domain						
RR71	Muscovite	Esmeralda Granite	1548.7 ± 1.3	Plateau	-18.4682	142.9466
RR71	Biotite	Esmeralda Granite	1536.5 ± 1.8	Plateau	-18.4682	142.9466
Western Domain						
SYC02	Hornblende	Cobbold Metadolerite	1539.5 ± 11.3	Plateau	-18.6067	143.2266
RR65	Hornblende	Dead Horse Metabasalt	1532.4 ± 19	Plateau	-19.1037	143.5191
Central Domain						
ROB1612	Muscovite	Corbett Formation garnet-staurolite schist	1497.0 ± 3.6	Plateau	-18.8472	143.5339
DMB03	Hornblende	Dead Horse Metabasalt	1573.2 ± 13.7	Plateau	-18.8693	143.5213
DMB03	Hornblende	Dead Horse Metabasalt	1534.5 ± 8.1	Plateau	-18.8693	143.5213
Eastern Domain						
EIN1603	Hornblende	Einasleigh Metamorphics	1491.6 ± 8.1	Plateau	-18.1830	144.0044

(1) Croydon Domain

Twenty-five km southwest of the Forest Home homestead, muscovite from sample RR71 Esmeralda Granite yielded a plateau age of **1549 ± 1 Ma** with 98% ^{39}Ar released in 15 steps (MSWD = 0.68, p=0.79), while biotite in the same sample yielded a plateau age of **1536 ± 2 Ma** with 94% ^{39}Ar released in 19 steps (MSWD = 1.17, p=0.27) (Fig. 4.8). Twenty km southeast of Croydon town, biotite from sample ESG02 of the Esmeralda Granite failed to yield any age and produced a saddle-like ^{40}Ar/^{39}Ar age spectrum with the step ages around 1.4 Ga and 1.2 Ga (Fig. D.4.4a). Forty-six km southeast, biotite from sample NG01 (the Nonda Granite) failed to yield an age and produced a saddle-like ^{40}Ar/^{39}Ar age spectrum around 1.4–0.8 Ga (Fig. D.4.4b).

(2) Western Domain

Ten km northwest of the Gilberton town, hornblende from the Dead Horse Metabasalt sample RR65 (Fig. 4.8) yielded a plateau age of **1532 ± 19 Ma** (60% of ^{39}Ar released at 10 steps; MSWD = 1.52, p=0.13). The high-temperature steps decrease to younger apparent age with a minimum of ca 0.8 Ga. Sixty km northwest, a hornblende and muscovite mineral pair was collected from the Cobbold Metadolerite and its hosting mica schist for dating. First attempt of hornblende dating for sample SYC02 failed to yield an age and instead produced a hump-shaped ^{40}Ar/^{39}Ar age spectrum around 1.5–1.2 Ga (Fig. D.4.4c). Reanalysis of a new hornblende grain from this sample yielded a plateau age of **1539 ± 11 Ma** with 75% ^{39}Ar released in 12 steps (MSWD = 1.27, p=0.23) (Fig. 4.8). The muscovite failed to yield an age, and produced a tilde-shape ^{40}Ar/^{39}Ar age spectrum around 1.3-1.1 Ga (Fig. D.4.4d). Twenty-five km northeast, another hornblende and biotite mineral pair was retrieved from the Cobbold Metadolerite sample WC03. Hornblende failed to yield any age, and produced a hump-shaped ^{40}Ar/^{39}Ar age spectrum with steps hovering around 1.6 Ga and 0.4 Ga (Fig. D.4.4e). The biotite also failed to yield any age, and produced a tilde-shape ^{40}Ar/^{39}Ar age spectrum around 1.3–1.0 Ga (Fig. D.4.4f). Eighteen km to the west, biotite sample FG04 from the Forsayth Granite failed to yield any age, and produced a hump-shaped ^{40}Ar/^{39}Ar age spectrum around 1.0–0.7 Ga (Fig. D.4.4g).

(3) Central Domain

Thirty km southwest of Forsayth township, hornblende sample DMB03 from Dead Horse Metabasalt first yielded a plateau age of 1573 ± 13 Ma with 84% of ^{39}Ar released in 14 steps (MSWD = 1.52, p=0.12). However, the reliability of this age was not high as the age spectrum shows excess argon effects, and most step ages recorded errors around 100 – 200 Ma. A reanalysis of a different hornblende grain from the same sample yielded a plateau age of **1534 ± 8 Ma** (Fig. 4.8), with 96% of ^{39}Ar released in 14 steps (MSWD = 0.62, p=0.84). Two km northeast, a muscovite and biotite mineral pair was chosen from the garnet-staurolite schist sample ROB1612 of the lower Etheridge Group (Fig. 4.8). The muscovite initially failed to yield plateau age and produced a total fusion error age of ~1472 Ma. A reanalysis of a different muscovite grain yielded a plateau age of **1497 ± 3 Ma** (Fig. 4.4), with 93% of ^{39}Ar released in 12 steps (MSWD = 1.28, p=0.21). The biotite from the same sample failed to yield any age, producing a hump-shaped ^{40}Ar/^{39}Ar age spectrum ranging between ca. 1.6 and 1.2 Ga (Fig. D.4.4h). Eight km east of the Cabbo Goerge stage, a mineral pair was collected from the mica schist sample (MSC01) and Cobbold Metadolerite (MDR02). Biotite and hornblende failed to yield any age, and produced ladder-shaped ^{40}Ar/^{39}Ar age of 0.7 Ga (Fig. D.4.4i) and discordant age of 1.49 Ga (Fig. D.4.4j), respectively. Eight km southeast, another mineral pair is also chosen to compare the cooling age spacial variation. In sample RR39, hornblende failed to yield any age, and produced a tidal shaped ^{40}Ar/^{39}Ar age spectrum (Fig. D.4.4k). The muscovite from sample RR40 also failed to yield any age and produced a ladder-shaped, monotonously increasing ^{40}Ar/^{39}Ar age spectrum rising to ca. 1.38 Ga (Fig. D.4.4l).

(4) Eastern Domain

In the northern part of this domain, hornblende dated from sample EIN1603 of the Einasleigh Metamorphics yielded a plateau age of **1492 ± 8 Ma**, with 78% of ^{39}Ar released at 6 steps (MSWD = 1.19, p=0.31). Near the Einasleigh township, hornblende from a migmatitic amphibolite (AME01) produced a hump-shaped ^{40}Ar/^{39}Ar age spectrum with steps around 1.45 Ga and 1.0 Ga (Fig. D.4.4m). Eight km southwest of the Gilberton township, hornblende from sample AME02 produced a tidal shaped ^{40}Ar/^{39}Ar age spectrum ranging between ca. 1.1 Ga and 0.4 Ga (Fig. D.4.4n).

4.5 Discussion

4.5.1 $^{40}Ar/^{39}Ar$ age interpretation

As discussed previously (section 3.5.3), to ascribe the dated $^{40}Ar/^{39}Ar$ ages as mineral thermal cooling ages, several assumptions need to be considered. These Include: (1) the dated minerals remain in a closed system without being interrupted by hydrothermal fluids; (2) all the radiogenic ^{40}Ar were produced from the decay of ^{40}K without additional K-bearing mineral contribution from secondary mineral growth or alteration. This requires the dated mineral to be least weathered and homogenous without incorporating other K-bearing mineral phases or inclusions. Although carefully examining single crystals under the optical microscopy, several samples are observed as being subjected to secondary potassium-rich mineral inter-growth (e.g., AME02, RR39) or chlorite alterations (e.g., RR39, SYC03). After careful mineral picking and separation to select the least altered grains, these samples still yield excess argon (e.g., WC03, RR39) or argon loss (e.g., ESG02, FG04, MSC01) as seen on their age spectrum (Fig. D.4.4), or a hybrid age spectrum mixing initial crystals and alteration products (FG04 & SYC03), and thus, are discarded in the following cooling history interpretation. The remainder eight ^{40}Ar/^{39}Ar geochronological results are combined with published geochronological, structural and petrological constraints (Boger and Hansen, 2004; Volante et al., 2020a, 2020b, 2020c; Pourteau et al., 2018) to reconstruct retrograde *P–T* paths (Fig. 4.9a) to evaluate the cooling histories of the different tectonic domains. Cooling rate calculations were also conducted to monitor the cooling behaviour, and decipher the timing and exhumation histories between different tectonic domains (Fig. 4.9). Calculated results are listed in Table 4.2.

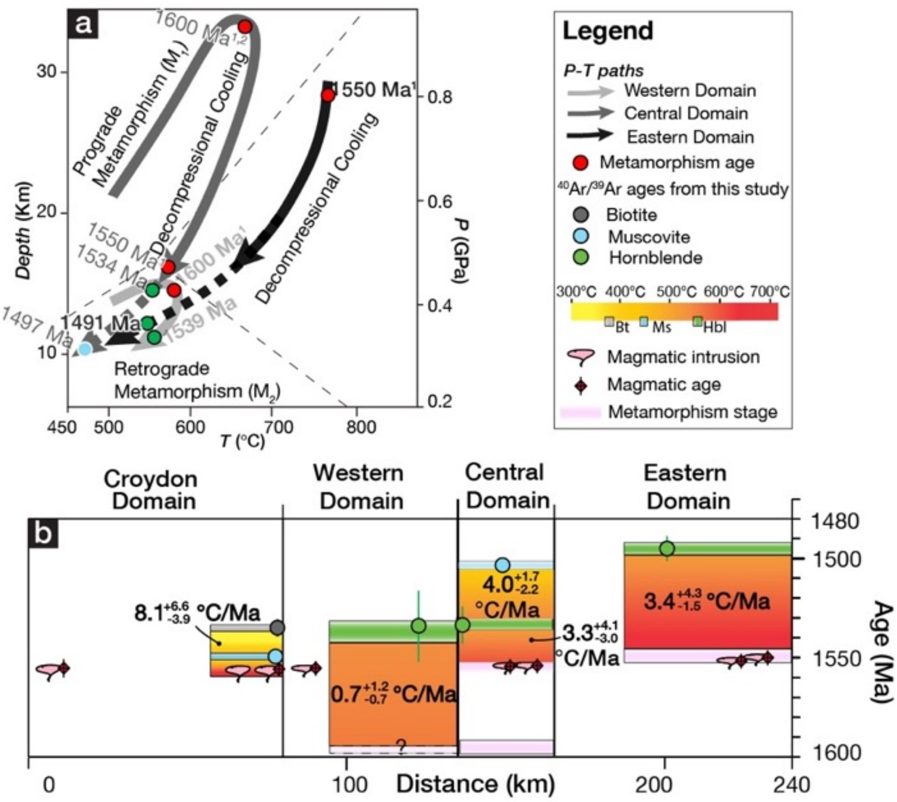

Fig 4.9: a. Reconstructed P–T evolution and tectonic interpretation of the Croydon, western, central and eastern domains (Bell and Rubenach, 1983; Pourteau et al., 2018; Volante et al., 2020a). Dashed lines represent the kyanite-andalusite-sillimanite stability fields. Ages of metamorphism stages referred from previous works: 1= Volante et al., 2020a; 2 = Pourteau et al., 2018. b. Time vs distance plot of $^{40}Ar/^{39}Ar$ ages along an E-W transect across the Georgetown Inlier (line A–A' in Fig. 4.1). Different domains are subdivided by the major boundary faults. Each of the green, blue and grey horizontal bars represents the cooling age dated from the hornblende, muscovite and biotite, respectively. Magmatic ages are from Black and McCulloch (1990), Black and Withnall (1993), and Neumann and Kositcin (2011).

(1) Croydon Domain

In the Croydon domain, the muscovite single aliquot from the Esmeralda Supersuite cooled down to closure temperatures of 478 ± 54°C at 1548.7 ± 1.3 Ma, and further down to the biotite closure temperature of 354 ± 60°C at 1536.5 ± 1.8 Ma at a cooling rate of $8.1^{+6.6}_{-3.9}$°C/Ma (Fig. 4.9b). Volante et al. (2020c) dated the Esmeralda Supersuite with a zircon U-Pb age of 1550 ± 6 Ma. Zircon and monazite thermometry coupled with thermodynamic modelling further indicate a magmatic crystallization temperature of 824 ± 17°C (Volante et al., 2020c). The muscovite cooling age from this study is within the error range of the granite crystallization age, suggesting that the magma cooled down to below muscovite closure temperature of ~480°C shortly after emplacement.

Based on petrological observation and phase equilibria modelling, Volante et al. (2020c) suggest that the Esmeralda Supersuite consists of hot and dry S-type granites derived from a lower crustal magma source that reached upper crustal levels with the contribution of additional mantle-like magma pulses. The hypabyssal texture of these S-type granites supports the interpretation that the magmas were emplaced at near-surface levels in a short duration. Thus, we associate the rapid cooling of the subvolcanic granites from ca. 830°C to 460°C within 2–6 Ma of magmatic crystallization to post-emplacement magmatic heat loss in shallow crustal levels. The second stage cooling rate is moderately fast, with a temperature decrease of ~110°C over a ~12 Myr period, which likely represents a steady thermal diffusion period following the granitic intrusion.

(2) Western Domain

In the western domain, both the Cobbold Metadolerite sample (SYC02) from the north and the the Dead Horse Metabasalt sample (RR65) from the south yield similar cooling ages of ca. 1.53 Ga at hornblende closure temperature of ~510°C. This indicates that the north and south sections of the western domain likely cooled coherently as a single block. Due to a lack of appropriate mineral assemblages, the metamorphic *P-T* condition cannot be precisely constrained. However, chloritoid reported 10–15 km south of the Cobbold Gorge location (Bell and Rubenach, 1983) indicates that the metamorphism reached at least greenschist facies conditions. Based on structural measurements and petrographical observations, Volante et al. (2020b) proposed that the western domain was subjected to the 1.60 Ga crustal thickening/metamorphic event in a low-*P* and medium-*T* metamorphic setting (M_1/D_1) with *P–T* conditions roughly estimate at 550–580°C and ~4 kbar (Volante et al. 2020b). Hornblende $^{40}Ar/^{39}Ar$ thermochronological results imply that the western domain cooled below a closure temperature of 513 ± 52°C at 1532 ± 19 Ma with a slow cooling rate of $0.7^{+1.2}_{-0.7}$°C/Ma (Fig. 4.9b). Slow cooing of the western domain post ca. 1.6 Ga crustal thickening/metamorphic event is consistent with structural and metamorphic studies, which show that this domain was not buried to great depths (over 15km), and was deformed at lower metamorphic *P-T* conditions than the central and eastern domains (Volantee et al., 2020a, 2020b). Thus, rapid tectonic exhumation is not expected. Here, we attribute the slow cooling in the western domain to mainly reflect surface erosion over low topographic relief.

(3) Central Domain

In the central domain, although nine (9) single grain aliquots metamorphic samples had been subjected to thermochronological analyses, only two (including 1 hornblende and 1 muscovite) crystals yielded robust argon cooling ages (Fig. 4.8). Based on petrological observations and phase equilibria modelling, Volante et al. (2020c) suggested that the central domain records fabric and mineral relicts of prograde metamorphism which occurred within the garnet and staurolite stability field from 530–550°C at 6–7 kbar to 620–650°C at 8–9 kbar (Fig. 4.9a, Volante et al., 2020a). This prograde metamorphic event has been precisely dated by garnet Lu-Hf isotopes at ca. 1598 ± 6 Ma (Volante et al., 2020a). The hornblende from the Dead Horse Metabasalt DMB03 in the southwest of Forsayth township dated the followed cooling to hornblende closure temperatures of 548 ± 46°C at 1534 ± 8 Ma, with a minimal cooling rate (because estimation may have started sometime after the 1.6 Ga metamorphic event) of $4.0^{+1.7}_{-2.2}$ °C/Ma (Fig. 4.9b). Replacement of staurolite by andalusite documented a decompression event from 8–9 kbar to <5 kbar (Fig. 4.9a) and marks the transition from medium- to low-pressure metamorphism stage between ca. 1.60 and 1.55 Ga (Volante et al., 2020a). Thus, the rapid cooling to hornblende closure temperature of 1534 ± 8 Ma following the decompressional event is consistent with the rapid crustal exhumation associated with the domain boundary detachment fault activation as normal faulting during the post-orogenic extensional stage (Volante et al., 2020a, 2020b). The nearby muscovite from garnet-staurolite schist sample ROB1612 of the lower Etheridge Group show the following cooling to the muscovite closure temperature of 401 ± 48°C at 1497 ± 3 Ma, with a minimal cooling rate of $3.3^{+4.1}_{-3.0}$ °C/Ma. The later stage of cooling likely accommodated the slow exhumation of the central domain, possibly from ~14 km to ~10 km (Fig. 4.9a) at a rate of ~0.11 mm yr^{-1}.

(4) Eastern Domain

In the eastern domain, based on petrostructural analyses and thermodynamic modeling, Volante et al. (2020a) suggested that partial melting of paragneisses and amphibolitic rocks occurred at a *P-T* condition of 730–770°C and 6–8 kbar. This high-temperature M_2 event occurred syn- to post-D_2 structures, and was dated at ca. 1554 ± 33 Ma (Volante et al., 2020b, 2020c). Subsequent cooling is documented by our new hornblende $^{40}Ar/^{39}Ar$ ages from the Einasleigh metamorphic migmatite, where the temperature cooled through the hornblende closure temperature of 541 ± 50°C at ca. 1491 ± 8 Ma with a cooling rate of $3.4^{+4.3}_{-1.5}$ °C/Ma (Fig. 4.9c). Growth of coronitic green amphibole in the migmatitic amphibolite is suggested to have formed during the retrograde event along the modelled *P-T* condition of 600–650°C and 4–5 kbar (Volante et al., 2020a). Brown amphibole from the dated migmatitic amphibolite sample EIN1603 has rims being replaced by quartz and chlorite, consistent with the regional retrograde overprinting record. Thus, the cooling to hornblende closure temperature of ca. 550 °C followed the projected retrograde *P-T* path (Fig. 4.9a), and is interpreted to have resulted from a continuing retrograde, extensional tectonic regime in the eastern domain. Contrasting to the central domain, where the crust cooled down to 548 ± 46°C by 1534 ± 8 Ma, the eastern domain remained buried at lower-crustal levels at ca. 1.55 Ga and did not cool down to hornblende closure temperature until at ca. 1491 ± 8 Ma.

Table 3: Cooling rates calculated from mineral pairs of hornblende (Hbl), muscovite (Ms), and biotite (Bt) from each tectonic domain at specific closure temperatures. Cooling rate values are reported as the median value and 90% inter-percentile range between 5% (I1) and 95% (I3).

Domain	**Cooling rate $^{I3}_{I1}$(°C/Ma)**	**Cooling period (Ma)**	**Cooling stage**	**Cooling temperature (°C ± 2 SD)**
Croydon Domain				
		1550–1548 Ma	Magmatic crystallisation–Ms cooling	~811 ± 32 °C
				478 ± 54
	$8.1^{+6.6}_{-3.9}$°C/Ma	1548–1536 Ma	Ms–Bt	478 ± 54
				354 ± 60
Western Domain				
	$0.7^{+1.2}_{-0.7}$°C/Ma	1595–1539 Ma	D_1 low-*P* metamorphic stage–Hbl cooling	550 ± 30
				513 ± 52
Central Domain				
	$3.3^{+4.1}_{-3.0}$°C/Ma	1554–1534 Ma	D_3 *MP* – *MP* metamorphic stage–Hbl cooling	640 ± 15
				548 ± 46
	$4.0^{+1.7}_{-2.2}$°C/Ma	1534–1497 Ma	Hbl–Ms	548 ± 46
				401 ± 48
Eastern Domain				
	$3.4^{+4.3}_{-1.5}$ °C/Ma	1549–1491 Ma	D_2 *MP* – *HP* metamorphic stage–Hbl cooling	740 ± 30
				541 ± 50

4.5.2 Tectonics events causing heterogeneous cooling post the assembly of Nuna

Here, we compare the Proterozoic cooling histories (Fig. 4.9) of the Georgetown Inlier (syn to post-Isa Orogeny) and that of the concurrent Isan Orogeny from the neighbouring Mount Isa Inlier (Li et al., 2020; Fig. 4.10 & 4.11), and discussed the tectonic processes of the late to post-orogenic cooling and exhumation history related to the final assembly of Nuna.

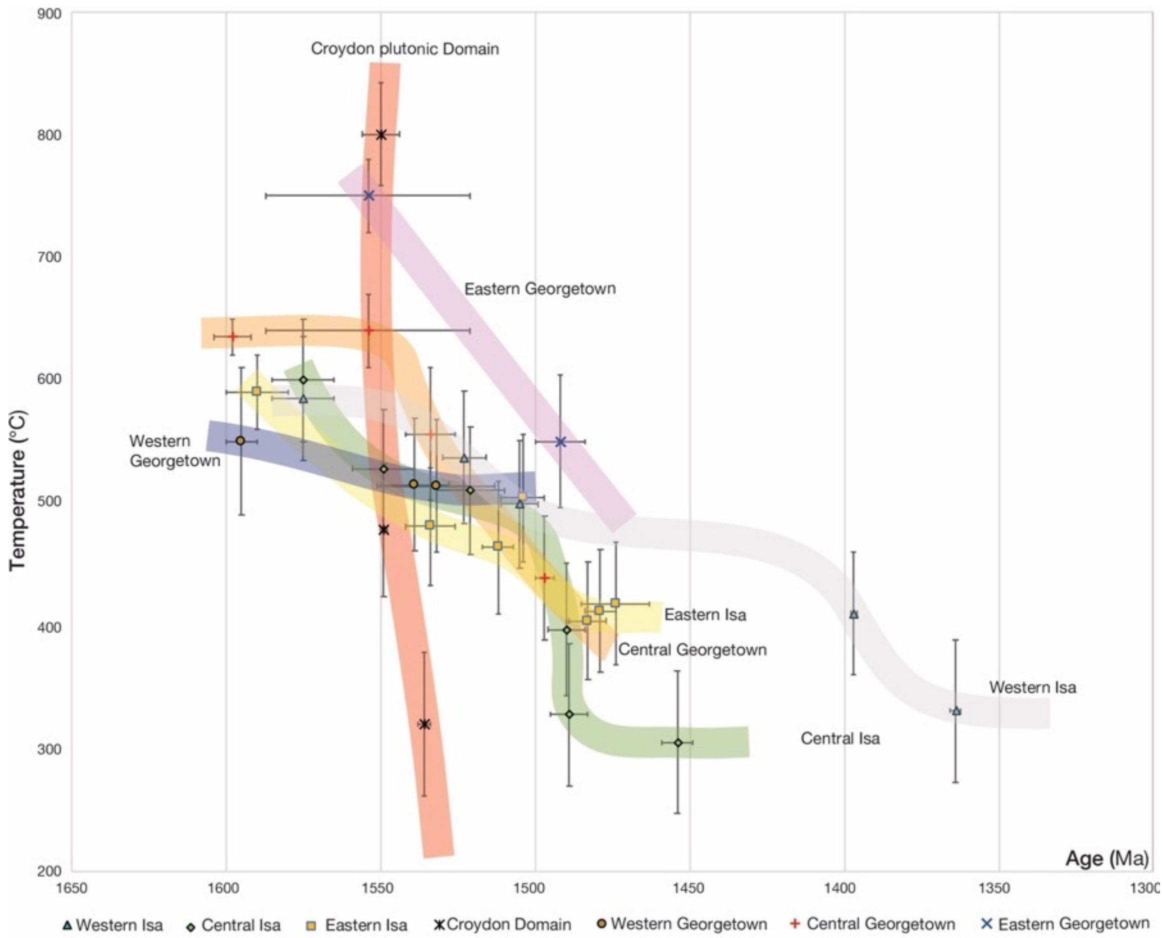

Fig. 4.10: A comparison of cooling paths between different domains from the Mount Isa and Georgetown inliers. For simplicity, Isa is short for the Mount Isa Inlier, and Georgetown is short for Georgetown Inlier. Slop of the cooling path represent the cooling rate from each domain at the different stage with the vertical slop representing the fastest cooling and the horizonal slop represent the slowest cooling.

a) *Rapid magmatic cooling in the Croydon Domain and slow late orogenic cooling in the western Georgetown Inlier*

In the cooling path plot (Fig. 4.10), the fastest cooling is shown in the Croydon Domain, where the magmatism cooled ~500 degrees in a short duration (ca. 10 Ma), and yield a sub-vertical cooling path slope. Both the hypabyssal subvolcanic texture of the granite and the fast cooling closely following intrusion indicate rapid cooling of the subvolcanic granites due to post-emplacement magmatic heat loss and steady thermal diffusion in shallow crustal levels. Further east, the western Georgetown domain recorded the minimum temperature drop of <50 degrees in ca. 100 Myr. with a shallow cooling path. Structural and metamorphic studies showed that this domain was not buried to great depths (e.g., over 15km), thus, was unlikely to have experienced isostatic crustal rebound during orogenic collapse as recorded by the shallow cooling slope.

b) *Differentiate cooling in the central and eastern Georgetown Inlier suggests either a possible crustal break in-between or block tilting*

Further east, the cooling history of the central domain is in stark contrast to that of the eastern domain (Fig. 4.10 & 4.11). The central domain cooled through 548 ± 46°C at 1534 ± 8 Ma with a minimal cooling rate of 3.3°C/Ma, on the contrary, the eastern domain cooled to 541 ± 50°C at ca. 1491 ± 8 Ma. Such different cooling behaviors across a short distance cannot be explained by a crustal tilting around a horizontal hinge east of the eastern domain, as the eastern domain reflect deeper crustal levels than the central domain (Volante et al., 2020a, 2020b).

Volante et al. (2020a, 2020b) proposed a post peak-metamorphism decompressional event in the region where a rapid crustal exhumation associated with the domain boundary detachment normal fault occurred during the post-orogenic extensional stage (Volante et al., 2020a, 2020b). Activation of this west dipping detachment fault along the eastern boundary of the western domain triggered a rapid crustal exhumation of the central domain, as recorded by the rapid cooling at a rate of $3.3^{+4.1}_{-3.0}$ °C/Ma around 1535 Ma. Fluid-fluxed crustal melting of mafic rocks in a post-collisional setting (Pourteau et al., 2020), which generated the ca. 1.55 Ga TTG emplacement in the western domain, accompanied this event. As constrained by both the metamorphic P-T-t path (Pourteau et al., 2018, Volante et al., 2020a, 2020b) and thermochronological record of this study, the western part of the central domain was exhumed from ~33 km to ~14 km between ca. 1600 Ma and 1535 Ma (Fig. 4.9a) at an exhumation rate of ~0.8 mm yr^{-1}. However, similar rapid cooling or exhumation was not observed from the eastern domain, suggesting the possible existence of a structural break in-between. The exact location of such a structural break is yet to be determined through detailed field mapping and geophysical interpretations.

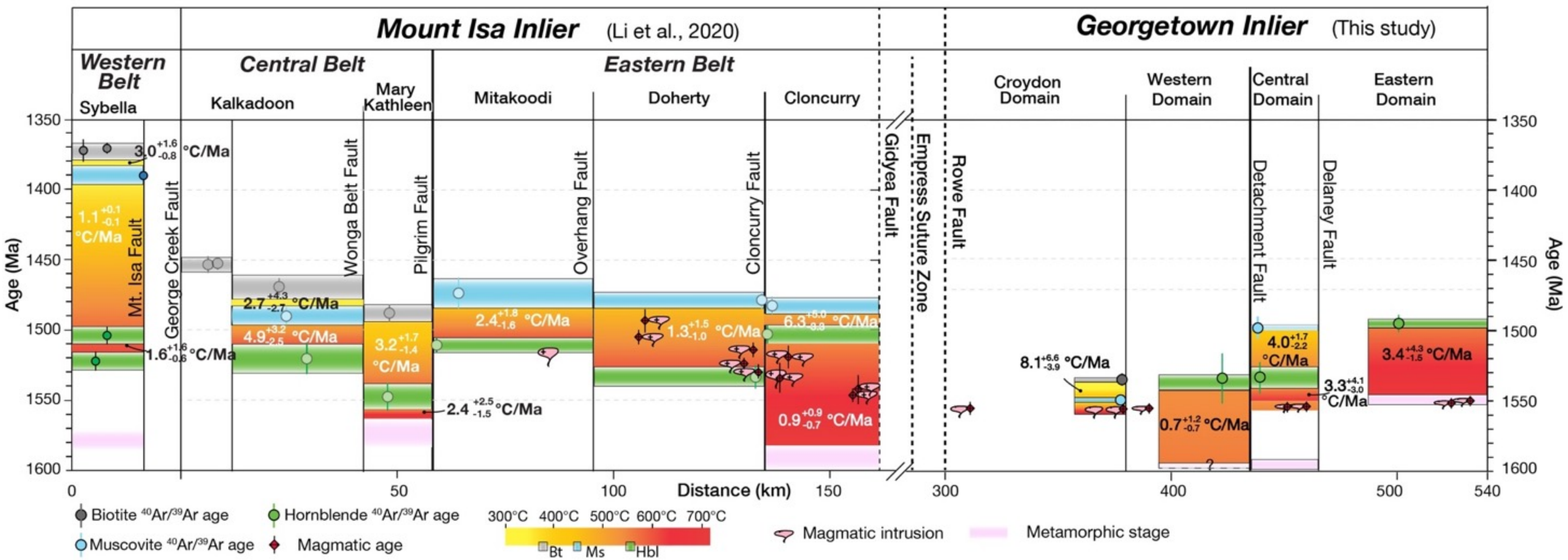

Fig. 4.11: Time vs distance plot of $^{40}Ar/^{39}Ar$ ages along an E-W transect across the Mount Isa and Georgetown inliers. Different domains are subdivided by the major boundary faults. Each of the green, blue and grey horizontal bars represents cooling ages dated from hornblende, muscovite and biotite, respectively. Solid circles represent $^{40}Ar/^{39}Ar$ ages determined in this study, while semitransparent circles are ages from Li et al. (2020). Magmatic ages for the Mount Isa Inlier are from Connors and Page (1995), Mark et al. (2006), Pollard and McNaughton (1997), and Page and Sun (1998). Magmatic ages for the Georgetown Inlier are from Black and McCulloch (1990), Black and Withnall (1993), and Neumann and Kositcin (2011)

c) Diachronous cooling in the Mount Isa Inlier indicates diachronous fault activation, and a comparison with the Georgetown Inlier

As discussed previously (section 3.6.), the diachronous cooling of the orogenic belts in Mount Isa Inlier were associated with reactivation of inherited normal (i.e., early basinal) and reverse (i.e., orogenic) faults. In the cooling path plot (Fig. 4.10), the central belt of the Mount Isa Inlier shows two stages of crustal cooling. The first stage occurred at ca. 1.58–1.50 Ga under the post-Isan Orogeny extensional tectonic regime, and is attributed either by E–W block tilting, or by east to west diachronous uplifting of horsts with the Mary Kathleen Domain the earliest, and the western Kalkadoon Domain the latest (Li et al., 2020). The second stage initiated at ca. 1.5 Ga, reflect the activation of the sub-vertical but slightly east-dipping Pilgrim Fault as a normal fault that exhumed the amphibolite facies Mary Kathleen Domain. Across the Pilgrim Fault, the eastern belt cooled consistently during ca. 1.58–1.48 Ga, with the crustal domains exhumed along the Pilgrim Fault and the Cloncurry Fault at different relative sense of vertical motions. The western belt recorded the most prolonged cooling history with the first stage cooling occurred at ca. 1.55 Ga and seconded stage occurred at ca. 1.40 Ga associated with the reactivation of the Mount Isa Fault. It is noted that although both Georgetown and Mount Isa inliers recorded ca. 1600 Ma peak metamorphism, the rapid cooling in the Georgetown Inlier started from ca. 1550 Ma, whereas that in the Mt Isa Inlier started after 1500 Ma.

d) 1.55 Ga crustal melting and exhumation due to lithospheric delamination

In the cooling path plot (Fig. 4.10), except for the sub-vertical magmatic fast cooling in the Croydon Domain and the delayed cooling in the Eastern Domain of the Georgetown Inlier, the cooling path from different tectonic domains of the Mount Isa and Georgetown inliers overlap within the time period of ca. 1.55 – 1.50 Ga (Fig. 4.11). This cooling period is also contemporary with the regional 1.55–1.50 Ga magmatic events, although the magmatism shows a Georgetown to the Mount Isa inliers westward younging trend. Thus, understanding the genesis for the extensive magmatic activity (Volante et al., 2020b, Pourteau et al., 2020) would provide insight into the cooling mechanism.

In the Mount Isa, the post-orogenic intrusions consist of localized ca. 1550 Ma trondhjemite (Mark, 2001) and widespread voluminous ca. 1540–1490 Ma A-type granitoids.

Geochemistry and petrogenesis studies revealed that the ca. 1.55 Ga trondhjemite is characterized by high Al_2O_3 contents, low heavy rare earth element, and no Sr anomaly, suggesting that it was derived by partial melting of a hydrated mafic source possibly at >0.8–1.0 GPa (Mark, 2001). As discussed previously (section 3.6), magmatism transiting from trondhjemite to A-type granitoids indicates a crustal melting at >900 °C and <0.8–1.0 GPa from a tonalitic to granodioritic source (Mark, 2001), pointing to an elevated geotherm and a decompression melting from the lower crust at ca. 1.55 Ga. The heating of the lower crust in the Mount Isa Inlier was proposed to have been caused by the delamination of a predominantly mafic lower crust (Li et al., 2020). Delamination of the dense orogenic root would have been accompanied by crustal isostatic rebound and extension (orogenic collapse; Li et al., 2010), which likely triggered the reactivation of inherited fault zones and crustal exhumation. In the Georgetown Inlier, structural and metamorphic studies suggested that the ca. 1.55 Ga partial melting in the eastern domain occurred at ca. 25–35 km depths under *MP-HT* conditions estimated at 730–770°C and 6–8 kbar (Volante et al., 2020a; Boger & Hansen, 2004).

Here we propose a coherent tectonic model to explain the regional partial melting, crustal exhumation and diachronous cooling histories. In our model, after the 1.6 Ga collision, the thickened mafic lower crust, together with the lithospheric mantle, started to delaminate at ca. 1.55 Ga due to the eclogitization of the mafic lower crust (Fig. 4.12). Water released from the newly accreted sedimentary rocks and the eclogitizing mafic lower crust triggered H_2O-enhanced, medium pressure melting of the Georgetown basaltic rocks in the eastern domain (Fig. 4.12), and generated the 1.55 Ga Forest Home TTGs that is featured low heavy rare earth elements and low high field strength elements contents (Pourteau et al., 2020). The model is also consistent with the zircon-monazite thermometry thermodynamic modelling which suggests that additional H_2O is required to produce sufficient melts with compositions similar to the 1.55 Ga S-type granites emplaced in the central domain (Volante et al., 2020c). Delamination of the dense orogenic root is expected to have been accompanied by local influx of hot asthenospheric mantle, which could have provided the extra heat for the melting event, including the likely formation of drier and hotter magmas during a slightly later stage of the process (Li et al., 2010; Yao et al., 2012). Petrological observation and phase equilibria modelling by Volante et al. (2020c) of the Esmeralda Supersuite in the western domain of the Georgetown Inlier indeed suggested that the ca. 1.55 Ga intrusion consists of hot and dry S-type granites derived from a lower crustal magma source that reached upper crustal levels with the contribution of additional mantle-like magma pulses. The crustal isostatic rebound and extension follow by the lithosphere delamination may have triggered renewed extensional faulting (D_2) along the main detachment fault proposed at the western boundary of the central Georgetown domain (Volante et al., 2020b). This is accompanied by a rapid crustal exhumation and cooling , causing the Georgetown's Eastern Domain being uplifted from a crustal depth of ~30 km to ~12 km at an exhumation rate of ~0.3 mm yr^{-1}, and the Central Domain uplifted from a depth of ~33 km to ~16 km, at an exhumation rate of ~0.34 mm yr^{-1}. (Fig. 4.9a, 4.12c-d).

Figure 4.11 also shows that ca. 1600–1500 Ma crustal exhumation and cooling occurred broadly synchronously between the Georgetown Inlier and all but the Western Belt of the Mount Isa Inlier. We therefore further propose that the delamination likely occurred across the two inliers, possibly centred close to the proposed ca. 1.6 Ga crustal suture zone which is now covered under Mesozoic Carpentaria Basin (Fig. 4.12). Elevated geotherm by hot mantle upwelling, together with water released from the sinking lower crust and reduced pressure caused by orogenic collapse, induced widespread post-kinematic felsic to mafic magmatism, with widespread melting and exhumation occurring synchronously between the Mount Isa and Georgetown inliers.

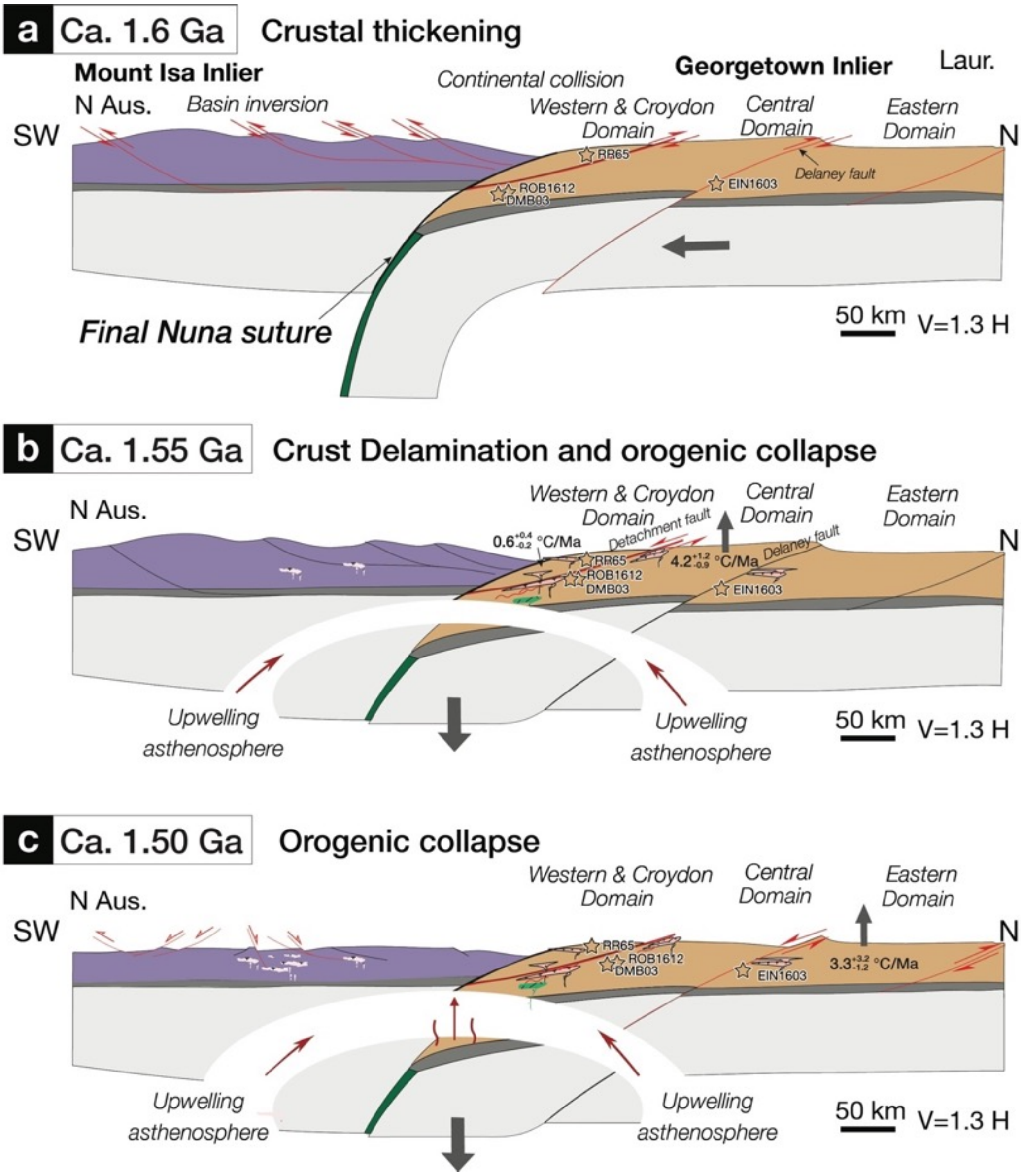

Fig 4.12: Conceptional model for the tectonic evolution of the NE Australia from 1.60 Ga to 1.50 Ga. a. The ca. 1.60 Ga continental collision event recorded westward accretion of the Georgetown Inlier with synchronous orogenesis and crust shortening recorded in both the Mount Isa and Georgetown inliers. b. The orogenic root started to delaminate at ca. 1.55 Ga, replaced by upwelling asthenosphere in both the Georgetown and Mt Isa inliers. c. Elevated geotherm by hot mantle upwelling, together with water released from the sinking lower crust and reduced pressure caused by orogenic collapse, induced widespread post-kinematic felsic to mafic magmatism, with widespread melting and exhumation in the Mount Isa and Georgetown inliers.

Acknowledgments

This study was supported by a China Scholarship Council and a Curtin Research Scholarship to JYL, and an Australian Research Council Laureate Fellow grant (FL150100133) to ZXL. We thank all the owners of land in the Etheridge Province for their hospitality and logistic help during our field work campaigns, with a particular thank you to Adelia and Simon Terry. We thank Sigma Zone company for providing licence for Quantum XL program to make Monte Carlo simulation possible, and Celia Mayers for their assistance during the $^{40}Ar/^{39}Ar$ data producing. Datasets for this research are available at https://doi.org/10.4121/14247125.v1

4.6 References

Abu Sharib, A. S. A. A., & I. V. Sanislav (2013), Polymetamorphism accompanied switching in horizontal shortening during Isan Orogeny: Example from the Eastern Fold Belt, Mount Isa Inlier, Australia, *Tectonophysics*, *587*, 146-167.

Anderson, J.R., Fraser, G.L., McLennan, S.M., Lewis, C.J., 2017, *A U-Pb geochronology compilation for northern Australia, Geoscience Australia. Record,* 2017/22, 17p + appendix

Baker, M. J., A. J. Crawford, and I. W. Withnall (2010), Geochemical, Sm-Nd isotopic characteristics and petrogenesis of Paleoproterozoic mafic rocks from the Georgetown Inlier, north Queensland: Implications for relationship with the Broken Hill and Mount Isa Eastern Succession, *Precambrian Research*, *177*(1-2), 39-54.

Begemann, F., K. Ludwig, G. Lugmair, K. Min, L. Nyquist, P. Patchett, P. Renne, C.-Y. Shih, I. M. Villa, and R. Walker (2001), Call for an improved set of decay constants for geochronological use, *Geochimica et Cosmochimica Acta*, *65*(1), 111-121

Bell, T. H., & M. J. Rubenach (1983), Sequential Porphyroblast Growth and Crenulation Cleavage Development during Progressive Deformation, *Tectonophysics*, *92*(1-3), 171-194.

Betts, P. G., D. Giles, & B. F. Schaefer (2008), Comparing 1800-1600 Ma accretionary and basin processes in Australia and Laurentia: Possible geographic connections in Columbia, *Precambrian Research*, *166*(1-4), 81-92.

Betts, P. G., R. J. Armit, J. Stewart, A. R. A. Aitken, L. Ailleres, P. Donchak, L. Hutton, I. Withnall, & D. Giles (2016), Australia and Nuna, *Geological Society, London, Special Publications*, *424*(1), 47-81.

Black, L. P., T. H. Bell, M. J. Rubenach, And I. W. Withnall (1979), Geochronology of discrete Structural-Metamorphic events in a multiply deformed Precambrian Terrain, *Tectonophysics*, *54*(1-2), 103-137.

Black, L. P., and M. T. McCulloch (1990), Isotopic evidence for the dependence of recurrent felsic Magmatism on new crust formation - An example from the Georgetown Region of Northeastern Australia, *Geochimica Et Cosmochimica Acta*, *54*(1), 183-196.

Black, L.P., Withnall, I.W., 1993, The ages of Proterozoic granites in the Georgetown Inlier of northeastern Australia and their relevance to the dating of tectonothermal events., AGSO Journal of Australian Geology and Geophysics, 14(4), p331-341

Black, L. P., P. Gregory, I. W. Withnall, and J. H. C. Bain (1998), U-Pb zircon age for the Etheridge Group, Georgetown region, north Queensland: implications for relationship with the Broken Hill and Mt Isa sequences, *Australian Journal of Earth Sciences*, *45*(6), 925-935.

Black, L. P., I. W. Withnall, P. Gregory, B. S. Oversby, and J. H. C. Bain (2005), U-Pb zircon ages from leucogneiss in the Etheridge Group and their significance for the early history of the Georgetown region, north Queensland, *Australian Journal of Earth Sciences*, *52*(3), 385-401.

Boger, S. D., & D. Hansen (2004), Metamorphic evolution of the Georgetown Inlier, northeast Queensland, Australia; evidence for an accreted Palaeoproterozoic terrane?, *Journal of Metamorphic Geology*, *22*(6), 511-527.

Brown, M. (2007), Metamorphic conditions in orogenic belts: A record of secular change, *International Geology Review*, *49*(3), 193-234.

Champion (1991), The felsic granites of far North Queensland

Champion, D.C., Heinemann, M.A., 1994, Igneous rocks of northern Queensland : 1:500 000 map and GIS explanatory notes., Australian Geological Survey Organisation. Record, 1994/11, 98p

Cihan, M., P. Evins, N. Lisowiec, and K. Blake (2006), Time constraints on deformation and metamorphism from EPMA dating of monazite in the Proterozoic Robertson River Metamorphics, NE Australia, *Precambrian Research*, *145*(1-2), 1-23.

Dodson, M. H. (1973), Closure temperature in cooling geochronological and petrological systems, *Contributions to Mineralogy and Petrology*, *40*(3), 259-274.

Duncan, A.C., Withnall, I.W., 1983, Definition of the Proterozoic Juntala Metamorphics, Georgetown Inlier, North Queensland, Queensland Government Mining Journal, 84(979), p191-192

Dunlap, W. J. (2000), Nature's diffusion experiment: The cooling-rate cooling-age correlation. *Geology*, *28*(2), 139-142.

Dong, Y., G. Zhang, F. Neubauer, X. Liu, J. Genser, and C. Hauzenberger (2011), Tectonic evolution of the Qinling orogen, China: Review and synthesis, *Journal of Asian Earth Sciences*, *41*(3), 213-237.

Evans, D. A. D., & R. N. Mitchell (2011), Assembly and breakup of the core of Paleoproterozoic-Mesoproterozoic supercontinent Nuna, *Geology*, *39*(5), 443-446.

Evans, D. A. D., R. V. Veselovsky, P. Y. Petrov, A. V. Shatsillo, & V. E. Pavlov (2016), Paleomagnetism of Mesoproterozoic margins of the Anabar Shield: A hypothesized billion-year partnership of Siberia and northern Laurentia, *Precambrian Research*, *281*, 639-655.

Furlanetto, F., D. J. Thorkelson, H. Daniel Gibson, D. D. Marshall, R. H. Rainbird, W. J. Davis, J. L. Crowley, & J. D. Vervoort (2013), Late Paleoproterozoic terrane accretion in northwestern Canada and the case for circum-Columbian orogenesis, *Precambrian Research*, *224*, 512-528.

Geological Survey of Queensland, 2011, North-West Queensland mineral and energy province report and data package, Queensland Department of Employment, Economic Development and Innovation, 1v, 123p, maps, CD-ROM

Grove, M., & T. M. Harrison (1996), ^{40}Ar* diffusion in Fe-rich biotite, *American Mineralogist*, *81*(7-8), 940-951.

Hansma, J., E. Tohver, C. Schrank, F. Jourdan, & D. Adams (2016), The timing of the Cape Orogeny: New 40 Ar/ 39 Ar age constraints on deformation and cooling of the Cape Fold Belt, South Africa, *Gondwana Research*, *32*, 122-137.

Harrison, T. M. (1981), Diffusion of ^{40}Ar in hornblende, *Contributions to Mineralogy & Petrology*, *78*(3), 324-331.

Harrison, T. M., I. Duncan, & I. McDougall (1985), Diffusion of 40Ar in biotite: Temperature, pressure and compositional effects, *Geochimica et Cosmochimica Acta*, *49*(11), 2461-2468.

Harrison, T. M., J. Célérier, A. B. Aikman, J. Hermann, & M. T. Heizler (2009), Diffusion of 40Ar in muscovite, *Geochimica et Cosmochimica Acta*, *73*(4), 1039-1051.

Hills, Q. G. (2004). *The tectonic evolution of the Georgetown Inlier* (PhD thesis). Melbourne, Australia: School of Geosciences, Monash University, 225 pp.

Johnson, M. R., Harley, S. L., & Harley, S. (2012). *Orogenesis: the making of mountains*. Cambridge University Press.

Kearey, P., K. A. Klepeis, & F. J. Vine (2009), *Global tectonics*, John Wiley & Sons.

Kelley, S. (2002), K-Ar and Ar-Ar Dating, Reviews in Mineralogy and Geochemistry, 47(1), 785-818.

Kirscher, U., Liu, Y., Li, Z. X., Mitchell, R. N., Pisarevsky, S. A., Denyszyn, S. W., & Nordsvan, A. (2019). Paleomagnetism of the Hart Dolerite (Kimberley, Western Australia)–A two-stage assembly of the supercontinent Nuna?. Precambrian Research, 329, 170-181.

Koppers, A. A. P. (2002), ArArCALC - software for Ar-40/Ar-39 age calculations, *Computers & Geosciences*, *28*(5), 605-619.

Lee, J. Y., K. Marti, J. P. Severinghaus, K. Kawamura, H. S. Yoo, J. B. Lee, and J. S. Kim (2006), A redetermination of the isotopic abundances of atmospheric Ar, Geochimica et Cosmochimica Acta, 70(17), 4507-4512.

Li, J. Y., Pourteau, A., Li, Z.-X., Jourdan, F., Nordsvan, A. R., Collins, W. J., & Volante, S. 2020, Heterogeneous exhumation of the Mount Isa orogen in NE Australia after 1.6 Ga Nuna assembly: new high-precision $^{40}Ar/^{39}Ar$ thermochronological constraints, *Tectonics, 39(12).* 10.1029/2020TC006129

Mackenzie, D.E., 1980, New and redefined igneous rock units in the Forest Home-North Head region, Georgetown Inlier, North Queensland, Queensland Government Mining Journal, 81(942), p208-214

McLaren (1999), High radiogenic heat–producing granites and metamorphism—An example from the western Mount Isa inlier, Australia, *Geology*, *27*(8), 679-682.

McLaren, S., M. Sandiford, and R. Powell (2005), Contrasting styles of Proterozoic crustal evolution: A hot-plate tectonic model for Australian terranes, *Geology*, *33*(8), 673-676.

Mark, G. (2001), Nd isotope and petrogenetic constraints for the origin of the Mount Angelay igneous complex: implications for the origin of intrusions in the Cloncurry district, NE Australia, *Precambrian Research*, *105*(1), 17-35.

McDougall, I., and Harrison, T.M. 1999. *Geochronology and Thermochronology by the 40Ar/39Ar Method*. Oxford University Press on Demand.

McDonald, C. S., D. Regis, C. J. Warren, S. P. Kelley, and S. C. Sherlock (2018), Recycling argon through metamorphic reactions: The record in symplectites, *Lithos*, *300-301*, 200-211.

Mcnaughton, N., and A. Wilson (1983), On the Age of D4 in the Georgetown Inlier, Northern-Queensland, *Search*, *14*(9-10), 272-273

Neumann, N. L., and G. L. Fraser (2007), Geochronological synthesis and Time-Space plots for Proterozoic Australia.

Neumann, N. L., and N. Kositcin (2011), New SHRIMP U-Pb zircon ages from North Queensland 2007-2010, Geoscience Australia Record, 2011(38)

Nordsvan, A. R., W. J. Collins, Z.-X. Li, C. J. Spencer, A. Pourteau, I. W. Withnall, P. G. Betts, & S. Volante (2018), Laurentian crust in northeast Australia: Implications for the assembly of the supercontinent Nuna, *Geology*, *46*(3), 251-254.

Olierook, H. K. H., R. G. Affleck, N. J. Evans, F. Jourdan, C. L. Kirkland, S. Volante, A. R. Nordsvan, B. I. A. McInnes, B. McDonald, C. Mayers, R. A. Frew, K. Rankenburg, N. d'Offay, M. Nind, and A. Larking (2021), Mineralization proximal to the final Nuna suture in northeastern Australia, *Gondwana Research*, *92*, 54-71.

Pisarevsky, S. A., S.-A. Elming, L. J. Pesonen, & Z.-X. Li (2014), Mesoproterozoic paleogeography: Supercontinent and beyond, *Precambrian Research*, *244*, 207-225.

Pourteau, A., M. A. Smit, Z.-X. Li, W. J. Collins, A. R. Nordsvan, S. Volante, & J. Li (2018), 1.6 Ga crustal thickening along the final Nuna suture, *Geology*, *46*(11), 959-962.

Renne, P. R., G. Balco, K. R. Ludwig, R. Mundil, & K. Min (2011), Response to the comment by W.H. Schwarz et al. on "Joint determination of K-40 decay constants and Ar-40*/K-40 for the Fish Canyon sanidine standard, and improved accuracy for Ar-40/Ar-39 geochronology" by PR Renne et al. (2010), *Geochimica Et Cosmochimica Acta*, *75*(17), 5097-5100.

Richards, J. R., Cooper, J. A. & Webb, A. W. (1963) Potassium-argon ages on micas from the Precambrian region of North-Western Queensland. *Journal of the Geological Society of Australia*, 10(2), 299-312.

Richards, J. e. a. (1966), *Isotopic ages of acid igneous rocks in the Cairns hinterland, north Queensland*, Bureau of Mineral Resources, Geology and Geophysics.

Richards, J. e. a. (1966), *Isotopic ages of acid igneous rocks in the Cairns hinterland, north Queensland*, Bureau of Mineral Resources, Geology and Geophysics.

Rogers, J. J. W., & M. Santosh (2002), Configuration of Columbia, a mesoproterozoic supercontinent, *Gondwana Research*, *5*(1), 5-22.

Scibiorski, E., E. Tohver, & F. Jourdan (2015), Rapid cooling and exhumation in the western part of the Mesoproterozoic Albany-Fraser Orogen, Western Australia, *Precambrian Research*, *265*, 232-248.

Skipton, D.R., Schneider, D.A., Kellett, D.A. and Joyce, N.L., 2017. Deciphering the Paleoproterozoic cooling history of the northeastern Trans-Hudson Orogen, Baffin Island (Canada), using 40Ar/39Ar step-heating and UV laser thermochronology. *Lithos*, *284*, pp.69-90.

Spikings, R. A., D. A. Foster, B. P. Kohn, and P. B. O'Sullivan (2001), Late Neoproterozoic to Holocene thermal history of the Precambrian Georgetown Inlier, northeast Australia, *Australian Journal of Earth Sciences*, *48*(1), 9-24.

Stübner, K., Grujic, D., Dunkl, I., Thiede, R. and Eugster, P., 2018. Pliocene episodic exhumation and the significance of the Munsiari thrust in the northwestern Himalaya. *Earth and Planetary Science Letters*, *481*, pp.273-283.

Thorkelson, D. J., J. A. Abbott, J. K. Mortensen, R. A. Creaser, M. E. Villeneuve, V. J. McNicoll, & P. W. Layer (2005), Early and Middle Proterozoic evolution of Yukon, Canada, *Canadian Journal of Earth Sciences*, *42*(6), 1045-1071.

Volante, S., A. Pourteau, W. J. Collins, E. Blereau, Z. X. Li, M. Smit, N. J. Evans, A. R. Nordsvan, C. J. Spencer, B. J. McDonald, J. Li, and C. Günter (2020a), Multiple P-T–d–t paths reveal the evolution of the final Nuna assembly in northeast Australia, *Journal of Metamorphic Geology*, *38*(6), 593-627.

Volante, S., W. J. Collins, A. Pourteau, Z. X. Li, J. Li, and A. R. Nordsvan (2020b), Structural Evolution of a 1.6 Ga Orogeny Related to the Final Assembly of the Supercontinent Nuna: Coupling of Episodic and Progressive Deformation, *Tectonics*, *39*(10).

Volante, S., Collins, W., Spencer, C., Blereau, E., Pourteau, A., Barrote, V., Nordsvan, A., Li, Z.X., Evans, N. and Li, J., (2020c), May. Reconciling zircon and monazite thermometry constrains H2O content in granitic melts. *Contributions to Mineralogy and Petrology,*

Warren, C. J., F. Hanke, and S. P. Kelley (2012), When can muscovite 40Ar/39Ar dating constrain the timing of metamorphic exhumation?, Chemical Geology, 291, 79-86.

Whitney, D.L. and Evans, B.W., 2010. Abbreviations for names of rock-forming minerals. *American mineralogist*, *95*(1), pp.185-187.

Yao, W.-H., Z.-X. Li, W.-X. Li, X.-C. Wang, X.-H. Li, & J.-H. Yang (2012), Post-kinematic lithospheric delamination of the Wuyi–Yunkai orogen in South China: Evidence from ca. 435Ma high-Mg basalts, *Lithos*, *154*, 115-129.

Yin, A., and T. M. Harrison (2000), Geologic evolution of the Himalayan-Tibetan orogen, *Annual Review of Earth and Planetary Sciences*, *28*(1), 211-280

Zhang, S., Z.-X. Li, D. A. D. Evans, H. Wu, H. Li, & J. Dong (2012), Pre-Rodinia supercontinent Nuna shaping up: A global synthesis with new paleomagnetic results from North China, *Earth and Planetary Science Letters*, *353-354*, 145-155.

Zhao, G., P. A. Cawood, S. A. Wilde, & M. Sun (2002), Review of global 2.1–1.8 Ga orogens: implications for a pre-Rodinia supercontinent, *Earth-Science Reviews*, *59*(1-4), 125-162.

Zou, Y., Li, Q.L., Mitchell, R.N., Zhai, M.G., Zou, X.Y., Zhao, L., Wang, Y.Q. and Liu, B., 2020. Local rapid exhumation and fast cooling in a long-lived Paleoproterozoic orogeny. Journal of Petrology.

Appendix D: Supplementary materials to Chapter 4

Attached at the end of the thesis.

Chapter 5

Proterozoic crustal evolution of NE Australia during Nuna assembly: new insights from coupled geophysical and radiogenic isotope analyses

This chapter is format to *Earth Science Review* as:

Li, J., Olierook, H. K. H., Li, Z.-X., Nordsvan, A. R., Collins, W. J., Elder, C., Volante, S., Pourteau, A., & Doucet, L.S. Proterozoic tectonic evolution of North Queensland, Australia: insights from seismic reflection profile reinterpretation, *Earth Science Review* (in preparison)

Abstract

The final assembly of the Proterozoic supercontinent Nuna is believed to have occurred via a collisional event between eastern Australia and western Laurentia at ca. 1.60 Ga. However, detailed orogenic evolution remains elusive due to a lack of systematic multidisciplinary regional analyses. This study combines aeromagnetic and gravity analyses, along with a reinterpretation of seismic profiles and integration with the surface geological data, to characterise the crustal architecture and explore the evolution of the collisional event. Based on geophysical data interpretation, three crustal-scale faults were recognized across the Mount Isa and Georgetown inliers. On the west, a N-S trending, sharp magnetic gradient was resolved on the eastern margin of the Mount Isa Inlier, coinciding with the lithosphere scale Gidyea Fault (previously named as the Gidyea Suture Zone) imaged from the seismic reflection profile. Between the Mount Isa and Georgetown inliers, a seismically identified, west-dipping crustal dissecting fault (the Empress Suture Zone) is interpreted as a terrane suture zone with additional smaller-scale thrusts antithetic to the main structures. The presence of duplexed crustal architecture indicates crustal thickening along the Empress Suture Zone, and is interpreted to be associated with the westward docking of the Georgetown Inlier. On the east, the Rowe Fault (previously named as the Rowe Fossil Subduction Zone) offsets the Moho within the Georgetown Inlier, and joins with the detachment fault which defines the boundary

between the western and central domains. Compiled Nd isotopic data shows that the Georgetown Inlier is distinguishable from the Mount Isa Inlier at ca. 1.68 Ga, but shares the same isotopic characteristics post ca. 1.56 Ga, therefore defining the age interval for the unification of the Georgetown Inlier with the North Australian Craton. Combining the geophysical and isotopic evidence, we propose that the Georgetown Inlier subducted westward to the Mount Isa Inlier during the final assembly of the Proterozoic supercontinent Nuna. Subduction may have initiated at ca. 1.64 Ga but likely ceased at ca. 1.60 Ga as signified by the metamorphic ages linked to a regional crustal thickening event, when the Georgetown Inlier accreted to the Mount Isa Inlier, possibly along the Empress Suture Zone.

5.1 Introduction

Despite the presence of a global orogenic episode between ca. 2.10 and 1.80 Ga, the supercontinent Nuna (also known as Columbia; Evans & Mitchell, 2011; Evans et al., 2016; Rogers & Santosh, 2002; Zhang et al., 2012; Zhao et al., 2002) was still assembling until the collision between Australia and Laurentia (North America) at ca. 1.60 Ga (Fig. 5.1a, Betts et al., 2016; Furlanetto et al., 2013; Nordsvan et al., 2018; Pehrsson et al., 2016; Pisarevsky et al., 2014; Pourteau et al., 2018; Verbaas, 2018). This final amalgamation event was marked by the Racklan and Forward orogenies in western Laurentia (Furlanetto et al., 2013; Thorkelson et al., 2001) and the coeval Isan and Jana orogenies in the Mount Isa and Georgetown inliers of NE Australia, respectively (Betts et al., 2008; Boger & Hansen, 2004; Withnall & Hutton, 2013). Here we collectively call the orogen across the Mount Isa and Georgetown inliers, linked to the ca. 1.6 Ga collisional event, the Isa orogen, although the orogenic events recorded by the two adjacent inliers have been given distinct names. The Isan Orogeny in NE Australia has been interpreted by recent sedimentological and metamorphic studies to be due to the collision of the Georgetown Inlier, an exotic terrane with Laurentian affinity, with the North Australian Craton at ca. 1.60 Ga (Nordsvan et al., 2018; Pourteau et al., 2018). However, detailed crustal boundaries and accretionary processes remain elusive due to the lack of clearly diagnostic plate-boundary features, such as ophiolites, accretionary complexes, pre-collisional arc magmatism, and high-pressure metamorphic rocks that can reflect the presence of a subduction zone (Foster & Rubenach, 2006; Pourteau et al., 2018). The orogenic evolution and processes involved thus remain hotly debated (Champion, 2013; Gibson et al., 2018; Gibson & Champion, 2019; Mark et al., 2005; Nordsvan et al., 2018; Korsch et al., 2012).

Understanding the orogenic process in the Proterozoic NE Australia thus demands further evidence for the purposes of: (i) distinguishing allochthonous terranes, (ii) identification of terrane boundaries, (iii) delineating crustal architecture of the orogen, (iv) deciphering the crustal evolutionary process and the magmatic history. In this study, three E–W and NE–SW trending seismic reflection surveys across the Proterozoic inliers in NE Australia (Fig. 5.1c) have been reinterpreted, in combination with filtered aeromagnetic and gravity images and the surface geological data, to address terrane boundaries and delineate the crustal architecture of the Isan orogen. Whole-rock Nd and Hf isotopic data of Proterozoic igneous intrusions are also compiled from each domain to distinguish periods of mantle input and crustal melting. Updated structural and metamorphic evolution (Pourteau et al., 2018, 2020; Volante et al., 2020a–c) are also integrated to establish the orogenic evolution.

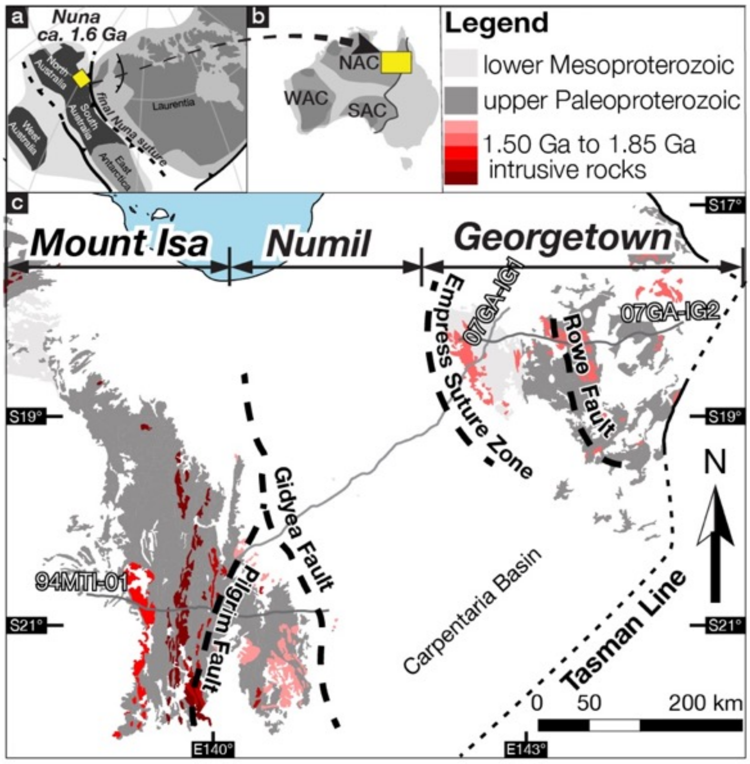

Fig. 5.1: a. Paleogeographic reconstruction of the Proterozoic supercontinent Nuna at ca. 1.60 Ga (adapted from Pourteau et al., 2018) showing the location of NE Australia (yellow box). b: Present-day map of Australia with Australian cratons, and show the location of study area. NAC, North Australian Craton; SAC, South Australian Craton; WAC, West Australian Craton. c: Simplified map of the NE Australian Proterozoic inliers (Modified after Pourteau et al., 2018) with E-W and NE-SW trending seismic transects, including 94MTI–01, 07GA–IG1, and 07GA–IG2. The discontinuous black line 'Tasman Line' depicts the eastern edge of the North Australia Craton (NAC). The thick discontinuous black lines represent deep crustal boundaries including, from west to east, the Pilgrim Fault (Blenkinsop et al., 2008), Gidyea Fault (Korsch et al., 2012), Empress Suture Zone (Olierook et al., 2021) and Rowe Fault (Korsch et al., 2012).

5.2 Geological setting

5.2.1 Mount Isa Inlier

The Proterozoic Mount Isa Inlier of the North Australia preserves evidence of ca. 1.90–1.50 Ga sedimentation and igneous activities with intermittent orogenic and metamorphic episodes (Betts et al., 1998; Foster & Austin, 2008; Jackson et al., 2000; Neumann et al., 2006; Neumann & Fraser, 2007; Withnall and Hutton, 2013). Traditionally, the Mount Isa Inlier has been subdivided into three major belts, including the western, central, and eastern fold belts, separated by N-S trending Mount Isa Fault zones and NE–SW-striking Pilgrim Fault, respectively (Fig. 5.2, Day et al., 1983; GSQ, 2011). More recently, based on discrete sedimentary records and geophysical characteristics, the Mount Isa Inlier has been divided into 15 geological domains, with 12 of them are outlined in Fig. 5.2 (GSQ, 2011; Withnall & Hutton, 2013).

The oldest rocks of the Mount Isa Inlier are high-grade metamorphic and crystalline basement rocks (the >1.85 Ga Kalkadoon–Leichhardt Complex; Blake, 1987; Etheridge et al., 1987) exposed in the western and central belts, which are overlain by three successive superbasins, including: the ca. 1.80–1.74 Ga Leichhardt Superbasin, the ca. 1.73–1.68 Ga Calvert Superbasin, and the ca. 1.67–1.58 Ga Isa Superbasin (Betts et al., 2006; Blake, 1987; Jackson et al., 2000; Neumann et al., 2009; Withnall & Hutton, 2013). The Leichhardt Superbasin comprises widespread bimodal magmatism, fluvial clastic sedimentary rocks and marine incursions (Betts et al., 2006; Derrick et al., 1980; Eriksson et al. 1994; Jackson et al., 2000), accumulated mainly under an extensional setting (Eriksson et al., 1993; GSQ, 2011; Scott et al., 2000), and are exposed in the western belt, central belt and western part of the eastern belt (Fig. 5.2). At ca. 1.73–1.72 Ga, an episode of basin inversion terminated the Leichhardt Superbasin deposition, and resulted in high-angle unconformities with the overlying Calvert Superbasin (Betts, 1999; Blaikie et al., 2017; Derrick, 1982). The Calvert Superbasin comprises ca. 1.73–1.68 Ga fluvial to shallow marine clastic sedimentary rocks (Derrick et al., 1980; GSQ, 2011; Hutton et al., 1981), temporarily interbedded with ca. 1.71 Ga bimodal Fiery Creek Volcanics (Jackson et al., 2005; Neumann et al., 2006), and deposited in the northern western and central belts under a NW–SE extensional setting (Betts et al., 2011; GSQ, 2011; Jackson et al., 2000; O'Dea et al., 1997b). Contemporaneous sequences in the eastern belt are dominated by rift-related turbidites and quartzite successions deposited at ca. 1.73–1.68 Ga (Foster & Austin, 2008; Neumann et al., 2009; Page & Sun, 1998). The youngest stratigraphic package of the Isa Superbasin comprises shallow marine carbonaceous shale, turbiditic sandstone, siltstone and quartz sandstone, exposed in the western and the eastern extremities of the Mount Isa Inlier between ca. 1.67 and 1.58 Ga (Betts et al., 1998; Betts & Lister, 2001; Foster & Austin, 2008; Gibson et al., 2005; Southgate et al., 2000; Vries et al., 2006; Withnall et al., 2013).

At ca. 1.60 Ga, sedimentation was disrupted throughout most of the Mount Isa Inlier by a predominately E–W shortening event—the Isan Orogeny (Abu Sharib and Sanislav, 2013; Betts et al., 2006; Blake, 1987; Giles et al., 2006b), with the supracrustal rocks being metamorphosed to sub-greenschist to upper amphibolite facies at low-pressure condition (Giles & Nutman, 2002; Rubenach 1992; Rubenach et al., 2008; Sayab, 2006). Although the kinematic evolution of Isan Orogeny was complex and aspects remain controversial (Betts et al., 2006; Connors & Lister, 1995; Giles et al., 2006b; O'Dea & Lister, 1995; O'Dea et al., 1997b), most studies suggest that the orogeny was poly-phased and initiated at ca. 1.60 Ga with N–S crustal shortening in the Western Belt, associated with reverse reactivation of E-W-trending normal faults (Bell, 1983, 1991; Bell et al., 1992; Betts et al., 2006; Blake, 1987; Lister et al., 1999; O'Dea & Lister, 1995; O'Dea et al., 1997a). Continuous deformation evolved into thick-skinned, E–W shortening, and produced N–S striking, basement-rooted reverse faults and upright to steeply inclined folds at all scales (Betts et al., 2000; Blenkinsop et al., 2008; MacCready et al., 1998; MacCready, 2006; O'Dea et al., 2006). A late-stage regional deformation event, interpreted to be transpressional (Lister et al., 1999; O'Dea et al., 1997b), is associated with crustal shortening accommodated by conjugate NW–striking sinistral and NE–striking dextral faults along inherited early normal faults (Lister et al., 1999). The activity of these faults has not been precisely dated, but post-dates the orogenic deformation phase (Betts et al., 2006; Williams & Phillips, 1992). Syn- to post-orogenic intrusions include an early episode of ca 1.60–1.58 Ga abyssal pegmatite in the southern inlier and the intrusion of a ca. 1.55 Ga small trondhjemitic pluton in the eastern inlier near the Cloncurry Fault (Mark, 2001; Page & Sun, 1998). Following the metamorphism and most of the deformation, the eastern belt was intruded by voluminous A-type, post-orogenic granite plutons of Williams and Naraku batholiths at ca. 1.54–1.49 Ga (Mark, 2001; Pollard et al., 1998; Wyborn, 1998), before transiting to a tectonic quiescent stage.

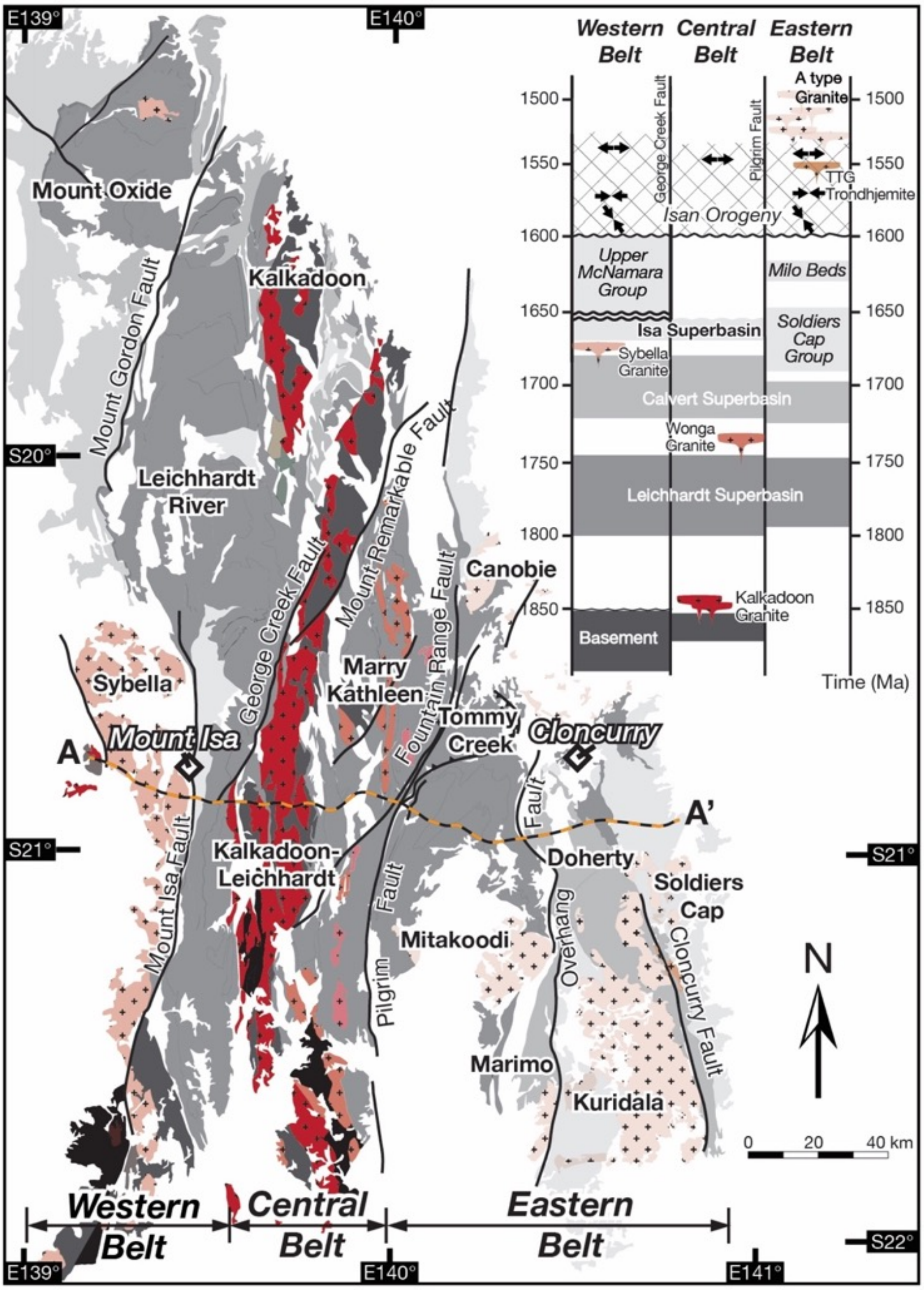

Fig. 5.2: Simplified lithological map of the Mount Isa Inlier showing the basement, successive stratigraphic packages (or "superbasins"), magmatic intrusions and main fault zones, modified from Blake, (1987). Transect A–A' shows the trace of Geoscience Australia geophysical imaging profile 94MTI-1. Stratigraphic columns are modified after Betts et al. (2006) and Withnall et al. (2013). Relative tectonic regimes during the Isan Orogeny are adapted from Bell et al.,1992; Bell, 1980; Giles et al., 2006b; O'Dea et al.,2006; Rubenach et al, 2008 and Sharib & Sanislav., 2013. Twelve out of 15 geological domains of the Mount Isa Inlier, separated by geophysically-imaged boundaries or major faults (Withnall & Hutton, 2013), are shown in light grey colour and outlined by thin continuous line.

5.2.2 Georgetown Inlier

The Georgetown Inlier exposes >ca. 1.70–1.56 Ga sedimentary and mafic volcanic rocks (Black et al., 1998, 2005; Withnall and Hutton, 2013), which were regionally deformed and locally metamorphosed up to granulite facies during the 1.60 Ga Jana Orogeny (Cihan et al., 2006; Pourteau et al., 2018; Volante et al., 2020a), and later being intruded by regional S-type and locally I-type plutons at ca. 1.56–1.54 Ga (Black & McCulloch, 1990; Black et al., 1998). Recent metamorphic and thermochronology studies (Volante et al., 2020b; Li et al., Tectonics, in review) have divided the Georgetown Inlier into four distinguished geological domains based on their distinct structural and metamorphic gradient variations, from west to east, including the Croydon, western, central, and eastern domains (Fig. 5.3).

Three primary stratigraphic successions are exposed within the Georgetown Inlier. From east to west, these include the ca. 1.72–1.60 Ga Etheridge Group (subdivided into upper and lower sequences, Blewett and Black, 1998; Geological Survey of Queensland, 2011), the ca. 1.57–1.56 Ga Langlovale Group (Withnall & Mackenzie, 1983; GSQ, 2011) and the ca. 1.55 Ga Croydon Volcanic Group (Fig. 5.3, Black et al., 1998; Withnall, 1996; Withnall et al., 2013; Withnall & Mackenzie, 1980). The lower Etheridge Group (ca. 1.70–1.65 Ga; Withnall et al., 2013; Neumann & Kositcin, 2011) exposed in the central domain, comprises paralic to deeper marine sedimentary rocks (Withnall, 1996; Lambeck, 2011) that are interlayered with ca. 1.66–1.65 Ga mafic intrusions (Baker et al., 2010; Black et al., 1998), represents the protolith of the high-grade migmatitic Einasleigh Metamorphics of the eastern domain (Withnall et al., 1988; Black et al., 2005; Neumann & Kositcin, 2011). The overlying upper Etheridge Group (ca. 1.65–1.60 Ga, GSQ, 2011; Withnall et al., 2013) is exposed in the western domain, and comprises tidal-flat deltaic carbonaceous siltstone and mudstone (Withnall et al., 1988; Withnall & Henderson, 2012), overlain by the ca. 1.57–1.56 Ga shallow marine sandstone and mudstone Langlovale Group package (Geological Survey of Queensland, 2011; Withnall & Mackenzie, 1983).

Syn- to post-ca. 1.60 Ga, the Georgetown Inlier was subjected to multiple deformational and metamorphic events during the Jana Orogeny (Withnall, 1996). Although the kinematic evolution of Jana Orogeny remains controversial (Black et al., 2005; Boger and Hansen 2004; Cihan and Parsons, 2005; Cihan et al., 2006; Withnall et al., 1988), updated geochronology and petrology studies have suggested that the Jana Orogeny initiated at ca. 1.6 Ga with an E–W compressional event (D_1/M_1, Pourteau et al., 2018; Volante et al., 2020a), before progressively evolving into an E-W extensional stage (D_2/M_2) at ca. 1.55 Ga (Volante et al., 2020a, 2020b). Metamorphic conditions had reached low pressure and mid-temperature (*LP-MT*) in the western domain, and mid-pressure and mid-temperature (*LP-MT*), upper amphibolite facies (600–680 °C and 4–6 kbar) in the central domain (Volante et al., 2020a). Syn- to post-orogenic intrusions include the ca. 1.56–1.55 Ga Forsayth Supersuite (Champion & Heinemann, 1994; Anderson et al., 2017), the ca. 1.56 Ga Forest Home Trondhjemite (Neumann & Kositcin, 2011) and the ca. 1.55 Ga Esmeralda Supersuite (Champion, 1991; Black and McCulloch, 1990; Withnall and Hutton, 2013). Synchronous volcanics erupted subaerially at ca. 1.55 Ga (Black & McCulloch, 1990; Withnall, 1996), comprising felsic ignimbrite and rhyolite, and is overlain the by stratigraphically younger undeformed Inorunie Group (Withnall et al., 1997), marking tectonic quiescence post-1.55 Ga.

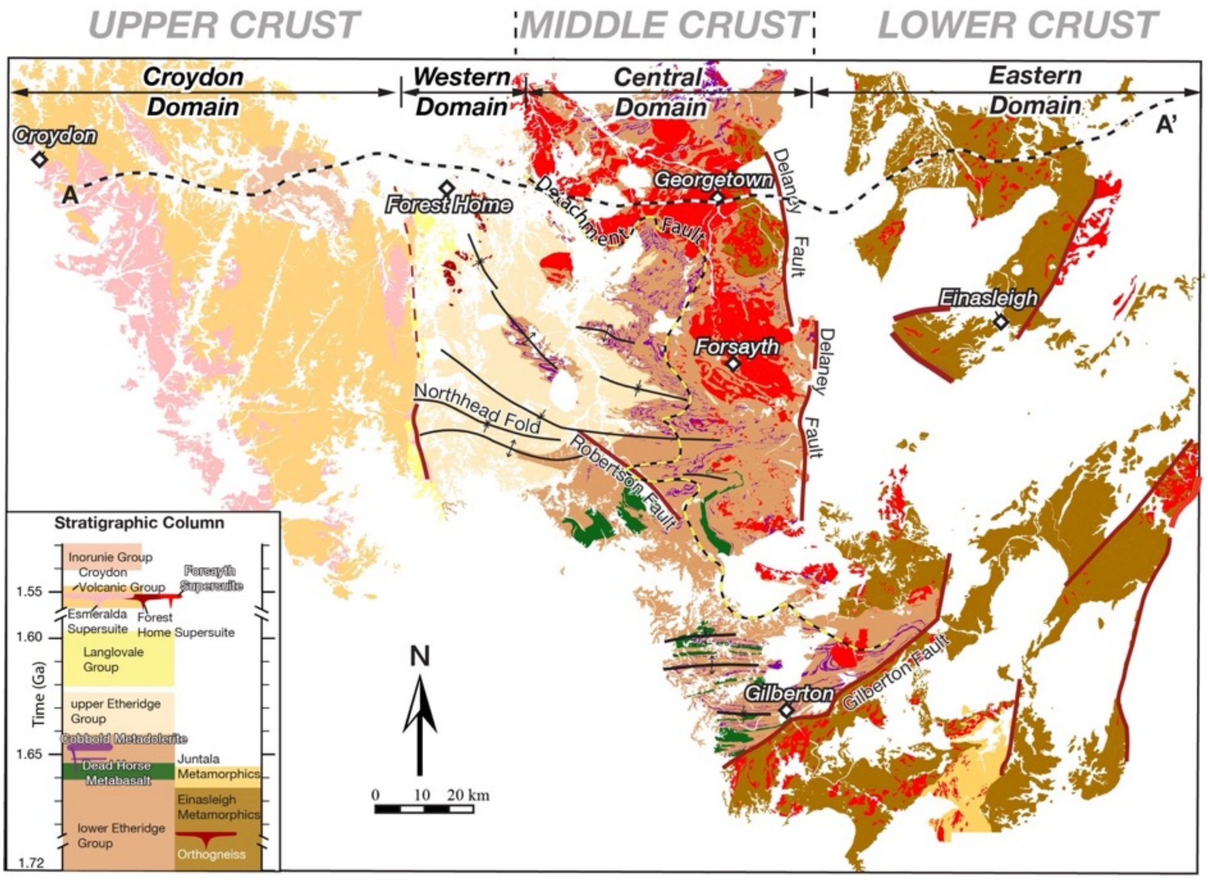

Fig 5.3: Simplified lithological map of the Georgetown Inlier, modified from Bain et al. (1985), showing the successive stratigraphic packages (or "superbasins"), magmatic intrusions and main fold and fault zones. Discontinuous yellow and black line depicts the regional detachment fault separating the upper-crustal western domain against lower-crustal central domain (Volante et al., 2020). Transect B–B' shows the trace of Geoscience Australia geophysical imaging profile 07GA–IG2. Stratigraphic columns are modified after Withnall et al. (2013) and Neumann and Fraser. (2007).

5.3 Previous studies

5.3.1 Cross-sectional crustal architecture determined from 2D seismic reflection data

In 1994, a deep seismic reflection survey (L138 Mount Isa) was conducted by the Australian Geological Survey Organization across the Mount Isa Inlier (Goleby et al., 1996) with the data reprocessed by Geoscience Australia in 2007 (Jones et al., 2008). A joint seismic survey (L184 Isa-Georgetown) that involved the Australian Government's Onshore Energy Security Programme, the Queensland Government's Smart Mining and Smart Exploration initiatives, and Auscope was also conducted in 2007 to collect the seismic data from the eastern edge of the Mount Isa Inlier towards the Georgetown Inlier, with the data being processed by Geoscience Australia. The above two surveys acquired a total length of 714 km seismic reflection data that were collected to 20s two-way travel time, equating to about 60 km in depth (Jones et al., 2008; Maher, 2009).

Previous seismic data interpretation suggested a weakly reflective and seismically heterogenous crust exists across the Mount Isa Inlier that extends to a depth of ~55 km (94MTI-01, Drummond et al., 2006; MacCready, 2006). MacCready. (2006) proposed that the eastern fold belt of the Mount Isa Inlier shows shallow, east-dipping continuous structures that are dissected by steep east-dipping reflective zones. This seismic reflective signature is different from that of the central and western belts which show subvertical east-dipping or west-dipping structures that cut across the crystalline basement. Towards east, between the Mount Isa and Georgetown inliers, two major crustal boundaries were identified from the seismic reflection profile 07GA-IG1 interpretation (Korsch et al., 2012). The Gidyea Suture, locates on the west, is a west-dipping, low reflective zone which dissects the Moho, and defines the boundary between the non-reflective, thick crust of the Mount Isa terrane from the thinner, two-layered crust beneath the Carpentaria Basin. The Rowe Fossil Subduction Zone, on the east, is a SW-dipping reflective zone that offsets the Moho below the Eitheridge Province at a crustal depth of ~36 km. This discontinuity has been interpreted to represent a major suture formed in relation to the juxtaposition of allochthonous terranes on the east margin of the North Australia (Korsch et al., 2012). In this study, we rename the Gidyea Suture Zone (Korsch et al., 2012) as the Gidyea Fault, and the Rowe Fossil Subduction Zone as the Rowe Fault after the recognition that these two major structures may not represent terrane sutures (see the detailed discussion in section 5.7). Between the Gidyea Fault and Rowe Fault, a series of west-dipping, crustal-scale faults were initially recognized by Korsch et al. (2012) and later termed by Olierook et al. (2021) as the Empress Suture Zone, which separates the Numil Seismic Province and the Georgetown Inlier on the west and east, respectively. Seismic reflection profile across the Georgetown Inlier (07GA-IG2) imaged a two-layered crust with an upper less reflective layer linked with the Etheridge Province, and a less understood, strong reflective lower crust corresponding to the deep basement (Korsch et al., 2012).

5.3.2 Crustal structures from aeromagnetic, gravity and magnetolluric data

Several studies have previously tackled the geophysical signature of the Mount Isa Inlier and surrounding areas (Spampinato et al., 2015; Blaikie et al., 2017; Jiang et al., 2019). By utilizing data filtering and image enhancement on the acquired gravity and airborne geophysics data, Spampinato et al. (2015) interpreted the Proterozoic basement lithologies that is concealed under Mesozoic sedimentary rocks in the southern Mount Isa terrane. By interpreting and modelling the high resolution geophysical data from the Leichhardt River Fault Trough of the Mount Isa Inlier, Blaikie et al. (2017) diagnosed the regional structural relationships, and concluded that a basin inversion event occurred at ca. 1.74–1.71 Ga following the ca. 1.78–1.74 Ga Leichhardt Superbasin deposition (Blaikie et al., 2017). A subsequent magnetotelluric study was undertaken on the eastern margin of the Mount Isa Province, and diagnosed a west-dipping conductivity anomaly zone that can be correlated with the Gidyea Fault. This lithosphere-scale magnetotelluric structure is regarded as a potential controlling structure for the the iron–oxide–copper–gold (IOCG) mineralization in its vicinity (Jiang et al., 2019).

Although previous geophysical studies had addressed the crustal geometry within or adjacent to the Mount Isa Inlier, little is known about the regional-scale architecture and its implications for terrane reconstruction. In addition, the nature of crustal boundaries identified from the seismic reflection profiles, and the timing and kinematics of their formation, remain enigmatic (Korsch et al., 2012; Olierook et al., 2021). In this study, through incorporating newly processed aeromagnetic and gravity results as well as geological constrains with seismic data reinterpretation, we present a new crustal architecture interpretation of terranes across the Mount Isa Inlier to the Georgetown Inlier, and establish a new tectonic model for terrane accretion in NE Australia during the assembly of the supercontinent Nuna.

5.4 Methodology

5.4.1 Aeromagnetic and gravity data processing

The publicly available, high-resolution airborne aeromagnetic and gravity data used in this study were merged by the Geological Survey of Queensland from individual states, the Federal Government of Australia, and open range and multi-client surveys, covering a total area of ~785,700 km^2 (Greenwood et al., 2018; Roger, 2014). Line spacing, direction and flight height vary between surveys and have been levelled using data from the Australia Wide Airborne Geophysical Survey (AWAGS). Small offsets occur related to levelling at the regional scale, but do not pose a problem for our investigation.

Filtering of the acquired geophysical grids had been conducted to enhance the geophysical signal and resolve source bodies at different crustal levels. The total magnetic intensity (TMI) grid was reduced-to-magnetic-pole (RTP) (Geological Survey of Queensland; Greenwood et al., 2018), using a background field value of 50696 nT, an inclination of –50.56° and declination of 6.11°, to reduce the dipolar effect and bring the anomalies directly over their geological sources. The normal gravity was corrected to reduce the free-air correction and produced a Bouguer gravity grid which shows gravity anomalies that are more representative of local geology (Geological Survey of Queensland; Roger, 2014). Upward continuation, which transfers the potential field measurement to an arbitrary surface (10 km) above the original measurement surface, is applied to RTP magnetic data to attenuate the subsurface wavelength signature (e.g., Blakely, 1995) and image the basement anomalies. A low pass filter is applied to the Bouguer gravity to remove high frequency and short wavelength responses near the upper surface and improve the geophysical signals of buried source bodies. Data processing and filtering were conducted via Geosoft Oasis montaj®, which allows visualistaion of multiple superimposed datasets for integrated spatial analysis. The upward continued aeromagnetic image is projected as an 80% transparent colour scale intensity layer overlying the regional RTP aeromagnetic image to facilitate later data interpretation.

5.4.2 Seismic data processing

The publicly available, seismic data used in this study (http://www.ga.gov.au/about/projects/resources/seismic/qld-datasets) including the L138 Mount Isa survey conducted by the Australian Geological Survey Organization in 1994

(Goleby et al., 1996), and the L184 Isa-Georgetown survey conducted by the National Research Facility for Earth Sounding in 2007. The L138 seismic data were acquired along two transects (94MTI-01 and 94MTI-02) with vibroseis using explosives. The L184 seismic data were acquired along two transects (07GA-IG1 and 07GA-IG2), using three Hemi-60 (60 000 lb) peak force vibrators as the energy source (Korsch et al., 2012). A total length of 255 km and 32 km of 2D seismic reflection data were collected to 20 s two-way travel time (TWT) for the 94MTI-01 and 94MTI-02 transects, respectively. For the 07GA-IG1 and 07GA-IG2 in the L184 survey, the seismic traverses were acquired at a total length of 440 km and 240 km, respectively. CDP lines used for geological interpretation are 10-fold for the L138 survey, 60-fold for the 07GA-IG1 traverse, and 75-fold for the 07GA-IG2 traverses in the L184 survey (Korsch et al., 2012). The seismic section is grid referenced to AGD84, AMG Zone 54, and displayed assuming an average crustal velocity of 6 km s^{-1} at a vertical to horizontal scale of 1:4. Detailed reflection survey and associated experiments are given in Goleby et al. (1996) for the L138 survey and Korsch et al. (2012) for the L184 survey.

In this study, we chose the three most extended E–W to NE–SW seismic transects (94MTI-01, 07GA-IG1, and 07GA-IG) across the Mount Isa and Georgetown inliers to best image the crustal architecture of Proterozoic terranes in NE Australia. Seismic reflection images were optimized using Schlumberger Petrel E&P to amplify the reflection signal. To further aid visualization and interpretation at large-scale, seismic images were uploaded into the tile display at HIVE (Hub for Immersive Visualisation and eResearch), Curtin University, and displayed on an array of 12 full-HD LCD panels at a resolution of 24 million active pixels. Seismic images were reinterpreted in the context of surface petrological studies, magnetic and gravity profiles and filtered aeromagnetic and gravity grids.

5.5 Aeromagnetic and gravity patterns of NE Australia

5.5.1 The Mount Isa Inlier

To facilitate linking ground-truthed lithologies with aeromagnetic responses, a simplified lithological map of the Mount Isa Inlier was made by grouping geological units into three major lithological categories (granitoids, mafic intrusions/flows and sedimentary rocks), which are further temporally subdivided into segments related to the geological history (Fig. 5.4). Localized excerpts of this lithology map are shown with the aeromagnetic and gravity regions of interest to link the surface geology with magnetic and gravity patterns (e.g., Fig. 5.5c–c'').

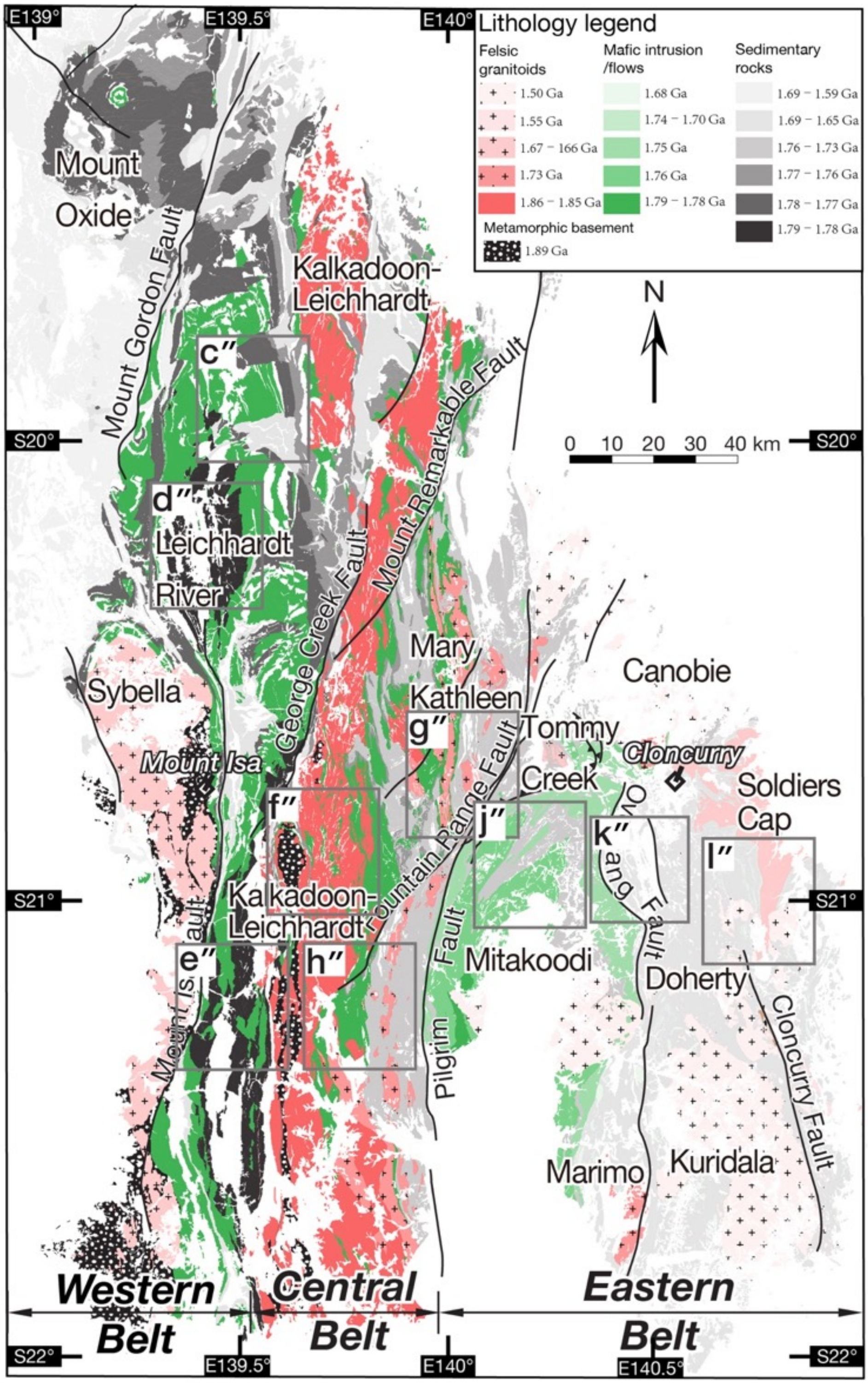

Fig. 5.4: Simplified lithological map of the Mount Isa Inlier from ca. 1.89 to 1.50 Ga, modified from Blake. (1987), mapped in four different lithologies, including metamorphic basement (black with white dots), mafic intrusions/flows (green), felsic intrusions (red) and sedimentary rocks (grey). (c'') – (l'') corresponding with the (c'') – (l'') in Fig. 5.5.

(1) Western Belt

In the RTP aeromagnetic anomaly grid (Fig. 5.5), the western margin of the western belt is defined by a N-S trending aeromagnetic anomaly that separates the Quaternary Basin on the west and the Proterozoic Mount Isa terrane on the east (Fig. 5.5a). The eastern margin of the western belt is defined by a N-S trending sharp anomaly boundary separating the high magnetic Leichhardt River Domain on the west from the low magnetic Kalkadoon Leichhardt Domain on the east. Within the western belt, the Leichhardt River Domain (Fig. 5.5d) is an elongated, positive (10–300 nT) and negative (∼ −100 nT) anomaly intersectant belt with an extent of ∼50 km by ∼15 km. This corresponds to a symmetric gravity anomaly ranging between -200 to 150 μm s^{-2} in the Bouguer gravity grid (Fig. 5.5d'). The N-S trending, positive anomaly belts are overprinted by the E-W trending, wedge-shaped negative anomaly domains in the north (Fig. 5.5c–c'), and superimposed by elliptical negative anomalies in the central west (Sybella Domain). In the southern western belt, prominent N-S-trending anomalies are displaced by NE-trending linear anomalies with apparent displacements of ∼3–6 km (Fig. 5.5e & e').

(2) Central Belt

The central belt is characterized by an approximately 35 km wide, 300 km long zone of low magnetic intensity (−200 to 50 nT), superimposed by narrow (~2–4 km-wide), N-S trending magnetic highs of varying frequency mainly on the eastern section (Fig. 5.5a). The bipartite geophysical signature of this domain is also evident in the Bouguer gravity grid (Fig. 5.5b), although it partly shows an inverse correlation (Figs. 5.5f' & h'). The western margin of this belt is bounded by the N-S trending positive magnetic anomalies that define the limit with the Leichhardt River Domain. A N-S trending sharp gradient in magnetic intensity defines its eastern margin (Fig. 5.5h), separating the low magnetic Kalkadoon-Leichhardt Domain from the high magnetic Mitakoodi Domain to its east. This anomaly margin is termed the Central Anomaly Boundary in this study, with its southern section corresponding to the surface projection of the NNE-trending Pilgrim Fault. By contrast, the Bouguer gravity anomaly shows a reversed decreasing trend in intensity signals across the Central Anomaly Boundary, with values reduced from 350 μm s^{-2} to -200 μm s^{-2} (Fig. 5.5h').

The Kalkadoon-Leichhardt Domain is characterized by a N-S trending, negative magnetic anomaly belt in the RTP magnetic grid, (east of Fig. 5.5c), and low intensity zones (−200 to 50 μm s^{-2}) in the Bouguer gravity grid in the north. In the central, geophysical grids show a bipartite signature where short wavelength (∼10 km) magnetic anomalies are superimposed onto the long wavelength signals (Fig. 5.5f-h, 20–25 km to ∼50 km). In the Bouguer gravity grid, the anomaly signature is relatively homogenous, characterized by N-S trending high intensity Bouguer gravity anomalies, regionally increasing to the east with values ranging between −50 and 350 μm s^{-2} (Fig. 5.5h' and 5.5e').

(3) Eastern Belt

The western margin of the eastern belt is defined by the N-S trending Central Anomaly Boundary, and its eastern margin corresponds to the outcropped Mesozoic Carpentaria Basin. The eastern belt is characterized by NE to NNW trending high magnetic anomaly belts in the north and N-S trending positive to negative magnetic zones in the south (Fig. 5.5a), correlating with an inverse pattern in the Bouguer gravity grid (Fig. 5.5b). On the west, the Mitakoodi Domain show NE-trending positive magnetic anomalies with wavelengths of ∼30 km and intensity values of ~300 nT, superimposed by shorter wave-length magnetic anomalies (∼2–10 km) with negative intensity values from -200 nT to -30 nT (Fig. 5.5j). Towards the east, the Doherty Domain is characterized by alternating NNW-trending intermediate to high linear magnetic anomalies at intensity values between 0 and ~200 nT (Fig. 5.5k), corresponding to the symmetric gravity response (Fig. 5.5k'). Across the Cloncurry Fault in the Soldiers Cap Domain, the magnetic pattern is characterized by an approximately 30 km wide, 100 km long, NNW-trending low magnetic intensity zone (-200 to -30 nT), superimposed by narrow (~5–10 km-wide), NNW-trending, curvilinear magnetic highs (100 to 350 nT) of varying frequency (Fig. 5.5l).

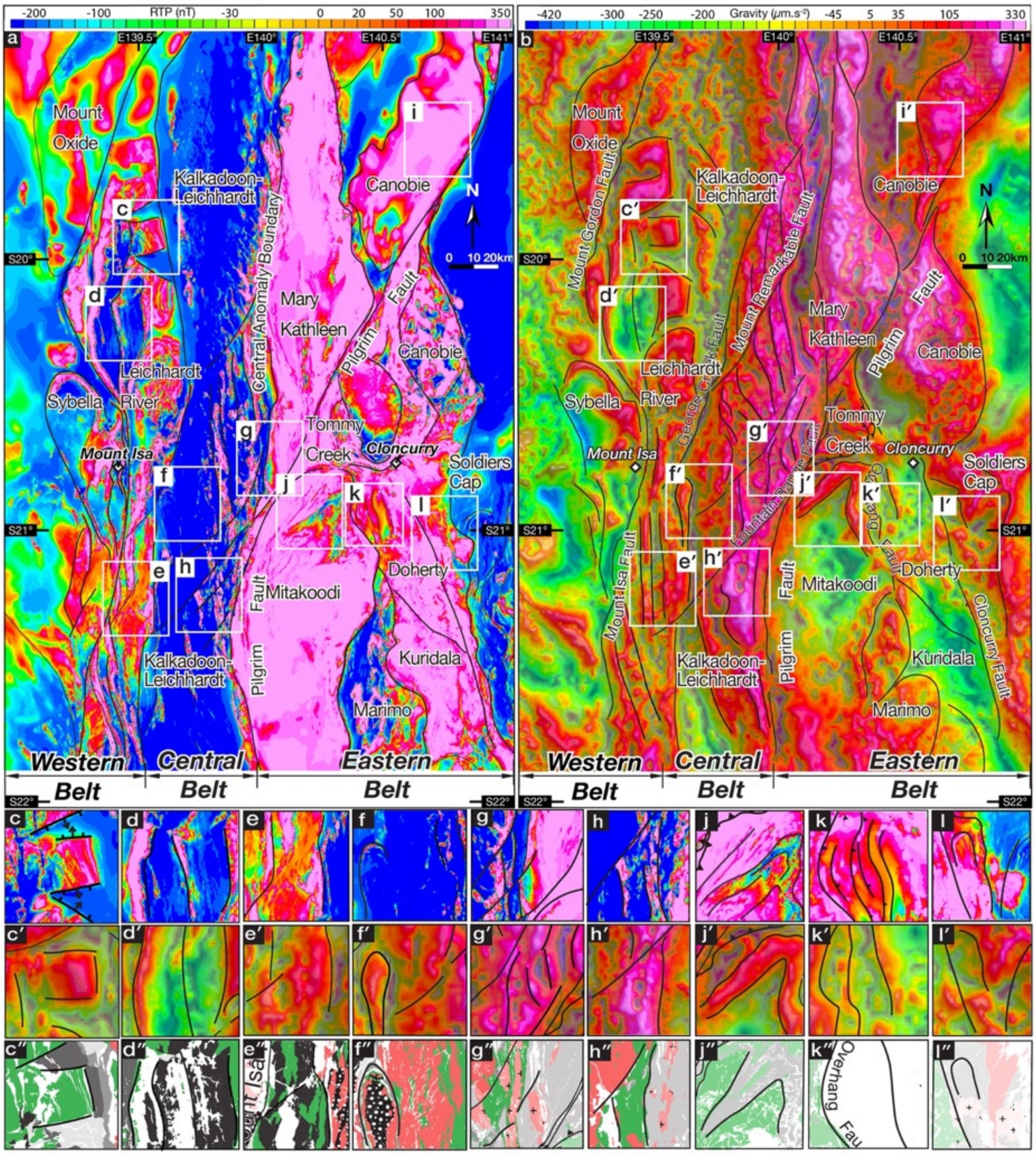

Fig 5.5: (a) Reduced-to-magnetic-pole (RTP) aeromagnetic and (b) Bouguer gravity anomaly image of the Mount Isa Inlier. (c)–(l) Zoomed-in RTP aeromagnetic images. (c')–(l') Zoomed-in Bouguer gravity regions. (c")–(l") Simplified lithological zoom-ins, facilitating correlations to zoomed-in aeromagnetic and gravity images.

5.5.2 Aeromagnetic and gravity patterns of the Georgetown Inlier

In the Georgetown Inlier, geological units are also temporally subdivided and grouped into four major lithological categories to facilitate correlations between rock types and geophysical responses (Fig. 5.6). Localized excerpts of magnetic and gravity images show a strong correlation with corresponding lithology areas (e.g., Fig. 5.7 c–c''), which will be further described below.

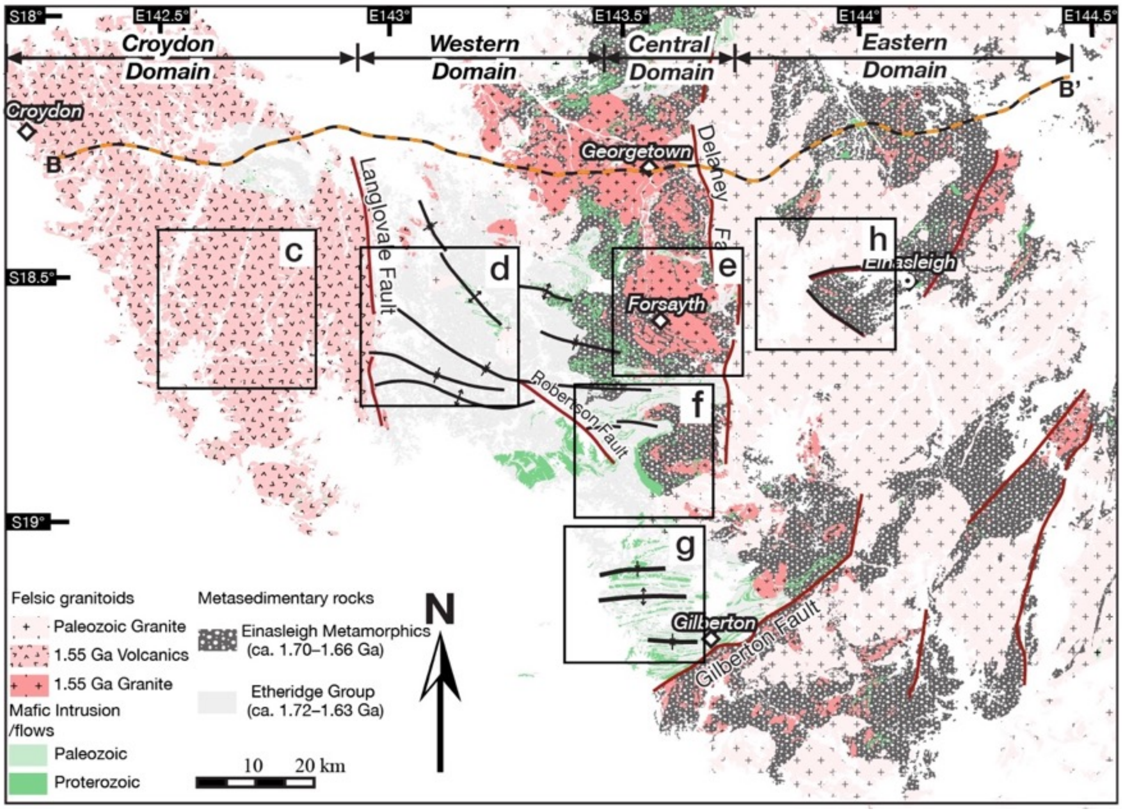

Fig. 5.6: Simplified lithological map of the Georgetown Inlier (modified from Bain et al., 1985) shown in four main lithological groups, including metamorphic basement (dark grey with white dots), mafic intrusions/flows (green), felsic intrusions and volcanics (red and pink) and sedimentary rocks (light grey). (c) – (h) correspond with the (c) – (h) in Fig. 5.7.

(1) Croydon Domain

In the RTP aeromagnetic anomaly grid (Fig. 5.5), the western margin of the Croydon Domain is defined by Quaternary and Mesozoic basins exposures. The eastern margin corresponds to a sharp N-S trending gradient zone that separates the elliptical and homogenous Croydon Volcanics on the west from the NW-trending lineated structures on the east. Within the Croydon Domain, the aeromagnetic image is characterized by N-S-trending negative magnetic anomalies superimposed by NNW-trending, elliptical, intermediate magnetic anomalies (Fig. 5.7c) with intensity of anomalies decreasing from the centre (+60 nT) to the edge (-30 nT). A similar pattern is also evident in the Bouguer gravity grid (Fig. 5.7c'), showing elliptical gravity high in the core (+100 μm s^{-2}) and gravity low (-30 μm s^{-2}) at the rim, respectively.

(2) Western Domain

The western domain is characterized by a series of NW–SE oriented, curvilinear positive magnetic and high intensity gravity anomalies of varying frequency, superimposed on the regional low to intermediate anomalies (Figs. 5.7d–d'). Further in the south, the regional magnetic anomalies are punctuated by short wavelength of stippled, E-W trending linear magnetic anomalies which correlate with more distinct E-W trending high intensity gravity anomalies belts (100 to 200 μms^{-2}) in the Bouguer gravity grid (west of Fig. 5.7g'). The boundary between the western and central domains is less well-defined due to similar magnetic and gravity signatures.

(3) Central Domain

The central domain is characterized by intermediate magnetic pattens being cross-cutted by NW- trending, short wavelength negative magnetic anomalies to the west of the Forsayth (Fig. 5.7e). Subrounded positive magnetic anomalies are superimposed onto intermediate anomalies in the central area (Fig. 5.7f). The Bouguer gravity grid shows a reverse pattern, with high gravity anomalies being overprinted by negative subrounded anomalies (Fig. 5.7f'). Further south, the E-W trending, high intensity linear magnetic and gravity anomalies identified in the western domain continuously extended into the central domain (Fig. 5.7g–g'). The eastern boundary of the central domain is defined by a N-S trending, sharp gradient variation that defines highly magnetic and lowly gravity eastern domain

(4) Eastern Domain

In contrast with the relatively smooth pattern in the western and central domains, the geophysical anomaly of the eastern domain shows a bipartite signature with N-S trending, high intensity magnetic anomalies (between +60 nT and 350 nT) lie along the western section with a lateral extent of ~70 km by ~20 km. On the eastern section (Fig. 5.7h), triangle magnetic low is locally superimposed on the regional intermediate magnetic anomalies (-50 nT), correspond with an inverse pattern in the gravity anomaly (Fig. 5.7h'). Further south, the geophysical pattern differs from regional structural grain and is characterized by prominent long wavelength (~20 km), circular positive magnetic and gravity anomalies (east of Figs. 5.7g–g').

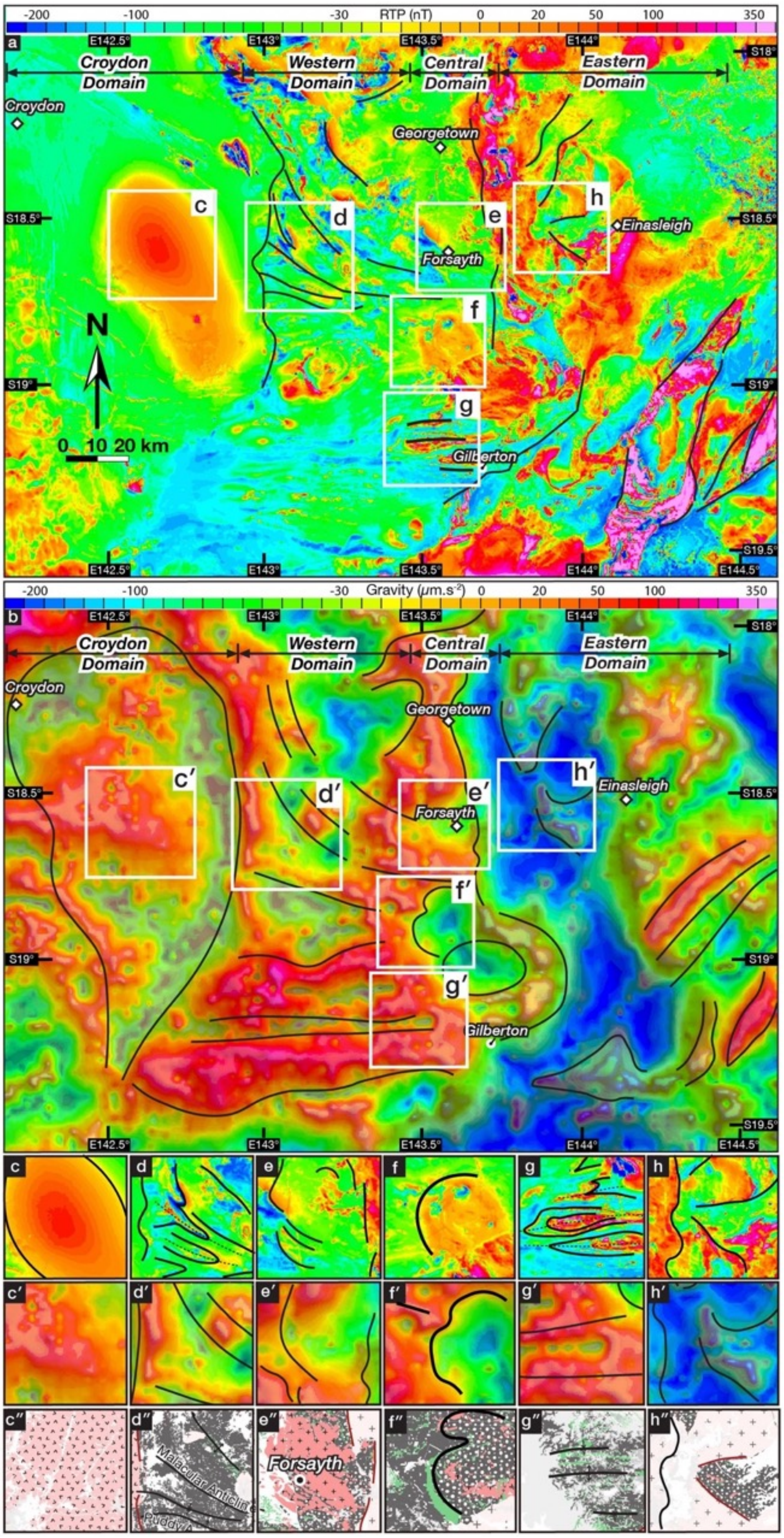

Fig. 5.7: (a) Reduced-to-magnetic-pole (RTP) aeromagnetic image and (b) Bouguer gravity anomaly image of the Georgetown Inlier. (c)–(h) Zoomed-in RTP aeromagnetic images. (c')–(h') Zoomed-in Bouguer gravity regions. (c")–(h") Simplified lithological zoom-ins. This layout is designed to facilitate correlations between zoomed-in aeromagnetic and gravity images.

5.5.3 Regional anomalies

Acquired geophysical grids have been applied with upward continuation and low pass filter methods to enhance deep source body signals, and diagnose distinctive crustal boundaries. In the Mount Isa Inlier, the filtered aeromagnetic data shows ~300 km-long, broad N-S trending belts of intermediate-, weak- and high-magnetic response that are broadly identical with the structurally defined western, central and eastern belts (Fig. 5.8a). The boundary between the central and eastern belts is well-defined in the filtered image by a NNW-SSE trending, sharp magnetic and gravity gradient zone (Fig. 5.8a-b), which was previously recognized from the RTP magnetic intensity grid and defined as the Central Anomaly Boundary (section 5.5.1). This geophysical boundary is also co-located with the surface Pilgrim Fault in the south. A N-S trending, distinctive aeromagnetic boundary is recognized on the eastern margin of the Mount Isa Inlier (Fig. 5.8f), which separates the high magnetic Mount Isa basement rock on the west from the low magnetic Millungera Basin on the east. Similar patterns are also evident in the filtered Bouguer gravity grid (Fig. 5.8b), where the alternating intermediate, low- and high-density N-S to NNE-trending belts are consistent with the magnetic patterns.

Between the Mount Isa and Georgetown inliers, the Numil seismic province is characterized by a bipartite geophysical signature showing weak- and strong-magnetic regions separated by a strong magnetic gradient (Fig. 5.8g), although is less well-defined in the filtered Bouguer gravity grid (Fig. 5.8b). This sharp magnetic boundary is named the Numil Thrust Front in this study, which is located to the east of the Millungera Basin (Fig. 5.8g). A distinct decrease of magnetic anomalies is observed on the eastern margin of the Numil seismic province, and is coincident with the Empress Suture Zone previously recognized from the seismic reflection data (Fig. 5.8a, Olierook et al., 2021). Further east, in the Georgetown Inlier, the magnetic pattern of the Croydon domain is homogenously N-S trending (Fig. 5.8a), and is characterized by elliptical, weak to intermediate magnetic anomalies, corresponds to a symmetric pattern in the filtered gravity grid (Fig. 5.8b). Similarly, the western domain is also characterized with a N-S and NNW-SSE trending, homogenous weak magnetic and intermediate gravity responses. The boundary between the western (Croydon and western domains) and eastern (central and eastern domains) Georgetown Inlier is defined by a NNW-SSE trending magnetic gradient zone, that separates western domains from the N-S trending high magnetic anomalies of the central and eastern domains to the east. This magnetic gradient zone also coincides with the exposed, N-S trending, regional detachment fault recognized from recent structural and metamorphic studies (Volante et al., 2020a; 2020b).

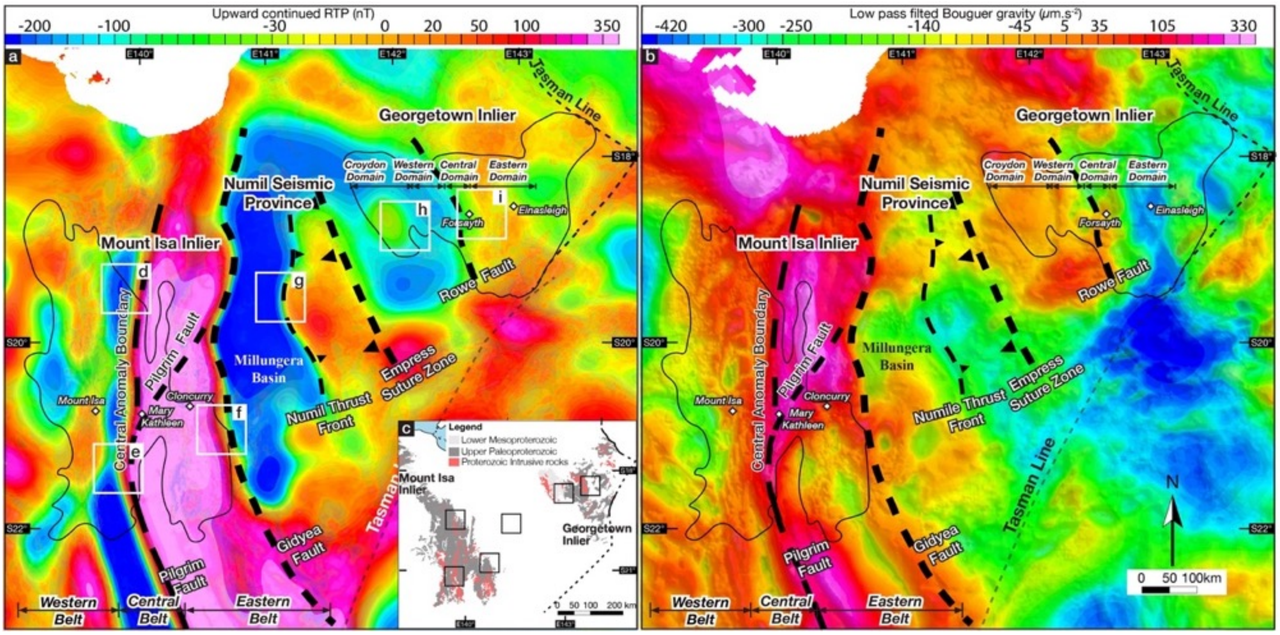

Fig. 5.8: (a) reduced-to-magnetic-pole (RTP) aeromagnetic image, upward continued to 10 km and (b) low pass filtered Bouguer gravity anomaly image of north Queensland. (c) Simplified lithological map of north Queensland correspond with the exposure aera of Fig. 5.8a. The square boxes in Fig. 5.8c are co-located with (d)–(i) in Fig. 5.8a.

5.6 Crustal architecture of NE Australia

Although magnetic and gravity data provide new insights into the geophysical texture of North Queensland, it is not an unique geological solution as the same geophysical response can be produced by different geological settings. Thus, to reduce the ambiguity remaining in the interpretation of the potential filed data, constraints from the surface geological data and regional seismic transects were also incorporated into the crustal architecture interpretation (Figs. 5.9–5.11). Via linking the regional geophysical signature with specific lithologies, regional fold geometry, and alteration textures of known age, definition of preserved architecture can be achieved. In this section, excerpts of upward-continued magnetic response (Figs. 5.9D, 5.10B & 5.11D) and low-pass filtered gravity images (Figs. 5.9G, 5.10E & 5.11G) are combined with seismic reflection profiles (Figs. 5.9B, 5.10C & 5.11B) across the Mount Isa and Georgetown inliers to further constrain the deep crustal architecture undercover. The surface geological maps are overlain to investigate the nature of the filtered geophysical boundaries (Figs. 5.9A & 5.11A). Field magnetic (Figs. 5.9C, 5.10A & 5.11C) and gravity value profiles overlapping the seismic transects are also presented to facilitate further correlations (Figs. 5.9F, 5.10D & 5.11F).

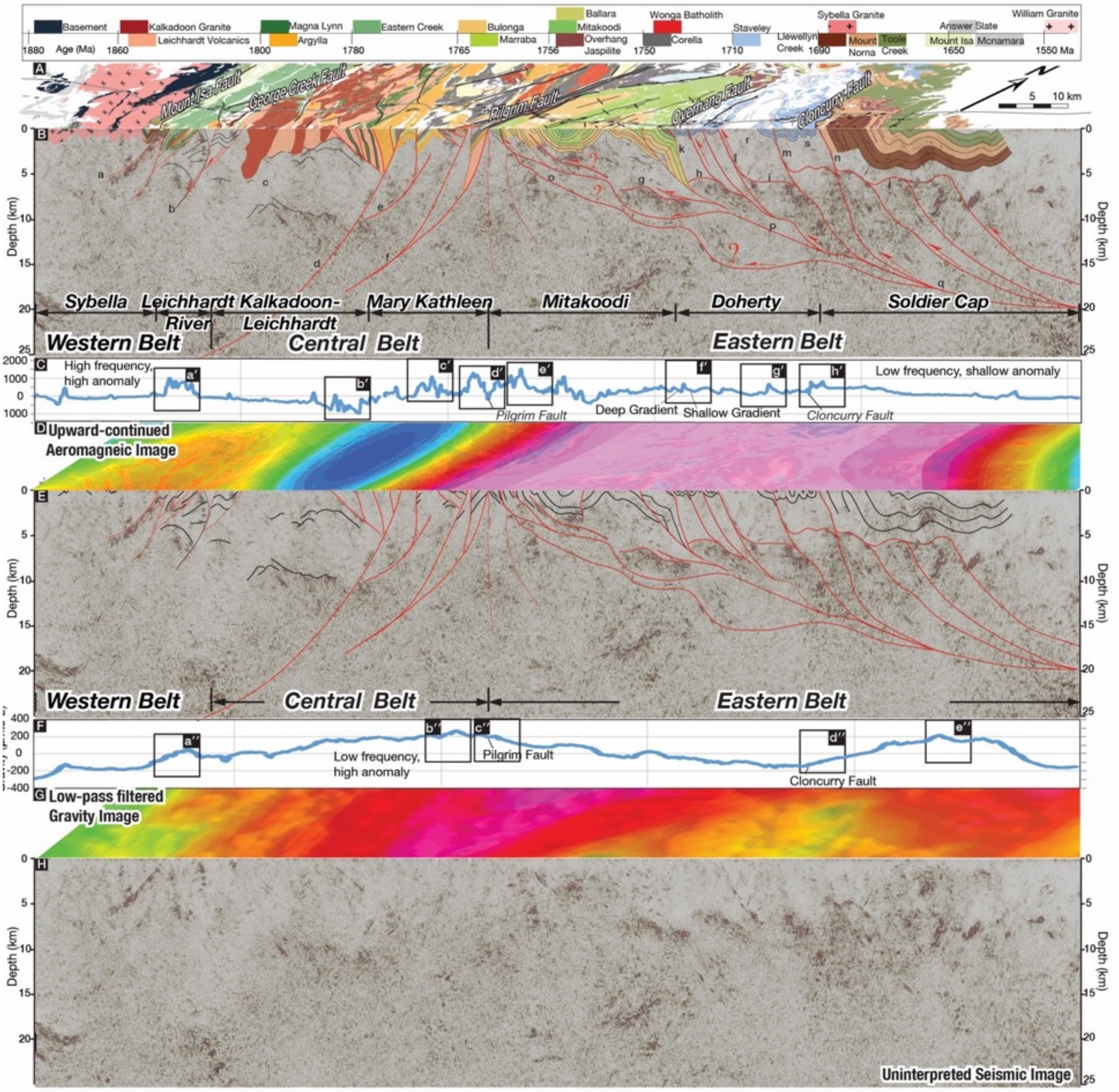

Fig. 5.9: Crustal architecture interpretation of the Mount Isa Inlier after combining the seismic transect (94MTI–01) with the surface geology (A) and filtered geophysical images (D). A. Surface geological map of the Mount Isa Inlier (adapted from Blake, 1987) that overlaps with the intersection of seismic line 94MTI–1. B. Crustal architecture of the Mount Isa Inlier interpreted from seismic reflection line 94MTI–01. a–q: various seismic locations referred to in the text. C. Magnetic response values along the seismic transect. a'–h': various magnetic line locations referred to in the text. D. Upward-continued RTP magnetic grid overlain on the seismic transect. E. Simplified crustal architecture of the Mount Isa Inlier interpreted from seismic reflection line 94MTI–01. F. Gravity response values along the seismic transect. a''–e'': various gravity line locations referred to in the text. G. Low-pass filtered Bouguer gravity grid overlain on with the seismic transect. H. Uninterpreted deep seismic reflection line 94MTI–01. Vertical to horizontal scale on the seismic sections is ~1:4, assuming an average crustal velocity of 6 km s^{-1}.

5.6.1 The Mount Isa Inlier

a) Western Belt

In the western belt, the stratigraphic sequences of the Leichhardt Superbasin (O'Dea et al., 1997b) were deposited in the Leichhardt River Domain (Derrick, 1982), accommodated by the N-S- to NNW-trending, west-dipping Mount Isa and the Gorge Creek faults in the west and east, respectively (O'Dea et al., 1997a). The rift controlled architecture is also evident in the seismic reflection image where parallel seismic reflections dip towards the subvertical highly reflective boundaries on the west, and is indicative of stratal growth thickened towards the Gorge Creek faults (Fig. 5.9B, O'Dea et al., 1997b). During the Leichhardt rift event (1.79–1.78 Ga, O'Dea et al. 1997b; Jackson et al., 2000), deposition of the intermediate density and low magnetic Mount Guide Quartzite (Barlow, 2004; MacCready, 2006; Pears et al., 2001) and extrusion of the high-density and highly magnetic Eastern Creek Volcanics in the Leichhardt River domain was controlled by N-S trending normal faults under an E-W extensional setting (Barlow, 2004; MacCready, 2006a; Pears et al., 2001). This structure corresponds to the N-S trending, long wavelength (~20–30 km) of positive to negative geophysical anomalies in the magnetic and gravity grid (see section 5.5.1). Consistently, on the magnetic and gravity profiles (Fig. 5.9C & 5.9F), a magnetic (Fig. 5.9a') and gravity (Fig. 5.9a'') elevated domain is also co-located with the fault-controlled, Eastern Creek Volcanics in the Leichhardt River Domain. Further west, the boundary between the Leichhardt and Sybella domains is well-defined on the seismic reflection image (a in Fig. 5.9B) as a strong reflective zone, dipping west to ~6 km depth, which coincides with the surface projection of the Mount Isa Fault (Fig. 5.9A). The Sybella Domain is characterized by non-reflective signatures on the seismic reflection profile (Fig. 5.9B) and elliptical negative anomalies in the magnetic (Fig. 5.9D) and gravity grid (Fig. 5.9G). This is correlated with the intermediate density and low magnetic ca. 1.68 Ga Sybella Granite outcrop area (Fig. 5.9A). During the ca. 1.6 Ga Isan Orogeny, reversal of the N-S trending, graben-bounding normal faults accommodated the shortening on the eastern margin of the Sybella Domain (Bierlein & Betts, 2004; Drummond et al., 1998), as shown on the seismic image as subparallel, steeply dipping fault zones.

b) Central Belt

The boundary between the western and central belts is defined by the surface exposure of the west-dipping Quilalar/Gorge Creek Fault zone (O’Dea et al., 1997a) that separates the western meta-sedimentary package from the eastern crystalline basement. In the central belt, its western section is characterized by non- to weakly- reflective signatures (c in Fig. 5.9B) and N-S trending negative magnetic (Fig. 5.9D) and positive gravity anomalies (Fig. 5.9G) in the processed geophysical grid. This is correlated with the low magnetic and intermediate density of ca. 1.86 Ga Kalkadoon Granite (Wyborn and Page, 1983) crystalline basement which is exposed on the surface (Fig. 5.9A). On the eastern section, the seismic reflection data imaged several E-dipping, subvertical faults that may control the surface expression of the ca. 1.79–1.74 Ga Leichhardt Superbasin depositing, before being truncated by W-dipping, reverse thrusts (d–f in Fig. 5.9B) during the Isan Orogeny (Korsch et al., 2008; MacCready, 2006; MacCready et al., 1998). The tectonic contact between the Kalkadoon Batholith (Barlow, 2004) and the Paleoproterozoic basinal successions is shown by NNW-trending, low angle thrusts that connect into an east-dipping detachment above the crystalline basement. In the Mary Kathleen Domain (Fig. 5.9B), west-dipping, sub-vertical reflections (d–f) have separated the Mary Kathleen Domain into several less reflective portions. The sub-vertical transects can be extrapolated to the surface, and are consistent with mapped NE-SW trending steep fault exposures, while the weakly-reflective areas correspond to the lithologically homogeneous, felsic volcanic rocks of the ca. 1.78 Ga Argylla Formation (Neumann et al., 2009). During the ca. 1.74 Ga Wonga Event (Withnall & Hutton, 2013), highly magnetic and density Lunch Creek mafic dykes and gabbro were intruded into the eastern Mary Kathleen Domain under an E-W extension (Derrick et al., 1977; GSQ, 2011). The long wavelength (~20–30 km) positive geophysical anomalies (Fig. 5.9c' & 5.9b'') correlate with mafic sills intruded into low magnetic and high-density Corella meta-sedimentary packages (Derrick et al., 1977).

c) Eastern Belt

On the seismic profile (Fig. 5.9B), although the boundary between the central and eastern belts is hardly resolved due to low penetrative strain contrast for sub-vertical structures, a sharp dissection of high magnetic signals by the weak magnetic signature is identified on the magnetic value profile (Fig. 5.9 d'), co-located with the Pilgrim Fault projection. Separated by the Pilgrim Fault on the east, the seismic reflection data show several east-dipping, sub-horizontal reflection zones (g, h, i, j in Fig. 5.9B) dissected by sub-vertical east-dipping reflection layers (k, l, m, n) before extending to a crustal depth of 15–20 km (Fig. 5.9B), and joining a laterally coherent band of sub-horizontal reflection (o, p, q). The sub-vertical, dissecting layers could be traced upward, and are consistent with the surface-mapped steep faults of the Overhang, Happy Value and Cloncurry faults (Blake, 1987). On the aeromagnetic value profile (Fig. 5.9 C), the magnetic values show repeating peaks flanked by steep gradients to the west and shallow slopes to the east (Figs. 5.9 f'-h'). This magnetic pattern is commonly interpreted as a westward thrust fault signature (Betts et al., 2004) as shown on the seismic reflection image (l–n in Fig. 5.9 B), with the steep and shallow gradients correspond to the subvertical, upper parts and the ramp of the thrust fault, respectively. In the Mitakoodi Domain, the magnetic value increase to the highest (e' in Fig. 5.9 C) at regions co-located with the surface expression of the Mitakoodi Anticline that is cored by the highly magnetic Argylla Formation (Barlow, 2004; Meixner, 2009) and the high density and highly magnetic Bulonga and Marraba Volcanics (Barlow, 2004; Blenkinsop et al., 2008; MacCready, 2006a; Pears et al., 2001). The regional seismic structure reflects a thrusting related duplex structure likely associated with the regional fold and thrust development, which is documented by the west-vergent Mitakoodi and Soldiers Cap anticlinorium on the surface (MacCready, 2006a; Withnall et al., 2013).

5.6.2 Crustal architecture between the Mount Isa and Georgetown inliers

Between the Mount Isa and Georgetown inliers, due to a lack exposure of Proterozoic rocks, linking the surface mapped Proterozoic structures with deep crustal architecture imaged by the seismic reflection data is difficult. However, as geophysical data filtering techniques can help to enhance or reduce the magnetic or gravity signals from specific rock units, upward-continued magnetic response (Fig. 5.10B) and low-pass filtered gravity image (Fig. 5.10E) are combined with seismic reflection profiles to further constrain the deep crustal architecture undercover. The magnetic (Fig. 5.10A) and gravity profiles (Fig. 5.10D) are also overlain on the seismic transects to provide further correlations.

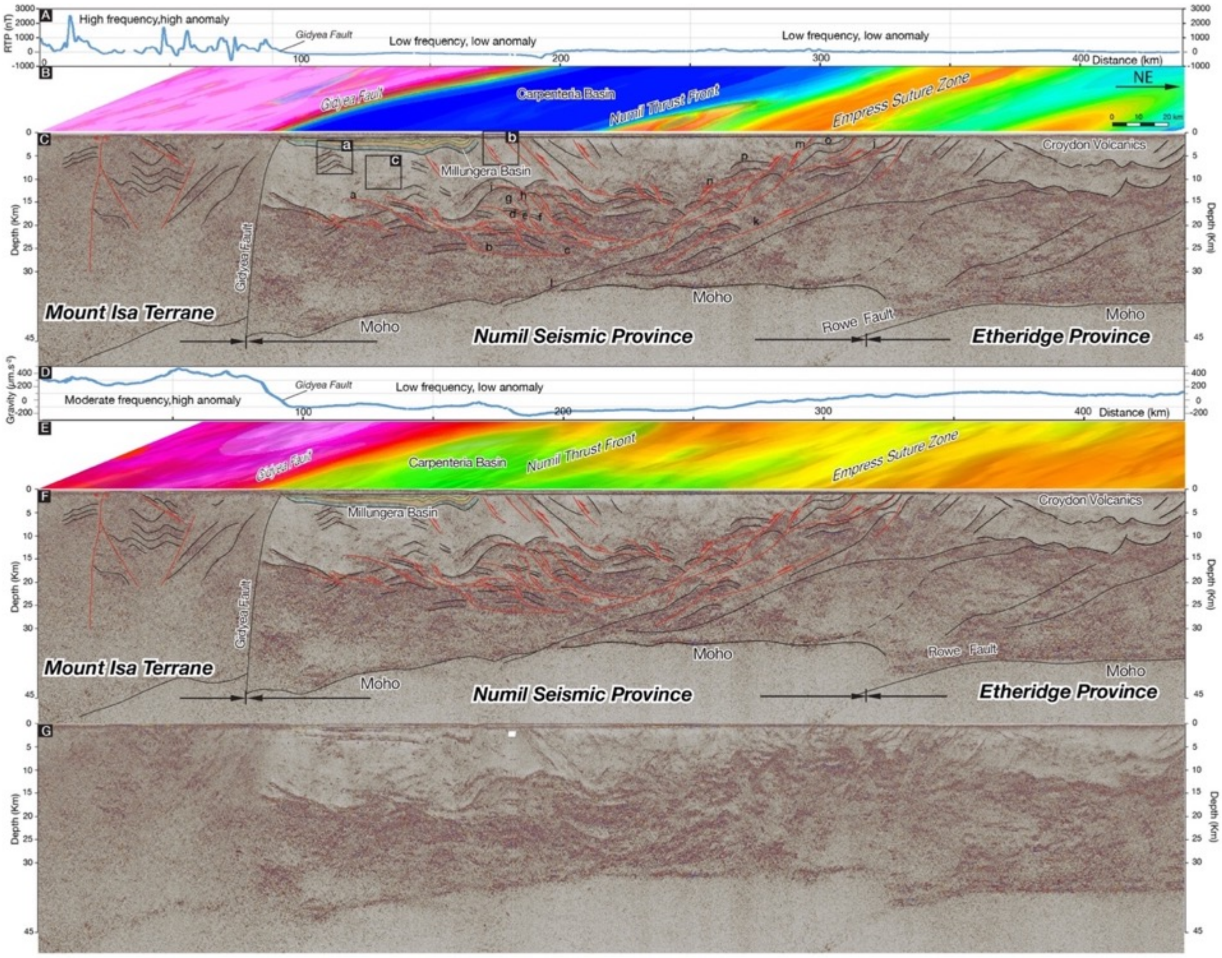

Fig. 5.10: Crustal architecture interpretation between the Mount Isa and Georgetown inliers after combining the seismic transect (07GA–IG1) with the surface geology and filtered geophysical image. A. Magnetic response along the seismic transect. B. Upward-continued RTP magnetic grid overlain on the seismic transect. C. Crustal architecture from the Mount Isa Terrane toward the Georgetown Terrane, interpreted from seismic reflection line 07GA–IG1. D. Gravity response along the seismic transect. E. Low-pass filtered Bouguer gravity grid overlain on the seismic transect. F. Same as C. G. Uninterpreted deep seismic reflection line 07GA–IG1. Vertical to horizontal scale is ~1:4, assuming an average crustal velocity of 6 km s^{-1}.

In the filtered aeromagnetic grid, the Gidyea Fault is resolved as the eastern geophysical margin of the Mount Isa Inlier (Fig. 5.10B). This distinctive aeromagnetic boundary is also recognized on the seismic image as a vertical crustal dissection, cut the Moho at a crustal depth of 45 km (Fig. 5.10 C). The Gidyea Fault zone separates highly-reflective, thicker crust of the Mount Isa Province on its west from the two-layered thinner crust under the Millungera Basin on its east. On the magnetic value profile, a sharp transit of high frequency and high magnetic signals to low frequency and low magnetic anomaly is identified on the magnetic value profile (Fig. 5.10 A), coinciding with the Gidyea Fault's surface projection (Fig. 5.10 B). On the west, the Mount

Isa Province is a highly-reflective, homogenous seismic domain with the Moho imaged at a depth of 40 km to 50 km tilting towards the southeast (Fig. 5.10 C). On the east, the seismic reflection shows a dual-layered, non-reflective upper crust (0–20 km) and highly reflective middle to lower crust (20–40 km). In the upper crust, the horizontal, flat reflection layers (0–2 km) and its underlying folded reflective structures (2–5 km) correspond to the surface exposure of the Mesozoic Carpentaria Basin and the underlying Millungera Basin, respectively (Korsch et al., 2011). Several east-dipping, sub-vertical, highly reflective layers are juxtaposed against the Millungera Basin to its east (b in Fig. 5.10 C), and are interpreted as west-verging thrust faults, related to the deformation of the Millungera Basin and fold geometry. These west-verging thrust faults can be extrapolated to the surface, and correspond to the surface exposure of the Numil Thrust Front that was previous recognized in the filtered aeromagnetic and gravity grid (Fig. 5.10 B & Fig. 5.10 D).

In the middle to lower crust, subparallel horizontal layers (d, e, f in Fig. 5.10 C) are displaced by sub-vertical, east-dipping non-reflective belts (g & h), which are in turn overlain by a dome-shaped structure above (i). The east-dipping reflection layers extend to a crustal depth of 15–25 km and laterally join a coherent band of sub-horizontal reflection (a-c). The cross-cutting structures are comparable with thrust-related duplex structures likely associated with the regional fold and thrust development, commonly found in convergent orogenic belts (Graciansky et al., 2010; Pfiffner, 2017). In the eastern Numil Seismic Province, a 100 km-long, west-dipping, laterally coherent band of planar reflection intersects the Moho at ~35 km (l in Fig. 5.10 C), and extends northeast-ward near-surface (j). This lithosphere-scale zone of high reflectivity was first recognized by Korsch et al. (2012) and was later termed the Empress Suture Zone by Olierook et al. (2021). In the filtered aeromagnetic image, a N-S trending magnetic gradient variation is also co-located with the surface projection of the Empress Suture Zone, separating high and low magnetic signals between its west and east. Further east across the Empress Suture Zone, the Rowe Fault, pervious named as Rowe Fossil Subduction Zone (Korsch et al. (2012), offsets the Moho at a crustal depth of ~35 km under the Etheridge Province. Tracing the surface exposure and linking its geological association is problematic due to the discontinuous nature of the seismic reflection profile (07GA–IG1). Above it, the Etheridge Province is characterized by a weakly reflective layer in the upper crust (0–10 km), correspond to the ca. 1.55 Ga Croydon Volcanic Group exposed on the surface, and a highly reflective layer in the middle to lower crust (10–40 km), ascribed as the underlying deep basement rock of unknown affinity.

5.6.3 Crustal architecture of the Georgetown Inlier

In the Georgetown Inlier, the 07GA–IG1 seismic reflection, which transects the western segment of the Georgetown Inlier, is overlain with the 07GA–IG2 seismic line to trace the geometry and eastward continuity of the Rowe Fault towards the Georgetown Inlier (Fig. 5.11 I). The seismic reflection image is also joined with the surface geological map (Fig. 5.11 A) and filtered geophysical image (Fig. 5.11 B & E) to better establish the 3D geometry of the regional crustal architecture.

In the joint seismic transect, the Rowe Fault, which dissects the Moho below the Etheridge Province, can be traced eastward and connected with west-dipping, sub-vertical, highly reflective layers that exposed on the surface near Forest Home homestead (Fig. 5.11 B). On the surface geological map (Fig. 5.11 A), this crustal boundary is co-located with the regional west-dipping detachment fault that defines the domain boundary between the low metamorphic grade western domain and high metamorphic amphibolite facies central domain (Volante et al., 2020a). In the filtered aeromagnetic image (Fig. 5.11 D), a N-S and NNW-SSE trending magnetic gradient variation marks the surface projection of the Rowe Fault. Separated by the Rowe Fault, the Croydon and western domains on the west preserve west-dipping reflective layers compared to the fold and thrust structure in the central domain. The eastern margin of the central domain is bound by a vertical lithosphere scale structure, which dissects the Moho at a crustal depth of 36 km and exposes on the surface as the N-S trending Delaney Fault (Fig. 5.11 B). On the magnetic profile (Fig. 5.11 C), a sharp dissection of high-magnetic signal by weak-magnetic response is consistent with the surface exposure the Delaney Fault (a' in Fig. 5.11C). Bounded by the Delaney Fault on the east, a two-layered crustal architecture identified in the central domain can be further traced toward the eastern domain (Fig. 5.11 B). The upper crust of the eastern domain shows a weakly reflective signature. In the middle to lower crust, sub-horizontally, laterally coherent high reflection layers can be traced eastward (g, h, i), and are dissected by east-dipping, non-reflective zones (j & k).

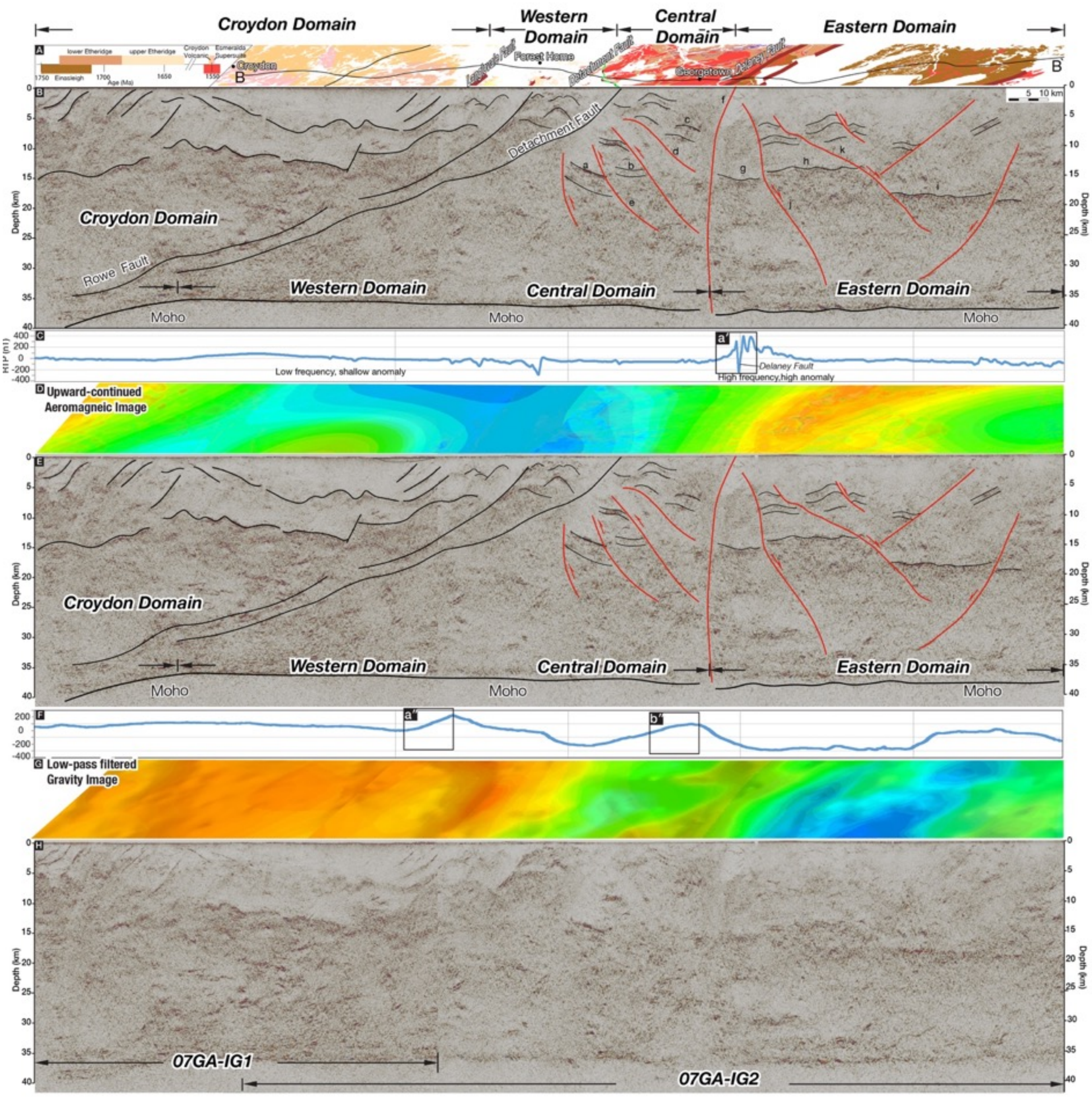

Fig. 5.11: Crustal architecture interpretation of the Georgetown Inlier after combining the seismic transect (07GA–IG2) with the surface geology and filtered geophysical image. A. Surface geological map of the Georgetown Inlier where intersected by 07GA–IG2, show showing stratigraphic distribution and main fault zones (adapted from Bain et al., 1985). B. Crustal architecture of the Georgetown Inlier interpreted from seismic reflection line 07GA–IG2. a–k: various seismic locations referred to in the text. C. Magnetic response values along the seismic transect. a': magnetic line location referred to in the text. D. Upward-continued RTP magnetic grid overlain on the seismic transect. E. Crustal architecture of the Georgetown Inlier interpreted from seismic reflection line 07GA–IG2. F. Gravity response along the seismic transect. a'': gravity line location referred to in the text. G. Low-pass filtered Bouguer gravity grid overlaying with the seismic transect. H. Same as E. I. Uninterpreted deep seismic reflection line 07GA–IG2. Vertical to horizontal scale is ~1:4, assuming an average crustal velocity of 6 km s^{-1}.

5.7 Discussion

Based on the distinctive crustal architecture resolved from seismic data and clear geophysical boundaries identified from the filtered aeromagnetic and grids, five major crustal boundaries, including the Central Anomaly Boundary (overlap with the Pilgrim Fault in the south), Gidyea Fault, Empress Suture Zone, Rowe Fault and the Delaney Fault, divide this part of the North Australian Craton into six separate crustal domains. However, whether these crustal-scale structures represent terrane suture zones or crustal-scale faults and detachment zones is a matter of debate (Betts et al., 2016; Bierlein et al., 2011; Nordsvan et al., 2020; Korsch et al., 2012; Volante et al., GR, in review). Here, we evaluate the potential allochthonous terranes preserved in NE Australia by investigating sedimentary records, structural evolution and Nd isotopic ratios and model ages of Proterozoic crystalline rocks (Fig. 5.12 & Fig. 5.13) from individual domains.

5.7.1 Dextral transpression between the eastern and central Mount Isa inlier at ca. 1.74 Ga via the Pilgrim Fault

In the seismic image (Fig. 5.9 B), there is significant contrast in the crustal architecture on the two sides of the Pilgrim Fault. In the eastern Mount Isa Inlier, the crustal architecture is homogenous and characterized by a laterally coherent band of sub-horizontal mid-crustal reflectors which are dissected by sub-vertical to steeply east-dipping reflectors. On the contrary, the western Mount Isa Inlier is characterized by non- to low-reflective domains, west-dipping thrust structures that cut the basement, and intense shortening accumulating at sub-vertical faults of domain boundaries. This distinct architecture leads us to propose that the eastern and western Mount Isa Inlier were controlled by different tectonic regimes, and were possibly deposited in discrete sedimentary basins with distinctive architecture that influenced the style and evolution of the orogenic structures.

In the eastern Mount Isa Inlier, the decoupled deformation between basement and supracrustal units is interpreted as due to a decollement layer preserved above the crystal basement (MacCready et al., 2006). This decollement layer is linked with the Marimo Slate Group where micaceous schistosity was developed parallel to bedding, causing impedance contrast between the upper unite and underlying basement (MacCready et al., 2006). By contrast, the western Mount Isa Inlier is dominated by N-S trending structures, with sub-vertical strata thrusting toward the basement on its eastern and western flanks (Gibson & Henson, 2005). Intracontinental rift setting has accommodated early superbasin deposition (ca. 1.8–1.73 Ga; O'Dea et al. 1997) and facilitated the N-S trending deep faulting development. Basin architecture, along with the underlying basement structures, therefore had a strong impact on post-depositional deformation and the crustal geometry development. In this scenario, the basement acted as a rigid buttress against the overlying rocks, which were compressed during the Isan Orogeny by the E-W shortening (Gibson & Henson, 2005). Thus, the differential crustal geometries between the western and eastern section of Mount Isa Inlier can be simply ascribed to the different tectonic regimes that controlled the early basin architecture.

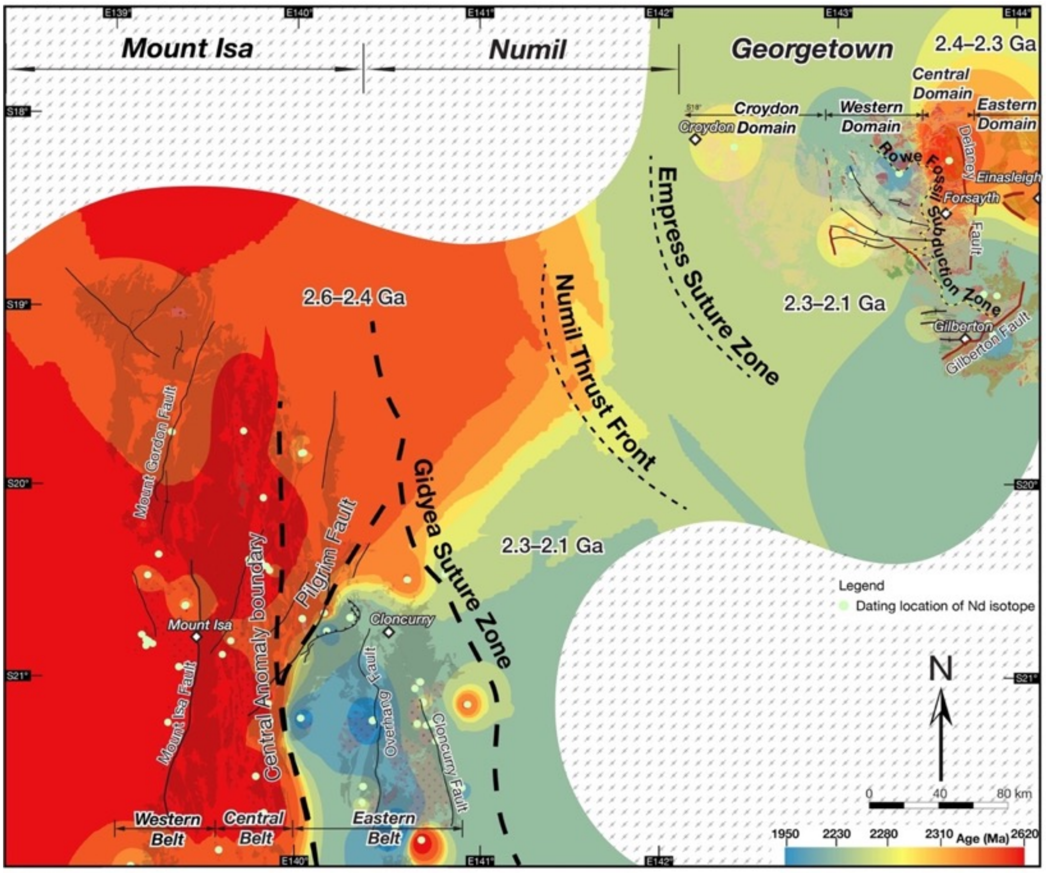

Fig 5.12: Neodymium two-stage depleted mantle model age map of felsic and mafic igneous rocks (ca. 1.89–1.50 Ga) from the Mount Isa and Georgetown inliers. Neodymium isotope data are from previous studies (Black & McCulloch, 1984, 1990; Bierlein & Betts, 2004; Bierlein et al., 2011; Geoscience Australia, unpublished; Lambeck et al., 2012; Mark, 2001; McDonald et al., 1997; Page & Sun 1988; Wyborn et al., 1988). Isotopic data were gridded using minium curvature in ArcGIS.

Detrital zircon analyses of the ca. 1.76 Ga synchronous sedimentary rocks from the western and eastern Mount Isa Inlier suggest that they were sourced from different regions (Nordsvan, 2020). The Mitakoodi Quartzite deposited in the eastern Mount Isa shares similarities with the contemporaneous sedimentary rocks from the Broken Hill in the South Australia Craton (Nordsvan, 2020), contrasting with the Ballara Quartzite (Page, 1998) that deposited in the western Mount Isa Inlier, and received North Australian sources (Nordsvan, 2020). Neodymium isotopic analyses of >ca. 1.8 Ga magmatic rocks in the western and central belts yielded consistent T_{2DM} age of ca. 2.6–2.3 Ga (Fig. 5.12), and suggests that these portions of the Mount Isa Inlier were underlain by an isotopically-similar lithospheric block, with granitic to dioritic intrusions sampling rocks with Neoarchean to Paleoproterozoic mantle extraction ages (Bierlein et al., 2011; Champion, 2013). Conversely, Nd isotopes dated from ca. 1.7–1.5 Ga intrusions in the Eastern Belt yield younger T_{2DM} ages of ca. 2.2 Ga (Bierlein et al., 2011), and suggests the eastern Belt underwent a separate evolutionary history.

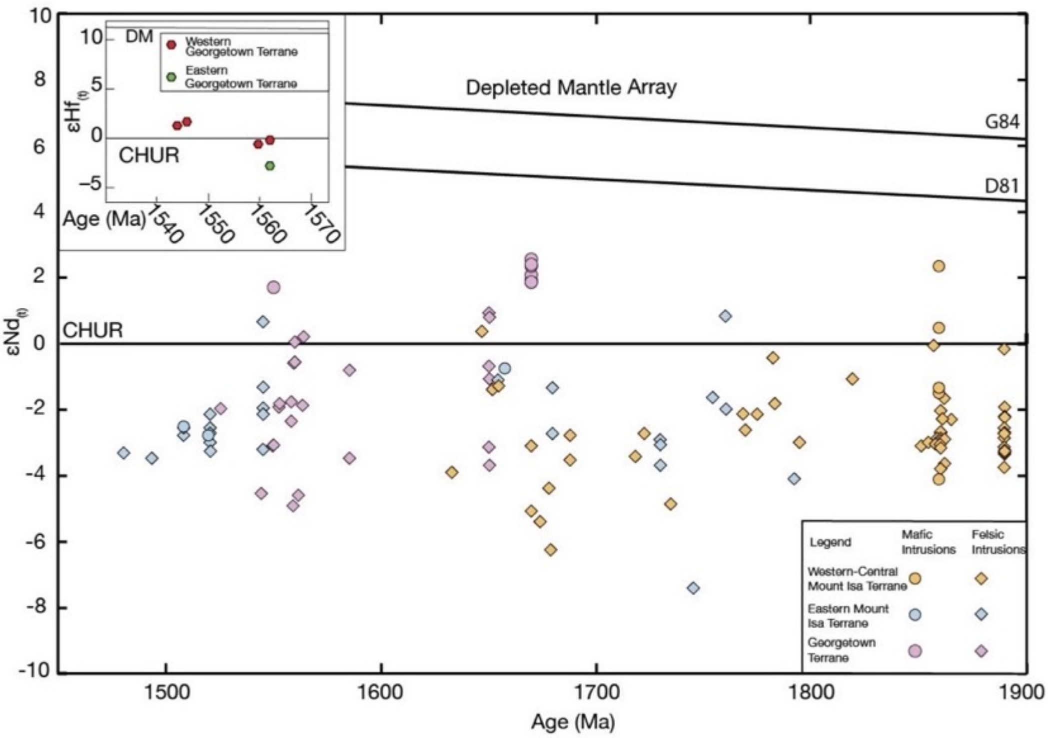

Fig 5.13: Initial Nd isotopic ratios of Proterozoic crystalline rocks from the western-central and eastern Mount Isa Inlier and Georgetown Inlier. The εNd values refer to the initial chondrite normalized $^{143}Nd/^{144}Nd$ isotopic ratio (Bouvieret al., 2008), while the depleted mantle arrays represent Nd isotopic evolution for the mantle rocks, each from Goldstein et al. (1984), and DePaolo (1981), respectively. Data sources are compiled from Blenkinsop. 2005, Bierlein and Betts. 2004, Bierlein et al. 2011, Champion. 2013, Geoscience Australia, unpublished, Lamback et al. 2012, Mark. 2001, McDonald et al. 1997, Page and Sun. 1998, Wyborn et al. 1988. Specific values are listed in the Table E.5.1 in Appendix E.

In the Initial Nd isotopic ratios plot (Fig. 5.13, modified from Champion, 2013), the $\varepsilon Nd_{(t)}$ values of the western Mount Isa Inlier show a progressive evolution to more negative and evolved nature with younging age during ca. 1.8–1.68 Ga. At ca. 1.68 Ga, an abrupt increase in $\varepsilon Nd_{(t)}$ values from -6 to –2 reflects a burst of juvenile input. In the eastern Mount Isa Inlier, the $\varepsilon Nd_{(t)}$ values fluctuate between + 1 and –7 during the ca. 1.76–1.65 Ga interval, with a trend toward less negative values (-1 to -3) at ca. 1.68 Ga comparable to that in the western Mount Isa Inlier. Synchronous juvenile inputs and undifferentiated crustal evolution between the western and eastern Mount Isa terranes suggest that these two terranes may have amalgamated predate ca. 1.68 Ga. Geophysical modelling suggests that the Pilgrim and Fountain Range Faults are the lithospheric-scale, N-S trending structures that accommodated an apparent dextral offset of up to 20 km (Betts et al., 2011; Blenkinsop et al., 2008). This is comparable to the 30 km of stratigraphic displacement previously recorded after the Malbon Group deposition at ca. 1.76 Ga (O'Dea et al., 1997; Withnall & Hudson, 2013). According to field observations and petrological investigations, a N-S trending, shearing and metamorphism event is recorded on the both sides of the Pilgrim Fault at ca. 1.74 Ga (Pearson, 1992; Withnall & Hudson, 2013). By interpreting and modelling of high resolution regional geophysical data in the Leichardt River Domain of the western belt, Blaikie et al. (2017) documented a basin inversion event occurred at ca. 1.74–1.71 Ga, associated with an E-W direct compressional event, following the ca. 1.78–1.74 Ga Leichhardt Superbasin deposition (Blaikie et al., 2017). Thus, based on various pieces of evidence, we propose that the western–central and eastern belts of the Mount Isa Inlier amalgamated at ca. 1.74 Ga, via transpressional dextral slip faulting of Pilgrim and Fountain Range Fault (Fig. 5.14 a-b).

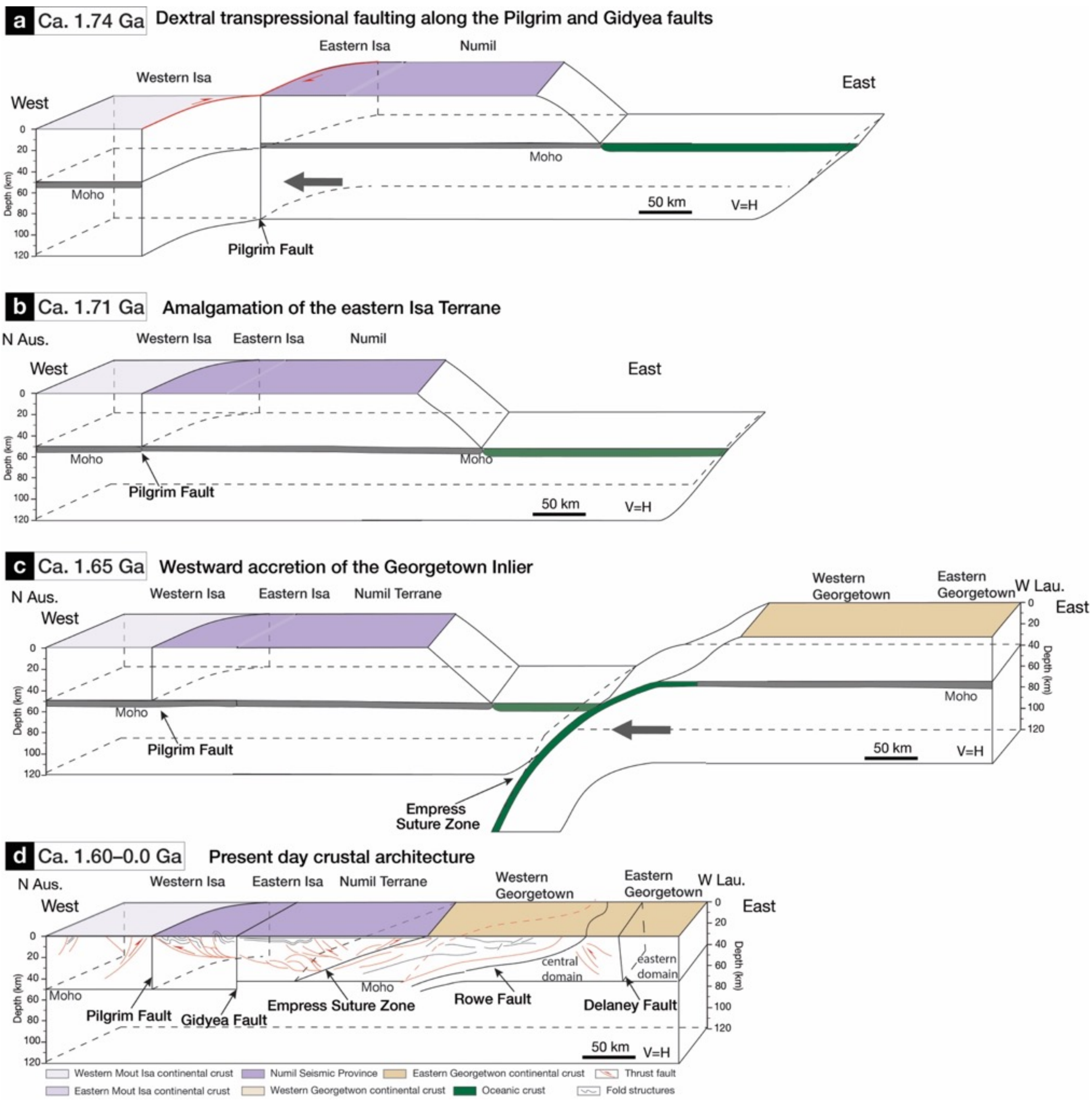

Fig. 5.14 : Proterozoic terrane accretionary history of NE Australia during the assembly of the supercontinent Nuna between ca. 1.74 and 1.60 Ga.

5.7.2 The Gidyea Fault is a domain boundary fault activated post the ca. 1.60 Ga Isan Orogeny

The crustal architecture separated by the Gidyea Fault is distinctly different, with the western crust characterized by uniform, highly reflective, thickened crust, compared to the two-layered, thinner crust covered by the Mesozoic Carpentaria Basin to the east. Based on seismic reflective geometry, Korsch et al. (2012) proposed that the Gidyea Fault was a broad zone of low reflectivity, dipping to the southwest at about 40°, and represented as a subduction zone formed priority to the ca. 1.70–1.62 Ga sedimentary succession in the Etheridge Province. Others, by investigating the depositional facies of the Soldiers Cap Group (ca. 1.68–1.65 Ga; Page and Sun, 1998), suggested that the sedimentary rocks were deposited continually across the Gidyea Fault under a continental margin setting (Foster & Austin 2008; Blenkinsop et al., 2008). Although limited exposure of Proterozoic basement rock within the Numil terrane inhibits a clear interpretation of the terrane accretionary event and formation age of the Gidyea Fault. Recent resistivity models indicate that the Gidyea Fault is a highly conductive zone, with conductivity interpreted to be the result of hydrous alteration associated with the period of subduction, and/or the mineralisation event responsible for the formation of the Earnest Henry IOCG deposit (Jiang et al., 2019). If the latter is true and the Gidyea Fault was once a suture, then the suture zone must be older than 1.52 Ga, the age of Earnest Henry deposit (Mark et al., 2006).

The Gidyea Fault truncates the Kowanyama Seismic Zone (Etheridge age or younger) on the east and the upper sequences of the Mount Isa Inlier (<1.71 Ga) on the west. This indicates that the Gidyea Fault should have formed postdate the Etheridge sequence (ca. 1.71 Ga). Although a gentle west dipping suture geometry has been previously proposed by Korsch et al. (2012) and Betts et al. (2016) based on seismic reinterpretation, on the seismic reflection image (Fig. 5.10 C), the Gidyea Fault is imaged as a subvertical boundary dissecting the Moho between the Mount Isa and Numil Seismic Province. In the RTP and filtered aeromagnetic grid, the Gidyea Fault can be traced northwards and be joined with the Pilgrim Fault on the east of the Canobie Domain, defining the eastern boundary of the Mount Isa Inlier. From the localised excerpts RTP pattern (Fig. 5.5a), the narrow, NNW-trending, S-shaped high magnetic lineaments indicate a right lateral strike slip displacement on the east of the Gidyea Fault (Fig. 5.5l). This strike slip pattern recognized east of the Cloncurry Fault is believed to have occurred during the transpressional stage post Isan Orogeny with crustal shortening accommodated by conjugate NW-striking sinistral and NE-striking dextral faults along inherited early normal faults (Lister et al., 1999; O'Dea et al., 1997b). Based on these evidences, we propose that the Gidyea Fault is a terrane boundary fault activated between ca. 1.60 and 1.52 Ga (Fig. 5.14 d). It joined with the Pilgrim Fault in the north, forming a transpressional fault system that rotated towards vertical via ongoing shortening during the Isan orogenic episode of the collision (Volante et al. 2020b).

5.7.3 The Empress Suture Zone is a Nuna-age suture zone formed at ca. 1.6 Ga

The Empress Suture Zone was first documented by Korsch et al. (2012) as a series of west-dipping, crustal-scale faults, and later interpreted by Pourteau et al. (2018) as a Nuna-age suture zone connecting Australian and Laurentian crusts during the ca. 1.6 Ga Isan Orogeny. Based on zircon U-Pb dating and whole-rock geochemical analyses, Olierook et al. (2021) supported Pourteau et al. (2018)'s interpretation and suggested that the scale of the suture zone is at least a ~10 km wide, west-dipping fault system. Mesozoic sedimentary basin coverage directly above the suture zone hampers a clear interpretation of its nature and formation age. Nevertheless, granites from drill hole sample situated on the southwest of the Empress Suture Zone yielded age of 1544 ± 5 and 1546 ± 4 Ma (Nordsvan, 2020). These granites, collectively termed the Cudgee Creek Granite, are classified as I-type, with significant hornblende and titanite ± allanite present in samples that are comparable with synchronous intrusions in the eastern belt of the Mount Isa Inlier. This indicates that the Mount Isa crustal material is preserved to the west of the suture zone. Based on seismic geometry reinterpretation, dual thrusting structures associated with terrane suturing event were developed on both sides of the Empress Suture Zone (see section 5.6.2). On the west, subparallel horizontal layers were displaced by sub-vertical, east-dipping non-reflective belts which can be related to the west-verging thrust duplex structures commonly developed in convergent orogenic belts. On the east, west dipping planar reflections point to an eastward trusting above the Empress Suture Zone.

As both the central Georgetown Inlier and eastern Mount Isa Inlier were intruded by synchronous mafic igneous rock at ca. 1.68-1.66 Ga (Dead Horse Metabasalt Vs Soldiers Cap Amphibolites), by comparing their Nd isotopic signatures could provide insights on the terrane accretion process. At ca. 1.66 Ga, the Georgetown Inlier, on the east of the Empress Suture Zone, yields a narrow cluster of positive εNd(t) data at ~+2, contrasting with the negative εNd(t) values obtained from contemporaneous intrusions from the eastern Mount Isa Terranes

(0 to –1). However, no statistical difference between εNd values is observed between the Georgetown and eastern Mount Isa inliers after ca. 1.56 Ga. This indicates a minimum suture age of ca. 1.56 Ga that unified the two crustal segments. Synchronous prograde collisional metamorphism occurred at ca. 1.6 Ga, recorded in both the Mount Isa and Georgetown inliers, further indicating the terrane accretionary timing. We concluded that the Empress Suture Zone is the ca. 1.6 Ga Nuna suture zone, with thrust-related duplex structures developed in the thickened crust (Fig. 5.14 c-d).

5.7.4 The Rowe Fault is a major crustal structure formed during Nuna assembly

The Rowe Fault was initially documented by Korsch et al. (2012) and recognized in this study as a west-dipping, crustal cutting fault system. The suture intersects the Moho with a significant thickness variation of ~ 32 km beneath the Numil Seismic Province and ~ 38 km beneath the Eitheridge Province. It can be traced eastward and connected with the regional detachment fault recognized in the upper crust (Volante et al., 2020a), separating the west-dipping reflectors in the Croydon-western domain from the dominantly east-dipping reflective crust in the central-eastern domain. At the surface, this major crustal boundary is imaged in the filtered magnetic grid as a N-S and NW-SE trending sharp geophysical gradient (Fig. 5.11D). By linking the seismic geometry of the Rowe Fault with similar reflections observed elsewhere in the world, Korsch et al. (2012) interpreted this structure as a fossil subduction zone that was formed associated with the subduction of a passive continental margin, though its formation timing and nature remains unknown. A recent metamorphic study has discovered a surface expression (the 'detachment fault') of the Rowe Fault, which separates highly-metamorphosed, lower crustal units in the east from weakly-metamorphosed upper crustal units in the west (Volante et al., 2020b). According to thermodynamic modelling and geochronological analyses, the eastern Georgetown Inlier had been buried to a crustal depth of ~28–32 km before being exhumed to a surface level of ~8–13 km during the ca. 1.55 Ga extensional stage (Volante et al., 2020a). This provides a minimum formation age of the Rowe Fault before it reactivated as a regional detachment fault. Stratigraphic investigations indicate that the Etheridge Group, which was deposited under paralic (Withnall, 1996) to deeper marine settings (Lambeck, 2011) between ca. 1.71–1.60 Ga, can be traced continuously across the Rowe Fault (Withnall et al., 2013) before being folded uniformly into N-S- and NNW-trending structures during the ca. 1.6 Ga Isan Orogeny (Volante et al., 2020b). Thus, if the Rowe Fault is a subduction related structure, it should be formed predate the above sedimentary rock depositional age of > ca. 1.70 Ga.

Interpretation of the Rowe Fault as subduction structure is problematic as no evidence suggests the basement rock separated by the Rowe Fault is different. Although it is possible that the subduction records were buried beneath the Mesoproterozoic Etheridge Group sedimentary rocks, no major crustal difference has been previously reported between the Croydon-western domain and central-eastern domain (Geological Survey of Queensland, 2011; Withnall et al., 2013). We propose another scenario to explain the genesis of the Rowe Fault, and suggest it representants a crustal-scale structure rather than a terrane boundary. Similar to the major crustal structures developed in the Himalaya-Tibetan Orogen, where subduction related suture zones were formed orthogonal to the northward accretion of the India Plate towards the Tibetan Craton (Yin &. Harrison, 2000), the Rowe Fault was also developed as a major structure orthogonal to the westward accretion of the Georgetown Terrane towards the NE Australian Terrane (Fig. 5.14 d). It was formed parallel with the Empress Suture Zone as a terrane accretionary structure during the final Nuna assembly, and was reactivated as a normal fault during the late-orogenic extensional stage (Volante et al., 2020b).

5.7.5 The Delaney Fault is a structural break formed pre-ca. 1.55 Ga and reactivated during the Palaeozoic extensional stage

The Delaney Fault is a newly identified major crust cutting fault from this study. It intersects the Moho and separates the east-dipping reflectors in the central domain from the dual-layer crust in the eastern domain. At the surface, this major crustal boundary is imaged in the filtered magnetic grid as a sharp geophysical gradient, elongating along a N–S and NNW–SSE direction. According to previous petrological and sedimentary investigations, Withnall (1996) and Withnall et al. (1988a) suggested that the Einasleigh Metamorphics, which are now preserved in the eastern domain (east of the Delaney Fault), are equivalent to rocks of the low Etheridge Formations that are exposed in the central domain (west of the Delaney Fault). Utilizing phase equilibrium and trace-element modelling, Pourteau et al. (2020) suggested that the ca. 1.56 Ga Forest Home TTG in the western domain was produced by fluid-fluxed crustal melting of mafic rocks in the eastern domain under a post-collisional setting. This suggests the eastern domain was connected with the western and central domains of the Georgetown Inlier at the latest from ca. 1.70 Ga. Further petrostructural analysis and thermodynamic modelling suggest that, separating by the Delaney Fault, the eastern domains underwent different crustal evolution (Volante et al., 2020a). At ca. 1.55 Ga, partial melting of paragneiss and amphibolite in the eastern domain occurred at P-T conditions of 730–770°C and 6–8 kbar (Volante et al., 2020a), syn- to post-peak thermal metamorphic stage. In the central domain, synchronous retrograde andalusite replacing staurolite, conversely, documented a decompression event with the pressure dropping from 8–9 kbar to <5 kbar (Volante et al., 2020a). This differential pressure condition and tectonic burial at ca. 1.55 Ga suggests a structural discontinuity between the central and eastern domains, which is also documented by thermochronology record (Chapter 4). Updated $^{40}Ar/^{39}Ar$ thermochronology information shows that the eastern domain did not exhume and cool through the hornblende closure temperature until ca. 80 million years later than the neighbouring central domain. Contrasting cooling across the Delaney Fault suggests it formed at least predate ca. 1.55 Ga as a structural break that separates the central and eastern domains (see detailed discussion in 4.5.2). The surface expression of intermediate to highly magnetic Palaeozoic feldspathic basin and granitoid intrusions along the Delaney Fault indicates a later staged reactivation under Palaeozoic E-W-direct extensional setting (Queensland Geological Survey, 2011; Withnall et al., 2013), correspond to the N-S trending, long wavelength of positive anomalies observed in the filtered magnetic grid. Combining previous metamorphic and petrological studies (Pourteau et al., 2020; Volante et al., 2020a; 2020b) with argon thermochronology analyses (Chapter 4) and sedimentary record (Withnall & Hutton, 2013), we suggest that the Delaney Fault is a major crustal break formed before ca. 1.55 Ga, but reactivated as a normal fault during the Palaeozoic extensional stage.

5.7.6 Allochthonous terrane accretion in NE Australia during the assembly of the supercontinent Nuna

Two crustal amalgamation events in Proterozoic eastern North Australian Craton involved three different crustal domains, from west to east, the western–central belt of the Mount Isa Inlier as part of the proto-North Australia Craton, the eastern Mount Isa-Numil Terrane, and the Georgetown Terrane. The first event occurred at ca. 1.74 Ga, with the N-S and NNE trending Pilgrim activated as a dextral transpressional fault, and amalgamated the eastern Mount Isa-Numil Terrane with the western–central belt of the Mount Isa Inlier (Fig. 5.14 a-b). Contractional basin inversion event at ca. 1.74–1.71 Ga in the Mount Isa Province (Betts, 1999; Blaikie et al., 2017) is a consequence record of this accretionary event.

At ca. 1.67–1.65 Ga, the Georgetown Inlier was rifted from the western margin of the Laurentian continent via a westward juvenile arc retreating (Nordsvan et al., 2018). Detrital zircon analyses on the Etheridge Group of Georgetown Inlier suggests its lower section (ca. 1.71–1.65 Ga; Neumann & Kositcin, 2011) was derived from Laurentian material whereas the upper sedimentary rocks were derived from Australian sources (Nordsvan et al., 2018). Nordsvan et al. (2018) proposed that this sedimentary source transition period represents the rifting stage of the Georgetown Inlier. This scenario is supported by the synchronous mantle-derived tholeiitic basalts intruded in the western domain of the Georgetown Inlier (Baker et al., 2010; Gibson et al., 2018; Withnall et al., 2013), and detrital zircon analyses showing large quantities of juvenile material from proximal sources (Nordsvan et al., 2018).

The second accretionary event occurred at ca. 1.60 Ga, synchronous with the prograde, collision-related Isan Orogeny recorded in both the Mount Isa and Georgetown inliers (Pourteau et al., 2018). This crustal unification occurred along a west dipping subduction zone, which is now preserved as the Empress Suture Zone below the Mesozoic Carpentaria Basin, that joined the Mount Isa Inlier as the upper plate with the Georgetown Inlier as the lower plate, during the final Nuna assembly (Fig. 5.14 d).

Acknowledgments

This study was supported by a China Scholarship Council and a Curtin Research Scholarship to JYL, and an Australian Research Council Laureate Fellow grant (FL150100133) to ZXL. We thank Matthew Greenwood from the Geological Survey of Queensland for guiding us through utilizing the aeromagnetic and gravity data of North Queensland. We thank Schlumberger company for providing student license for Petrel E&P software to imaging seismic profiles, and Seequent company for providing student licence for Geosoft Oasis montaj® software to make aeromagnetic and gravity data filtering possible. We also thank HIVE (Hub for Immersive Visualisation and eResearch) at Curtin University for facilitating imaging high-resolution seismic images utilizing tile display panels.

5.8 References

Abu Sharib, A. S. A. A., & I. V. Sanislav (2013), Polymetamorphism accompanied switching in horizontal shortening during Isan Orogeny: Example from the Eastern Fold Belt, Mount Isa Inlier, Australia, *Tectonophysics*, *587*, 146-167.

Anderson, J. R., Fraser, G. L., McLennan, S. M. and Lewis, C. J. 2017. *A U–Pb geochronology compilation for northern Australia: version 1, November 2017.* Record 2017/22. Geoscience Australia, Canberra.

Bain, JHC, Withnall, IW, Oversby, BS & Mackenzie, DE 1985, Geology of the Georgetown region, Queensland, 1:250 000 map, Bureau of Mineral Resources, Australia, Canberra.

Baker, M. J., A. J. Crawford, and I. W. Withnall (2010), Geochemical, Sm-Nd isotopic characteristics and petrogenesis of Paleoproterozoic mafic rocks from the Georgetown Inlier, north Queensland: Implications for relationship with the Broken Hill and Mount Isa Eastern Succession, *Precambrian Research*, *177*(1-2), 39-54.

Barlow, M.A., 2004. Density and susceptibility characterization of major rock units and rock types of Mount Isa Inlier I1 & I2 Projects PMD*CRC.

Beardsmore, T.J., Newbery, S.P., Laing, W.P., 1988. The Maronan Supergroup: an inferred early volcanosedimentary rift sequence in the Mount Isa Inlier, and its implications for ensialic rifting in the Middle Proterozoic of northwest Queens- land. Precambrian Res. 40–41, 487–507.

Bell, TH 1980, 'The deformation history of northeastern Queensland a new framework', in RA Henderson & PJ Stephenson (eds), The geology and geophysics of northeastern Australia, Geological Society of Australia Queensland Division, Brisbane, pp. 307 13.

Bell, T. H. (1983), Thrusting and duplex formation at Mount Isa, Queensland, Australia, *Nature*, *304*(5926), 493-497.

Bell, T. H. (1991), The role of thrusting in the structural development of the Mount Isa Mine and its relevance to exploration in the surrounding region, *Economic Geology*, *86*(8), 1602-1625.

Bell, T., J. Reinhardt, & R. Hammond (1992), Multiple foliation development during thrusting and synchronous formation of vertical shear zones, *Journal of Structural Geology*, *14*(7), 791-805.

Betts, P. G., G. S. Lister, & M. G. O'Dea (1998), Asymmetric extension of the Middle Proterozoic lithosphere, Mount Isa terrane, Queensland, Australia, *Tectonophysics*, *296*(3-4), 293-316.

Betts, P. G. (1999), Palaeoproterozoic mid-basin inversion in the northern Mt Isa terrane, Queensland, *Australian Journal of Earth Sciences*, *46*(5), 735-748.

Betts, P. G., L. Ailleres, D. Giles, & M. Hough (2000), Deformation history of the Hampden Synform in the Eastern fold Belt of the Mt Isa terrane, *Australian Journal of Earth Sciences*, *47*(6), 1113-1125.

Betts, P. G., and G. S. Lister (2001), Comparison of the 'strike-slipe' versus 'episodic rift-sag' models for the origin of the Isa superbasin, Australian Journal of Earth Sciences, 48(2), 265-280.

Betts, PG, Giles, D & Lister, GS 2004, 'Aeromagnetic patterns of half-graben and basin inversion: implications for sediment-hosted massive sulfide Pb–Zn–Ag exploration', Journal of Structural Geology, vol. 26, pp. 1137–56.

Betts, P. G., D. Giles, G. Mark, G. S. Lister, B. R. Goleby, & L. Ailleres (2006), Synthesis of the proterozoic evolution of the Mt Isa Inlier, *Australian Journal of Earth Sciences*, *53*(1), 187-211.

Betts, P. G., D. Giles, & B. F. Schaefer (2008), Comparing 1800-1600 Ma accretionary and basin processes in Australia and Laurentia: Possible geographic connections in Columbia, *Precambrian Research*, *166*(1-4), 81-92.

Betts, P. G., D. Giles, and A. Aitken (2011), Palaeoproterozoic accretion processes of Australia and comparisons with Laurentia, International Geology Review, 53(11-12), 1357-1376.

Betts, P. G., R. J. Armit, J. Stewart, A. R. A. Aitken, L. Ailleres, P. Donchak, L. Hutton, I. Withnall, & D. Giles (2016), Australia and Nuna, *Geological Society, London, Special Publications*, *424*(1), 47-81.

Bierlein, FP & Betts, PG 2004, 'The Proterozoic Mount Isa Fault Zone, northeastern Australia: is it really a ca 1.9 Ga terrane-bounding suture?', Earth and Planetary Science Letters, vol. 225, pp. 279–94.

Bierlein, F. P., R. Maas, and J. Woodhead (2011), Pre-1.8 Ga tectono-magmatic evolution of the Kalkadoon–Leichhardt Belt: implications for the crustal architecture and metallogeny of the Mount Isa Inlier, northwest Queensland, Australia, *Australian Journal of Earth Sciences*, *58*(8), 887-915.

Blake, D. H. (1987), Geology of the Mount Isa inlier and environs, Queensland and Northern Territory, Australian Govt. Pub. Service.

Black, LP & McCulloch, MT 1984, 'Sm Nd ages of the Arunta, Tennant Creek and Georgetown inliers of northern Australia', Australian Journal of Earth Sciences, vol. 31, pp. 49–60.

Black, LP & McCulloch, MT 1990, 'Isotopic evidence for the dependence of recurrent felsic magmatism on new crust formation: an example from the Georgetown region of northeastern Australia', Geochimica et Cosmochimica Acta, vol. 54, pp. 183–96.

Black, LP, Withnall, IW, Gregory, P, Oversby, BS & Bain, JHC 2005, 'U–Pb zircon ages from leucogneiss in the Etheridge Group and their role in the early history of the Georgetown region', *Australian Journal of Earth Sciences*, vol. 52, pp. 385–401.

Blaikie, T. N., P. G. Betts, R. J. Armit, and L. Ailleres (2017), The ca. 1740–1710 Ma Leichhardt Event: Inversion of a continental rift and revision of the tectonic evolution of the North Australian Craton, Precambrian Research, 292, 75-92.

Blenkinsop, T. G., C. R. Huddlestone-Holmes, D. R. W. Foster, M. A. Edmiston, P. Lepong, G. Mark, J. R. Austin, F. C. Murphy, A. Ford, & M. J. Rubenach (2008), The crustal scale architecture of the Eastern Succession, Mount Isa: The influence of inversion, *Precambrian Research*, *163*(1-2), 31-49.

Blakely, R.J., 1995. Potential Theory in Gravity and Magnetic Applications. Cambridge University Press, New York.

Blewett, RS & Black, LP 1998, 'Structural and temporal framework of the Coen region North Queensland; implications for major tectonothermal events in east and north Australia', *Australian Journal of Earth Sciences*, vol. 45, pp. 597–609.

Boger, S. D., & D. Hansen (2004), Metamorphic evolution of the Georgetown Inlier, northeast Queensland, Australia; evidence for an accreted Palaeoproterozoic terrane?, *Journal of Metamorphic Geology*, *22*(6), 511-527.

Boger, S.D. and Miller, J.M., 2004. Terminal suturing of Gondwana and the onset of the Ross–Delamerian Orogeny: the cause and effect of an Early Cambrian reconfiguration of plate motions. Earth and Planetary Science Letters, 219(1-2), pp.35-48.

Bouvier, A., Vervoort, J.D., Patchett, P.J., 2008. The Lu–Hf and Sm–Nd isotopic composition of CHUR: Constraints from unequilibrated chondrites and implications for the bulk composition of terrestrial planets. Earth and Planetary Science Letters 273, 48-57.

Carson, CJ, Hutton, LJ, Withnall, IW, Perkins, WG, Donchak, PJT, Parsons, A, Blake, PR, Sweet, IP, Neumann, NL & Lambeck, A 2011, Joint GSQ–GA NGA geochronology project—Mount Isa region, 2009–2010, record, no. 2011/3, Geological Survey of Queensland, Brisbane

Champion, DC 1991, ‘Petrogenesis of the felsic granitoids of far north Queensland’, PhD thesis, Australian National University, Canberra.

Champion DC & Heinemann, MA 1994, *Igneous rocks of northern Queensland: 1:500 000 map and explanatory notes,* record no. 1994/11, Australian Geological Survey Organisation, Canberra.

Champion, D.C. 2013. Neodymium depleted mantle model age map of Australia: explanatory notes and user guide. Record 2013/44. Geoscience Australia: Canberra.

Cihan, M., and A. Parsons (2005), The use of porphyroblasts to resolve the history of macro-scale structures: an example from the Robertson River Metamorphics, North-Eastern Australia, Journal of Structural Geology, 27(6), 1027-1045.

Cihan, M., P. Evins, N. Lisowiec, and K. Blake (2006), Time constraints on deformation and metamorphism from EPMA dating of monazite in the Proterozoic Robertson River Metamorphics, NE Australia, Precambrian Research, 145(1-2), 1-23.

Connors, K. A., & G. S. Lister (1995), Polyphase deformation in the western Mount Isa Inlier, Australia: episodic or continuous deformation?, *Journal of structural geology*, *17*(3), 305-328.

Day, RW, Whitaker, WG, Murray, CG, Wilson, IH & Grimes, KG 1983, *Queensland Geology. A companion volume to the 1:2 500 000 scale geological map (1975)*, publication no. 383, Geological Survey of Queensland, Brisbane.

DePaolo, D. J. (1981), Nd Isotopic Studies: Some New Perspectives on Earth Structure and Evolution

Derrick, GM, Wilson, IH, Hill, RM, Glikson, AY & Mitchell, JE 1977, ‘Geology of the Mary Kathleen 1:100 000 sheet area, north-west Queensland’, Bulletin of the Bureau of Mineral Resources, vol. 193, pp. 1–113.

Derrick, G. M., I. H. Wilson, and I. P. Sweet (1980), The Quilalar and Surprise Creek Formations - new Proterozoic units from the Mount Isa Inlier (Australia): their regional sedimentology and application to regional correlation, BMR Journal of Australian Geology & Geophysics, 5(3), 215-223

Derrick, GM 1982, 'A Proterozoic rift zone at Mount Isa, Queensland, and implications for mineralisation', BMR Journal of Australian Geology & Geophysics, vol. 7, pp. 81–92.

Eriksson, K., E. Simpson, & M. Jackson (1994), Stratigraphical Evolution of a Proterozoic Syn-Rift to Post-Rift Basin: Constraints on the Nature of Lithospheric Extension in the Mount Isa Inlier, Australia, *Tectonic controls and signatures in sedimentary successions*, 203-221.

Eriksson, KA, Simpson, EL & Jackson, MJ 1993, 'Stratigraphical evolution of a Proterozoic syn-rift to post-rift basin: constraints on the nature of lithospheric extension in the Mount Isa Inlier, Australia', Special Publications of the International Association of Sedimentologists, vol. 20, pp. 203–21.

Etheridge, M. A., R. W. R. Rutland, & L. A. I. Wyborn (1987), Orogenesis and tectonic process in the early to middle Proterozoic of northern Australia, *Precambrian Lithospheric Evolution*, *17*, 131-147.

Evans, D. A. D., & R. N. Mitchell (2011), Assembly and breakup of the core of Paleoproterozoic-Mesoproterozoic supercontinent Nuna, *Geology*, *39*(5), 443-446.

Evans, D. A. D., R. V. Veselovsky, P. Y. Petrov, A. V. Shatsillo, & V. E. Pavlov (2016), Paleomagnetism of Mesoproterozoic margins of the Anabar Shield: A hypothesized billion-year partnership of Siberia and northern Laurentia, *Precambrian Research*, *281*, 639-655.

Foster, D. R. W., & M. J. Rubenach (2006), Isograd pattern and regional low-pressure, high-temperature metamorphism of pelitic, mafic and calc-silicate rocks along an east – west section through the Mt Isa Inlier, *Australian Journal of Earth Sciences*, *53*(1), 167-186.

Foster, D., & J. Austin (2008), The 1800–1610Ma stratigraphic and magmatic history of the Eastern Succession, Mount Isa Inlier, and correlations with adjacent Paleoproterozoic terranes, *Precambrian Research*, *163*(1-2), 7-30.

Furlanetto, F., D. J. Thorkelson, H. Daniel Gibson, D. D. Marshall, R. H. Rainbird, W. J. Davis, J. L. Crowley, & J. D. Vervoort (2013), Late Paleoproterozoic terrane accretion in northwestern Canada and the case for circum-Columbian orogenesis, *Precambrian Research*, *224*, 512-528. http://doi.org/10.1016/j.precamres.2012.10.010.

Geological Survey of Queensland, 2011: North-West Queensland Mineral and Energy Province Report. Queensland Department of Employment, Economic Development and Innovation, Brisbane.

Geoscience Australia, 2009. Geophysical Archive Data Delivery System (GADDS). http://www.geoscience.gov.au/gadds/.

Gibson, GM, Debenham, S, Henson, PA, Hutton, LJ, Lambeck, A, Neumann, NL & Southgate, PN 2005, 'Geodynamic setting and structural evolution of the Western Succession', in GM Gibson & AP Hitchman (eds), *Final report Project I1 – 3D basin architecture and mineral systems in the Mt Isa Western Succession*, Predictive Mineral Discovery, Cooperative Research Centre, Melbourne, pp. 61–82.

Gibson, G. M., A. J. Meixner, I. W. Withnall, R. J. Korsch, L. J. Hutton, L. E. A. Jones, J. Holzschuh, R. D. Costelloe, P. A. Henson, and E. Saygin (2016), Basin architecture and evolution in the Mount Isa mineral province, northern Australia: Constraints from deep seismic reflection profiling and implications for ore genesis, *Ore Geology Reviews*, *76*, 414-441.

Gibson, G. M., L. J. Hutton, and J. Holzschuh (2017), Basin inversion and supercontinent assembly as drivers of sediment-hosted Pb–Zn mineralization in the Mount Isa region, northern Australia, *Journal of the Geological Society*, *174*(4), 773-786.

Gibson, G. M., D. C. Champion, I. W. Withnall, N. L. Neumann, & L. J. Hutton (2018), Assembly and breakup of the Nuna supercontinent: Geodynamic constraints from 1800 to 1600 Ma sedimentary basins and basaltic magmatism in northern Australia, *Precambrian Research*, *313*, 148-169.

Gibson, G. M., and D. C. Champion (2019), Antipodean fugitive terranes in southern Laurentia: How Proterozoic Australia built the American West, *Lithosphere*, *11*(4), 551-559.

Giles, D., & A. P. Nutman (2002), SHRIMP U-Pb monazite dating of 1600-1580 Ma amphibolite facies metamorphism in the southeastern Mt Isa Block, Australia, *Australian Journal of Earth Sciences*, *49*(3), 455-465.

Giles, D., L. Ailléres, D. Jeffries, P. Betts, & G. Lister (2006a), Crustal architecture of basin inversion during the Proterozoic Isan Orogeny, Eastern Mount Isa Inlier, Australia, *Precambrian Research*, *148*(1-2), 67-84.

Giles, D., P. G. Betts, L. Aillères, B. Hulscher, M. Hough, and G. S. Lister (2006b), Evolution of the Isan Orogeny at the southeastern margin of the Mt Isa Inlier, Australian Journal of Earth Sciences, 53(1), 91-108.http://doi.org/10.1080/08120090500432470

Goldstein, S.L., O'Nions, R.K., Hamilton, P.J., 1984. A Sm-ND isotopic study of atmospheric dusts and particulates from major river systems. Earth and Planetary Science Letters 70, 221-236.

Goleby, B., Drummond, B., MacCready, T., 1996, The deep Seismic relfection profile south of Mount Isa and Cloncurry, AGSO Research Newsletter, 24, p6-7

De Graciansky, P.C., Roberts, D.G. and Tricart, P., 2010. The Western Alps, from rift to passive margin to orogenic belt: an integrated geoscience overview. Elsevier.

Greenwood, M., 2018. Queensland Digital Exploration Reports System (QDEX). https://qdexdata.dnrme.qld.gov.au or https://geoscience.data.qld.gov.au

Holcombe, RJ, Pearson, PJ & Oliver, NHS 1991, 'Geometry of a Middle Proterozoic extensional décollement in northeastern Australia', Tectonophysics, vol. 191, pp. 255–74.

Hutton, LJ, Cavaney, RJ & Sweet, IP 1981, 'New and revised stratigraphic units, Lawn Hill Platform, northwest Queensland', *Queensland Government Mining Journal*, vol. 82, pp. 423–34.

Jackson, M. J., P. N. Southgate, L. P. Black, P. R. Blake, and J. Domagala (2005), Overcoming Proterozoic quartzite sand-body miscorrelations: integrated sequence stratigraphy and SHRIMP U–Pb dating of the Surprise Creek Formation, Torpedo Creek and Warrina Park Quartzites, Mt Isa Inlier, Australian Journal of Earth Sciences, 52(1), 1-25.

Jackson, M. J., D. L. Scott, & D. J. Rawlings (2000), Stratigraphic framework for the Leichhardt and Calvert Superbasins: review and correlations of the pre-1700 Ma successions between Mt Isa and McArthur River, *Australian Journal of Earth Sciences*, *47*(3), 381-403.

Jiang, W., R. J. Korsch, M. P. Doublier, J. Duan, and R. Costelloe (2019), Mapping Deep Electrical Conductivity Structure in the Mount Isa region, Northern Australia: Implications for Mineral Prospectivity, Journal of Geophysical Research: Solid Earth, 124(11), 10655-10671.

Johnson, M. R., Harley, S. L., & Harley, S. (2012). *Orogenesis: the making of mountains*. Cambridge University Press.

Jones, L., Goleby, B., Barton, T., Owen, A. 2008. L138 Mt Isa Basin seismic survey, QLD, 1994 Stacked and migrated seismic data and images for lines 94MTI-01, 94MTI-02, 94ISA-01, 94ISA-02, 94ISA-03, and 94ISA-04. Geoscience Australia, Canberra.

Kearey, P., K. A. Klepeis, & F. J. Vine (2009), *Global tectonics*, John Wiley & Sons.

Korsch, R., Henson, P., Gibson, G., Withnall, I., Hutton, L., Saygin, E., Jones, L., Stewart, L., Huston, D., Maidment, D., 2008. Results from the central and southern Mt Isa Inlier (Lines 06GA-MI6 and 94AGS-MTI1). Mt Isa Seismic Workshop, 24 June 2008.

Korsch, R.J., Struckmeyer, H.I.M., Kirkby, A., Hutton, L.J., Carr, L.K., Hoffmann, K.L., Chopping, R., Roy, I.G., Fitzell, M., Totterdell, J.M., Nicoll, M.G., Talebi, B., 2011. Energy potential of the Millungera Basin; a newly discovered basin in north Queensland. APPEA J. 51, 295–332.

Korsch, R. J., D. L. Huston, R. A. Henderson, R. S. Blewett, I. W. Withnall, C. L. Fergusson, W. J. Collins, E. Saygin, N. Kositcin, A. J. Meixner, R. Chopping, P. A. Henson, D. C. Champion, L. J. Hutton, R. Wormald, J. Holzschuh, and R. D. Costelloe (2012), Crustal architecture and geodynamics of North Queensland, Australia: Insights from deep seismic reflection profiling, Tectonophysics, 572-573, 76-99.

Lambeck, L 2011, 'Basin analysis and the geochemical and isotopic signature of Paleoproterozoic sedimentary successions in northern Australia', PhD thesis, University of Adelaide.

Lambeck, A., Barovich, K., Gibson, G., Huston, D., and Pisarevsky, S., 2012, An abrupt change in Nd isotopic composition in Australian basins at 1655 Ma: Implications for the tectonic evolution of Australia and its place in NUNA: Precambrian Research, v. 208, p. 213–221,

Li, J., Pourteau, A., Li, Z.X., Jourdan, F., Nordsvan, A.R., Collins, W.J. and Volante, S., 2020. Heterogeneous Exhumation of the Mount Isa Orogen in NE Australia After 1.6 Ga Nuna Assembly: New High-Precision $^{40}Ar/^{39}Ar$ Thermochronological Constraints. *Tectonics*, *39*(12), p.e2020TC006129.

Li, J. Y., Li, Z.-X., Pourteau, A., Jourdan, F., Volante, S., Olierook, H. K. H., Nordsvan, A. R., & Collins, W. J. Crustal extrusion and orogenic collapse in the Georgetown Inlier of NE Australia after 1.6 Ga Nuna assembly: new insights from Ar thermochronology *Tectonics*, In review

Lister, G. S., M. G. O'Dea, & I. Somaia (1999), A tale of two synclines: Rifting, inversion and transpressional popouts at Lake Julius, northwestern Mt Isa terrane, Queensland, *Australian Journal of Earth Sciences*, *46*(2), 233-250.

MacCready, T. (2006), Structural cross-section based on the Mt Isa deep seismic transect, *Australian Journal of Earth Sciences*, *53*(1), 5-26.

MacCready, T., B. R. Goleby, A. Goncharov, B. J. Drummond, & G. S. Lister (1998), A framework of overprinting orogens based on interpretation of the Mount Isa deep seismic transect, *Economic Geology*, *93*(8), 1422-1434.

Magee, C.W., Withnall, I.W., Hutton, L.J., Perkins, W.G., Donchak, P.J.T., Parsons, A., Blake, P.R., Sweet, I.P., Carson, C.J., 2012, Joint GSQ-GA geochronology project, Mount Isa Region, 2008-2009, Queensland Geological Record, 2012/07, 134p

Maher, J.L. 2009. L184 Isa-Georgetown Deep Crustal Seismic Survey, QLD, 2007. Stacked and migrated data and images for lines 07GA-IG1 and 07GA-IG2. Geoscience Australia, Canberra.

Mark, G. (2001), Nd isotope and petrogenetic constraints for the origin of the Mount Angelay igneous complex: implications for the origin of intrusions in the Cloncurry district, NE Australia, *Precambrian Research*, *105*(1), 17-35.

Mark, G., A. Wilde, N. H. S. Oliver, P. J. Williams, and C. G. Ryan (2005), Modeling outflow from the Ernest Henry Fe oxide Cu–Au deposit: implications for ore genesis and exploration, *Journal of Geochemical Exploration*, *85*(1), 31-46.

McDonald, GD, Collerson, KD & Kinny, PD 1997, 'Late Archean and early Proterozoic crustal evolution of the Mount Isa Block, Northwest Queensland, Australia', Geology, vol. 25, pp. 1095–8.

Meixner, A.J., 2009. Rock property data (densities and magnetic suceptibilities) of the Mount Isa region. Geoscience Australia/OEMD.

Murphy, F.C., 1987. Evidence for late Ordovician amalgamation of volcanogenic terranes in the Iapetus suture zone, eastern Ireland. Earth and Environmental Science Transactions of the Royal Society of Edinburgh, 78(3), pp.153-167.

Neumann, N. L., P. N. Southgate, G. M. Gibson, & A. McIntyre (2006), New SHRIMP geochronology for the Western Fold Belt of the Mt Isa Inlier: Developing a 1800 - 1650 Ma event framework, *Australian Journal of Earth Sciences*, *53*(6), 1023-1039.

Neumann, N.L. & Fraser, G.L. (Eds.), 2007. Geochronological synthesis and Time-Space plots for Proterozoic Australia. Geoscience Australia Record 2007/06.

Neumann, N. L., G. M. Gibson, & P. N. Southgate (2009), New SHRIMP age constraints on the timing and duration of magmatism and sedimentation in the Mary Kathleen Fold Belt, Mt Isa Inlier, Australia, *Australian Journal of Earth Sciences*, *56*(7), 965-983.

Neumann, N.L. and Kositcin, N., 2011. New SHRIMP U-Pb zircon ages from north Queensland, 2007–2010. Geoscience Australia, Record, 2011/38, 82 p.

Nordsvan, A. R., W. J. Collins, Z.-X. Li, C. J. Spencer, A. Pourteau, I. W. Withnall, P. G. Betts, & S. Volante (2018), Laurentian crust in northeast Australia: Implications for the assembly of the supercontinent Nuna, *Geology*, *46*(3), 251-254.

O'Dea, M. G., & G. S. Lister (1995), The role of ductility contrast and basement architecture in the structural evolution of the Crystal Creek block, Mount Isa Inlier, NW Queensland, Australia, Journal of Structural Geology, 17(7), 949-960.

O'Dea, M. G., G. S. Lister, P. G. Betts, & K. S. Pound (1997a), A shortened intraplate rift system in the Proterozoic Mount Isa terrane, NW Queensland, Australia, *Tectonics*, *16*(3), 425-441.

O'Dea, M. G., G. S. Lister, T. Maccready, P. G. Betts, N. H. S. Oliver, K. S. Pound, W. Huang, R. K. Valenta, N. H. S. Oliver, & R. K. Valenta (1997b), Geodynamic evolution of the Proterozoic Mount Isa terrain, *Geological Society, London, Special Publications*, *121*(1), 99-122.

O'Dea, M. G., P. G. Betts, T. MacCready, & L. Aillères (2006), Sequential development of a mid-crustal fold-thrust complex: evidence from the Mitakoodi Culmination in the eastern Mt Isa Inlier, Australia, *Australian Journal of Earth Sciences*, *53*(1), 69-90.

Olierook, H. K. H., R. G. Affleck, N. J. Evans, F. Jourdan, C. L. Kirkland, S. Volante, A. R. Nordsvan, B. I. A. McInnes, B. McDonald, C. Mayers, R. A. Frew, K. Rankenburg, N. d'Offay, M. Nind, and A. Larking (2021), Mineralization proximal to the final Nuna suture in northeastern Australia, *Gondwana Research*, *92*, 54-71.

Page, R. W., & S. S. Sun (1998), Aspects of geochronology and crustal evolution in the Eastern Fold Belt, Mt Isa Inlier, *Australian Journal of Earth Sciences*, *45*(3), 343-361.

Page, RW 1988, 'Geochronology of Early to Middle Proterozoic fold belts in northern Australia: a review', Precambrian Research, vol. 40–41, pp. 1–19.

Pearson, P. J. (1992), Synkinematic emplacement of the Middle Proterozoic Wonga batholith into a midcrustal extensional shear zone, Mount Isa Inlier, Queensland, Australia, Detailed studies of the Mount Isa Inlier, 289-328

Pearson P.J. 1989.Structural andtectonic evolution ofthe Wonga Belt, northwest Queensland: A Proterozoic extensional detachment zone . PhD thesis , University of Queensland, Brisbane (unpubl.).

Pears, G., Fullagar, P., Andrews, P., 2001. 3D gravity modelling and interpretation for the 1:250,000 Boulia map sheet, Queensland. Preview 93, 90.

Pehrsson, S. J., B. M. Eglington, D. A. D. Evans, D. Huston, & S. M. Reddy (2016), Metallogeny and its link to orogenic style during the Nuna supercontinent cycle, *Geological Society, London, Special Publications*, *424*(1), 83-94.

Pfiffner, O.A., 2017. Thick-skinned and thin-skinned tectonics: a global perspective. Geosciences, 7(3), p.71.

Pisarevsky, S. A., S.-A. Elming, L. J. Pesonen, & Z.-X. Li (2014), Mesoproterozoic paleogeography: Supercontinent and beyond, *Precambrian Research*, *244*, 207-225.

Pollard, P. J., G. Mark, & L. C. Mitchell (1998), Geochemistry of post-1540 Ma granites in the Cloncurry district, northwest Queensland, *Economic Geology and the Bulletin of the Society of Economic Geologists*, *93*(8), 1330-1344.

Potma, WA & Betts, PG 2006, 'Extension-related structures in the Mitakoodi Culmination: implications for the nature and timing of extension, and effect on later shortening in the eastern Mt Isa Inlier', Australian Journal of Earth Sciences, vol. 53, pp. 55–67.

Pourteau, A., M. A. Smit, Z.-X. Li, W. J. Collins, A. R. Nordsvan, S. Volante, & J. Li (2018), 1.6 Ga crustal thickening along the final Nuna suture, *Geology*, *46*(11), 959-962.

Roger, C., 2014. Queensland Digital Exploration Reports System (QDEX). https://qdexdata.dnrme.qld.gov.au

Rogers, J. J. W., & M. Santosh (2002), Configuration of Columbia, a mesoproterozoic supercontinent, *Gondwana Research*, *5*(1), 5-22.

Rubenach, M. J. (1992), Proterozoic low-pressure/high-temperature metamorphism and an anticlockwise P–T–t path for the Hazeldene area, Mount Isa Inlier, Queensland, Australia, *Journal of Metamorphic Geology*, *10*(3), 333-346.

Rubenach, M. J., D. R. W. Foster, P. M. Evins, K. L. Blake, & C. M. Fanning (2008), Age constraints on the tectonothermal evolution of the Selwyn Zone, Eastern Fold Belt, Mount Isa Inlier, *Precambrian Research*, *163*(1-2), 81-107.

Sayab, M. (2006), Decompression through clockwise P–T path: implications for early N–S shortening orogenesis in the Mesoproterozoic Mt Isa Inlier (NE Australia).

Scott, DL, Rawlings, DJ, Page, RS, Tarlowski, CZ, Idnurm, M, Jackson, MJ & Southgate, PN 2000, 'Basement framework and geodynamic evolution of the Palaeoproterozoic superbasins of north-central Australia: an integrated review of geochemical, geochronological and geophysical data', Australian Journal of Earth Sciences, vol. 47, pp. 341–480.

Southgate, P. N., D. L. Scott, T. T. Sami, J. Domagala, M. J. Jackson, N. P. James, & T. K. Kyser (2000), Basin shape and sediment architecture in the Gun Supersequence: A strike-slip model for Pb–Zn–Ag ore genesis at Mt Isa, *Australian Journal of Earth Sciences*, *47*(3), 509-531.

Spampinato, G. P. T., P. G. Betts, L. Ailleres, and R. J. Armit (2015), Structural architecture of the southern Mount Isa terrane in Queensland inferred from magnetic and gravity data, Precambrian Research, 269, 261-280.

Thorkelson, D. J., J. K. Mortensen, R. A. Creaser, G. J. Davidson, and J. G. Abbott (2001), Early Proterozoic magmatism in Yukon, Canada: Constraints on the evolution of northwestern Laurentia, *Canadian Journal of Earth Sciences*, *38*(10), 1479-1494.http://doi.org/10.1139/e01-032

Verbaas, J. (2018), A sedimentary overlap assemblage links Australia to northwestern Laurentia at 1.6 Ga, *Precambrian Research*.

Volante, S., A. Pourteau, W. J. Collins, E. Blereau, Z. X. Li, M. Smit, N. J. Evans, A. R. Nordsvan, C. J. Spencer, B. J. McDonald, J. Li, and C. Günter (2020a), Multiple P-T–d–t paths reveal the evolution of the final Nuna assembly in northeast Australia, Journal of Metamorphic Geology, 38(6), 593-627.10.1111/jmg.12532

Volante, S., W. J. Collins, A. Pourteau, Z. X. Li, J. Li, and A. R. Nordsvan (2020b), Structural Evolution of a 1.6 Ga Orogeny Related to the Final Assembly of the Supercontinent Nuna: Coupling of Episodic and Progressive Deformation, Tectonics, 39(10).10.1029/2020tc006162

Volante, S., Collins, W., Spencer, C., Blereau, E., Pourteau, A., Barrote, V., Nordsvan, A., Li, Z.X., Evans, N. and Li, J., (2020c), May. Reconciling zircon and monazite thermometry constrains H2O content in granitic melts. Contributions to Mineralogy and Petrology

de Vries, ST, Fry, N & Pryer, L 2006, 'OZ SEEBASE Proterozoic Basins Study', report to Geoscience Australia and consortium partners by FrOG Tech Pty Ltd, public domain GIS and report available from www.frogtech.com.au

Williams, P. J., & G. N. Phillips (1992), Cloncurry mapping project 1990: geology of the Selwyn Range (McKinlay River and Maramungee Creek areas), *Contributions - James Cook University, Economic Geology Research Unit*, *40*.

Withnall, I. W. (1996), Stratigraphy, structure and metamorphism of the Proterozoic Etheridge and Langlovale Groups, Georgetown region, north Queensland, Australian Geological Survey Organisation Record (15)

Withnall, I. W., & Henderson, R. A. (2012). Accretion on the Long-Lived Continental Margin of Northeastern Australia. Episodes, 35, 166–176.

Withnall, I. W., & Hutton, L. J. (2013). Chapter 2 Proterozoic - North Australian Craton. In P. A. Jell (Ed.), Geology of Queensland (pp. 23–112): Department of Natural Resources and Mines, Queensland.

Withnall, IW & Mackenzie, DE 1983, 'Definition of the Proterozoic Langlovale Group, Georgetown Inlier, north Queensland', *Queensland Government Mining Journal*, vol. 84, pp. 193–4.

Withnall, IW & Mackenzie, DE 1980, 'New and revised stratigraphic units in the Proterozoic Georgetown Inlier, north Queensland', Queensland Government Mining Journal, vol. 81, pp. 28–43.

Withnall, I. W., Bain, J. H. C., Draper, J. J., MacKenzie, D. E., & Oversby, B. S. (1988). Proterozoic stratigraphy and tectonic history of the Georgetown Inlier, northeastern Queensland. Precambrian Research, 40/41, 429–446.

Withnall, I. W., MacKenzie, D. E., Denaro, T. J., Bain, J. H. C., Oversby, B. S., Knutson, J., . . . Pain, C. F. (1997) Georgetown Region. North Queensland Geology (pp. 19–116): Australian Geological Survey Organisation Bulletin 240/Queensland Geology 9.

Withnall, IW., Hutton, LJ., Armit, RJ., Betts, PG., Blewett, RS., Champion, DC. & Jell, PA., 2013, Geology of Queensland. Jell, P. A. (ed.). Brisbane Qld Australia: Geological Survey of Queensland, p. 23-112 90 p.

Wyborn, L. (1998), Younger ca 1500 Ma granites of the Williams and Naraku Batholiths, Cloncurry district, eastern Mt Isa Inlier: Geochemistry, origin, metallogenic significance and exploration indicators, *Australian Journal of Earth Sciences*, *45*(3), 397-411.

Wyborn, L. A. I., and R. W. Page (1983), The Proterozoic Kalkadoon and Ewen Batholiths, Mount Isa Inlier, Queensland - Source, Chemistry, Age, and Metamorphism, *Bmr Journal of Australian Geology & Geophysics*, *8*(1), 53-69

Wyborn, L., R. Page, & M. McCulloch (1988), Petrology, geochronology and isotope geochemistry of the post-1820 Ma granites of the Mount Isa Inlier: mechanisms for the generation of Proterozoic anorogenic granites, *Precambrian Research*, *40-41*(C), 509-541.

Zhang, S., Z.-X. Li, D. A. D. Evans, H. Wu, H. Li, & J. Dong (2012), Pre-Rodinia supercontinent Nuna shaping up: A global synthesis with new paleomagnetic results from North China, *Earth and Planetary Science Letters*, *353-354*, 145-155. http://doi.org/10.1016/j.epsl.2012.07.034.

Zhao, G., P. A. Cawood, S. A. Wilde, & M. Sun (2002), Review of global 2.1–1.8 Ga orogens: implications for a pre-Rodinia supercontinent, *Earth-Science Reviews*, *59*(1-4), 125-162.

Appendix E:
Supplementary materials to Chapter 5

Attached at the end of the thesis.

Chapter 6

Conclusions

This thesis primary focus on the NE Australian Craton, with particular interests in the Protozoic rocks of the Mount Isa and Georgetown inliers, to resolve the crustal evolution record across this region that reflect on tectonic processes and crustal history related to the assembly of the supercontinent Nuna.

New high-precision $^{40}Ar/^{39}Ar$ thermochronological data acquired along an E-W transect across the Proterozoic Mount Isa and Georgetown inliers in NE Australia provided new constraints on the timing and magnitude of vertical crustal motions syn- to post-orogenic events. The thermochronological results are combined with published geochronological and petrological constraints to reconstruct retrograde P–T paths, and decipher the crustal evolution from individual domain. In addition, aeromagnetic and gravity analyses, along with a reinterpretation of seismic profiles, were also utilized to reveal the crustal architecture and understand syn- to post-crustal accretionary processes through integration with surface geology, published isotopic data, and the new thermo-geochronological results. Major scientific findings of this thesis regarding the Proterozoic tectonic evolution of NE Australia include:

1) A N-S trending, sharp magnetic gradient was resolved on the eastern margin of the Mount Isa Inlier, coinciding with the lithosphere scale Gidyea Fault imaged from the seismic reflection profile.

2) The eastern Mount Isa-Numil Terrane connected with the western and central Mount Isa Inlier at ca. 1.74 Ga along the N-S and NNE-trending Pilgrim and Fountain Range faults via a dextral transpressional faulting. A contractional basin inversion event at ca. 1.74–1.71 Ga recorded in the western Mount Isa Inlier (Betts, 1999; Blaikie et al., 2017) is a consequence of this accretion, and provide partial support for this interpretation.

3) The Rowe Fault (previously named as the Rowe Fossil Subduction Zone), which offsets the Moho within the Georgetown Inlier, is joined with the detachment fault and defines the boundary between the western and central domains.

4) Between the Mount Isa and Georgetown inliers, a seismically identified west-dipping, crustal dissecting Empress Suture Zone is interpreted to be a Nuna suture zone with additional smaller-scale thrusts antithetic to the main suture.

5) A duplexed crustal architecture identified between the Mount Isa and Georgetown inliers is interpreted to reflect a crustal thickening event associated with the docking of the Georgetown Inlier along the west-dipping Empress Suture subduction zone.

6) The presence of a major structural break between the central and eastern domains of the Georgetown Inlier is demanded by both the thermochronological data and geophysical images.

7) Regional exhumation, initiated at ca. 1.55 Ga and accompanied by high-temperature lower crustal melting and occurred in both the Mount Isa and Georgetown inliers, is interpreted to reflect orogenic collapse due to the delamination of a thickened mafic lower crust. This event led to diachronous extensional faulting and heterogeneous exhumation between crustal domains of both inliers during 1.55–1.40 Ga.

8) Heterogeneous exhumation within the central domain of the Mount Isa Inlier is interpreted to represent westward crustal tilting during the orogenic collapse.

Appendix A

Supplementary materials to Chapter 1

FIRST AUTHOR JOURNAL PUBLICATIONS

Paper title: Heterogeneous exhumation of the Mount Isa orogen in NE Australia after 1.6 Ga Nuna assembly: new high-precision $^{40}Ar/^{39}Ar$ thermochronological constraints

Tectonics (2020), Volume 39, Issue 12

Jiangyu Li, Amaury Pourteau, Zheng-Xiang Li, Fred Jourdan, Adam R. Nordsvan, William J. Collins, Silvia Volante

JOHN WILEY AND SONS LICENSE
TERMS AND CONDITIONS

May 01, 2021

This Agreement between Mr. Jiangyu Li ("You") and John Wiley and Sons ("John Wiley and Sons") consists of your license details and the terms and conditions provided by John Wiley and Sons and Copyright Clearance Center.

License Number	5060090308473
License date	May 01, 2021
Licensed Content Publisher	John Wiley and Sons
Licensed Content Publication	Tectonics
Licensed Content Title	Heterogeneous Exhumation of the Mount Isa Orogen in NE Australia After 1.6 Ga Nuna Assembly: New High-Precision 40Ar/39Ar Thermochronological Constraints
Licensed Content Author	Silvia Volante, William J. Collins, Adam R. Nordsvan, et al
Licensed Content Date	Dec 4, 2020
Licensed Content Volume	39

Licensed Content Issue	12
Licensed Content Pages	27
Type of use	Dissertation/Thesis
Requestor type	Author of this Wiley article
Format	Electronic
Portion	Full article
Will you be translating?	No
Title	Proterozoic crustal evolution history of NE Australia during the supercontinent Nuna assembly: new insights from coupled geophysical, isotopic and thermochronological data
Institution name	Curtin University
Expected presentation date	Oct 2021
Requestor Location	Mr. Jiangyu Li 2 Rangeview Place, Canning Vale Perth, 6155 Australia Attn: Mr. Jiangyu Li

Publisher Tax ID	EU826007151
Total	0.00 AUD

Terms and Conditions

TERMS AND CONDITIONS

This copyrighted material is owned by or exclusively licensed to John Wiley & Sons, Inc. or one of its group companies (each a"Wiley Company") or handled on behalf of a society with which a Wiley Company has exclusive publishing rights in relation to a particular work (collectively "WILEY"). By clicking "accept" in connection with completing this licensing transaction, you agree that the following terms and conditions apply to this transaction (along with the billing and payment terms and conditions established by the Copyright Clearance Center Inc., ("CCC's Billing and Payment terms and conditions"), at the time that you opened your RightsLink account (these are available at any time at http://myaccount.copyright.com).

Terms and Conditions

- The materials you have requested permission to reproduce or reuse (the "Wiley Materials") are protected by copyright.

- You are hereby granted a personal, non-exclusive, non-sub licensable (on a stand-alone basis), non-transferable, worldwide, limited license to reproduce the Wiley Materials for the purpose specified in the licensing process. This license, **and any CONTENT (PDF or image file) purchased as part of your order,** is for a one-time use only and limited to any maximum distribution number specified in the license. The first instance of republication or reuse granted by this license must be completed within two years of the date of the grant of this license (although copies prepared before the end date may be distributed thereafter). The Wiley Materials shall not be used in any other manner or for any other purpose, beyond what is granted in the license. Permission is granted subject to an appropriate acknowledgement given to the author, title of the material/book/journal and the publisher. You shall also duplicate the copyright notice that appears in the Wiley publication in your use of the Wiley Material. Permission is also granted on the understanding that nowhere in the text is a previously published source acknowledged for all or part of this Wiley Material. Any third party content is expressly excluded from this permission.

- With respect to the Wiley Materials, all rights are reserved. Except as expressly granted by the terms of the license, no part of the Wiley Materials may be copied, modified, adapted (except for minor reformatting required by the new Publication), translated, reproduced, transferred or distributed, in any form or by any means, and no derivative works may be made based on the Wiley Materials without the prior permission of the respective copyright owner.**For STM Signatory Publishers clearing permission under the terms of the STM Permissions Guidelines only, the**

FAILURE OF ESSENTIAL PURPOSE OF ANY LIMITED REMEDY PROVIDED HEREIN.

- Should any provision of this Agreement be held by a court of competent jurisdiction to be illegal, invalid, or unenforceable, that provision shall be deemed amended to achieve as nearly as possible the same economic effect as the original provision, and the legality, validity and enforceability of the remaining provisions of this Agreement shall not be affected or impaired thereby.

- The failure of either party to enforce any term or condition of this Agreement shall not constitute a waiver of either party's right to enforce each and every term and condition of this Agreement. No breach under this agreement shall be deemed waived or excused by either party unless such waiver or consent is in writing signed by the party granting such waiver or consent. The waiver by or consent of a party to a breach of any provision of this Agreement shall not operate or be construed as a waiver of or consent to any other or subsequent breach by such other party.

- This Agreement may not be assigned (including by operation of law or otherwise) by you without WILEY's prior written consent.

- Any fee required for this permission shall be non-refundable after thirty (30) days from receipt by the CCC.

- These terms and conditions together with CCC's Billing and Payment terms and conditions (which are incorporated herein) form the entire agreement between you and WILEY concerning this licensing transaction and (in the absence of fraud) supersedes all prior agreements and representations of the parties, oral or written. This Agreement may not be amended except in writing signed by both parties. This Agreement shall be binding upon and inure to the benefit of the parties' successors, legal representatives, and authorized assigns.

- In the event of any conflict between your obligations established by these terms and conditions and those established by CCC's Billing and Payment terms and conditions, these terms and conditions shall prevail.

- WILEY expressly reserves all rights not specifically granted in the combination of (i) the license details provided by you and accepted in the course of this licensing transaction, (ii) these terms and conditions and (iii) CCC's Billing and Payment terms and conditions.

- This Agreement will be void if the Type of Use, Format, Circulation, or Requestor Type was misrepresented during the licensing process.

- This Agreement shall be governed by and construed in accordance with the laws of the State of New York, USA, without regards to such state's conflict of law rules. Any legal action, suit or proceeding arising out of or relating to these Terms and Conditions or the breach thereof shall be instituted in a court of competent jurisdiction in New York County in the State of New York in the United States of America and each party hereby consents and submits to the personal jurisdiction of such court, waives any objection to venue in such court and consents to service of process by registered or certified mail, return receipt requested, at the last known address of such party.

WILEY OPEN ACCESS TERMS AND CONDITIONS

Wiley Publishes Open Access Articles in fully Open Access Journals and in Subscription journals offering Online Open. Although most of the fully Open Access journals publish open access articles under the terms of the Creative Commons Attribution (CC BY) License only, the subscription journals and a few of the Open Access Journals offer a choice of Creative Commons Licenses. The license type is clearly identified on the article.

The Creative Commons Attribution License

The Creative Commons Attribution License (CC-BY) allows users to copy, distribute and transmit an article, adapt the article and make commercial use of the article. The CC-BY license permits commercial and non-

Creative Commons Attribution Non-Commercial License

The Creative Commons Attribution Non-Commercial (CC-BY-NC)License permits use, distribution and reproduction in any medium, provided the original work is properly cited and is not used for commercial purposes.(see below)

Creative Commons Attribution-Non-Commercial-NoDerivs License

The Creative Commons Attribution Non-Commercial-NoDerivs License (CC-BY-NC-ND) permits use, distribution and reproduction in any medium, provided the original work is properly cited, is not used for commercial purposes and no modifications or adaptations are made. (see below)

Use by commercial "for-profit" organizations

Use of Wiley Open Access articles for commercial, promotional, or marketing purposes requires further explicit permission from Wiley and will be subject to a fee.

Further details can be found on Wiley Online Library
http://olabout.wiley.com/WileyCDA/Section/id-410895.html

Other Terms and Conditions:

v1.10 Last updated September 2015

Questions? customercare@copyright.com or +1-855-239-3415 (toll free in the US) or +1-978-646-2777.

Appendix B:
Supplementary materials to Chapter 2

Table B.2.4: Summary of the dated $^{40}Ar/^{39}Ar$ thermochronological results with relevant sample information

Sample ID	$^{40}Ar/^{39}Ar$ dates phase	Lithology	Argon age (Ma)	Age type	Latitude	Longitude
Mount Isa Inlier						
Eastern Belt						
AML01	Hornblende	Amphibolite	1504 ± 7	Plateau	-20.932	140.640
AMS01	Hornblende	Amphibolite	1534 ± 8	Plateau	-21.124	140.671
MMB03	Hornblende	Marraba Metabasalt	1511 ± 5	Plateau	-20.831	140.086
LCF01	Muscovite	Muscovite schist	1483 ± 6	Plateau	-20.959	140.660
MnMs01	Muscovite	Muscovite schist	1479 ± 5	Plateau	-21.022	140.651
CF05	Muscovite	Muscovite schist	1474 ± 11	Plateau	-20.7737	140.144
Central Belt						
LCG01	Hornblende	Lunch Creek Metagabbro	1549 ± 10	Plateau	-20.784	139.986
KLB1604	Hornblende	Kurbayia Amphibolite	1843 ± 6	Plateau	-20.917	139.615
MLMB01	Hornblende	Magna Lynn Metabasalt	1521 ± 11	Plateau	-20.442	139.839
WG01	Biotite	Wonga Granite	1489 ± 6	Plateau	-20.815	139.995
KLB1602	Biotite	Kurbayia Biotite Gneiss	1454 ± 5	Plateau	-20.918	139.609
Western Belt						
SG01	Hornblende	Sybella Granite	1523 ± 7	Plateau	-20.688	139.364
CRS01	Hornblende	Alpha Centauri Amphibolite	1505 ± 6	Plateau	-20.651	139.396

Georgetown Inlier						
Croydon Domain						
ESG02	Biotite	Esmeralda Granite	1284.4 ± 1.3	Total Fusion	-18.247	142.358
NG01	Biotite	Nonda Granite	1015.7 ± 17.5	Total Fusion	-18.614	142.578
RR71	Muscovite	Esmeralda Granite	1548.7 ± 1.3	Plateau	-18.468	142.946
RR71	Biotite	Esmeralda Granite	1536.5 ± 1.8	Plateau	-18.468	142.946
Western Domain						
SYC02	Hornblende	Cobbold Metadolerite	1512.8 ± 7.8	Total Fusion	-18.606	143.226
SYC02	Hornblende	Cobbold Metadolerite	1539.6 ± 11.3	Plateau	-18.606	143.226
SYC03	Biotite	Lane Creek Formation mica schist	1205.3 ± 1.4	Total Fusion	-18.607	143.205
FG04	Biotite	Forsayth Granite	984.2 ± 16.4	Total Fusion	-18.433	143.229
WC03	Hornblende	Cobbold Metadolerite	1546.5 ± 3.7	Total Fusion	-18.466	143.423
WC03	Biotite	Cobbold Metadolerite	1214.2 ± 1.3	Total Fusion	-18.466	143.423
RR65	Hornblende	Dead Horse Metabasalt	1532.4 ± 19	Plateau	-19.103	143.519
Central Domain						
ROB1612	Muscovite	Corbett Formation garnet-staurolite schist	1472.1 ± 2.3	Total Fusion	-18.847	143.533
ROB1612	Muscovite	Corbett Formation garnet-staurolite schist	1497.0 ± 3.7	Plateau	-18.847	143.533
ROB1612	Biotite	Corbett Formation garnet -staurolite schist	1584.3 ± 2.7	Total Fusion	-18.847	143.531
DMB03	Hornblende	Dead Horse Metabasalt	1573.2 ± 13.7	Plateau	-18.869	143.521
DMB03	Hornblende	Dead Horse Metabasalt	1534.5 ± 8.1	Plateau	-18.869	143.521
MSC01	Biotite	Corbett Formation mica schist	740.3 ± 7.9	Total Fusion	-18.836	143.517
RR39	Hornblende	Daniel Creek Formation amphibolite	1285.7 ± 7.7	Total Fusion	-18.875	143.607

RR40	Muscovite	Daniel Creek Formation mica schist	1039.0 ± 4.4	Total Fusion	-18.869	143.601
LHG01	Muscovite	Light House Granite	478.1 ± 2.3	Plateau	-18.300	143.582
MGE01	Muscovite	Micaschist from Einasleigh group	418.8 ± 2.4	Plateau	-19.061888	143.854752
Eastern Domain						
EIN1603	Hornblende	Einasleigh Metamorphics	1491.6 ± 8.1	Plateau	-18.183	144.004
EIN1603	Biotite	Einasleigh Metamorphics	429.5 ± 1.3	Plateau	-18.183	144.004
EIN1603	Muscovite	Einasleigh Metamorphics	408.4 ± 0.6	Plateau	-18.183	144.004
ES18B	Muscovite	Sillimanite-bearing migmatitic paragneiss	409.8 ± 0.6	Plateau	-18.549	143.974
AME01	Hornblende	Einasleigh Metamorphics	1374.7 ± 6.8	Total Fusion	-18.506	144.100
AME02	Hornblende	Einasleigh Metamorphics	991.7 ± 2.5	Total Fusion	-19.322	143.656
Dargalong Inlier						
DAR1701	Muscovite	McDewitt Schist	1098.2 ± 2.7	Total Fusion	-17.37753	144.190
DAR1702	Hornblende	Amphibolite	1910.5 ± 17.8	Total Fusion	-17.96917	145.157
DAR1712	Biotite	McDewitt Schist	1450.8 ± 1.1	Total Fusion	-17.96917	145.157
Yambo Inlier						
YAM1705	Hornblende	Chelmstone Gneiss	991.7 ± 2.5	Total Fusion	-15.99712	144.057
YAM1709	Hornblende	Amphibolite	397.9 ± 0.5	Plateau	-15.97243	143.763
YAM1713	Muscovite	Mica Schist	409.3 ± 6.6	Plateau	-16.37591	143.977
Cone Inlier						
COE1706	Muscovite	Muscovite Schist	407.9 ± 1.2	Plateau	-14.64985	143.097
COE1708	Hornblende	Amphibolite/Metadolerite	2127.6.7 ± 6.6	Total Fusion	-14.74791	142.980
COE1712	Biotite	Biotite Schist	1266.4 ± 1.3	Total Fusion	-14.57379	142.897

Table B.2.5: Initial inputs to Dodson's (1973) equation used to calculate mineral closure temperatures and cooling rates. Abbreviations are: *Q*, activation energy; D_0, diffusion coefficient; *R*, volume constant; T_{i_c} , initial closure temperature value; *A*, geometric factor; *a*, effective diffusion radius; *dT/dt,* initial cooling rate. Recalibrate samples from previous research are in italic, given at a moderate mineral grain size. Closure temperature values are calculated by Monte Carlo simulation, and reported at ± 2σ. Average closure temperatures estimated for hornblende, muscovite, and biotite are 518 ± 53℃, 405 ± 49 ℃, and 329 ± 57 ℃ respectively.

Sample name	Mineral	T_{i_c} (°C)	a (µm)	E (kcal/mol)	D_0 (cm²/s)	A	dT/dt (°C/Ma)	T_c (°C ± 2σ)
Mount Isa Inlier								
Eastern Belt								
AML01	Hbl	510	250–300	64.1 ± 1.7	$0.024^{+0.053}_{-0.011}$	55	1.2	516 ± 52
AMS01	Hbl	510	75–150	64.1 ± 1.7	$0.024^{+0.053}_{-0.011}$	55	2.1	472 ± 48
MMB03	Hbl	510	100–150	64.1 ± 1.7	$0.024^{+0.053}_{-0.011}$	55	0.4	488 ± 54
LCF01	Ms	390	125–150	63 ± 7	$2.3^{+70}_{-2.2}$	55	1.7	385 ± 48
MnMs01	Ms	390	200–250	63 ± 7	$2.3^{+70}_{-2.2}$	55	0.9	399 ± 50
CF05	Ms	390	150–250	63 ± 7	$2.3^{+70}_{-2.2}$	55	1.7	398 ± 50
Central Belt								
LCG01	Hbl	510	250–300	64.1 ± 1.7	$0.024^{+0.053}_{-0.011}$	55	4.3	521 ± 48
KLB1604	Hbl	510	150–200	64.1 ± 1.7	$0.024^{+0.053}_{-0.011}$	55	3.7	506 ± 52
MLMB01	Hbl	510	200–300	64.1 ± 1.7	$0.024^{+0.053}_{-0.011}$	55	1.6	514 ± 54
KG07	Ms	390	150–250	63 ± 7	$2.3^{+70}_{-2.2}$	55	0.4	369 ± 58
WG01	Bt	320	250–300	50.5 ± 2.2	$0.4^{+0.96}_{-0.28}$	27	3.4	328 ± 56
KLB1602	Bt	320	100–200	50.5 ± 2.2	$0.4^{+0.96}_{-0.28}$	27	1.45	309 ± 56
KG03	Bt	320	250–300	50.5 ± 2.2	$0.4^{+0.96}_{-0.28}$	27	4.3	329 ± 58
AG6065	*Bt*	320	*200–400*	*50.5 ± 2.2*	*$0.4^{+0.96}_{-0.28}$*	*27*	*2.5*	324 ± 57
Western Belt								

SG01	Hbl	510	300–450	64.1 ± 1.7	$0.024^{+0.053}_{-0.011}$	55	2	535 ± 54
CRS01	Hbl	510	150–250	64.1 ± 1.7	$0.024^{+0.053}_{-0.011}$	55	1.5	506 ± 54
DF75	*Ms*	390	*200–400*	*63 ± 7*	$2.3^{+70}_{-2.2}$	*55*	*0.96*	393 ± 48
RS54	*Bt*	320	*200–400*	*50.5 ± 2.2*	$0.4^{+0.96}_{-0.28}$	*27*	*1.45*	329 ± 59
Georgetown Inlier								
Croydon Domain								
RR71	Ms	390	200–300	63 ± 7	$2.3^{+70}_{-2.2}$	55	69.6	461 ± 52
RR71	Bt	320	200–300	50.5 ± 2.2	$0.4^{+0.96}_{-0.28}$	27	29.6	354 ± 61
Western Domain								
RR65	Hbl	510	400–600	64.1 ± 1.7	$0.024^{+0.053}_{-0.011}$	55	2.6	502 ± 46
SYC02	Hbl	510	400–600	64.1 ± 1.7	$0.024^{+0.053}_{-0.011}$	55	2.6	513 ± 52
Central Domain								
DMB03	Hbl	510	500–700	64.1 ± 1.7	$0.024^{+0.053}_{-0.011}$	55	12.1	548 ± 46
ROB1612	Mus	390	*200–400*	*63 ± 7*	$2.3^{+70}_{-2.2}$	*55*	*0.96*	401 ± 48
Eastern Domain								
EIN1603	Hbl	510	500–700	64.1 ± 1.7	$0.024^{+0.053}_{-0.011}$	55	3.2	541 ± 50

Table B.2.6: Probability distributions and values of variables used in the Monte Carlo simulation. The uncertainty of each random variable used in the Monte Carlo simulation was modelled using either a uniform, triangular or normal probability distribution.

Variable	Input Probability Distribution	Value (± 2 SD)	Source
Hornblende			
E	Triangular (min, mode, max)	64.1 ± 1.7 kcal/mol	*Harrison,* 1981
D_0	Triangular (min, mode, max)	$0.024^{+0.053}_{-0.011}$ cm^2/s	
Biotite			
E	Triangular (min, mode, max)	50.5 ± 2.2 kcal/mol	*Grove and Harrison,* 1996
D_0	Triangular (min, mode, max)	$0.4^{+0.96}_{-0.28}$ cm^2/s	

Muscovite			
E	Triangular (min, mode, max)	63 ± 7 kcal/mol	*Harrison et al,*. 2009
D_0	Triangular (min, mode, max)	$2.3^{+70}_{-2.2}$ cm^2/s	
Metamorphic age (Ma)	Normal (mean, σ)	Varies for each mineral	See Chapter 3 & 4
Metamorphic temperature (°C)	Uniform (min, max)	Varies for each mineral	See Chapter 3 & 4
$^{40}Ar/^{39}Ar$ cooling age (°C)	Normal (mean, σ)	Varies for each mineral	Table B.2.1
Closure temperature (°C)	Not modelled with a probability distribution	The value of the closure temperature is directly calculated by iterating Equation 2 as part of each trial	
Cooling rate (°C/Ma)	Not modelled with a probability distribution	Initially calculated based on metamorphic age, metamorphism temperature, $^{40}Ar/^{39}Ar$ cooling age and the initial estimate of $^{40}Ar/^{39}Ar$ closure temperature. The cooling rate is recalculated after every propagation of Equation 2, using the new closure temperature directly calculated as part of each calculation	

Appendix C:
Supplementary materials to Chapter 3

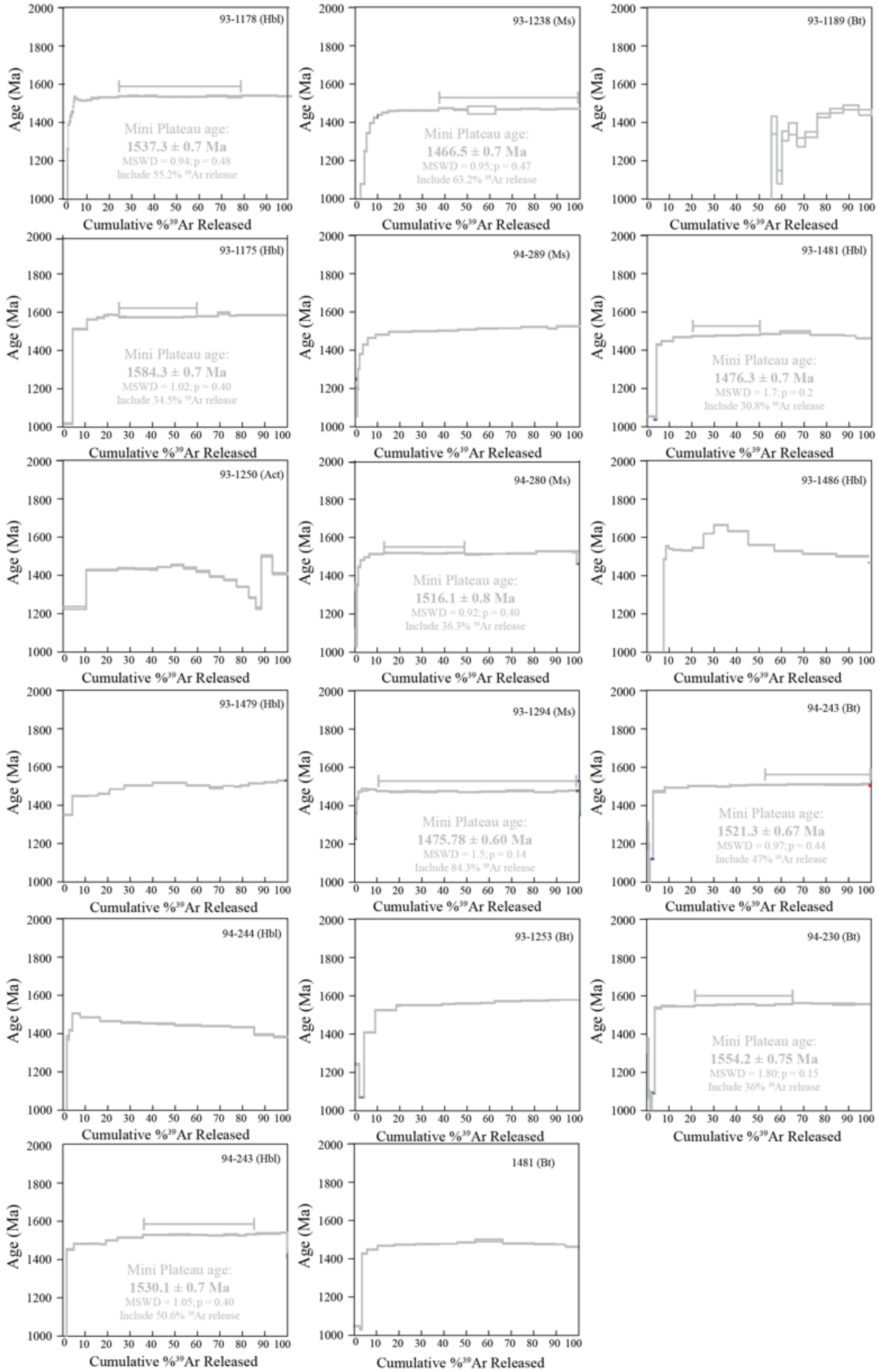

Fig. C.3.1: ${}^{40}Ar/{}^{39}Ar$ age spectra recalculated from Perkins and Wyborn (1998) using updated argon decay constant. Spectra with ages in light grey or no quoted ages are the 40Ar/39Ar results discarded in this paper. Whereas those we retained are shown with age plateaus in black (Bt) or blue (Ms). Specific sample information including sample lithology, locations, and stratigraphic positions are listed in Table C.3.1.

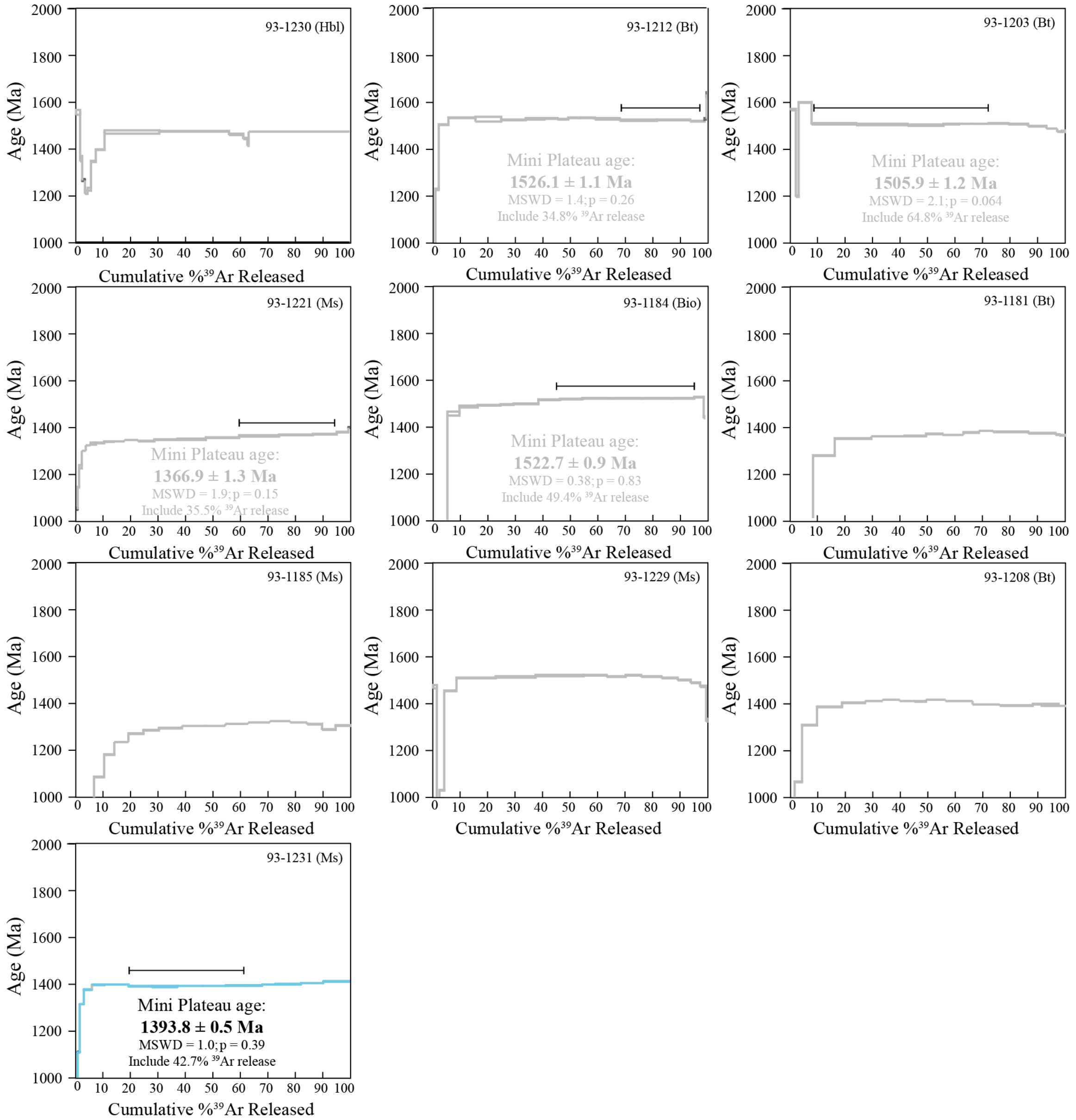

Fig. C.3.2: $^{40}Ar/^{39}Ar$ age spectra recalculated from Perkins et al. (1999) using updated decay constant. Spectra with ages in light grey or no quoted ages are the $^{40}Ar/^{39}Ar$ results discarded in this paper. Whereas those we retained are shown with age plateaus in black (Bt) or blue (Ms). Specific sample information including sample lithology, locations, and stratigraphic positions are listed in Table C.3.1.

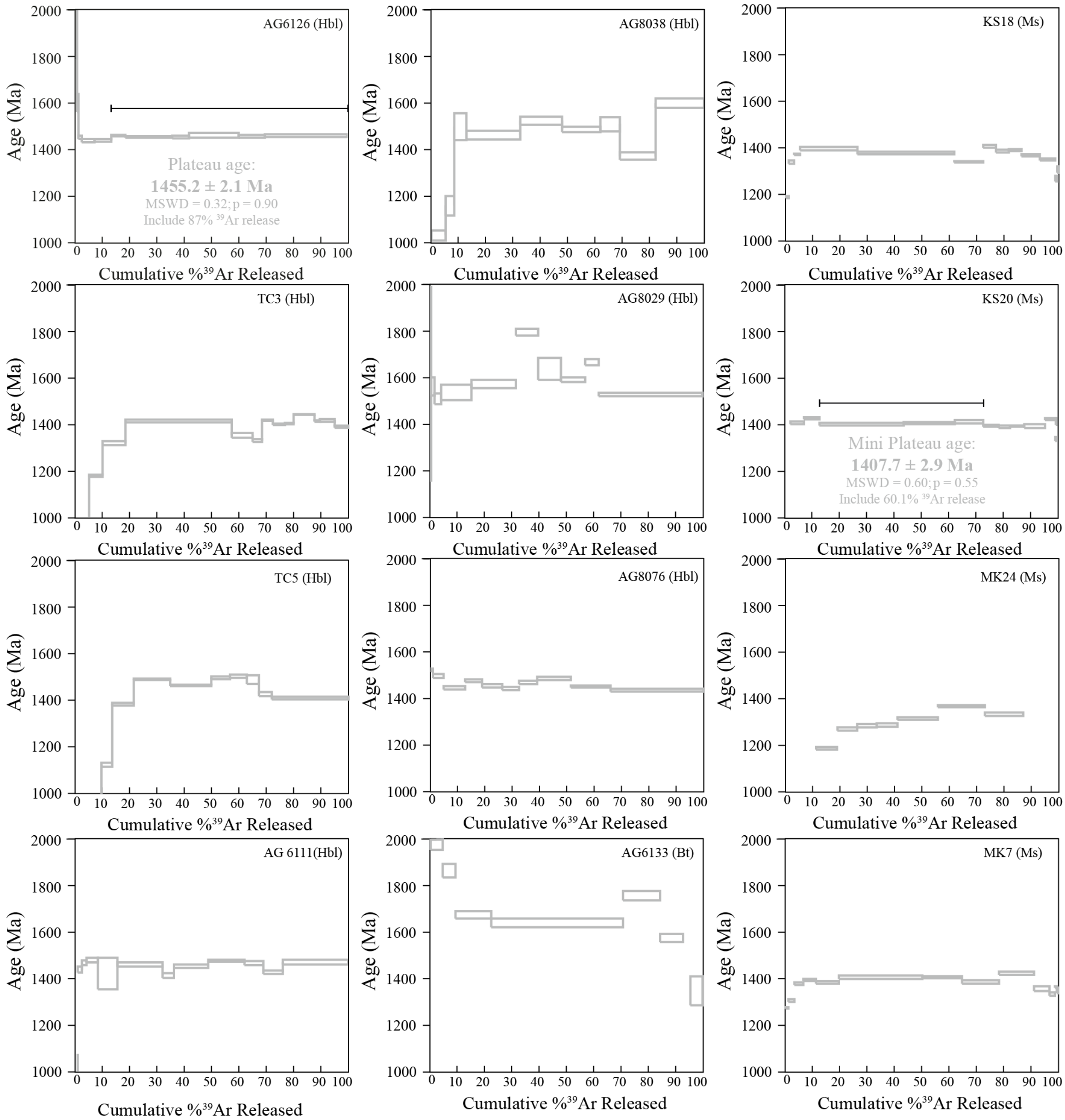
AG6126 (Hbl)
Plateau age:
1455.2 ± 2.1 Ma
MSWD = 0.32; p = 0.90
Include 87% 39Ar release
AG8038 (Hbl)
KS18 (Ms)
TC3 (Hbl)
AG8029 (Hbl)
KS20 (Ms)
Mini Plateau age:
1407.7 ± 2.9 Ma
MSWD = 0.60; p = 0.55
Include 60.1% 39Ar release
TC5 (Hbl)
AG8076 (Hbl)
MK24 (Ms)
AG 6111(Hbl)
AG6133 (Bt)
MK7 (Ms)
Age (Ma)
Cumulative %39Ar Released

Continue

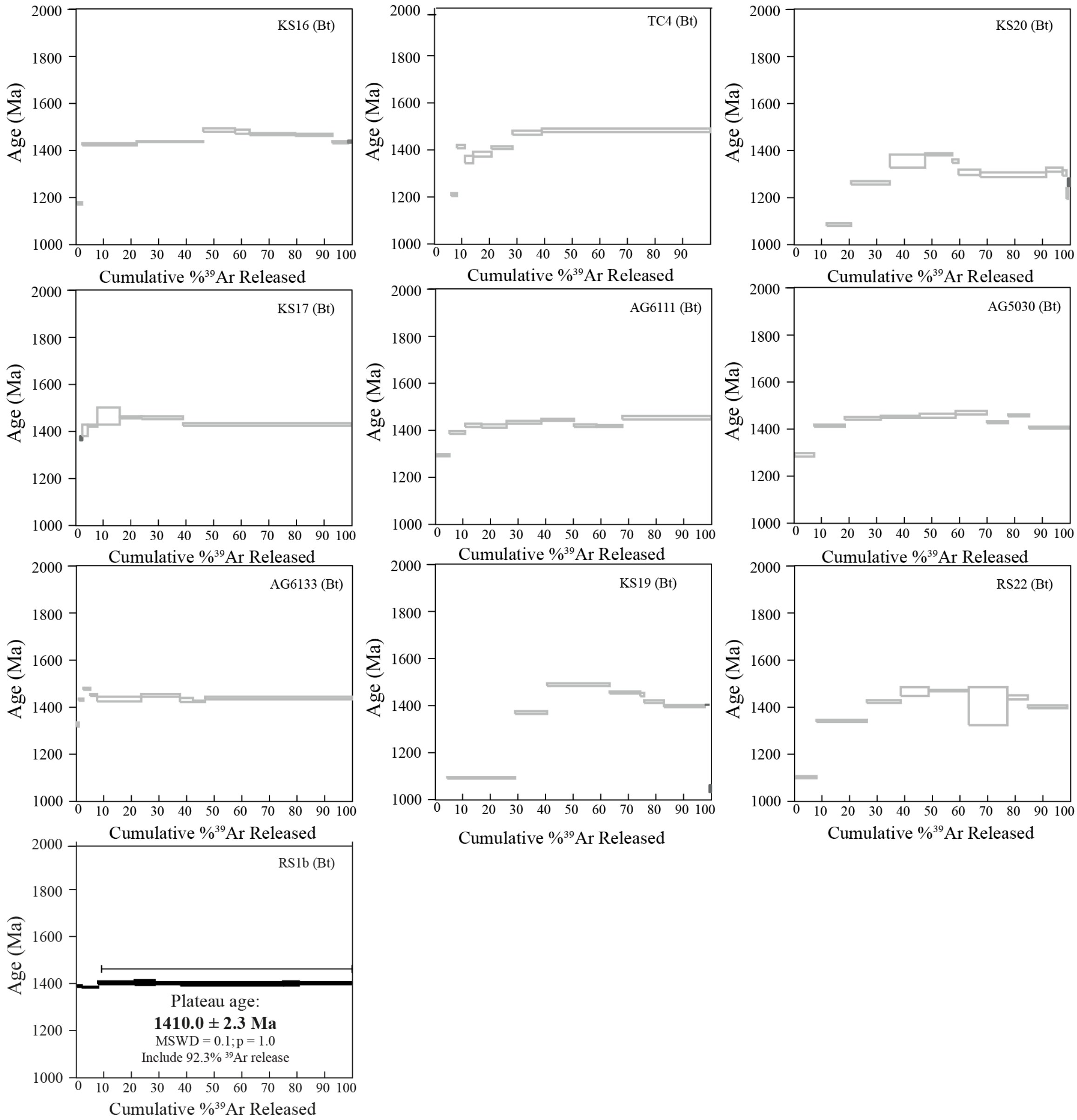

Fig. C.3.3: $^{40}Ar/^{39}Ar$ age spectra recalculated from Spikings et al., (2001) using updated decay constant. Spectra with ages in light grey or no quoted ages are the $^{40}Ar/^{39}Ar$ results discarded in this paper. Whereas those we retained are shown with age plateaus in black (Bt) or blue (Ms). Specific sample information including sample lithology, locations, and stratigraphic positions are listed in Table C.3.1.

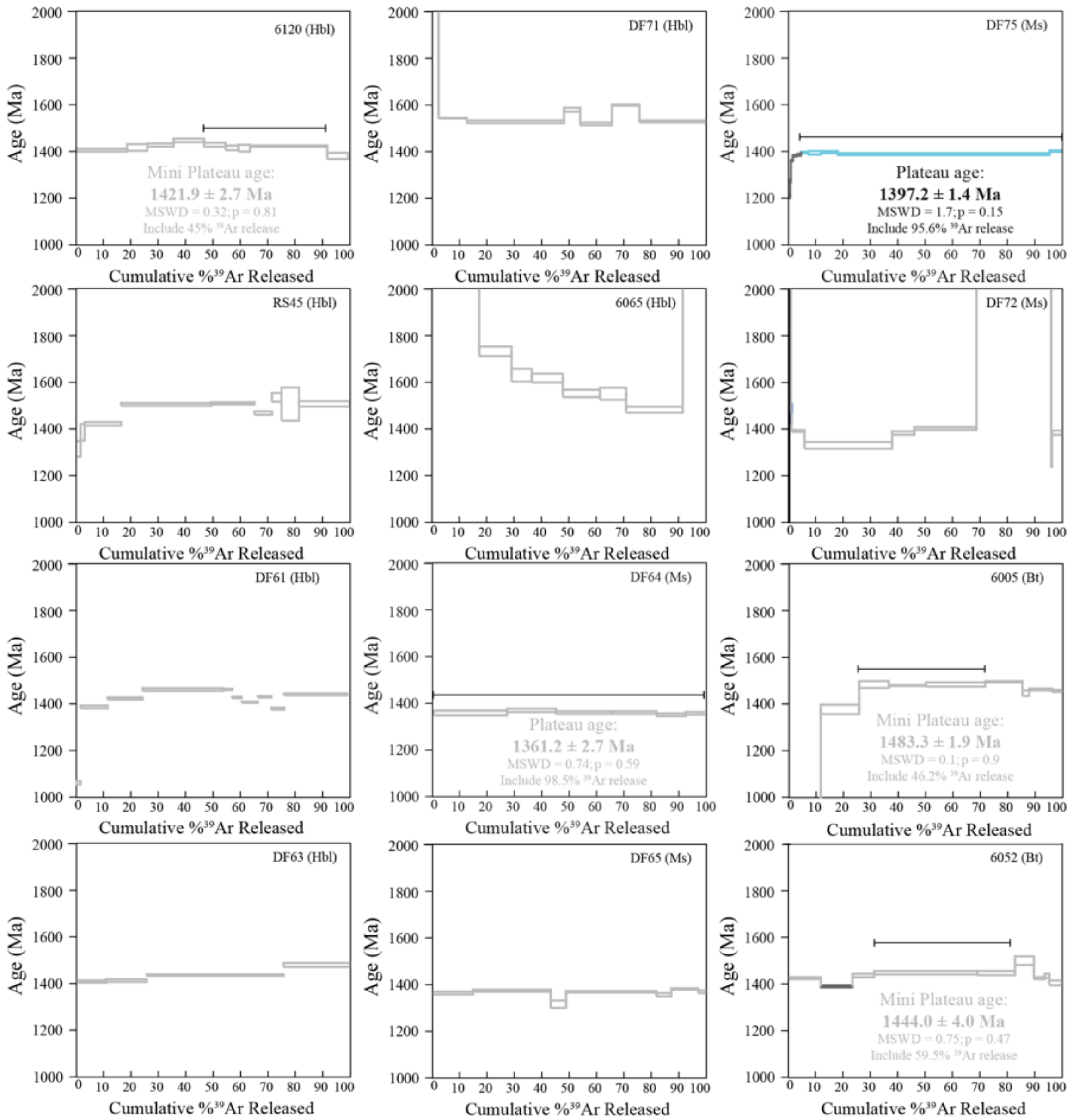
6120 (Hbl)
Mini Plateau age:
1421.9 ± 2.7 Ma
MSWD = 0.32; p = 0.81
Include 45% ³⁹Ar release
DF71 (Hbl)
DF75 (Ms)
Plateau age:
1397.2 ± 1.4 Ma
MSWD = 1.7; p = 0.15
Include 95.6% ³⁹Ar release
RS45 (Hbl)
6065 (Hbl)
DF72 (Ms)
DF61 (Hbl)
DF64 (Ms)
Plateau age:
1361.2 ± 2.7 Ma
MSWD = 0.74; p = 0.59
Include 98.5% ³⁹Ar release
6005 (Bt)
Mini Plateau age:
1483.3 ± 1.9 Ma
MSWD = 0.1; p = 0.9
Include 46.2% ³⁹Ar release
DF63 (Hbl)
DF65 (Ms)
6052 (Bt)
Mini Plateau age:
1444.0 ± 4.0 Ma
MSWD = 0.75; p = 0.47
Include 59.5% ³⁹Ar release
Age (Ma)
Cumulative %³⁹Ar Released

Continue

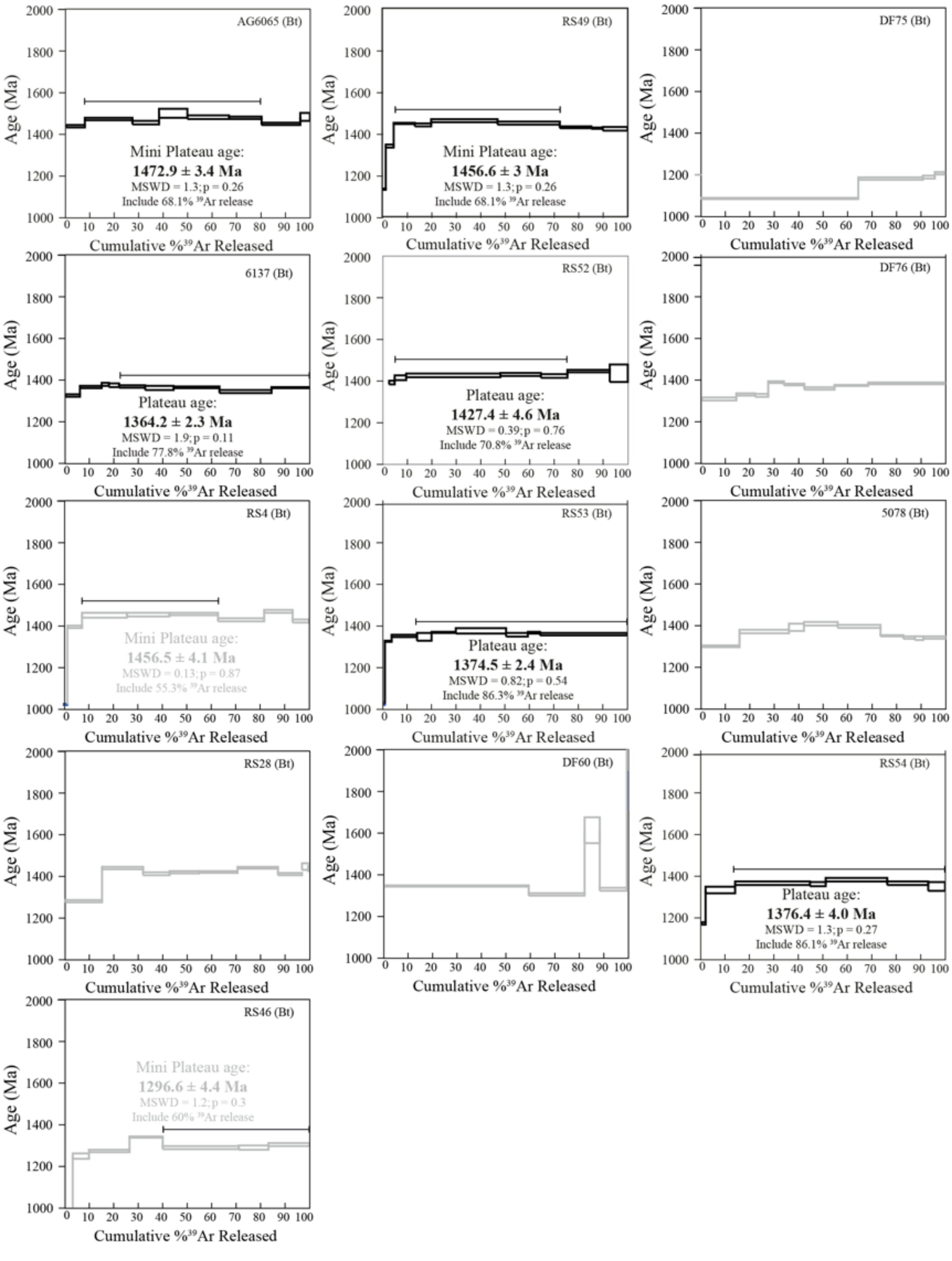

Fig. C.3.4: $^{40}Ar/^{39}Ar$ age spectra recalculated from Spikings et al., (2002) using updated decay constant. Spectra with ages in light grey or no quoted ages are the $^{40}Ar/^{39}Ar$ results discarded in this paper. Whereas those we retained are shown with age plateau in black (Bt) or blue (Ms). Specific sample information including sample lithology, locations, and stratigraphic positions are listed in Table C.3.1.

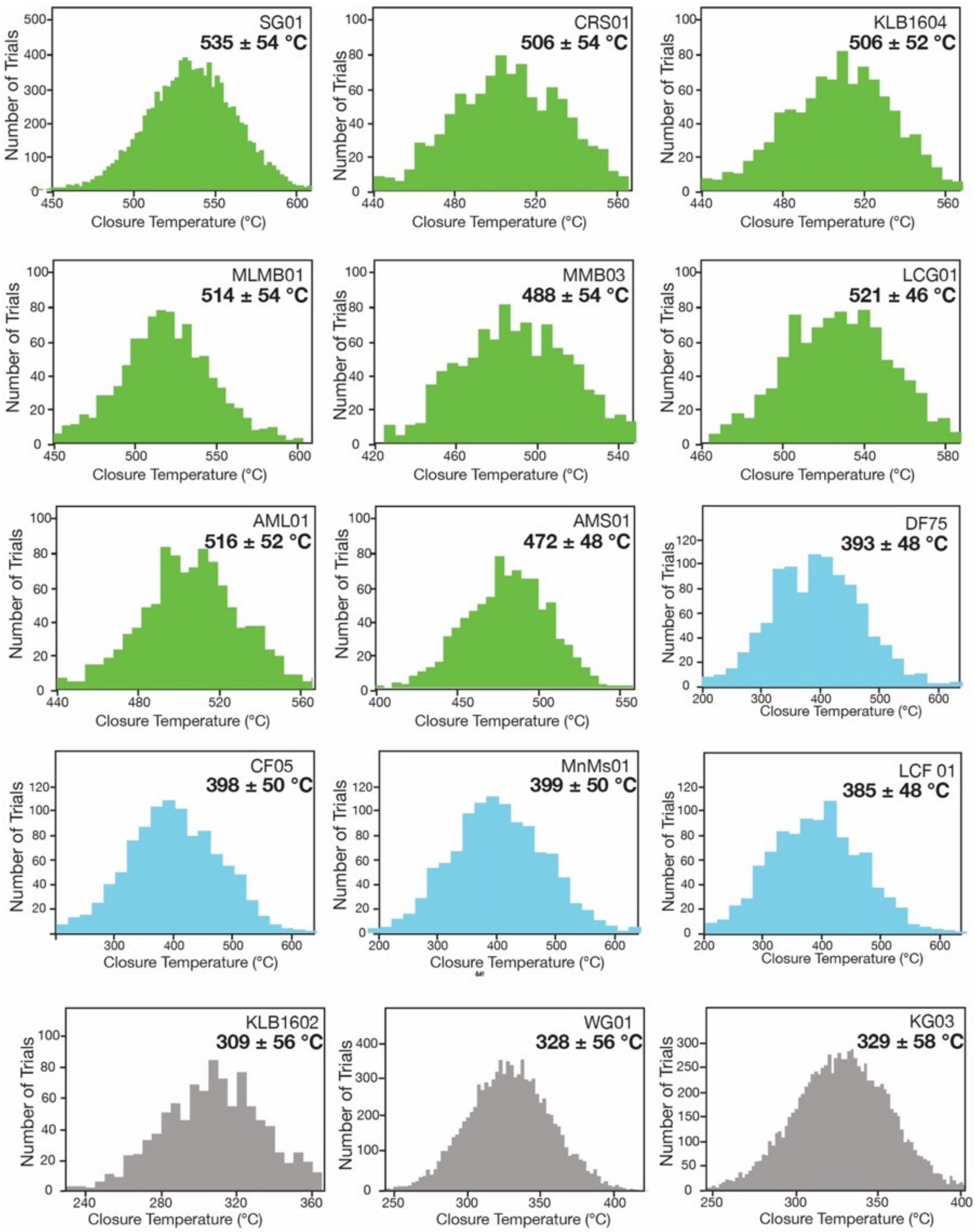

Fig. C.3.5: Probability diagrams of Monte Carlo simulation for 10,00 computations of the argon closure temperature in hornblende, biotite and muscovite from this study. The closure temperature values are reported at mean with 2σ.

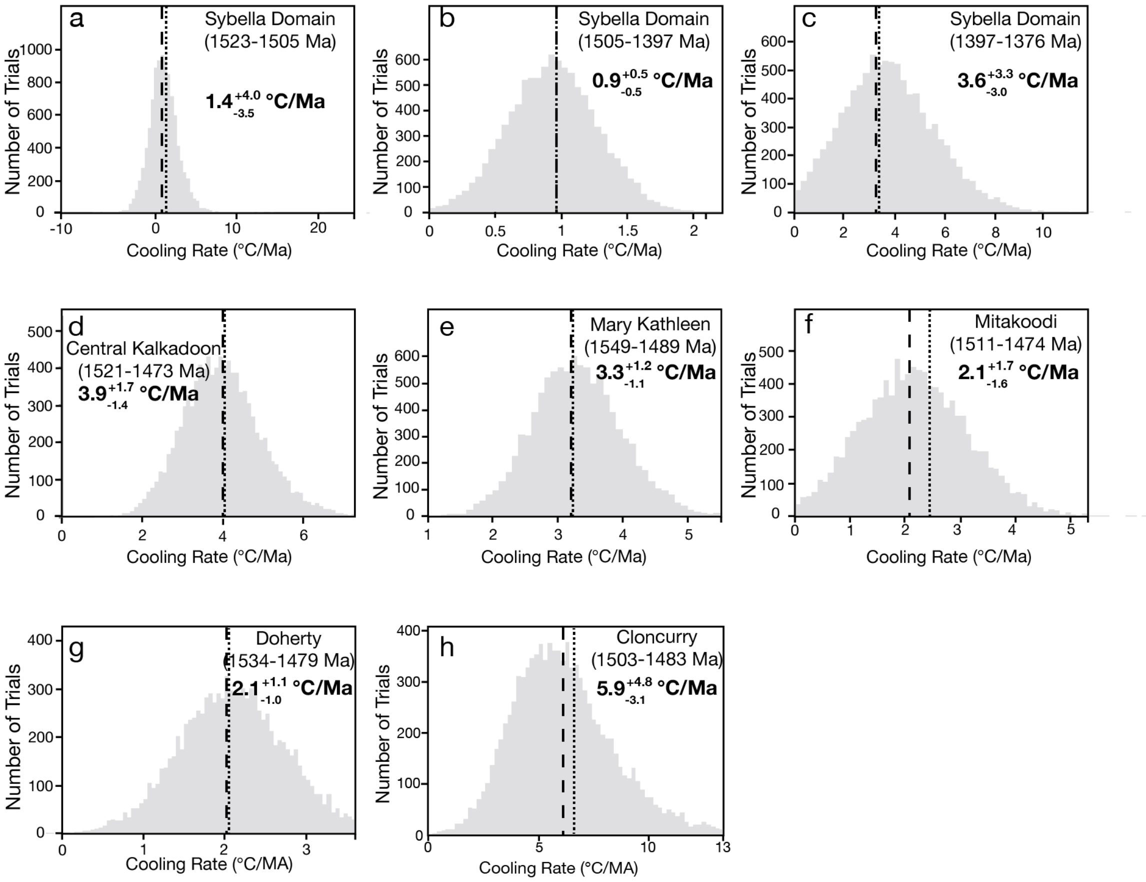

Fig. C.3.15: Probability diagrams of Monte Carlo simulation for 10,000 computation of the cooling rate between argon closure in hornblende, muscovite and biotite at different cooling stages. Mineral pair calculated in each domain include hornblende-hornblende (a); hornblende-muscovite (b, f–h); hornblende-biotite (d, e); muscovite-biotite (c). The cooling rate values are reported at median value and 90% inter-percentile range, between 5% and 95% ($\frac{I_3}{I_1}$), for measuring such a tendency of a shewed population. Specific values for different stage are list in Table 3.1 in the main text. The dashed and dot line each represents the approximate location of the population median and mean.

Table C.3.1. Previously published $^{40}Ar/^{39}Ar$ thermochronology results from the Mount Isa Inlier.

Sample ID	Mineral	Lithology	Domain	Age (Ma)	Plateau age	Reference	Latitude	Longitude	Age interpretation
93-1178	Hornblende	Ore, Kuridala Group, Osborne Deposit	Kuridala-Selwyn Domain	1530±2	Mini	Perkins & Wyborn, 1998	-22.0815	140.5841	Mineralization
93-1175	Hornblende	Ore, Kuridala Group, Osborne Deposit	Kuridala-Selwyn Domain	1564±2	Mini	Perkins & Wyborn, 1998	-22.0815	140.5841	Alteration or mineralization
93-1250	Actinolite	Ore, Mt. Elliott Deposit	Kuridala-Selwyn Domain	1396±4	No Plateau	Perkins & Wyborn, 1998	N/A	N/A	Fluid
93-1479	Hornblende	Ore, Ernest Henry Deposit	Kuridala-Selwyn Domain	1490±1	No Plateau	Perkins & Wyborn, 1998	N/A	N/A	Alteration or mineralization
94-244	Hornblende	Ore, Mt. Elliott Deposit	Kuridala-Selwyn Domain	1431±2	No Plateau	Perkins & Wyborn, 1998	N/A	N/A	Alteration or mineralization
94-243	Hornblende	Ore, Mt. Elliott Deposit	Kuridala-Selwyn Domain	1513±2	Mini	Perkins & Wyborn, 1998	N/A	N/A	Alteration or mineralization
93-1238	Muscovite	Altered William Granite Suite	Kuridala-Selwyn Domain	1439±4	Mini	Perkins & Wyborn, 1998	N/A	N/A	Alteration
94-289	Muscovite	Ore, Maronan Deposit	Kuridala-Selwyn Domain	1481±1	No Plateau	Perkins & Wyborn, 1998	N/A	N/A	Alteration or mineralization
94-280	Muscovite	Ore, Mt. Elliott Deposit	Kuridala-Selwyn Domain	1512±2	Mini	Perkins & Wyborn, 1998	N/A	N/A	Alteration or mineralization

93-1294	Biotite	Ore, Osborne Deposit	Kuridala-Selwyn Domain	1476±1	Yes	Perkins & Wyborn, 1998	N/A	N/A	Alteration or mineralization
93-1253	Biotite	Ore, Mt. Elliott Deposit	Kuridala-Selwyn Domain	1447±2	No Plateau	Perkins & Wyborn, 1998	N/A	N/A	Alteration or mineralization
93-1481	Biotite	Ore, Ernest Henry Deposit	Kuridala-Selwyn Domain	1461±2	No Plateau	Perkins & Wyborn, 1998	N/A	N/A	Alteration or mineralization
93-1189	Biotite	Ore, Ernest Henry Deposit	Kuridala-Selwyn Domain	1100±9	No Plateau	Perkins & Wyborn, 1998	N/A	N/A	Alteration or mineralization
93-1481	Biotite	William Suit, Ernest Henry Deposit	Kuridala-Selwyn Domain	1478±16	Mini	Perkins & Wyborn, 1998	-22.0815	140.5841	Alteration or mineralization
93-1486	Biotite	Ore, Ernest Henry Deposit	Kuridala-Selwyn Domain	1483±1	No Plateau	Perkins & Wyborn, 1998	N/A	N/A	Alteration or mineralization
94-243	Biotite	Ore, Mt. Elliott Deposit	Kuridala-Selwyn Domain	1505±2	Mini	Perkins & Wyborn, 1998	N/A	N/A	Alteration or mineralization
94-230	Biotite	Ore, Mt. Elliott Deposit	Kuridala-Selwyn Domain	1540±2	Mini	Perkins & Wyborn, 1998	N/A	N/A	Alteration or mineralization
93-1230	Hornblende	Alpha Centauri Metamorphics	Sybella Domain	1457±3	No Plateau	Perkins, 1999	-20.8192	139.4396	Fault activity
93-1221	Muscovite	Urquhart Shale, Holley Fault	Leichardt River Domain	1367±1	Mini	Perkins, 1999	-20.7245	139.4781	Fault activity
93-1185	sericite	Buck Quartz Fault	Leichardt River Domain	1261±1	No Plateau	Perkins, 1999	N/A	N/A	Alteration or mineralization

93-1231	Muscovite	Chlorite-Muscovite metasomatic zone	Sybella Domain	1394±1	Mini	Perkins, 1999	-20.8246	139.4433	Cooling
93-1212	Biotite	Orebody	Leichardt River Domain	1526±1	Mini	Perkins, 1999	N/A	N/A	Mineralization
93-1184	Biotite	Ore	Sybella Domain	1523±1	Mini	Perkins, 1999	N/A	N/A	Alteration or mineralization
93-1229	Muscovite	Ore	Sybella Domain	1496±2	No Plateau	Perkins, 1999	N/A	N/A	Alteration or mineralization
93-1203	Biotite	Altered Vein	Sybella Domain	1506±1	Mini	Perkins, 1999	N/A	N/A	Alteration or mineralization
93-1181	Biotite	Eastern Creek Volcanics	Sybella Domain	1320±1	No Plateau	Perkins, 1999	N/A	N/A	Alteration or mineralization
93-1208	Biotite	Altered Basalt	Leichardt River Fault Domain	1515±1	No Plateau	Perkins, 1999	N/A	N/A	Alteration or mineralization
AG6126	Hornblende	Squirrel Hills Granite, William	Kuridala-Selwyn Domain	1455±2	Yes	Spikings et al., 2001	-21.7286	140.8463	Cooling
TC3	Hornblende	Rhyolite, Corella Formation	Tommy Creek Domain	1398±5	No Plateau	Spikings et al., 2001	-20.7619	140.1788	Cooling
TC5	Hornblende	Dolerite,	Tommy Creek Domain	1457±5	No Plateau	Spikings et al., 2001	-20.7488	140.165	Cooling
AG6111	Hornblende	Wimberu Granite	Mitakoodi Domain	1456±2	No Plateau	Spikings et al., 2001	-21.3091	140.3483	Cooling

AG8038	Hornblende	Mount Margaret Granite, Naraku	Kuridala-Selwyn Domain	1493±8	No Plateau	Spikings et al., 2001	-20.4580	140.8158	Cooling
AG8029	Hornblende	Rhyolite, Mount Fort Constantine Volcanics	Cloncurry Domain	1550±5	No Plateau	Spikings et al., 2001	-20.4886	140.6097	Cooling
AG8076	Hornblende	Boomarra Metamorphics	Mary Kathleen Domain	1458±6	No Plateau	Spikings et al., 2001	-19.7680	140.24	Cooling
AG6133	Biotite	Gin Creek Granite	Kuridala-Selwyn Domain	1435±3	No Plateau	Spikings et al., 2001	-21.6627	140.45	Cooling
KS18	Muscovite	Schist, Kuridala Group	Kuridala-Selwyn Domain	1370±6	No Plateau	Spikings et al., 2001	-21.6980	140.5311	Cooling
KS20	Muscovite	Schist, New Hope Sandstone	Kuridala-Selwyn Domain	1400±5	Mini	Spikings et al., 2001	-21.7011	140.5377	Cooling
MK24	Muscovite	Quartzite, Overhang Jaspilite	Mitakoodi Domain	1316±7	No Plateau	Spikings et al., 2001	-20.7656	140.2080	Cooling
MK7	Muscovite	Limestone, Overhang Jaspilite	Mitakoodi Domain	1400±5	No Plateau	Spikings et al., 2001	-20.7869	140.16	Cooling
KS16	Biotite	Wimberu Granite	Kuridala-Selwyn Domain	1446±3	No Plateau	Spikings et al., 2001	-21.6988	140.53	Cooling
KS17	Biotite	Wimberu Granite	Kuridala-Selwyn Domain	1428±8	No Plateau	Spikings et al., 2001	-21.6988	140.5311	Cooling

AG6133	Biotite	Gin Creek Granite	Marimo-Staveley Domain	1576±18	Mini	Spikings et al., 2001	-21.6627	140.45	Cooling
RS1b	Biotite	Naraku Granite	Kuridala-Selwyn Domain	1408±5	Yes	Spikings et al., 2001	-20.1225	140.2336	Cooling
TC4	Biotite	Milo Bed Schist	Tommy Creek Domain	1481±5	No Plateau	Spikings et al., 2001	-20.7530	140.18	Cooling
AG6111	Biotite	Wimberu Granite	Mitakoodi Domain	1456±2	No Plateau	Spikings et al., 2001	-21.3091	140.3483	Cooling
KS19	Biotite	Schist, Corella Formation	Mary Kathleen Domain	1405±5	No Plateau	Spikings et al., 2001	-21.6969	140.5455	Cooling
KS20	Biotite	Schist, New Hope Sandstone	Kuridala-Selwyn Domain	1400±5	No Plateau	Spikings et al., 2001	-21.7011	140.5377	Cooling
AG5030	Biotite	Jessie Granite	Kuridala-Selwyn Domain	1435±5	No Plateau	Spikings et al., 2001	-20.7011	140.4761	Cooling
RS22	Biotite	Capsize Granodiorite	Kuridala-Selwyn Domain	1436±8	No Plateau	Spikings et al., 2001	-20.3672	140.2608	Cooling
6120	Hornblende	Kalkadoon Granite	Kalkadoon Domain	1419±7	Mini	Spikings et al., 2002	-21.6655	139.7763	Cooling
RS45	Hornblende	Kurbayia Metamorphic Complex	Kalkadoon Domain	1489±12	No Plateau	Spikings et al., 2002	-20.8716	139.5694	Alteration
DF61	Hornblende	Widgewarra Granite	Sybella Domain	1378±10	No Plateau	Spikings et al., 2002	-20.975	139.4063	Cooling
DF63	Hornblende	Alpha Centauri Metamorphics	Sybella Domain	1439±5	No Plateau	Spikings et al., 2002	-20.9686	139.4083	Cooling

DF71	Hornblende	Kalkadoon Granodiorite	Kalkadoon Domain	1501±5	No Plateau	Spikings et al., 2002	-20.6605	139.6872	Cooling
6052	Hornblende	Kalkadoon Granodiorite	Kalkadoon Domain	1483±14	No Plateau	Spikings et al., 2002	-20.32	139.78	Cooling
DF64	Muscovite	Myally Subgroup	Sybella Domain	1363±8	Mini	Spikings et al., 2002	-20.9272	139.4447	Cooling
DF65	Muscovite	Queen Elizabeth Granite	Sybella Domain	1225±7	Mini	Spikings et al., 2002	-20.9444	139.4447	Cooling
DF75	Muscovite	Eastern Creek Volcanics	Sybella Domain	1390±4	Yes	Spikings et al., 2002	-20.8630	139.4611	Cooling
DF72	Muscovite	Kalkadoon Granodiorite	Kalkadoon Domain	1388±7	No Plateau	Spikings et al., 2002	-20.5547	139.7502	Cooling
6005	Biotite	Kalkadoon Granodiorite	Kalkadoon Domain	1488±2	No Plateau	Spikings et al., 2002	-19.75	139.96	Cooling
6052	Biotite	Kalkadoon Granodiorite	Kalkadoon Domain	1444±4	No Plateau	Spikings et al., 2002	-20.32	139.78	Cooling
6065	Biotite	Kalkadoon Granodiorite	Leichardt River Fault Domain	1470±9	Yes	Spikings et al., 2002	-20.8513	139.75	Cooling
6137	Biotite	Leichhardt Volcanics	Leichardt River Fault Domain	1361±6	Yes	Spikings et al., 2002	-21.7522	139.5638	Cooling
RS4	Biotite	Kalkadoon Granodiorite	Kalkadoon Domain	1456±4	No Plateau	Spikings et al., 2002	-19.9925	139.5483	Cooling
RS28	Biotite	Rhyodacite, Leichhardt volcanics	Kalkadoon Domain	1426±6	No Plateau	Spikings et al., 2002	-20.3111	139.8511	Cooling
RS46	Biotite	Kalkadoon Granodiorite	Kalkadoon Domain	1295±7	No Plateau	Spikings et al., 2002	-20.9361	139.5638	Cooling
RS49	Biotite	Kalkadoon Granodiorite	Kalkadoon Domain	1453±4	Yes	Spikings et al., 2002	-21.1133	139.6472	Cooling

RS52	Biotite	Kalkadoon Granodiorite	Kalkadoon Domain	1432±3	Yes	Spikings et al., 2002	-21.5205	139.6744	Cooling
RS53	Biotite	Steeles Granite	Sybella Domain	1372±8	Yes	Spikings et al., 2002	-20.6747	139.3405	Cooling
DF60	Biotite	Widgewarra Granite, Sybella	Sybella Domain	1378±10	No Plateau	Spikings et al., 2002	-20.975	139.4063	Cooling
DF75	Biotite	Schist, Eastern Creek Volcanics	Leichhardt River Domain	1122±4	No Plateau	Spikings et al., 2002	-20.8630	139.4611	Cooling
DF76	Biotite	Kitty Plain Microgranite	Sybella Domain	1362±5	No Plateau	Spikings et al., 2002	-20.5388	139.4372	Cooling
5078	Biotite	Big Toby Granite	Sybella Domain	1361±7	No Plateau	Spikings et al., 2002	-20.7638	139.1969	Cooling
RS54	Biotite	Gidyea Granite, Sybella	Sybella Domain	1377±4	Yes	Spikings et al., 2002	-21.1966	139.3094	Cooling
0257	Biotite	Gabbro	Mary Kathleen Domain	1442±20	No Plateau	Page, 1983	-20.7503	140.0722	Cooling
AG5032	Biotite	Malakoff Granite	Kuridala-Selwyn Domain	1454±4	No Plateau	Page & Sun, 1998	-20.57	140.4561	Cooling
AG6111	Hornblende	Wimberu Granite	Kuridala-Selwyn Domain	1456±2	No Plateau	Page & Sun, 1998	-21.3091	140.3483	Cooling

Table C.3.2. Summary of published geochronological constraints and thermo conditions for the peak metamorphism stage in each tectonic domain.

Location	Metamorphic zone	Peak metamorphism temperature (°C)	Reference	Peak metamorphism age	Reference
Eastern Belt					

Central Snake Creek Anticline (Cloncurry Domain)	Staurolite/Andalusite	580–605 °C	Rubenach, 1997	1570–1590 Ma; 1600–1608 Ma	Rubenach, 2008; Pourteau et al., 2018.
South Snake Creek Anticline (Cloncurry Domain)	Sillimanite/K-Feldspar	675 °C	Foster, 2003		
Middle Creek Anticline (Cloncurry Domain)	Staurolite/Andalusite	580–605 °C	Foster & Rubenach, 2006	1599±10 Ma;	Hand & Rubatto, 2002
Osborne Mine (Cloncurry Domain)	Sillimanite/K-feldspar	678–700 °C	Foster, 2003	1595±6 Ma; 1595±6 Ma	Hand & Rubatto, 2002; Gautier et al., 2001
Cannington (Cloncurry Domain)	Sillimanite/K-Feldspar	665–690 °C	Foster & Rubenach, 2006	1577±5 Ma;	Hand & Rubatto, 2002
Cloncurry Domain	Sillimanite	600–690 °C	Rubenach, 1997; Foster, 2003; Foster & Rubenach, 2006	1570–1600 Ma; 1585–1600 Ma; 1584 Ma	Rubenach et al., 2008; Giles & Nutman, 2002; Page & Sun, 1998
Doherty Domain	Calc-silicate Biotite	500–520 °C			
Mitakoodi Domain	Lower Greenschist	510–530 ° C	Foster & Rubenach, 2006		
Tommy Creek Domain	Amphibolite	550–600 ° C	Foster & Rubenach, 2006	1575–1585 Ma	Hand & Rubatto, 2002
Central Belt					
Mary Kathleen Domain	Andalusite/Sillimanite	580–640 °C; 596 °C	Reinhardt, 1992; Foster, 2003	1570 Ma; 1590 Ma;	Hand & Rubatto, 2002; Blenkinsop 2005
Central Kalkadoon Domain	Mid-amphibolite	570–600 °C	Foster, 2002		

Rifle Creek Domain	Upper amphibolite	500 °C			
Western Belt					
Sybella Domain	Lower Sillimanite	570–600 °C	Rubenach, 1992	1575 Ma; 1584±3 Ma	Hand & Rubatto, 2002; Geoscience Australia

Table C.3.3. $^{40}Ar/^{39}Ar$ analytical data corrected for blank, mass discrimination and radioactive decay for Mount Isa Inlier. Bold numbers represent the steps used for plateau age calculation.

Step	36Ar	%1σ	37Ar	1%σ	38Ar	%1σ	39Ar	%1σ	40Ar	%1σ	Age	± 2σ	40Ar (r)	39Ar (k)	K/Ca	± 2σ
	[fA]		[fA]		[fA]		[fA]		[fA]		(Ma)		(%)	(%)		
SG01 **Hornblende**: J = 0.01078250 ± 0.00002264 (1σ)																
1	0.0000123	42.693	0.0005236	158.272	0.0000011	532.327	0.0000021	298.839	0.017322	0.517	0.00	± 13262.92	121.04	0.00	0.002	± 0.013
2	0.0000161	46.191	0.0003377	221.504	0.0000220	26.549	0.0004366	2.937	0.046968	0.181	1288.99	± 111.51	89.69	0.41	0.673	± 2.980
3	0.0000028	231.299	0.0012238	56.232	0.0000203	36.649	0.0010881	0.839	0.133943	0.146	1522.55	± 34.35	99.46	1.03	0.462	± 0.520
4	0.0000067	86.458	0.0023561	32.916	0.0000200	33.322	0.0011488	1.232	0.137579	0.149	1487.23	± 36.03	98.69	1.08	0.253	± 0.167
5	0.0000198	42.721	0.0198961	4.054	0.0001930	6.060	0.0086404	0.319	1.063500	0.037	1524.70	± 8.25	99.59	8.16	0.225	± 0.018
6	0.0000077	74.082	0.0082805	8.252	0.0000829	9.774	0.0035038	0.557	0.419361	0.035	1496.24	± 14.09	99.61	3.31	0.220	± 0.036
7	0.0000049	112.128	0.0098987	8.675	0.0000819	9.177	0.0038217	0.711	0.464655	0.064	1514.98	± 16.38	99.85	3.61	0.200	± 0.035
8	0.0000060	108.824	0.0010421	76.454	0.0000048	145.873	0.0002534	3.185	0.031450	0.234	1587.79	± 140.92	105.41	0.24	0.127	± 0.194
9	0.0000143	42.949	0.0339735	3.227	0.0003206	3.881	0.0141493	0.380	1.715408	0.031	1512.47	± 8.14	99.91	13.36	0.216	± 0.014
10	0.0000025	186.871	0.0019698	41.936	0.0000265	23.763	0.0010334	1.872	0.125920	0.168	1525.62	± 45.05	100.72	0.98	0.272	± 0.229
11	0.0000165	54.656	0.0569870	2.406	0.0005220	1.284	0.0233074	0.264	2.860119	0.022	1525.75	± 5.81	99.99	22.00	0.212	± 0.010
12	0.0000186	40.090	0.0494218	2.257	0.0004779	2.804	0.0202661	0.360	2.462050	0.035	1514.87	± 7.66	99.93	19.13	0.213	± 0.010

13	0.0000194	28.047	0.0295622	3.110	0.0002758	3.770	0.0119489	0.467	1.456715	0.086	1516.74	± 10.02	99.76	11.28	0.210	± 0.013
14	0.0000135	45.735	0.0355249	2.974	0.0003235	3.597	0.0137175	0.351	1.690858	0.039	1529.87	± 7.65	99.93	12.95	0.200	± 0.012
15	0.0000050	146.842	0.0061131	14.580	0.0000576	12.134	0.0026074	0.565	0.319042	0.081	1529.25	± 18.46	100.62	2.46	0.221	± 0.065
Step	36Ar	%1σ	37Ar	1%σ	38Ar	%1σ	39Ar	%1σ	40Ar	%1σ	Age	± 2σ	40Ar (r)	39Ar (k)	K/Ca	± 2σ
	[fA]		[fA]		[fA]		[fA]		[fA]		(Ma)		(%)	(%)		
CRS01 **Hornblende**: J = 0.01078250 ± 0.00002264 (1σ)																
1	0.0000032	148.263	0.0008257	84.234	0.0000010	413.982	0.0000264	21.500	0.0775982	0.274	6285.88	± 742.92	101.15	0.09	0.017	± 0.030
2	0.0000032	154.967	0.0002831	200.394	0.0000005	594.473	0.0000651	10.185	0.0504637	0.472	4008.12	± 341.65	98.09	0.21	0.120	± 0.481
3	0.0000041	124.584	0.0043912	13.592	0.0000306	12.434	0.0012533	0.897	0.1776736	0.124	1674.49	± 27.50	99.50	3.99	0.148	± 0.040
4	0.0000065	87.458	0.0061934	11.615	0.0000283	16.081	0.0015120	1.077	0.1786305	0.144	1479.93	± 29.39	99.18	4.81	0.127	± 0.030
5	0.0000064	77.161	0.0127932	4.200	0.0000437	13.503	0.0030286	0.653	0.3793020	0.143	1545.86	± 16.09	99.77	9.64	0.123	± 0.010
6	0.0000052	112.775	0.0267561	2.752	0.0000948	4.934	0.0058425	0.532	0.7059453	0.061	1512.33	± 12.13	100.08	18.59	0.113	± 0.006
7	0.0000089	58.965	0.0449288	1.256	0.0001613	5.032	0.0099966	0.266	1.1974335	0.045	1503.36	± 6.14	100.08	31.80	0.115	± 0.003
8	0.0000009	458.462	0.0112320	5.643	0.0000367	11.602	0.0026073	0.788	0.3085720	0.103	1493.99	± 18.10	100.37	8.30	0.120	± 0.014
9	0.0000019	282.669	0.0198500	3.439	0.0000557	9.655	0.0034136	0.405	0.4077076	0.088	1505.87	± 11.55	100.52	10.85	0.089	± 0.006
10	0.0000031	161.594	0.0030201	19.003	0.0000052	66.987	0.0003337	2.697	0.0401314	0.456	1539.25	± 94.28	102.90	1.06	0.057	± 0.022
11	0.0000012	457.083	0.0085118	8.924	0.0000144	32.941	0.0012878	1.110	0.1512189	0.139	1490.86	± 32.19	100.69	4.09	0.078	± 0.014
12	0.0000017	244.855	0.0104083	5.197	0.0000122	38.145	0.0012622	1.079	0.1513379	0.201	1515.11	± 27.96	100.87	4.01	0.063	± 0.007
13	0.0000018	267.849	0.0071418	9.653	0.0000038	120.753	0.0006643	1.510	0.0809307	0.256	1524.78	± 48.44	100.04	2.10	0.048	± 0.009
14	0.0000052	87.135	0.0021620	29.978	0.0000021	179.174	0.0001487	5.987	0.0212509	0.780	1624.90	± 195.84	93.52	0.47	0.035	± 0.022
Step	36Ar	%1σ	37Ar	1%σ	38Ar	%1σ	39Ar	%1σ	40Ar	%1σ	Age	± 2σ	40Ar (r)	39Ar (k)	K/Ca	± 2σ

	[fA]		[fA]		[fA]		[fA]		[fA]		(Ma)		(%)	(%)		
KLB1604 **Hornblende**: J = 0.01081180 ± 0.00000597 (1σ)																
1	0.0000004	1485.901	0.0002767	265.229	0.0000024	169.872	0.0000050	120.474	0.0158771	0.534	6374.74	± 4106.89	99.07	0.01	0.010	± 0.056
2	0.0000242	23.678	0.0001417	570.068	0.0000110	41.094	0.0000087	66.380	0.0429455	0.294	6926.78	± 2392.79	83.18	0.02	0.031	± 0.361
3	0.0000030	219.623	0.0002704	260.820	0.0000042	88.767	0.0000962	7.039	0.0316841	0.223	2700.94	± 265.72	97.13	0.23	0.185	± 0.967
4	0.0000017	365.622	0.0061345	12.295	0.0000176	26.068	0.0012103	1.081	0.2067980	0.062	1901.76	± 32.91	100.48	2.89	0.102	± 0.025
5	0.0000140	45.855	0.0529884	1.789	0.0001499	5.119	0.0096234	0.311	1.5938234	0.027	1860.12	± 7.80	100.00	22.94	0.094	± 0.003
6	0.0000027	274.709	0.0132040	6.671	0.0000341	16.628	0.0026178	0.736	0.4243067	0.035	1835.42	± 20.90	100.05	6.24	0.103	± 0.014
7	0.0000102	69.493	0.0568112	2.047	0.0001580	4.251	0.0105842	0.433	1.7285636	0.098	1844.74	± 10.68	100.08	25.23	0.097	± 0.004
8	0.0000029	259.109	0.0341306	3.063	0.0000877	7.307	0.0065296	0.431	1.0648025	0.053	1843.93	± 11.19	100.17	15.57	0.099	± 0.006
9	0.0000035	159.928	0.0116768	5.927	0.0000286	16.269	0.0020818	0.786	0.3345630	0.089	1825.00	± 21.53	99.97	4.96	0.092	± 0.011
10	0.0000073	93.189	0.0143514	4.959	0.0000447	11.155	0.0027710	0.605	0.4516339	0.119	1838.63	± 17.66	99.77	6.61	0.100	± 0.010
11	0.0000149	45.741	0.0069104	11.686	0.0000181	26.045	0.0013451	1.119	0.2170862	0.046	1856.15	± 33.66	102.30	3.21	0.101	± 0.024
12	0.0000080	70.942	0.0058334	12.372	0.0000172	23.565	0.0009495	1.758	0.1553369	0.118	1867.45	± 48.15	101.83	2.26	0.084	± 0.021
13	0.0000044	135.990	0.0155771	4.340	0.0000392	17.724	0.0025892	0.461	0.4241791	0.067	1847.68	± 14.53	99.98	6.17	0.086	± 0.008
14	0.0000036	169.669	0.0066517	14.732	0.0000190	24.659	0.0010589	1.074	0.1732778	0.106	1857.39	± 34.76	100.92	2.52	0.082	± 0.024
15	0.0000037	207.980	0.0039803	21.586	0.0000103	43.370	0.0004787	1.845	0.0771297	0.207	1851.76	± 80.84	101.85	1.14	0.062	± 0.027

Step	36Ar	%1σ	37Ar	1%σ	38Ar	%1σ	39Ar	%1σ	40Ar	%1σ	Age	± 2σ	40Ar (r)	39Ar (k)	K/Ca	± 2σ
	[fA]		[fA]		[fA]		[fA]		[fA]		(Ma)		(%)	(%)		
MLMB01 **Hornblende**: J = 0.01081180 ± 0.00000597 (1σ)																
1	0.0000040	179.756	0.0013080	95.974	0.0000009	426.574	0.0001269	5.404	0.0149550	0.346	1416.25	± 326.83	92.61	1.00	0.0501	± 0.0963
2	0.0000173	45.003	0.0363654	3.862	0.0000525	9.219	0.0025502	0.523	0.3086068	0.125	1515.16	± 19.20	99.25	20.04	0.0361	± 0.0028

3	0.0000137	59.170	0.0348450	4.118	0.0000503	14.765	0.0022726	0.376	0.2767815	0.098	1525.28	± 19.82	99.52	17.85	0.0336	± 0.0028
4	0.0000115	65.806	0.0417397	2.912	0.0000588	11.585	0.0027742	0.521	0.3393130	0.125	1534.03	± 17.76	99.96	21.79	0.0342	± 0.0020
5	0.0000004	1867.135	0.0065641	19.125	0.0000082	51.371	0.0005633	2.052	0.0666789	0.213	1504.44	± 80.17	100.60	4.44	0.0443	± 0.0170
6	0.0000015	519.537	0.0221694	5.603	0.0000301	19.149	0.0016660	1.337	0.2031458	0.129	1536.61	± 36.66	100.64	13.10	0.0387	± 0.0045
7	0.0000004	2248.587	0.0083961	14.588	0.0000071	62.643	0.0005694	1.400	0.0684942	0.307	1525.48	± 76.55	100.82	4.47	0.0349	± 0.0102
8	0.0000026	327.740	0.0166494	7.441	0.0000259	22.223	0.0011322	1.071	0.1312993	0.125	1484.01	± 44.35	100.42	8.90	0.0350	± 0.0053
9	0.0000015	507.607	0.0128625	9.981	0.0000208	25.567	0.0010689	1.268	0.1228409	0.132	1480.68	± 45.57	101.20	8.41	0.0429	± 0.0086

Step	36Ar	%1σ	37Ar	1%σ	38Ar	%1σ	39Ar	%1σ	40Ar	%1σ	Age	± 2σ	40Ar (r)	39Ar (k)	K/Ca	± 2σ
	[fA]		[fA]		[fA]		[fA]		[fA]		(Ma)		(%)	(%)		
LCG01 **Hornblende**: J = 0.01081180 ± 0.00000595 (1σ)																
1	0.0000362	15.000	0.0007260	69.107	0.0000232	19.045	0.0000261	21.743	0.0720022	0.226	5949.65	± 778.88	85.09	0.13	0.018	± 0.027
2	0.0000042	147.035	0.0018096	19.440	0.0000065	51.807	0.0001202	4.616	0.0265619	0.420	2166.33	± 218.45	95.80	0.59	0.034	± 0.014
3	0.0000042	134.037	0.0033920	14.547	0.0000369	15.355	0.0006273	1.313	0.0822021	0.147	1619.11	± 51.50	101.86	3.07	0.096	± 0.028
4	0.0000048	116.715	0.0008983	41.366	0.0000124	35.813	0.0002579	3.070	0.0324850	0.385	1603.79	± 123.12	104.60	1.27	0.149	± 0.124
5	0.0000006	927.607	0.0004154	95.075	0.0000009	469.585	0.0001232	5.203	0.0150905	0.610	1542.50	± 256.91	101.44	0.60	0.154	± 0.293
6	0.0000238	19.994	0.0443226	2.082	0.0003120	3.491	0.0057215	0.446	0.7408165	0.161	1583.50	± 10.86	99.52	28.00	0.067	± 0.003
7	0.0000041	149.156	0.0140197	7.527	0.0001178	4.964	0.0024074	0.763	0.3004865	0.070	1548.39	± 20.36	99.97	11.80	0.089	± 0.013
8	0.0000016	376.984	0.0004896	181.556	0.0000008	366.496	0.0001156	6.457	0.0149196	0.653	1551.77	± 288.90	97.11	0.57	0.122	± 0.445
9	0.0000025	227.588	0.0038575	22.835	0.0000143	27.714	0.0004865	1.738	0.0599797	0.385	1529.69	± 70.14	99.25	2.38	0.065	± 0.030
10	0.0000259	26.843	0.0828223	1.399	0.0005013	2.236	0.0095933	0.515	1.1970764	0.086	1549.49	± 11.53	99.90	46.92	0.060	± 0.002
11	0.0000059	92.884	0.0057026	16.093	0.0000240	15.188	0.0006480	1.617	0.0808420	0.383	1533.39	± 55.08	98.37	3.17	0.059	± 0.019
12	0.0000008	703.964	0.0014323	66.733	0.0000068	47.320	0.0003095	1.958	0.0406555	0.480	1598.33	± 98.07	99.69	1.52	0.112	± 0.150

Step	36Ar [fA]	%1σ	37Ar [fA]	1%σ	38Ar [fA]	%1σ	39Ar [fA]	%1σ	40Ar [fA]	%1σ	Age (Ma)	± 2σ	40Ar (r) (%)	39Ar (k) (%)	K/Ca	± 2σ
MMB03 **Hornblende**: J = 0.01081180 ± 0.00000595 (1σ)																
1	0.0000331	14.960	0.0001384	472.945	0.0000096	33.374	0.0000260	22.294	0.0170948	0.614	2514.94	± 825.46	42.31	0.14	0.0973	± 0.9215
2	0.0000123	39.344	0.0016306	43.678	0.0000192	26.152	0.0003318	2.715	0.0400859	0.357	1421.17	± 95.00	91.15	1.78	0.1055	± 0.0923
3	0.0000120	40.515	0.0062111	12.195	0.0000852	7.398	0.0010972	1.690	0.1245995	0.183	1427.34	±41.18	97.52	5.87	0.0915	± 0.0225
4	0.0000302	24.815	0.0653280	2.062	0.0006753	0.852	0.0075566	0.299	0.9126763	0.076	1512.52	± 8.13	99.58	40.34	0.0598	± 0.0025
5	0.0000053	121.811	0.0013914	51.714	0.0000262	16.869	0.0002717	1.969	0.0325249	0.226	1458.77	±129.87	95.51	1.45	0.1012	± 0.1047
6	0.0000040	140.500	0.0018567	37.586	0.0000264	19.350	0.0003311	1.675	0.0394587	0.328	1535.14	±92.14	103.40	1.77	0.0924	± 0.0695
7	0.0000020	261.613	0.0120934	7.080	0.0001019	5.667	0.0011709	1.316	0.1429671	0.171	1531.85	±35.65	100.26	6.24	0.0500	± 0.0072
8	0.0000173	33.274	0.0670481	1.699	0.0004727	2.231	0.0056745	0.235	0.6803226	0.084	1511.74	± 7.32	100.02	30.23	0.0436	± 0.0015
9	0.0000013	393.278	0.0013903	52.758	0.0000041	104.073	0.0001361	4.567	0.0161906	0.708	1534.10	±217.00	103.14	0.73	0.0505	± 0.0535
10	0.0000091	60.363	0.0103601	6.626	0.0000855	7.724	0.0010826	0.848	0.1294070	0.194	1491.84	±31.62	98.54	5.78	0.0540	± 0.0072
11	0.0000004	1656.241	0.0037863	18.527	0.0000181	25.970	0.0002926	2.828	0.0343253	0.367	1495.76	±118.95	100.57	1.56	0.0398	± 0.0149
12	0.0000057	120.884	0.0019088	33.878	0.0000097	37.610	0.0001853	3.566	0.0231527	0.317	1481.42	±206.92	93.27	0.99	0.0501	± 0.0342
13	0.0000029	219.969	0.0082050	8.828	0.0000392	14.586	0.0005892	1.450	0.0693964	0.215	1491.61	±64.14	99.68	3.13	0.0370	± 0.0066

Step	36Ar [fA]	%1σ	37Ar [fA]	1%σ	38Ar [fA]	%1σ	39Ar [fA]	%1σ	40Ar [fA]	%1σ	Age (Ma)	± 2σ	40Ar (r) (%)	39Ar (k) (%)	K/Ca	± 2σ
AMS01 **Hornblende**: J = 0.01081180 ± 0.00000597 (1σ)																
1	0.0000334	16.447	0.0009241	81.579	0.0000099	38.053	0.0001128	5.216	0.0181770	1.003	1061.90	± 330.58	45.61	0.55	0.063	± 0.103
2	0.0000347	15.663	0.0284676	3.271	0.0002219	4.150	0.0033173	0.849	0.4167995	0.120	1537.22	± 19.69	98.06	16.02	0.060	± 0.004
3	0.000015	38.184	0.0581522	1.662	0.0004779	2.191	0.0070907	0.604	0.8734809	0.072	1536.83	± 13.34	100.00	34.26	0.063	± 0.002

	5															
4	0.0000126	45.127	0.0574224	1.715	0.0004730	2.279	0.0070230	0.566	0.8617749	0.092	1533.74	± 12.61	100.09	33.94	0.063	± 0.002
5	0.0000057	84.513	0.0032842	19.289	0.0000243	14.542	0.0003515	2.106	0.0417888	0.452	1548.38	± 81.97	104.70	1.70	0.055	± 0.021
6	0.0000011	425.398	0.0038225	20.313	0.0000222	18.530	0.0003805	2.368	0.0458052	0.440	1528.64	± 80.27	101.39	1.84	0.051	± 0.021
7	0.0000091	54.399	0.0014607	59.966	0.0000110	30.192	0.0001219	5.224	0.0137643	1.445	1645.97	± 226.07	120.66	0.59	0.043	± 0.052
8	0.0000028	204.221	0.0029005	21.791	0.0000297	13.180	0.0004193	2.901	0.0508014	0.362	1540.33	± 92.17	102.12	2.03	0.075	± 0.033
9	0.0000007	725.716	0.0033255	21.744	0.0000438	10.223	0.0005448	1.981	0.0627677	0.358	1467.97	± 63.10	100.09	2.64	0.085	± 0.037
10	0.0000036	132.543	0.0002737	212.142	0.0000162	23.812	0.0002724	2.808	0.0280388	0.623	1316.74	± 113.69	96.20	1.32	0.517	± 2.194
11	0.0000087	58.126	0.0034862	20.259	0.0000436	10.064	0.0009171	1.244	0.0816645	0.279	1196.22	± 40.21	97.16	4.45	0.136	± 0.055
12	0.0000066	78.845	0.0003852	166.920	0.0000118	30.470	0.0001397	5.302	0.0160966	1.242	1332.42	± 231.41	87.62	0.68	0.189	± 0.631

Step	36Ar	%1σ	37Ar	1%σ	38Ar	%1σ	39Ar	%1σ	40Ar	%1σ	Age	± 2σ	40Ar (r)	39Ar (k)	K/Ca	± 2σ
	[fA]		[fA]		[fA]		[fA]		[fA]		(Ma)		(%)	(%)		
AML01 **Hornblende**: J = 0.01081180 ± 0.00000595 (1σ)																
1	0.0000626	10.928	0.0006746	96.752	0.0000100	36.195	0.0000178	31.952	0.0308757	0.466	3799.87	± 1126.43	39.34	0.07	0.014	± 0.029
2	0.0000137	40.460	0.0169568	4.529	0.0001681	3.678	0.0023100	0.807	0.2787827	0.158	1504.91	± 20.89	99.01	8.28	0.070	± 0.006
3	0.0000050	116.379	0.0149742	5.196	0.0001484	3.477	0.0021475	0.437	0.2571654	0.120	1505.60	± 16.73	99.88	7.70	0.074	± 0.008
4	0.0000066	90.642	0.0124947	6.299	0.0001260	6.814	0.0017313	0.638	0.2067247	0.085	1518.64	± 21.96	101.43	6.20	0.072	± 0.009
5	0.0000197	41.749	0.0495720	1.832	0.0004854	2.487	0.0071493	0.493	0.8508650	0.097	1498.18	± 11.85	99.77	25.62	0.075	± 0.003
6	0.0000152	46.600	0.0514085	1.602	0.0005104	2.175	0.0072908	0.273	0.8652342	0.144	1497.17	± 8.04	99.95	26.13	0.073	± 0.002
7	0.0000017	355.351	0.0061833	10.739	0.0000595	8.518	0.0009144	1.782	0.1126164	0.251	1535.42	± 50.16	99.98	3.28	0.077	± 0.017
8	0.0000018	336.755	0.0070515	10.505	0.0000722	7.473	0.0010266	0.676	0.1223993	0.157	1502.57	± 32.96	100.03	3.68	0.075	± 0.016
9	0.0000052	105.797	0.0107897	7.326	0.0001041	6.573	0.0015368	0.939	0.1845570	0.150	1523.05	± 26.69	101.30	5.51	0.074	± 0.011

10	0.0000024	222.863	0.0041132	16.162	0.0000387	9.010	0.0006098	1.554	0.0725955	0.318	1495.35	± 54.76	99.48	2.19	0.077	± 0.025
11	0.0000094	66.054	0.0072622	10.867	0.0000612	7.753	0.0009451	0.994	0.1143868	0.196	1548.31	± 38.88	102.95	3.39	0.067	± 0.015
12	0.0000031	161.407	0.0066238	9.789	0.0000558	7.674	0.0009389	1.367	0.1137019	0.212	1531.31	± 39.08	101.27	3.36	0.073	± 0.015
13	0.0000055	87.187	0.0080890	7.878	0.0000608	6.623	0.0009918	0.793	0.1179956	0.181	1520.69	± 29.78	101.94	3.55	0.063	± 0.010
14	0.0000030	193.650	0.0029093	23.560	0.0000111	35.560	0.0002950	2.752	0.0360425	0.409	1561.16	± 112.63	103.09	1.06	0.052	± 0.025

Step	36Ar	%1σ	37Ar	1%σ	38Ar	%1σ	39Ar	%1σ	40Ar	%1σ	Age	± 2σ	40Ar (r)	39Ar (k)	K/Ca	± 2σ
	[fA]		[fA]		[fA]		[fA]		[fA]		(Ma)		(%)	(%)		
CF05 **Muscovite**: J = 0.01078250 ± 0.00002264 (1σ)																
1	0.0000022	353.195	0.0000184	530.490	0.0000544	8.284	0.0048550	0.540	0.5638307	0.046	1466.90	± 13.67	99.88	33.05	137	± 1455
2	0.0000010	852.839	0.0000636	140.883	0.0001177	4.773	0.0090478	0.376	1.0594360	0.064	1476.61	± 9.01	100.03	61.59	74	± 208
3	0.0000008	844.679	0.0000342	344.240	0.0000029	120.301	0.0004055	2.340	0.0482667	0.137	1498.09	± 100.95	100.51	2.76	6	± 42
4	0.0000063	89.587	0.0000885	155.213	0.0000028	134.033	0.0003821	1.844	0.0464697	0.235	1556.49	± 82.57	104.07	2.60	2	± 7

Step	36Ar	%1σ	37Ar	1%σ	38Ar	%1σ	39Ar	%1σ	40Ar	%1σ	Age	± 2σ	40Ar (r)	39Ar (k)	K/Ca	± 2σ
	[fA]		[fA]		[fA]		[fA]		[fA]		(Ma)		(%)	(%)		
MnMs01 **Muscovite**: J = 0.01078250 ± 0.00002264 (1σ)																
1	0.0000026	189.216	0.0000479	200.077	0.0000038	89.821	0.0004739	2.190	0.0493334	0.244	1345.29	± 71.85	98.39	0.84	5.1	± 20.6
2	0.0000242	26.796	0.0000315	319.017	0.0000470	6.491	0.0034356	0.617	0.4143828	0.050	1488.53	± 15.84	98.26	6.10	56.7	± 362.0
3	0.0000019	261.966	0.0000093	986.847	0.0000237	16.517	0.0022357	0.694	0.2614564	0.072	1472.91	± 18.05	99.79	3.97	125.6	± 2479.2
4	0.0000025	186.116	0.0000147	673.111	0.0000727	6.997	0.0069202	0.309	0.8125719	0.037	1478.22	± 7.20	99.91	12.28	244.1	± 3285.6
5	0.0000038	162.175	0.0000651	142.447	0.0001904	7.251	0.0162405	0.237	1.9092287	0.050	1479.76	± 5.26	99.94	28.81	129.8	± 369.7
6	0.0000008	628.034	0.0000164	562.126	0.0000707	6.015	0.0050584	0.451	0.5924559	0.092	1476.20	± 10.51	99.96	8.97	160.6	± 1805.3
7	0.0000032	143.912	0.0000236	433.641	0.0000171	19.663	0.0012509	0.961	0.1431783	0.156	1446.80	± 27.41	99.33	2.22	27.5	± 238.9

8	0.0000018	267.670	0.0000734	148.488	0.0000355	10.950	0.0027471	0.898	0.3225868	0.060	1477.59	± 20.31	99.83	4.87	19.5	± 57.8
9	0.0000013	473.781	0.0000062	1846.934	0.0000297	10.577	0.0026649	1.155	0.3154494	0.075	1488.57	± 26.23	100.12	4.73	224.4	± 8287.5
10	0.0000044	112.256	0.0000906	121.994	0.0000087	41.959	0.0011737	0.727	0.1362356	0.095	1477.02	± 26.16	100.95	2.08	6.7	± 16.4
11	0.0000042	108.043	0.0000872	121.237	0.0000110	23.673	0.0006338	2.195	0.0735442	0.063	1449.72	± 57.64	98.28	1.12	3.8	± 9.2
12	0.0000008	598.951	0.0000358	287.179	0.0000034	77.906	0.0004834	2.045	0.0564919	0.242	1478.29	± 64.44	100.40	0.86	7.0	± 40.3
13	0.0000019	249.138	0.0001009	104.643	0.0000019	143.660	0.0004243	2.134	0.0500072	0.174	1494.27	± 72.36	101.14	0.75	2.2	± 4.6
14	0.0000001	5350.465	0.0001357	76.146	0.0000494	5.389	0.0040627	0.882	0.4862160	0.100	1498.50	± 18.99	100.00	7.21	15.6	± 23.7
15	0.0000019	279.437	0.0000276	340.717	0.0000526	9.391	0.0043851	0.550	0.5122262	0.057	1474.99	± 12.71	100.11	7.78	82.6	± 563.0
16	0.0000012	417.338	0.0001223	78.931	0.0000497	5.941	0.0038338	0.618	0.4552288	0.117	1489.62	± 14.52	99.92	6.80	16.3	± 25.7
17	0.0000007	757.724	0.0000577	172.559	0.0000044	57.849	0.0003372	1.999	0.0390433	0.339	1460.13	± 88.23	99.50	0.60	3.0	± 10.5

Step	36Ar	%1σ	37Ar	1%σ	38Ar	%1σ	39Ar	%1σ	40Ar	%1σ	Age	± 2σ	40Ar (r)	39Ar (k)	K/Ca	± 2σ
	[fA]		[fA]		[fA]		[fA]		[fA]		(Ma)		(%)	(%)		
LCF01 **Muscovite**: J = 0.01078250 ± 0.00002264 (1σ)																
1	0.0000179	91.445	0.0012862	95.554	0.0000602	10.655	0.0045277	0.399	0.5342363	0.099	1473.52	± 20.42	98.98	7.18	1.8	± 3.5
2	0.0000211	83.996	0.0005634	206.449	0.0004332	4.356	0.0366179	0.217	4.3186724	0.094	1482.12	± 5.39	99.85	58.07	33.8	± 139.6
3	0.0000073	230.201	0.0008178	143.089	0.0000497	10.603	0.0037720	0.359	0.4561086	0.093	1503.82	± 23.89	99.51	5.98	2.4	± 6.9
4	0.0000078	208.947	0.0005847	183.860	0.0000100	50.123	0.0012257	0.835	0.1455235	0.170	1473.34	± 70.88	98.36	1.94	1.1	± 4.0
5	0.0000023	728.087	0.0012243	98.764	0.0000014	332.080	0.0003133	3.467	0.0376022	0.279	1514.26	± 274.16	101.54	0.50	0.1	± 0.3
6	0.0000053	311.965	0.0003632	317.006	0.0000013	329.404	0.0004437	3.252	0.0533065	0.181	1473.17	± 201.47	97.11	0.70	0.6	± 4.0
7	0.0000055	297.263	0.0002134	487.284	0.0000081	70.736	0.0009550	0.873	0.1137260	0.198	1507.71	± 88.21	101.42	1.51	2.3	± 22.7
8	0.0000017	975.946	0.0004923	222.281	0.0000338	18.149	0.0028142	1.038	0.3350581	0.070	1491.93	± 36.29	99.86	4.46	3.0	± 13.2
9	0.0000030	542.275	0.0000424	2562.980	0.0000519	11.106	0.0036966	0.682	0.4372976	0.065	1488.78	± 26.66	100.21	5.86	45.3	± 2323.3

10	0.0000025	655.764	0.0002870	389.639	0.0000206	28.386	0.0014348	1.037	0.1743360	0.149	1518.65	± 61.29	100.44	2.27	2.6	± 20.3
11	0.0000027	621.755	0.0003417	354.231	0.0000148	33.576	0.0014033	0.833	0.1663868	0.127	1493.57	± 63.11	100.47	2.23	2.1	± 15.1
12	0.0000095	61.474	0.0004837	321.556	0.0000544	12.138	0.0037414	0.573	0.4445841	0.184	1484.55	± 14.62	99.35	5.93	4.0	± 25.9
13	0.0000008	630.874	0.0000967	1578.448	0.0000214	18.995	0.0016364	1.528	0.1926320	0.245	1480.54	± 35.13	99.88	2.59	8.8	± 277.8
14	0.0000007	837.823	0.0005033	312.776	0.0000088	50.803	0.0004781	1.473	0.0573523	0.285	1498.58	± 71.35	99.69	0.76	0.5	± 3.1

Step	36Ar	%1σ	37Ar	1%σ	38Ar	%1σ	39Ar	%1σ	40Ar	%1σ	Age	± 2σ	40Ar (r)	39Ar (k)	K/Ca	± 2σ
	[fA]		[fA]		[fA]		[fA]		[fA]		(Ma)		(%)	(%)		
KLB1602 **Biotite**: J = 0.01078250 ± 0.00002264 (1σ)																
1	0.0000273	17.461	0.0000969	88.698	0.0000417	9.918	0.0033062	0.647	0.3431576	0.078	1335.04	± 14.70	97.62	8.88	18	± 31
2	0.0000169	23.830	0.0000460	160.051	0.0001037	4.806	0.0085277	0.336	0.9801058	0.047	1452.46	± 7.22	99.48	22.90	96	± 308
3	0.0000181	25.666	0.0001398	56.529	0.0001346	4.339	0.0103982	0.262	1.1979794	0.041	1455.51	± 5.79	99.55	27.93	39	± 44
4	0.0000056	73.715	0.0000725	105.729	0.0000833	6.322	0.0070982	0.334	0.8155072	0.065	1455.20	± 7.44	99.79	19.06	51	± 108
5	0.0000042	102.590	0.0000242	283.087	0.0000223	11.810	0.0021294	0.929	0.2441956	0.054	1450.30	± 21.31	99.49	5.72	46	± 259
6	0.0000069	52.823	0.0000308	208.811	0.0000324	12.463	0.0027443	0.793	0.3126211	0.096	1442.16	± 17.35	99.34	7.37	46	± 193
7	0.0000062	78.449	0.0002132	39.985	0.0000149	31.301	0.0019008	0.519	0.2186228	0.109	1450.01	± 17.04	99.16	5.10	5	± 4
8	0.0000027	165.708	0.0000348	231.370	0.0000047	55.472	0.0001896	2.513	0.0216002	0.242	1410.51	± 136.17	96.23	0.51	3	± 13
9	0.0000008	517.226	0.0000341	298.645	0.0000024	126.925	0.0003573	2.518	0.0440254	0.296	1533.97	± 79.23	100.55	0.96	5	± 33
10	0.0000000	20287.090	0.0001091	56.785	0.0000026	160.968	0.0002368	2.463	0.0285174	0.608	1504.63	± 98.06	99.99	0.64	1	± 1
11	0.0000031	123.905	0.0001293	66.325	0.0000024	131.216	0.0003435	1.671	0.0402418	0.350	1453.21	± 66.83	97.71	0.92	1	± 2

Step	36Ar	%1σ	37Ar	1%σ	38Ar	%1σ	39Ar	%1σ	40Ar	%1σ	Age	± 2σ	40Ar (r)	39Ar (k)	K/Ca	± 2σ
	[fA]		[fA]		[fA]		[fA]		[fA]		(Ma)		(%)	(%)		
KG03 **Biotite**: J = 0.01078250 ± 0.00002264 (1σ)																

1	0.0000024	180.408	0.0001450	110.097	0.0000118	31.552	0.0007827	1.307	0.046927	0.265	891.18	± 43.12	98.52	0.84	2.8	± 6.2
2	0.0000053	80.434	0.0000962	170.337	0.0001317	6.064	0.0080872	0.320	0.885794	0.070	1408.24	± 7.00	99.82	8.67	43.7	± 148.9
3	0.0000045	105.644	0.0000688	245.165	0.0000123	28.620	0.0011148	1.131	0.135301	0.089	1522.97	± 31.54	100.99	1.19	8.4	± 41.3
4	0.0000051	80.487	0.0000165	996.329	0.0000615	6.864	0.0038251	0.798	0.471577	0.100	1532.27	± 17.47	100.32	4.10	120.8	± 2408.1
5	0.0000106	38.644	0.0000276	605.423	0.0000915	6.568	0.0061389	0.519	0.756477	0.052	1532.76	± 11.29	100.42	6.58	115.8	± 1402.0
6	0.0000091	55.434	0.0000790	206.594	0.0002339	3.551	0.0146012	0.158	1.809209	0.083	1535.70	± 4.08	100.15	15.65	96.1	± 397.3
7	0.0000055	84.586	0.0001404	118.324	0.0001168	5.444	0.0074145	0.810	0.916934	0.091	1534.02	± 17.15	100.18	7.95	27.5	± 65.0
8	0.0000082	84.943	0.0016429	11.114	0.0004516	1.414	0.0300939	0.283	3.735820	0.045	1535.45	± 6.03	99.94	32.26	9.5	± 2.1
9	0.0000037	122.059	0.0030253	6.080	0.0002550	4.781	0.0167461	0.428	2.051981	0.050	1522.34	± 8.98	99.96	17.95	2.9	± 0.4
10	0.0000011	417.591	0.0015685	12.269	0.0000485	7.643	0.0028897	0.929	0.360358	0.080	1542.47	± 20.92	100.13	3.10	1.0	± 0.2
11	0.0000005	893.434	0.0008411	21.715	0.0000227	14.156	0.0016058	1.036	0.198261	0.122	1530.43	± 25.32	99.96	1.72	1.0	± 0.4

Step	36Ar	%1σ	37Ar	1%σ	38Ar	%1σ	39Ar	%1σ	40Ar	%1σ	Age	± 2σ	40Ar (r)	39Ar (k)	K/Ca	± 2σ
	[fA]		[fA]		[fA]		[fA]		[fA]		(Ma)		(%)	(%)		
WG01 **Biotite**: J = 0.01078250 ± 0.00002264 (1σ)																
1	0.0000165	26.483	0.0000166	501.289	0.0000278	13.860	0.0013150	1.183	0.1395496	0.120	1344.76	± 29.13	96.46	2.26	41	± 413
2	0.0000082	61.161	0.0000056	1519.933	0.0001639	5.498	0.0087490	0.808	1.0358491	0.083	1485.13	± 16.71	99.76	15.05	814	± 24739
3	0.0000024	228.338	0.0000450	187.010	0.0000427	9.064	0.0022388	0.438	0.2635637	0.091	1484.53	± 15.27	100.27	3.85	26	± 97
4	0.0000025	206.164	0.0001610	58.168	0.0001843	6.455	0.0109018	0.496	1.2836003	0.171	1481.36	± 10.89	99.94	18.76	35	± 41
5	0.0000031	169.029	0.0002344	41.566	0.0001835	3.409	0.0100642	0.479	1.1978095	0.065	1493.68	± 10.20	100.08	17.32	22	± 19
6	0.0000041	122.103	0.0000068	1257.959	0.0000967	6.474	0.0058436	0.501	0.6945747	0.053	1493.29	± 11.11	100.17	10.05	446	± 11211
7	0.0000029	215.442	0.0000348	323.862	0.0000423	12.237	0.0022834	0.820	0.2743766	0.094	1499.33	± 21.94	99.68	3.93	34	± 221
8	0.000004	116.293	0.0000764	111.987	0.0000712	6.159	0.0041536	0.612	0.4935965	0.089	1488.79	± 13.85	99.75	7.15	28	± 63

	1															
9	0.0000006	649.310	0.0000520	157.310	0.0001232	7.085	0.0075588	0.635	0.8966268	0.175	1489.24	± 13.64	99.98	13.01	76	± 238
10	0.0000077	51.383	0.0000705	114.078	0.0000486	10.475	0.0032080	0.534	0.3770218	0.078	1486.21	± 12.65	100.61	5.52	24	± 54
11	0.0000031	138.211	0.0000243	330.004	0.0000040	69.936	0.0001944	2.775	0.0228556	0.420	1521.41	± 125.14	104.07	0.33	4	± 27
12	0.0000029	162.754	0.0000534	163.221	0.0000197	12.714	0.0010543	1.203	0.1252159	0.153	1483.70	± 33.44	99.31	1.81	10	± 34
13	0.0000014	283.604	0.0000862	99.959	0.0000071	38.787	0.0003881	1.966	0.0470756	0.284	1521.12	± 66.55	100.89	0.67	2	± 5
14	0.0000036	128.625	0.0001070	79.315	0.0000016	169.888	0.0001665	3.577	0.0201124	0.409	1451.13	± 162.72	94.58	0.29	1	± 1

Appendix D:
Supplementary materials to Chapter 4

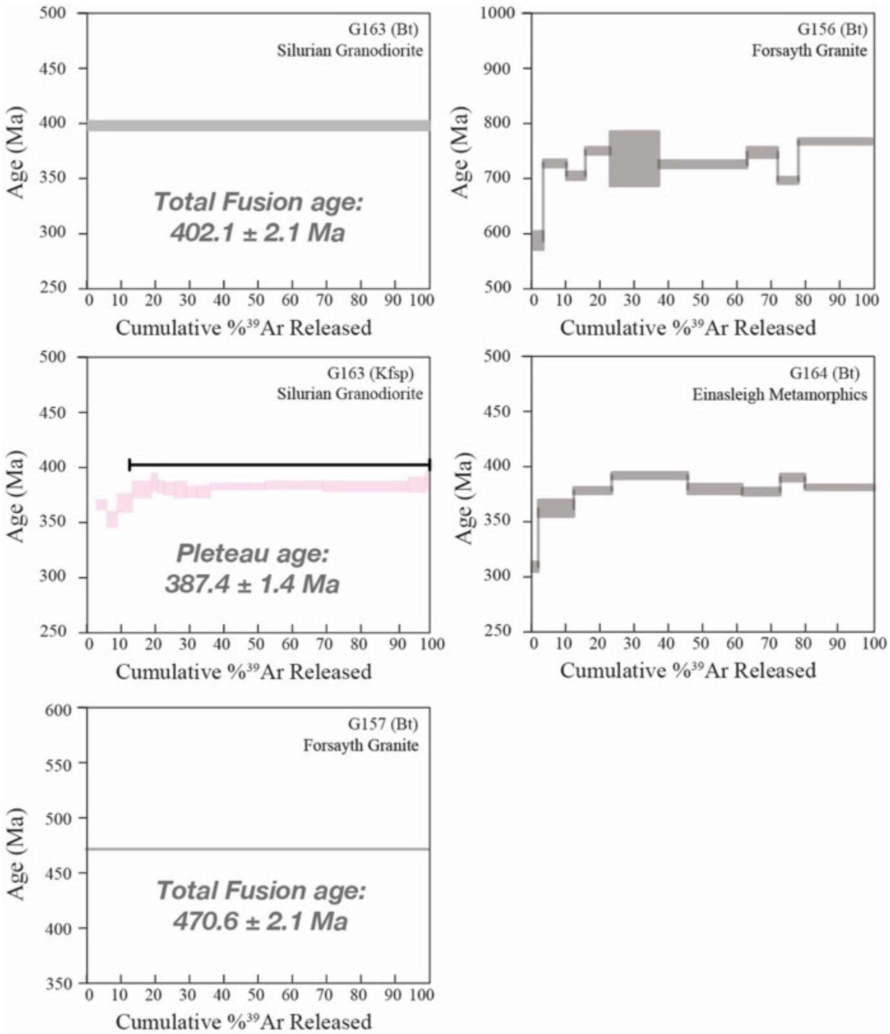

Fig. D.4.16: $^{40}Ar/^{39}Ar$ age spectra recalculated from Spikings et al., (2001) using updated argon decay constant. Spectra shown in black and pink each represent the argon dating on biotite and K-feldspar, respectively. Specific sample information including sample lithology, locations, and stratigraphic positions are listed in Table D.4.1.

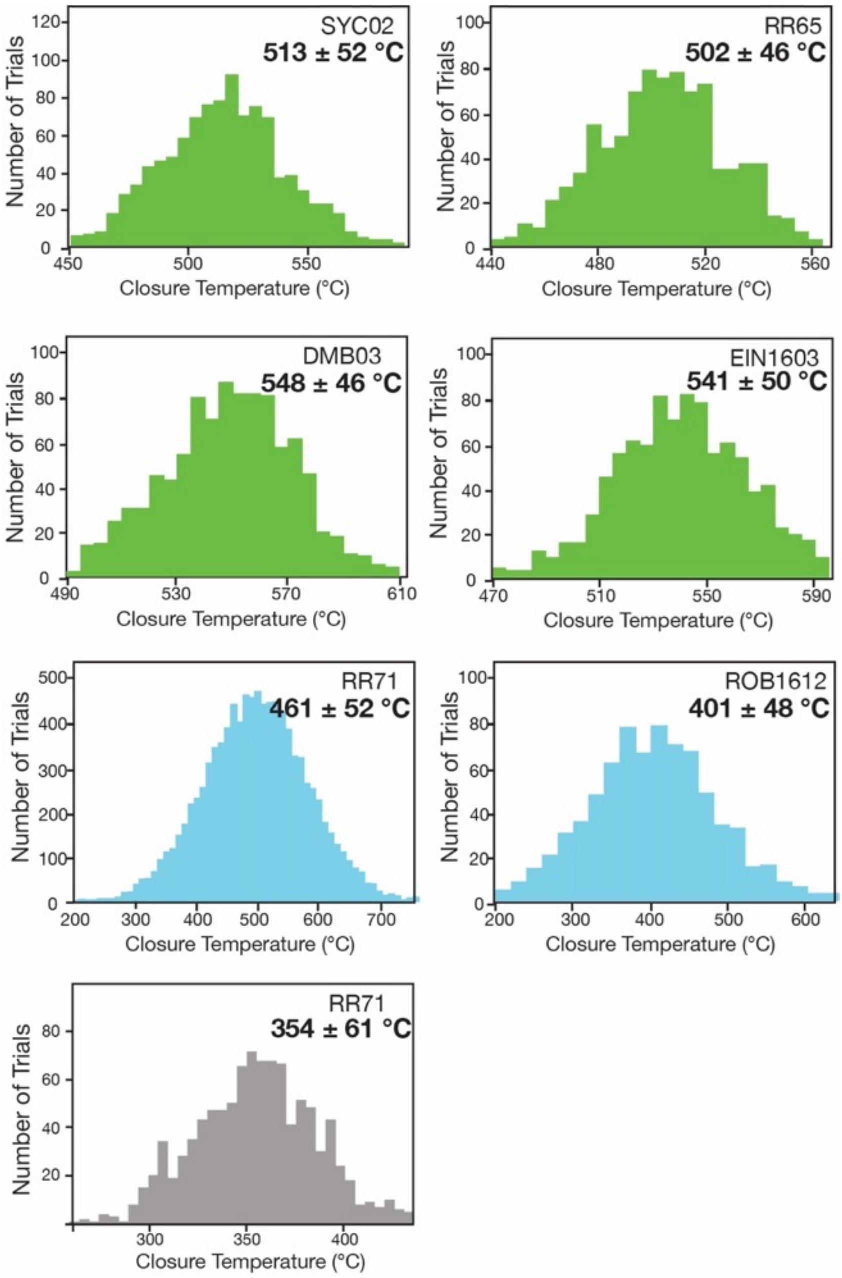

Fig. D.4.17: Probability diagrams of Monte Carlo simulation for 10,000 computations of the argon closure temperature in hornblende, biotite, and muscovite from this study. The closure temperature values are reported at mean with 2 standard deviations

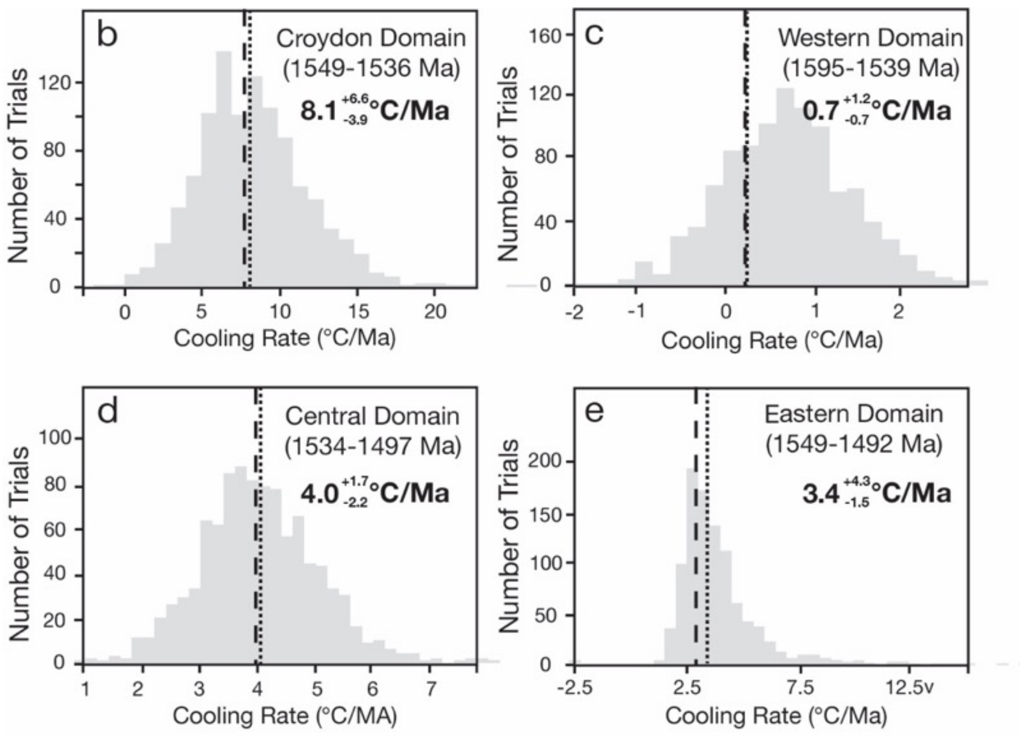

Fig. D.4.18: Probability diagrams of Monte Carlo simulation for 10,00 computation of the cooling rate between peak metamorphism to argon closure in hornblende, muscovite and biotite at different cooling stages. Cooling stage calculated in each domain include magmatism-muscovite (a); muscovite–biotite (b); peak metamorphism–hornblende (c, d & e). The cooling rate values are reported at median value and 90% inter-percentile range, between 5% and 95% ($^{I_3}_{I_1}$), for measuring such a tendency of a shewed population. Specific values for different stage are list in Table 1 in the main text. The dashed and dot line each represents the approximate location of the population median and mean.

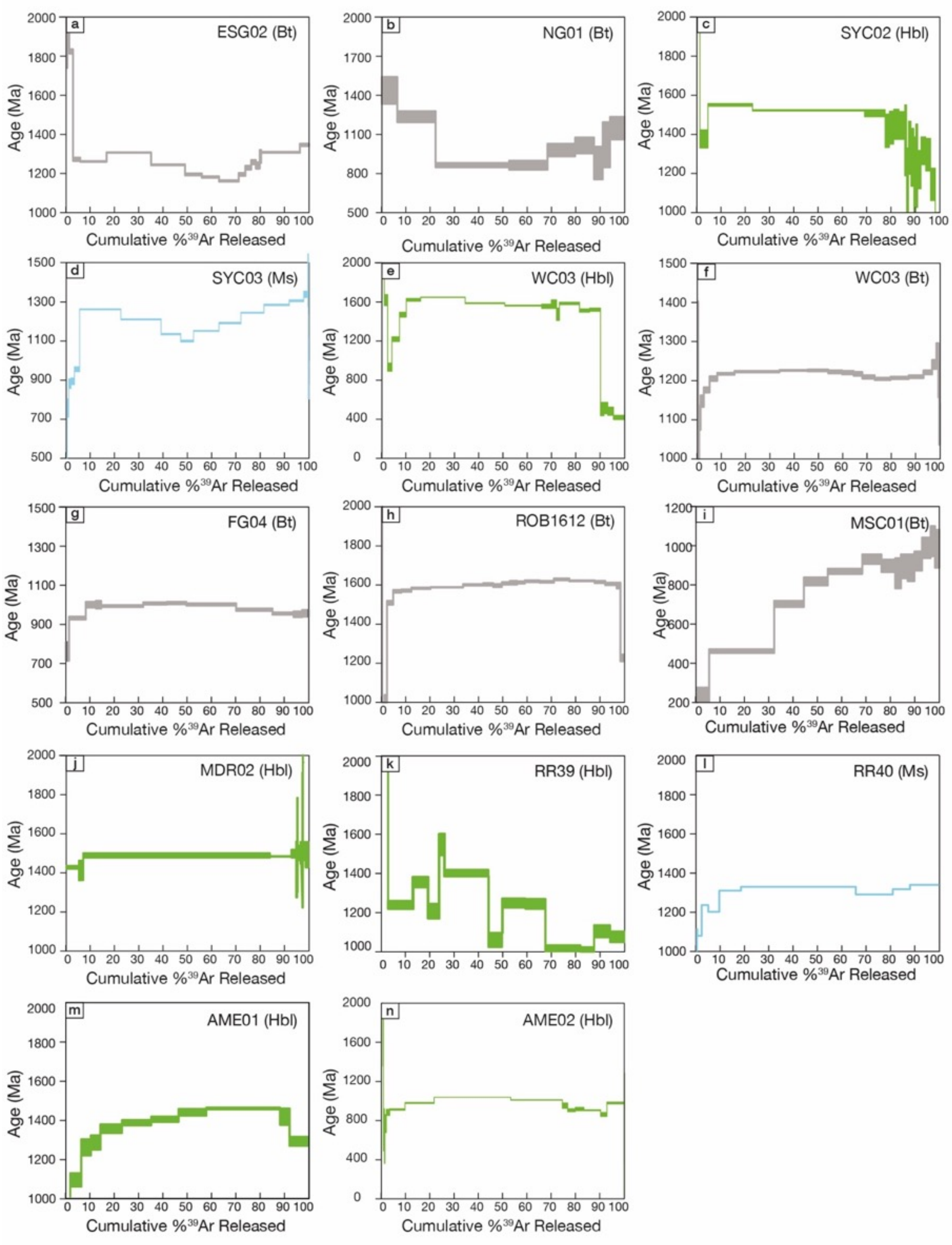

Fig. D.4.19: ^{40}Ar/^{39}Ar total fusion ages discard in this study. Spectra shown in green, blue and gray each represent the argon dating with hornblende, muscovite and biotite, respectively. Specific sample information including sample lithology, locations, and stratigraphic positions are listed in Table 4.1 of the main text.

Table D.4.1: Previously published argon thermochronology results from the Georgetown Inlier

G163

Sample ID	Mineral	Method	Lithology	Domain	Age (Ma)	Age type	Reference	Latitude	Longitude	Age interpretation
N/A	Muscovite	K/Ar	N/A	N/A	439	N/A	Richards et al., 1966	N/A	N/A	Thermal disturbance
N/A	Biotite	K/Ar	N/A	N/A	421	N/A	Richards et al., 1996	N/A	N/A	Thermal disturbance
73300487	Hornblende	$^{40}Ar/^{39}Ar$	Einasleigh Metamorphics	Eastern	1444	N/A	Black et al., 1979	N/A	N/A	Cooling
73300476	Muscovite	$^{40}Ar/^{39}Ar$	Einasleigh Metamorphics	Eastern	415	N/A	Black et al., 1979	N/A	N/A	Cooling
73303007	Muscovite	$^{40}Ar/^{39}Ar$	Lower Etheridge	Central	1456	TF	Black et al., 1979	N/A	N/A	Cooling
73303008	Muscovite	$^{40}Ar/^{39}Ar$	Lower Etheridge	Central	1478	TF	Black et al., 1979	N/A	N/A	Cooling
73303005	Biotite	$^{40}Ar/^{39}Ar$	Forsayth Batholith	Central	297	N/A	Black et al., 1979	N/A	N/A	Cooling
N/A	Muscovite	K/Ar	Einasleigh Metamorphics	Eastern	414–410 ± 12	N/A	McNaughton & Wilson, 1983	N/A	N/A	N/A
N/A	Biotite	K/Ar	Awring Granodiorite	Central	281 ± 3	N/A	MacKenzie, 1987	N/A	N/A	N/A
G164	Biotite	$^{40}Ar/^{39}Ar$	Gneiss	Eastern	380	TF	Spikings et al., 2001	-18.220	144.108	Cooling
G157	Biotite	$^{40}Ar/^{39}Ar$	Granite	Central	471	TF	Spikings et al., 2001	-18.292	143.406	Cooling
G163	Biotite	$^{40}Ar/^{39}Ar$	Granodiorite	Eastern	402	Plateau	Spikings et al., 2001	-18.273	143.841	Cooling
G156	Biotite	$^{40}Ar/^{39}Ar$	Forsayth Granite	Central	735	TF	Spikings et al., 2001	-18.383	143.521	Cooling

Table D.4.2: Summary of published geochronological constraints and temperature conditions estimated for each metamorphic stage for each domain.

Location	Metamorphic stage	Metamorphism temperature (°C)	Reference	Metamorphism age	Reference
Western Domain					
	M1 static growth of andalusite	500–550 °C	Bell and Rubenach, 1983	1.60 Ga	Volante et al., 2020a
	M1 static growth of andalusite	550–580 °C	Volante et al., 2020a	1.60 Ga	Volante et al., 2020a
Central Domain					
	M1 medium- *P* (*MP*) medium-*T (MT) stage*	600–650 °C	Boger and Hansen, 2004; Hills, 2004	1.60 Ga	Volante et al., 2020a
	M2 *low-P (LP)*–high-*T* (*HT*) *stage*	600–650 °C	Boger and Hansen, 2004	1.56-1.55 Ga	Black et al., 1998; Neumann and Kositcin, 2011
	M1 *MP-MT stage*	530–550 °C	Cihan et al., 2006	1.66-1.58 Ga	Cihan et al., 2006
	M2 *LP-HT stage*	600–620 °C	Cihan et al., 2006	1.55-1.51 Ga	Cihan et al., 2006
	M1 *MP-MT stage*	530-570 °C	Pourteau et al., 2018	1.60 Ga	Pourteau et al., 2018;
	M1 *MP-MT stage*	530–550 °C	Volante et al., 2020a	1.60 Ga	Volante et al., 2020a, 2020b
	M2 *LP-HT stage*	620–650 °C	Volante et al., 2020a	1.55 Ga	Volante et al., 2020a
Eastern Domain					
Einasleigh	M2 *MP-HT stage*	700–800 °C	Boger & Hansen, 2004	1.55 Ga	Black et al., 2005; Neumann & Kositcin, 2011.

Table D.4.3: $^{40}Ar/^{39}Ar$ analytical data from the North Queensland corrected for blanks, mass discrimination, and radioactive decay.

Step	36Ar [fA]	%1σ	37Ar [fA]	1%σ	38Ar [fA]	%1σ	39Ar [fA]	%1σ	40Ar [fA]	%1σ	40(r)/39(K)	± 2σ	Age (Ma)	± 2σ	40Ar (r) (%)	39Ar (k) (%)	K/Ca	± 2σ
ESG02 **Muscovite**: J = 0.01057910 ± 0.00000476 (1σ)																		
1	0.0000041	70.771	0.0046753	68.074	0.0000786	46.052	0.0002281	4.946	0.041500	2.319	172.54030	± 20.56056	1877.99	± 139.20	96.19	0.15	0.0	± 0.0
2	0.0000099	28.951	0.0055639	85.225	0.0000107	340.393	0.0010163	1.322	0.367528	0.262	356.91235	± 10.03281	2827.17	± 40.18	99.07	0.68	0.1	± 0.2
3	0.0000037	78.092	0.0061976	74.177	0.0000499	79.007	0.0024734	0.387	0.406833	0.237	164.52358	± 1.72624	1822.88	± 12.05	99.85	1.64	0.2	± 0.3
4	0.0000034	85.832	0.0049671	67.624	0.0000559	57.201	0.0043066	0.331	0.416399	0.231	96.28462	± 0.89172	1270.06	± 8.45	99.66	2.87	0.5	± 0.6
5	0.0000080	36.087	0.0007688	713.822	0.0002284	17.999	0.0164111	0.099	1.565343	0.062	95.23076	± 0.25493	1260.05	± 2.43	99.84	10.92	11.1	± 158.5
6	0.0000122	23.665	0.0004539	1002.737	0.0004444	9.176	0.0276129	0.073	2.763534	0.035	99.95108	± 0.17670	1304.47	± 1.64	99.87	18.38	31.6	± 634.4
7	0.0000070	41.130	0.0028158	126.816	0.0002992	11.359	0.0210686	0.070	1.967872	0.049	93.32207	± 0.18352	1241.77	± 1.77	99.90	14.02	3.9	± 9.9
8	0.0000051	56.240	0.0053112	77.243	0.0001486	23.619	0.0104539	0.166	0.925367	0.105	88.30040	± 0.39175	1192.77	± 3.87	99.79	6.96	1.0	± 1.6
9	0.0000046	62.061	0.0005149	655.612	0.0001575	23.760	0.0107341	0.168	0.934154	0.103	86.90468	± 0.38278	1178.91	± 3.81	99.86	7.15	10.8	± 142.1
10	0.0000030	96.633	0.0026932	162.329	0.0000887	41.380	0.0120093	0.150	1.019817	0.095	84.87599	± 0.34065	1158.58	± 3.43	99.93	7.99	2.3	± 7.5
11	0.0000018	163.329	0.0037179	88.946	0.0001093	32.830	0.0042738	0.263	0.378715	0.254	88.36882	± 0.77709	1193.45	± 7.68	99.78	2.85	0.6	± 1.1
12	0.0000005	526.903	0.0009645	431.133	0.0000273	139.950	0.0035431	0.354	0.325189	0.296	91.69500	± 1.00577	1226.04	± 9.77	99.93	2.36	1.9	± 16.5
13	0.0000028	102.918	0.0002884	1291.559	0.0000445	91.192	0.0031115	0.339	0.295724	0.326	94.76075	± 1.07731	1255.56	± 10.29	99.71	2.07	5.6	± 144.9
14	0.0000022	132.580	0.0032752	134.557	0.0000122	351.714	0.0021197	0.560	0.197094	0.488	92.89547	± 1.65877	1237.65	± 16.00	99.80	1.41	0.3	± 0.9
15	0.0000058	49.739	0.0023500	164.194	0.0000919	40.759	0.0009962	1.226	0.098878	0.974	97.87938	± 3.62877	1285.11	± 34.10	98.45	0.66	0.2	± 0.7
16	0.0000169	17.242	0.0015455	204.963	0.0003630	9.964	0.0241371	0.071	2.420627	0.040	100.06711	± 0.18008	1305.55	± 1.67	99.79	16.07	8.1	± 33.3
17	0.0000265	10.894	0.0023413	169.906	0.0000978	38.815	0.0057189	0.191	0.604336	0.159	104.22837	± 0.61985	1343.81	± 5.64	98.66	3.81	1.3	± 4.3

Step	36Ar	%1σ	37Ar	1%σ	38Ar	%1σ	39Ar	%1σ	40Ar	%1σ	40(r)/39(K)	± 2σ	Age	± 2σ	40Ar (r)	39Ar (k)	K/Ca	± 2σ
	[fA]		[fA]		[fA]		[fA]		[fA]				(Ma)		(%)	(%)		
NG01 **Biotite**: J = 0.01078250 ± 0.00002264 (1σ)																		
1	0.0000904	7.501	0.0009651	13.866	0.0000275	15.846	0.0003854	2.076	0.0702875	0.213	112.69682	± 11.55134	1438.06	± 101.67	61.69	6.20	0.207	± 0.058
2	0.0001400	4.461	0.0029110	5.217	0.0000467	10.145	0.0009906	1.223	0.1316051	0.212	91.08054	± 4.42119	1237.04	± 43.49	68.41	15.94	0.177	± 0.019
3	0.0000208	19.605	0.0039164	4.026	0.0000292	19.367	0.0018847	0.558	0.1128464	0.158	56.82205	± 1.45453	864.12	± 17.58	94.77	30.34	0.250	± 0.020
4	0.0000069	65.024	0.0028010	6.262	0.0000105	48.533	0.0009695	0.894	0.0568306	0.262	56.83257	± 2.96854	864.24	± 35.89	96.76	15.60	0.180	± 0.023
5	0.0000081	56.302	0.0021085	6.570	0.0000096	52.944	0.0007088	1.277	0.0494359	0.240	66.71563	± 4.21179	979.93	± 47.76	95.46	11.40	0.174	± 0.023
6	0.0000051	68.307	0.0020305	7.784	0.0000065	69.300	0.0004859	2.348	0.0352818	0.346	69.98783	± 5.45830	1016.66	± 60.65	96.11	7.81	0.124	± 0.020
7	0.0000070	53.614	0.0013431	10.551	0.0000025	181.947	0.0002282	2.596	0.0152124	0.630	58.17600	± 10.38597	880.41	± 124.43	86.91	3.66	0.088	± 0.019
8	0.0000040	119.441	0.0013851	11.296	0.0000001	3930.140	0.0001897	3.018	0.0143598	0.652	70.42773	± 15.57055	1021.54	± 172.54	92.54	3.04	0.071	± 0.017
9	0.0000052	88.648	0.0032960	5.611	0.0000071	62.968	0.0003750	2.490	0.0319880	0.424	82.35419	± 8.48746	1149.10	± 87.65	95.96	6.01	0.059	± 0.007

Step	36Ar	%1σ	37Ar	1%σ	38Ar	%1σ	39Ar	%1σ	40Ar	%1σ	40(r)/39(K)	± 2σ	Age	± 2σ	40Ar (r)	39Ar (k)	K/Ca	± 2σ
	[fA]		[fA]		[fA]		[fA]		[fA]				(Ma)		(%)	(%)		
NG71 **Muscovite**: J = 0.01057910 ± 0.00000476 (1σ)																		
1	0.0000001	2278.492	0.0030062	148.179	0.0000316	158.600	0.0000590	17.306	0.0066110	9.523	103.85752	± 46.75813	1340.43	± 426.17	96.04	0.08	0.01	± 0.03
2	0.0000011	154.772	0.0010132	440.136	0.0000427	110.144	0.0013814	0.800	0.1761895	0.358	127.41940	± 2.48300	1543.36	± 20.23	99.85	1.83	0.71	± 6.24
3	0.0000048	36.958	0.0035909	130.603	0.0001641	34.785	0.0058299	0.168	0.7458803	0.085	127.79833	± 0.54967	1546.45	± 4.47	99.85	7.73	0.84	± 2.20
4	0.0000047	39.748	0.0037516	116.832	0.0001685	25.916	0.0086305	0.144	1.1100384	0.057	128.52818	± 0.43574	1552.37	± 3.53	99.90	11.44	1.20	± 2.79
5	0.0000193	9.347	0.0016314	275.250	0.0005132	8.952	0.0373197	0.042	4.7844946	0.014	128.05558	± 0.11990	1548.54	± 0.97	99.88	49.50	11.90	± 65.48
6	0.0000063	28.522	0.0024193	239.012	0.0001485	29.233	0.0074947	0.130	0.9612710	0.066	128.06340	± 0.44033	1548.60	± 3.58	99.82	9.94	1.61	± 7.70

7	0.0000032	57.335	0.0028599	158.035	0.0001342	36.188	0.0055634	0.179	0.7121493	0.089	127.92214	± 0.58017	1547.45	± 4.72	99.90	7.38	1.01	± 3.20
8	0.0000014	129.330	0.0002247	2385.444	0.0000943	48.493	0.0025372	0.412	0.3274932	0.192	128.89704	± 1.34772	1555.36	± 10.91	99.87	3.37	5.87	± 280.10
9	0.0000008	223.950	0.0008597	666.311	0.0000274	165.537	0.0015892	0.673	0.2036669	0.310	128.10079	± 2.18736	1548.90	± 17.77	99.92	2.11	0.96	± 12.81
10	0.0000001	1478.790	0.0047606	98.159	0.0000492	108.009	0.0009509	1.072	0.1211065	0.521	128.16206	± 3.46810	1549.40	± 28.16	100.28	1.26	0.10	± 0.20
11	0.0000015	119.280	0.0002848	1642.770	0.0000860	53.150	0.0007706	1.519	0.1003409	0.628	129.67057	± 4.72683	1561.61	± 38.12	99.56	1.02	1.41	± 46.22
12	0.0000007	279.765	0.0000460	12856.318	0.0000169	274.678	0.0005114	2.309	0.0659770	0.956	128.64581	± 7.32422	1553.33	± 59.34	99.71	0.68	5.78	± 1486.45
13	0.0000024	77.743	0.0027226	196.417	0.0000135	323.334	0.0003872	2.385	0.0501680	1.255	126.58112	± 8.06629	1536.52	± 65.96	98.17	0.52	0.07	± 0.29
14	0.0000034	52.182	0.0016957	281.209	0.0000137	311.921	0.0005970	1.644	0.0781278	0.806	129.62203	± 5.44076	1561.22	± 43.89	98.86	0.79	0.18	± 1.03
15	0.0000063	29.201	0.0014773	383.289	0.0000468	100.218	0.0000487	20.033	0.0079535	7.917	120.03945	± 63.47878	1482.22	± 534.94	75.02	0.07	0.02	± 0.13
16	0.0000051	35.280	0.0008237	543.647	0.0000013	3913.211	0.0002462	5.043	0.0261498	2.408	99.53083	± 12.64669	1300.56	± 117.84	93.92	0.33	0.16	± 1.69
17	0.0000218	8.559	0.0031912	138.760	0.0000554	98.932	0.0007407	1.806	0.0866835	0.727	107.57304	± 4.67193	1373.99	± 41.80	92.20	0.99	0.12	± 0.34
18	0.0000218	8.559	0.0031912	138.760	0.0000554	98.932	0.0007407	1.806	0.0866835	0.727	107.57304	± 4.67193	1373.99	± 41.80	92.20	0.99	0.12	± 0.34

Step	36Ar	%1σ	37Ar	1%σ	38Ar	%1σ	39Ar	%1σ	40Ar	%1σ	40(r)/39(K)	± 2σ	Age	± 2σ	40Ar(r)	39Ar (k)	K/Ca	± 2σ
	[fA]		[fA]		[fA]		[fA]		[fA]				(Ma)		(%)	(%)		
NG71 **Biotite**: J = 0.01057910 ± 0.00000476 (1σ)																		
1	0.0000003	322.177	0.0071168	57.970	0.0000572	87.929	0.0000124	120.759	0.001186	62.651	96.14734	± 195.82220	0.00	± 218385.61	140.86	0.02	0.00	± 0.00
2	0.0000009	105.230	0.0024369	229.094	0.0000093	542.245	0.0000123	124.230	0.002775	26.785	255.71737	± 779.75315	2368.24	± 4025.53	97.46	0.01	0.00	± 0.01
3	0.0000007	129.052	0.0019968	203.899	0.0000345	143.695	0.0002266	7.609	0.030070	2.474	130.25205	± 21.34044	1566.29	± 171.67	98.75	0.26	0.06	± 0.24
4	0.0000005	198.276	0.0008509	517.760	0.0000171	264.679	0.0002546	6.033	0.033100	2.246	128.88727	± 17.21970	1555.28	± 139.36	99.38	0.29	0.16	± 1.62
5	0.0000074	12.331	0.0018726	235.213	0.0001066	44.269	0.0016243	1.047	0.200746	0.371	122.04654	± 2.80475	1499.05	± 23.42	98.83	1.85	0.45	± 2.12

6	0.0000074	13.413	0.0015278	321.598	0.0001081	42.171	0.0030772	0.500	0.386606	0.192	125.00537	± 1.40465	1523.59	± 11.57	99.46	3.50	1.05	± 6.73
7	0.0000028	34.545	0.0015395	308.229	0.0000850	59.280	0.0046186	0.352	0.584037	0.128	126.32646	± 0.98419	1534.44	± 8.06	99.88	5.25	1.56	± 9.61
8	0.0000039	23.361	0.0061091	68.616	0.0001117	47.298	0.0061499	0.256	0.777249	0.096	126.35878	± 0.71528	1534.70	± 5.86	99.91	6.99	0.52	± 0.72
9	0.0000074	13.132	0.0051730	81.999	0.0000871	58.119	0.0073309	0.256	0.925703	0.081	126.08986	± 0.69565	1532.50	± 5.70	99.81	8.34	0.74	± 1.21
10	0.0000034	28.280	0.0020449	255.493	0.0001967	24.402	0.0093495	0.165	1.184840	0.063	126.65634	± 0.47167	1537.14	± 3.86	99.93	10.64	2.38	± 12.15
11	0.0000087	11.561	0.0000482	8132.472	0.0002691	19.282	0.0142909	0.114	1.809765	0.041	126.45547	± 0.31665	1535.49	± 2.59	99.86	16.26	154.28	± 25093.66
12	0.0000069	15.296	0.0005511	1039.700	0.0001733	30.249	0.0124714	0.140	1.583569	0.047	126.81777	± 0.39269	1538.45	± 3.21	99.87	14.19	11.77	± 244.68
13	0.0000050	18.699	0.0029221	174.057	0.0001448	33.225	0.0068287	0.250	0.862553	0.086	126.16809	± 0.69505	1533.14	± 5.69	99.86	7.77	1.21	± 4.23
14	0.0000045	22.032	0.0066693	58.513	0.0000290	168.019	0.0042864	0.349	0.545201	0.136	127.14058	± 0.98773	1541.09	± 8.06	99.85	4.87	0.33	± 0.39
15	0.0000026	35.306	0.0038317	115.387	0.0000425	114.523	0.0024925	0.632	0.319198	0.233	128.01080	± 1.79221	1548.17	± 14.56	99.85	2.83	0.34	± 0.78
16	0.0000016	58.193	0.0003889	1174.594	0.0000806	66.750	0.0017597	0.873	0.223747	0.333	126.84988	± 2.46798	1538.72	± 20.16	99.78	2.00	2.35	± 55.28
17	0.0000044	22.007	0.0094865	72.139	0.0000411	121.574	0.0015869	1.017	0.203555	0.365	128.45591	± 2.99457	1551.79	± 24.28	99.72	1.80	0.09	± 0.12
18	0.0000030	28.441	0.0050766	77.144	0.0000959	49.262	0.0030945	0.471	0.391014	0.190	125.79537	± 1.32258	1530.08	± 10.85	99.67	3.52	0.32	± 0.49
19	0.0000049	18.309	0.0001572	2716.447	0.0000809	60.080	0.0035403	0.447	0.454911	0.164	128.07226	± 1.26101	1548.67	± 10.24	99.68	4.03	11.71	± 636.16
20	0.0000061	16.305	0.0072372	71.468	0.0000876	53.816	0.0017384	0.894	0.220855	0.337	126.70106	± 2.55376	1537.50	± 20.87	99.44	1.97	0.12	± 0.18
21	0.0000027	33.446	0.0013928	349.181	0.0000703	69.470	0.0009543	1.698	0.124066	0.601	129.41818	± 4.85974	1559.57	± 39.24	99.44	1.08	0.36	± 2.49
22	0.0000034	30.539	0.0023815	180.543	0.0000453	113.701	0.0005272	3.119	0.069397	1.071	128.93589	± 8.79583	1555.67	± 71.17	98.25	0.60	0.12	± 0.42
23	0.0000075	12.916	0.0009116	484.686	0.0000526	99.526	0.0003337	4.457	0.045311	1.640	129.58708	± 12.92255	1560.94	± 104.26	95.24	0.38	0.19	± 1.84
24	0.0000023	43.368	0.0003951	961.185	0.0000184	269.072	0.0011349	1.393	0.145650	0.510	127.67717	± 3.90694	1545.46	± 31.79	99.51	1.29	1.49	± 28.72
25	0.0000193	5.528	0.0036962	124.028	0.0000797	58.293	0.0002547	6.142	0.038404	1.936	130.69109	± 17.98243	1569.82	± 144.37	85.81	0.29	0.04	± 0.09

Step	36Ar	%1σ	37Ar	1%σ	38Ar	%1σ	39Ar	%1σ	40Ar	%1σ	40(r)/ 39(K)	± 2σ	Age	± 2σ	40Ar (r)	39Ar (k)	K/Ca	± 2σ
	[fA]		[fA]		[fA]		[fA]		[fA]				(Ma)		(%)	(%)		

SYC02 (1) **Hornblende**: J = 0.01057910 ± 0.00000476 (1σ)

1	0.0000960	1.341	0.0007927	299.126	0.0000074	542.384	0.0000165	60.831	0.0776526	0.443	2864.79634	± 3418.58200	6227.00	± 2088.76	63.02	0.11	0.0112	± 0.0684
2	0.0000136	10.501	0.0012621	186.780	0.0000260	144.760	0.0000334	29.466	0.0238900	1.438	575.79418	± 336.89820	3541.96	± 908.77	82.57	0.23	0.0141	± 0.0534
3	0.0000078	16.761	0.0014606	158.182	0.0000251	149.117	0.0000581	20.639	0.0222014	1.548	350.23702	± 149.70959	2800.23	± 608.63	90.02	0.38	0.0203	± 0.0648
4	0.0000094	14.115	0.0094423	23.341	0.0000056	633.990	0.0005291	2.140	0.0584926	0.589	107.97194	± 5.17785	1377.55	± 46.23	96.46	3.44	0.0288	± 0.0135
5	0.0000374	3.377	0.0436868	5.710	0.0000098	377.027	0.0028225	0.349	0.3663285	0.094	128.44059	± 1.00071	1551.66	± 8.12	97.90	18.36	0.0332	± 0.0038
6	0.0000468	3.109	0.0940993	2.536	0.0000881	38.363	0.0070946	0.171	0.8851992	0.040	125.00239	± 0.46890	1523.56	± 3.86	99.26	46.21	0.0388	± 0.0020
7	0.0000157	8.298	0.0175333	10.788	0.0000106	313.111	0.0012857	0.813	0.1601785	0.215	123.19381	± 2.20797	1508.61	± 18.34	97.95	8.37	0.0378	± 0.0082
8	0.0000105	12.053	0.0023792	84.387	0.0000022	1888.699	0.0002736	3.947	0.0336018	1.023	112.71113	± 9.84834	1419.38	± 85.93	91.21	1.79	0.0594	± 0.1004
9	0.0000111	12.161	0.0016228	128.257	0.0000101	418.823	0.0002850	3.838	0.0356885	0.963	114.50578	± 9.72051	1434.97	± 84.08	91.09	1.87	0.0910	± 0.2335
10	0.0000121	10.594	0.0052170	62.059	0.0000238	130.210	0.0003475	3.480	0.0432353	0.795	116.46865	± 8.97584	1451.87	± 76.92	92.64	2.26	0.0343	± 0.0426
11	0.0000118	11.776	0.0026297	90.817	0.0000017	2298.440	0.0003355	3.241	0.0419164	0.820	115.71157	± 8.36111	1445.37	± 71.91	92.10	2.19	0.0660	± 0.1199
12	0.0000088	15.003	0.0021754	112.093	0.0000210	207.130	0.0001290	8.330	0.0161044	2.133	107.03346	± 20.25581	1369.15	± 181.71	84.73	0.84	0.0305	± 0.0685
13	0.0000096	14.931	0.0015585	172.013	0.0000206	174.593	0.0001358	8.808	0.0141102	2.433	84.42737	± 17.50722	1154.06	± 176.89	80.58	0.89	0.0449	± 0.1548
14	0.0000095	14.434	0.0027685	89.218	0.0000110	403.200	0.0001557	6.073	0.0184233	1.866	102.81022	± 14.82476	1330.86	± 135.84	85.83	1.01	0.0289	± 0.0517
15	0.0000148	9.533	0.0001730	1394.396	0.0000327	137.871	0.0001780	7.313	0.0218037	1.577	97.56801	± 15.76751	1282.18	± 148.42	79.69	1.17	0.5353	± 14.9299
16	0.0000122	11.097	0.0017420	132.341	0.0000089	486.719	0.0001118	10.746	0.0130580	2.631	86.34092	± 21.47662	1173.29	± 214.71	73.13	0.73	0.0330	± 0.0877
17	0.0000206	6.462	0.0034948	66.301	0.0000043	922.200	0.0001310	10.733	0.0178181	1.927	93.00744	± 22.22478	1238.73	± 214.29	67.11	0.85	0.0191	± 0.0257

18	0.0000273	4.841	0.0000802	3487.443	0.0000550	61.530	0.0002141	4.589	0.0276189	1.243	91.06576	± 10.03811	1219.92	± 97.80	70.57	1.41	1.3881	± 96.8195
19	0.0000244	5.223	0.0046524	41.585	0.0000119	421.976	0.0002995	3.322	0.0369030	0.930	101.17737	± 7.75119	1315.84	± 71.62	81.22	1.95	0.0331	± 0.0276
20	0.0000413	3.551	0.0050325	48.580	0.0000255	134.364	0.0003106	3.989	0.0423084	0.812	98.96459	± 8.92626	1295.28	± 83.42	71.83	2.02	0.0317	± 0.0309
21	0.0000303	4.851	0.0014288	190.995	0.0000350	112.535	0.0002793	4.109	0.0321375	1.069	83.43565	± 8.19017	1144.01	± 83.22	72.24	1.83	0.1013	± 0.3869
22	0.0000688	2.410	0.0013637	151.747	0.0000117	411.528	0.0003222	3.257	0.0385267	0.896	55.35151	± 5.30594	833.46	± 64.01	46.42	2.12	0.1232	± 0.3740
SYC02 (2) **Hornblende**: J = 0.01057910 ± 0.00000476 (1σ)																		
1	0.0000436	1.832	0.0005602	264.104	0.0000354	128.564	0.0000269	43.469	0.0308306	0.772	673.58256	± 597.10724	3829.92	± 1410.11	57.90	0.42	0.0246	± 0.1318
2	0.0000128	6.292	0.0003645	383.047	0.0000197	212.614	0.0000347	28.952	0.0064427	3.691	73.81603	± 47.26142	1064.52	± 515.14	40.03	0.55	0.0498	± 0.3830
3	0.0000033	23.505	0.0007604	163.640	0.0000138	316.032	0.0001051	9.781	0.0086193	2.765	71.72798	± 15.47260	1041.61	± 170.80	87.87	1.66	0.0722	± 0.2368
4	0.0000058	13.279	0.0068197	19.643	0.0000198	247.546	0.0005489	2.053	0.0613116	0.393	110.47707	± 4.76738	1425.55	± 42.56	98.05	8.55	0.0415	± 0.0164
5	0.0000025	29.279	0.0055228	19.093	0.0000500	89.957	0.0003759	2.643	0.0435079	0.547	116.09204	± 6.47603	1474.99	± 56.25	99.26	5.84	0.0350	± 0.0135
6	0.0000143	5.916	0.0271592	4.965	0.0000099	408.878	0.0019536	0.528	0.2436363	0.098	124.83452	± 1.38826	1549.37	± 11.57	99.13	30.39	0.0370	± 0.0037
7	0.0000050	14.496	0.0120874	13.158	0.0000748	53.092	0.0009784	1.154	0.1174125	0.203	120.48610	± 2.90687	1512.76	± 24.73	99.54	15.24	0.0417	± 0.0110
8	0.0000021	36.607	0.0044813	22.637	0.0000111	352.992	0.0003200	3.409	0.0390702	0.611	122.45855	± 8.71485	1529.46	± 73.45	99.33	4.98	0.0368	± 0.0168
9	0.0000010	72.011	0.0023162	60.888	0.0000270	164.742	0.0001974	4.701	0.0245757	0.968	124.89294	± 12.41498	1549.86	± 103.46	99.49	3.08	0.0439	± 0.0537
10	0.0000006	148.321	0.0018692	74.794	0.0000029	1370.141	0.0001437	6.466	0.0168366	1.412	118.08576	± 16.30855	1492.22	± 140.31	99.88	2.24	0.0396	± 0.0595
11	0.0000015	54.568	0.0002213	608.627	0.0000171	251.178	0.0000921	10.259	0.0104353	2.282	108.14702	± 23.55814	1404.62	± 212.75	95.61	1.45	0.2168	± 2.6390
12	0.0000012	66.369	0.0012990	100.173	0.0000409	95.509	0.0000479	21.568	0.0072726	3.278	149.34264	± 67.57651	1742.93	± 506.13	96.53	0.74	0.0188	± 0.0386

13	0.0000002	337.793	0.0009274	170.652	0.0000464	90.440	0.0000552	20.800	0.0070819	3.367	130.00972	± 56.49853	1592.01	± 460.00	100.07	0.86	0.0306	± 0.1051
14	0.0000020	35.093	0.0003038	381.180	0.0000043	878.589	0.0000481	20.573	0.0070173	3.398	132.04034	± 55.99605	1608.47	± 451.78	90.96	0.76	0.0828	± 0.6318
15	0.0000038	17.756	0.0033340	33.782	0.0000300	139.207	0.0002069	6.258	0.0248031	0.959	116.89664	± 15.16234	1481.96	± 131.19	96.44	3.21	0.0319	± 0.0219
16	0.0000021	38.247	0.0033172	34.164	0.0000065	691.222	0.0002158	6.091	0.0262267	0.907	121.22463	± 15.30233	1519.03	± 129.72	98.66	3.35	0.0335	± 0.0232
17	0.0000096	10.987	0.0097419	13.459	0.0000070	557.347	0.0005681	2.094	0.0692053	0.345	119.52625	± 5.28580	1504.57	± 45.17	96.95	8.82	0.0300	± 0.0082
18	0.0000047	16.795	0.0017146	62.780	0.0000563	68.410	0.0003266	3.174	0.0363434	0.655	107.78506	± 7.20780	1401.35	± 65.21	96.51	5.11	0.0987	± 0.1241
19	0.0000129	7.839	0.0017230	65.340	0.0000289	142.941	0.0001775	5.926	0.0195439	1.216	89.79956	± 11.64059	1230.84	± 115.73	81.00	2.77	0.0532	± 0.0698

Step	36Ar [fA]	%1σ	37Ar [fA]	1%σ	38Ar [fA]	%1σ	39Ar [fA]	%1σ	40Ar [fA]	%1σ	40(r)/39(K)	± 2σ	Age (Ma)	± 2σ	40Ar (r) (%)	39Ar (k) (%)	K/Ca	± 2σ
SYC03 **Muscovite**: J = 0.01057910 ± 0.00000476 (1σ)																		
1	0.0000066	13.851	0.0006833	543.848	0.0000090	386.024	0.0001430	9.701	0.0063105	7.372	30.93026	± 10.56673	511.86	± 152.29	69.84	0.15	0.11	± 1.18
2	0.0000069	15.496	0.0008355	456.279	0.0000609	60.213	0.0004934	2.621	0.0261403	1.781	48.99520	± 3.69398	755.10	± 46.54	92.38	0.51	0.31	± 2.80
3	0.0000009	108.994	0.0002922	1366.588	0.0000093	422.440	0.0009768	1.306	0.0582483	0.800	59.33178	± 2.04374	880.85	± 24.02	99.51	1.01	1.74	± 47.51
4	0.0000004	225.234	0.0026802	147.409	0.0000196	197.626	0.0013886	0.912	0.0836849	0.556	60.41011	± 1.44555	893.48	± 16.87	100.10	1.44	0.27	± 0.79
5	0.0000011	85.134	0.0017110	206.896	0.0000118	382.681	0.0020414	0.691	0.1341595	0.347	65.65907	± 1.09986	953.72	± 12.42	99.85	2.12	0.62	± 2.57
6	0.0000064	15.254	0.0022735	171.112	0.0002246	21.062	0.0165080	0.093	1.5783873	0.030	95.51684	± 0.19562	1262.77	± 1.86	99.89	17.13	3.78	± 12.92
7	0.0000048	19.912	0.0001252	2971.634	0.0001687	31.010	0.0160200	0.110	1.4447634	0.033	90.09517	± 0.21446	1210.43	± 2.10	99.90	16.63	66.51	± 3953.12
8	0.0000025	42.952	0.0008034	476.917	0.0000471	79.360	0.0077208	0.159	0.6391488	0.073	82.67226	± 0.31550	1136.23	± 3.22	99.87	8.01	5.00	± 47.67
9	0.0000014	74.199	0.0020253	178.620	0.0000361	146.717	0.0052309	0.256	0.4144490	0.112	79.20382	± 0.47707	1100.49	± 4.97	99.94	5.43	1.34	± 4.80
10	0.0000044	24.836	0.0002874	1313.566	0.0000676	54.388	0.0100672	0.142	0.8488376	0.055	84.19130	± 0.27476	1151.67	± 2.78	99.85	10.45	18.21	± 478.51

11	0.0000033	28.782	0.0000061	61066.436	0.0000746	49.561	0.0087264	0.191	0.7699708	0.061	88.12279	± 0.36959	1191.01	± 3.66	99.87	9.06	749.20	± 915016.70
12	0.0000042	23.750	0.0014555	247.056	0.0001188	28.527	0.0091867	0.159	0.8612374	0.055	93.63507	± 0.33167	1244.78	± 3.19	99.87	9.53	3.28	± 16.22
13	0.0000052	19.278	0.0022969	154.069	0.0001227	28.855	0.0100926	0.132	0.9898589	0.047	97.95675	± 0.29056	1285.84	± 2.73	99.86	10.47	2.28	± 7.04
14	0.0000037	27.562	0.0026404	153.805	0.0000308	112.638	0.0057504	0.254	0.5766853	0.081	100.16115	± 0.56528	1306.43	± 5.25	99.84	5.97	1.13	± 3.48
15	0.0000058	16.898	0.0007800	534.272	0.0000336	133.894	0.0017776	0.740	0.1863123	0.250	103.76323	± 1.73001	1339.57	± 15.78	99.03	1.85	1.19	± 12.67
16	0.0000066	16.566	0.0023720	155.925	0.0000162	249.522	0.0002076	6.284	0.0255953	1.820	111.99025	± 15.49420	1413.08	± 135.66	91.54	0.22	0.05	± 0.14
17	0.0000172	7.363	0.0049074	83.427	0.0000267	151.229	0.0000397	32.509	0.0097876	4.755	139.28587	± 108.18182	1637.54	± 836.61	51.63	0.04	0.00	± 0.01

Step	36Ar [fA]	%1σ	37Ar [fA]	1%σ	38Ar [fA]	%1σ	39Ar [fA]	%1σ	40Ar [fA]	%1σ	40(r)/39(K)	± 2σ	Age (Ma)	± 2σ	40Ar (r) (%)	39Ar (k) (%)	K/Ca	± 2σ
FG04 **Biotite**: J = 0.01057910 ± 0.00000476 (1σ)																		
1	0.0000144	37.247	0.0000707	147.928	0.0000208	11.507	0.0008889	1.036	0.0474905	0.264	48.60825	± 3.74323	761.99	± 47.88	90.98	1.00	6.5	± 19.4
2	0.0000101	40.912	0.0001436	74.368	0.0000832	5.062	0.0062101	0.433	0.3925269	0.094	62.72548	± 0.68275	934.11	± 7.94	99.24	6.96	22.5	± 33.5
3	0.0000083	72.228	0.0001669	57.651	0.0000550	6.232	0.0037680	0.558	0.2613579	0.105	68.70954	± 1.23039	1002.40	± 13.78	99.06	4.22	11.7	± 13.5
4	0.0000030	151.670	0.0000727	141.043	0.0000258	12.687	0.0019034	0.723	0.1318121	0.070	68.77911	± 1.75936	1003.18	± 19.70	99.31	2.13	13.6	± 38.4
5	0.0000149	39.964	0.0002582	42.122	0.0002066	3.835	0.0155025	0.235	1.0594103	0.063	68.05230	± 0.40359	995.03	± 4.54	99.58	17.38	31.2	± 26.3
6	0.0000036	127.745	0.0000284	350.212	0.0000987	5.901	0.0087295	0.374	0.6058159	0.083	69.27685	± 0.61511	1008.75	± 6.86	99.82	9.79	159.9	± 1119.9
7	0.0000046	106.840	0.0000197	476.998	0.0000905	7.086	0.0072227	0.345	0.5032150	0.081	69.48004	± 0.64005	1011.01	± 7.13	99.73	8.10	190.8	± 1820.6
8	0.0000027	175.962	0.0002853	44.465	0.0002461	5.228	0.0182169	0.412	1.2531723	0.044	68.74813	± 0.59167	1002.84	± 6.62	99.94	20.42	33.2	± 29.5
9	0.0000102	59.786	0.0001834	54.436	0.0001720	5.358	0.0135461	0.355	0.9021199	0.048	66.37360	± 0.54533	976.05	± 6.20	99.66	15.19	38.4	± 41.8
10	0.0000050	89.047	0.0001386	70.422	0.0001044	7.970	0.0076799	0.309	0.4989000	0.089	64.76782	± 0.54302	957.71	± 6.23	99.70	8.61	28.8	± 40.6
11	0.0000026	165.690	0.0000533	192.650	0.0000316	14.394	0.0030848	0.670	0.1978091	0.101	64.37775	± 1.21663	953.23	± 14.00	100.40	3.46	30.1	± 116.1

Step	36Ar [fA]	%1σ	37Ar [fA]	1%σ	38Ar [fA]	%1σ	39Ar [fA]	%1σ	40Ar [fA]	%1σ	40(r)/39(K)	± 2σ	Age (Ma)	± 2σ	40Ar(r) (%)	39Ar (k) (%)	K/Ca	± 2σ
12	0.0000052	84.521	0.0001747	60.573	0.0000346	9.491	0.0024468	0.839	0.1602169	0.148	64.83624	± 1.54158	958.50	± 17.69	99.02	2.74	7.3	± 8.8
WC03 **Hornblende**: J = 0.01069480 ± 0.00000588 (1σ)																		
1	0.0001422	2.037	0.0010880	306.572	0.0000766	36.804	0.0003304	2.981	0.3872121	0.196	1040.93556	± 64.01972	4512.97	± 102.04	89.01	0.84	0.158	± 0.970
2	0.0000364	7.574	0.0029776	113.000	0.0000292	111.875	0.0005398	2.038	0.0837297	0.907	135.93241	± 7.11790	1623.05	± 56.10	87.30	1.37	0.094	± 0.212
3	0.0000202	13.502	0.0019279	212.146	0.0000671	57.054	0.0007302	1.427	0.0523693	1.450	63.12501	± 3.68030	932.79	± 42.49	88.18	1.86	0.197	± 0.837
4	0.0000153	18.256	0.0068019	65.146	0.0000421	94.162	0.0012304	0.752	0.1144876	0.663	90.12027	± 2.40223	1220.31	± 23.65	96.48	3.12	0.094	± 0.122
5	0.0000155	17.915	0.0064080	64.700	0.0000051	835.410	0.0011363	0.800	0.1372615	0.553	117.62105	± 2.86615	1472.65	± 24.55	96.99	2.88	0.092	± 0.119
6	0.0000258	10.716	0.0131828	35.403	0.0000548	99.879	0.0022734	0.610	0.3142995	0.242	135.86886	± 2.00165	1622.55	± 15.78	97.88	5.77	0.089	± 0.063
7	0.0000449	6.085	0.0352775	11.412	0.0001270	27.244	0.0072939	0.169	1.0244985	0.075	139.47375	± 0.58024	1650.74	± 4.50	98.96	18.51	0.107	± 0.024
8	0.0000381	7.284	0.0329827	11.180	0.0001042	34.867	0.0064571	0.152	0.8562161	0.089	131.70867	± 0.54985	1589.45	± 4.41	98.98	16.39	0.101	± 0.023
9	0.0000419	6.918	0.0230312	20.268	0.0000258	162.652	0.0059366	0.187	0.7717008	0.099	128.53677	± 0.64662	1563.80	± 5.27	98.62	15.08	0.134	± 0.054
10	0.0000353	7.729	0.0100649	43.681	0.0000328	119.526	0.0015918	0.879	0.2126708	0.358	128.03533	± 2.74441	1559.71	± 22.40	95.41	4.04	0.082	± 0.072
11	0.0000382	7.110	0.0076068	57.834	0.0000431	69.692	0.0008653	1.737	0.1230794	0.617	130.53655	± 5.38602	1580.01	± 43.47	91.21	2.19	0.059	± 0.068
12	0.0000598	4.742	0.0054241	89.792	0.0000254	121.910	0.0004751	2.166	0.0731589	1.038	118.26858	± 7.45097	1478.19	± 63.62	76.20	1.20	0.045	± 0.081
13	0.0000752	3.677	0.0193488	21.895	0.0001520	37.296	0.0032350	0.463	0.4447099	0.171	131.54525	± 1.44285	1588.14	± 11.59	95.29	8.20	0.087	± 0.038
14	0.0001167	2.434	0.0151537	29.560	0.0000131	311.158	0.0016725	0.620	0.2372525	0.320	122.50769	± 2.14700	1514.03	± 17.97	85.82	4.23	0.057	± 0.034
15	0.0001235	2.332	0.0146945	26.336	0.0000211	137.926	0.0018281	0.586	0.2607938	0.291	123.81255	± 1.99316	1524.92	± 16.58	86.30	4.63	0.064	± 0.034
16	0.0001740	1.694	0.0073739	54.401	0.0000438	89.633	0.0005339	2.023	0.0687556	1.104	30.09466	± 4.64552	504.54	± 67.96	23.59	1.37	0.038	± 0.041
17	0.0001488	1.848	0.0012345	333.334	0.0000875	45.056	0.0006294	1.975	0.0636206	1.193	30.68757	± 3.91228	513.20	± 56.96	30.32	1.60	0.265	± 1.765
18	0.0002020	1.397	0.0033013	138.301	0.0000407	94.990	0.0008757	1.353	0.0849507	0.894	28.51239	± 2.84463	481.25	± 42.15	29.31	2.22	0.138	± 0.381

19	0.0003062	1.022	0.0024050	165.802	0.0000861	39.168	0.0017601	0.668	0.1344037	0.565	24.28384	± 1.45533	417.47	± 22.34	31.83	4.49	0.381	± 1.263

Step	36Ar [fA]	%1σ	37Ar [fA]	1%σ	38Ar [fA]	%1σ	39Ar [fA]	%1σ	40Ar [fA]	%1σ	40(r)/39(K)	± 2σ	Age (Ma)	± 2σ	40Ar (r) (%)	39Ar (k) (%)	K/Ca	± 2σ
WC03 **Biotite**: J = 0.01057910 ± 0.00000476 (1σ)																		
1	0.0000849	2.213	0.0072756	62.041	0.0000227	148.749	0.0001178	12.645	0.031497	1.542	45.46117	± 17.50907	710.02	± 226.16	17.74	0.07	0.0	± 0.0
2	0.0000253	6.951	0.0025476	184.793	0.0001202	37.662	0.0000697	19.740	0.012034	4.036	69.06448	± 37.28205	991.76	± 412.08	39.01	0.04	0.0	± 0.1
3	0.0000159	11.429	0.0000006	835491.300	0.0000407	74.233	0.0001016	14.760	0.010715	4.534	58.83915	± 24.15244	875.05	± 284.75	55.80	0.06	88.5	± 1478676.0
4	0.0000114	15.659	0.0005085	859.629	0.0000662	45.552	0.0002042	6.637	0.013597	3.574	49.73995	± 10.32183	764.46	± 129.37	74.84	0.12	0.2	± 3.6
5	0.0000174	10.171	0.0058275	74.283	0.0001040	39.772	0.0004052	4.128	0.029796	1.634	62.48224	± 6.61892	917.50	± 76.23	84.12	0.24	0.0	± 0.1
6	0.0000264	6.697	0.0029998	130.896	0.0001195	35.603	0.0009630	1.574	0.085011	0.572	79.68569	± 3.01588	1105.50	± 31.30	90.46	0.59	0.2	± 0.4
7	0.0000357	4.926	0.0012724	488.467	0.0000926	37.332	0.0021336	0.706	0.189256	0.258	83.79408	± 1.47678	1147.65	± 14.97	94.43	1.30	0.9	± 8.5
8	0.0000374	4.771	0.0005162	783.884	0.0000504	65.512	0.0041233	0.338	0.368633	0.132	86.71012	± 0.71067	1176.97	± 7.09	96.98	2.51	4.2	± 65.1
9	0.0000284	6.474	0.0049172	88.066	0.0001196	22.795	0.0050336	0.288	0.460058	0.106	89.57783	± 0.61700	1205.36	± 6.06	98.08	3.06	0.5	± 0.9
10	0.0001155	1.613	0.0001097	3443.558	0.0002406	12.626	0.0118246	0.123	1.108471	0.044	90.82828	± 0.26453	1217.60	± 2.58	96.89	7.19	56.1	± 3860.7
11	0.0001245	1.494	0.0004634	997.101	0.0004284	7.392	0.0303010	0.068	2.807396	0.018	91.42557	± 0.13668	1223.42	± 1.33	98.68	18.42	34.0	± 678.0
12	0.0000367	5.040	0.0037166	146.512	0.0002509	16.540	0.0194196	0.083	1.792053	0.027	91.74322	± 0.18021	1226.50	± 1.75	99.40	11.80	2.7	± 8.0
13	0.0000233	7.759	0.0016312	238.552	0.0001920	20.905	0.0137378	0.111	1.267107	0.039	91.71132	± 0.23687	1226.19	± 2.30	99.44	8.35	4.4	± 20.9
14	0.0000169	10.500	0.0042530	119.004	0.0001190	32.249	0.0096471	0.188	0.887210	0.055	91.37919	± 0.38880	1222.97	± 3.78	99.39	5.87	1.2	± 2.8
15	0.0000134	13.311	0.0002852	1817.459	0.0001022	40.644	0.0075982	0.203	0.696757	0.070	91.16574	± 0.43834	1220.89	± 4.27	99.42	4.62	13.9	± 503.6
16	0.0000134	13.452	0.0056790	70.211	0.0000447	101.941	0.0060554	0.246	0.553368	0.088	90.85595	± 0.52443	1217.87	± 5.12	99.36	3.68	0.6	± 0.8

17	0.0000204	8.564	0.0001006	4598.127	0.0001517	22.672	0.0082637	0.202	0.750157	0.065	90.03974	± 0.41906	1209.89	± 4.11	99.19	5.02	42.7	± 3928.9
18	0.0000184	9.623	0.0020029	259.936	0.0000928	39.807	0.0108391	0.143	0.976186	0.050	89.52873	± 0.30421	1204.88	± 2.99	99.42	6.59	2.8	± 14.6
19	0.0000220	8.577	0.0106349	43.099	0.0001301	25.893	0.0125078	0.141	1.128268	0.043	89.79942	± 0.29013	1207.54	± 2.85	99.49	7.60	0.6	± 0.5
20	0.0000193	9.253	0.0100522	42.194	0.0001323	34.292	0.0098059	0.183	0.887552	0.055	90.06929	± 0.37156	1210.18	± 3.64	99.44	5.96	0.5	± 0.4
21	0.0000132	13.490	0.0007005	612.774	0.0000537	66.404	0.0061057	0.242	0.561048	0.087	91.25838	± 0.52079	1221.79	± 5.07	99.31	3.71	4.5	± 55.5
22	0.0000113	15.179	0.0054956	74.044	0.0000281	140.101	0.0029021	0.566	0.274940	0.177	93.30248	± 1.19688	1241.58	± 11.52	98.61	1.77	0.3	± 0.4
23	0.0000126	14.078	0.0000970	5386.216	0.0000547	71.881	0.0010718	1.442	0.106522	0.457	95.87867	± 3.23606	1266.21	± 30.73	96.47	0.65	5.7	± 618.9
24	0.0000067	26.231	0.0022548	205.994	0.0000211	182.188	0.0006993	2.176	0.064805	0.750	89.36710	± 4.58189	1203.29	± 45.05	96.65	0.43	0.2	± 0.7
25	0.0000332	5.373	0.0000422	11242.618	0.0000406	97.861	0.0005692	2.642	0.054417	0.893	78.17799	± 5.10415	1089.78	± 53.44	81.78	0.35	7.0	± 1577.0

Step	36Ar	%1σ	37Ar	1%σ	38Ar	%1σ	39Ar	%1σ	40Ar	%1σ	40(r)/39(K)	± 2σ	Age	± 2σ	40Ar (r)	39Ar (k)	K/Ca	± 2σ
	[fA]		[fA]		[fA]		[fA]		[fA]				(Ma)		(%)	(%)		
RR65 **Hornblende**: J = 0.01057910 ± 0.00000476 (1σ)																		
1	0.0000435	10.813	0.0010803	376.895	0.0000040	1157.892	0.0000899	11.057	0.0145577	8.576	18.63319	± 42.96586	328.02	± 691.74	11.41	0.83	0.0429	± 0.3237
2	0.0000123	38.351	0.0021120	222.119	0.0000181	276.296	0.0000823	15.025	0.0066877	18.675	39.41102	± 49.03164	634.95	± 666.16	47.66	0.75	0.0199	± 0.0887
3	0.0000116	40.494	0.0024700	159.132	0.0000226	192.894	0.0000712	14.610	0.0069257	18.028	52.62294	± 57.21421	806.09	± 707.13	52.78	0.65	0.0146	± 0.0468
4	0.0000222	21.276	0.0010158	361.041	0.0000330	153.217	0.0001050	10.395	0.0145126	8.603	73.85120	± 39.31926	1051.09	± 424.38	53.79	0.99	0.0541	± 0.3909
5	0.0000144	32.838	0.0042997	99.304	0.0000225	228.104	0.0001168	8.899	0.0180171	6.930	123.63172	± 40.97692	1521.51	± 340.96	78.12	1.06	0.0138	± 0.0275
6	0.0000193	24.337	0.0036889	106.853	0.0000081	635.354	0.0002957	3.385	0.0402839	3.099	118.76271	± 15.47440	1480.54	± 131.71	86.41	2.73	0.0413	± 0.0883
7	0.0000121	38.955	0.0118476	31.317	0.0000062	834.795	0.0005217	2.176	0.0670911	1.861	125.47286	± 9.33641	1536.77	± 77.03	96.03	4.79	0.0225	± 0.0142

8	0.0000157	30.059	0.0140951	24.723	0.0000474	97.375	0.0006133	1.756	0.0765662	1.631	120.97637	± 7.69543	1499.28	± 64.82	95.36	5.63	0.0223	± 0.0110
9	0.0000329	14.334	0.0351672	11.206	0.0000037	1225.568	0.0009126	1.394	0.1183493	1.055	125.34149	± 5.65024	1535.68	± 46.65	94.06	8.28	0.0131	± 0.0030
10	0.0000350	13.437	0.0614783	7.109	0.0000096	525.635	0.0019100	0.468	0.2429163	0.514	127.09527	± 2.41829	1550.10	± 19.81	97.70	17.41	0.0158	± 0.0023
11	0.0000153	30.798	0.0146706	24.230	0.0000634	75.804	0.0006652	1.798	0.0838133	1.490	122.77207	± 7.39026	1514.35	± 61.74	95.95	6.11	0.0232	± 0.0113
12	0.0000233	20.134	0.0118947	34.363	0.0000080	652.312	0.0005213	2.223	0.0659542	1.893	116.83383	± 9.19785	1464.05	± 79.00	90.88	4.78	0.0224	± 0.0155
13	0.0000184	25.783	0.0058715	68.701	0.0000079	621.947	0.0001820	7.071	0.0232229	5.376	102.26582	± 26.31804	1334.38	± 242.86	78.34	1.66	0.0158	± 0.0218
14	0.0000344	13.702	0.0165599	23.502	0.0000037	1242.278	0.0008005	1.544	0.1038088	1.203	120.22213	± 6.18273	1492.92	± 52.26	91.37	7.36	0.0248	± 0.0117
15	0.0000367	12.774	0.0258418	15.671	0.0000117	546.196	0.0008639	1.305	0.1077168	1.159	116.78238	± 5.52780	1463.60	± 47.49	91.72	7.89	0.0170	± 0.0054
16	0.0000675	6.984	0.0104960	43.085	0.0000269	177.406	0.0005026	2.048	0.0622828	2.005	86.72512	± 8.60341	1184.96	± 86.23	68.97	4.62	0.0245	± 0.0212
17	0.0000490	9.594	0.0100904	41.248	0.0000289	177.943	0.0004490	3.327	0.0449234	2.780	70.37676	± 9.89673	1013.19	± 109.08	69.23	4.12	0.0228	± 0.0189
18	0.0000636	7.429	0.0132211	31.732	0.0000025	1879.484	0.0004581	2.358	0.0481567	2.593	67.34125	± 9.15747	979.42	± 102.83	62.77	4.19	0.0177	± 0.0112
19	0.0001418	3.442	0.0320407	11.342	0.0000450	109.963	0.0017543	0.741	0.1422275	0.878	59.13047	± 2.41693	884.79	± 28.60	72.01	16.15	0.0281	± 0.0064

Step	36Ar [fA]	%1σ	37Ar [fA]	1%σ	38Ar [fA]	%1σ	39Ar [fA]	%1σ	40Ar [fA]	%1σ	40(r)/39(K)	± 2σ	Age (Ma)	± 2σ	40Ar(r) (%)	39Ar (k) (%)	K/Ca	± 2σ
LHG01 **Muscovite**: J = 0.01078250 ± 0.00002264 (1σ)																		
1	0.0000013	412.719	0.0000120	1194.142	0.0000114	50.008	0.0005944	1.806	0.0155848	0.391	25.55689	± 5.54688	440.09	± 84.78	97.48	0.39	26	± 617
2	0.0000000	13439.408	0.0000029	4876.711	0.0000103	50.772	0.0007873	0.981	0.0200993	0.534	25.54467	± 4.09116	439.90	± 62.54	100.06	0.51	143	± 13916
3	0.0000025	225.838	0.0000452	296.966	0.0001050	9.742	0.0088494	0.553	0.2359624	0.101	26.74698	± 0.48057	458.19	± 7.27	100.31	5.73	102	± 605
4	0.0000036	133.366	0.0000355	358.543	0.0000874	8.748	0.0077138	0.470	0.2029129	0.088	26.44363	± 0.45031	453.59	± 6.83	100.53	5.00	113	± 811
5	0.0000087	59.185	0.0000210	678.819	0.0004908	2.639	0.0407016	0.212	1.1360978	0.077	27.97581	± 0.14688	476.69	± 2.20	100.23	26.37	1007	± 13672
6	0.0000022	318.585	0.0000148	954.990	0.0010613	1.815	0.0897348	0.180	2.5246306	0.032	28.12633	± 0.11296	478.94	± 1.69	99.97	58.15	3152	± 60193
7	0.0000023	213.008	0.0000037	3483.292	0.0000464	13.654	0.0040896	0.941	0.1143177	0.182	28.12129	± 0.89706	478.87	± 13.42	100.60	2.65	579	± 40307

8	0.0000034	143.543	0.0001374	111.436	0.0000225	28.029	0.0018532	0.492	0.0477044	0.275	26.28774	± 1.61921	451.22	± 24.60	102.13	1.20	7	± 16

Step	36Ar [fA]	%1σ	37Ar [fA]	1%σ	38Ar [fA]	%1σ	39Ar [fA]	%1σ	40Ar [fA]	%1σ	40(r)/ 39(K)	± 2σ	Age (Ma)	± 2σ	40Ar(r) (%)	39Ar (k) (%)	K/Ca	± 2σ
ROB1612 (1) **Muscovite**: J = 0.01057910 ± 0.00000476 (1σ)																		
1	0.0000000	4650.758	0.0020912	176.568	0.0000058	700.753	0.0025374	0.378	0.2897884	0.116	114.33720	± 0.97980	1433.51	± 8.48	100.06	5.04	0.63	± 2.23
2	0.0000010	85.827	0.0028843	116.032	0.0000211	216.371	0.0008857	1.181	0.1019133	0.328	115.25178	± 3.01298	1441.41	± 25.97	99.94	1.76	0.16	± 0.37
3	0.0000294	3.231	0.0010460	300.962	0.0004939	9.795	0.0387277	0.044	4.6683482	0.007	120.31960	± 0.10934	1484.58	± 0.92	99.81	77.03	19.25	± 115.89
4	0.0000028	31.953	0.0002184	1667.571	0.0000801	48.194	0.0045197	0.244	0.5486435	0.062	121.21399	± 0.64879	1492.09	± 5.44	99.85	8.99	10.76	± 358.86
5	0.0000004	211.075	0.0026187	140.455	0.0000348	135.336	0.0010059	0.879	0.1230472	0.271	122.61663	± 2.47870	1503.81	± 20.64	100.06	2.00	0.20	± 0.56
6	0.0000008	115.170	0.0012610	282.628	0.0000150	235.988	0.0001597	6.579	0.0184885	1.800	113.11194	± 16.47472	1422.87	± 143.47	98.24	0.32	0.07	± 0.37
7	0.0000002	420.521	0.0001478	2260.583	0.0000525	84.281	0.0000980	10.658	0.0125764	2.648	127.89775	± 29.77318	1547.26	± 242.04	99.59	0.19	0.34	± 15.58
8	0.0000014	59.117	0.0054789	63.292	0.0000074	612.471	0.0006120	1.600	0.0747922	0.446	123.01593	± 4.39292	1507.13	± 36.51	100.03	1.21	0.06	± 0.07
9	0.0000014	59.097	0.0030347	110.672	0.0000161	260.908	0.0004186	2.528	0.0514259	0.647	123.05961	± 6.82538	1507.49	± 56.72	99.66	0.83	0.07	± 0.16
10	0.0000009	92.472	0.0012390	292.058	0.0000304	121.009	0.0000686	14.851	0.0090381	3.692	131.02763	± 43.22806	1572.52	± 346.54	98.17	0.13	0.03	± 0.17
11	0.0000001	859.176	0.0015763	246.578	0.0000491	86.143	0.0000612	13.580	0.0092339	3.602	155.13574	± 48.47844	1756.14	± 351.10	101.06	0.12	0.02	± 0.10
12	0.0000016	50.577	0.0016749	214.252	0.0000513	88.373	0.0000034	254.804	0.0008446	39.429	225.32190	± 1855.28898	2204.09	± 10488.27	60.83	0.00	0.00	± 0.01
13	0.0000008	109.720	0.0022716	150.058	0.0000143	273.219	0.0000088	102.134	0.0006256	53.238	20.48618	± 102.89360	354.69	± 1617.63	34.06	0.02	0.00	± 0.01
14	0.0000020	42.070	0.0003055	1100.213	0.0000182	225.252	0.0000048	235.981	0.0012991	25.645	145.68067	± 764.96191	0.00	± 27038.97	51.78	0.01	0.01	± 0.18
15	0.0000010	81.128	0.0053482	78.673	0.0000519	76.239	0.0000098	126.288	0.0014150	23.533	252.89577	± 1075.64645	2353.61	± 5598.20	107.84	0.01	0.00	± 0.00

16	0.0000051	17.730	0.0018537	204.121	0.0000558	63.777	0.0000476	25.108	0.0052494	6.342	83.81542	± 49.68762	1147.86	± 503.77	73.99	0.09	0.01	± 0.05
17	0.0000070	14.031	0.0014763	258.392	0.0000328	132.574	0.0001009	10.103	0.0086464	3.852	66.91309	± 17.73997	967.82	± 198.69	77.26	0.20	0.04	± 0.18
18	0.0000105	8.509	0.0015051	229.253	0.0000557	77.113	0.0001843	4.832	0.0168522	1.975	73.35295	± 9.12104	1038.55	± 98.24	80.68	0.37	0.06	± 0.29
19	0.0000247	3.561	0.0009948	368.853	0.0000463	97.055	0.0008460	1.237	0.0578326	0.577	59.51590	± 1.94190	883.01	± 22.79	87.13	1.68	0.44	± 3.26
ROB1612 (2) **Muscovite**: J = 0.01057910 ± 0.00000476 (1σ)																		
1	0.0000006	185.631	0.0000147	174.755	0.0000344	118.152	0.0001106	9.066	0.0123358	1.848	110.04149	± 21.24328	1395.94	± 187.77	98.65	0.51	4	± 14
2	0.0000011	97.277	0.0000177	194.681	0.0000599	75.357	0.0002239	5.217	0.0257477	0.883	113.64369	± 12.36398	1427.50	± 107.39	98.82	1.02	7	± 26
3	0.0000013	86.804	0.0000251	116.349	0.0001331	33.516	0.0005190	1.723	0.0580083	0.392	111.16998	± 4.12688	1405.88	± 36.28	99.45	2.37	11	± 25
4	0.0000016	68.328	0.0000021	1212.054	0.0000889	43.687	0.0011128	0.960	0.1370044	0.168	122.72025	± 2.46152	1504.67	± 20.49	99.68	5.09	273	± 6609
5	0.0000043	25.954	0.0000065	466.235	0.0000973	49.448	0.0041053	0.252	0.5027360	0.046	122.14714	± 0.64764	1499.89	± 5.40	99.75	18.79	327	± 3047
6	0.0000023	48.346	0.0000205	132.861	0.0000583	68.856	0.0007404	1.490	0.0879462	0.261	117.86894	± 3.67832	1463.83	± 31.31	99.24	3.39	19	± 50
7	0.0000041	26.607	0.0000112	296.538	0.0000050	864.420	0.0018465	0.707	0.2235684	0.102	120.41712	± 1.75482	1485.40	± 14.76	99.46	8.45	86	± 508
8	0.0000059	17.130	0.0000260	117.747	0.0000804	52.416	0.0060794	0.254	0.7429990	0.032	121.92499	± 0.63102	1498.04	± 5.27	99.76	27.82	122	± 287
9	0.0000001	1427.502	0.0000176	185.534	0.0000013	3409.528	0.0014373	0.712	0.1727881	0.133	120.22720	± 1.79289	1483.80	± 15.10	100.01	6.58	42	± 157
10	0.0000011	89.270	0.0000055	513.268	0.0000337	144.594	0.0010857	1.036	0.1306498	0.176	120.03829	± 2.58272	1482.21	± 21.76	99.75	4.97	104	± 1063
11	0.0000016	65.008	0.0000081	393.488	0.0000796	62.881	0.0023914	0.401	0.2917125	0.079	121.78474	± 1.03168	1496.86	± 8.62	99.84	10.94	154	± 1215
12	0.0000010	107.242	0.0000148	205.306	0.0000119	393.706	0.0010395	0.876	0.1276198	0.179	122.48751	± 2.27246	1502.73	± 18.93	99.77	4.76	36	± 150

13	0.0000003	388.394	0.0000182	211.605	0.0000905	58.172	0.0003764	3.019	0.0477141	0.478	126.61228	± 7.94254	1536.77	± 64.94	99.89	1.72	11	± 46
14	0.0000022	46.714	0.0000194	148.908	0.0000556	72.466	0.0000976	9.791	0.0110265	2.069	106.54654	± 22.27496	1364.78	± 200.31	94.28	0.45	3	± 8
15	0.0000020	52.964	0.0000400	70.476	0.0000424	110.135	0.0000804	13.781	0.0114703	1.988	135.52440	± 38.55938	1608.22	± 303.07	95.00	0.37	1	± 2
16	0.0000017	61.929	0.0000259	117.011	0.0000987	42.624	0.0001749	5.839	0.0221569	1.031	123.75026	± 15.11778	1513.22	± 125.23	97.70	0.80	4	± 8
17	0.0000020	56.543	0.0000151	183.987	0.0000522	82.238	0.0003363	3.690	0.0418004	0.546	122.54322	± 9.35652	1503.19	± 77.94	98.60	1.54	12	± 43
18	0.0000001	1063.839	0.0000115	275.943	0.0000258	154.054	0.0000831	11.866	0.0114228	1.997	138.04493	± 34.08904	1627.92	± 265.03	100.36	0.38	4	± 21
19	0.0000076	15.215	0.0000021	1286.245	0.0000316	121.419	0.0000114	93.768	0.0033627	6.770	96.84150	± 195.49061	1275.33	± 1847.11	32.84	0.05	3	± 74

Step	36Ar [fA]	%1σ	37Ar [fA]	1%σ	38Ar [fA]	%1σ	39Ar [fA]	%1σ	40Ar [fA]	%1σ	40(r)/ 39(K)	± 2σ	Age (Ma)	± 2σ	40Ar (r) (%)	39Ar (k) (%)	K/Ca	± 2σ
ROB1612 **Biotite**: J = 0.01057910 ± 0.00000476 (1σ)																		
1	0.0000001	775.576	0.0035015	119.252	0.0000518	65.672	0.0000014	1017.533	0.000643	188.310	103.43361	± 1029.27210	1345.12	± 9441.87	61.63	0.00	0.00	± 0.00
2	0.0000011	66.355	0.0004143	1294.354	0.0000515	73.987	0.0000199	72.226	0.001569	77.196	59.65760	± 156.18861	891.01	± 1841.82	76.65	0.01	0.03	± 0.66
3	0.0000045	13.012	0.0025647	195.983	0.0000332	167.782	0.0001742	8.737	0.004978	24.333	22.25937	± 15.46510	385.48	± 241.20	77.09	0.11	0.03	± 0.14
4	0.0000136	4.523	0.0016989	313.233	0.0000016	2531.852	0.0005343	2.370	0.012633	9.591	15.77053	± 4.90174	281.34	± 80.98	66.84	0.36	0.16	± 1.03
5	0.0000433	1.757	0.0027689	184.004	0.0000883	41.377	0.0010358	1.270	0.040267	3.009	26.66215	± 2.60580	452.88	± 39.15	68.45	0.69	0.19	± 0.71
6	0.0000533	0.958	0.0022355	217.959	0.0000265	134.296	0.0014929	0.960	0.121222	1.000	70.72644	± 2.21379	1017.04	± 24.35	87.01	0.99	0.35	± 1.51
7	0.0000431	1.593	0.0014402	367.049	0.0000274	126.010	0.0038210	0.410	0.480851	0.252	122.53802	± 1.23550	1512.39	± 10.33	97.35	2.54	1.38	± 10.13

8	0.0000216	3.077	0.0003487	1424.986	0.0000024	1288.594	0.0049691	0.277	0.650209	0.187	129.54061	± 0.90364	1570.02	± 7.32	99.00	3.30	7.41	± 211.19
9	0.0000233	4.005	0.0045141	112.396	0.0000913	44.262	0.0062471	0.282	0.820777	0.148	130.14679	± 0.85717	1574.93	± 6.92	99.11	4.15	0.72	± 1.62
10	0.0000354	2.122	0.0053440	77.885	0.0001701	27.470	0.0117919	0.130	1.563831	0.078	131.64442	± 0.40950	1586.98	± 3.29	99.30	7.83	1.15	± 1.79
11	0.0000318	1.919	0.0072683	79.222	0.0002260	16.898	0.0202267	0.081	2.685483	0.045	132.23802	± 0.25570	1591.74	± 2.05	99.62	13.44	1.45	± 2.29
12	0.0000119	5.444	0.0002878	1523.350	0.0001117	37.946	0.0126331	0.120	1.693264	0.072	133.74924	± 0.38550	1603.80	± 3.06	99.79	8.39	22.83	± 695.46
13	0.0000078	5.983	0.0024080	205.120	0.0000006	6948.514	0.0061424	0.213	0.825393	0.147	134.06296	± 0.72244	1606.29	± 5.74	99.74	4.08	1.33	± 5.44
14	0.0000056	11.036	0.0004642	1087.190	0.0000013	2794.651	0.0054607	0.263	0.730229	0.166	133.43068	± 0.86283	1601.26	± 6.87	99.77	3.63	6.12	± 133.01
15	0.0000067	7.843	0.0021907	227.102	0.0000198	168.993	0.0051090	0.262	0.690901	0.175	134.76525	± 0.88494	1611.86	± 7.00	99.68	3.39	1.21	± 5.51
16	0.0000051	12.653	0.0042323	109.080	0.0000143	294.009	0.0043176	0.377	0.584433	0.208	135.17625	± 1.19754	1615.11	± 9.46	99.79	2.87	0.53	± 1.16
17	0.0000070	9.371	0.0000631	8184.797	0.0000765	46.615	0.0049136	0.260	0.667120	0.182	135.34141	± 0.90214	1616.41	± 7.12	99.68	3.26	40.51	± 6631.54
18	0.0000071	11.628	0.0001389	3895.161	0.0000551	76.278	0.0090237	0.173	1.230759	0.099	136.15530	± 0.56391	1622.83	± 4.44	99.83	5.99	33.77	± 2631.14
19	0.0000076	7.981	0.0002294	1930.576	0.0001136	36.056	0.0091278	0.180	1.242335	0.098	135.86092	± 0.57191	1620.51	± 4.51	99.82	6.06	20.69	± 798.72
20	0.0000104	5.366	0.0027234	191.971	0.0001662	24.672	0.0093995	0.188	1.293961	0.094	137.28099	± 0.59414	1631.66	± 4.65	99.74	6.24	1.80	± 6.89
21	0.0000141	4.336	0.0050321	93.243	0.0002063	17.706	0.0159534	0.104	2.181841	0.056	136.55351	± 0.33141	1625.96	± 2.60	99.82	10.59	1.65	± 3.07
22	0.0000085	12.006	0.0002840	2015.144	0.0001565	29.631	0.0063352	0.250	0.861892	0.141	135.64024	± 0.81500	1618.77	± 6.43	99.70	4.21	11.60	± 467.44
23	0.0000128	5.816	0.0049170	96.877	0.0000988	42.970	0.0070963	0.241	0.958014	0.127	134.34191	± 0.75361	1608.50	± 5.98	99.56	4.72	0.75	± 1.45
24	0.0000075	6.340	0.0010452	476.038	0.0000503	73.106	0.0026172	0.525	0.351443	0.345	133.35441	± 1.74583	1600.66	± 13.90	99.34	1.74	1.30	± 12.40
25	0.0000422	1.755	0.0023581	187.515	0.0000793	56.290	0.0021105	0.677	0.205262	0.590	91.13845	± 1.74884	1228.66	± 17.11	93.78	1.40	0.47	± 1.75

Step	36Ar	%1σ	37Ar	1%σ	38Ar	%1σ	39Ar	%1σ	40Ar	%1σ	40(r)/ 39(K)	± 2σ	Age	± 2σ	40Ar (r)	39Ar (k)	K/Ca	± 2σ
	[fA]		[fA]		[fA]		[fA]		[fA]				(Ma)		(%)	(%)		
DMB03 (1) **Hornblende**: J = 0.01078250 ± 0.00002264 (1σ)																		
1	0.0000041	164.284	0.0011160	67.334	0.0000040	112.659	0.0000032	175.666	0.0431778	0.251	17372.39979	± 81049.63434	0.00	± 8481.09	96.95	0.02	0.0011	± 0.0055

2	0.0000155	46.153	0.0016619	43.836	0.0000042	120.583	0.0000561	11.239	0.0757114	0.349	1295.62979	± 308.37372	4892.97	± 401.61	94.08	0.43	0.0172	± 0.0156
3	0.0000180	38.863	0.0385997	2.609	0.0000407	12.339	0.0019518	0.914	0.2777123	0.118	143.06840	± 3.44425	1687.37	± 26.41	99.17	15.07	0.0259	± 0.0014
4	0.0000096	79.802	0.0447037	1.934	0.0000366	12.951	0.0023695	0.477	0.3025132	0.102	129.65610	± 2.33235	1581.49	± 18.96	100.23	18.30	0.0272	± 0.0011
5	0.0000266	28.585	0.0655106	1.794	0.0000517	8.899	0.0034064	0.506	0.4401392	0.057	130.13580	± 1.90911	1585.38	± 15.49	99.37	26.30	0.0267	± 0.0010
6	0.0000026	270.946	0.0156249	6.227	0.0000144	34.588	0.0007883	1.666	0.0969698	0.138	125.31417	± 6.92975	1545.84	± 57.46	100.47	6.08	0.0259	± 0.0033
7	0.0000126	67.078	0.0396298	2.876	0.0000444	13.540	0.0021711	0.870	0.2661154	0.111	123.85105	± 3.23126	1533.67	± 26.98	99.76	16.78	0.0281	± 0.0017
8	0.0000012	623.115	0.0026424	26.847	0.0000030	140.966	0.0001543	7.120	0.0189364	0.268	123.21287	± 34.40628	1528.33	± 288.08	99.20	1.19	0.0300	± 0.0167
9	0.0000008	901.803	0.0031621	21.984	0.0000006	838.907	0.0002102	2.864	0.0247453	0.425	118.99826	± 21.84625	1492.69	± 186.56	100.05	1.63	0.0342	± 0.0152
10	0.0000019	391.498	0.0048577	15.255	0.0000044	106.208	0.0002616	1.976	0.0303869	0.378	116.93271	± 18.02056	1474.97	± 155.40	99.38	2.02	0.0276	± 0.0085
11	0.0000023	314.216	0.0059489	12.940	0.0000027	162.850	0.0002648	2.193	0.0326153	0.429	124.31326	± 17.43540	1537.52	± 145.24	99.35	2.04	0.0228	± 0.0060
12	0.0000009	763.915	0.0040462	19.035	0.0000045	100.120	0.0002170	3.161	0.0259501	0.526	121.38795	± 21.14580	1512.98	± 178.56	100.17	1.68	0.0275	± 0.0106
13	0.0000019	363.085	0.0011977	58.458	0.0000006	728.307	0.0001235	3.886	0.0139673	0.452	119.21161	± 34.59027	1494.51	± 295.08	104.70	0.96	0.0533	± 0.0624
14	0.0000030	232.795	0.0062029	13.180	0.0000029	171.409	0.0003282	2.161	0.0405124	0.260	129.33125	± 14.03037	1578.85	± 114.24	103.41	2.54	0.0272	± 0.0073
15	0.0000080	88.825	0.0113096	6.215	0.0000057	81.215	0.0006473	2.424	0.0850326	0.267	130.65073	± 9.23849	1589.56	± 74.78	98.25	5.00	0.0294	± 0.0039
DMB03 (2) **Hornblende**: J = 0.01078250 ± 0.00002264 (1σ)																		
1	0.0000291	3.022	0.0002583	50.461	0.0000058	789.286	0.0000022	503.839	0.0278326	0.097	9573.03343	± 105113.31396	8414.58	± 19664.67	68.90	0.04	0.0040	± 0.0445
2	0.0000037	10.911	0.0002543	49.134	0.0000212	242.447	0.0000005	2680.310	0.0016408	1.677	1584.16794	± 126718.95595	5246.75	± 136691.16	34.68	0.01	0.0007	± 0.0587

3	0.0000014	45.240	0.0000742	140.310	0.0000474	59.534	0.0000001	10218.676	0.0023759	1.453	10425.59461	#############	0.00	± 271315.00	83.14	0.00	0.0013	± 0.1974
4	0.0000005	104.061	0.0003838	27.315	0.0000000	118796.387	0.0000066	172.264	0.0009695	3.405	134.38251	± 484.88696	1627.26	± 3871.60	88.12	0.13	0.0086	± 0.0313
5	0.0000003	220.430	0.0008687	12.315	0.0000899	35.141	0.0000343	33.610	0.0030022	1.102	94.40183	± 66.01243	1276.03	± 640.09	105.81	0.67	0.0201	± 0.0146
6	0.0000014	44.861	0.0015054	6.725	0.0000528	49.223	0.0000710	14.540	0.0065036	0.340	100.63547	± 30.17828	1335.48	± 283.16	108.20	1.39	0.0242	± 0.0078
7	0.0000011	55.070	0.0024282	4.212	0.0000177	92.927	0.0001064	10.660	0.0106871	0.225	100.80046	± 22.11244	1337.03	± 207.30	98.74	2.09	0.0224	± 0.0052
8	0.0000004	141.266	0.0029064	2.665	0.0000285	77.197	0.0001200	8.876	0.0134057	0.204	116.56345	± 21.21947	1479.08	± 183.90	102.55	2.35	0.0211	± 0.0040
9	0.0000156	3.035	0.0562960	0.314	0.0000500	58.901	0.0024264	0.409	0.2941852	0.021	123.13749	± 1.03508	1535.17	± 8.70	99.93	47.62	0.0221	± 0.0002
10	0.0000053	8.935	0.0230153	0.447	0.0000076	415.522	0.0010106	1.094	0.1221352	0.021	123.03668	± 2.75228	1534.33	± 23.13	100.20	19.84	0.0225	± 0.0005
11	0.0000005	91.437	0.0074600	1.507	0.0000414	81.206	0.0003296	4.164	0.0394434	0.072	122.96643	± 10.43797	1533.73	± 87.77	101.13	6.47	0.0226	± 0.0020
12	0.0000067	9.321	0.0043140	3.134	0.0000321	114.781	0.0001867	5.852	0.0196279	0.150	119.57211	± 14.37222	1504.97	± 122.79	111.93	3.67	0.0221	± 0.0030
13	0.0000041	14.631	0.0071923	1.954	0.0000492	98.922	0.0003023	3.604	0.0348644	0.101	123.29214	± 9.12123	1536.47	± 76.58	105.15	5.93	0.0215	± 0.0018
14	0.0000037	16.540	0.0070540	1.850	0.0000431	88.484	0.0002989	3.430	0.0352987	0.102	125.72719	± 8.86030	1556.80	± 73.56	104.70	5.86	0.0217	± 0.0017
15	0.0000407	2.413	0.0010895	8.999	0.0001284	27.015	0.0000216	35.492	0.0011769	1.977	642.38742	± 473.39589	3754.71	± 1165.44	1139.07	0.42	0.0100	± 0.0075
16	0.0000403	2.307	0.0096233	1.277	0.0001142	29.365	0.0003844	2.307	0.0449712	0.057	152.94626	± 7.33250	1769.73	± 54.11	128.46	7.53	0.0204	± 0.0011
17	0.0000433	2.240	0.0003791	23.181	0.0001196	31.798	0.0000099	79.789	0.0078134	0.431	498.32171	± 776.81978	3359.91	± 2379.10	65.10	0.20	0.0140	± 0.0227
18	0.0000405	2.299	0.0007561	11.037	0.0000948	38.853	0.0000347	29.457	0.0086439	0.258	98.81851	± 61.32937	0.00	± 16442.57	39.05	0.68	0.0235	± 0.0150
19	0.0000420	2.256	0.0007791	10.571	0.0001423	34.159	0.0000420	19.461	0.0091882	0.226	79.22674	± 34.11253	3561.06	± 4800.99	35.73	0.83	0.0277	± 0.0124

Step	36Ar [fA]	%1σ	37Ar [fA]	1%σ	38Ar [fA]	%1σ	39Ar [fA]	%1σ	40Ar [fA]	%1σ	40(r)/39(K)	± 2σ	Age (Ma)	± 2σ	40Ar(r) (%)	39Ar (k) (%)	K/Ca	± 2σ
20	0.0000374	2.497	0.0006767	15.428	0.0000663	65.011	0.0000464	18.041	0.0080460	0.322	66.63836	± 27.18260	2326.07	± 1932.32	38.04	0.92	0.0353	± 0.0169
21	0.0000390	2.411	0.0007995	13.252	0.0000881	48.766	0.0000513	13.239	0.0085422	0.281	60.01289	± 19.53995	1907.50	± 1101.99	35.66	1.01	0.0330	± 0.0124
22	0.0000312	3.088	0.0005278	16.785	0.0001143	35.514	0.0000399	23.098	0.0063383	0.417	73.97661	± 37.46143	2941.53	± 3742.81	46.12	0.79	0.0389	± 0.0224
MSC01 **Biotite**: J = 0.01078250 ± 0.00002264 (1σ)																		
1	0.0000143	35.491	0.0000010	24166.541	0.0000192	16.704	0.0010865	1.111	0.0180377	0.589	12.67905	± 2.80556	231.70	± 48.12	76.37	4.77	570.4	± 275701.9
2	0.0000494	12.836	0.0000754	329.057	0.0000841	6.059	0.0061305	0.513	0.1817488	0.120	27.24223	± 0.68151	465.67	± 10.27	91.89	26.92	42.3	± 278.3
3	0.0000204	23.949	0.0000364	640.397	0.0000375	11.825	0.0028076	0.704	0.1307532	0.132	44.40704	± 1.21738	707.43	± 16.05	95.35	12.33	40.1	± 513.7
4	0.0000134	40.535	0.0000041	5669.497	0.0000283	13.791	0.0022322	0.810	0.1234208	0.149	53.50107	± 1.69867	823.52	± 21.00	96.76	9.80	282.8	± 32071.3
5	0.0000179	27.829	0.0000111	2187.074	0.0000456	9.075	0.0032300	0.532	0.1920646	0.099	57.80206	± 1.11575	875.93	± 13.40	97.21	14.19	151.3	± 6617.0
6	0.0000119	52.445	0.0000935	250.981	0.0000231	17.760	0.0018033	0.606	0.1173213	0.135	63.08208	± 2.20836	938.26	± 25.63	96.97	7.92	10.0	± 50.4
7	0.0000099	51.413	0.0000338	702.689	0.0000182	21.378	0.0013031	1.141	0.0813259	0.196	60.14327	± 2.71119	903.83	± 32.06	96.37	5.72	20.1	± 281.9
8	0.0000076	71.557	0.0000995	242.696	0.0000047	61.179	0.0005361	1.753	0.0328769	0.393	57.05176	± 6.41553	866.89	± 77.44	93.05	2.35	2.8	± 13.6
9	0.0000001	8967.444	0.0001027	228.059	0.0000104	32.541	0.0006669	1.905	0.0399228	0.310	59.86795	± 5.18872	900.57	± 61.48	100.02	2.93	3.4	± 15.4
10	0.0000083	63.369	0.0000450	515.292	0.0000157	17.204	0.0005911	2.048	0.0375591	0.255	59.32799	± 5.86718	894.16	± 69.76	93.37	2.60	6.8	± 70.4
11	0.0000056	80.712	0.0001308	179.562	0.0000111	23.581	0.0007303	1.593	0.0471708	0.218	62.29113	± 4.18762	929.05	± 48.84	96.45	3.21	2.9	± 10.4
12	0.0000038	154.828	0.0000414	572.808	0.0000097	22.239	0.0008046	1.177	0.0558953	0.262	68.03969	± 4.70634	994.89	± 52.93	97.94	3.53	10.1	± 115.9
13	0.0000004	1203.378	0.0000744	318.910	0.0000049	46.309	0.0004232	1.911	0.0300279	0.538	71.19334	± 6.94988	1030.01	± 76.65	100.35	1.86	3.0	± 18.9
14	0.0000043	126.375	0.0000786	307.317	0.0000050	45.387	0.0004237	2.950	0.0299642	0.391	67.70512	± 8.58521	991.12	± 96.75	95.74	1.86	2.8	± 17.2

Step	36Ar	%1σ	37Ar	1%σ	38Ar	%1σ	39Ar	%1σ	40Ar	%1σ	40(r)/39(K)	± 2σ	Age	± 2σ	40Ar(r)	39Ar (k)	K/Ca	± 2σ
	[fA]		[fA]		[fA]		[fA]		[fA]				(Ma)		(%)	(%)		
RR39 **Hornblende**: J = 0.01081180 ± 0.00000597 (1σ)																		
1	0.0000114	64.747	0.0007259	169.218	0.0000058	82.527	0.0000160	33.564	0.0890549	0.231	5195.84196	± 3434.10610	7316.05	± 1174.17	96.13	0.07	0.0118	± 0.0407
2	0.0000068	82.372	0.0008248	147.375	0.0000034	111.513	0.0000451	12.261	0.0169764	0.647	326.34924	± 108.37995	2730.99	± 467.88	87.72	0.19	0.0288	± 0.0851
3	0.0000171	29.871	0.0023956	52.852	0.0000188	23.875	0.0005577	1.732	0.1429842	0.193	248.31321	± 10.30466	2358.18	± 54.67	96.57	2.31	0.1207	± 0.1277
4	0.0000246	23.093	0.0125227	9.718	0.0000585	8.171	0.0025245	0.911	0.2349077	0.114	90.84610	± 2.15305	1237.16	± 21.23	97.29	10.45	0.1045	± 0.0204
5	0.0000071	84.590	0.0115174	11.690	0.0000458	12.001	0.0014605	0.690	0.1510367	0.162	103.14571	± 2.88891	1354.57	± 26.70	99.20	6.03	0.0656	± 0.0154
6	0.0000158	39.635	0.0077668	18.865	0.0000351	12.768	0.0011314	1.028	0.1028496	0.189	87.70236	± 3.80462	1205.89	± 38.18	96.02	4.68	0.0754	± 0.0285
7	0.0000136	35.342	0.0042076	29.933	0.0000237	26.320	0.0005143	1.401	0.0678396	0.316	125.36691	± 6.70819	1549.10	± 55.68	94.51	2.12	0.0632	± 0.0379
8	0.0000291	23.197	0.0398042	4.097	0.0001212	4.695	0.0044167	0.779	0.4807907	0.083	108.28449	± 1.93952	1401.45	± 17.47	98.85	18.23	0.0573	± 0.0048
9	0.0000039	178.255	0.0108773	11.467	0.0000459	10.511	0.0013778	1.061	0.1007350	0.141	73.30745	± 3.39096	1055.35	± 36.98	99.71	5.69	0.0655	± 0.0151
10	0.0000018	307.719	0.0194188	6.148	0.0000758	6.007	0.0023302	0.980	0.2119900	0.114	91.93451	± 2.33033	1247.86	± 22.85	100.47	9.62	0.0620	± 0.0077
11	0.0000098	65.455	0.0162591	8.256	0.0000567	10.345	0.0019720	0.878	0.1808403	0.208	91.40208	± 2.55952	1242.64	± 25.17	99.10	8.14	0.0627	± 0.0104
12	0.0000094	60.173	0.0290620	5.325	0.0000995	7.692	0.0035151	0.765	0.2429923	0.063	69.38641	± 1.44284	1012.07	± 16.12	99.80	14.52	0.0625	± 0.0067
13	0.0000058	111.196	0.0156174	7.693	0.0000341	16.049	0.0013376	1.058	0.0888917	0.233	66.61594	± 3.27346	980.86	± 37.20	99.43	5.51	0.0442	± 0.0069
14	0.0000028	224.789	0.0205653	6.571	0.0000449	13.601	0.0016085	1.030	0.1230310	0.142	77.66509	± 2.89468	1102.26	± 30.76	100.64	6.62	0.0403	± 0.0054
15	0.0000038	148.604	0.0202989	8.105	0.0000322	15.467	0.0014147	0.576	0.1044593	0.179	74.91506	± 2.60238	1072.79	± 28.11	100.44	5.82	0.0359	± 0.0058

Step	36Ar	%1σ	37Ar	1%σ	38Ar	%1σ	39Ar	%1σ	40Ar	%1σ	40(r)/39(K)	± 2σ	Age	± 2σ	40Ar(r)	39Ar (k)	K/Ca	± 2σ
	[fA]		[fA]		[fA]		[fA]		[fA]				(Ma)		(%)	(%)		
RR40 Muscovite: J = 0.01078250 ± 0.00002264 (1σ)																		

1	0.0000040	175.486	0.0003855	199.934	0.0000011	698.803	0.0002664	2.974	0.017105	0.676	59.50752	± 16.30801	896.29	± 193.68	92.76	0.13	0.4	± 1.4
2	0.0000063	124.832	0.0000269	3256.880	0.0000028	278.366	0.0004938	2.416	0.035644	0.397	68.36884	± 10.09966	998.58	± 113.35	94.71	0.23	9.5	± 620.7
3	0.0000194	42.360	0.0008483	80.717	0.0000545	15.111	0.0036360	0.736	0.287227	0.096	77.37221	± 1.77186	1096.91	± 18.83	97.96	1.71	2.2	± 3.6
4	0.0000088	87.536	0.0010510	71.565	0.0000648	11.798	0.0060076	0.611	0.541810	0.090	89.72270	± 1.34935	1223.63	± 13.37	99.50	2.83	3.0	± 4.3
5	0.0000152	51.271	0.0013973	52.955	0.0001325	8.297	0.0096834	0.278	0.858917	0.033	88.21207	± 0.68817	1208.60	± 6.88	99.46	4.56	3.6	± 3.8
6	0.0000048	143.638	0.0006872	98.074	0.0002072	5.324	0.0188844	0.248	1.854854	0.031	98.13933	± 0.53718	1305.17	± 5.09	99.92	8.90	14.3	± 28.0
7	0.0000219	38.226	0.0002570	288.085	0.0012013	1.759	0.1005529	0.133	10.164213	0.029	101.01784	± 0.27949	1332.24	± 2.61	99.94	47.36	203.5	± 1172.3
8	0.0000080	125.324	0.0011673	70.272	0.0003886	3.373	0.0325146	0.205	3.130974	0.074	96.21512	± 0.45723	1286.85	± 4.38	99.92	15.32	14.5	± 20.4
9	0.0000045	190.438	0.0007708	107.527	0.0001842	6.902	0.0151323	0.349	1.517530	0.065	100.36569	± 0.78954	1326.14	± 7.39	100.08	7.13	10.2	± 22.0
10	0.0000083	128.756	0.0003399	188.865	0.0003274	3.569	0.0251182	0.418	2.540792	0.111	101.05206	± 0.90991	1332.56	± 8.49	99.90	11.83	38.4	± 145.1

Step	36Ar	%1σ	37Ar	1%σ	38Ar	%1σ	39Ar	%1σ	40Ar	%1σ	40(r)/39(K)	± 2σ	Age	± 2σ	40Ar(r)	39Ar (k)	K/Ca	± 2σ
	[fA]		[fA]		[fA]		[fA]		[fA]				(Ma)		(%)	(%)		
MGE01 Muscovite: J = 0.01078250 ± 0.00002264 (1σ)																		
1	0.0000073	58.611	0.0000632	175.009	0.0000839	5.980	0.0070118	0.446	0.1699249	0.126	23.92527	± 0.42482	414.98	± 6.58	98.73	12.42	57.7	± 201.8
2	0.0000036	131.479	0.0007909	15.573	0.0004540	2.789	0.0391339	0.180	0.9462505	0.123	24.20848	± 0.12783	419.36	± 1.98	100.12	69.34	25.7	± 8.0
3	0.0000013	331.694	0.0001002	84.618	0.0000903	6.950	0.0080829	0.305	0.1952767	0.106	24.11179	± 0.35387	417.86	± 5.48	99.80	14.32	42.0	± 71.0
4	0.0000020	204.895	0.0001224	68.292	0.0000110	30.228	0.0007448	1.428	0.0181778	0.332	23.60414	± 3.29142	409.99	± 51.15	96.73	1.32	3.2	± 4.3
5	0.0000043	104.825	0.0000630	149.534	0.0000190	21.043	0.0014611	1.369	0.0343287	0.202	24.38684	± 1.98088	422.12	± 30.58	103.79	2.59	12.1	± 36.0

Step	36Ar	%1σ	37Ar	1%σ	38Ar	%1σ	39Ar	%1σ	40Ar	%1σ	40(r)/39(K)	± 2σ	Age	± 2σ	40Ar(r)	39Ar (k)	K/Ca	± 2σ
	[fA]		[fA]		[fA]		[fA]		[fA]				(Ma)		(%)	(%)		

MHG01 Biotite: J = 0.01078250 ± 0.00002264 (1σ)

1	0.0000307	18.517	0.0000480	204.020	0.0000919	6.185	0.0065927	0.660	0.2073039	0.112	30.05344	± 0.65380	507.54	± 9.63	95.58	14.33	71	± 292
2	0.0000060	81.230	0.0000986	93.104	0.0001334	5.919	0.0106673	0.151	0.3383928	0.128	31.55332	± 0.30220	529.49	± 4.40	99.47	23.19	56	± 105
3	0.0000031	135.172	0.0000839	84.894	0.0001675	3.747	0.0123113	0.237	0.3869508	0.130	31.35332	± 0.26587	526.58	± 3.87	99.75	26.76	76	± 130
4	0.0000029	151.182	0.0000194	372.832	0.0000824	4.500	0.0065879	0.582	0.2066661	0.151	31.50130	± 0.54832	528.74	± 7.98	100.42	14.32	176	± 1314
5	0.0000042	109.974	0.0000254	368.911	0.0000616	7.296	0.0044269	0.496	0.1385267	0.164	31.57705	± 0.70879	529.84	± 10.31	100.91	9.62	91	± 668
6	0.0000036	133.238	0.0001143	71.450	0.0000270	18.157	0.0022200	0.813	0.0681579	0.258	31.18436	± 1.37948	524.12	± 20.13	101.57	4.83	10	± 14
7	0.0000027	176.610	0.0000056	1487.359	0.0000189	18.664	0.0015005	1.018	0.0468100	0.205	31.74144	± 2.03898	532.23	± 29.62	101.75	3.26	138	± 4113
8	0.0000027	141.522	0.0001139	61.617	0.0000114	32.063	0.0008387	1.064	0.0260356	0.293	31.99430	± 2.82137	535.90	± 40.90	103.07	1.82	4	± 5
9	0.0000048	82.416	0.0000352	206.282	0.0000037	104.239	0.0008528	1.330	0.0269600	0.258	33.27839	± 2.89580	554.42	± 41.55	105.27	1.85	13	± 52

Step	36Ar [fA]	%1σ	37Ar [fA]	1%σ	38Ar [fA]	%1σ	39Ar [fA]	%1σ	40Ar [fA]	%1σ	40(r)/39(K)	± 2σ	Age (Ma)	± 2σ	40Ar(r) (%)	39Ar (k) (%)	K/Ca	± 2σ
EIN1605 Muscovite: J = 0.01057910 ± 0.00000476 (1σ)																		
1	0.0000028	40.400	0.0048763	88.714	0.0000133	245.917	0.0001525	8.137	0.0034784	11.746	20.28939	± 9.15990	351.60	± 144.25	86.96	0.11	0.02	± 0.03
2	0.0000057	19.493	0.0008674	439.905	0.0000031	1222.043	0.0007778	1.713	0.0182811	2.236	21.41451	± 1.73305	369.23	± 27.03	91.04	0.58	0.47	± 4.10
3	0.0000050	24.768	0.0070748	48.916	0.0000548	76.838	0.0014158	0.770	0.0327868	1.250	22.57524	± 0.94407	387.24	± 14.58	97.14	1.05	0.10	± 0.10
4	0.0000039	29.645	0.0089895	38.673	0.0000027	1164.873	0.0021817	0.486	0.0513428	0.796	23.39271	± 0.60019	399.82	± 9.20	99.12	1.62	0.13	± 0.10
5	0.0000077	15.504	0.0015674	324.094	0.0000257	157.509	0.0036682	0.332	0.0883154	0.463	23.48848	± 0.40265	401.29	± 6.17	97.53	2.73	1.22	± 7.89
6	0.0000175	6.693	0.0023005	150.751	0.0005640	7.964	0.0496402	0.042	1.1935546	0.035	23.94258	± 0.03173	408.23	± 0.48	99.57	37.02	11.22	± 33.83
7	0.0000018	73.565	0.0032856	110.762	0.0002702	14.071	0.0233254	0.063	0.5558459	0.074	23.79271	± 0.06288	405.94	± 0.96	99.85	17.40	3.69	± 8.18
8	0.0000019	58.262	0.0008744	516.434	0.0002128	19.328	0.0188328	0.076	0.4512064	0.091	23.92251	± 0.07753	407.93	± 1.18	99.85	14.04	11.20	± 115.68
9	0.0000013	85.559	0.0014764	349.975	0.0000670	52.852	0.0062504	0.189	0.1504342	0.272	23.98141	± 0.23419	408.82	± 3.57	99.66	4.66	2.20	± 15.41

10	0.0000009	135.234	0.0043738	87.354	0.0000556	73.747	0.0047677	0.254	0.1146901	0.357	23.91072	± 0.29007	407.75	± 4.43	99.46	3.56	0.57	± 0.99
11	0.0000013	88.331	0.0011711	413.074	0.0000711	55.805	0.0041641	0.293	0.1012693	0.404	24.25583	± 0.34647	413.01	± 5.27	99.72	3.10	1.85	± 15.27
12	0.0000013	89.700	0.0065969	58.882	0.0000129	341.024	0.0020365	0.698	0.0494444	0.829	24.39757	± 0.70333	415.16	± 10.69	100.26	1.52	0.16	± 0.19
13	0.0000034	32.647	0.0037840	97.210	0.0001403	32.391	0.0125144	0.108	0.3025400	0.135	24.12199	± 0.10995	410.97	± 1.68	99.76	9.33	1.72	± 3.34
14	0.0000030	40.935	0.0070300	57.987	0.0000452	91.009	0.0003485	3.044	0.0086769	4.709	24.23058	± 4.03262	412.62	± 61.40	95.94	0.26	0.03	± 0.03
15	0.0000059	19.920	0.0020642	251.538	0.0000054	773.084	0.0032208	0.346	0.0799334	0.511	24.20943	± 0.45573	412.30	± 6.94	97.59	2.40	0.81	± 4.08
16	0.0000061	18.832	0.0049738	76.586	0.0000563	68.479	0.0006350	1.653	0.0166239	2.458	24.06271	± 2.10779	410.06	± 32.14	91.42	0.47	0.07	± 0.10
17	0.0000163	7.491	0.0000169	22383.113	0.0000155	299.508	0.0001887	5.107	0.0095983	4.256	25.02526	± 7.12795	424.68	± 107.81	49.19	0.14	5.81	± 2601.56

Step	36Ar	%1σ	37Ar	1%σ	38Ar	%1σ	39Ar	%1σ	40Ar	%1σ	40(r)/ 39(K)	± 2σ	Age	± 2σ	40Ar(r)	39Ar (k)	K/Ca	± 2σ
	[fA]		[fA]		[fA]		[fA]		[fA]				(Ma)		(%)	(%)		
EIN1605 Biotite: J = 0.01057910 ± 0.00000476 (1σ)																		
1	0.0000090	14.810	0.0012888	297.927	0.0000560	73.946	0.0000935	12.117	0.0031622	14.506	6.35926	± 14.72928	117.73	± 263.99	18.62	0.10	0.0	± 0.2
2	0.0000256	5.028	0.0009067	442.919	0.0000584	63.405	0.0005928	1.923	0.0120163	3.818	7.50310	± 2.30876	138.11	± 40.92	36.97	0.67	0.3	± 3.0
3	0.0000245	5.272	0.0014028	271.285	0.0000565	64.975	0.0019339	0.725	0.0397313	1.155	16.69427	± 0.73612	294.07	± 11.97	81.30	2.18	0.7	± 3.9
4	0.0000038	32.139	0.0008270	476.451	0.0000303	143.051	0.0013070	0.882	0.0283087	1.622	20.84348	± 1.08745	360.30	± 17.04	96.19	1.47	0.8	± 7.8
5	0.0000043	30.384	0.0007320	555.027	0.0001027	31.759	0.0027656	0.435	0.0638556	0.719	22.65058	± 0.53427	388.40	± 8.24	98.08	3.11	2.0	± 21.8
6	0.0000078	15.332	0.0018980	194.403	0.0000684	48.988	0.0040970	0.365	0.0963572	0.477	22.99098	± 0.36114	393.65	± 5.56	97.72	4.61	1.1	± 4.4
7	0.0000037	35.893	0.0001705	2520.003	0.0000607	79.552	0.0031942	0.401	0.0789326	0.581	24.37422	± 0.47796	414.81	± 7.27	98.63	3.60	9.7	± 491.1
8	0.0000026	47.313	0.0000631	6798.109	0.0000647	61.767	0.0028880	0.443	0.0732680	0.626	25.09912	± 0.52429	425.80	± 7.92	98.93	3.25	23.8	± 3237.8
9	0.0000043	29.386	0.0005549	741.094	0.0001257	37.548	0.0073106	0.157	0.1851319	0.248	25.15421	± 0.20288	426.63	± 3.07	99.33	8.23	6.9	± 101.5
10	0.0000041	30.141	0.0013828	294.663	0.0001407	30.067	0.0086992	0.147	0.2230673	0.206	25.51779	± 0.17221	432.12	± 2.59	99.50	9.80	3.3	± 19.3
11	0.0000082	14.797	0.0020035	210.047	0.0001218	32.022	0.0119169	0.104	0.3059164	0.150	25.48197	± 0.12516	431.58	± 1.89	99.25	13.42	3.1	± 13.0

12	0.0000043	28.619	0.0020486	183.897	0.0001359	27.779	0.0067864	0.196	0.1724257	0.266	25.24622	± 0.21946	428.02	± 3.31	99.34	7.64	1.7	± 6.3
13	0.0000031	40.026	0.0009437	458.126	0.0000458	73.836	0.0030378	0.376	0.0778800	0.589	25.30122	± 0.49005	428.85	± 7.39	98.71	3.42	1.7	± 15.3
14	0.0000032	39.611	0.0007765	539.212	0.0000445	87.514	0.0027046	0.491	0.0679374	0.675	24.78852	± 0.56371	421.10	± 8.54	98.66	3.05	1.8	± 19.5
15	0.0000021	57.886	0.0003122	1420.196	0.0000031	1072.433	0.0018920	0.633	0.0469269	0.977	24.45020	± 0.79066	415.96	± 12.02	98.59	2.13	3.2	± 89.5
16	0.0000027	49.075	0.0011840	338.451	0.0000169	198.829	0.0018537	0.639	0.0465650	0.985	24.63030	± 0.80102	418.70	± 12.16	98.09	2.09	0.8	± 5.5
17	0.0000035	34.436	0.0000157	26087.765	0.0000717	52.608	0.0028402	0.442	0.0714637	0.643	24.79605	± 0.51996	421.21	± 7.88	98.55	3.20	94.3	± 49199.8
18	0.0000020	63.924	0.0005366	725.125	0.0000755	60.312	0.0039606	0.319	0.1003063	0.457	25.18964	± 0.37626	427.17	± 5.68	99.45	4.46	3.8	± 55.7
19	0.0000043	28.172	0.0005787	720.529	0.0001160	29.897	0.0083026	0.180	0.2114195	0.218	25.30071	± 0.18695	428.84	± 2.82	99.36	9.35	7.5	± 107.5
20	0.0000049	25.535	0.0012495	337.656	0.0000838	47.402	0.0060962	0.221	0.1556615	0.295	25.27391	± 0.25048	428.44	± 3.78	98.99	6.87	2.5	± 17.1
21	0.0000011	114.906	0.0007015	593.923	0.0001108	39.998	0.0009313	1.430	0.0242991	1.887	25.67893	± 1.63763	434.54	± 24.63	98.47	1.05	0.7	± 8.2
22	0.0000029	43.527	0.0006764	590.656	0.0000239	161.239	0.0030543	0.388	0.0783558	0.586	25.35252	± 0.48294	429.62	± 7.28	98.84	3.44	2.3	± 27.7
23	0.0000034	36.983	0.0021064	197.498	0.0000248	181.911	0.0002615	4.103	0.0078058	5.873	25.18302	± 5.57966	427.07	± 84.28	84.84	0.30	0.1	± 0.3
24	0.0000031	40.112	0.0015468	274.685	0.0000317	138.471	0.0020429	0.617	0.0532009	0.863	25.66440	± 0.73971	434.32	± 11.13	98.50	2.30	0.7	± 3.8
25	0.0000080	14.979	0.0032731	120.256	0.0000025	1745.154	0.0002399	4.609	0.0087514	5.244	25.19771	± 5.94610	427.29	± 89.80	69.72	0.27	0.0	± 0.1

Step	36Ar	%1σ	37Ar	1%σ	38Ar	%1σ	39Ar	%1σ	40Ar	%1σ	40(r)/ 39(K)	± 2σ	Age	± 2σ	40Ar(r)	39Ar (k)	K/Ca	± 2σ
	[fA]		[fA]		[fA]		[fA]		[fA]				(Ma)		(%)	(%)		
EIN1603 Hornblende: J = 0.01078250 ± 0.00002264 (1σ)																		
1	0.0000024	199.067	0.0084450	10.057	0.0000119	34.196	0.0008788	1.191	0.0929852	0.238	106.47732	± 4.15692	1382.48	± 37.73	99.96	3.20	0.0537	± 0.0109
2	0.0000019	250.332	0.0107608	7.588	0.0000137	32.700	0.0011046	1.227	0.1199529	0.137	109.58255	± 3.79855	1410.44	± 33.95	100.23	4.02	0.0530	± 0.0082
3	0.0000111	50.224	0.0361139	2.445	0.0000412	13.210	0.0033762	0.608	0.3893438	0.116	116.04626	± 1.75615	1467.31	± 15.21	99.88	12.28	0.0483	± 0.0024
4	0.0000038	132.122	0.0105392	8.888	0.0000182	28.970	0.0009516	1.097	0.1083289	0.206	114.41118	± 4.07070	1453.09	± 35.53	99.73	3.46	0.0466	± 0.0083
5	0.0000011	454.302	0.0198452	4.700	0.0000269	16.410	0.0018826	0.858	0.2197136	0.107	118.23329	± 2.60247	1486.15	± 22.30	100.57	6.85	0.0490	± 0.0047
6	0.0000422	12.188	0.1377480	1.190	0.0001803	3.577	0.0136198	0.335	1.6122740	0.143	119.08849	± 0.90170	1493.46	± 7.70	99.89	49.54	0.0511	± 0.0013

7	0.0000084	57.081	0.0218732	3.702	0.0000306	14.663	0.0022056	0.957	0.2600861	0.103	118.37923	± 2.64527	1487.40	± 22.66	99.69	8.02	0.0521	± 0.0040
8	0.0000062	91.213	0.0229463	3.541	0.0000239	19.133	0.0022448	0.536	0.2661621	0.068	119.40191	± 1.99306	1496.14	± 16.99	99.99	8.16	0.0505	± 0.0036
9	0.0000004	1038.906	0.0065024	12.842	0.0000063	66.596	0.0006651	2.200	0.0789985	0.077	120.57788	± 6.81040	1506.13	± 57.73	100.82	2.42	0.0528	± 0.0138
10	0.0000014	399.339	0.0061729	14.711	0.0000130	36.451	0.0005652	1.617	0.0696888	0.249	125.84895	± 7.18110	1550.27	± 59.40	101.29	2.05	0.0472	± 0.0140

Step	36Ar	%1σ	37Ar	1%σ	38Ar	%1σ	39Ar	%1σ	40Ar	%1σ	40(r)/39(K)	± 2σ	Age	± 2σ	40Ar(r)	39Ar (k)	K/Ca	± 2σ
	[fA]		[fA]		[fA]		[fA]		[fA]				(Ma)		(%)	(%)		
ES18B Muscovite: J = 0.01057910 ± 0.00000476 (1σ)																		
1	0.0000002	413.181	0.0072634	66.352	0.0000083	485.008	0.0001626	7.601	0.0036994	7.933	26.68457	± 8.37886	449.61	± 124.99	113.62	0.12	0.01	± 0.02
2	0.0000030	35.302	0.0000185	31251.074	0.0000313	151.568	0.0006773	2.071	0.0163280	1.804	22.79120	± 2.10163	390.57	± 32.39	94.54	0.51	19.00	± 11873.98
3	0.0000017	57.468	0.0028199	218.248	0.0000120	381.539	0.0009981	1.222	0.0241249	1.215	23.93387	± 1.42372	408.10	± 21.73	98.83	0.75	0.18	± 0.80
4	0.0000022	44.900	0.0020137	188.310	0.0000662	58.965	0.0026641	0.486	0.0639721	0.460	23.83648	± 0.45349	406.61	± 6.93	99.22	2.01	0.69	± 2.59
5	0.0000032	35.600	0.0075050	57.197	0.0002160	16.213	0.0169367	0.090	0.4081706	0.073	24.00045	± 0.07981	409.12	± 1.22	99.62	12.79	1.17	± 1.34
6	0.0000038	27.192	0.0016247	254.433	0.0003011	14.095	0.0245049	0.066	0.5915342	0.050	24.09844	± 0.05455	410.61	± 0.83	99.83	18.50	7.84	± 39.91
7	0.0000035	33.853	0.0070781	73.717	0.0003602	11.491	0.0307580	0.051	0.7400155	0.040	24.04685	± 0.04746	409.82	± 0.72	99.93	23.21	2.26	± 3.33
8	0.0000007	161.179	0.0003210	1607.968	0.0000758	46.337	0.0050488	0.285	0.1205147	0.244	23.83508	± 0.27669	406.59	± 4.23	99.85	3.81	8.18	± 262.99
9	0.0000032	29.917	0.0066343	83.176	0.0000844	70.229	0.0070976	0.177	0.1708983	0.172	24.03074	± 0.19132	409.58	± 2.92	99.74	5.35	0.56	± 0.92
10	0.0000029	42.522	0.0006814	811.651	0.0001459	28.897	0.0136371	0.108	0.3281695	0.090	23.99599	± 0.10831	409.05	± 1.65	99.72	10.29	10.41	± 168.94
11	0.0000042	25.650	0.0015812	364.629	0.0001145	36.295	0.0080890	0.180	0.1954720	0.151	23.99170	± 0.17973	408.98	± 2.74	99.30	6.11	2.66	± 19.40
12	0.0000033	31.426	0.0019734	244.595	0.0000784	47.967	0.0060279	0.219	0.1452282	0.202	23.96119	± 0.21833	408.52	± 3.33	99.43	4.55	1.59	± 7.77
13	0.0000054	18.584	0.0031078	150.881	0.0000268	120.191	0.0034973	0.363	0.0857340	0.343	23.97077	± 0.36654	408.66	± 5.59	97.84	2.64	0.59	± 1.77
14	0.0000039	28.612	0.0078957	63.226	0.0000138	328.210	0.0014403	0.890	0.0353934	0.829	24.29846	± 0.94045	413.66	± 14.31	98.50	1.08	0.09	± 0.12
15	0.0000086	12.737	0.0019802	232.796	0.0000407	115.499	0.0014763	0.856	0.0378285	0.778	24.00605	± 0.88480	409.20	± 13.50	93.60	1.11	0.39	± 1.80
16	0.0000159	7.934	0.0070889	73.563	0.0000661	61.419	0.0031168	0.434	0.0793232	0.371	24.14495	± 0.46025	411.32	± 7.01	94.72	2.35	0.23	± 0.34

Step	36Ar [fA]	%1σ	37Ar [fA]	1%σ	38Ar [fA]	%1σ	39Ar [fA]	%1σ	40Ar [fA]	%1σ	40(r)/39(K)	± 2σ	Age (Ma)	± 2σ	40Ar(r) (%)	39Ar (k) (%)	K/Ca	± 2σ
17	0.0000384	2.875	0.0007997	607.983	0.0000619	72.743	0.0063732	0.231	0.1663297	0.177	24.31093	± 0.21721	413.85	± 3.30	93.14	4.81	4.14	± 50.39

Step	36Ar [fA]	%1σ	37Ar [fA]	1%σ	38Ar [fA]	%1σ	39Ar [fA]	%1σ	40Ar [fA]	%1σ	40(r)/39(K)	± 2σ	Age (Ma)	± 2σ	40Ar(r) (%)	39Ar (k) (%)	K/Ca	± 2σ
AME01 Hornblende: J = 0.01078250 ± 0.00002264 (1σ)																		
1	0.0000206	42.147	0.0006390	111.027	0.0000142	20.421	0.0005171	0.701	0.0220623	0.302	30.89413	± 10.05439	519.88	± 147.04	72.34	1.38	0.420	± 0.934
2	0.0000098	86.997	0.0081128	11.698	0.0000412	12.347	0.0017029	0.767	0.1324091	0.151	76.66638	± 3.23724	1089.39	± 34.55	98.27	4.53	0.109	± 0.026
3	0.0000102	83.516	0.0065763	14.191	0.0000308	18.004	0.0014411	1.257	0.1361879	0.189	93.04937	± 4.25826	1256.30	± 41.44	98.15	3.83	0.114	± 0.032
4	0.0000055	166.553	0.0075227	9.472	0.0000399	7.603	0.0014857	0.521	0.1424491	0.126	95.51405	± 3.82187	1280.13	± 36.71	99.27	3.95	0.102	± 0.019
5	0.0000143	69.661	0.0175892	5.027	0.0000862	5.684	0.0034020	0.750	0.3524720	0.108	103.13002	± 2.35630	1351.84	± 21.75	99.18	9.04	0.100	± 0.010
6	0.0000185	47.262	0.0246374	3.277	0.0001164	6.180	0.0045024	0.384	0.4812598	0.128	106.50009	± 1.45191	1382.69	± 13.18	99.26	11.96	0.095	± 0.006
7	0.0000098	85.633	0.0230446	3.931	0.0001169	4.733	0.0042585	0.432	0.4614717	0.096	108.51536	± 1.52464	1400.88	± 13.70	99.76	11.32	0.096	± 0.008
8	0.0000072	119.615	0.0243654	3.331	0.0001074	3.894	0.0043605	0.679	0.4887028	0.057	112.46179	± 1.93887	1435.99	± 17.08	99.96	11.59	0.093	± 0.006
9	0.0000125	68.557	0.0597215	1.443	0.0002901	2.442	0.0114948	0.228	1.3127904	0.050	114.70925	± 0.69744	1455.69	± 6.08	100.08	30.55	0.100	± 0.003
10	0.0000047	179.662	0.0086282	10.164	0.0000386	8.606	0.0014709	1.398	0.1617162	0.121	109.90186	± 4.62765	1413.30	± 41.29	99.56	3.91	0.088	± 0.018
11	0.0000053	166.382	0.0175064	4.137	0.0000749	9.874	0.0029900	0.790	0.2866816	0.132	96.20790	± 2.34548	1286.78	± 22.44	99.93	7.94	0.088	± 0.007

Step	36Ar [fA]	%1σ	37Ar [fA]	1%σ	38Ar [fA]	%1σ	39Ar [fA]	%1σ	40Ar [fA]	%1σ	40(r)/39(K)	± 2σ	Age (Ma)	± 2σ	40Ar(r) (%)	39Ar (k) (%)	K/Ca	± 2σ
AME02 Hornblende: J = 0.01057910 ± 0.00000476 (1σ)																		
1	0.0000027	N/A	0.0001956	N/A	0.0000507	N/A	0.0000597	N/A	0.0226404	N/A	N/A	N/A	2913.88	± 596.79	96.51	0.17	0.159	± 5.727
2	0.0000027	N/A	0.0000251	N/A	0.0000534	N/A	0.0000668	N/A	0.0107032	N/A	N/A	N/A	1791.93	± 434.22	92.94	0.19	1.386	± 322.191
3	0.0000015	N/A	0.0007322	N/A	0.0000197	N/A	0.0000821	N/A	0.0037107	N/A	N/A	N/A	706.63	± 216.59	89.29	0.24	0.058	± 0.609
4	0.0000023	N/A	0.0015306	N/A	0.0000270	N/A	0.0001054	N/A	0.0031310	N/A	N/A	N/A	494.30	± 135.76	82.15	0.30	0.036	± 0.146
5	0.0000013	N/A	0.0034980	N/A	0.0000900	N/A	0.0001850	N/A	0.0092931	N/A	N/A	N/A	770.59	± 93.13	95.86	0.53	0.028	± 0.051

6	0.0000076	N/A	0.0036628	N/A	0.0000322	N/A	0.0005061	N/A	0.0301635	N/A	N/A	N/A	884.00	± 32.52	93.04	1.45	0.072	± 0.133
7	0.0000407	N/A	0.0077029	N/A	0.0001042	N/A	0.0021774	N/A	0.1353704	N/A	N/A	N/A	913.92	± 8.95	91.76	6.25	0.147	± 0.124
8	0.0000218	N/A	0.0113211	N/A	0.0000331	N/A	0.0042541	N/A	0.2899079	N/A	N/A	N/A	981.61	± 4.63	97.80	12.21	0.195	± 0.105
9	0.0000172	N/A	0.0350491	N/A	0.0001079	N/A	0.0109644	N/A	0.8052480	N/A	N/A	N/A	1039.50	± 1.87	99.36	31.46	0.163	± 0.038
10	0.0000078	N/A	0.0243150	N/A	0.0001366	N/A	0.0074833	N/A	0.5301733	N/A	N/A	N/A	1011.36	± 2.99	99.56	21.47	0.160	± 0.050
11	0.0000039	N/A	0.0016556	N/A	0.0000341	N/A	0.0007249	N/A	0.0475920	N/A	N/A	N/A	953.67	± 25.75	97.61	2.08	0.228	± 0.819
12	0.0000033	N/A	0.0074576	N/A	0.0000712	N/A	0.0011304	N/A	0.0693588	N/A	N/A	N/A	904.49	± 14.97	98.59	3.24	0.079	± 0.065
13	0.0000052	N/A	0.0039901	N/A	0.0000239	N/A	0.0012363	N/A	0.0773434	N/A	N/A	N/A	918.41	± 15.35	98.04	3.55	0.161	± 0.261
14	0.0000085	N/A	0.0067193	N/A	0.0000924	N/A	0.0023908	N/A	0.1471108	N/A	N/A	N/A	906.52	± 7.08	98.30	6.86	0.185	± 0.175
15	0.0000047	N/A	0.0003570	N/A	0.0000509	N/A	0.0008990	N/A	0.0518978	N/A	N/A	N/A	861.87	± 20.61	97.38	2.58	1.310	± 30.840
16	0.0000076	N/A	0.0110144	N/A	0.0000327	N/A	0.0024650	N/A	0.1673581	N/A	N/A	N/A	978.77	± 9.16	98.66	7.07	0.116	± 0.073
17	0.0000076	N/A	0.0030646	N/A	0.0000236	N/A	0.0000479	N/A	0.0021973	N/A	N/A	N/A	715.71	± 358.40	49.14	0.14	0.008	± 0.019
18	0.0000076	N/A	0.0013550	N/A	0.0000071	N/A	0.0000412	N/A	0.0024103	N/A	N/A	N/A	870.38	± 414.19	36.43	0.12	0.016	± 0.086
19	0.0000076	N/A	0.0001859	N/A	0.0000348	N/A	0.0000269	N/A	0.0008868	N/A	N/A	N/A	540.78	± 531.87	13.34	0.08	0.075	± 2.647

Step	36Ar	%1σ	37Ar	1%σ	38Ar	%1σ	39Ar	%1σ	40Ar	%1σ	40(r)/ 39(K)	± 2σ	Age	± 2σ	40Ar(r)	39Ar (k)	K/Ca	± 2σ
	[fA]		[fA]		[fA]		[fA]		[fA]				(Ma)		(%)	(%)		
AME02 Biotite: J = 0.01057910 ± 0.00000476 (1σ)																		
1	0.0000008	132.939	0.0033648	170.260	0.0000354	100.219	0.0000074	150.115	0.0002390	112.030	26.97053	± 141.99283	607.41	± 3800.51	110.40	0.01	0.0	± 0.0
2	0.0000003	435.422	0.0047715	135.456	0.0000096	413.913	0.0000125	93.871	0.0006505	41.269	103.44858	± 318.14476	1336.70	± 2905.70	146.28	0.01	0.0	± 0.0
3	0.0000013	89.595	0.0005741	876.194	0.0000454	75.546	0.0000310	36.904	0.0011606	23.091	23.31837	± 41.58142	398.68	± 638.01	63.06	0.05	0.0	± 0.5
4	0.0000038	31.074	0.0047587	120.303	0.0000189	235.979	0.0002946	4.402	0.0041508	6.459	11.62934	± 4.48686	209.80	± 76.43	81.63	0.42	0.0	± 0.1
5	0.0000042	30.207	0.0014850	380.653	0.0000223	169.455	0.0004333	2.391	0.0048341	5.529	8.58346	± 3.00414	157.16	± 52.68	76.75	0.63	0.2	± 1.2
6	0.0000036	31.457	0.0052886	111.273	0.0000126	293.244	0.0004127	2.448	0.0069602	3.847	13.16234	± 3.11490	235.72	± 52.30	78.74	0.60	0.0	± 0.1
7	0.0000038	30.385	0.0017807	297.940	0.0000266	147.361	0.0007202	1.422	0.0186345	1.436	24.52465	± 1.84379	417.09	± 28.00	94.63	1.04	0.2	± 1.3
8	0.0000073	14.808	0.0034740	124.164	0.0000103	334.613	0.0013187	0.965	0.0385102	0.696	27.81322	± 0.98966	466.36	± 14.63	95.07	1.91	0.2	± 0.5
9	0.0000058	20.432	0.0053653	89.301	0.0000308	115.470	0.0027508	0.358	0.0750232	0.358	26.82894	± 0.47236	451.76	± 7.04	98.24	3.98	0.3	± 0.5

10	0.0000065	17.259	0.0041969	124.255	0.0000476	79.113	0.0061562	0.184	0.1634975	0.164	26.30885	± 0.21854	443.99	± 3.27	99.01	8.92	0.8	± 1.9
11	0.0000060	19.646	0.0023311	240.796	0.0001046	34.516	0.0102070	0.117	0.2709239	0.101	26.38790	± 0.13972	445.17	± 2.09	99.40	14.80	2.3	± 11.0
12	0.0000020	58.033	0.0013679	334.168	0.0000053	670.823	0.0055420	0.236	0.1480151	0.181	26.62260	± 0.24315	448.68	± 3.63	99.66	8.03	2.1	± 14.1
13	0.0000024	48.460	0.0026448	216.325	0.0000504	80.598	0.0035783	0.293	0.0964041	0.278	26.67098	± 0.38837	449.40	± 5.79	99.05	5.19	0.7	± 3.0
14	0.0000047	23.113	0.0052461	88.480	0.0000470	86.813	0.0040557	0.313	0.1105513	0.242	26.78162	± 0.32570	451.05	± 4.85	98.34	5.89	0.4	± 0.7
15	0.0000026	44.208	0.0051816	119.384	0.0000194	183.446	0.0034859	0.344	0.0946527	0.283	26.78164	± 0.42446	451.05	± 6.33	98.73	5.06	0.4	± 0.8
16	0.0000020	54.108	0.0014255	315.576	0.0000146	301.765	0.0037202	0.310	0.1011203	0.264	26.98240	± 0.34281	454.04	± 5.10	99.29	5.40	1.4	± 8.6
17	0.0000058	18.839	0.0015076	320.739	0.0000818	42.298	0.0045581	0.325	0.1227639	0.219	26.52213	± 0.30601	447.18	± 4.57	98.50	6.61	1.6	± 10.1
18	0.0000045	24.219	0.0028376	192.257	0.0000396	76.845	0.0048761	0.213	0.1305400	0.205	26.55040	± 0.27565	447.60	± 4.12	99.13	7.07	0.9	± 3.4
19	0.0000053	22.375	0.0085190	63.507	0.0000772	62.007	0.0060946	0.166	0.1625331	0.165	26.27063	± 0.22279	443.42	± 3.33	98.60	8.85	0.4	± 0.5
20	0.0000068	16.490	0.0032162	155.594	0.0000294	104.755	0.0041836	0.239	0.1121399	0.240	26.24219	± 0.30921	442.99	± 4.63	97.95	6.07	0.7	± 2.1
21	0.0000033	34.283	0.0008378	645.956	0.0000276	116.545	0.0028258	0.428	0.0754434	0.355	26.37758	± 0.49085	445.02	± 7.34	98.78	4.10	1.8	± 22.7
22	0.0000055	20.069	0.0029687	187.734	0.0000596	47.063	0.0016093	0.784	0.0443661	0.603	26.73186	± 0.87869	450.31	± 13.10	96.84	2.33	0.3	± 1.1
23	0.0000077	15.348	0.0017186	288.461	0.0000210	166.463	0.0005990	1.976	0.0183516	1.457	26.51559	± 2.25318	447.08	± 33.66	86.71	0.87	0.2	± 1.0
24	0.0000026	45.233	0.0034519	151.712	0.0000335	114.908	0.0009499	1.145	0.0257784	1.037	25.98525	± 1.41044	439.14	± 21.16	95.99	1.38	0.1	± 0.4
25	0.0000193	6.287	0.0011849	527.637	0.0000152	196.748	0.0005616	2.268	0.0206454	1.299	26.68158	± 2.70979	449.56	± 40.42	72.48	0.81	0.2	± 2.6

Step	36Ar	%1σ	37Ar	1%σ	38Ar	%1σ	39Ar	%1σ	40Ar	%1σ	40(r)/39(K)	± 2σ	Age	± 2σ	40Ar(r)	39Ar (k)	K/Ca	± 2σ
	[fA]		[fA]		[fA]		[fA]		[fA]				(Ma)		(%)	(%)		
MDE01 Hornblende: J = 0.01081180 ± 0.00000597 (1σ)																		
1	0.0000010	N/A	0.0144341	N/A	0.0000210	N/A	0.0011583	N/A	0.0289098	N/A	N/A	N/A	431.97	± 46.00	98.99	7.65	0.0417	± 0.0079
2	0.0000044	N/A	0.0304043	N/A	0.0000278	N/A	0.0023106	N/A	0.0584697	N/A	N/A	N/A	437.28	± 26.46	102.28	15.25	0.0395	± 0.0039
3	0.0000005	N/A	0.0586970	N/A	0.0000588	N/A	0.0044501	N/A	0.1081128	N/A	N/A	N/A	421.71	± 14.71	99.87	29.38	0.0394	± 0.0021
4	0.0000028	N/A	0.0090551	N/A	0.0000040	N/A	0.0006454	N/A	0.0147742	N/A	N/A	N/A	399.88	± 87.93	94.62	4.26	0.0371	± 0.0091
5	0.0000033	N/A	0.0292516	N/A	0.0000280	N/A	0.0021620	N/A	0.0512462	N/A	N/A	N/A	412.53	± 27.82	98.13	14.27	0.0384	± 0.0031
6	0.0000003	N/A	0.0424747	N/A	0.0000377	N/A	0.0031856	N/A	0.0772804	N/A	N/A	N/A	421.16	± 17.80	99.88	21.03	0.0390	± 0.0022

7	0.0000024	N/A	0.0077336	N/A	0.0000034	N/A	0.0005797	N/A	0.0147697	N/A	N/A	N/A	439.97	± 99.51	105.07	3.83	0.0390	± 0.0127
8	0.0000021	N/A	0.0081822	N/A	0.0000091	N/A	0.0006562	N/A	0.0159458	N/A	N/A	N/A	421.82	± 76.43	104.06	4.33	0.0417	± 0.0110

Step	36Ar	%1σ	37Ar	1%σ	38Ar	%1σ	39Ar	%1σ	40Ar	%1σ	40(r)/ 39(K)	± 2σ	Age	± 2σ	40Ar(r)	39Ar (k)	K/Ca	± 2σ
	[fA]		[fA]		[fA]		[fA]		[fA]				(Ma)		(%)	(%)		

EIN1603 Biotite: J = 0.01057910 ± 0.00000476 (1σ)

1	0.0000090	14.810	0.0012888	297.927	0.0000560	73.946	0.0000935	12.117	0.0031622	14.506	6.35926	± 14.72928	117.73	± 263.99	18.62	0.10	0.0	± 0.2
2	0.0000256	5.028	0.0009067	442.919	0.0000584	63.405	0.0005928	1.923	0.0120163	3.818	7.50310	± 2.30876	138.11	± 40.92	36.97	0.67	0.3	± 3.0
3	0.0000245	5.272	0.0014028	271.285	0.0000565	64.975	0.0019339	0.725	0.0397313	1.155	16.69427	± 0.73612	294.07	± 11.97	81.30	2.18	0.7	± 3.9
4	0.0000038	32.139	0.0008270	476.451	0.0000303	143.051	0.0013070	0.882	0.0283087	1.622	20.84348	± 1.08745	360.30	± 17.04	96.19	1.47	0.8	± 7.8
5	0.0000043	30.384	0.0007320	555.027	0.0001027	31.759	0.0027656	0.435	0.0638556	0.719	22.65058	± 0.53427	388.40	± 8.24	98.08	3.11	2.0	± 21.8
6	0.0000078	15.332	0.0018980	194.403	0.0000684	48.988	0.0040970	0.365	0.0963572	0.477	22.99098	± 0.36114	393.65	± 5.56	97.72	4.61	1.1	± 4.4
7	0.0000037	35.893	0.0001705	2520.003	0.0000607	79.552	0.0031942	0.401	0.0789326	0.581	24.37422	± 0.47796	414.81	± 7.27	98.63	3.60	9.7	± 491.1
8	0.0000026	47.313	0.0000631	6798.109	0.0000647	61.767	0.0028880	0.443	0.0732680	0.626	25.09912	± 0.52429	425.80	± 7.92	98.93	3.25	23.8	± 3237.8
9	0.0000043	29.386	0.0005549	741.094	0.0001257	37.548	0.0073106	0.157	0.1851319	0.248	25.15421	± 0.20288	426.63	± 3.07	99.33	8.23	6.9	± 101.5
10	0.0000041	30.141	0.0013828	294.663	0.0001407	30.067	0.0086992	0.147	0.2230673	0.206	25.51779	± 0.17221	432.12	± 2.59	99.50	9.80	3.3	± 19.3
11	0.0000082	14.797	0.0020035	210.047	0.0001218	32.022	0.0119169	0.104	0.3059164	0.150	25.48197	± 0.12516	431.58	± 1.89	99.25	13.42	3.1	± 13.0
12	0.0000043	28.619	0.0020486	183.897	0.0001359	27.779	0.0067864	0.196	0.1724257	0.266	25.24622	± 0.21946	428.02	± 3.31	99.34	7.64	1.7	± 6.3
13	0.0000031	40.026	0.0009437	458.126	0.0000458	73.836	0.0030378	0.376	0.0778800	0.589	25.30122	± 0.49005	428.85	± 7.39	98.71	3.42	1.7	± 15.3
14	0.0000032	39.611	0.0007765	539.212	0.0000445	87.514	0.0027046	0.491	0.0679374	0.675	24.78852	± 0.56371	421.10	± 8.54	98.66	3.05	1.8	± 19.5
15	0.0000021	57.886	0.0003122	1420.196	0.0000031	1072.433	0.0018920	0.633	0.0469269	0.977	24.45020	± 0.79066	415.96	± 12.02	98.59	2.13	3.2	± 89.5
16	0.0000027	49.075	0.0011840	338.451	0.0000169	198.829	0.0018537	0.639	0.0465650	0.985	24.63030	± 0.80102	418.70	± 12.16	98.09	2.09	0.8	± 5.5
17	0.0000035	34.436	0.0000157	26087.765	0.0000717	52.608	0.0028402	0.442	0.0714637	0.643	24.79605	± 0.51996	421.21	± 7.88	98.55	3.20	94.3	± 49199.8

18	0.0000020	63.924	0.0005366	725.125	0.0000755	60.312	0.0039606	0.319	0.1003063	0.457	25.18964	± 0.37626	427.17	± 5.68	99.45	4.46	3.8	± 55.7
19	0.0000043	28.172	0.0005787	720.529	0.0001160	29.897	0.0083026	0.180	0.2114195	0.218	25.30071	± 0.18695	428.84	± 2.82	99.36	9.35	7.5	± 107.5
20	0.0000049	25.535	0.0012495	337.656	0.0000838	47.402	0.0060962	0.221	0.1556615	0.295	25.27391	± 0.25048	428.44	± 3.78	98.99	6.87	2.5	± 17.1
21	0.0000011	114.906	0.0007015	593.923	0.0001108	39.998	0.0009313	1.430	0.0242991	1.887	25.67893	± 1.63763	434.54	± 24.63	98.47	1.05	0.7	± 8.2
22	0.0000029	43.527	0.0006764	590.656	0.0000239	161.239	0.0030543	0.388	0.0783558	0.586	25.35252	± 0.48294	429.62	± 7.28	98.84	3.44	2.3	± 27.7
23	0.0000034	36.983	0.0021064	197.498	0.0000248	181.911	0.0002615	4.103	0.0078058	5.873	25.18302	± 5.57966	427.07	± 84.28	84.84	0.30	0.1	± 0.3
24	0.0000031	40.112	0.0015468	274.685	0.0000317	138.471	0.0020429	0.617	0.0532009	0.863	25.66440	± 0.73971	434.32	± 11.13	98.50	2.30	0.7	± 3.8
25	0.0000080	14.979	0.0032731	120.256	0.0000025	1745.154	0.0002399	4.609	0.0087514	5.244	25.19771	± 5.94610	427.29	± 89.80	69.72	0.27	0.0	± 0.1

Step	36Ar	%1σ	37Ar	1%σ	38Ar	%1σ	39Ar	%1σ	40Ar	%1σ	40(r)/39(K)	± 2σ	Age	± 2σ	40Ar(r)	39Ar (k)	K/Ca	± 2σ
	[fA]		[fA]		[fA]		[fA]		[fA]				(Ma)		(%)	(%)		

LHG01 Muscovite: J = 0.01078250 ± 0.00002264 (1σ)

1	0.0000013	412.719	0.0000120	1194.142	0.0000114	50.008	0.0005944	1.806	0.0155848	0.391	25.55689	± 5.54688	440.09	± 84.78	97.48	0.39	26	± 617
2	0.0000000	13439.408	0.0000029	4876.711	0.0000103	50.772	0.0007873	0.981	0.0200993	0.534	25.54467	± 4.09116	439.90	± 62.54	100.06	0.51	143	± 13916
3	0.0000025	225.838	0.0000452	296.966	0.0001050	9.742	0.0088494	0.553	0.2359624	0.101	26.74698	± 0.48057	458.19	± 7.27	100.31	5.73	102	± 605
4	0.0000036	133.366	0.0000355	358.543	0.0000874	8.748	0.0077138	0.470	0.2029129	0.088	26.44363	± 0.45031	453.59	± 6.83	100.53	5.00	113	± 811
5	0.0000087	59.185	0.0000210	678.819	0.0004908	2.639	0.0407016	0.212	1.1360978	0.077	27.97581	± 0.14688	476.69	± 2.20	100.23	26.37	1007	± 13672
6	0.0000022	318.585	0.0000148	954.990	0.0010613	1.815	0.0897348	0.180	2.5246306	0.032	28.12633	± 0.11296	478.94	± 1.69	99.97	58.15	3152	± 60193
7	0.0000023	213.008	0.0000037	3483.292	0.0000464	13.654	0.0040896	0.941	0.1143177	0.182	28.12129	± 0.89706	478.87	± 13.42	100.60	2.65	579	± 40307
8	0.0000034	143.543	0.0001374	111.436	0.0000225	28.029	0.0018532	0.492	0.0477044	0.275	26.28774	± 1.61921	451.22	± 24.60	102.13	1.20	7	± 16

Step	36Ar	%1σ	37Ar	1%σ	38Ar	%1σ	39Ar	%1σ	40Ar	%1σ	40(r)/39(K)	± 2σ	Age	± 2σ	40Ar(r)	39Ar (k)	K/Ca	± 2σ
	[fA]		[fA]		[fA]		[fA]		[fA]				(Ma)		(%)	(%)		

MGE01 Muscovite: J = 0.01078250 ± 0.00002264 (1σ)

1	0.0000013	412.719	0.0000120	1194.142	0.0000114	50.008	0.0005944	1.806	0.0155848	0.391	25.55689	± 5.54688	440.09	± 84.78	97.48	0.39	26	± 617
2	0.0000000	13439.408	0.0000029	4876.711	0.0000103	50.772	0.0007873	0.981	0.0200993	0.534	25.54467	± 4.09116	439.90	± 62.54	100.06	0.51	143	± 13916
3	0.0000025	225.838	0.0000452	296.966	0.0001050	9.742	0.0088494	0.553	0.2359624	0.101	26.74698	± 0.48057	458.19	± 7.27	100.31	5.73	102	± 605
4	0.0000036	133.366	0.0000355	358.543	0.0000874	8.748	0.0077138	0.470	0.2029129	0.088	26.44363	± 0.45031	453.59	± 6.83	100.53	5.00	113	± 811
5	0.0000087	59.185	0.0000210	678.819	0.0004908	2.639	0.0407016	0.212	1.1360978	0.077	27.97581	± 0.14688	476.69	± 2.20	100.23	26.37	1007	± 13672

Step	36Ar	%1σ	37Ar	1%σ	38Ar	%1σ	39Ar	%1σ	40Ar	%1σ	40(r)/ 39(K)	± 2σ	Age	± 2σ	40Ar(r)	39Ar (k)	K/Ca	± 2σ
	[fA]		[fA]		[fA]		[fA]		[fA]				(Ma)		(%)	(%)		

ES18B Muscovite: J = 0.01057910 ± 0.00000476 (1σ)

1	0.0000002	413.181	0.0072634	66.352	0.0000083	485.008	0.0001626	7.601	0.0036994	7.933	26.68457	± 8.37886	449.61	± 124.99	113.62	0.12	0.01	± 0.02
2	0.0000030	35.302	0.0000185	31251.074	0.0000313	151.568	0.0006773	2.071	0.0163280	1.804	22.79120	± 2.10163	390.57	± 32.39	94.54	0.51	19.00	± 11873.98
3	0.0000017	57.468	0.0028199	218.248	0.0000120	381.539	0.0009981	1.222	0.0241249	1.215	23.93387	± 1.42372	408.10	± 21.73	98.83	0.75	0.18	± 0.80
4	0.0000022	44.900	0.0020137	188.310	0.0000662	58.965	0.0026641	0.486	0.0639721	0.460	23.83648	± 0.45349	406.61	± 6.93	99.22	2.01	0.69	± 2.59
5	0.0000032	35.600	0.0075050	57.197	0.0002160	16.213	0.0169367	0.090	0.4081706	0.073	24.00045	± 0.07981	409.12	± 1.22	99.62	12.79	1.17	± 1.34
6	0.0000038	27.192	0.0016247	254.433	0.0003011	14.095	0.0245049	0.066	0.5915342	0.050	24.09844	± 0.05455	410.61	± 0.83	99.83	18.50	7.84	± 39.91
7	0.0000035	33.853	0.0070781	73.717	0.0003602	11.491	0.0307580	0.051	0.7400155	0.040	24.04685	± 0.04746	409.82	± 0.72	99.93	23.21	2.26	± 3.33
8	0.0000007	161.179	0.0003210	1607.968	0.0000758	46.337	0.0050488	0.285	0.1205147	0.244	23.83508	± 0.27669	406.59	± 4.23	99.85	3.81	8.18	± 262.99
9	0.0000032	29.917	0.0066343	83.176	0.0000844	70.229	0.0070976	0.177	0.1708983	0.172	24.03074	± 0.19132	409.58	± 2.92	99.74	5.35	0.56	± 0.92
10	0.0000029	42.522	0.0006814	811.651	0.0001459	28.897	0.0136371	0.108	0.3281695	0.090	23.99599	± 0.10831	409.05	± 1.65	99.72	10.29	10.41	± 168.94
11	0.0000042	25.650	0.0015812	364.629	0.0001145	36.295	0.0080890	0.180	0.1954720	0.151	23.99170	± 0.17973	408.98	± 2.74	99.30	6.11	2.66	± 19.40
12	0.0000033	31.426	0.0019734	244.595	0.0000784	47.967	0.0060279	0.219	0.1452282	0.202	23.96119	± 0.21833	408.52	± 3.33	99.43	4.55	1.59	± 7.77
13	0.0000054	18.584	0.0031078	150.881	0.0000268	120.191	0.0034973	0.363	0.0857340	0.343	23.97077	± 0.36654	408.66	± 5.59	97.84	2.64	0.59	± 1.77
14	0.0000039	28.612	0.0078957	63.226	0.0000138	328.210	0.0014403	0.890	0.0353934	0.829	24.29846	± 0.94045	413.66	± 14.31	98.50	1.08	0.09	± 0.12
15	0.0000086	12.737	0.0019802	232.796	0.0000407	115.499	0.0014763	0.856	0.0378285	0.778	24.00605	± 0.88480	409.20	± 13.50	93.60	1.11	0.39	± 1.80

16	0.0000159	7.934	0.0070889	73.563	0.0000661	61.419	0.0031168	0.434	0.0793232	0.371	24.14495	± 0.46025	411.32	± 7.01	94.72	2.35	0.23	± 0.34
17	0.0000384	2.875	0.0007997	607.983	0.0000619	72.743	0.0063732	0.231	0.1663297	0.177	24.31093	± 0.21721	413.85	± 3.30	93.14	4.81	4.14	± 50.39

Step	36Ar	%1σ	37Ar	1%σ	38Ar	%1σ	39Ar	%1σ	40Ar	%1σ	40(r)/39(K)	± 2σ	Age	± 2σ	40Ar(r)	39Ar (k)	K/Ca	± 2σ
	[fA]		[fA]		[fA]		[fA]		[fA]				(Ma)		(%)	(%)		

AME02 Biotite: J = 0.01057910 ± 0.00000476 (1σ)

1	0.0000008	132.939	0.0033648	170.260	0.0000354	100.219	0.0000074	150.115	0.0002390	112.030	26.97053	± 141.99283	607.41	± 3800.51	110.40	0.01	0.0	± 0.0
2	0.0000003	435.422	0.0047715	135.456	0.0000096	413.913	0.0000125	93.871	0.0006505	41.269	103.44858	± 318.14476	1336.70	± 2905.70	146.28	0.01	0.0	± 0.0
3	0.0000013	89.595	0.0005741	876.194	0.0000454	75.546	0.0000310	36.904	0.0011606	23.091	23.31837	± 41.58142	398.68	± 638.01	63.06	0.05	0.0	± 0.5
4	0.0000038	31.074	0.0047587	120.303	0.0000189	235.979	0.0002946	4.402	0.0041508	6.459	11.62934	± 4.48686	209.80	± 76.43	81.63	0.42	0.0	± 0.1
5	0.0000042	30.207	0.0014850	380.653	0.0000223	169.455	0.0004333	2.391	0.0048341	5.529	8.58346	± 3.00414	157.16	± 52.68	76.75	0.63	0.2	± 1.2
6	0.0000036	31.457	0.0052886	111.273	0.0000126	293.244	0.0004127	2.448	0.0069602	3.847	13.16234	± 3.11490	235.72	± 52.30	78.74	0.60	0.0	± 0.1
7	0.0000038	30.385	0.0017807	297.940	0.0000266	147.361	0.0007202	1.422	0.0186345	1.436	24.52465	± 1.84379	417.09	± 28.00	94.63	1.04	0.2	± 1.3
8	0.0000073	14.808	0.0034740	124.164	0.0000103	334.613	0.0013187	0.965	0.0385102	0.696	27.81322	± 0.98966	466.36	± 14.63	95.07	1.91	0.2	± 0.5
9	0.0000058	20.432	0.0053653	89.301	0.0000308	115.470	0.0027508	0.358	0.0750232	0.358	26.82894	± 0.47236	451.76	± 7.04	98.24	3.98	0.3	± 0.5
10	0.0000065	17.259	0.0041969	124.255	0.0000476	79.113	0.0061562	0.184	0.1634975	0.164	26.30885	± 0.21854	443.99	± 3.27	99.01	8.92	0.8	± 1.9
11	0.0000060	19.646	0.0023311	240.796	0.0001046	34.516	0.0102070	0.117	0.2709239	0.101	26.38790	± 0.13972	445.17	± 2.09	99.40	14.80	2.3	± 11.0
12	0.0000020	58.033	0.0013679	334.168	0.0000053	670.823	0.0055420	0.236	0.1480151	0.181	26.62260	± 0.24315	448.68	± 3.63	99.66	8.03	2.1	± 14.1
13	0.0000024	48.460	0.0026448	216.325	0.0000504	80.598	0.0035783	0.293	0.0964041	0.278	26.67098	± 0.38837	449.40	± 5.79	99.05	5.19	0.7	± 3.0
14	0.0000047	23.113	0.0052461	88.480	0.0000470	86.813	0.0040557	0.313	0.1105513	0.242	26.78162	± 0.32570	451.05	± 4.85	98.34	5.89	0.4	± 0.7
15	0.0000026	44.208	0.0051816	119.384	0.0000194	183.446	0.0034859	0.344	0.0946527	0.283	26.78164	± 0.42446	451.05	± 6.33	98.73	5.06	0.4	± 0.8
16	0.0000020	54.108	0.0014255	315.576	0.0000146	301.765	0.0037202	0.310	0.1011203	0.264	26.98240	± 0.34281	454.04	± 5.10	99.29	5.40	1.4	± 8.6

17	0.0000058	18.839	0.0015076	320.739	0.0000818	42.298	0.0045581	0.325	0.1227639	0.219	26.52213	± 0.30601	447.18	± 4.57	98.50	6.61	1.6	± 10.1
18	0.0000045	24.219	0.0028376	192.257	0.0000396	76.845	0.0048761	0.213	0.1305400	0.205	26.55040	± 0.27565	447.60	± 4.12	99.13	7.07	0.9	± 3.4
19	0.0000053	22.375	0.0085190	63.507	0.0000772	62.007	0.0060946	0.166	0.1625331	0.165	26.27063	± 0.22279	443.42	± 3.33	98.60	8.85	0.4	± 0.5
20	0.0000068	16.490	0.0032162	155.594	0.0000294	104.755	0.0041836	0.239	0.1121399	0.240	26.24219	± 0.30921	442.99	± 4.63	97.95	6.07	0.7	± 2.1
21	0.0000033	34.283	0.0008378	645.956	0.0000276	116.545	0.0028258	0.428	0.0754434	0.355	26.37758	± 0.49085	445.02	± 7.34	98.78	4.10	1.8	± 22.7
22	0.0000055	20.069	0.0029687	187.734	0.0000596	47.063	0.0016093	0.784	0.0443661	0.603	26.73186	± 0.87869	450.31	± 13.10	96.84	2.33	0.3	± 1.1
23	0.0000077	15.348	0.0017186	288.461	0.0000210	166.463	0.0005990	1.976	0.0183516	1.457	26.51559	± 2.25318	447.08	± 33.66	86.71	0.87	0.2	± 1.0
24	0.0000026	45.233	0.0034519	151.712	0.0000335	114.908	0.0009499	1.145	0.0257784	1.037	25.98525	± 1.41044	439.14	± 21.16	95.99	1.38	0.1	± 0.4
25	0.0000193	6.287	0.0011849	527.637	0.0000152	196.748	0.0005616	2.268	0.0206454	1.299	26.68158	± 2.70979	449.56	± 40.42	72.48	0.81	0.2	± 2.6

Step	36Ar [fA]	%1σ	37Ar [fA]	1%σ	38Ar [fA]	%1σ	39Ar [fA]	%1σ	40Ar [fA]	%1σ	40(r)/39(K)	± 2σ	Age (Ma)	± 2σ	40Ar(r) (%)	39Ar(k) (%)	K/Ca	± 2σ

DAR1701 Muscovite: J = 0.01057910 ± 0.00000476 (1σ)

1	0.0000008	117.570	0.0005958	416.464	0.0000165	227.626	0.0001917	5.131	0.0123081	1.530	65.87545	± 8.04319	956.16	± 90.67	102.40	0.59	0.17	± 1.39
2	0.0000008	132.388	0.0007684	331.031	0.0000144	324.416	0.0006299	1.770	0.0362926	0.518	57.07890	± 2.45292	854.18	± 29.26	99.15	1.95	0.43	± 2.82
3	0.0000028	35.282	0.0039944	71.202	0.0000368	111.869	0.0029358	0.345	0.4400509	0.043	149.85511	± 1.09360	1717.48	± 8.09	99.88	9.06	0.38	± 0.54
4	0.0000048	24.329	0.0030226	82.291	0.0001832	19.731	0.0156353	0.107	1.2122334	0.016	77.46438	± 0.17635	1082.30	± 1.85	99.90	48.32	2.69	± 4.43
5	0.0000011	92.549	0.0009268	248.914	0.0000005	7485.048	0.0011892	0.973	0.0716087	0.262	59.85168	± 1.35190	886.95	± 15.83	99.45	3.68	0.67	± 3.32
6	0.0000003	341.669	0.0001834	1585.617	0.0000144	276.353	0.0007617	1.520	0.0456980	0.411	59.91219	± 2.15281	887.66	± 25.21	99.84	2.35	2.16	± 68.46
7	0.0000012	83.413	0.0031077	74.712	0.0000245	195.294	0.0012288	0.670	0.0694816	0.272	56.56560	± 1.00122	848.05	± 11.98	99.86	3.79	0.21	± 0.31
8	0.0000002	492.713	0.0020105	114.122	0.0000583	68.935	0.0042942	0.237	0.2474135	0.076	57.68549	± 0.33454	861.40	± 3.97	100.09	13.27	1.11	± 2.53
9	0.0000004	265.370	0.0031688	82.339	0.0000494	79.893	0.0023555	0.351	0.1681368	0.112	71.49944	± 0.63985	1018.47	± 6.97	100.07	7.27	0.39	± 0.64
10	0.0000003	338.574	0.0002326	842.520	0.0000095	522.723	0.0010573	0.778	0.0790090	0.238	74.67241	± 1.39057	1052.70	± 14.86	99.91	3.27	2.36	± 39.82
11	0.0000008	123.566	0.0024877	116.947	0.0000103	388.180	0.0006372	1.652	0.0518842	0.362	81.58375	± 3.04462	1125.09	± 31.26	99.93	1.96	0.13	± 0.31

12	0.0000005	221.821	0.0013596	258.994	0.0000044	834.247	0.0004567	2.463	0.0382643	0.493	84.51143	± 4.73813	1154.90	± 47.85	100.66	1.41	0.17	± 0.90
13	0.0000068	14.622	0.0016357	175.138	0.0000083	479.329	0.0000463	22.275	0.0055809	3.364	81.63327	± 42.22657	1125.60	± 433.43	66.08	0.14	0.01	± 0.05
14	0.0000018	59.013	0.0009195	246.165	0.0000021	1948.690	0.0003177	3.251	0.0275596	0.685	85.42196	± 6.21186	1164.08	± 62.42	98.26	0.98	0.18	± 0.88
15	0.0000036	31.324	0.0005997	380.802	0.0000418	93.413	0.0005271	1.852	0.0430162	0.440	79.74695	± 3.39961	1106.13	± 35.27	97.65	1.63	0.46	± 3.48
16	0.0000064	17.115	0.0020322	127.865	0.0000260	144.354	0.0000471	22.881	0.0116185	1.614	197.13469	± 90.54843	2037.28	± 561.36	82.25	0.15	0.01	± 0.03
17	0.0000134	8.192	0.0009593	292.344	0.0000021	2351.556	0.0000585	23.035	0.0066684	2.809	47.57478	± 27.02975	737.12	± 343.94	41.26	0.18	0.03	± 0.18

Step	36Ar	%1σ	37Ar	1%σ	38Ar	%1σ	39Ar	%1σ	40Ar	%1σ	40(r)/39(K)	± 2σ	Age	± 2σ	40Ar(r)	39Ar (k)	K/Ca	± 2σ
	[fA]		[fA]		[fA]		[fA]		[fA]				(Ma)		(%)	(%)		

DAR1702 Hornblende: J = 0.01057910 ± 0.00000476 (1σ)

1	0.0000223	6.219	0.0020807	174.030	0.0000369	175.813	0.0000261	52.837	0.3530216	0.061	12579.19596	± 12802.84792	8857.09	± 1826.58	98.07	0.33	0.0069	± 0.0249
2	0.0000089	13.640	0.0075585	47.085	0.0000819	40.161	0.0000213	61.110	0.1058554	0.201	6487.05378	± 10721.13827	7672.28	± 2945.41	98.05	0.19	0.0011	± 0.0021
3	0.0000095	13.610	0.0045179	96.993	0.0000006	5660.552	0.0000087	145.508	0.0733127	0.290	12639.61992	± 59013.61200	8865.69	± 8379.50	96.62	0.07	0.0006	± 0.0033
4	0.0000055	24.245	0.0018346	222.727	0.0000013	2827.725	0.0000125	112.804	0.0505734	0.422	3533.55154	± 7380.67126	6595.40	± 3678.37	96.44	0.17	0.0039	± 0.0192
5	0.0000037	34.084	0.0012992	267.572	0.0000288	142.425	0.0000207	61.773	0.0124563	1.704	520.30738	± 628.65438	3385.73	± 1848.80	90.27	0.26	0.0086	± 0.0474
6	0.0000056	22.925	0.0043260	82.215	0.0000197	187.665	0.0000206	62.174	0.0076616	2.772	358.84355	± 535.19578	2834.88	± 2134.50	82.58	0.21	0.0021	± 0.0047
7	0.0000034	39.080	0.0045574	84.251	0.0000401	108.446	0.0000017	861.287	0.0101244	2.103	1796.83873	± 10992.46814	5417.56	± 10508.86	86.39	0.06	0.0006	± 0.0035
8	0.0000037	34.580	0.0019017	214.061	0.0000289	131.160	0.0000233	59.244	0.0056759	3.758	179.16104	± 209.77094	1922.27	± 1385.88	77.86	0.30	0.0067	± 0.0299

9	0.0000072	18.084	0.0007722	500.179	0.0000223	204.565	0.0000491	33.596	0.0101460	2.100	165.64728	± 116.16292	1830.71	± 807.31	79.29	0.58	0.0327	± 0.3280
10	0.0000044	28.628	0.0027920	155.464	0.0000308	124.881	0.0000566	21.797	0.0141763	1.502	239.70861	± 113.21437	2283.64	± 612.47	92.34	0.65	0.0102	± 0.0320
11	0.0000102	12.110	0.0118822	30.464	0.0000196	224.516	0.0002026	8.357	0.0327294	0.649	157.53182	± 28.24849	1773.41	± 202.64	93.55	2.33	0.0085	± 0.0054
12	0.0000408	3.127	0.0756318	5.617	0.0001361	26.068	0.0012145	1.136	0.2586598	0.083	217.29103	± 5.36811	2158.11	± 31.13	97.61	13.90	0.0080	± 0.0009
13	0.0000213	6.655	0.0275914	18.834	0.0000253	194.099	0.0005420	2.342	0.1053260	0.206	193.48730	± 10.06052	2014.52	± 63.16	96.04	6.25	0.0099	± 0.0037
14	0.0000202	6.788	0.0001184	3349.508	0.0000050	698.736	0.0001538	9.697	0.0559099	0.380	324.49152	± 64.44063	2692.41	± 278.08	89.21	1.84	0.6750	± 45.2183
15	0.0000181	7.097	0.0100809	38.349	0.0000345	102.042	0.0002669	5.137	0.0479003	0.448	166.57270	± 18.37607	1837.13	± 127.26	90.38	3.11	0.0134	± 0.0104
16	0.0000379	3.599	0.0099272	35.499	0.0000701	47.971	0.0004460	3.109	0.0572661	0.373	106.43284	± 7.25317	1363.76	± 65.26	81.60	5.25	0.0230	± 0.0164
17	0.0000420	3.757	0.0112452	30.668	0.0000508	87.477	0.0007044	1.749	0.0645227	0.331	75.88224	± 3.20934	1065.59	± 34.05	81.93	8.33	0.0322	± 0.0198
18	0.0000604	2.438	0.0005092	694.960	0.0000032	1705.062	0.0007284	1.774	0.0643786	0.331	63.70910	± 2.77439	931.57	± 31.70	72.05	8.71	0.7436	± 10.3349
19	0.0002306	0.649	0.0189869	16.103	0.0000295	129.462	0.0039811	0.370	0.3052578	0.070	59.96167	± 0.52992	888.24	± 6.20	77.94	47.47	0.1087	± 0.0350

Step	36Ar	%1σ	37Ar	1%σ	38Ar	%1σ	39Ar	%1σ	40Ar	%1σ	40(r)/39(K)	± 2σ	Age	± 2σ	40Ar(r)	39Ar (k)	K/Ca	± 2σ
	[fA]		[fA]		[fA]		[fA]		[fA]				(Ma)		(%)	(%)		

DAR1712 Biotite: J = 0.01057910 ± 0.00000476 (1σ)

1	0.0000010	126.911	0.0002809	963.095	0.0000176	216.621	0.0001140	9.506	0.003926	12.525	32.01215	± 13.20887	527.38	± 188.75	92.76	0.06	0.2	± 4.1
2	0.0000061	21.713	0.0000334	6311.284	0.0000070	704.208	0.0009350	1.206	0.022450	2.191	22.06821	± 1.49349	379.40	± 23.16	91.91	0.53	14.6	± 1839.3
3	0.0000058	22.947	0.0000504	5291.826	0.0000329	113.897	0.0017631	0.569	0.039264	1.254	21.28790	± 0.79628	367.25	± 12.43	95.59	1.00	18.2	± 1926.2
4	0.0000074	17.589	0.0028842	97.708	0.0000778	54.177	0.0027931	0.371	0.097763	0.504	34.11014	± 0.54066	557.12	± 7.60	97.52	1.59	0.5	± 1.0

5	0.0000061	21.615	0.0005631	370.326	0.0000020	1486.302	0.0018808	0.514	0.131677	0.374	69.07555	± 0.99932	991.88	± 11.04	98.64	1.07	1.7	± 12.9
6	0.0000045	29.896	0.0019932	114.232	0.0000270	134.004	0.0017067	0.725	0.174674	0.282	101.72999	± 1.67821	1320.94	± 15.46	99.32	0.97	0.4	± 1.0
7	0.0000075	16.790	0.0002679	855.842	0.0000126	324.107	0.0031603	0.323	0.348196	0.141	109.47976	± 0.82328	1390.97	± 7.30	99.36	1.80	6.1	± 105.0
8	0.0000103	12.602	0.0013851	137.354	0.0000844	47.949	0.0056509	0.240	0.635719	0.077	111.91524	± 0.58561	1412.42	± 5.13	99.50	3.22	2.1	± 5.8
9	0.0000116	11.512	0.0034736	63.099	0.0001579	25.667	0.0093414	0.129	1.067637	0.047	113.97878	± 0.32916	1430.41	± 2.85	99.70	5.32	1.4	± 1.8
10	0.0000142	9.160	0.0012669	186.316	0.0002537	12.792	0.0148788	0.083	1.709771	0.029	114.64099	± 0.21133	1436.14	± 1.83	99.76	8.48	6.1	± 22.8
11	0.0000284	5.096	0.0062923	40.529	0.0004228	7.964	0.0290743	0.064	3.451545	0.014	118.45753	± 0.15866	1468.84	± 1.35	99.77	16.57	2.4	± 1.9
12	0.0000161	8.817	0.0030717	75.916	0.0002620	12.916	0.0202321	0.075	2.455814	0.020	121.11928	± 0.19460	1491.29	± 1.63	99.79	11.53	3.4	± 5.2
13	0.0000124	11.101	0.0011318	238.290	0.0001842	21.652	0.0141968	0.073	1.719312	0.029	120.85610	± 0.20261	1489.09	± 1.70	99.79	8.09	6.5	± 31.1
14	0.0000104	12.622	0.0003860	661.336	0.0001418	31.878	0.0105644	0.108	1.277533	0.039	120.62708	± 0.29280	1487.16	± 2.46	99.75	6.02	14.2	± 188.2
15	0.0000065	19.624	0.0026724	94.983	0.0001634	25.279	0.0100614	0.125	1.221517	0.041	121.25656	± 0.33234	1492.44	± 2.78	99.86	5.73	2.0	± 3.7
16	0.0000039	33.184	0.0002741	1015.887	0.0000783	47.645	0.0064391	0.183	0.788217	0.063	122.22374	± 0.49795	1500.53	± 4.15	99.85	3.67	12.2	± 248.2
17	0.0000083	17.222	0.0031399	79.510	0.0000969	37.076	0.0089729	0.113	1.092939	0.045	121.58373	± 0.31859	1495.18	± 2.67	99.79	5.11	1.5	± 2.4
18	0.0000082	15.169	0.0007384	262.739	0.0001665	23.833	0.0093871	0.120	1.148393	0.043	122.06326	± 0.32397	1499.19	± 2.70	99.78	5.35	6.6	± 34.7
19	0.0000087	14.360	0.0009969	254.838	0.0001070	34.939	0.0077333	0.167	0.961610	0.053	124.03145	± 0.45227	1515.55	± 3.74	99.74	4.41	4.0	± 20.6
20	0.0000089	14.741	0.0037233	70.870	0.0000299	137.301	0.0059275	0.182	0.755424	0.065	127.10154	± 0.51993	1540.77	± 4.24	99.69	3.38	0.8	± 1.2
21	0.0000054	25.713	0.0013083	208.697	0.0000473	90.069	0.0031903	0.279	0.407269	0.121	127.08218	± 0.83983	1540.61	± 6.85	99.58	1.82	1.3	± 5.3
22	0.0000062	21.701	0.0020073	121.012	0.0000170	204.022	0.0024108	0.448	0.310211	0.159	127.77030	± 1.28168	1546.22	± 10.43	99.35	1.37	0.6	± 1.5
23	0.0000079	17.469	0.0011285	203.214	0.0000558	81.961	0.0019008	0.561	0.250505	0.197	130.44838	± 1.63777	1567.87	± 13.16	99.02	1.08	0.9	± 3.6
24	0.0000060	22.953	0.0014567	149.956	0.0000190	268.129	0.0013852	0.855	0.178033	0.276	127.05616	± 2.38828	1540.40	± 19.49	98.93	0.79	0.5	± 1.5
25	0.0000162	8.014	0.0024121	108.395	0.0000248	171.581	0.0017551	0.760	0.230161	0.214	128.15060	± 2.10160	1549.31	± 17.07	97.82	1.00	0.4	± 0.8
Step	36Ar	%1σ	37Ar	1%σ	38Ar	%1σ	39Ar	%1σ	40Ar	%1σ	40(r)/39(K)	± 2σ	Age	± 2σ	40Ar(r)	39Ar (k)	K/Ca	± 2σ
	[fA]		[fA]		[fA]		[fA]		[fA]				(Ma)		(%)	(%)		

YAM1705 Hornblende: J = 0.01067510 ± 0.00001228 (1σ)

1	0.0000588	1.491	0.0005193	673.520	0.0000471	82.405	0.0000131	70.318	0.0637510	0.332	3639.04186	± 5444.64680	6663.14	± 2637.43	72.53	1.07	0.013	± 0.172
2	0.0000037	23.688	0.0007464	623.543	0.0000167	255.928	0.0000086	137.619	0.0042729	4.983	341.16193	± 924.42813	2775.76	± 3843.98	73.11	0.77	0.006	± 0.081
3	0.0000015	49.114	0.0016809	247.213	0.0000067	630.658	0.0000111	97.326	0.0011460	18.445	56.51961	± 156.37552	1672.01	± 7609.77	48.88	0.83	0.003	± 0.017
4	0.0000006	134.396	0.0041117	114.193	0.0000168	286.504	0.0000095	124.434	0.0003395	62.348	25.85417	± 177.36583	440.70	± 2683.05	50.61	0.56	0.001	± 0.004
5	0.0000025	29.494	0.0005089	826.067	0.0000349	106.124	0.0000042	261.112	0.0005312	39.932	47.81543	± 367.93917	1291.45	± 14506.84	34.59	0.32	0.004	± 0.069
6	0.0000026	32.899	0.0009563	444.930	0.0000563	87.673	0.0000033	353.337	0.0007861	26.978	35.85106	± 487.06429	585.93	± 6799.26	11.93	0.22	0.001	± 0.018
7	0.0000006	142.465	0.0022528	192.534	0.0000321	126.014	0.0000093	152.723	0.0004786	44.245	11.18467	± 93.18477	203.94	± 1606.82	25.28	0.91	0.002	± 0.012
8	0.0000020	38.631	0.0058175	64.660	0.0000714	55.358	0.0000029	410.992	0.0008115	26.133	37.49398	± 181.93581	924.41	± 5855.40	32.12	0.58	0.001	± 0.002
9	0.0000032	28.781	0.0052018	75.425	0.0000004	11922.932	0.0000932	12.186	0.0033439	6.325	31.29793	± 13.19912	521.22	± 190.97	83.87	7.53	0.009	± 0.014
10	0.0000024	30.807	0.0075755	52.478	0.0000339	112.321	0.0003178	3.482	0.0079715	2.651	25.13996	± 3.34905	429.86	± 50.97	98.58	26.25	0.021	± 0.023
11	0.0000040	18.566	0.0016587	205.453	0.0000050	873.725	0.0000718	15.714	0.0034750	6.128	34.32174	± 16.08236	564.45	± 227.19	69.79	5.93	0.022	± 0.091
12	0.0000068	10.994	0.0023743	140.673	0.0000505	77.793	0.0001074	10.575	0.0050675	4.180	30.59632	± 10.18290	511.05	± 148.16	63.84	8.88	0.023	± 0.065
13	0.0000119	9.595	0.0004240	970.837	0.0000114	321.742	0.0001091	9.756	0.0074543	2.855	35.31834	± 11.83584	578.48	± 165.91	51.85	9.19	0.134	± 2.606
14	0.0000284	3.001	0.0031954	154.817	0.0000211	203.926	0.0000755	14.080	0.0109460	1.939	36.94882	± 17.96866	601.19	± 248.73	24.74	6.16	0.012	± 0.037
15	0.0000132	6.452	0.0014311	289.107	0.0000453	81.029	0.0000166	62.256	0.0047561	4.447	39.66437	± 71.60405	638.39	± 970.98	14.70	1.48	0.006	± 0.038

J.Y. Li Appendix E: Supplementary material to Chapter 5

16	0.0000233	4.419	0.0025231	172.317	0.0000493	74.535	0.0000317	38.877	0.0094417	2.242	68.66444	± 60.28246	994.22	± 671.43	24.33	2.81	0.007	± 0.024
17	0.0000152	5.098	0.0028466	122.126	0.0000188	210.258	0.0000411	23.721	0.0054764	3.884	29.43092	± 26.19181	494.01	± 384.70	21.01	3.28	0.007	± 0.018
18	0.0000322	2.829	0.0059287	76.369	0.0000039	974.544	0.0000602	16.979	0.0135520	1.562	53.92884	± 23.67392	822.16	± 290.00	25.60	5.40	0.006	± 0.009
19	0.0000578	1.520	0.0017010	219.542	0.0000556	77.277	0.0002465	4.692	0.0227134	0.930	22.85316	± 4.27043	394.72	± 66.26	24.68	20.60	0.075	± 0.329

Step	36Ar	%1σ	37Ar	1%σ	38Ar	%1σ	39Ar	%1σ	40Ar	%1σ	40(r)/ 39(K)	± 2σ	Age	± 2σ	40Ar(r)	39Ar (k)	K/Ca	± 2σ
	[fA]		[fA]		[fA]		[fA]		[fA]				(Ma)		(%)	(%)		

YAM1709 Hornblend: J = 0.01067510 ± 0.00001228 (1σ)

1	0.0000122	8.285	0.0020697	186.136	0.0000565	108.411	0.0000576	29.214	0.0057267	4.098	32.55361	± 25.05763	539.30	± 358.93	33.56	0.69	0.0148	± 0.0559
2	0.0000045	16.239	0.0033630	95.788	0.0000130	465.125	0.0000328	52.592	0.0018293	12.844	24.43842	± 38.78482	419.15	± 593.74	40.71	0.36	0.0047	± 0.0105
3	0.0000052	14.124	0.0009578	385.719	0.0000377	137.774	0.0001203	13.956	0.0041726	5.623	21.12242	± 9.30614	367.66	± 146.58	61.25	1.42	0.0657	± 0.5071
4	0.0000090	9.588	0.0092212	37.900	0.0000032	1700.527	0.0004997	3.326	0.0138951	1.690	24.21557	± 2.44280	415.74	± 37.47	85.97	5.79	0.0278	± 0.0212
5	0.0000206	3.944	0.0514986	8.513	0.0000416	132.273	0.0023269	0.731	0.0573152	0.410	24.10897	± 0.55846	414.10	± 8.57	96.37	26.87	0.0231	± 0.0040
6	0.0000141	7.734	0.0202412	18.254	0.0001071	55.864	0.0014623	1.303	0.0368897	0.638	23.67039	± 0.93143	407.36	± 14.35	92.92	16.98	0.0372	± 0.0136
7	0.0000074	10.517	0.0039871	99.612	0.0000211	238.913	0.0002835	7.299	0.0086976	2.698	24.22796	± 4.85204	415.93	± 74.41	78.21	3.29	0.0366	± 0.0732
8	0.0000091	8.978	0.0036009	105.293	0.0000009	6621.301	0.0001490	11.808	0.0054435	4.322	20.52440	± 7.94321	358.22	± 125.77	55.22	1.72	0.0211	± 0.0448
9	0.0000138	6.012	0.0013021	280.423	0.0000375	132.619	0.0002808	6.067	0.0100715	2.341	20.80294	± 4.07022	362.62	± 64.29	58.18	3.30	0.1125	± 0.6310
10	0.0000127	6.855	0.0024943	163.554	0.0000494	108.354	0.0003113	5.315	0.0104014	2.264	22.01596	± 3.89614	381.68	± 60.89	65.53	3.63	0.0645	± 0.2112
11	0.0000152	5.311	0.0024229	180.375	0.0000036	1413.484	0.0001884	9.565	0.0084267	2.788	21.91728	± 6.71449	380.14	± 105.03	48.57	2.19	0.0401	± 0.1448
12	0.0000260	3.402	0.0083350	51.550	0.0000299	187.209	0.0003192	5.372	0.0145166	1.618	23.71092	± 4.08961	407.98	± 62.99	51.19	3.68	0.0196	± 0.0203
13	0.0000243	4.064	0.0010367	408.864	0.0000290	207.600	0.0003681	4.567	0.0154120	1.529	22.45859	± 3.45076	388.59	± 53.73	53.53	4.31	0.1843	± 1.5068

14	0.0000374	2.913	0.0037572	106.426	0.0000456	122.255	0.0003536	4.723	0.0184699	1.276	21.63862	± 3.58610	375.77	± 56.23	41.12	4.12	0.0486	± 0.1035
15	0.0000347	2.382	0.0071038	53.566	0.0000404	137.289	0.0004293	4.019	0.0193772	1.213	22.60375	± 2.83754	390.85	± 44.12	49.50	4.98	0.0311	± 0.0334
16	0.0000527	1.510	0.0056203	62.588	0.0000361	157.563	0.0002594	6.769	0.0212268	1.107	23.23470	± 4.69038	400.63	± 72.54	27.97	3.00	0.0236	± 0.0298
17	0.0000543	1.692	0.0128983	26.822	0.0000211	257.569	0.0005817	2.959	0.0281195	0.835	22.57129	± 2.09414	390.34	± 32.57	45.97	6.72	0.0231	± 0.0125
18	0.0000755	1.943	0.0007772	510.057	0.0000394	130.918	0.0001273	13.483	0.0244419	0.959	14.44421	± 10.00482	259.29	± 167.32	7.55	1.50	0.0855	± 0.8726
19	0.0001718	0.799	0.0044034	102.773	0.0000059	899.419	0.0004690	3.563	0.0634478	0.372	26.80178	± 3.21852	454.97	± 48.30	19.68	5.47	0.0550	± 0.1132

Step	36Ar	%1σ	37Ar	1%σ	38Ar	%1σ	39Ar	%1σ	40Ar	%1σ	40(r)/ 39(K)	± 2σ	Age	± 2σ	40Ar(r)	39Ar (k)	K/Ca	± 2σ
	[fA]		[fA]		[fA]		[fA]		[fA]				(Ma)		(%)	(%)		

YAM1713 Muscovite: J = 0.01057910 ± 0.00000476 (1σ)

1	0.0000009	82.742	0.0009633	263.368	0.0000427	123.331	0.0001124	9.643	0.0020096	7.959	14.67399	± 6.73480	260.93	± 111.52	82.58	0.10	0.1	± 0.3
2	0.0000024	33.810	0.0038073	72.471	0.0000169	198.091	0.0003981	3.175	0.0096534	1.666	23.33841	± 2.38835	398.99	± 36.64	95.60	0.35	0.1	± 0.1
3	0.0000085	10.123	0.0004752	612.500	0.0004332	8.044	0.0334474	0.051	0.7802322	0.021	23.25194	± 0.03306	397.66	± 0.51	99.68	29.56	36.6	± 448.4
4	0.0000053	14.252	0.0028148	115.355	0.0006362	5.778	0.0522725	0.044	1.2175014	0.016	23.26537	± 0.02558	397.87	± 0.39	99.88	46.19	9.7	± 22.3
5	0.0000018	38.492	0.0027890	128.376	0.0000994	34.962	0.0070969	0.191	0.1659499	0.097	23.34514	± 0.14155	399.09	± 2.17	99.81	6.27	1.3	± 3.4
6	0.0000002	252.910	0.0005556	484.225	0.0000418	86.937	0.0035915	0.311	0.0842253	0.190	23.44565	± 0.23218	400.63	± 3.56	99.96	3.17	3.4	± 32.6
7	0.0000014	44.690	0.0016615	149.062	0.0000516	71.836	0.0057381	0.198	0.1343686	0.120	23.31634	± 0.14398	398.65	± 2.21	99.59	5.07	1.8	± 5.4
8	0.0000013	60.003	0.0011815	229.985	0.0000607	67.811	0.0029567	0.416	0.0691772	0.234	23.30793	± 0.30849	398.52	± 4.73	99.59	2.61	1.3	± 6.0
9	0.0000010	50.081	0.0000322	8167.098	0.0000582	59.141	0.0018968	0.641	0.0444516	0.359	23.26975	± 0.44131	397.93	± 6.77	99.30	1.68	30.6	± 5000.0
10	0.0000017	38.125	0.0000795	3759.282	0.0000562	63.208	0.0032112	0.431	0.0753174	0.212	23.29444	± 0.29552	398.31	± 4.54	99.32	2.84	21.0	± 1578.3
11	0.0000024	21.408	0.0020461	136.291	0.0000509	73.279	0.0014445	0.688	0.0339750	0.470	22.89263	± 0.53807	392.14	± 8.29	97.43	1.28	0.4	± 1.0
12	0.0000005	135.510	0.0005313	538.510	0.0000405	134.279	0.0003211	3.138	0.0072623	2.207	22.28131	± 2.62287	382.70	± 40.60	98.42	0.28	0.3	± 3.4
13	0.0000023	26.432	0.0000225	13227.741	0.0000201	214.135	0.0004944	2.198	0.0118215	1.348	22.55780	± 1.69210	386.97	± 26.13	94.34	0.44	11.4	± 3016.5

14	0.0000022	25.628	0.0033126	76.776	0.0000504	64.661	0.0000335	35.490	0.0015516	10.332	17.51588	± 20.89109	307.38	± 337.14	40.42	0.03	0.0	± 0.0
15	0.0000037	16.589	0.0013910	197.315	0.0000115	467.583	0.0000280	35.350	0.0011329	14.049	2.98695	± 22.62565	58.06	± 446.92	7.64	0.03	0.0	± 0.0
16	0.0000033	19.616	0.0019014	168.263	0.0000545	71.721	0.0000633	16.857	0.0022896	6.948	23.37998	± 14.16061	399.63	± 217.16	63.29	0.05	0.0	± 0.1
17	0.0000100	7.131	0.0034452	69.533	0.0000284	159.654	0.0000626	15.533	0.0040699	3.936	12.38423	± 10.75848	222.61	± 181.96	19.77	0.06	0.0	± 0.0

Step	36Ar	%1σ	37Ar	1%σ	38Ar	%1σ	39Ar	%1σ	40Ar	%1σ	40(r)/ 39(K)	± 2σ	Age	± 2σ	40Ar(r)	39Ar (k)	K/Ca	± 2σ
	[fA]		[fA]		[fA]		[fA]		[fA]				(Ma)		(%)	(%)		

COE1706 Muscovite: J = 0.01057910 ± 0.00000476 (1σ)

1	0.0000009	312.754	0.0016192	259.372	0.0000769	63.726	0.0000073	198.118	0.0003326	220.802	6.45803	± 854.36735	127.96	± 17541.32	11.99	0.00	0.00	± 0.01
2	0.0000022	119.129	0.0006742	631.730	0.0000044	1103.243	0.0002183	7.187	0.0062409	11.764	18.86860	± 24.60543	329.08	± 392.35	66.14	0.10	0.17	± 2.13
3	0.0000043	61.224	0.0002309	1481.847	0.0000069	663.681	0.0013877	1.101	0.0353869	2.076	22.75804	± 3.87348	390.06	± 59.72	89.25	0.66	3.13	± 92.62
4	0.0000096	28.024	0.0010347	376.094	0.0001111	43.626	0.0086157	0.197	0.2127022	0.345	23.68225	± 0.75263	404.25	± 11.51	95.93	4.11	4.33	± 32.57
5	0.0000078	33.981	0.0008311	479.142	0.0003533	15.317	0.0281078	0.070	0.6808241	0.109	23.97107	± 0.21677	408.67	± 3.31	98.97	13.40	17.59	± 168.52
6	0.0000138	19.103	0.0010204	449.084	0.0010390	4.651	0.0871386	0.040	2.0976283	0.035	23.93635	± 0.08617	408.14	± 1.32	99.43	41.55	44.41	± 398.84
7	0.0000008	334.506	0.0014792	309.279	0.0002124	23.669	0.0174771	0.117	0.4200531	0.175	23.97290	± 0.31134	408.69	± 4.75	99.75	8.33	6.14	± 38.01
8	0.0000003	772.732	0.0076450	72.765	0.0000948	60.487	0.0077319	0.249	0.1850824	0.397	23.73022	± 0.72286	404.99	± 11.05	99.20	3.69	0.53	± 0.77
9	0.0000001	2829.345	0.0030757	154.210	0.0001185	45.920	0.0060075	0.252	0.1427652	0.514	23.65393	± 0.91924	403.82	± 14.06	99.57	2.87	1.02	± 3.13
10	0.0000011	236.450	0.0002053	1874.071	0.0000747	79.121	0.0093460	0.166	0.2213602	0.332	23.58504	± 0.56064	402.77	± 8.58	99.58	4.46	23.67	± 887.08
11	0.0000014	184.210	0.0027976	162.240	0.0001065	50.332	0.0091910	0.175	0.2205792	0.333	23.78598	± 0.59021	405.84	± 9.02	99.13	4.38	1.71	± 5.54
12	0.0000017	153.721	0.0041022	107.631	0.0000614	86.677	0.0087177	0.171	0.2097444	0.350	23.76762	± 0.62692	405.56	± 9.58	98.82	4.16	1.11	± 2.38
13	0.0000065	41.512	0.0035439	117.835	0.0001654	31.976	0.0124392	0.122	0.3033232	0.243	23.85741	± 0.48498	406.93	± 7.41	97.86	5.93	1.83	± 4.30

14	0.0000042	62.907	0.0001118	3993.802	0.0000924	53.155	0.0042820	0.379	0.1075189	0.683	24.24538	± 1.30177	412.85	± 19.82	96.56	2.04	19.92	± 1591.53
15	0.0000100	26.832	0.0028492	158.403	0.0001044	56.037	0.0058511	0.296	0.1484528	0.495	23.76201	± 1.15062	405.47	± 17.59	93.69	2.79	1.07	± 3.38
16	0.0000082	33.405	0.0039936	105.197	0.0000353	136.864	0.0024492	0.678	0.0860088	0.854	31.79334	± 2.63553	524.25	± 37.73	90.64	1.17	0.32	± 0.67
17	0.0000333	8.475	0.0042110	122.334	0.0000505	106.887	0.0007311	1.908	0.0937141	0.784	86.74227	± 19.51601	1177.30	± 194.67	67.94	0.35	0.09	± 0.22

COE1708 Hornblende: J = 0.01067510 ± 0.00001228 (1σ)

Step	36Ar	%1σ	37Ar	1%σ	38Ar	%1σ	39Ar	%1σ	40Ar	%1σ	40(r)/39(K)	± 2σ	Age	± 2σ	40Ar(r)	39Ar (k)	K/Ca	± 2σ
	[fA]		[fA]		[fA]		[fA]		[fA]				(Ma)		(%)	(%)		
1	0.0000702	2.311	0.0035080	107.227	0.0000051	809.514	0.0000574	17.342	0.2381457	0.358	3626.28532	± 1247.89195	6656.95	± 606.56	91.08	0.27	0.009	± 0.019
2	0.0000589	2.894	0.0066177	49.360	0.0000053	720.688	0.0000237	38.974	0.1152679	0.739	3431.79643	± 2308.26666	6559.86	± 1183.87	84.30	0.13	0.002	± 0.003
3	0.0000345	4.848	0.0007108	560.058	0.0000257	149.583	0.0000685	16.569	0.0433763	1.964	478.48677	± 164.79227	3272.00	± 520.78	76.14	0.31	0.050	± 0.566
4	0.0000230	7.226	0.0001057	3918.942	0.0000155	286.255	0.0001020	9.065	0.0274976	3.098	201.96105	± 43.39310	2078.10	± 265.40	74.98	0.46	0.502	± 39.365
5	0.0000125	14.203	0.0017737	213.380	0.0000267	168.311	0.0001633	8.034	0.0269075	3.166	143.94785	± 27.04940	1683.12	± 205.83	86.70	0.72	0.048	± 0.203
6	0.0000112	15.200	0.0023081	135.991	0.0000006	6820.563	0.0003648	3.034	0.0529593	1.609	137.10124	± 10.21212	1630.25	± 80.01	94.02	1.62	0.082	± 0.223
7	0.0000065	24.842	0.0012744	380.069	0.0000639	60.263	0.0005127	2.086	0.0899538	0.947	172.15183	± 8.59203	1885.92	± 58.44	97.95	2.28	0.209	± 1.587
8	0.0000128	12.895	0.0011392	272.940	0.0000186	160.042	0.0008235	1.489	0.2118255	0.403	252.93270	± 8.04189	2365.71	± 41.95	98.24	3.67	0.376	± 2.050
9	0.0001245	1.579	0.0348384	9.808	0.0001514	25.349	0.0057964	0.166	1.5628158	0.055	264.78819	± 0.98410	2426.52	± 4.96	97.80	25.75	0.086	± 0.017
10	0.0000558	3.009	0.0519185	7.568	0.0001829	17.730	0.0087895	0.138	1.4414382	0.059	163.23918	± 0.52018	1824.26	± 3.66	99.13	39.05	0.088	± 0.013
11	0.0000067	24.386	0.0035372	102.101	0.0000266	102.769	0.0004814	1.952	0.0819817	1.039	167.60624	± 8.03554	1854.73	± 55.61	97.91	2.14	0.070	± 0.144
12	0.0000120	13.723	0.0047600	92.683	0.0000413	94.081	0.0008641	1.137	0.1493455	0.571	169.77873	± 4.72916	1869.70	± 32.46	97.85	3.84	0.094	± 0.174

13	0.0000106	15.295	0.0038254	102.836	0.0000219	227.882	0.0007443	1.476	0.1507978	0.565	199.46705	± 6.69191	2062.78	± 41.28	98.10	3.31	0.101	± 0.207
14	0.0000124	13.973	0.0001607	2410.223	0.0000155	264.682	0.0003468	2.971	0.0705570	1.208	192.74259	± 13.27079	2020.82	± 83.78	94.76	1.55	1.122	± 54.100
15	0.0000222	7.496	0.0076490	47.913	0.0000297	172.693	0.0015324	0.810	0.2940642	0.290	188.61906	± 3.40808	1994.60	± 21.83	97.95	6.81	0.104	± 0.099
16	0.0000230	6.912	0.0024119	134.877	0.0000122	288.417	0.0004559	2.030	0.0897245	0.950	182.79523	± 8.86283	1956.90	± 57.96	92.55	2.03	0.098	± 0.264
17	0.0000183	9.249	0.0021834	197.338	0.0000199	228.116	0.0005242	2.508	0.0923822	0.923	165.00576	± 9.35751	1836.65	± 65.41	93.90	2.35	0.125	± 0.494
18	0.0000447	3.613	0.0036328	89.779	0.0000090	407.244	0.0005077	2.016	0.0903005	0.944	152.92643	± 7.50564	1750.18	± 55.03	85.55	2.25	0.072	± 0.130
19	0.0000747	2.380	0.0068719	61.852	0.0000166	183.240	0.0003272	3.768	0.0633699	1.345	122.06656	± 11.29737	1508.44	± 94.68	63.95	1.48	0.025	± 0.031

Step	36Ar	%1σ	37Ar	1%σ	38Ar	%1σ	39Ar	%1σ	40Ar	%1σ	40(r)/ 39(K)	± 2σ	Age	± 2σ	40Ar(r)	39Ar (k)	K/Ca	± 2σ
	[fA]		[fA]		[fA]		[fA]		[fA]				(Ma)		(%)	(%)		

YAM1712 Biotite: J = 0.01067510 ± 0.00001228 (1σ)

1	0.0000183	4.761	0.0006730	507.388	0.0000031	1390.928	0.0015027	0.799	0.103433	0.601	65.14319	± 1.43532	947.89	± 16.25	94.67	1.33	1.16	± 11.79
2	0.0001523	0.678	0.0039741	84.227	0.0002074	25.309	0.0172322	0.111	1.393681	0.045	78.26871	± 0.19555	1090.73	± 2.05	96.76	15.26	2.25	± 3.80
3	0.0001033	1.001	0.0059371	59.686	0.0002365	16.197	0.0172491	0.078	1.700075	0.037	96.82217	± 0.17714	1275.15	± 1.67	98.21	15.28	1.51	± 1.80
4	0.0001092	0.926	0.0021540	165.946	0.0000196	255.260	0.0193013	0.087	1.932729	0.032	98.42896	± 0.18963	1290.27	± 1.78	98.30	17.10	4.66	± 15.47
5	0.0000788	1.304	0.0002677	1250.633	0.0001809	27.199	0.0144968	0.083	1.402770	0.045	95.13870	± 0.19122	1259.17	± 1.82	98.32	12.84	28.16	± 704.32
6	0.0000400	1.837	0.0048196	67.228	0.0000988	37.846	0.0070650	0.175	0.684755	0.091	95.13343	± 0.39269	1259.12	± 3.74	98.20	6.26	0.76	± 1.03
7	0.0000202	3.979	0.0012031	273.515	0.0000998	49.897	0.0037357	0.333	0.377880	0.165	99.58521	± 0.77542	1301.07	± 7.22	98.43	3.31	1.61	± 8.83
8	0.0000209	4.208	0.0025790	169.253	0.0000545	99.828	0.0035941	0.367	0.365006	0.171	99.92434	± 0.86314	1304.23	± 8.03	98.34	3.18	0.72	± 2.45
9	0.0000166	4.279	0.0072691	48.156	0.0000267	169.714	0.0027898	0.519	0.289567	0.215	102.41348	± 1.19493	1327.22	± 10.97	98.49	2.47	0.20	± 0.19
10	0.0000378	2.269	0.0039868	99.991	0.0001137	45.251	0.0062969	0.217	0.691107	0.090	108.05936	± 0.53373	1378.33	± 4.76	98.41	5.58	0.82	± 1.64
11	0.0000300	3.010	0.0017470	214.978	0.0000648	62.987	0.0054797	0.266	0.569979	0.110	102.33150	± 0.61524	1326.47	± 5.65	98.40	4.85	1.63	± 7.01
12	0.0000268	2.974	0.0042258	79.877	0.0000454	90.888	0.0051040	0.223	0.552137	0.113	106.48389	± 0.56029	1364.22	± 5.04	98.49	4.52	0.63	± 1.00

13	0.0000339	2.136	0.0005259	684.235	0.0000617	76.185	0.0066494	0.217	0.726613	0.086	107.74188	± 0.52128	1375.50	± 4.66	98.60	5.89	6.58	± 89.98
14	0.0000121	6.615	0.0009790	397.681	0.0000345	137.699	0.0022516	0.550	0.223254	0.279	97.61773	± 1.27821	1282.65	± 12.03	98.42	1.99	1.20	± 9.51
15	0.0000037	19.905	0.0030914	154.039	0.0000024	1773.169	0.0001582	7.167	0.011490	5.412	68.22122	± 14.18681	982.41	± 157.62	92.63	0.14	0.03	± 0.08
16	0.0000019	45.195	0.0026353	131.014	0.0000003	12673.374	0.0000215	52.202	0.004043	15.382	187.48623	± 230.83656	1976.45	± 1480.04	91.31	0.02	0.00	± 0.01
17	0.0000091	8.318	0.0003574	1051.590	0.0000157	266.742	0.0000200	70.294	0.009666	6.434	345.29472	± 492.95747	0.00	± 3554.44	72.23	0.02	0.03	± 0.62

Appendix E:
Supplementary materials to Chapter 5

Table E.5.1 Previously published Nd isotopic analyses the North Queensland (Modified from Champion et al., 2013).

Sample Id	Lithology	Age (Ma)	εNd	T_{2DM} (Ga)	Reference	Longitude	Latitude	Group	Domain	Sm (ppm)	Nd (ppm)	$^{147}Sm/^{144}Nd$	$^{143}Nd/^{144}Nd$
Mount Isa Inlier													
8223	igneous	1890	-0.17	2.34	Bierlein & Betts 2004	139.6582	-20.8105	Kurbayia Migmatite	western belt	15.74	90.52	0.1051	0.51149
8218	igneous	1890	-2.68	2.53	Bierlein & Betts 2004	139.8372	-21.7068	Plum Mountain Gneiss	western belt	8.1	42.32	0.1158	0.511495
828	igneous	1890	-2.7	2.53	Bierlein & Betts 2004	139.2090	-20.8097	Yaringa Metamorphics	western belt	5.22	29.64	0.1064	0.511377
829	igneous	1890	-2.81	2.54	Bierlein & Betts 2004	139.1976	-20.8014	Yaringa Metamorphics	western belt	7.96	44.6	0.1078	0.511389
8210	igneous	1890	-3.17	2.57	Bierlein & Betts 2004	139.1729	-20.7759	Yaringa Metamorphics	western belt	7.43	38.7	0.1161	0.511474
8212	igneous	1890	-2.26	2.5	Bierlein & Betts 2004	139.1970	-20.8329	Yaringa Metamorphics	western belt	12.19	69.97	0.1053	0.511386
8211	igneous	1890	-3.18	2.57	Bierlein & Betts 2004	N/A	N/A	Yaringa Metamorphics	western belt	6.13	33.49	0.1107	0.511406
FBMI6514	igneous mafic intrusive	1860	2.32	2.13	Bierlein et al. 2011	139.3979	-20.6420	Dolerite	western belt	9.146	41.716	0.132	0.512
FBMI6510	igneous felsic intrusive	1775	-2.15	2.4	Bierlein et al. 2011	139.8228	-20.3975	Plagioclase porphyry, KG	western belt	13.241	67.087	0.119	0.512
FBMI6504	igneous felsic intrusive	1855	-2.98	2.53	Bierlein et al. 2011	139.8355	-20.0562	Felsic KG	western belt	7.983	50.841	0.095	0.511
FBMI6511C	igneous felsic intrusive	1860	-3.82	2.59	Bierlein et al. 2011	139.7888	-20.4500	Felsic KG	western belt	8.711	49.615	0.106	0.511
FBMI5601	igneous felsic intrusive	1718	-3.4	2.44	Bierlein et al. 2011	139.8716	-21.2296	Mt Erle Igneous Complex	western belt	16.413	88.3	0.112	0.512
FBMI5605	igneous felsic intrusive	1722	-2.71	2.4	Bierlein et al. 2011	139.8573	-21.1377	Revenue Granite	western belt	11.006	70.046	0.095	0.511
FBMI6508B	igneous mafic intrusive	1860	-4.13	2.62	Bierlein et al. 2011	139.7991	-20.3226	Diorite phase, KG	western belt	8.479	46.171	0.111	0.511
FBMI5604	igneous mafic intrusive	1860	-1.53	2.42	Bierlein et al. 2011	139.8532	21.36816	Dolerite	western belt	3.378	14.534	0.14	0.512
FBMI5608	igneous felsic intrusive	1860	-3.04	2.54	Bierlein et al. 2011	139.8317	-21.1317	N/A	western belt	5.973	27.8	0.13	0.512
FBMI6501	igneous felsic intrusive	1718	-6.8	2.52	Bierlein et al. 2011	N/A	N/A	Intermediate enclave in KG	western belt	10.059	44.879	0.135	0.512
FBMI5602	Amphibolitic gneiss	1860	-2.45	2.47	Bierlein et al. 2011	N/A	N/A	Amphibolitic gneiss	western belt	5.851	30.182	0.117	0.512

Mt Whelan 1	igneous felsic intrusive	1769	-2.6	2.43	GA unpublished	N/A	N/A	N/A	western belt	N/A	N/A	N/A	N/A
PDMT173B	igneous felsic intrusive	1861	-2.31	2.48	GA unpublished	N/A	N/A	N/A	western belt	N/A	N/A	N/A	N/A
IWMI2799	igneous felsic volcanic	1782	-0.41	2.27	GA unpublished	N/A	N/A	N/A	western belt	N/A	N/A	N/A	N/A
LJHMI576	igneous felsic volcanic	1857	-0.04	2.31	GA unpublished	N/A	N/A	N/A	western belt	N/A	N/A	N/A	N/A
LJHMI 775	igneous volcanic	1633	-3.9	2.41	GA unpublished	N/A	N/A	N/A	western belt	N/A	N/A	N/A	N/A
LJHMI 900	igneous felsic intrusive	1735	-4.84	2.57	GA unpublished	N/A	N/A	N/A	western belt	N/A	N/A	N/A	N/A
PDMT 174	igneous felsic intrusive	1792	-4.09	2.56	GA unpublished	N/A	N/A	N/A	eastern belt	N/A	N/A	N/A	N/A
LJHMI 420	igneous felsic intrusive	1679	-6.23	2.62	GA unpublished	N/A	N/A	N/A	western belt	N/A	N/A	N/A	N/A
PDMT 149	igneous felsic	1862	-3.63	2.58	GA unpublished	N/A	N/A	N/A	western belt	N/A	N/A	N/A	N/A
95208068	igneous	1890	-3.37	2.59	GA unpublished	N/A	N/A	N/A	western belt	N/A	N/A	N/A	N/A
PDMT155	igneous	1851	-3.12	2.53	GA unpublished	N/A	N/A	N/A	western belt	N/A	N/A	N/A	N/A
WPMI 1051	igneous felsic intrusive	1858	-3.04	2.53	GA unpublished	N/A	N/A	N/A	western belt	N/A	N/A	N/A	N/A
LJHMI 565A	igneous felsic intrusive	1795	-3	2.48	GA unpublished	N/A	N/A	N/A	western belt	N/A	N/A	N/A	N/A
WPMI1464	igneous felsic intrusive	1859	-2.91	2.52	GA unpublished	N/A	N/A	N/A	eastern belt	N/A	N/A	N/A	N/A
85206003	igneous mafic intrusive	1508	-2.52	2.2	GA unpublished	N/A	N/A	N/A	eastern belt	N/A	N/A	N/A	N/A
86206117	igneous mafic	1545	-2.9	2.26	GA unpublished	N/A	N/A	N/A	eastern belt	N/A	N/A	N/A	N/A
92208016	igneous felsic volcanic	1680	-2.7	2.36	GA unpublished	N/A	N/A	N/A	eastern belt	N/A	N/A	N/A	N/A
IWMI2804	igneous felsic volcanic	1768	-2.14	2.39	GA unpublished	N/A	N/A	N/A	eastern belt	N/A	N/A	N/A	N/A
92208025	igneous felsic volcanic	1745	-7.42	2.77	GA unpublished	N/A	N/A	N/A	eastern belt	N/A	N/A	N/A	N/A
95208052	igneous felsic volcanic	1760	0.83	2.16	GA unpublished	N/A	N/A	N/A	eastern belt	N/A	N/A	N/A	N/A
95208053	igneous felsic volcanic	1760	-1.96	2.37	GA unpublished	N/A	N/A	N/A	eastern belt	N/A	N/A	N/A	N/A
86206081	igneous mafic intrusive	1520	-2.78	2.23	GA unpublished	N/A	N/A	N/A	eastern belt	N/A	N/A	N/A	N/A
86206122	igneous felsic intrusive	1545	0.63	2	GA unpublished	N/A	N/A	N/A	eastern belt	N/A	N/A	N/A	N/A

LJHMI 752	igneous felsic volcanic	1819	-1.06	2.35	GA unpublished	N/A	N/A	N/A	western belt	N/A	N/A	N/A	N/A
85206007	igneous felsic intrusive	1508	-2.79	2.22	GA unpublished	N/A	N/A	N/A	eastern belt	N/A	N/A	N/A	N/A
86206120	igneous felsic intrusive	1545	-2.15	2.21	GA unpublished	N/A	N/A	N/A	eastern belt	N/A	N/A	N/A	N/A
92208038	igneous felsic intrusive	1680	-1.35	2.26	GA unpublished	N/A	N/A	N/A	eastern belt	N/A	N/A	N/A	N/A
2008165076	igneous felsic	1668	-25.09	4.04	Lambeck et al. 2012	325933	7819949	Gun Supersequence Pinkite	western belt	3.4	9.2	0.22524	0.51167
95779098	igneous felsic	1668	-2.77	2.35	Lambeck et al. 2012	325620	7819772	Lower Gunpowder Creek Pinkite	western belt	8.9	61.4	0.0888	0.511313
2008165068	igneous felsic	1668	-3.54	2.41	Lambeck et al. 2012	325479	7819811	Prize Supersequence Pinkite	western belt	9.6	59.9	0.09877	0.511383
92208013	igneous felsic intrusive	1654	-1.12	2.22	Lambeck et al. 2012	471900	7663200	Mount Norna Rhyolite	eastern belt	1.3	6.7	0.1181	0.511726
2004169015	igneous felsic intrusive	1674	-5.41	2.56	Lambeck et al. 2012	332902	771552	Guns Knob Granite	western belt	10.5	64.6	0.0985	0.511281
2004169018	igneous felsic intrusive	1670	-5.09	2.53	Lambeck et al. 2012	330928	7682946	Widgewarra Granite	western belt	19.6	108.6	0.1089	0.511414
74205211	igneous felsic volcanic	1678	-4.39	2.49	Lambeck et al. 2012	317700	7745700	Carters Bore Rhyolite	western belt	14.1	77.7	0.1099	0.511456
95779090	igneous volcanic	1647	0.4	2.1	Lambeck et al. 2012	295692	7811922	Lady Loretta -felsic tuff	western belt	10.9	74.1	0.0891	0.511493
95779104	igneous volcanic	1654	-1.28	2.23	Lambeck et al. 2012	325920	7819872	Paradise Creek- felsic tuff	western belt	4.6	32.5	0.0854	0.511362
91779005	igneous volcanic	1652	-1.34	2.23	Lambeck et al. 2012	340856	7724416	Urquhart Shale	western belt	3.8	25	0.0927	0.51144
2009165033	igneous mafic intrusive	1658	-0.73	2.19	Lambeck et al. 2012	448041	7647452	Toole Creek Volcanics	eastern belt	2	5.8	0.2071	0.512714
91779034	igneous volcanic	1639	-2.24	2.29	Lambeck et al. 2012	N/A	N/A	N/A	N/A	N/A	N/A	N/A	N/A
42732	igneous felsic intrusive	1520	-3.27	2.27	Mark 2001	140.7682	-21.3331	Granite	eastern belt	1.32	9.9	0.0803	0.511308
42704	igneous felsic intrusive	1545	-3.18	2.28	Mark 2001	140.6689	-21.2433	Granite	eastern belt	12.64	72.2	0.10593	0.511554
42709	igneous felsic intrusive	1520	-2.16	2.18	Mark 2001	140.7682	-21.3331	Granite	eastern belt	17.2	105.8	0.09831	0.5115
42708	igneous felsic intrusive	1545	-2	2.19	Mark 2001	140.7682	-21.3331	Monzonite	eastern belt	16.22	118.7	0.08267	0.511378
42739	igneous felsic intrusive	1520	-2.99	2.25	Mark 2001	140.6689	-21.2433	Monzonite	eastern belt	11.24	63	0.10798	0.511599
42762	igneous felsic intrusive	1520	-2.55	2.21	Mark 2001	140.7682	-21.3331	Monzonite	eastern belt	14.07	74.1	0.09842	0.511526
42737	igneous felsic intrusive	1520	-2.97	2.25	Mark 2001	140.7682	-21.3331	Qtz-Monzonite	eastern belt	18.89	119.2	0.09586	0.511479

42696	igneous felsic intrusive	1520	-2.74	2.23	Mark 2001	140.6689	-21.2433	Trondhjemite	eastern belt	2.06	10.4	0.1192	0.511724
A34L	Andesite	1740	0.2	2.18	Mark 2005	N/A	N/A	N/A	eastern belt	0.1669	0.5123	-17.3	0.5104
A27L	Meta-andesite	1740	-0.2	2.21	Mark 2005	N/A	N/A	N/A	eastern belt	0.1021	0.5115	-21.3	0.5104
A41	Andesite	1740	-1.3	2.29	Mark 2005	N/A	N/A	N/A	eastern belt	0.1413	0.5119	-17.3	0.5103
A8	Diorite	1650	-1.6	2.24	Mark 2005	N/A	N/A	N/A	eastern belt	0.136	0.5119	-14.5	0.5104
22	Amphibolite	1600	3.2	1.84	Mark 2005	N/A	N/A	N/A	eastern belt	0.1873	0.5127	1.2	0.5107
27B	K-rich pegmatite	1590	-5.2	2.45	Mark 2005	N/A	N/A	N/A	eastern belt	0.1481	0.5119	-15	0.5103
44A	Pegmatite	1590	-6.7	2.57	Mark 2005	N/A	N/A	N/A	eastern belt	0.2113	0.5124	-3.7	0.5102
103	Trondjhemite	1550	-2.5	2.21	Mark 2005	N/A	N/A	N/A	eastern belt	0.1192	0.5117	-17.8	0.5105
163-1	Quartz monzodiorite	1530	-2.2	2.18	Mark 2005	N/A	N/A	N/A	eastern belt	0.0827	0.5114	-24.6	0.5105
JTGC14	Quartz diorite	1530	-2.2	2.18	Mark 2005	N/A	N/A	N/A	eastern belt	0.1071	0.5116	-19.8	0.5105
JTGC03	Quartz monzogranite	1530	-2.7	2.22	Mark 2005	N/A	N/A	N/A	eastern belt	0.0916	0.5114	-23.3	0.5105
JTGC09	Quartz monzogranite	1530	-2.9	2.23	Mark 2005	N/A	N/A	N/A	eastern belt	0.1082	0.5116	-20.2	0.5105
95080	Quartz monzonite	1530	-2.8	2.23	Mark 2005	N/A	N/A	N/A	eastern belt	0.0959	0.5115	-22.6	0.5105
163-3	Quartz monzonite	1530	-2.9	2.23	Mark 2005	N/A	N/A	N/A	eastern belt	0.0983	0.5115	-22.2	0.5105
138	Quartz monzonite	1530	-3.4	2.27	Mark 2005	N/A	N/A	N/A	eastern belt	0.1059	0.5116	-21.1	0.5105
95019	Syenogranite	1530	-3.3	2.25	Mark 2005	N/A	N/A	N/A	eastern belt	0.0803	0.5113	-25.9	0.5105
JTGC04	Aplite	1530	-2	2.16	Mark 2005	N/A	N/A	N/A	eastern belt	0.1123	0.5117	-18.5	0.5106
LM26.04	Diorite	1520	-1	2.08	Mark 2005	N/A	N/A	N/A	eastern belt	0.144	0.5121	N/A	N/A
LM26.15	Monzogranite	1520	-1.8	2.14	Mark 2005	N/A	N/A	N/A	eastern belt	0.126	0.5118	N/A	N/A
LM26.18	Two-mica granite	1536	-3	2.25	Mark 2005	N/A	N/A	N/A	eastern belt	0.1304	0.5118	N/A	N/A
42766	Syenogranite	1530	-3.1	2.25	Mark 2005	N/A	N/A	N/A	eastern belt	0.0879	0.5114	-24.4	0.5105
72205032A	igneous felsic intrusive	1480	-3.32	2.24	Page & Sun 1988; reanalysed GA	N/A	N/A	N/A	eastern belt	N/A	N/A	N/A	N/A
72205030A	igneous felsic intrusive	1754	-1.67	2.34	Page & Sun 1988; reanalysed GA	N/A	N/A	N/A	eastern belt	N/A	N/A	N/A	N/A
72205044F	igneous felsic intrusive	1670	-3.1	2.38	Wyborn et al. 1988/GA unpublihed	N/A	N/A	N/A	eastern belt	N/A	N/A	N/A	N/A
72205018A	igneous felsic intrusive	1730	-2.92	2.42	Page & Sun, 1998	140.0447	-20.6914	N/A	eastern belt	N/A	N/A	N/A	N/A
79205320	igneous felsic intrusive	1493	-3.46	2.26	Page & Sun, 1998	N/A	N/A	N/A	eastern belt	N/A	N/A	N/A	N/A

79205322	igneous felsic intrusive	1508	-2.58	2.21	Page & Sun, 1998	140.4239	-21.2265	N/A	eastern belt	N/A	N/A	N/A	N/A
86206124	igneous felsic intrusive	1545	-1.32	2.14	Page & Sun, 1998	N/A	N/A	N/A	eastern belt	N/A	N/A	N/A	N/A
72205017A	igneous felsic intrusive	1730	-3.07	2.43	Page & Sun, 1998	N/A	N/A	N/A	eastern belt	N/A	N/A	N/A	N/A
72205013G	igneous felsic intrusive	1730	-3.69	2.48	Page & Sun, 1998	N/A	N/A	N/A	eastern belt	N/A	N/A	N/A	N/A
72-514D	igneous felsic intrusive	1670	+1.8	1.79	Wyborn et al., 1988	N/A	N/A	Sybella Batholith:	western belt	9.80	92.'7	0.09063	0.51158
74-360	intrusive	1,783	-1.8	2.17	Wyborn et al., 1988	N/A	N/A	Argylla Formation:	western belt	13.00	65.8	0.1197	0.511655
74-368A	intrusive	1865	-2.3	2.21	Wyborn et al., 1988	N/A	N/A	Leichhardt Metamorphics:	western belt	8.40	50.5	0.1007	0.511355
7920.5312	igneous felsic intrusive	1886	-2.7	2.30	Wyborn et al., 1988	N/A	N/A	Leichhardt Metamorphics:	western belt	8.50	47.5	0.1080	0.511415
7920.5309	igneous felsic intrusive	18621	-1.6	2.14	Wyborn et al., 1988	N/A	N/A	Kalkadoon Granodiorite:	western belt	8.30	56.5	0.0888	0.511245
72-251A	igneous felsic intrusive	1754	+2.5	1.82	Wyborn et al., 1988	N/A	N/A	Naraku Batholith:	eastern belt	6.32	53.9	0.1073	0.51175
72-248	igneous felsic intrusive	1480	+2.0	1.63	Wyborn et al., 1988	N/A	N/A	Naraku Batholith:	eastern belt	7.95	70.8	0.06782	0.511476
5320	igneous felsic intrusive	1480	+3.5	1.53	Wyborn et al., 1988	N/A	N/A	Williams Batholith:	eastern belt	4.78	62.8	0.06831	0.511585
5322	igneous felsic intrusive	1560	+3.0	1.62	Wyborn et al., 1988	N/A	N/A	Williams Batholith:	eastern belt	11.45	94.4	0.07334	0.511551
72-237	igneous felsic intrusive	1740	-3.7	2.28	McCulloch 1987	N/A	N/A	Wonga Batholith:	western belt	8.87	44.5	0.1206	0.511596
72-241	igneous felsic intrusive	1740	-3.1	2.16	McCulloch 1987	N/A	N/A	Wonga Batholith:	western belt	10.17	59.1	0.1040	0.511439
72-242 A	igneous felsic intrusive	1740	-2.9	2.17	McCulloch 1987	N/A	N/A	Wonga Batholith:	western belt	11.12	62.5	0.1077	0.5114890
Georgetown Inlier													
79300059	igneous felsic volcanic	1650	0.93	2.06	Black & McCulloch 1984	143.0561	-18.6783	Candlow Formation	western domain	1.14	5.33	0.1291	0.511149
79300062	igneous felsic volcanic	1650	-0.71	2.18	Black & McCulloch 1984	143.0561	-18.6783	Candlow Formation	western domain	1.28	6.67	0.1162	0.510906
79300062	igneous felsic volcanic	1650	-1.09	2.21	Black & McCulloch 1984	143.0561	-18.6783	Candlow Formation	western domain	1.33	6.85	0.1171	0.510935
79300060	igneous felsic volcanic	1650	-3.67	2.41	Black & McCulloch 1984	143.0561	-18.6783	Candlow Formation	western domain	1.62	6.84	0.1434	0.511069
79300060	igneous felsic volcanic	1650	-3.14	2.37	Black & McCulloch 1984	143.0561	-18.6783	Candlow Formation	western domain	1.66	7.06	0.142	0.511081
79300058	igneous felsic volcanic	1650	0.82	2.07	Black & McCulloch 1984	143.0561	-18.6783	Candlow Formation	western domain	1. 19	5.76	0.1251	0.5111
80303065	igneous mafic	1670	4.22	1.83	Black & McCulloch 1984	144.1167	-18.525	Einasleigh Metamorphics	eastern domain	2.48	7.62	0.1971	0.512053

80303066	igneous mafic	1670	3.42	1.89	Black & McCulloch 1984	144.1167	-18.525	Einasleigh Metamorphics	eastern domain	2.11	6.52	0.1958	0.511998
73303006	igneous mafic intrusive	1670	1.41	2.04	Black & McCulloch 1984	143.5166	-18.6167	Cobbold metadolerite	western domain	2.476	8.521	0.1757	0.511675
82303068	igneous felsic intrusive	1670	-5.49	2.56	Black & McCulloch 1984	143.5013	-19.1731	granophyre	western domain	4.74	27.43	0.1045	0.510543
79300232	igneous mafic intrusive	1670	4.4	1.82	Black & McCulloch 1984	143.5013	-19.1731	Cobbold metadolerite	western domain	1.76	5.59	0.1905	0.51199
82303067	igneous mafic intrusive	1670	-2.27	2.32	Black & McCulloch 1984	143.5013	-19.1731	quartz diorite	western domain	45.75	247.7	0.1116	0.510785
92836584	metamorphic protolith unknown	1585	7.53	1.51	GA unpublished	N/A	N/A	N/A	N/A	N/A	N/A	N/A	N/A
2007167007-01	igneous felsic intrusive	1559	-4.91	2.43	GA unpublished	N/A	N/A	N/A	N/A	N/A	N/A	N/A	N/A
2008839059	igneous felsic intrusive	1560	-0.57	2.1	GA unpublished	N/A	N/A	N/A	N/A	N/A	N/A	N/A	N/A
2008839057	igneous felsic intrusive	1560	0.05	2.05	GA unpublished	N/A	N/A	N/A	N/A	N/A	N/A	N/A	N/A
IWGT342	igneous felsic intrusive	1563	-1.88	2.2	GA unpublished	N/A	N/A	N/A	N/A	N/A	N/A	N/A	N/A
2008839046	igneous felsic intrusive	1558	-1.74	2.19	GA unpublished	N/A	N/A	N/A	N/A	N/A	N/A	N/A	N/A
2008839056	igneous felsic intrusive	1559	-0.61	2.1	GA unpublished	N/A	N/A	N/A	N/A	N/A	N/A	N/A	N/A
2008839008	igneous felsic volcanic	1552	-1.81	2.19	GA unpublished	N/A	N/A	N/A	N/A	N/A	N/A	N/A	N/A
2008839064	igneous felsic intrusive	1550	-3.06	2.28	GA unpublished	N/A	N/A	N/A	N/A	N/A	N/A	N/A	N/A
92836584	metamorphic protolith unknown	1585	7.75	1.49	GA unpublished	N/A	N/A	N/A	N/A	N/A	N/A	N/A	N/A
68480227	igneous mafic intrusive	1550	4.83	1.68	GA unpublished	N/A	N/A	N/A	N/A	N/A	N/A	N/A	N/A
77303064	igneous felsic volcanic	1552	-1.91	2.19	Black & McCulloch 1990	N/A	N/A	Croydon Volcanic	Croydon domain	6.04	28.11	0.1298	0.51187
81303066	igneous felsic intrusive	1544	-4.55	2.39	Black & McCulloch 1990	N/A	N/A	Mistletoe Granite	central domain	9.33	61.11	0.0924	0.511359
81303068	igneous felsic intrusive	1550	-3.12	2.28	Black & McCulloch 1990	N/A	N/A	Forsayth Granite	central domain	5.57	34.89	0.0964	0.511469
81303071	igneous felsic intrusive	1558	-2.37	2.23	Black & McCulloch 1990	N/A	N/A	Esmerada Granite	Croydon domain	3.08	12.72	0.1463	0.512013

81303067	igneous felsic intrusive	1561	-4.59	2.4	Black & McCulloch 1990	N/A	N/A	Lighthouse Granite	central domain	1.16	6.21	0.1135	0.511562
81303069	igneous felsic intrusive	1564	0.2	2.04	Black & McCulloch 1990	N/A	N/A	Forest Home Trondhjemite	western domain	1.35	6.58	0.1242	0.511915
BB2234	igneous felsic intrusive	1525	-1.98	2.18	Knutson and Sun in Blewett et al. 1997	N/A	N/A	N/A	N/A	N/A	N/A	N/A	N/A
BB2236	high grade metamorphic rock	1585	-0.44	2.11	Knutson and Sun in Blewett et al. 1997	N/A	N/A	N/A	N/A	N/A	N/A	N/A	N/A
93834299A	igneous felsic	1585	-0.8	2.14	Knutson and Sun in Blewett et al. 1997	N/A	N/A	N/A	N/A	N/A	N/A	N/A	N/A
93836592	high grade metamorphic rock	1585	-3.27	2.32	Knutson and Sun in Blewett et al. 1997	N/A	N/A	N/A	N/A	N/A	N/A	N/A	N/A
92836572	igneous felsic	1585	-3.45	2.34	Knutson and Sun in Blewett et al. 1997	N/A	N/A	N/A	N/A	N/A	N/A	N/A	N/A
92836504B	igneous mafic intrusive	1670	-3.37	2.4	Knutson In Withnall et al. 1997	N/A	N/A	N/A	N/A	N/A	N/A	N/A	N/A
92836540	metamorphic protolith unknown	1670	3.7	1.87	Knutson In Withnall et al. 1997	N/A	N/A	N/A	N/A	N/A	N/A	N/A	N/A